Jens Als-Nielsen • Des McMorrow

Elements of Modern X-ray Physics

Second Edition

Elements of Modern X-ray Physics

Second Edition

Elements of Modern X-ray Physics

Second Edition

Jens Als-Nielsen

Ørsted Laboratory
Niels Bohr Institute
Copenhagen University

Des McMorrow

London Centre for Nanotechnology
University College London

Preface

In the decade or so since *Elements of Modern X-ray Physics* first appeared there has continued to be astonishing progress in the development of X-ray sources and the understanding of how to exploit them. This fact, taken together with the kind and generous comments we received in response to the first edition, has encouraged us to produce a second edition.

The second edition differs from the first in several key regards:

- An entirely new chapter on X-ray imaging has been included.

- The chapter dealing with kinematical diffraction has been divided into two separate chapters, which deal with non-crystalline and crystalline materials, respectively. This change has allowed us to include new material on the use of X-rays in the determination of the structure of liquids, glasses, and most importantly polymers and biomolecules.

- We have made many adjustments to various sections in the book with a view to improving the overall exposition.

- Small typographical errors have been corrected.

- Exercises have been included at the ends of all chapters except the first.

In preparing the second edition we have enjoyed the support and encouragement of many of our colleagues and friends without which our task would have been impossible. We would like to extend our deep gratitude to everyone who has contributed, most especially David Attwood, Martin Bech, Christian David, Martin Dierolf, Paul Emma, Kenneth Evans-Lutterodt, Per Hedegård, Mikael Häggström, John Hill, Moritz Hoesch, Torben Jensen, James Keeler, Ken Kelton, Carolyn Larabell, Bruno Lengeler, Anders Madsen, David Moncton, Theyencheri Narayan, Franz Pfeiffer, Harald Reichert, Ian Robinson, Jan Rogers, Joachim Stöhr, Joan Vila-Comamala, Simon Ward, and Tim Weitkamp.

Work on the second edition was initiated in Provence, France, during the summer of 2008 thanks to the generous support of the Ib Henriksen Foundation.

The front cover was designed by Marusa Design from an image kindly provided by Michael Wulff.

This book is dedicated to our respective families.

Jens Als-Nielsen and Des McMorrow

London, November 2010

Preface to the first edition

The construction of the first dedicated X-ray beamlines at synchrotron sources in the late 1970s heralded the start of a new era in X-ray science. In the intervening years tremendous progress has been made, both with respect to improvements to the sources, and with our knowledge of how to exploit them. Today's third-generation sources deliver extremely bright beams of radiation over the entire X-ray band (c. 1–500 keV), and with properties such as polarization, energy resolution, etc., that can be tailored to meet almost any requirement. These improvements have driven a surge of activity in X-ray science, and phenomena over a diverse range of disciplines can now be studied with X-rays that were undreamt of before the advent of synchrotron sources.

In light of these developments we believed that it was timely to produce a textbook at an introductory level. Our intention is to offer a coherent overview, which covers the basic physical principles underlying the production of X-rays, their interaction with matter, and also to explain how these properties are used in a range of applications. The main target audience for this book are final year undergraduates, and first year research students. Although the book has been written from the perspective of two physicists, we hope that it will be useful to the wider community of biologists, chemists, material scientists, etc., who work at synchrotron radiation facilities around the world. The main challenge in writing for a wider audience has been to convey the physical concepts without obscuring them in too much mathematical rigour. Therefore, many of the more difficult mathematical manipulations and theorems are explained in shaded boxes that may be studied separately. In addition appendices covering some of the required introductory physics have been included.

It is also our hope that this book will have appeal to more experienced research workers. Synchrotron radiation facilities are large laboratories where many different groups work on disparate areas of science. Cross fertilization of ideas is often the driving force of scientific progress. In order that these different groups, often working on neighbouring beamlines, can communicate their ideas, a common background is required. It is our intention that this book should provide at least some of this background knowledge. In addition, many X-ray techniques are becoming viewed as standard analytical tools, and it is no longer necessary to understand every aspect of the design of an instrument in order to be able to perform experiments. While this is undoubtedly a positive development, it can also be argued that a greater knowledge of the underlying principles not only adds to the overall feeling of satisfaction, but also allows better experiments to be designed.

This book has emerged from a lecture course that has been running for several years at the University of Copenhagen. The material covered in this book is taught in one semester, and is augmented by practical lessons both in an X-ray laboratory at the university, and also during a week long trip to the HASYLAB synchrotron facility. The list of subjects covered in this book inevitably reflects to some degree our own areas of specialization. There is, for example, very little on the vast and important subject of imaging. It was also decided at an early stage not to focus on subjects, such as classical crystallography, that we felt were well described in other texts. In spite of these shortcomings we hope that the reader, whatever his or her background, will learn something by studying this book, and be inspired to think of new ways to exploit the great opportunities that the development of synchrotron radiation offers.

Jens Als-Nielsen and Des McMorrow

Copenhagen, September 2000

Acknowledgements from the first edition

Notes on the use of this book

The material in this book follows a more or less linear development. The scene is set in the first chapter, where the predominant mechanisms for the interaction of X-rays and matter are described. Many of the important concepts and results are introduced in this chapter, and forward references are made to the remaining chapters where these concepts are discussed more fully and the results derived. An attempt has been made to reduce to a minimum the level of mathematical skill required to follow the arguments. This has been done by placing most of the more taxing manipulations and theorems in shaded boxes, or in one of the appendices.

Computers are of course now an indispensable tool for helping to visualize mathematical and physical concepts. For this reason we have chosen to include a listing in the last appendix of some of the computer programmes that were used to generate the figures in this book. The hope is that this will ease the process of turning mathematical formulae into computer algorithms, and also aid the design of more complex programmes required for the analysis of data, etc. The programmes have been written using the MATLAB® programming environment, although the way that they are derived from the mathematics is transparent enough that they can easily be converted to other languages. Figures for which programme listings are given are indicated by a star, ★.

Contents

1

X-rays and their interaction with matter

X-rays were discovered by Wilhelm Conrad Röntgen in 1895. Since that time they have become established as an invaluable probe of the structure of matter. The range of materials for which X-rays have proved to be decisive in unravelling the structure is truly staggering. These include at one limit of complexity simple compounds, through to more complex and celebrated examples, such as DNA. In more recent times the structure of proteins, and even functional units of living organisms, can be solved on a regular basis. Progress in both our theoretical understanding of the interaction of X-rays with matter, and in our knowledge of how to exploit them experimentally, was steady from the period covering their discovery through to the mid 1970s. The main limitation in this period was the source, which had remained essentially unchanged from about 1912. In the 1970s it was realized that the synchrotron radiation emitted from charged particles circulating in storage rings constructed for high energy nuclear physics experiments was potentially a much more intense and versatile source of X-rays. Indeed synchrotrons have proven to be such vastly better sources that many storage rings have been constructed around the world dedicated solely to the production of X-rays.

This has culminated to date in the so-called third-generation synchrotron sources, which are more brilliant than the early lab-based sources by a factor of approximately 10^{12}, as indicated in Fig. 1.1. With the advent of synchrotron sources the pace of innovation in X-ray science increased markedly (though perhaps not a trillion fold!), and today shows no signs of slowing. The first X-ray free-electron lasers have recently come into service, and when they become fully operational further important breakthroughs will undoubtedly follow. In Chapter 2 we explain the basic physical principles of X-ray sources and outline their salient properties.

In Fig. 1.2 we show a schematic of the key components of a typical experimental beamline at a third-generation source. The details will of course vary considerably depending on the particular requirements, but many of the components shown will be found in one form or another on most beamlines. First there is the source itself. In this case the electrons do not follow a purely circular orbit in the storage ring, but traverse through straight sections where lattices of magnets, so-called undulator insertion devices, force them to execute small-amplitude oscillations. At each oscillation X-rays are emitted and, if the amplitude of the oscillations is small, then the different contributions from the passage of a single electron add coherently, and a very intense beam of X-rays results. The second key component is the monochromator, as in many applications it is required to work at a particular average wavelength. It may also be desirable to choose the wavelength bandwidth, and monochromators made
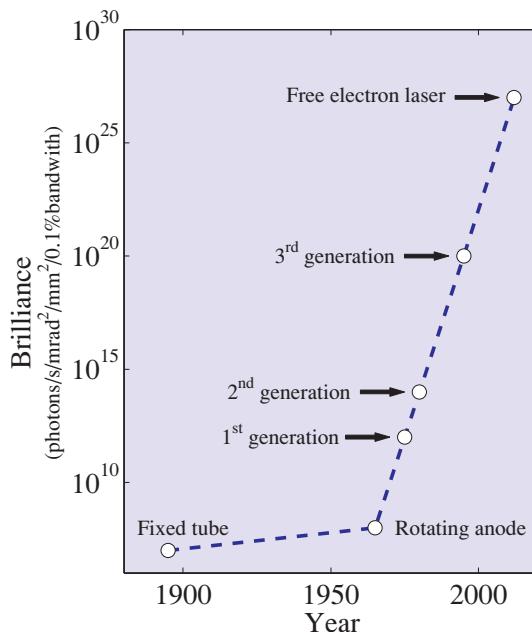
Fig. 1.1 The brilliance of X-ray sources as a function of time. Source brilliance is defined and discussed in Chapter 2, along with the principles underlying the production of X-rays from synchrotrons and free-electron lasers. For free-electron laser sources we plot the average brilliance. Due to the extremely short X-ray pulse length from a free-electron laser – of order 100 fs – the peak brilliance exceeds the average brilliance by a large factor.

from perfect crystals through to multilayers allow for a considerable variation in this parameter. Thirdly, if working with small samples it may be desirable to focus the monochromatic beam down to as small a size as achievable. This is accomplished by devices such as X-ray mirrors and refractive Fresnel lenses. Finally, X-rays are delivered to the sample itself on which the experiment is performed.

   One of the main goals of this book is to explain the physical principles underlying the operation of the key components shown in Fig. 1.2. As a first step it is necessary to understand some of the basic aspects of the interaction of X-rays with matter.

1.1 X-rays: waves and photons

X-rays are electromagnetic waves with wavelengths in the region of an Ångström (10^{-10}m). In many cases one is interested in a monochromatic beam of X-rays as depicted in Fig. 1.3. The direction of the beam is taken to be along the z-axis, perpendicular to the electric, $\mathbf{E}$, and magnetic, $\mathbf{H}$, fields. For simplicity, we shall start by considering the electric field only and neglect the magnetic field. The top part of Fig. 1.3 shows the spatial dependence of the electromagnetic field at a given instance of time. It is characterized by the wavelength λ, or equivalently the wavenumber $k = 2\pi/\lambda$. Mathematically the electric field amplitude is expressed as a sine wave, either in its real form, $E_0 \sin(kz)$, or in its more compact complex form, $E_0 e^{ikz}$.

   The lower part of Fig. 1.3 is an alternative illustration of the monochromatic plane wave. Only the wave crests are shown (full lines perpendicular to the z-axis), emphasizing that it is a plane wave with
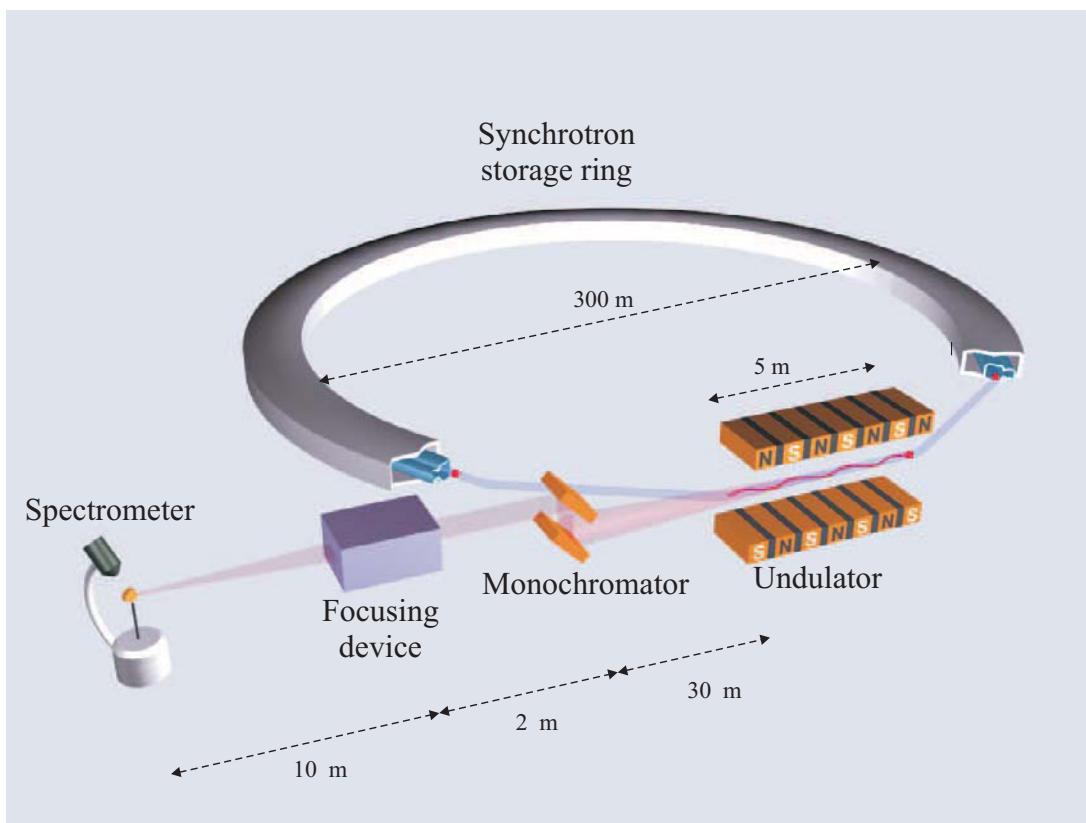
Fig. 1.2 A schematic of a typical X-ray beamline at a third generation X-ray source. Bunches of charged particles (electrons or positrons) circulate in a storage ring (typical diameter around 300 m). The ring is designed with straight sections, where an insertion device, such as undulator, is placed. The lattice of magnets in an insertion device forces the particles to execute small oscillations which produce intense beams of radiation. This radiation then passes through a number of optical elements, such as a monochromator, focusing device, etc., so that a beam of radiation with the desired properties is delivered to the sample. Typical distances are indicated.

an electric field that is constant anywhere in a plane perpendicular to the z-axis. Although a beam is never ideally collimated, the approximation of a plane wave is often valid. The spatial and temporal variation of a plane wave propagating along the z-axis can be encompassed in one simple expression, $E_0 \, e^{i(kz-\omega t)}$. More generally in three dimensions the polarization of the electric field is written as a unit vector $\hat{\boldsymbol{\varepsilon}}$, and the wavevector along the direction of propagation as $\mathbf{k}$, so that

$$\mathbf{E}(\mathbf{r}, t) = \hat{\boldsymbol{\varepsilon}} \, E_0 \, e^{i(\mathbf{k}\cdot\mathbf{r}-\omega t)}$$

Since electromagnetic waves are transverse we have $\hat{\boldsymbol{\varepsilon}} \cdot \mathbf{k}=0$, and $\mathbf{k} \cdot \mathbf{E}= \mathbf{k} \cdot \mathbf{H}=0$ as shown in Fig. 1.4.

This is the classical description of a linearly polarized, electromagnetic plane wave. From a quantum mechanical perspective, a monochromatic beam is viewed as being quantized into photons, each having an energy $\hbar\omega$ and momentum $\hbar\mathbf{k}$. The intensity of a beam is then given by the number of photons passing through a given area per unit time. As the intensity is also proportional to the square of the electric field, it follows that the magnitude of the field is quantized. Instead of quantizing the $\mathbf{E}$ and $\mathbf{H}$ fields separately, it turns out to be more convenient to work with the vector potential $\mathbf{A}$, since both $\mathbf{E}$
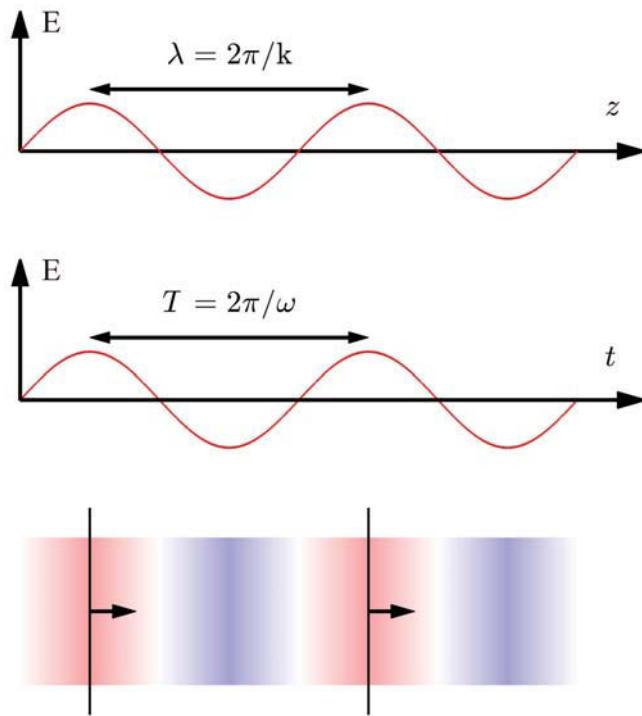
Fig. 1.3 Three representations of an electromagnetic plane wave. Only the electric field **E** is shown. Top: spatial variation, described by the wavelength λ or the wavenumber k, at a given instant in time. Middle: temporal variation, described by the period T or the cyclic frequency ω, at a given point in space. Bottom: Top view of a plane wave with the wave crests indicated by the heavy lines, and the direction of propagation by the arrows. The shading indicates the spatial variation of the amplitude of the field.
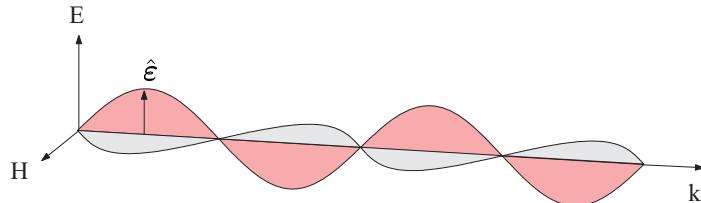
Fig. 1.4 An X-ray is a transverse electromagnetic wave, where the electric and magnetic fields, **E** and **H**, are perpendicular to each other and to the direction of propagation **k**. The direction of the electric field is given by the polarization unit vector $\hat{\varepsilon}$.

and **H** can be derived from **A**. In Appendix C it is explained how the vector potential is quantized, and the explicit form of the quantum mechanical Hamiltonian of the electromagnetic field is given. In this book we shall move freely between the classical and quantum descriptions, choosing whichever one leads us to the quickest and clearest understanding of the problem at hand.

The numerical relation[1] between wavelength λ in Å and photon energy $\mathcal{E}$ in keV is

$$\lambda\left[\text{Å}\right] = \frac{hc}{\mathcal{E}} = \frac{12.398}{\mathcal{E}\,[\text{keV}]} \tag{1.1}$$

An X-ray photon interacts with an atom in one of two ways: it can be scattered or it can be absorbed, and we shall discuss these processes in turn. When X-rays interact with a dense medium consisting of a very large number of atoms or molecules it is sometimes more convenient to treat the material as a continuum, with an interface to the surrounding vacuum (or air). At the interface the X-ray beam is refracted and reflected, and this is an alternative way in which the interaction may be discussed. The scattering and refraction descriptions are of course equivalent. In Chapter 3 we derive the X-ray reflectivity equations, and exploit this equivalence to relate the reflectivity to the microscopic properties of the medium of interest.

1.2   Scattering

To start with we shall consider the scattering of an X-ray by a single electron. In the classical description of the scattering event the electric field of the incident X-ray exerts a force on the electronic charge, which then accelerates and radiates the scattered wave. Classically, the wavelength of the scattered wave is the same as that of the incident one, and the scattering is necessarily *elastic*. This is not true in general in a quantum mechanical description, where the incident X-ray photon has a momentum of $\hbar\mathbf{k}$ and an energy of $\hbar\omega$. Energy may be transferred to the electron with the result that the scattered photon has a lower frequency relative to that of the incident one. This *inelastic* scattering process is known as the Compton effect, and is discussed at the end of this section. However, the elastic scattering of X-rays is the main process that is exploited in investigations of the structure of materials, and in this case it suffices to adopt what is essentially a classical approach.

One electron

The most elementary scattering object that we shall consider is a single, free electron. The ability of an electron to scatter an X-ray is expressed in terms of a *scattering length*, which we shall now derive.

Figure 1.5 shows a schematic of a generic scattering experiment. The fundamental quantity determined in such an experiment is the *differential scattering cross-section* $(d\sigma/d\Omega)$ which is defined by

$$\left(\frac{d\sigma}{d\Omega}\right) = \frac{I_{sc}}{\Phi_0\,\Delta\Omega} \tag{1.2}$$

The strength of the incident beam is given by the flux, Φ_0, which is simply the number of photons passing through unit area per second. The incident beam interacts with the scattering object and is scattered. The number of scattered photons recorded per second in a detector is I_{sc}, where the detector is positioned a distance R away from the object and subtends a solid angle $\Delta\Omega$. The differential cross-section is thus a measure of the efficiency of the scattering process where details of the experiment,

---

[1]In this book we shall mostly limit the wavelength band to $0.1 - 2$ Å corresponding to the energy band $120 - 6$ keV. The first limit, 0.1 Å or 120 keV, ensures that relativistic effects are negligible since the X-ray energy is considerably lower than the rest mass of the electron, $mc^2 = 511$ keV. The second limit, 2 Å or 6 keV, is a practical limit ensuring that the X-rays have a high penetration power through light materials, such as beryllium. In many X-ray tubes, and in synchrotron radiation beam lines, the X-rays must be transmitted through a Be window, and above 6 keV the transmission of a 0.5 mm Be window exceeds 90%. Lower energy X-rays are called soft X-rays and will not be dealt with in this book.
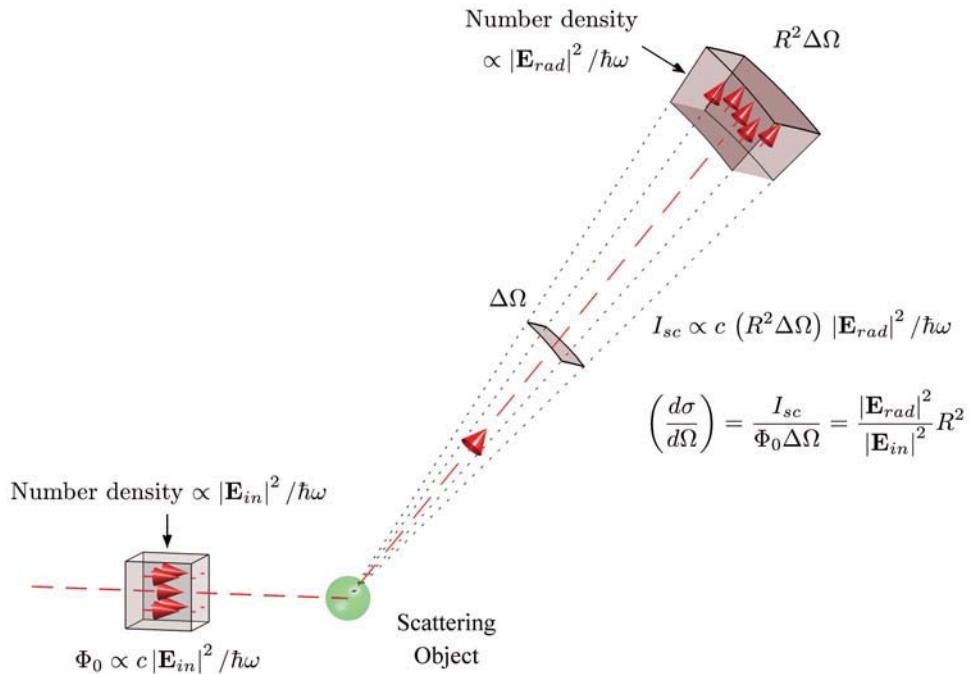
Fig. 1.5 Schematic layout of a generic scattering experiment used to determine the differential cross-section ($d\sigma/d\Omega$): see Eq. (1.2). The incident beam flux Φ_0 is the number of particles per second per unit area. For an electromagnetic wave this is proportional to $|\mathbf{E}_{in}|^2$ times the velocity of light, c. The incident beam interacts with the target object to produce the scattered beam. A detector records the scattered intensity, I_{sc}, defined as the number of counts recorded per second, which is proportional to $|\mathbf{E}_{rad}|^2$ times the area of the detector and the velocity of light. The detector is located a distance R from the target object, and subtends a solid angle of $\Delta\Omega$.

specifically the flux of the incident beam and size of the detector, have been normalized away. (See Appendix A for a more complete discussion.)

For the particular case of the scattering of an electromagnetic wave indicated in Fig. 1.5 an expression for Φ_0 can be obtained in terms of the electric field $\mathbf{E}_{in}$ of the incident beam. Since the energy density is proportional to $|\mathbf{E}_{in}|^2$, the number density of photons is proportional to $|\mathbf{E}_{in}|^2/\hbar\omega$, while the flux Φ_0 is the number density multiplied by speed of light, c. (This follows from the realisation that in one second a beam of area A sweeps out a volume equal to $A\,c$.) A similar argument applies to the intensity I_{sc} of the scattered beam. In this case the number density is proportional to the modulus squared of the radiated electric field, $|\mathbf{E}_{rad}|^2$. This quantity then must be multiplied by the area of the detector, $R^2\Delta\Omega$, and c to yield and expression for I_{sc}. With these considerations, the differential cross-section is given by

$$\left(\frac{d\sigma}{d\Omega}\right) = \frac{|\mathbf{E}_{\text{rad}}|^2 R^2}{|\mathbf{E}_{\text{in}}|^2} \tag{1.3}$$

In a classical description of the scattering process an electron will be forced to vibrate when placed in the electric field of an incident X-ray beam, as illustrated in Fig. 1.6(a). A vibrating electron acts as a source, and radiates a spherical wave $\mathbf{E}_{rad} \propto \hat{\varepsilon}'\, e^{ikR}/R$. The problem then is to evaluate the radiated field at an observation point X. This calculation is performed in Appendix B starting from
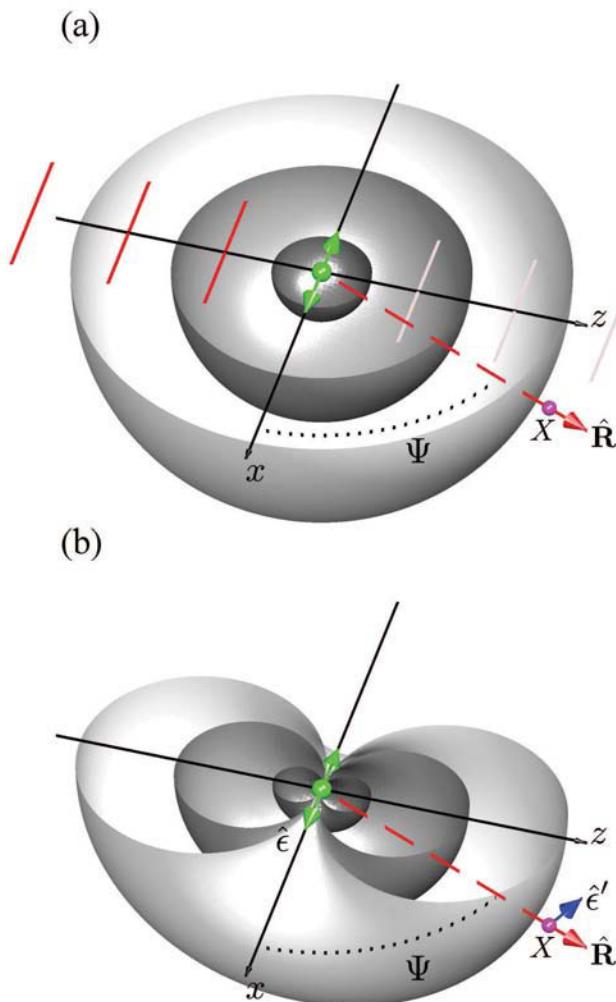
Fig. 1.6 The classical description of the scattering of an X-ray by an electron. (a) The electric field of an incident plane wave sets an electron in oscillation which then radiates a spherical wave. (For clarity the radiated wave is shown for positive values of y only, and for the simplest case of an isotropic spherical wave the phase and amplitude are constant on spherical surfaces.) The incident wave propagates along the z axis and has its electric field polarized along x. The wave crests of the incident wave lie in between those of the scattered spherical wave because of the 180° phase shift in Thomson scattering. In the text the radiated field at an observation point X is calculated. Point X lies in the plane spanned by the polarization vector and the propagation direction of the incident wave, and the observed acceleration has to be multiplied by a factor of $\sin \Psi$. (b) From geometry, $\sin \Psi = -\hat{\varepsilon} \cdot \hat{\varepsilon}'$ where $\hat{\varepsilon}$ ($\hat{\varepsilon}'$) represents the polarization of the incident (scattered) beam. The effect of this factor on the radiated wave is illustrated by plotting surfaces of constant amplitude.

Maxwell's equations. Here, an heuristic argument is outlined. Initially we consider the situation where the observation point X lies in the plane spanned by the polarization vector and the propagation direction of the incident wave, and at an angle $90° − \Psi$ with respect to the direction of propagation of the incident beam (Fig. 1.6(a)).

The radiated field is proportional to the charge of the electron, $−e$, and to the acceleration, $a_X(t')$, evaluated at a time t' earlier than the observation time t due to finite speed c at which the radiation propagates. The radiated field is thus expected to be of the form

$$E_{rad}(R, t) \propto \frac{-e}{R} \, a_X(t') \sin \Psi \tag{1.4}$$

where $t' = t − R/c$. The total energy flow through a spherical shell of radius R is the energy density, proportional to $|E_{rad}|^2$, multiplied by the surface area, proportional to R^2, so with $|E_{rad}| \propto R^{-1}$ the total energy flow becomes independent of R, as it must[2]. A further factor of $\sin \Psi$ has been included to allow for the variation of the acceleration with observation angle. For an observer at point X in the $x−z$ plane, the acceleration observed is zero for $\Psi = 0°$, and a maximum for $\Psi = 90°$. Therefore, the acceleration observed is the full acceleration multiplied by $\sin \Psi$.

To proceed we evaluate the full acceleration from the force on the electron divided by its mass, which yields

$$a_X(t') = \frac{-e \, E_0 \, e^{-i\omega t'}}{m} = \frac{-e}{m} \, E_{in} \, e^{i\omega(R/c)} = \frac{-e}{m} \, E_{in} \, e^{ikR}$$

where $E_{in} = E_0 e^{-i\omega t}$ is the electric field of the incident wave. Hence Eq. (1.4) can be rearranged to read

$$\frac{E_{rad}(R, t)}{E_{in}} \propto \left(\frac{e^2}{m}\right) \frac{e^{ikR}}{R} \sin \Psi \tag{1.5}$$

For an observation point at an arbitrary angle with respect to the polarization of the incident beam, the factor of $\sin \Psi$ must be reevaluated. If $\hat{\varepsilon}$ is the polarization of the incident field, and $\hat{\varepsilon}'$ that of the radiated field, then from Fig. 1.5(b), $\hat{\varepsilon} \cdot \hat{\varepsilon}' = \cos(90° + \Psi) = − \sin(\Psi)$. The advantage of writing the trigonometric factor for the apparent acceleration in this way is that it is valid for all possible angles of observation. This is ensured by the azimuthal symmetry evident in Fig. 1.6(b) of the radiated field around the x axis.

To complete the derivation of the differential cross-section it is necessary to check whether we have the correct units. Clearly, the ratio of electric fields given in Eq. (1.5) is dimensionless. This requires that whatever the factor is multiplying the spherical wave form e^{ikR}/R, it must have units of length. The appropriate length can be found by noting that in SI units the Coulomb energy at distance r from a point charge $−e$ is $e^2/(4\pi\epsilon_0 r)$, while dimensionally the energy is also of the form mc^2. Thus equating these two expressions for energy and rearranging provides an expression for the fundamental length scale in the problem, namely

$$r_0 = \left(\frac{e^2}{4\pi\epsilon_0 mc^2}\right) = 2.82 \times 10^{-5} \, \text{Å} \tag{1.6}$$

This is referred to as the Thomson scattering length, or classical radius, of the electron. While these arguments fix the magnitude of the scattering length, they do not fix its phase. As shown in Appendix

---

[2]Equation (1.4) represents the electric field radiated by an oscillating dipole in the far-field limit.

B, the scattering amplitude from a single electron is in fact equal to $-r_0 \left| \hat{\boldsymbol{\varepsilon}} \cdot \hat{\boldsymbol{\varepsilon}}' \right|$. Physically, the factor of -1 represents the fact that there is a $180°$ phase shift between the incident and scattered waves. This phase shift also has consequences for the refractive index n which in the X-ray region is less than unity, as discussed in Section 1.4 and Chapter 3.

The ratio of radiated to incident electric fields is therefore

$$\frac{\mathrm{E}_{\mathrm{rad}}(R, t)}{\mathrm{E}_{\mathrm{in}}} = -r_0 \frac{e^{ikR}}{R} \left| \hat{\boldsymbol{\varepsilon}} \cdot \hat{\boldsymbol{\varepsilon}}' \right| \tag{1.7}$$

and from Eq. (1.3) the differential cross-section becomes

$$\left(\frac{d\sigma}{d\Omega} \right) = r_0^2 \left| \hat{\boldsymbol{\varepsilon}} \cdot \hat{\boldsymbol{\varepsilon}}' \right|^2 \tag{1.8}$$

This equation describes the Thomson differential scattering cross-section of an electromagnetic wave by a free electron.
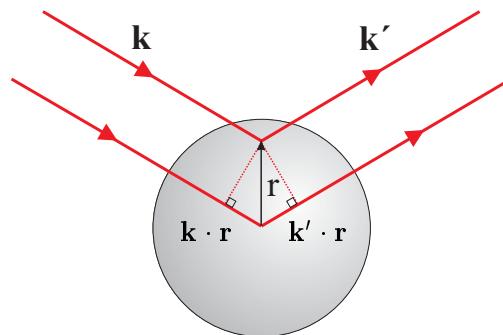
The factor of $\left| \hat{\boldsymbol{\varepsilon}} \cdot \hat{\boldsymbol{\varepsilon}}' \right|^2$ has important implications for the choice of optimal geometry for different types of X-ray experiments. For example, synchrotron sources naturally produce X-rays which are linearly polarized in the horizontal plane of the synchrotron. It follows that scattering experiments are best performed in a vertical scattering plane as then $\left| \hat{\boldsymbol{\varepsilon}} \cdot \hat{\boldsymbol{\varepsilon}}' \right|^2 = 1$ independent of the scattering angle, $\psi = 90° - \Psi$. Conversely, if one wants to study fluorescence from a sample, then it is possible to suppress the scattering by working in the horizontal plane at $\psi = 90°$ since $\left| \hat{\boldsymbol{\varepsilon}} \cdot \hat{\boldsymbol{\varepsilon}}' \right|^2 = 0$. These considerations lead us to define P, the polarization factor for scattering, which depends on the X-ray source:

$$P = \left| \hat{\boldsymbol{\varepsilon}} \cdot \hat{\boldsymbol{\varepsilon}}' \right|^2 = \begin{cases} 1 & \text{synchrotron: vertical scattering plane} \\ \cos^2 \psi & \text{synchrotron: horizontal scattering plane} \\ \frac{1}{2} \left(1 + \cos^2 \psi \right) & \text{unpolarized source} \end{cases} \tag{1.9}$$
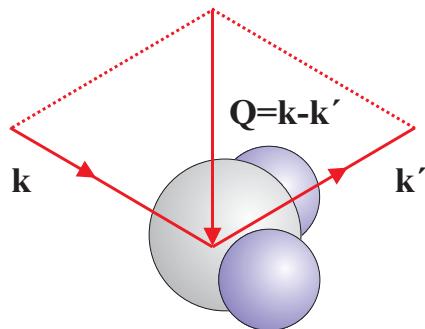
The *total* cross-section for Thomson scattering is found by integrating the differential cross-section over all possible scattering angles. Exploiting the rotational symmetry of the radiated field around $\hat{\boldsymbol{\varepsilon}}$, it can be shown that the average value of $< (\hat{\boldsymbol{\varepsilon}} \cdot \hat{\boldsymbol{\varepsilon}}')^2 >$ over the unit sphere is $(2/3)$. Thus the total cross-section σ_{T} is equal to $4\pi r_0^2 \times (2/3) = 8\pi r_0^2/3 = 0.665 \times 10^{-24}$ cm^2 $= 0.665$ barn. It is evident that the classical cross-section, both the differential and total, for the scattering of an electromagnetic wave by a free electron is a constant, independent of energy. This result is particularly relevant to the X-ray part of the electromagnetic spectrum, as here a photon is energetic enough that even atomic electrons respond to a good approximation as if they are free. Where it breaks down entirely is at low energies in the optical part of the spectrum, or when the energy of photon passes a threshold for resonantly exciting electrons from deeply bound atomic states, as outlined later in this section. In Chapter 8 we discuss the origin and consequences of such resonant scattering processes.

Finally in this section we note that the classical derivation of the scattering of a photon by a free electron given here yields the same result as the full quantum mechanical derivation given in Appendix C.

(a) One atom

(b) One molecule

(c) A crystal
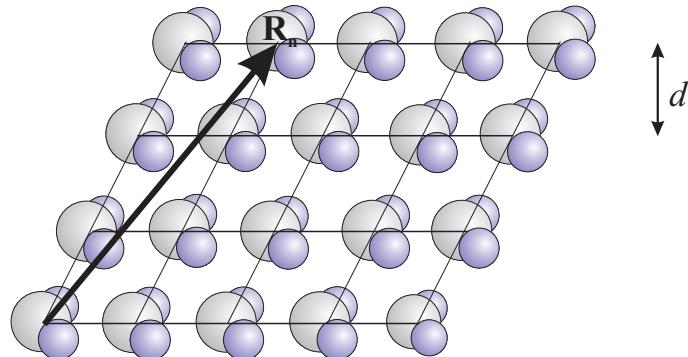
Fig. 1.7 (a) Scattering from an atom. An X-ray with a wavevector $\mathbf{k}$ scatters from an atom to the direction specified by $\mathbf{k}'$. The scattering is assumed to be elastic, i.e. $|\mathbf{k}| = |\mathbf{k}'| = 2\pi/\lambda$. The difference in phase between a wave scattered at the origin and one at a position $\mathbf{r}$ is $(\mathbf{k} - \mathbf{k}') \cdot \mathbf{r} = \mathbf{Q} \cdot \mathbf{r}$. This defines the wavevector transfer $\mathbf{Q}$. (b) The scattering from a molecule. Here the scattering triangle is shown which relates $\mathbf{k}$, $\mathbf{k}'$ and $\mathbf{Q}$. (c) Scattering from a molecular crystal. The molecules are organized on a lattice with position vectors $\mathbf{R_n}$, and a lattice plane spacing of d.

One atom

Let us now proceed from the scattering by a single electron to consider the elastic scattering from an atom with Z electrons.

To start with a purely classical description will be used, so that the electron distribution is specified by a number density, $\rho(\mathbf{r})$. The scattered radiation field is a superposition of contributions from different volume elements of this charge distribution. In order to evaluate this superposition one must keep track of the phase of the incident wave as it interacts with the volume element at the origin and the one at position $\mathbf{r}$, as shown in Fig. 1.7(a). The phase difference between two successive crests is 2π. The phase difference between the two volume elements is 2π multiplied by the ratio of $\mathbf{r}$, projected onto the incident direction, and the wavelength. This is nothing other than the scalar product of the two vectors $\mathbf{k}$ and $\mathbf{r}$. The simplicity of this expression is one of the reasons why it is so convenient to use the wavevector $\mathbf{k}$ to describe the incident wave. In the vicinity of the observation point X in Fig. 1.6, the scattered wave is locally like a plane wave with wavevector $\mathbf{k}'$. The phase difference, between the scattered wave from a volume element around the origin and one around $\mathbf{r}$ is $-\mathbf{k}' \cdot \mathbf{r}$. The resulting phase difference is thus

$$\Delta\phi(\mathbf{r}) = (\mathbf{k} - \mathbf{k}') \cdot \mathbf{r} = \mathbf{Q} \cdot \mathbf{r}$$

where

$$\boxed{\mathbf{Q} = \mathbf{k} - \mathbf{k}'} \tag{1.10}$$

$\mathbf{Q} = \mathbf{k} - \mathbf{k}'$ is known as the *wavevector transfer* or *scattering vector*. The scattering events depicted in Fig. 1.7 are elastic, with $|\mathbf{k}| = |\mathbf{k}'|$, so that from the scattering triangle we have $|\mathbf{Q}| = 2|\mathbf{k}| \sin\theta = (4\pi/\lambda)\sin\theta$. As we shall see, $\mathbf{Q}$ is the natural variable to describe elastic scattering processes and is usually expressed in units of Å^{-1}.

Thus a volume element $d\mathbf{r}$ at $\mathbf{r}$ will contribute an amount $-r_0\rho(\mathbf{r})d\mathbf{r}$ to the scattered field with a phase factor of $e^{i\mathbf{Q}\cdot\mathbf{r}}$. The total scattering length of the atom is

$$\boxed{-r_0\, f^0(\mathbf{Q}) = -r_0 \int \rho(\mathbf{r})\, e^{i\mathbf{Q}\cdot\mathbf{r}}\, d\mathbf{r}} \tag{1.11}$$

where $f^0(\mathbf{Q})$ is known as the *atomic form factor*. In the limit that $Q \to 0$ all of the different volume elements scatter in phase so that $f^0(\mathbf{Q} = 0) = Z$, the number of electrons in the atom. As Q increases from zero the different volume elements start to scatter out of phase and consequently $f^0(Q \to \infty) = 0$. The right hand side of Eq. (1.11) is recognizable as a Fourier transform. Indeed one of the recurrent themes of this book is that the scattering length may be calculated from the Fourier transform of the distribution of electrons in the sample[3]. It should be clear that to calculate the scattered intensity we have to evaluate Eq. (1.11) and multiply by its complex conjugate (see Eq. (1.2) and accompanying discussion).

Atomic electrons are of course governed by quantum mechanics, and have discrete energy levels. The most tightly bound electrons are those in the K shell, which have energies comparable to those of a typical X-ray photon. If the X-ray photon has an energy much less than the binding energy of the K shell, the response of these electrons to an external driving field is reduced by virtue of the fact that they are bound. Electrons in shells that are less tightly bound (L, M, etc.) will be able to respond to the

---

[3]The reader is reminded of the definition and properties of Fourier transforms in Appendix E.
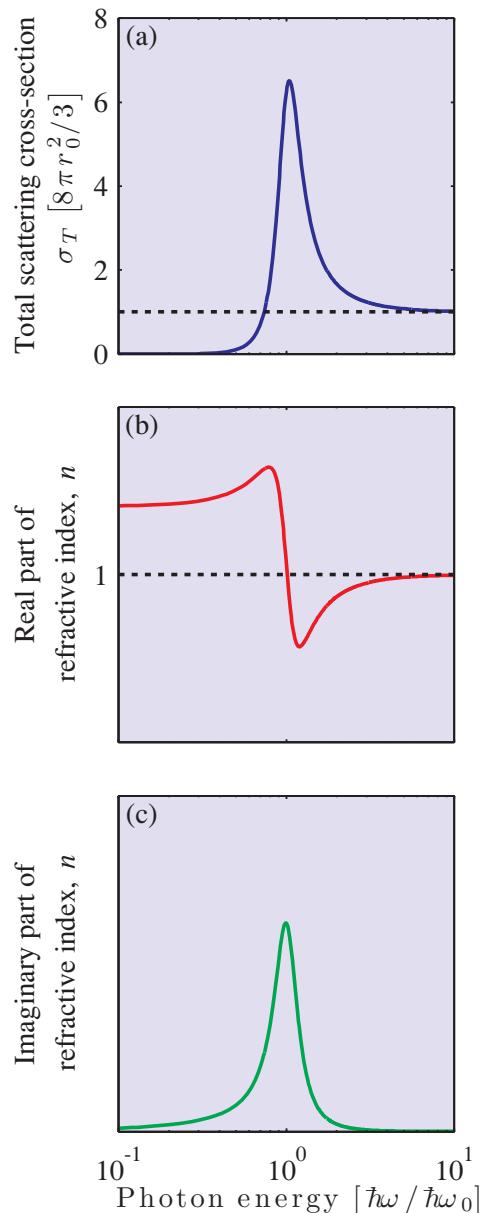
Fig. 1.8 The calculated frequency dependence of (a) the total Thomson scattering cross-section, and the real (b) and imaginary (c) parts of the refractive index, n, when including the dispersion corrections to the Thomson scattering (see Section 8.1). In general, the X-ray part of the electromagnetic spectrum corresponds to the high-frequency (or energy) limit. In this limit, the total scattering cross-section approaches that from a free electron, $\sigma_T = 8\pi r_0^2/3$, and the real part of the refractive index is less than one. It should be noted that important resonances, associated with the K, L and M absorption edges, occur in the X-ray part of the spectrum as discussed in Chapters 7 and 8. For clarity the width of the resonance at $\hbar\omega_0$ has been exaggerated.

driving field more closely, but overall we expect that the scattering length of an atom to be reduced by some amount, which is by convention denoted f'. At energies much greater than the binding energy the electrons can be treated as if they are free and f' is zero. For energies in between these limits f' displays resonant behaviour at energies corresponding to atomic absorption edges, which are discussed in Section 1.3. In addition to altering the real part of the scattering length, we also expect that, by analogy with a forced harmonic oscillator, the response of the electron to have a phase lag with respect to the driving field. This is allowed for by including a term if'', which represents the dissipation in the system, and, as we shall see in Chapters 3 and 8, it is related to the absorption. Collecting these results together means that the atomic form factor is

$$\boxed{f(\mathbf{Q}, \hbar\omega) = f^0(\mathbf{Q}) + f'(\hbar\omega) + if''(\hbar\omega)} \tag{1.12}$$

where f' and f'' are known as the dispersion corrections[4] to f^0. We have written f' and f'' as functions of the X-ray energy $\hbar\omega$ to emphasize that their behaviour is dominated by tightly bound inner-shell electrons, and as a consequence cannot have any appreciable dependence on $\mathbf{Q}$. As might be expected from these introductory remarks, f' and f'' assume their extremal values when the X-ray energy is equal to one of the absorption edge energies of the atom. This resonant behaviour is manifestly element specific, and in Chapter 8 it is explained how it may be exploited to solve the structure of complex materials.

In Fig. 1.8(a) we illustrate the effects of including the dispersion corrections in a calculation of the total scattering cross-section (see Section 8.1). For frequencies much less than $\hbar\omega_0$ the binding of the electron drastically reduces the cross-section. When $\omega \approx \omega_0$ the cross section is significantly enhanced. It is only at high frequencies that the electrons behave as if they are free and the value of the total cross-section calculated for Thomson scattering is realised. Figure 1.8(b) shows the calculated variation in the real part of the refractive index n as a function of photon energy. For $\hbar\omega \ll \hbar\omega_0$ the real part of the refractive index tends to a constant greater than unity, whereas above $\hbar\omega_0$ it is less than unity as is found to be true for X-rays. The consequences of the real part of n being less than unity for X-rays are introduced in Section 1.4 and discussed further in Chapter 3. Figure 1.8 also serves to further underline the fact that scattering and refraction of electromagnetic waves are essentially different views of the same physical phenomenon.

One molecule

So far we have introduced the scattering length for an electron and subsequently for an atom composed of electrons. The next step in complexity is naturally molecules composed of atoms (Fig. 1.7(b)). It is obvious that just as the scattering length of an atom has a form factor, so will the scattering length of a molecule. Labelling the different atoms in the molecule by index j we may write

$$F^{\text{mol}}(\mathbf{Q}) = \sum_j f_j(\mathbf{Q}) \, e^{i\mathbf{Q}\cdot\mathbf{r}_j}$$

where as before $f_j(\mathbf{Q})$ is the atomic form factor of the j'th atom in the molecule, and it must be remembered to include the multiplicative factor of $-r_0$ if the intensity is required in absolute units. If one can determine $\left|F^{\text{mol}}(\mathbf{Q})\right|^2$ experimentally for sufficiently many values of scattering vector $\mathbf{Q}$ then

---

[4]These are also sometimes referred to as the anomalous dispersion corrections, but it is generally agreed that there is in fact nothing anomalous about them. It should be noted that with our sign convention f'' is negative.

one can (at least by trial and error) determine the positions $\mathbf{r}_j$ of the atoms in the molecule. However, the scattering length of a single molecule is not sufficient to produce a measurable signal, even in the very intense X-ray beams produced by today's synchrotron sources. For that bulk samples containing many molecules are required, assembled either as non-crystalline or crystalline forms of matter. The scattering from these distinct phases of matter are dealt with in Chapters 4 and 5, respectively. However, it is expected that in the future, the spectacular increase in peak brilliance offered by free-electron sources will permit the imaging of single molecules.

A crystal

The defining property of a crystalline material is that it is periodic in space[5], as shown for a molecular crystal in Fig. 1.7(c). In elementary treatments of the scattering of X-rays from a crystal lattice, Bragg's law

$$m\lambda = 2d \sin \theta$$

is derived, where m is an integer. This is the condition for the constructive interference of waves which have an angle of incidence θ to a set of lattice planes a distance d apart. While this is a useful construction, it does have its limitations, principal among which is that it does not enable us to calculate the intensity of the scattering for which constructive interference occurs.

For that we need to build on what we have already developed and write down the scattering amplitude of the crystal. To do so we note that a crystal structure may be specified in the following way. First, a lattice of points is defined in space, which must reflect the symmetry of the crystal, and then a choice of unit cell is made, in other words a choice is made over which atoms to associate with each lattice site. If $\mathbf{R_n}$ are the lattice vectors that define the lattice, and $\mathbf{r}_j$ the position of the atoms with respect to any one particular lattice site, then the position of any atom in the crystal is given by $\mathbf{R_n} + \mathbf{r}_j$. It follows that the scattering amplitude for the crystal factorizes into the product of two terms, which we write as

$$F^{\text{crystal}}(\mathbf{Q}) = \overbrace{\sum_j f_j(\mathbf{Q})e^{i\mathbf{Q}\cdot\mathbf{r}_j}}^{\text{Unit cell structure factor}} \overbrace{\sum_n e^{i\mathbf{Q}\cdot\mathbf{R_n}}}^{\text{Lattice sum}} \tag{1.13}$$

where the first term is the *unit cell structure factor*, the second term is a sum over lattice sites, and where again we have neglected a leading factor of $-r_0$. In applications, such as solid state physics it is the structure of the material that is of interest in its own right. For many other applications, such as in molecular and protein crystallography, the lattice is of no interest whatsoever, and assembling the molecules on a lattice merely serves to amplify the signal.

All the terms in the lattice sum given in Eq. (1.13) are phase factors located on the unit circle in the complex plane. The sum will therefore be of order unity unless the scattering vector happens to fulfill

$$\mathbf{Q} \cdot \mathbf{R_n} = 2\pi \times \text{integer} \tag{1.14}$$

in which case it becomes of order N, the number of unit cells. The lattice vectors $\mathbf{R_n}$ are of the form

$$\mathbf{R_n} = n_1 \mathbf{a}_1 + n_2 \mathbf{a}_2 + n_3 \mathbf{a}_3$$

where $(\mathbf{a}_1, \mathbf{a}_2, \mathbf{a}_3)$ are the basis vectors of the lattice and (n_1, n_2, n_3) are integers. A unique solution to Eq. (1.14) can be found by introducing the important concept of the reciprocal lattice. This new lattice

---

[5]See, however, Section 5.2 on quasicrystals.

is spanned by the *reciprocal lattice basis* vectors which are defined by

$$\mathbf{a}_1^* = 2\pi\frac{\mathbf{a}_2 \times \mathbf{a}_3}{\mathbf{a}_1 \cdot (\mathbf{a}_2 \times \mathbf{a}_3)}, \quad \mathbf{a}_2^* = 2\pi\frac{\mathbf{a}_3 \times \mathbf{a}_1}{\mathbf{a}_1 \cdot (\mathbf{a}_2 \times \mathbf{a}_3)}, \quad \mathbf{a}_3^* = 2\pi\frac{\mathbf{a}_1 \times \mathbf{a}_2}{\mathbf{a}_1 \cdot (\mathbf{a}_2 \times \mathbf{a}_3)}$$

so that any lattice site in the reciprocal lattice is given by

$$\mathbf{G} = h\,\mathbf{a}_1^* + k\,\mathbf{a}_2^* + l\,\mathbf{a}_3^*$$

where (h, k, l) are all integers. We can see that the product of a lattice vector in the reciprocal ($\mathbf{G}$) and direct ($\mathbf{R_n}$) spaces is

$$\mathbf{G} \cdot \mathbf{R_n} = 2\pi(hn_1 + kn_2 + ln_3) = 2\pi \times \text{integer}$$

and hence the solution to Eq. (1.14) that we are seeking is to require that

$$\boxed{\mathbf{Q} = \mathbf{G}}$$

This proves that $F^{\text{crystal}}(\mathbf{Q})$ is non-vanishing if and only if $\mathbf{Q}$ coincides with a reciprocal lattice vector. This is the Laue condition for the observation of diffraction from a crystalline lattice which may be shown to be completely equivalent to Bragg's law (Chapter 5, page 155).

Scattering from a crystal is therefore confined to distinct points in reciprocal space. The intensity in each point is modulated by the absolute square of the unit cell structure factor. From a (large) set of intensities from a given crystal it is possible to deduce the positions of the atoms in the unit cell. These considerations may of course be generalized to crystals containing molecules. Indeed these methods have had an enormous impact on our knowledge of molecular structure. More than 95% of all molecular structures come from X-ray diffraction studies. Data sets from crystals of large molecules such as proteins or even viruses encompass tens of thousands of reflections and sophisticated methods have been developed to get from the measured intensities to the atomic positions in the molecule. In Chapter 5 these concepts will be further developed, and the principles behind these methods will be explained.

In this section it has been tacitly assumed that the interaction between the X-ray and crystal is weak, since we have not allowed for the possibility that the scattered beam may be scattered a second or third time before leaving the crystal. This assumption leads to considerable simplicity and is known as the *kinematical approximation*. In Chapter 6 it is explained how this assumption breaks down when dealing with macroscopic perfect crystals, where multiple scattering effects become important, and we are then in what is known as the *dynamical* scattering limit.

Compton scattering by a free electron

The alternative to the classical description used so far in this section, is to view the incident X-ray as a beam of photons. For simplicity assume that the electron is initially at rest and is free. In a collision energy will be transferred from the photon to the electron, with the result that the scattered photon has a lower energy than that of the incident one. This is the Compton effect. Historically this was of considerable importance as it could not be explained using classical concepts, and thus gave further support to the then emerging quantum theory. The energy loss of the photon is readily calculated by considering the conservation of energy and momentum during the collision. The collision process is sketched in Fig. 1.9, while the kinematics of the collision are worked through in the box on page 17.
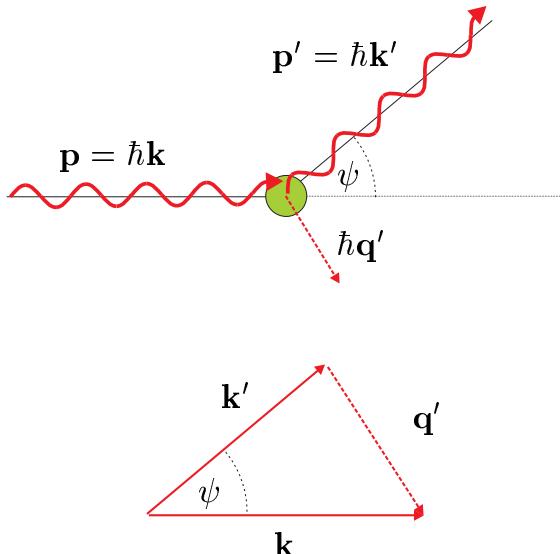
Fig. 1.9 Compton scattering. A photon with energy $\mathcal{E} = \hbar c k$ and momentum $\hbar \mathbf{k}$ scatters from an electron at rest with energy mc^2. The electron recoils with a momentum $\hbar \mathbf{q}' = \hbar(\mathbf{k} - \mathbf{k}')$ as indicated in the scattering triangle in the bottom half of the figure.
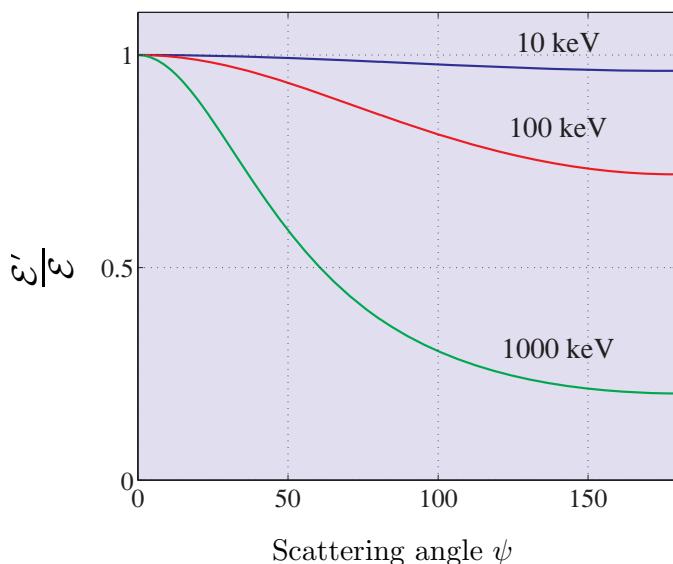
Fig. 1.10 The ratio of the energy $\mathcal{E}'$ of the scattered photon to the energy $\mathcal{E}$ of the incident one as function of scattering angle. The curves have been calculated from Eq. (1.15) with $\lambdabar_C k = \mathcal{E}/mc^2 = \mathcal{E}[\text{keV}]/511$.

Kinematics of Compton scattering

Conservation of energy for the scattering of a photon by an electron shown in Fig. 1.9 leads to

$$mc^2 + \hbar ck = \sqrt{(mc^2)^2 + (\hbar cq')^2} + \hbar ck'$$

Dividing both sides by mc^2, and using the definition of the Compton wavelength, $\lambda_C = \hbar c/(mc^2)$, leads to

$$1 + \lambda_C(k - k') = \sqrt{1^2 + (\lambda_C q')^2}$$

This can be rewritten to obtain an expression for q'^2 by squaring both sides and collecting terms to give

$$q'^2 = (k - k')^2 + 2\frac{(k - k')}{\lambda_C}$$

Conservation of momentum (or equivalently wavevector) reads

$$\mathbf{q}' = \mathbf{k} - \mathbf{k}'$$

Taking the scalar product of $\mathbf{q}'$ with itself gives

$$\mathbf{q}' \cdot \mathbf{q}' = q'^2 = (\mathbf{k} - \mathbf{k}') \cdot (\mathbf{k} - \mathbf{k}')$$
$$= k^2 + k'^2 - 2kk' \cos\psi$$

Equating this with the expression for q'^2 derived from energy conservation yields

$$k^2 + k'^2 - 2kk' \cos\psi = k^2 + k'^2 - 2kk' + 2\frac{(k - k')}{\lambda_C}$$

or

$$kk'(1 - \cos\psi) = \frac{(k - k')}{\lambda_C}$$

which may be recast in the form

$$\frac{k}{k'} = 1 + \lambda_C k(1 - \cos\psi) = \frac{\mathcal{E}}{\mathcal{E}'} = \frac{\lambda'}{\lambda} \tag{1.15}$$

The result of the calculation is that the change in wavelength is proportional to the Compton scattering length defined by

$$\lambda_C = \frac{\hbar}{mc} = \quad 3.86 \times 10^{-3} \text{ Å}$$

(1.16)

There are thus two fundamental scattering lengths for the X-ray, the Thomson scattering length, r_0, and the Compton scattering length, λ_C. The ratio of these two is the fine structure constant

$$\alpha = \frac{r_0}{\lambda_C} \approx \frac{1}{137}$$

The ratio of the final to initial energy of the photon is given in Eq. (1.15) and is plotted in Fig. 1.10. For a given scattering angle, the scattering becomes progressively more inelastic as the energy $\mathcal{E}$ of the incident X-ray is increased. The energy scale is set by the rest mass energy of the electron, $mc^2 = 511$ keV.

One important difference between Thomson and Compton scattering is that the latter is *incoherent*. It has already been shown how X-rays that are elastically scattered from a crystal add up coherently when Bragg's law (or equivalently the Laue condition) is fulfilled. The scattering is then restricted to lie at points on the reciprocal lattice. The same is not true for Compton scattering, as it is the interaction between a single photon and electron, and the variation of the Compton cross-section[6] varies only slowly with scattering angle. As far as diffraction experiments are concerned, Compton scattering gives rise to a smoothly varying background which sometimes needs to be subtracted from the data.

Compton scattering may be used to obtain unique information on the electronic structure of materials. So far we have assumed that the electron in the Compton scattering process is initially at rest. This assumption breaks down for electrons in a solid, which instead have a finite momentum. When the kinematics are worked through for this case, it turns out that the Compton cross-section gives a measure of the electronic momentum distribution.

1.3   Absorption

Now let us turn to the absorption process. It is depicted in Fig. 1.11(a). An X-ray photon is absorbed by an atom, and the excess energy is transferred to an electron, which is expelled from the atom, leaving it ionized.

The process is known as *photoelectric absorption*. Quantitatively, the absorption is given by the linear absorption coefficient μ. By definition μdz is the attenuation of the beam through an infinitesimal sheet of thickness dz at a depth z from the surface (Fig. 1.12). The intensity $I(z)$ through the sample must therefore fulfill the condition
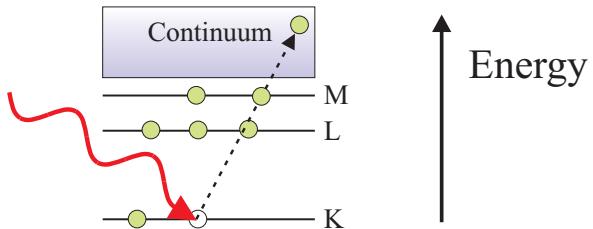
$$-dI = I(z)\,\mu\,dz$$

(1.17)

which leads to the differential equation
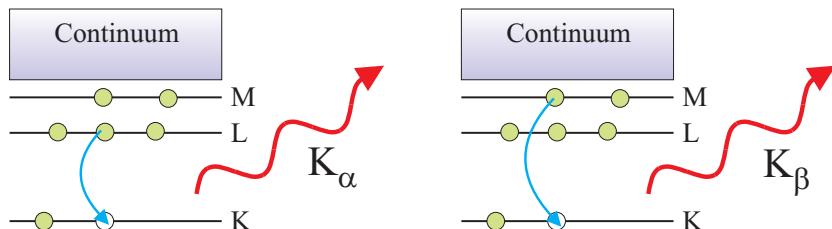
$$\frac{dI}{I(z)} = -\mu\,dz$$

---

[6]The calculation of the Compton cross-section is beyond the scope of this book. It is discussed by Lovesey and Collins [1996].

(a)   Photoelectric absorption

(b)   Fluorescent X-ray emission

(c)   Auger electron emission
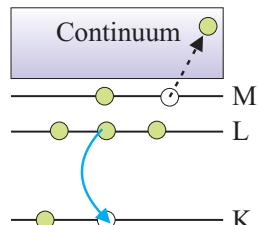
Fig. 1.11 Schematic energy level diagram of an atom. For clarity we have indicated only the energy of the three lowest shells; the rest are merged into the continuum. (a) The photoelectric absorption process. An X-ray photon is absorbed and an electron ejected from the atom. The hole created in the inner shell can be filled by one of two distinct processes: (b) Fluorescent X-ray emission. One of the electrons in an outer shell fills the hole, creating a photon. In this example the outer electron comes either from the L or M shell. In the former case the fluorescent radiation is referred to as the K_{α} line, and in the latter as K_{β}. (c) Auger electron emission. The atom may also relax to its ground state energy by liberating an electron.
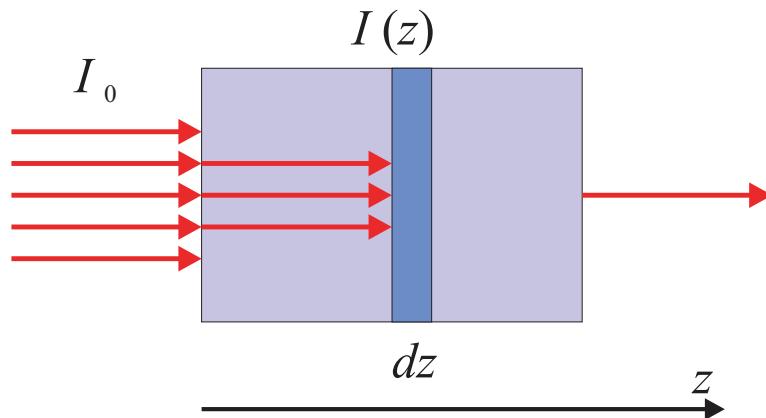
Fig. 1.12 The attenuation of an X-ray beam through a sample due to absorption. The attenuation follows an exponential decay with a characteristic linear attenuation length $1/\mu$, where μ is the absorption coefficient.

The solution is found by requiring that $I(z = 0) = I_0$, the incident beam intensity at $z = 0$, and we have

$$I(z) = I_0 \, e^{-\mu z}$$

One can therefore readily determine μ experimentally as the ratio of beam intensities with and without the sample. The number of absorption events, W, in the thin sheet is proportional to I, and to the number of atoms per unit area, $\rho_{at} \, dz$, where ρ_{at} is the atomic number density. The proportionality factor is by definition the absorption cross-section, σ_a, so that

$$W = I(z) \rho_{at} \, dz \, \sigma_a = I(z) \mu \, dz$$

where in the last step we have used Eq. (1.17). The absorption coefficient is therefore related to σ_a by

$$\mu = \rho_{at} \sigma_a = \left(\frac{\rho_m N_A}{M} \right) \sigma_a \tag{1.18}$$

where N_A, ρ_m and M are Avogadro's number, the mass density, and molar mass, respectively. In a composite material with several kinds of atoms, each with a number density $\rho_{at,j}$ and absorption cross section $\sigma_{a,j}$, the total probability for absorption in a layer dz is obtained by summing over $\rho_{at,j} \sigma_{a,j} dz$, the total probability of absorption for an atom of type j. Thus the absorption coefficient for a composite material is

$$\mu = \sum_j \rho_{at,j} \sigma_{a,j} \tag{1.19}$$

When an X-ray photon expels an electron from an inner atomic shell it creates a hole in that shell. In Fig. 1.11(a) we illustrate this for the case of an electron excited from a K shell. The hole is subsequently filled by an electron from an outer shell, L say, with the simultaneous emission of a photon with an energy equal to the difference in the binding energies of the K and L electrons (Fig. 1.11(b)). The emitted radiation is known as fluorescence. Alternatively, the energy released by an electron hopping from the L shell to the hole in the K shell can be used to expel yet another electron from one of the
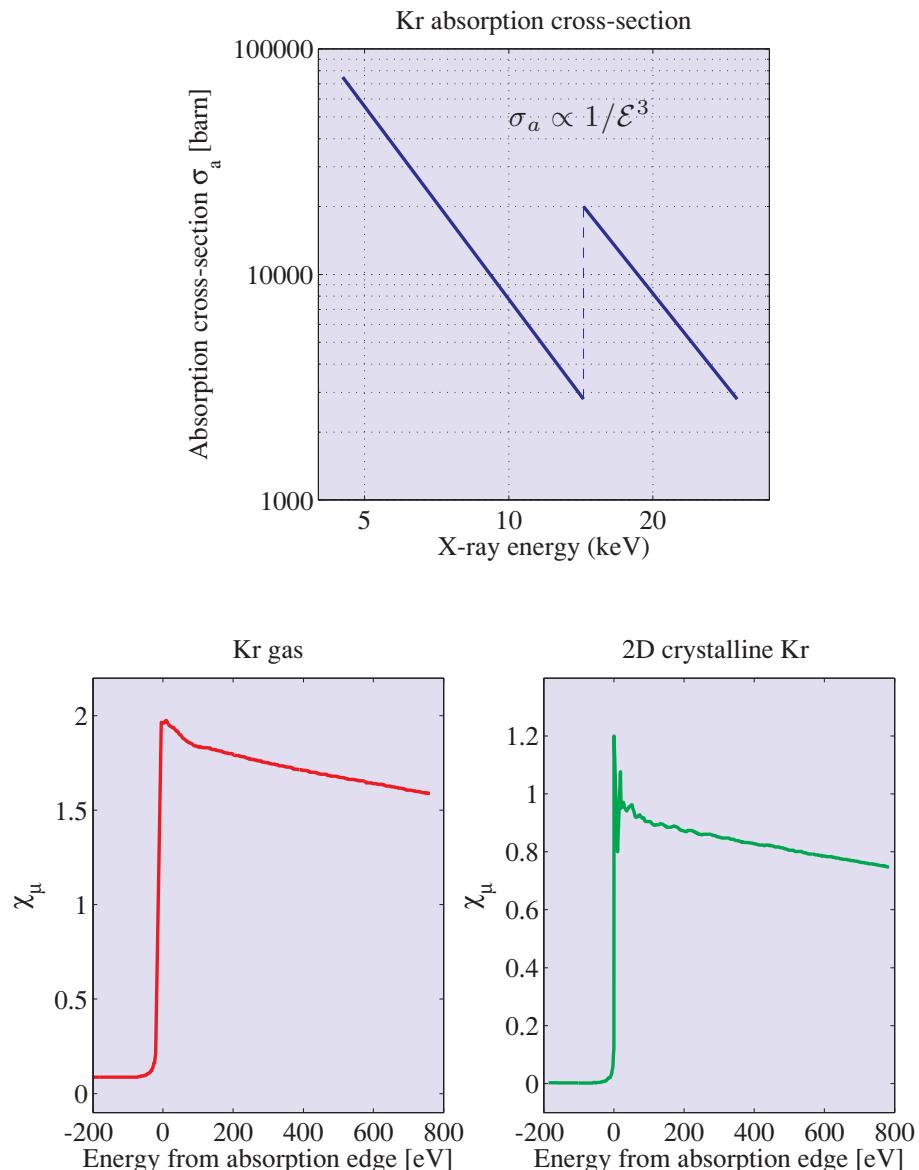
Fig. 1.13 Top: The absorption cross-section of gaseous krypton. Above a photon energy of 14.325 keV a K shell electron can be expelled from the atom and a new absorption 'channel' opens. The double logarithmic plot illustrates that the cross-section varies as $1/\mathcal{E}^3$. Bottom: A comparison of the absorption spectra of krypton in its gaseous form and physisorbed on graphite where the krypton atoms form a two-dimensional lattice. In the latter case fine structure, or wiggles, are evident which are known as EXAFS. The quantity χ_μ is proportional to the absorption cross-section σ_a.
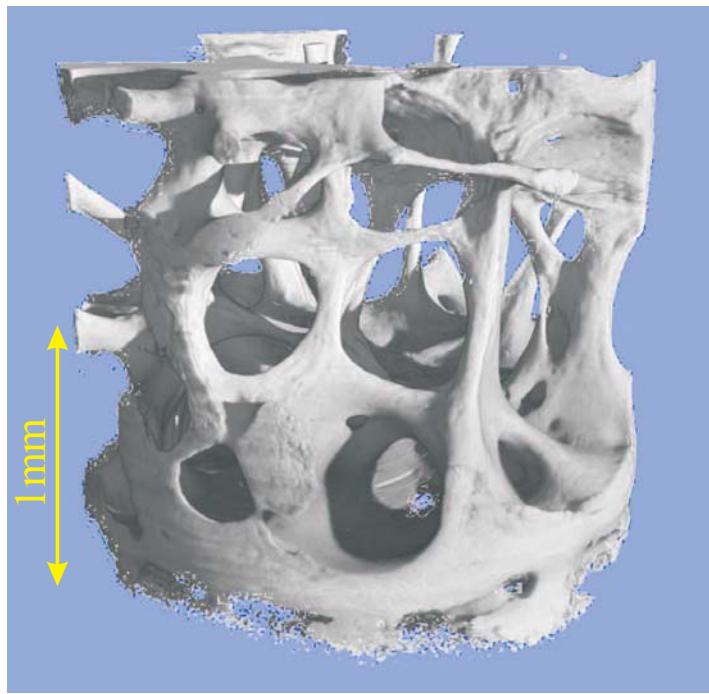
Fig. 1.14 Three-dimensional micro-CAT reconstruction of a cylindrical human vertebral bone specimen scanned with 3.6 μm spatial resolution. Note the difference between the cortical end-plate and the underlying trabecular bone. (Image courtesy of a collaboration between Aarhus University, Denmark, and HASYLAB at DESY, Germany.)

outer shells, as sketched in Fig. 1.11(c). This secondary emitted electron is called an Auger electron, named after the French physicist who first discovered the process.

The monochromatic nature of fluorescent X-rays is a unique fingerprint of the kind of atom that produces the fluorescence. It was Moseley who first discovered the empirical law

$$\mathcal{E}_{K_\alpha} \, [\text{keV}] \approx 1.017 \times 10^{-2} \, (Z-1)^2 \tag{1.20}$$

where $\mathcal{E}_{K_\alpha}$ is the energy of the K_α line of a given element and Z is its atomic number[7]. The analysis of fluorescent radiation can be utilized for non-destructive chemical analysis of samples, and has the advantage that it is very sensitive. The radiation that creates the hole in the first place does not have to be an X-ray: it could also be from a beam of particles, such as of protons or electrons. For example, the latter is a standard option on electron microscopes, enabling the chemical composition of samples to be determined with a very fine spatial resolution.

The absorption cross-section has a distinct dependence on photon energy. An example is shown in the top panel of Fig. 1.13 for the rare gas krypton. Below a photon energy of 14.32 keV the X-ray photon

[7]Moseley's original work, published in 1913 against the backdrop of the emergence of quantum mechanics, played a key role in establishing the Bohr model of the atom. Moseley's law also allowed the position of elements to be understood in terms of Z, and was used to predict the existence of elements that up until that point had not been discovered.

can only expel electrons from the L and M shells. The cross-section is approximately proportional to $1/\mathcal{E}^3$. At a characteristic energy, the so-called K-edge energy, the X-ray photon has enough energy to also expel a K electron, with a concomitant discontinuous rise in the cross-section of about one decade. From then on the cross-section continues to fall off as $1/\mathcal{E}^3$.

If we examine the fine structure of the absorption just around the edge it is apparent that it depends on the structure of the material. This is again illustrated for Krypton in Fig. 1.13 [taken from Stern and Heald, 1983]. The wiggles in the spectrum from two-dimensional crystalline Krypton on graphite demonstrate the phenomenon of Extended X-ray Absorption Fine Structure (EXAFS) in condensed matter systems. We shall return to the interpretation of EXAFS data in Chapter 7.

The photoelectric absorption cross-section varies with the atomic number Z of the absorber, approximately as Z^4. It is this variation, and thus the contrast, between different elements that make X-rays so useful for imaging, as we describe in Chapter 9. Tissue is mainly water and hydrocarbons and thus has a 1/e thickness of many centimetres for hard X-rays, whereas bone contains a lot of Ca and a correspondingly smaller X-ray transmission. It was this, by now well-known, ability to look through the body that produced a sensation, when Wilhelm Conrad Röntgen discovered X-rays over a 100 years ago. When coupled with the computer power available today one can obtain the internal structure of parts of the body with remarkable precision. The technique is called CAT scanning, an acronym for Computer Axial Tomography (or Computer Aided Tomography). The idea is to take two-dimensional 'shadow' pictures from many angles, and then reconstruct the three-dimensional object using a computer program. An example of the type of exquisite images that can be obtained with modern CAT scanning is given in Fig. 1.14. Another tomography application where computer power is essential, utilizes subtraction of pictures taken above and below the K edge of the element one is particularly interested in. In this way the element-sensitivity is enhanced dramatically.

While photoelectric absorption arises from a physical process that is distinct from the scattering of a photon, it should always be bourne in mind that the two are nonetheless related (see Fig. 1.8). In Section 3.3 the relationship between the absorption cross section and the imaginary part of the scattering amplitude is established, while this interrelationship is more fully explored in Chapter 8.
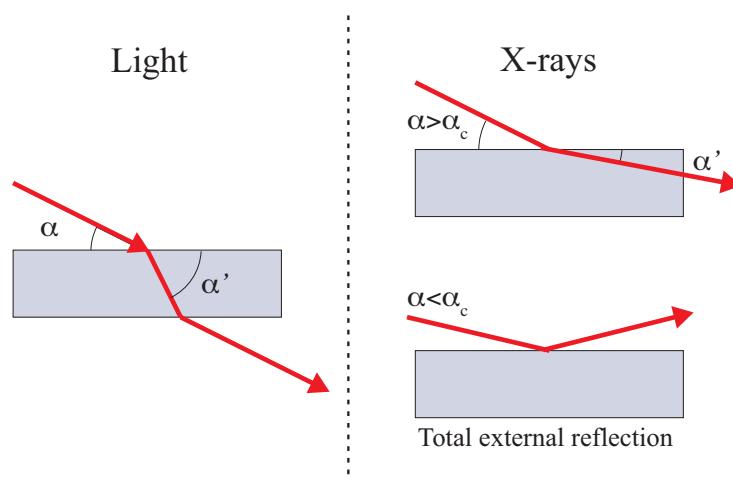
1.4   Refraction and reflection

The interaction of X-ray photons with matter has so far been discussed mostly at the atomic level. However, since X-rays are electromagnetic waves, one should also expect some kind of refraction phenomena at interfaces between different media. To describe such refractive phenomena, the media of interest are taken to be homogeneous with sharp boundaries between them, each having its own refractive index n. By definition the refractive index of vacuum is one. It is well known that for visible light in glass n is large and can vary considerably, ranging from 1.5 to 1.8 depending on the type of glass. This of course enables lenses to be designed for focusing light and thereby obtaining magnified images. For X-rays the difference from unity of n is very small, and as we shall see in Chapter 3 is of order 10^{-5} or so. In general for X-rays, the refractive index can be expressed as
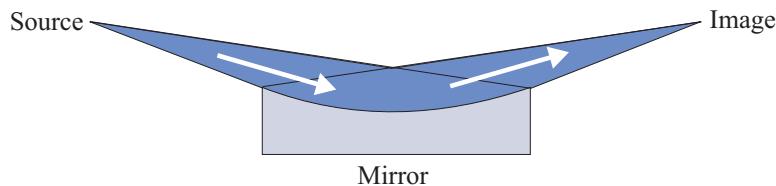
$$\boxed{n = 1 - \delta + i\beta} \tag{1.21}$$

where δ is of order 10^{-5} in solids and only around 10^{-8} in air. The imaginary part β is usually much smaller than δ. That the real part of n is less than unity is due to the fact that the X-ray spectrum generally lies to the high-frequency side of various resonances associated with the binding of electrons,
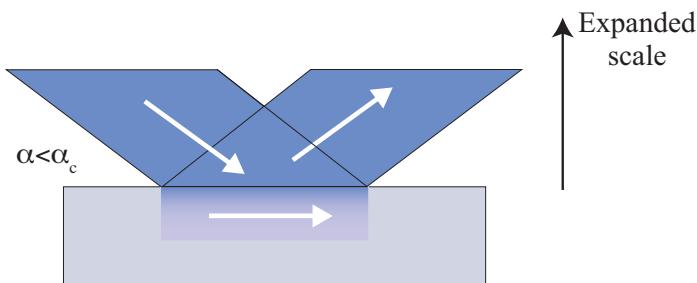
Fig. 1.15 (a) The refraction of light shows that in the visible part of the spectrum the refractive index of glass is considerably greater than one. In contrast, the index of refraction for X-rays is slightly less than one, implying total external reflection at glancing angles below the critical angle α_c. (b) A focusing X-ray mirror can be constructed by arranging that the incident angle is below the critical angle for total external reflection. (c) At glancing angles below the critical angle the reflectivity is almost 100%, and the X-ray only penetrates into the material as an evanescent wave with a typical penetration depth of ≈ 10 Å. In this way X-rays can be made to be surface sensitive.

as illustrated in Fig. 1.8. One consequence of the real part of n being less than unity is that it implies that the phase velocity inside the material, c/n, is larger than the velocity of light, c. This does not, however, violate the law of relativity, which requires that only signals carrying 'information' do not travel faster than c. Such signals move with the group velocity, not the phase velocity, and it can be shown that the group velocity is in fact less than c.

Snell's law relates the incident grazing angle α to the refracted grazing angle α' (see Fig. 1.15(a))

$$\cos \alpha = n \cos \alpha' \tag{1.22}$$

An index of refraction less than unity, implies that below a certain incident grazing angle called the critical angle, α_c, X-rays undergo total external reflection. Expansion of the cosine in Eq. (1.22) with $\alpha = \alpha_c$, $\alpha' = 0$ and using Eq. (1.21) allows us to relate δ to the critical angle α_c:

$$\alpha_c = \sqrt{2\delta}$$

where for simplicity we have taken $\beta = 0$. With δ being typically around 10^{-5}, α_c is of the order of a milli-radian. We shall see in Chapter 3, that the refractive constants δ and β can be derived from the scattering and absorption properties of the medium, respectively.

Total external reflection has several important implications for X-ray physics. First, total reflection from a curved surface enables focusing optics to be constructed as shown in the Fig. 1.15(b). A small source size is thus desirable, since from geometrical optics, a small source will be focused to a small image. A second consequence of total external reflection is that for $\alpha < \alpha_c$ there is a so-called evanescent wave within the refracting medium, see Fig. 1.15(c). It propagates parallel to the flat interface, and its amplitude decays rapidly in the material: typically with a penetration depth of only a few nanometers. This should be compared with a penetration depth of several micrometers at a glancing angle of several times α_c.

The much-reduced penetration of X-rays for angles less than α_c increases their surface sensitivity. This allows the scattering from the surface and near surface region to be studied, often in great detail, and indeed X-rays have become a valuable tool for the investigation of surfaces and interfaces.

1.5 Coherence

Throughout this introductory survey we have assumed that we are dealing with an X-ray beam in a perfect plane-wave state. This is obviously an idealization, and in this section we shall briefly discuss its limitation by recalling the concept of a *coherence length* of a real beam, and its relation to the source and monochromator. A real beam deviates from an ideal plane wave in two ways: it is not perfectly monochromatic, and it does not propagate in a perfectly well defined direction. Let us discuss these limitations in turn.

The top part of Fig. 1.16 shows two plane waves A and B with slightly different wavelengths, λ and $\lambda - \Delta\lambda$ say, but both propagating in exactly the same direction. The two waves are exactly in phase at the wavefront P. The question is how far do we have to go away from P before the two waves are out of phase? This defines the *longitudinal* coherence length L_L. If the two waves are out of phase after travelling L_L, then they will be in phase again after travelling $2L_L$. Let that distance be N wavelengths λ, or equivalently $(N + 1)(\lambda - \Delta\lambda)$, i.e.

$$2L_L = N\lambda = (N + 1)(\lambda - \Delta\lambda)$$
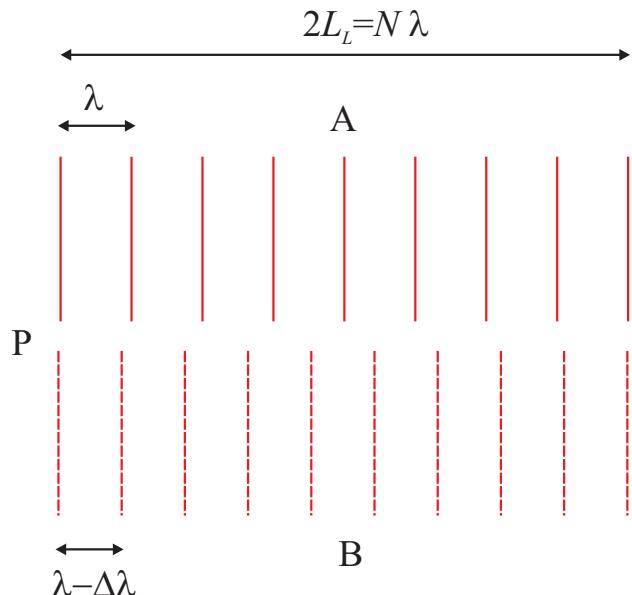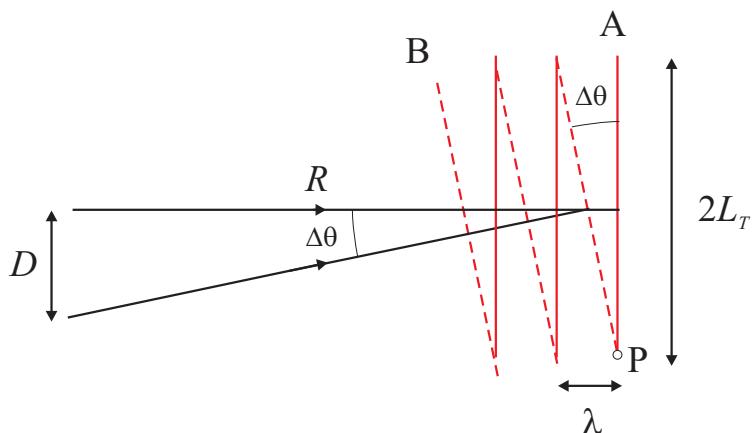
(a) Longitudinal coherence length, L_L

(b) Transverse coherence length, L_T

Fig. 1.16 Longitudinal and transverse coherence lengths. (a) Two plane waves with different wavelengths are emitted in the same direction. For clarity we have shown the waves displaced from each other in the vertical direction. After a distance L_L, the longitudinal coherence length, the two are out of phase by a factor of π. (b) Two waves with the same wavelength are emitted from the ends of a finite sized source of height D.

The second equation implies that $(N + 1)\Delta\lambda = \lambda$, or $N \approx \lambda/\Delta\lambda$, and using this result the first equation can be rearranged to read

$$L_L = \frac{1}{2}\frac{\lambda^2}{\Delta\lambda} \qquad (1.23)$$

The bottom panel of Fig. 1.16 shows the other case: two waves A and B of the same wavelength, but with slightly different directions of propagation, say by an angle of $\Delta\theta$. Their wavefronts coincide at point P, and the question is now how far do we have to go from P along the wavefront of wave A before it is out of phase with wave B? By definition that distance is the *transverse* coherence length L_T. Clearly, if proceeding to a distance of $2L_T$, the two waves will be in phase again, and it is obvious from the figure that $2L_T\Delta\theta = \lambda$, i.e. $L_T = \lambda/(2\Delta\theta)$. Suppose that the different directions of propagation arise because the two waves originate from two different points on the source, let us say a distance D apart. If the distance from the observation point P to the source is R, then $\Delta\theta = D/R$ and we have

$$L_T = \frac{1}{2}\frac{\lambda}{(D/R)} = \frac{\lambda}{2}\left(\frac{R}{D}\right) \qquad (1.24)$$

It is instructive to consider typical values for the coherence lengths, but to do so we need to make some assumptions about the source. At a third generation synchrotron the vertical source size is around 100 μm, and the experiment may be performed some 20 m away, so that for 1 Å X-rays L_T is approximately 10 μm in the vertical plane. To calculate the longitudinal coherence length we need to make some additional assumption about the device used to monochromate the beam. If a perfect crystal is used, $\Delta\lambda/\lambda \approx 10^{-5}$ (see Chapter 6), and then, according to Eq. (1.23), L_L is ≈ 5 μm for 1 Å X-rays, similar in order of magnitude to L_T. The consequence of a finite coherence length is that it places an upper limit on the separation of two objects if they are to give rise to interference effects. To take a simple example, consider the scattering from two electrons. If the projection of their separation on the wavevector transfer $\mathbf{Q}$ is much greater than the coherence length, then the total scattered intensity is the sum of scattered intensities from the individual electrons, and not the modulus squared of the sum of amplitudes as has been described thus far.

In Chapter 9 we describe how coherent beams of X-rays are utilized in modern imaging methods.

1.6   Magnetic interactions

The discussion so far has centred on the interaction between the electric field of the X-ray and the charge of the electron. What has been neglected is the magnetic field of the X-ray and the spin of the electron. When these are included in a full treatment of the interaction, terms emerge in the scattering cross-section that are sensitive to the spin and orbital magnetic moments of the electron. In this way it is possible to use X-rays to investigate magnetic structures. The history of X-ray magnetic scattering is much more recent than that of classical X-ray diffraction. In fact the first observation of X-ray magnetic scattering had to wait until 1972 and the pioneering experiments of de Bergevin and Brunel on antiferromagnetic NiO [de Bergevin and Brunel, 1972].

The reason for this is simply that magnetic scattering is much weaker than charge scattering. The

amplitude ratio of magnetic to charge scattering for a *single electron* is

$$\frac{A_{\text{magnetic}}}{A_{\text{charge}}} = \left(\frac{\hbar\omega}{mc^2}\right)$$

[Blume, 1985]. For 5.11 keV X-rays this ratio is 0.01, so the intensity of Bragg peaks that are purely magnetic in origin are weaker than the charge peaks by a factor of approximately 10^{-4}. In fact, as only relatively few atomic electrons contribute to the magnetic scattering (namely those with unpaired angular momenta in open shells), while all of them contribute to the charge scattering, the intensity ratio is typically depressed by an additional factor of 10^{-2} or so. Progress in the field of X-ray magnetic scattering was at first slow, but the routine availability of synchrotron radiation has given a tremendous boost to this subject, to the extent that it has now flourished into a field in its own right.

Sensitivity to magnetism is not restricted to scattering experiments, however, but also occurs in absorption processes. For example, the difference in absorption of left- and right-hand circularly polarized light by a solid (known generally as circular dichroism, or more specifically in the case of magnetic systems as X-ray magnetic circular dichroism (XMCD)) can be directly related to the ferromagnetic magnetization density, as described in Chapter 7. It has also been found that magnetic scattering itself is a much richer phenomena than early expectations, with the discovery that resonant magnetic scattering processes occur when the energy of the incident X-ray is tuned close to certain atomic absorption edges [Namikawa et al., 1985, Gibbs et al., 1988]. These subjects take us beyond the scope of this volume, but it is important to realize that the study of the interaction of X-rays with matter is still an active field of research some 100 years or so after the discovery of the X-ray [see, for example, Lovesey and Collins, 1996].

1.7   Further reading

Röntgen Centennial – X-rays in Natural and Life Sciences, Eds. A Haase, G. Landwehr, and E. Umbach (World Scientific, Singapore, 1997).

Fifty Years of X-ray Diffraction, P. P. Ewald, (International Union of Crystallographers, N. V. A. Oosthoek's uitgeversmaatchappj, Utrecht, 1962).

X-rays 100 Years Later, Physics Today (special issue) **48**, (1995).

2

Sources

2.1 Early history and the X-ray tube

Röntgen discovered X-rays in November 1895 in his laboratory at the University of Würzburg, Germany. He was examining the light and other radiation associated with the discharge from electrodes in an evacuated glass tube. He had covered the tube, a so-called Geisler discharge tube, so that no visible light could escape. The laboratory was also darkened. All that could be seen was a faint yellow-green light from a fluorescent screen placed close to the tube. The fluorescent light was flickering, since the high voltage was supplied by the *ac* output of an induction coil, and could be seen even when the screen was several metres away from the tube. To his amazement the radiation from the tube passed through paper and wood, whereas metal pieces of equipment cast a shadow on the screen. The most stunning phenomenon occurred when he placed his hand into the space between the tube and the screen and saw the bones inside. Röntgen was a keen amateur photographer and he quickly had the idea to photograph the X-ray beam instead of using the fluorescent screen. The photographs were convenient scientific documentation of his discovery, which was first published in the annals of the local Würzburg Scientific Society in late December of 1895. The paper is entitled 'Uber eine neue Art von Strahlen – vorläufige Mitteilung'[1]. The fact that one could now 'see' inside the human body was a sensation that spread worldwide within a few weeks, with implications for medical science that can hardly be overstated.

It became clear from Röntgen's subsequent investigations that the imaging of bones in the body is based on the fact that X-ray absorption is strongly dependent on the atomic number of the elements; it varies approximately as Z^4. The other important application of X-rays, based on diffraction phenomena, showing how crystalline matter is built up by atoms forming a periodic lattice, had to wait until 1912 when von Laue and his coworkers obtained the first diffraction pattern from a crystal of copper sulfate. In the following year W.H. Bragg and W.L. Bragg (father and son) examined the diffraction of X-rays from a number of crystals and laid the foundations of the field of crystallography, which subsequently allowed one to determine the structure of molecules.

The younger Bragg also found a particular simple way to interpret the diffraction patterns which

[1] 'On a new kind of radiation – preliminary communication'

proved unambiguously that X-rays are nothing other than electromagnetic radiation of short wavelength: Röntgen had also played with the same idea, and tried to prove it experimentally, but without success. His influence in German physics at the time was so great that even von Laue and coworkers were not tempted to reach the same conclusion from their diffraction experiments as Bragg.

The standard X-ray tube and the rotating anode

The X-ray tube Röntgen used was a tricky business to run reliably. It was therefore a tremendous practical step forward when in 1912 W.D. Coolidge from General Electric Research Laboratories in New York developed a new tube, where electrons were produced by a glowing filament and subsequently accelerated towards a water-cooled metal anode (see Fig. 2.1). Now one could vary the high voltage and the current independently, and the limitation of intensity was set only by the cooling efficiency. It turns out that the maximal power for such a device is around 1 kW. The Coolidge tube served as the standard X-ray tube for many decades with only marginal technical improvements.

Although it was appreciated early on that by spinning the anode the heat could be dissipated over a much larger volume than in a standard tube, allowing the total power to be correspondingly increased, it was not until the 1960s that so-called rotating anode generators became available on a commercial basis. One of the technical difficulties to overcome had been the problem of how to make a high-vacuum seal on the rotating shaft, inside which the cooling water must flow in and out.

The spectrum of X-rays generated from electrons impinging on a metal anode has two distinct components. There is a continuous part due to the electrons being decelerated, and eventually stopped in the metal. This is consequently known as *bremsstrahlung* radiation (after the German *bremsen* for brake), and has a maximum energy that corresponds to the high voltage applied to the tube. Superimposed on this broad spectrum is a sharp line spectrum. In a collision with an atom the incident electron may also cause an atomic electron to be removed from one of the inner shells, creating a vacancy. The subsequent relaxation of an electron from an outer shell into the vacancy may produce an X-ray with a characteristic energy equal to the difference in energy between the two shells. This is the fluorescent radiation. For experiments requiring a monochromatic beam one often utilizes the K_α line which is several orders of magnitude more intense than the bremsstrahlung spectrum. However, only a very small fraction of the photons emitted into the solid angle of 2π can be utilised in a beam requiring an angular divergence of a few squared milli-radian. In addition, the line source is not continuously tuneable so the optimal wavelength for the experiment cannot be chosen, or scanned, at will. As we shall see in the following sections, X-rays generated from synchrotron sources do not have these drawbacks, and have a brilliance which is enormously higher than that of standard laboratory sources.

2.2   Introduction to synchrotron radiation

Synchrotron radiation takes its name from a specific type of particle accelerator. However, synchrotron radiation has become a generic term to describe radiation from charged particles travelling at relativistic speeds in applied magnetic fields which force them to travel along curved paths. Besides synchrotrons themselves, synchrotron radiation is produced in storage rings where electrons or positrons are kept circulating at constant energy. In a storage ring the synchrotron radiation is produced either in the bending magnets needed to keep the electrons in a closed orbit, or in insertion devices such as wigglers or undulators situated in the straight sections of the storage ring. In these devices an alternating magnetic field forces the electrons to follow oscillating paths rather than moving in a straight line. In a wiggler the amplitude of the oscillations is rather large, and the radiation from different wiggles
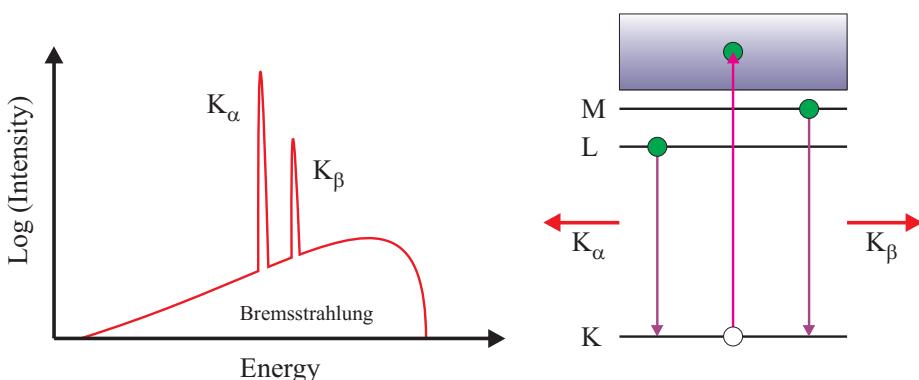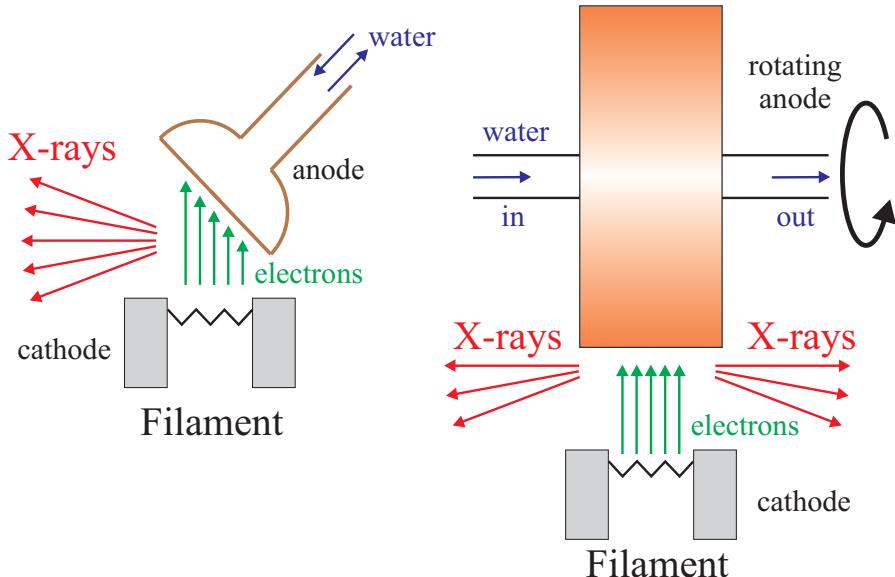
Fig. 2.1 The standard X-ray tube (upper, left) was developed by Coolidge around 1912. The intensity limitation is set by the maximum power a cooled metal anode can withstand. The power can be increased by dissipating it over a larger volume which is achieved by rotating the anode (upper, right). The spectrum from an X-ray tube has discrete fluorescent lines superimposed on the continuous bremsstrahlung radiation (bottom, left). Schematic atomic energy level diagram (bottom, right): the K_α line results from transitions between an L and K shell, whereas the K_β comes from an M to K transition.

add incoherently, whereas in undulators, as we shall see, the small-amplitude oscillations from the passage of a single electron produce a coherent addition of the radiation from each oscillation. It is also interesting to note that synchrotron radiation in fact occurs naturally, and has been observed, for example, from plasmas around stellar nebula.

For X-ray research, however, practically all modern sources[2] of synchrotron radiation are storage rings. The researcher new to the field of synchrotron X-ray science will encounter the usual set of abbreviations, such as SR (for synchrotron radiation), BM (from bending magnets), ID (from insertion devices), etc. We shall not use them in this book, but the reader is warned.

2.2.1   Characterizing the beam: brilliance

Several aspects of an X-ray source determine the quality of the X-ray beam it produces. These aspects can be combined into a single quantity, called the brilliance, which allows one to compare the quality of X-ray beams from different sources. First of all, there is the number of photons emitted per second. Next, there is the collimation of the beam. This describes how much the beam diverges, or spreads out, as it propagates. Usually the collimation of the beam is given in milli-radian, both for the horizontal and for the vertical direction. Third, it may be of importance how large the source area is: if it is small, one may be able to focus the X-ray beam to a correspondingly small image size. The source area is usually given in mm^2. Finally, there is the issue of the spectral distribution. Some X-ray sources produce very smooth spectra, others have peaks at certain photon energies. So it matters, when making comparisons, what range of photon energies contribute to the measured intensity. The convention is therefore to define the photon energy range as a fixed relative energy bandwidth (BW), which has been chosen to be 0.1%. There are several reasons why the relative rather than the absolute bandwidth is chosen. One reason is that monochromator crystals are often perfect crystals, and as we shall see in Chapter 6 the relative bandwidth for a perfect crystal in symmetric reflection geometry is independent of the photon energy, and depends only on the Miller indices of the reflection. Altogether then, one defines the figure-of-merit for the source as:

$$\text{Brilliance} = \frac{\text{Photons/second}}{(\text{mrad})^2 \ (\text{mm}^2 \ \text{source area}) \ (0.1\% \ \text{BW})} \qquad (2.1)$$

The intensity in photons per second after the monochromator crystal is the product of the brilliance, angular divergences set by the horizontal and vertical apertures (in milli-radian), the source area (in mm^2), and the relative bandwidth of the monochromator crystal relative to 0.1%.

The brilliance is a function of the photon energy. The maximum brilliance from third generation undulators (see Fig. 1.1) is approximately 10 orders of magnitude higher than that from a rotating anode at the K$_\alpha$ line! This dramatic improvement has in many ways led to a paradigm shift in experimental X-ray science. Experiments inconceivable only a few decades ago are now performed on almost a routine basis.

---

[2]As we write, X-ray free-electron lasers, as described in Section 2.6, are entering service. While these have unique capabilities, and will undoubtedly allow new branches of science to develop, we believe that for the foreseeable future, synchrotron storage rings will remain the principal source for many types of important experiments.
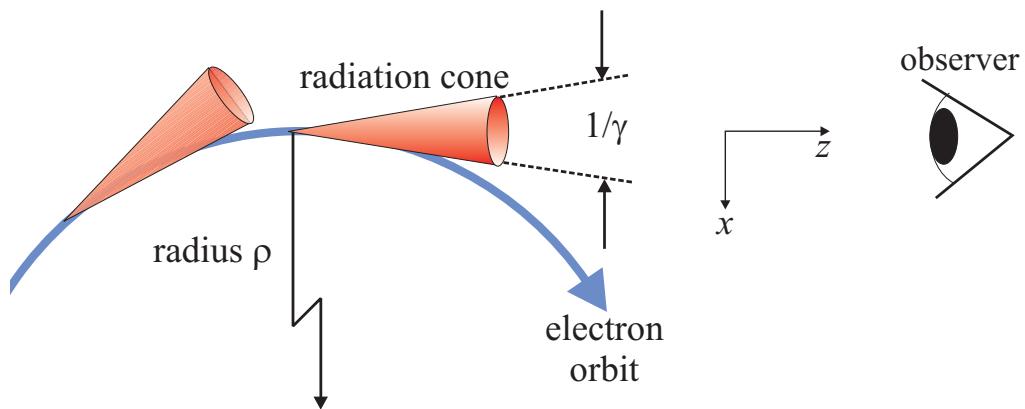
Fig. 2.2 A relativistic electron moving in a circular trajectory of radius ρ. The radiation emitted is confined to a narrow cone with an opening angle of $1/\gamma$ around the instantaneous velocity.

2.3   Synchrotron radiation from a circular arc

In this section we describe the basic characteristics of the radiation emitted by an electron moving in a constant magnetic field. The effect of the field is to accelerate the electron and bend its trajectory into a circular orbit, producing so-called bending magnet radiation in the process. While this type of radiation is not the most brilliant, it nonetheless has many useful properties that are widely exploited in synchrotron research.

A non-relativistic electron of momentum $\mathbf{p} = m\mathbf{v}$ moving in a constant magnetic field $\mathbf{B}$ experiences the Lorentz force $\mathbf{F} = d\mathbf{p}/dt = -e\mathbf{v} \times \mathbf{B}$. In response to this force the electron accelerates and moves in a circular orbit in a plane perpendicular to $\mathbf{B}$. The radius ρ of the orbit is determined by the magnetic field $\mathbf{B}$ in the following way. The magnitude of the Lorentz force is $ev\mathrm{B}$. For a non-relativistic particle this force is equal to the centripetal acceleration v^2/ρ times the mass m. With $m\mathrm{v} = \mathrm{p}$, one obtains $\mathrm{p} = \rho e\mathrm{B}$. This relation is also valid for relativistic particles, in which case p is equal to $\gamma m\mathrm{v}$, where $\gamma = \mathcal{E}_e/mc^2$, the electron energy in units of the rest mass energy. For the case of super-relativistic particles $v \cong c$ which pertains to synchrotrons, we have

$$\gamma\, m\, c = \rho\, e\, \mathrm{B} \tag{2.2}$$

so that in practical units the radius of an electron orbiting in a synchrotron is given by

$$\rho[\mathrm{m}] = 3.3 \frac{\mathcal{E}_e\,[\mathrm{GeV}]}{\mathrm{B}\,[\mathrm{T}]} \tag{2.3}$$

As discussed on page 8, the electric field radiated from an accelerating charge is directly proportional to the apparent acceleration. Hence an electron moving in a circular arc experiences a constant acceleration and radiates continuously throughout its entire orbit. However, as we shall see, the radiation from a relativistic charged particle moving in a circular orbit is compressed into tightly collimated cones of radiation, as indicated schematically in Fig. 2.2. The radiation from an
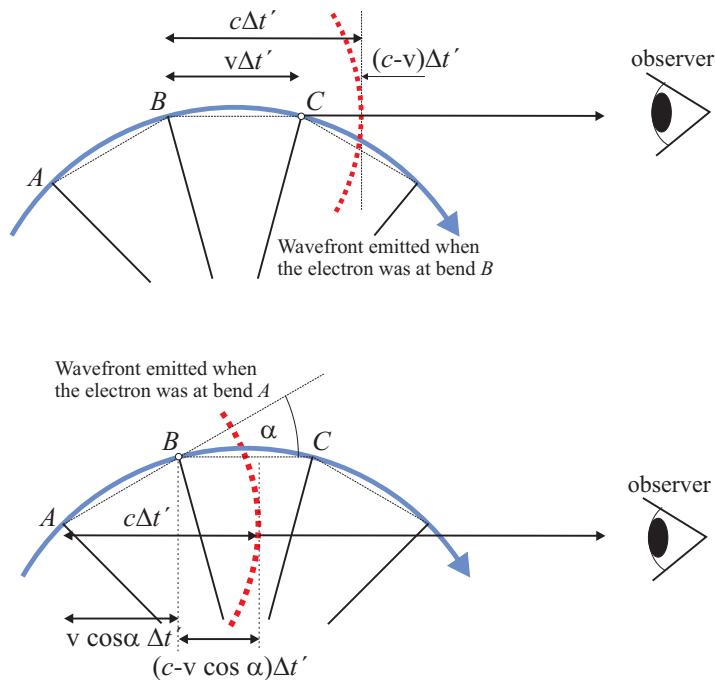
Fig. 2.3 A circular arc is approximated by straight segments connected by bends at A, B, C, etc. When the electron passes a bend, a wavefront (thick dotted line) is emitted and propagates with velocity c. The wavefront in the top (bottom) was emitted from bend B (A). The electron velocity is $\mathbf{v}$, and the time for the electron to travel from one bend to the next is $\Delta t'$. The observer experiences a time interval of $\Delta t = (c - v \cos \alpha) \Delta t'/c$ between wavefronts, where α is the angle between the electron velocity and the direction towards the observer.

electron orbiting at relativistic speeds in a circle can thus be likened to a sweeping search light. The characteristic features of the radiation depend on two key parameters: the cyclic frequency ω_o of the orbiting electron and $\gamma = \mathcal{E}_e/mc^2$.

The instantaneous direction of the radiation cone is that of the instantaneous velocity of the electron, and the opening angle of the cone is $\gamma^{-1} = mc^2/\mathcal{E}_e$. This is typically around 10^{-4}, or 0.1 milli-radian. The emitted spectrum is very broad, ranging from the far infrared to the hard X-ray region. However, the spectrum falls off quickly for photon frequencies higher than $\gamma^3 \omega_\mathrm{o}$. The angular frequency of an electron in the storage ring ω_o is typically of order 10^6 cycles per second, so the hard X-ray frequency cut-off is around 10^{18} cycles per second. We shall now show how one can understand these basic features from simple physical arguments. A few facts from the theory of relativity have to be recollected first, and these are given in the box on the facing page. The other important ingredient of basic physics we need is the Doppler effect.

2.3.1   The Doppler effect and the natural opening angle of synchrotron radiation

Rather than consider a circular path, we will first analyse the simpler case of an electron travelling on a path comprised of short straight segments, with abrupt bends at points A, B, C, etc., as shown in Fig. 2.3. Subsequently the limit will be taken where the straight sections become infinitesimally small and the path becomes a circular arc.

Relativistic formulae

The energy $\mathcal{E}_e$ of an electron at speed v is

$$\mathcal{E}_e = \frac{mc^2}{\sqrt{1 - \left(\frac{v}{c}\right)^2}}$$

It is convenient to use the electron energy γ, measured in units of its rest mass energy, $\gamma \equiv \mathcal{E}_e/mc^2$, and the speed β_e, measured in units of the velocity of light, $\beta_e \equiv v/c$. The formula above then reads

$$\gamma \equiv \frac{1}{\sqrt{1 - \beta_e^2}} \qquad (2.4)$$

The electron energy in a typical X-ray synchrotron storage ring is 5 GeV. The rest mass of an electron is 0.511 MeV, so γ is of order 10^4. We can therefore expand Eq. (2.4) to obtain:

$$\beta_e = \left[1 - \frac{1}{\gamma^2}\right]^{1/2} \cong 1 - \frac{1}{2\gamma^2} \qquad (2.5)$$

While in linear, uniform motion the electron does not radiate. At each bend it changes its velocity (but not its speed), and therefore it has a short period of acceleration during which it radiates. The observer is along the direction BC, and the time the electron spends in getting from one bend to the next is denoted $\Delta t'$. Consider in the top part of Fig. 2.3 the propagation of a wavefront emitted by the electron when passing the bend at B. During the time the electron spends in getting from B to C the wavefront has moved the distance $c\Delta t'$ towards the observer, at which point a new wavefront is emitted from C, which is $v\Delta t'$ closer to the observer than B. These two wavefronts will thus be $(c - v)\Delta t'$ apart, and the observer experiences[3] that they arrive within a time interval $\Delta t = (c - v)\Delta t'/c = (1 - \beta_e)\Delta t'$. The same kind of arguments can be made for the pair of wavefronts emitted when the electron was at A and B; the only difference is that the distance travelled by the electron towards the observer is $v\Delta t' \cos \alpha$, α being the angle between the velocity and the direction to the observer. The wavefront from A is therefore not $(c - v)\Delta t'$ ahead of the wavefront emitted from B, but a distance $(c - v \cos \alpha)\Delta t'$. In other words, the time compression of wavefronts – the Doppler effect – appears less pronounced to the observer.

The time interval, Δt, between wavefronts measured by the observer is related to the time interval $\Delta t'$ by

$$\Delta t = (1 - \beta_e \cos \alpha)\Delta t'$$

---

[3]Following our discussion of the field radiated by an accelerating charge on page 8, due to the finite velocity of light, it will again prove necessary to distinguish between the time t at which the radiation arrives at the observer, and the time t' at which it is emitted. The latter is often referred to as the retarded time, but here we shall also refer to it as the emitter time. In order to avoid a possible source of confusion, it is important to note that t and t' are both measured in one and the same inertial frame. In many other treatments of synchrotron radiation, use is made of Lorentz transformations to move between the rest frame of the electron and that of the observer, with space and time coordinates in the former often being denoted by primed quantities.
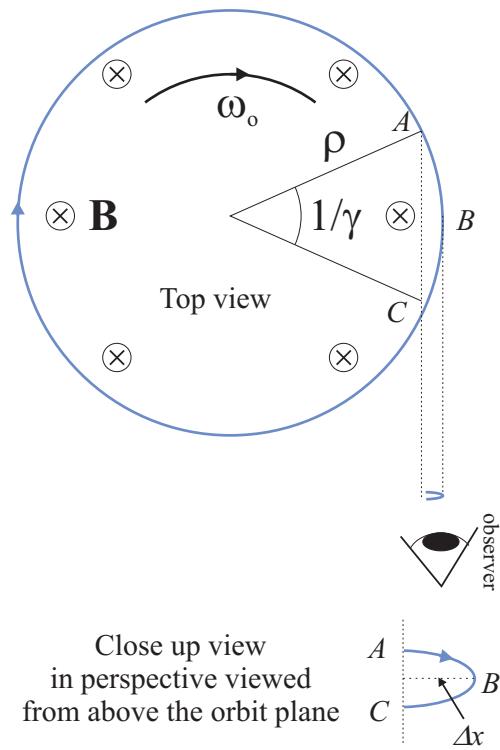
Fig. 2.4 An electron is kept in a circular orbit by the magnetic field **B**. An observer in the direction of the tangent at point B will, due to the Doppler effect, see the electron as having a large acceleration when it is between points A and C. The close-up view indicates that the observer will experience something that resembles half a period of an oscillation.

Since β_e and $\cos\alpha$ are both very close to unity they can be expanded

$$\Delta t \approx \left[1 - \left(1 - \frac{1}{2\gamma^2}\right)\left(1 - \frac{\alpha^2}{2}\right)\right]\Delta t'$$

which simplifies to read

$$\Delta t \approx \left[\frac{1 + (\alpha\gamma)^2}{2\gamma^2}\right]\Delta t' \tag{2.6}$$

With $\alpha \approx 0$ and $\gamma \approx 10^4$ the time compression of the wavefronts experienced by the observer is enormous. The Doppler effect is in fact maximal when $\alpha=0$, and has decreased by a factor of two when $\alpha = 1/\gamma$. This then explains why the natural opening angle of synchrotron radiation is of order γ^{-1}. Note that this is the opening angle in all directions. In the vertical plane the angular divergence is γ^{-1}, whereas in the horizontal plane the angular divergence of the fan of radiation depends on how long a segment of the circular arc is viewed by the observer.

Taking the limit $\Delta t' \to 0$, the general relation between the observer time t and the retarded (or
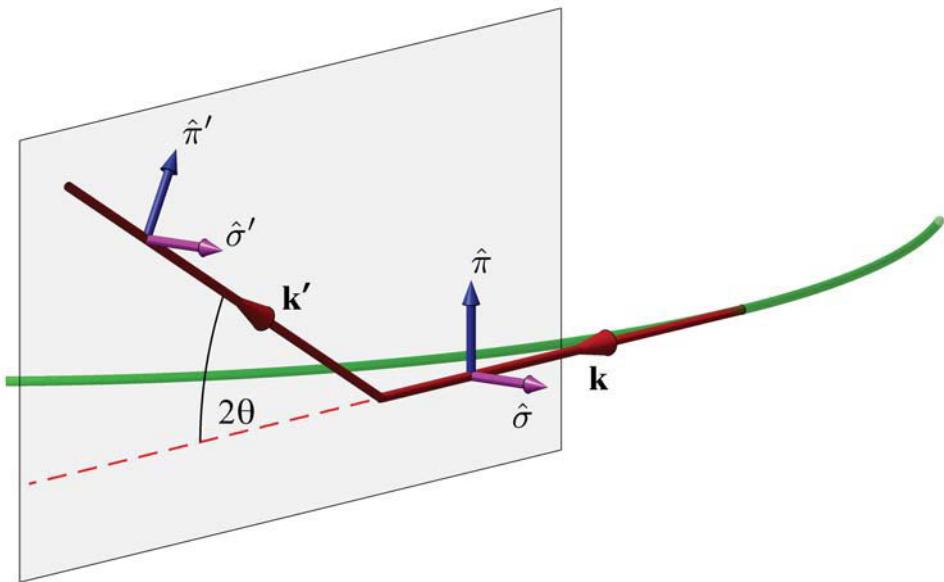
Fig. 2.5 Illustration of the vertical scattering geometry typically employed at synchrotrons. The component of the X-ray's electric field perpendicular to the scattering plane is labelled $\hat{\sigma}$, while the component in the plane is labelled $\hat{\pi}$. When viewed exactly in the orbit plane the radiation from an electron traversing a circular arc is purely $\hat{\sigma}$ polarized.

emitter) time t' is therefore given by the differential equation

$$\frac{dt}{dt'} = (1 - \beta_e \cos\alpha) \qquad (2.7)$$

where β_e is the electron velocity in units of c, and α is the angle between the instantaneous velocity and the direction to the observer. We shall return to the solution of this differential equation in Section 2.4.1.

An electron radiates during its entire cycle around its orbit, but an observer located in the direction of the tangent to point B (see Fig. 2.4) sees a significant amount of radiation only while the electron passes from A to C. This is because the amplitude of the far-field radiation is proportional to the apparent acceleration, which is itself overwhelmingly large when the electron is in the vicinity of B due to the enormous time compression given by Eq. (2.6). Thus in evaluating the radiation from a circular arc we are justified in restricting our considerations to segment $A - C$. (A quantitative estimate of the radiated flux from the arc segment $A - C$ is presented in Section 2.3.3.)

As well as being highly collimated, synchrotron radiation from a circular arc is also polarized. When viewed in the orbit plane of the synchrotron, the acceleration of the electron is strictly horizontal, and as electric field of the radiated field is parallel to the electron acceleration it is linearly polarized in the same plane. As discussed on page 9, the polarization factor P associated with Thomson scattering determines how different types of experiment are configured. Diffraction experiments, for example, are mostly performed utilising a vertical scattering plane (see Fig. 2.5), as in that case $P = 1$, and no correction has to be applied to the data. In general, the polarization state of the X-ray beam can be

decomposed into an orthogonal basis. By convention, the component perpendicular (parallel) to the scattering plane spanned by **k** and **k′** is labelled $\hat{\sigma}$ ($\hat{\pi}$).

When the electron trajectory is viewed out of the orbit plane the polarization of the emitted radiation is no longer linear. As can be seen in the lower part of Fig. 2.4, when the arc ABC is viewed from above the orbit plane, it appears as part of an ellipse with the electron orbiting clockwise. If looked at from below the orbit plane, on the other hand, A and C are interchanged. As the arrow must run from A to C via B, it is apparent that the electron now appears to move in a counter clockwise direction. Therefore when viewed out of the orbit plane the electron has non-zero angular momentum, which it imparts to the emitted X-rays. From this it may be concluded that the radiation viewed above the orbit plane has a right-handed circular component, whereas below the orbit plane the circular polarization is in the opposite sense of rotation. This subject is returned to in Section 7.3 on X-ray magnetic dichroism.

2.3.2 Characteristic frequency of synchrotron radiation

As an electron moves along the arc AC it generates an intense pulse of radiation of finite duration. Here we estimate the duration of that pulse Δt as witnessed by an observer viewing the motion of the electron as indicated in Fig. 2.4. The finite duration of the pulse in time implies, from the general property of Fourier transforms (see Appendix E), that there is a characteristic, cut-off frequency $\omega_c \sim 1/\Delta t$.

From the observer's point of view, the motion of the electron resembles one half of the period T of an entire oscillation. The time the electron spends in getting from A to C is $[\gamma^{-1}/(2\pi)]\,T = 1/(\gamma\omega_o)$, but the observer experiences the time to be $\sim \gamma^2$ shorter (Eq. (2.6)), i.e. $\Delta t \sim 1/(\gamma^3\omega_o)$. Thus the characteristic frequency ω_c is of order $\gamma^3\omega_o$. With ω_0 being typically of order a MHz, and γ around 10^4 for a third-generation synchrotron, bending magnet radiation has a characteristic frequency of around 10^{18} Hz, i.e. a wavelength of around 1 Å.

In a more rigorous treatment it can be shown that the characteristic frequency is given by $\omega_c = \left(\frac{3}{2}\right)\gamma^3\omega_o$. Since $\omega_o = 2\pi/T = 2\pi/(2\pi\rho/c) = c/\rho$, which by Eq. (2.2) is proportional to $B/\mathcal{E}_e$, the corresponding characteristic photon energy is given in practical units by

$$\hbar\omega_c[\text{keV}] = 0.665\,\mathcal{E}_e^2[\text{GeV}]\,B[\text{T}] \tag{2.8}$$

2.3.3 Flux, emitted power and the spectrum

The flux of photons emitted by an electron accelerated under the influence of a constant field in a bending magnet can be estimated by following arguments similar to those given in Section 1.2 where we derived the Thomson scattering cross-section. In both cases it is necessary to consider the power density of the radiated field. This is given by the magnitude of the Poynting vector $S = B_{\text{rad}}E_{\text{rad}}/\mu_0 = c\epsilon_0 E_{\text{rad}}^2$ with units of Wm^{-2}. The magnitude of the radiated electric field at a large distance R from the source in the case a single electron is $E_{\text{rad}} = \mathcal{A}e/(4\pi\epsilon_0 c^2 R)$, where $\mathcal{A}$ is the apparent acceleration (see Eq. (1.4)).

In the present context of a relativistic electron in a bending magnet, the acceleration d^2x/dt^2 is approximated by $\Delta x/(\Delta t)^2$, where Δx is the distance from B to the direct line from A to C in Fig. 2.4, and Δt is the time interval as seen by the observer that it takes for the electron to cover the arc length AC. From Fig. 2.4, the distance Δx can be approximated from $\Delta x = \rho(1 - \cos(\gamma^{-1}/2)) \sim \rho/\gamma^2$, while

the relevant time interval is $\Delta t \sim \rho/(c\gamma^3)$ (Section 2.3.2), so that the acceleration can be estimated as

$$\mathcal{A} = \frac{d^2x}{dt^2} \approx \frac{\Delta x}{(\Delta t)^2} \sim \frac{\rho/\gamma^2}{(\rho/c\gamma^3)^2} \sim \frac{\gamma^4 c^2}{\rho}$$

This equation reinforces our earlier comment that the apparent acceleration, and hence the radiated electric field, is massively boosted by the Doppler effect which gives rise to the factor of order γ^4.

The energy, $\mathcal{E}_{rad}$, radiated by the electron as it transits from A to C can then be calculated by multiplying S by product the of the area of the radiated field at the observer, equal to $R^2 \Delta\Omega$ with the solid angle $\Delta\Omega \sim \gamma^{-2}$, and the time interval Δt:

$$\begin{aligned}
\mathcal{E}_{rad} &= c\epsilon_0 \mathcal{A}^2 \left(\frac{e}{4\pi\epsilon_0 c^2 R}\right)^2 (R^2 \Delta\Omega)\Delta t \\
&\sim c\epsilon_0 \left(\frac{c^4\gamma^8}{\rho^2}\right)\left(\frac{e^2}{(4\pi\epsilon_0)^2 c^4 R^2}\right)(R^2\gamma^{-2})\frac{\rho}{c\gamma^3} \\
&= \frac{1}{4\pi}\frac{e^2}{4\pi\epsilon_0}\frac{\gamma^3}{\rho}
\end{aligned} \tag{2.9}$$

The number of photons emitted from the passage of a single electron, $\mathcal{N}_{rad}$, is of order $\mathcal{E}_{rad}/\hbar\omega_c$, and since the characteristic energy $\hbar\omega_c \sim \hbar(\gamma^3 c/\rho)$, one obtains from Eq. (2.9) that

$$\boxed{\mathcal{N}_{rad} \sim \frac{1}{4\pi}\frac{e^2/(4\pi\epsilon_0)}{\hbar c} = \frac{1}{4\pi}\alpha} \tag{2.10}$$

where $\alpha = e^2/(4\pi\epsilon_0\hbar c)$ is the fine structure constant. For a current I of electrons passing the point A per second, the photon flux is $\sim \alpha I/e$. This remarkably simple and elegant result[4] establishes that a current of relativistic electrons transiting a bending magnet radiates an enormous flux of photons, of order 10^{17} per Ampere, into a very narrow cone with an opening angle of $1/\gamma$.

We can also use Eq. (2.9) to obtain an expression for the power radiated by a current of electrons as it traverses a bending magnet. Equation (2.9) refers to the energy emitted from an electron path length of ρ/γ, so per unit length the energy is $\sim \gamma^4/\rho^2$. From Eq. (2.3) we have $\rho \propto \mathcal{E}_e/B$, and as $\gamma \propto \mathcal{E}_e$, we obtain a dependence of $\mathcal{E}_e^2 B^2$. This result is in agreement with a full analysis which provides an expression for the total radiated power in practical units of

$$\boxed{\mathcal{P}[\text{kW}] = 1.266\,\mathcal{E}_e^2[\text{GeV}]\,B^2[\text{T}]\,L[\text{m}]\,I[\text{A}]} \tag{2.11}$$

where L is the length of the electron trajectory through the bending magnet. The radiated power can be substantial, of order 1 MW for a third generation synchrotron, and has to be supplied to the electrons to keep them orbiting with the same energy.

Thus far we have not considered the exact spectral distribution of bending magnet radiation, other than to establish that it has a characteristic energy given by Eq. (2.8). The derivation of the spectral distribution involves a level of mathematical complexity not in keeping with the spirit of this book. (The interested reader should consult the references given in Further Reading at the end of this chapter.) It

---

[4]Here and elsewhere in this chapter we have borrowed heavily from the work of Kim: see under Further Reading.
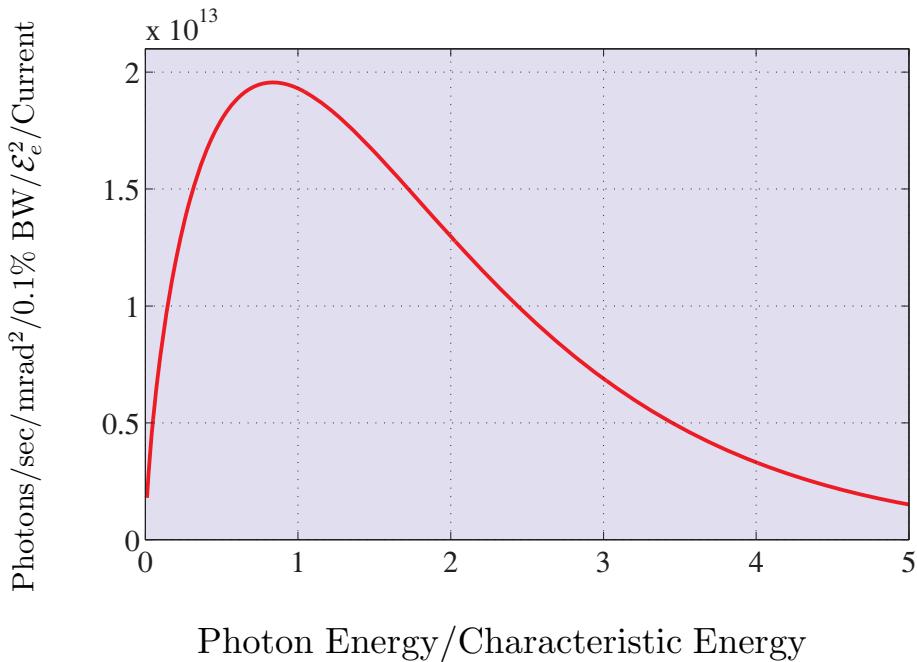
Fig. 2.6 The spectrum from a bending magnet, normalised by the square of the electron energy and the beam current. The abscissa is $x = \hbar\omega/(\hbar\omega_c)$, i.e. the photon energy normalized by the characteristic energy $\hbar\omega_c = \left(\frac{3}{2}\right)\gamma^3\hbar\omega_o$. The numerical formula is $1.33 \times 10^{13} x^2 K_{2/3}^2(x/2)$, where $K_{2/3}(x/2)$ is a modified Bessel function. The electron energy $\mathcal{E}_e$ is in GeV, and the beam current in Amperes.

transpires that the spectrum from a bending magnet is a universal function of (ω/ω_c) and is plotted in Fig. 2.6. It scales with the square of the electron energy, $\mathcal{E}_e$, and is proportional to the current I in the storage ring. In practical units, the spectral distribution of bending magnet radiation in the horizontal plane can be expressed as

$$\frac{\text{Photons/second}}{(\text{mrad}^2)\,(0.1\%\ \text{BW})} = 1.33 \times 10^{13}\mathcal{E}^2[\text{GeV}]I[\text{A}]x^2 K_{2/3}^2(x/2) \tag{2.12}$$

where $x = \omega/\omega_c$ and $K_{2/3}(x/2)$ is a modified Bessel function.

In a storage ring the electrons are stored in bunches. For certain applications one may choose to have a single bunch, but in general the storage ring is filled with a sequence of bunches. For example, the duty cycle for one bunch in a 300 m long storage ring is 1 μs, and as the bunch length is of order a centimetre, the pulse duration from the passage of one bunch is of order of a hundred pico-seconds. The resulting synchrotron radiation is consequently pulsed with a sub-nano second pulse width and a duty cycle in the μs range.

2.3.4   Example: bending magnet radiation at the ESRF

The European Synchrotron Radiation Facility (ESRF) in Grenoble, France, was the world's first third-generation X-ray source, and started regular operation for users in 1994. The storage ring consists of a number of straight sections where insertion devices may be placed, and in between these the electron beam passes through bending magnets where the electrons describe circular arcs.

The energy of the electrons in the storage ring at the ESRF is $\mathcal{E}_e = 6$ GeV, the ring electron current is typically around 200 mA, and the bending magnets produce a field of 0.8 T. Assume that the bending magnet is viewed through a 1×1 mm^2 aperture at 20 m from the tangent point of the arc. The angular acceptance of the aperture is 1/20=0.05 mrad, somewhat smaller than the natural divergence of the radiation. The opening angle of the synchrotron beam from an ESRF bending magnet is $1/\gamma = 5.11 \times 10^5/6 \times 10^9 = 0.08$ mrad.

The radius of the electron orbit through the bending magnet can be found from Eq. (2.3). The result is

$$\rho = 3.3 \times \frac{6}{0.8} = 24.8 \text{ m}$$

The characteristic energy is given in Eq. (2.8) and is equal to

$$\hbar\omega_c = 0.665 \times 6^2 \times 0.8 = 19.2 \text{ keV}$$

In Fig. 2.6 the generic spectrum of a bending magnet is shown. To calculate the peak flux at the characteristic energy it is necessary to multiply by the solid angle of the aperture, the square of the electron energy and the current. The peak flux is then

$$\text{Flux} = 1.95 \times 10^{13} \times \left(\frac{1}{20}\right)^2 \times 6^2 \times 0.2$$
$$= 3.5 \times 10^{11} \text{ photons/s/0.1\% BW}$$
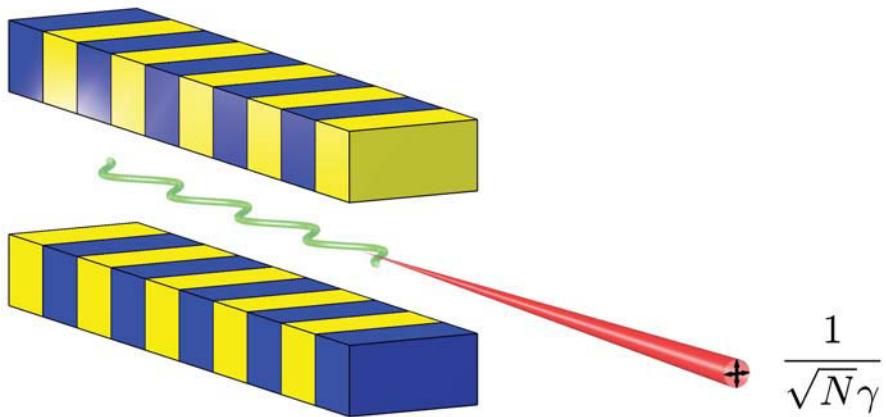
in a bandwidth of 0.1%. According to Eq. (2.11) the observed radiated power from the bending magnet is determined by the length, L, of the electron orbit viewed through the aperture. As the radiation is viewed from the tangent point, L is equal to the radius of the electron orbit, ρ, multiplied by the acceptance angle in the horizontal plane of the aperture, i.e. L=24.8 m $\times$ 0.05 mrad= 1.24 mm. The power radiated is then

$$\mathcal{P} = 1.266 \times 6^2 \times 0.8^2 \times 1.24 \times 10^{-3} \times 0.2 = 7.3 \text{ W}$$

The observed power is smaller than this value for a number of reasons. First, the value given above is the value integrated over the vertical direction, and it is therefore necessary to correct for the finite angular acceptance of the slit. Second, there may be beryllium vacuum windows, and possibly other components such as filters, etc., in a beamline at a synchrotron which act to dissipate the power.

Beamlines which use a bending magnet as a radiation source usually make use of focusing optics to collect a fan of the emitted radiation in the horizontal plane. Typically the optics are designed to collect and focus a fan of 1 mrad, rather than the 1/20 mrad in our example above. The values of the flux and power given above are then increased by a factor of 20.

(a) Undulator

$$\frac{1}{\sqrt{N}\gamma}$$

$$\frac{1}{\sqrt{N}\gamma}$$

(b) Wiggler

$$\frac{1}{\gamma}$$

$$\frac{K}{\gamma}$$
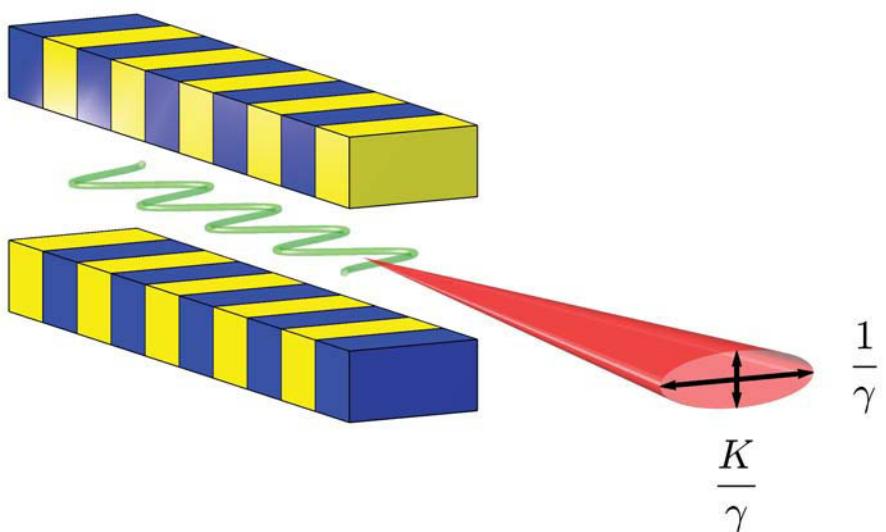
Fig. 2.7 Radiation from insertion devices: (a) an undulator, (b) a wiggler. The difference in the performance of these devices arises from differences in the maximum angles of the electron oscillations in the horizontal plane: K is around 20 for a wiggler, and 1 for an undulator. The consequence is that the radiation cone from an undulator is compressed by a factor of approximately $1/\sqrt{N}$ (Eq. (2.20)) relative to the natural opening angle of synchrotron radiation, $1/\gamma$. The number of periods N is typically around 50.

2.3.5   Summary: bending magnet radiation

We summarize the salient properties of the radiation from a circular arc as follows:

(a) The radiation power is particularly intense at the moment when the instantaneous electron velocity points directly towards the observer, since at that instant the Doppler effect is maximal.

(b) This glimpse of radiation dies away when the angle between the direction to the observer and the electron velocity is of order γ^{-1}.

(c) A typical frequency in the spectrum is γ^3 times the cyclic frequency of the orbiting electron in the storage ring.

(d) The on-axis radiation is linearly polarized in the horizontal plane, whereas a circularly component is obtained out of the orbit plane, with opposite helicities above and below the plane.

(e) The radiation is pulsed, the pulse duration as seen through a pin hole being the electron bunch length divided by c.

2.4   Undulator radiation
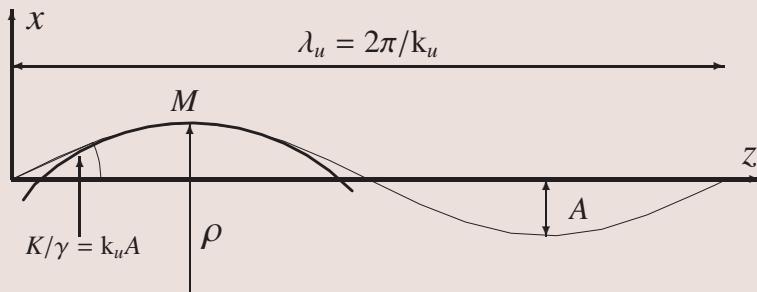
There is a much more efficient way to produce X-ray beams from a synchrotron than by having the electrons orbiting in a purely circular arc. In a typical storage ring there are straight sections followed by circular arc segments. In any one of these straight sections a device can be inserted that forces the electron to execute oscillations in the horizontal plane as it traverses through the section. This is achieved by an array of magnets which produces a field that alternates from up to down along the path.

It is possible to construct an insertion device such that the radiation emitted by a given electron at one oscillation is in phase with the radiation from the following oscillations. This implies that the amplitudes of the radiated waves are first added, and then the sum is squared to obtain the resulting intensity. An insertion device designed to operate in this way is known as an undulator, for which a schematic is shown in Fig. 2.7. A necessary condition for the coherent addition of amplitudes is that electrons transiting an undulator execute small angular oscillations on a scale set by γ^{-1}. The coherent addition of amplitudes implies a monochromatic spectrum (with harmonics), but one that is only quasi-monochromatic due to the finite number of periods in an undulator.

2.4.1   The undulator parameters

For bending magnet radiation the basic parameters are γ, the cyclic frequency and the bending radius ρ. For undulator radiation, the basic parameters are γ and the undulator spatial period λ_u. In addition we need something to characterize the amplitude of the oscillations. It could be the amplitude itself, but it turns out to be more convenient to use the maximum angular deviation from the undulator axis, as indicated in the drawing in the box on the next page. This maximum angle is some dimensionless number, of order unity and denoted K, times the natural opening angle for synchrotron radiation, γ^{-1}. Thus, in addition to γ and λ_u, we shall use the parameter K defined in this way to characterize the undulator. From Eq. (2.2) we have an expression for ρ in terms of the magnetic field, and from the drawing in the box on the following page we have an alternative expression for ρ in terms of $K\gamma^{-1}$, so

Properties of small-amplitude sinusoidal waves

In the vicinity of M we can approximate the cosine wave by a circle of radius ρ, which for the amplitude $A \ll \lambda_u$ can be related to A and k_u from the following considerations:

Circle: $\qquad x + (\rho - A) = \sqrt{\rho^2 - z^2} \quad \Rightarrow \quad x \cong A - \dfrac{1}{2}\dfrac{z^2}{\rho}$

Cosine path: $\qquad x = A \cos(k_u z) \quad \Rightarrow \quad x \cong A - \dfrac{A}{2}k_u^2 z^2$

Identifying the two expressions leads to the result $\rho \cong (A k_u^2)^{-1}$.

The electron path length S for one period of the undulator is evaluated as

$$S \cdot \lambda_u = \int ds \qquad\quad = \int \sqrt{1 + (dx/dz)^2}\, dz$$
$$\cong \lambda_u[1 + (A k_u)^2/4] \quad = \lambda_u[1 + K^2\gamma^{-2}/4]$$

one finds K readily in terms of the maximum magnetic field B_0 in the undulator as:

$$K = \frac{eB_0}{mck_u} = 0.934\,\lambda_u\,[\text{cm}]\,B_0\,[\text{T}] \tag{2.13}$$

where $k_u = 2\pi/\lambda_u$.

2.4.2   The fundamental wavelength, λ_1

An expression for the fundamental wavelength λ_1 in the undulator spectrum is now derived. It is a simple matter to find the relation between λ_1 and the undulator period λ_u. Consider, as shown in Fig. 2.8, one undulation of the electron path. At emitter time $t' = 0$ the electron is at point A. The electron is one undulation further downstream at $t' = T'$. The signal from A is then at a position $c\,T'$ and the condition for coherence is that $(c\,T' - \lambda_u)$ is one wavelength λ_1 (or a multiple thereof). The electron path length between A and B is a factor S larger than the period λ_u, so $T' = S\,\lambda_u/\text{v}$ or $cT' = (S/\beta_e)\lambda_u$. In the box on this page the path length is derived for one period in the limit of small amplitude oscillations.
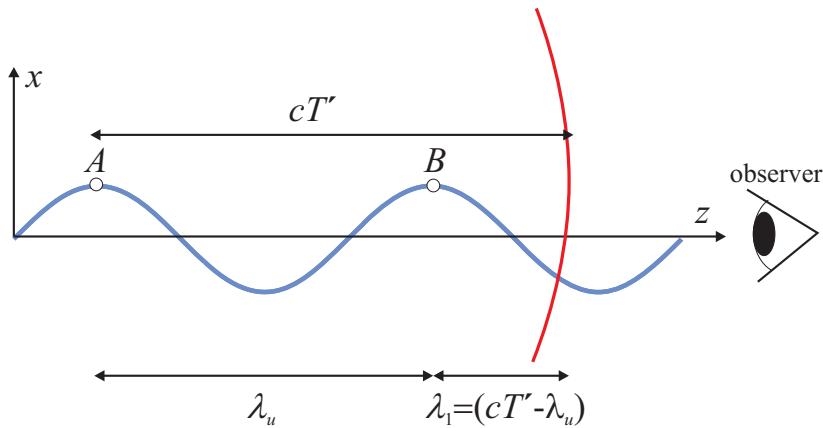
Fig. 2.8 Constructive interference occurs when the wavefront emitted by the electron when it was at A is one wavelength λ_1 ahead of the wavefront emitted by the electron when it reaches B. This is then the fundamental wavelength emitted from the undulator.

Altogether then we find

$$\lambda_1(\theta = 0) = \lambda_u(\frac{S}{\beta_e} - 1) \quad \xrightarrow[S=1+\gamma^{-2}K^2/4]{} \quad \frac{\lambda_u}{2\gamma^2}(1 + \frac{K^2}{2}) \tag{2.14}$$

Here it has been tacitly assumed that the direction of observation is on-axis – if the observation direction had been at angle θ with the undulator axis, then $(S/\beta_e - 1)$ should be substituted by $(S/\beta_e - \cos\theta)$ with the result

$$\lambda_1(\theta) = \lambda_u(\frac{S}{\beta_e} - \cos\theta) \quad \xrightarrow[S=1+\gamma^{-2}K^2/4]{} \quad \frac{\lambda_u}{2\gamma^2}(1 + \frac{K^2}{2} + (\gamma\theta)^2) \tag{2.15}$$

It has been shown above that γ^{-2} is of order 10^{-8}, so that with λ_u of order 1 cm, λ_1 becomes of order an Ångström, and is hence in the X-ray region. It is also important to note that the radiated, first-order wavelength λ_1 is tuneable: by changing the magnetic field by varying the gap between the poles, one changes K according to Eq. (2.13), and thereby the wavelength in accordance with Eq. (2.14). Somewhat counter-intuitively a larger field produces a softer X-ray fundamental.

2.4.3 Higher harmonics

Let us now look at the time dependence of the transverse electron oscillations, both in terms of the emitter time t' and in terms of the observer time t. The fundamental differential equation relating t' to t has already been derived (Eq. (2.7)). Here it is rewritten in terms of a unit vector $\mathbf{n}$ pointing towards the observer, and the instantaneous velocity vector $\boldsymbol{\beta}_e$:

$$\frac{dt}{dt'} = 1 - \mathbf{n} \cdot \boldsymbol{\beta}_e(t')$$

It is necessary to distinguish between the angle φ in the horizontal plane where the undulations occur, and the vertical angle ψ, the combination of which gives the total deviation angle θ. We assume that
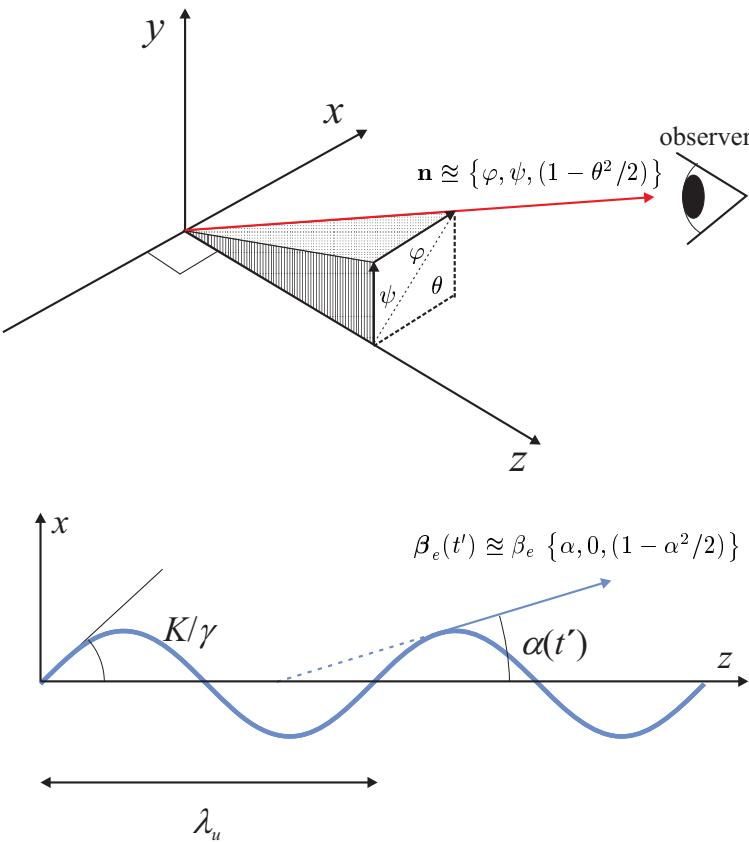
Fig. 2.9 The electron undulations take place in the horizontal $x - z$ plane. The direction to the observer is at angle ψ from the horizontal plane and at a horizontal angle φ from the undulator axis. The resulting angle θ is then given by $\theta^2 = \psi^2 + \varphi^2$ and the unit vector $\mathbf{n}$ has the coordinates as indicated. The other vector of interest is the velocity vector $\boldsymbol{\beta}_e(t')$. Its angle with the z-axis varies sinusoidally, or rather as a $\cos(\omega_u t')$, with a maximum value of K/γ.

both φ and ψ are small. The geometry is shown in the top part of Fig. 2.9. Since $\mathbf{n}$ is a unit vector it has the coordinates

$$\mathbf{n} = \left\{\varphi, \psi, \ \sqrt{1 - (\varphi^2 + \psi^2)}\right\} \cong \left\{\varphi, \psi, (1 - \theta^2/2)\right\}$$

The components of the velocity vector can be written in terms of the instantaneous angular deviation $\alpha(t')$ as

$$\boldsymbol{\beta}_e(t') = \beta_e \left\{\alpha, 0, \ \sqrt{1 - \alpha^2}\right\} \cong \beta_e \left\{\alpha, 0, (1 - \alpha^2/2)\right\}$$
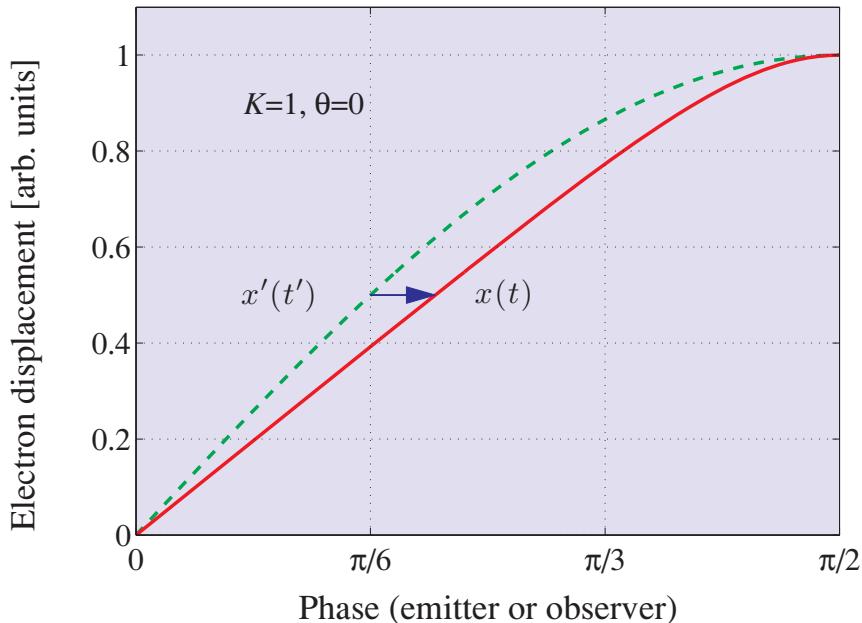
Fig. 2.10 Construction to show the relationship between the displacement as a function of emitter time for the electron (dashed sinusoidal line) and observer time (solid line). For example, the difference between the emitter, $\omega_u t'$, and observer, $\omega_1 t$, phases at the point $\omega_u t' = \pi/6$ is represented by the arrow (see Eq. (2.18)).

so that the differential equation for dt/dt' becomes

$$\frac{dt}{dt'} = 1 - \mathbf{n} \cdot \boldsymbol{\beta}_e(t') \cong 1 - \beta_e \left[\alpha\,\varphi + (1 - \theta^2/2 - \alpha^2/2)\right]$$

$$\cong 1 - (1 - \gamma^{-2}/2)\left[\alpha\,\varphi + (1 - \theta^2/2 - \alpha^2/2)\right]$$

$$\cong \frac{1}{2}\left[\gamma^{-2} + \theta^2 + \alpha^2(t')\right] - \alpha(t')\,\varphi \tag{2.16}$$

where $\beta_e = 1 - \gamma^{-2}/2$ from Eq. (2.5). The solution to this equation is

$$\omega_1 t = \omega_u t' + \frac{K^2/4}{[1 + (\gamma\theta)^2 + K^2/2]}\,\sin(2\omega_u t') - \frac{2K\gamma}{[1 + (\gamma\theta)^2 + K^2/2]}\,\varphi\,\sin(\omega_u t') \tag{2.17}$$

where $\omega_u t'$ and $\omega_1 t$ are the phases of the displacements with respect to emitter and observer time, respectively. The derivation is given in the box on the following page.

We can use the solution given in Eq. (2.17) to estimate quantitatively the content of higher harmonics in the undulator spectrum in the following way. The electron displacement varies sinusoidally in emitter time, but the observed displacement will, in general, have a different time dependence according to Eq. (2.17). Only in the limit $K \to 0$ will $\omega_1 t$ and $\omega_u t'$ be proportional to one another over an entire period, and only in this limit will the displacement also appear sinusoidal to the observer. Let us discuss a numerical example to understand how the observer in general experiences deviations from harmonic time variation. For simplicity the example is restricted to the case of on-axis radiation, i.e. $\theta = \varphi = 0$,

Solution of the differential equation (2.16)

With a sinusoidal path $x' = (K\gamma^{-1})k_u^{-1}\sin(k_u z)$, which has the required maximal deviation angle $(dx'/dz)_{max} = (K\gamma^{-1})$, one finds that the general deviation angle α is

$$\alpha \approx \tan(\alpha) = \frac{dx'}{dz} = (K\gamma^{-1})\cos(k_u z) = (K\gamma^{-1})\cos(\omega_u t')$$

Therefore $\alpha^2/2$ in Eq. (2.16) can be expressed as

$$\frac{\alpha^2}{2} = \frac{1}{2}(K\gamma^{-1})^2\cos^2(\omega_u t') = \frac{1}{4}(K\gamma^{-1})^2[1 + \cos(2\omega_u t')]$$

and the differential equation reads

$$\frac{dt}{dt'} = \frac{\gamma^{-2}}{2}[1 + (\gamma\theta)^2 + K^2/2] + \frac{(K\gamma^{-1})^2}{4}\cos(2\omega_u t')$$
$$- (K\gamma^{-1})\varphi\cos(\omega_u t')$$

This expression can be simplified by introducing the parameter χ, where

$$\chi = [1 + (\gamma\theta)^2 + K^2/2]$$

and multiplying both sides in the differential equation with $\omega_u dt' = d(\omega_u t')$ we obtain

$$\omega_u dt = \frac{\gamma^{-2}}{2}\chi d(\omega_u t') + \frac{\gamma^{-2}}{2}\frac{K^2}{2}\cos(2\omega_u t')d(\omega_u t')$$
$$- \frac{\gamma^{-2}}{2}(2K\gamma\varphi)\cos(\omega_u t')d(\omega_u t')$$

Further, by introducing the frequency ω_1 where

$$\omega_1 = \omega_u(2\gamma^2/\chi)$$

and multiplying by $2\gamma^2/\chi$ gives

$$d(\omega_1 t) = d(\omega_u t') + (K^2/2)\chi^{-1}\cos(2\omega_u t')d(\omega_u t')$$
$$- 2K\gamma\chi^{-1}\varphi\cos(\omega_u t')d(\omega_u t')$$

which is readily integrated to give

$$\omega_1 t = \omega_u t' + (K^2/4)\chi^{-1}\sin(2\omega_u t') - 2K\gamma\chi^{-1}\varphi\sin(\omega_u t')$$

and a value of $K=1$ is chosen as the undulation parameter. The solution Eq. (2.17) then reads

$$\omega_1 t = \omega_u t' + \left(\frac{1}{4}\right)\left(\frac{2}{3}\right)\sin(2\omega_u t') = \omega_u t' + \left(\frac{1}{6}\right)\sin(2\omega_u t') \tag{2.18}$$

The emitter displacement $x'(t')$ is proportional to $\sin(\omega_u t')$, which (in arbitrary units) is represented by the dashed curve in Fig. 2.10, when plotted against the emitter phase $\omega_u t'$. When plotted against the observer phase $\omega_1 t$ the result is the solid curves, $x(t)$. The two curves of course coincide when $\omega_1 t = \omega_u t'$, i.e. at $\omega_u t' = 0$ or at $\pi/2$, but differ at other points. For example, when $\omega_u t' = \pi/6$, the displacement is $\sin(\pi/6) = 1/2$, and $\omega_1 t$ is larger than $\omega_u t'$ by the amount $\sin(\pi/3)/6$, as indicated by the arrow. Hence by writing a simple computer program it is possible to generate the displacement as it appears to the observer. The resulting apparent displacement can then be resolved into Fourier components and the apparent acceleration calculated, since from elementary considerations it is expected that the apparent acceleration is proportional to the square of the frequency times the apparent displacement. Then as the amplitude of the observed radiation is proportional to the apparent acceleration, the observed undulator spectrum for any K and for any angle (φ, ψ) can be computed.

By way of example, in Fig. 2.11(a)$\star$ we plot the transverse displacement for $K = 1$, 2 and 5 as seen by an on-axis observer. The displacement is shown both versus emitter time t', or rather the emitter phase $\omega_u t'$, (dashed curves), for which the variation is sinusoidal, and versus observer time t, or rather the observer phase $\omega_1 t$, (full line). It is evident that the observed displacement, $x(t)$, deviates more and more from a sinusoidal variation the larger the value of K. This immediately implies that the frequency spectrum is dominated by the first harmonic at low K, but as K increases the spectrum acquires a successively greater content of higher harmonics. In Fig. 2.11(c)$\star$ the on-axis, $K = 2$, displacement seen by the observer is decomposed into its Fourier components with the contributions from the first three odd harmonics plotted. This allows us to estimate the intensity of the harmonics from the square of the acceleration, which is itself proportional to the displacement multiplied by the frequency (or harmonic number) squared. The results of this exercise, shown in Fig. 2.11(d)$\star$, illustrate that the intensities of higher harmonics do not decrease with harmonic number, in this case illustrated for $K = 2$. One consequence of this is that higher order undulator harmonics can be exploited in experiments requiring high energy X-ray photons.

A particular point of interest is the symmetry of the electron displacement as it appears to an on-axis observer: the curves are symmetric around $\pi/2$, $3\pi/2$, etc. This implies that all even harmonics vanish. Figure 2.11(b)$\star$ shows the electron displacement as seen from the observer in the off-axis case with $\psi = 0$, and $\varphi = \theta = \gamma^{-1}$, and for $K = 2$. Now it is apparent that the symmetry around $\pi/2$, $3\pi/2$, etc., is broken, and as a result even harmonics can be expected to appear in the spectrum.

2.4.4 Monochromaticity and angular collimation

So far we have only discussed one oscillation of an electron in the undulator, although in deriving the coherence condition (Eq. (2.14)) it was tacitly assumed that if there was coherence between waves emitted from A and B, then there was also coherence between waves from all subsequent oscillations in the undulator. The coherence condition, however, does not imply that the undulator emits perfectly monochromatic radiation. An electron traversing through an undulator of N periods produces a train of radiation pulses at the extremal points of its trajectory. As the pulse train is of finite duration, this implies that it also has a finite frequency, or wavelength, distribution proportional to $1/N$. (See, for example, our discussion of the characteristic frequency of bending magnet radiation in Section 2.3.2.)

The monochromaticity of undulator radiation can be derived by evaluating the total radiation amplitude from the pulse train. This involves performing a sum over the contributions from each
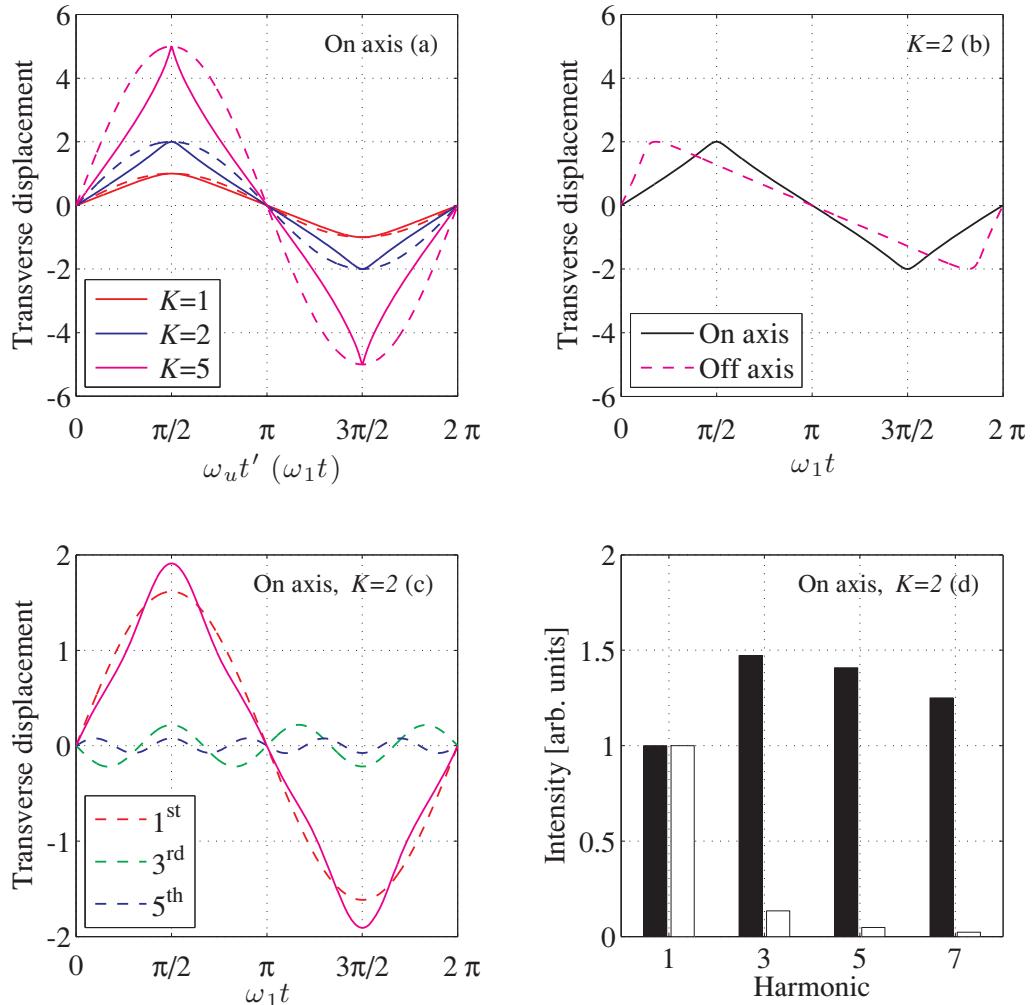
Fig. 2.11 ⋆ Undulator characteristics. (a) The transverse displacement of the electron which is sinusoidal versus emitter phase (dashed lines) adopts a progressively more triangular shape versus observer phase (solid lines) as K is increased. (b) On-axis the observed displacement is symmetric around $\omega_1 t = \pi/2$, $3\pi/2$, etc. (solid line), while off axis in the horizontal plane (here with $\psi = 0$ and $\varphi = 1/\gamma$) this symmetry is broken (dashed lines). Thus when the off-axis curve is Fourier transformed even harmonics are produced. For the sake of definiteness, a value of $K = 2$ was used in these calculations. (c) The on-axis $K=2$ displacement is decomposed into first, third and fifth harmonics; their sum is indicated by the full line. (d) The calculated intensities in arbitrary units observed on axis for the first four odd-order harmonics for $K = 2$ (black bars). The intensity is proportional to the square of the apparent acceleration which here is calculated from the displacement (white bars) multiplied by the frequency, or harmonic number, squared.

undulator period, taking into account the relevant phase factors. The total amplitude of the radiation field is then the radiation from a single undulator period multiplied by a phase factor sum of the form

$$S_N(\omega) \equiv \sum_{n=0}^{N-1} e^{in\omega T}$$
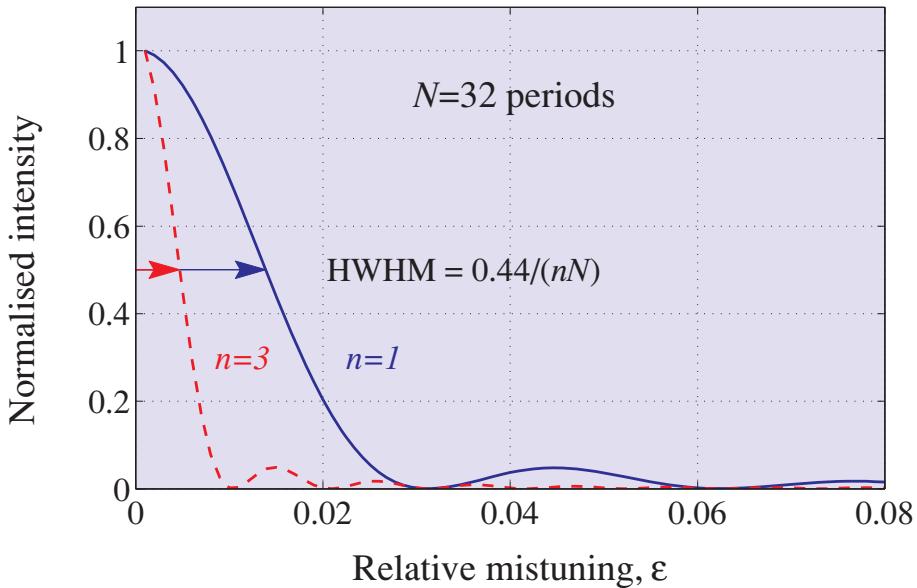
Fig. 2.12 Monochromaticity of the first ($n = 1$) and third ($n = 3$) harmonic for an undulator with $N =32$ periods as seen through an on-axis pin hole from a zero emittance source. The monochromaticity half width at half maximum (HWHM) is approximately equal to $0.44/(nN)$.

This phase factor sum is a particular example of a discrete Fourier transform which can be evaluated as shown in the box on the next page with the result that

$$|S_N(\omega)| = \frac{\sin(N\omega T/2)}{\sin(\omega T/2)}$$

Now suppose that we consider a wavelength, or a frequency for that matter, which has a relative deviation of ϵ from the coherence condition:

$$\omega = \omega_1(1 + \epsilon)$$

where ω_1 is the frequency of the first harmonic. The phase factor sum becomes

$$\left|S_{N,1}(\epsilon)\right| = \frac{\sin(\pi N \epsilon)}{\sin(\pi \epsilon)}$$

with $\epsilon = (\omega - \omega_1)/\omega_1 = \Delta\omega/\omega_1 = \Delta\lambda/\lambda_1$. This result can be generalized to the n'th harmonic to give

$$\left|S_{N,n}(\epsilon)\right| = \frac{\sin(\pi N n \epsilon)}{\sin(\pi n \epsilon)} \quad \text{now with} \quad \omega = n\omega_1(1 + \epsilon)$$

The radiated intensity is proportional to $\left|S_{N,n}\right|^2$ and this is normalized by N^2 and plotted in Fig. 2.12 for $N = 32$ with $n=1$ and $n=3$. The full width at half maximum (FWHM) is approximately $0.88/nN$. In other words the monochromaticity ($\Delta\lambda/\lambda$) of undulator radiation is inversely proportional to the number

Phase factor summation and the geometrical series

Throughout this book we shall be interested in evaluating sums over N phase factors of the form

$$S_N(x) = \sum_{n=0}^{N-1} e^{i\,2\pi n x}$$

with x a continuous variable. This is nothing other than the geometrical series

$$S_N = \sum_{n=0}^{N-1} k^n = 1 + k + k^2 + \cdots + k^{N-1} = \frac{1 - k^N}{1 - k}$$
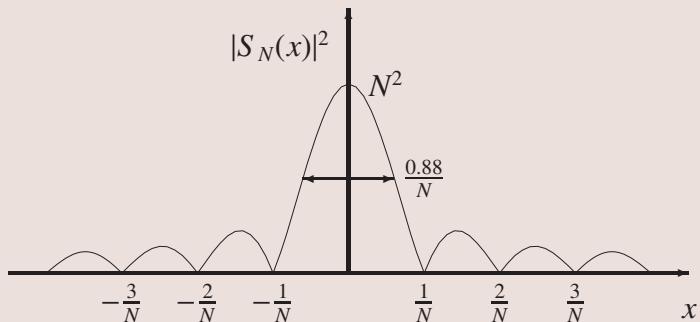
The proof follows once it is realised that $S_N - S_{N-1} = k^{N-1}$ and $kS_{N-1} + 1 = S_N$. The sum is convergent in the limit $N \to \infty$ if and only if $|k| < 1$, for which

$$S_\infty = \frac{1}{1 - k}$$

We can now evaluate the sum over phase factors as

$$S_N(x) = \frac{1 - e^{i\,2\pi N x}}{1 - e^{i\,2\pi x}} = \frac{e^{-i\pi N x} - e^{i\pi N x}}{e^{-i\pi x} - e^{i\pi x}} \frac{e^{i\pi N x}}{e^{i\pi x}}$$

$$= \frac{\sin(\pi N x)}{\sin(\pi x)} e^{i(N-1)\pi x}$$

and below we plot its modulus squared.

The full width at half of the maximum value (FWHM) is approximately $0.88/N$.

of periods N and to the harmonic index n:

$$\boxed{\frac{\Delta\omega}{\omega_n} = \frac{\Delta\lambda}{\lambda_n} \approx \frac{1}{nN}} \qquad (2.19)$$

Thus, although undulator radiation is not ideally monochromatic, it can be said to be quasi-monochromatic with a typical bandwidth of around 1%. This property of undulator radiation stands in stark contrast with the broad spectral distribution of bending magnet radiation (Fig. 2.6). The quasi-monochromatic, and tuneable, nature of undulator radiation means that experiments that do not require the typical monochromatic bandwidth of 0.01% delivered by perfect crystal optics (see Chapter 6) can benefit greatly from the flux enhancement associated with forgoing the monochromator and using directly the more relaxed bandwidth delivered by an undulator.

It is also important to understand how the angular collimation of undulator radiation compares with the natural opening angle γ^{-1} of bending magnet radiation. For an undulator, off-axis observation implies a change in the coherence condition, which means that a finite θ (see Fig. 2.9) corresponds to an offset in wavelength. Quantitatively it follows from Eq. (2.14) and (2.15) that

$$\lambda_1(\theta) = \lambda_1(0)\left[1 + \frac{(\gamma\theta)^2}{1 + K^2/2}\right] \equiv \lambda_1(0)\left[1 + \epsilon_\theta\right]$$

so a certain value of θ corresponds to a relative offset ϵ_θ in wavelength. Above it was shown that a relative mistuning of the frequency or wavelength by ϵ implied that the radiated intensity had a FWHM of approximately $1/nN$. It can therefore be concluded that the FWHM in θ must fulfil the equation

$$\epsilon_\theta = \frac{(\gamma\theta_{\mathrm{FWHM}})^2}{1 + K^2/2} \cong \frac{1}{nN}$$

which can be rearranged to yield

$$\boxed{\theta_{\mathrm{FWHM}} \approx \frac{1}{\gamma}\sqrt{\frac{1 + K^2/2}{nN}}} \qquad (2.20)$$

There is therefore a substantial reduction in the angular divergence of undulator radiation compared with the natural divergence γ^{-1} of synchrotron radiation. As sketched in Fig. 2.7, this reduction is independent of the azimuthal angle relative to the undulator axis.

In comparing with experiments one has to consider the effect of the finite angular divergence of the *electron* beam. This can be added in quadrature to the intrinsic divergence as given by Eq. (2.20) in order to obtain the observed divergence. The electron beam divergence within the plane of undulation is usually different from that in the perpendicular direction, so the observable synchrotron radiation divergence will not be symmetric around the undulator axis. These issues are further explored in Section 2.4.6.

2.4.5   Helical undulators

The *linear* undulator that has been discussed so far in this section is the most common insertion device used at present day synchrotron facilities, but it is by no means the only one. In some applications it is

useful to have an undulator with specific characteristics, for example one that is capable of producing circularly polarized instead of linearly polarized radiation. The *helical* undulator is such a device, and it is instructive to consider the difference between a linear and helical undulator in terms of the higher-harmonic content in their spectra.

The content of harmonics of undulator radiation can be understood qualitatively by considering the apparent electron acceleration that an on-axis observer experiences. First, recall the linear undulator. The electron executes harmonic, sinusoidal motion, but it is not sinusoidal seen from the on-axis observer. Here the Doppler shift is a little different when the electron is at its maximum displacement (where its instantaneous direction is exactly towards the observer), compared to when it is passing the undulator axis (where its instantaneous direction makes the angle K/γ with the direction to the observer). Therefore the observer does not see a sinusoidal displacement versus time: he sees the sinusoidal curve distorted more towards a triangular shape, which of course can be resolved into Fourier components (see Fig. 2.11). By symmetry the on-axis observer will see odd harmonics only (in contrast to the off-axis observer who will also see even harmonics). Clearly the distortion from sinusoidal shape increases with increasing K, so the content of higher harmonics also increases with K. Now consider the helical undulator. The electron path is a spiral. Seen from the on-axis observer though, the electron trajectory describes a circle, and by the symmetry of the circle there are no points where the Doppler effect is more pronounced than at other points. In other words the observer sees the same Doppler shift all the time, and therefore no distortion of the circular motion. Thus, projected onto a plane perpendicular to the undulator axis, the electron describes circular motion either as a function of emitter time, or as a function of observer time: the only difference being that the observer witnesses the circular movement as being much faster. However, there is no distortion, and hence there are no harmonics. As the electrons execute a circular path, the emitted radiation is circularly polarized. In practice, helical undulators are capable of producing intense X-ray beams with a circular polarization exceeding 99%.

2.4.6   Emittance and the diffraction limit

In the last section it was shown that an undulator is a highly brilliant source of radiation. The question naturally arises whether the brilliance of an undulator, or indeed any source, can be increased without limit. According to its definition in Eq. (2.1) the brilliance is inversely proportional to the square of the product of the linear source size and angular divergence. The product of source size and divergence is known as the *emittance*, ε, of a source. In this section the lower limit of the emittance of the photon beam is discussed. This turns out to be determined by the *convolution* of the emittance of the electron beam circulating in the storage ring, and the emittance of the photon beam for the passage of a single electron through the source path that is visible to the observer.

For a synchrotron storage ring, the electron beam emittance is a constant along the orbit around the ring. This is a consequence of Liouville's theorem, which states that for beams of particles the product of beam size and divergence is a constant. Although the product of source size and angular divergence is a constant, the two individual components may be manipulated by magnetic fields. It is therefore convenient to represent the electron beam emittance at a given position around the ring by a plot in phase space, with the spatial coordinate along the abscissa and the divergence along the ordinate, as shown in Fig. 2.13(a). Here y is the spatial coordinate in the vertical direction, and y' is the angular divergence in the same direction. In the figure the source size and divergence are written as σ_y and σ'_y respectively, and the contour representing the root-mean squared (r.m.s.) value of these quantities is shown as an ellipse. It follows from Liouville's theorem that the phase-space ellipse has a constant area around the orbit. But the ellipse can be tilted by magnetic fields as indicated in the figure.
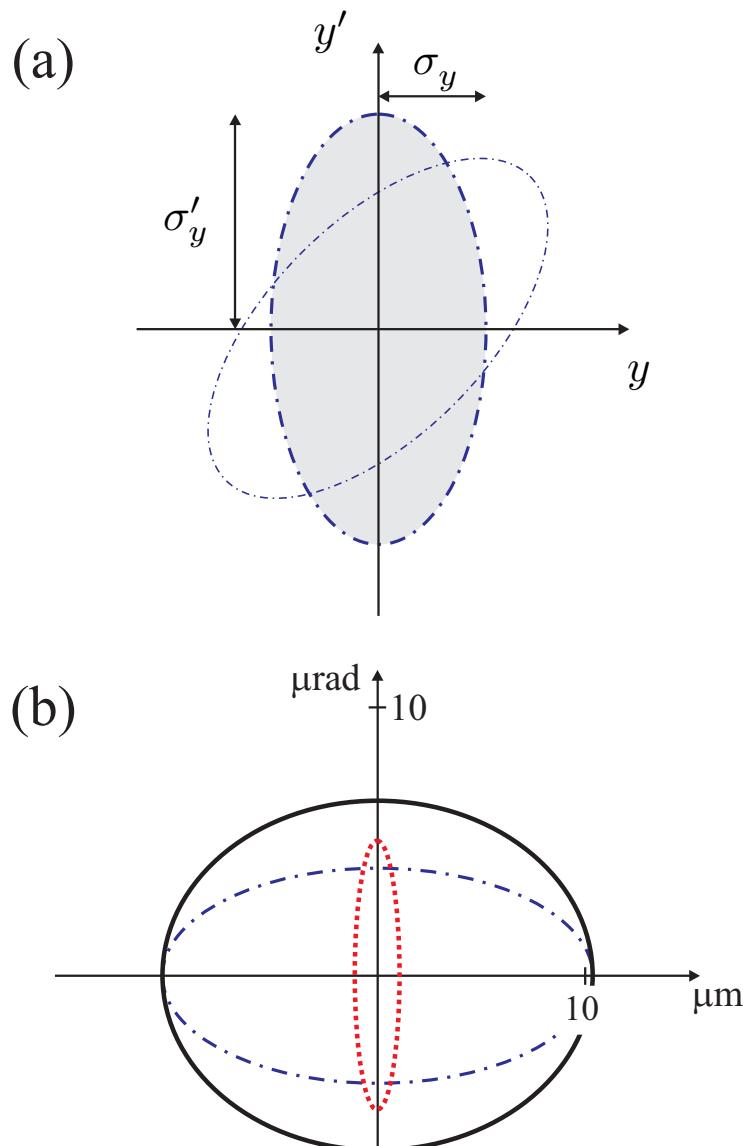
Fig. 2.13 Phase-space representation of the emittance ellipse, where the abscissa is the spatial dimension, y, and the ordinate is the divergence, y'. The emittance is defined to be the product of source size and divergence. (a) For the electron beam in the vertical direction, y, the emittance is written as $\varepsilon_y = \sigma_y \sigma_y'$. It is a constant around the orbit of the ring, and may therefore be represented at different points on the orbit by ellipses of equal area. (b) The photon beam emittance from an undulator at the ESRF in the vertical direction. Dotted line: the diffraction limit of a 1 Å photon beam arising from the passage of a single electron through a 4 m undulator. Dashed-dotted line: electron beam parameters in the vertical direction for a bunch of electrons in the storage ring. Full line: the phase-space ellipse of the resulting photon beam.

Typical values for the electron beam parameters of an undulator at the ESRF in the vertical direction are σ_y = 10.3 μm and σ'_y = 3.8 μrad. The vertical emittance is thus $\varepsilon_y = \sigma_y \sigma'_y$ = 39 pm rad. The ratio of the emittances in the vertical and horizontal directions is known as the *coupling*. For the ESRF the coupling is currently chosen to be 1 %, and the horizontal emittance is a factor of 100 times larger than in the vertical direction. In the future the coupling is likely to be reduced by a factor of between two to four.

The concept of a phase-space ellipse is also a convenient way to visualize the properties of the X-ray photon beam. Let us discuss this for an undulator source by considering the passage of a single electron. The angular divergence is given in Eq. (2.20), which for the first harmonic can be re-written as

$$\theta_{\mathrm{FWHM}} \cong \frac{1}{\gamma} \sqrt{\frac{1 + K^2/2}{N}} = \sqrt{2} \sqrt{\frac{\lambda_1}{L}}$$

where Eq. (2.14) has been used to relate the undulator length $L = N\lambda_u$ to the X-ray photon wavelength λ_1 of the first harmonic. Converting from FWHM to r.m.s. introduces a factor of $2\sqrt{2\ln 2} \approx 2.355$, but neglecting the difference between that and the factor of $\sqrt{2}$ in the equation above, leads to the expression for the r.m.s. photon beam divergence of

$$\sigma'_r \approx \sqrt{\frac{\lambda}{L}}$$

On the other hand, we know that the photon source size, σ_r, can never be smaller than the value set by the diffraction limit. Beyond the diffraction limit any reduction in source size leads to an increase in source divergence, and vice versa. The condition for the diffraction limit can be obtained from Heisenberg's uncertainty relation. In the present context this is written as

$$\sigma_r \Delta\mathrm{p} \geq \frac{\hbar}{2}$$

where $\Delta\mathrm{p}$ is the uncertainty in the transverse momentum of the photon. This in turn can be related to the angular divergence of the photon beam through

$$\Delta\mathrm{p} = \hbar\Delta\mathrm{k}$$

$$= \hbar\,\mathrm{k}\,\sigma'_r = \hbar\,\frac{2\pi}{\lambda}\,\sqrt{\frac{\lambda}{L}}$$

$$= \hbar\,\frac{2\pi}{\sqrt{L\lambda}}$$

It follows that the diffraction limited source size and angular divergence for an undulator are

$$\sigma_r = \frac{\sqrt{L\lambda}}{4\pi} \qquad \text{and} \qquad \sigma'_r = \sqrt{\frac{\lambda}{L}}$$

To take a definite example we consider an undulator at the ESRF, and show how the emittance of the electron beam and the diffraction limit of the photon beam combine to produce the final emittance of the X-ray beam. From the above, a 4 m long undulator at a wavelength of 1 Å has σ_r = 1.6 μm and σ'_r = 5 μrad. The source size and divergence of the electron beam in the vertical direction were stated

earlier as $\sigma_y = 10.3\,\mu m$ and $\sigma_y' = 3.8\,\mu rad$. These are shown graphically in Fig. 2.13(b). The phase-space ellipse for the X-ray photon due to passage of a single electron through the undulator is represented by the dotted line, while the ellipse from the passage of all the electrons in a bunch (approximately 10^{11} electrons) is shown by dashed-dotted line. The resulting photon beam pulse is the convolution of the two, as indicated by the solid line. From this it is clear that a further reduction in the electron beam size would be beneficial for the brilliance of the resulting photon beam, but a reduction in the electron beam divergence will not make much difference. Similar considerations apply to the horizontal direction.

If the electron beam phase-space ellipse could be made considerably smaller than the diffraction limit ellipse, the source would have full transverse coherence (Section 1.5). This is difficult to achieve at a synchrotron source for both the vertical and horizontal directions. For that it is necessary to consider a radically different type of source, the free-electron laser, which is described in Section 2.6.

2.4.7 Undulator brilliance

It is beyond the scope of this book to derive the formula for the brilliance of an undulator. (Derivations can be found in the references given in Further Reading at the end of this chapter). For completeness we quote one important result, which is the flux in the central cone[5] of an undulator:

$$\boxed{\frac{\text{Photons/second}}{(0.1\%BW)} \approx 1.43 \times 10^{14} NI[\text{A}] \frac{K^2}{1 + K^2/2}} \tag{2.21}$$

where this expression refers to the first harmonic and is approximately valid for $K \leq 1$. The brilliance is then given by the above expression for the flux divided by the product of source area (in mm^2) and the angular divergence (in mrad^2), or equivalently by dividing by the product of the vertical and horizontal emittances as discussed in Section 2.4.6.

A particular simple case to analyse, but one that is difficult to achieve in practice, is when the undulator radiation is fully diffraction limited. The brilliance can then be calculated by dividing the expression for the flux (Eq. (2.21)) by a factor of $(\lambda/4\pi)^2$. By way of example, we take $K = 1$, $N = 50$, $I = 0.5$ A and $\lambda = 1$ Å, for which the maximum (diffraction limited) brilliance[6] would be of order 10^{37} in photons/s/mm^2/mrad^2/0.1%BW. In practice, finite electron beam emittance means that undulator radiation is very far from being diffraction limited, especially for hard X-rays. Nonetheless, undulator brilliances in the range $10^{20} - 10^{23}$ can be achieved, exceeding the brilliance of bending magnet radiation by at least five orders of magnitude.

2.4.8 Summary: undulator radiation

The salient features of undulator radiation can be summarized as follows:

(a) An undulator is characterized by the K parameter (proportional to the peak magnetic field), the period λ_u, and the number of periods N.

---

[5]The reader may wonder why the central-cone flux scales with N, the number of undulator periods, and not with N^2. The reason is that it is the peak flux that scales with N^2, which is then averaged over the horizontal and vertical cone angles, each of which scales like $N^{-1/2}$, to obtain the flux in the central cone.

[6]For the parameters chosen the flux in the central cone is $\sim 2.4 \times 10^{15}$ photons/s/0.1%BW. Converting the diffraction-limited emittance, $(\lambda/4\pi)^2$, to practical units of (mm^2 mrad^2) introduces factors of 10^{-7} (Å to mm) squared, 10^{-3} (mrad) squared, plus an additional factor of $\sim 10^{-2}$ from $(1/4\pi)^2$. Thus the diffraction-limited brilliance is of order $10^{15+14+6+2} = 10^{37}$ in the appropriate units.
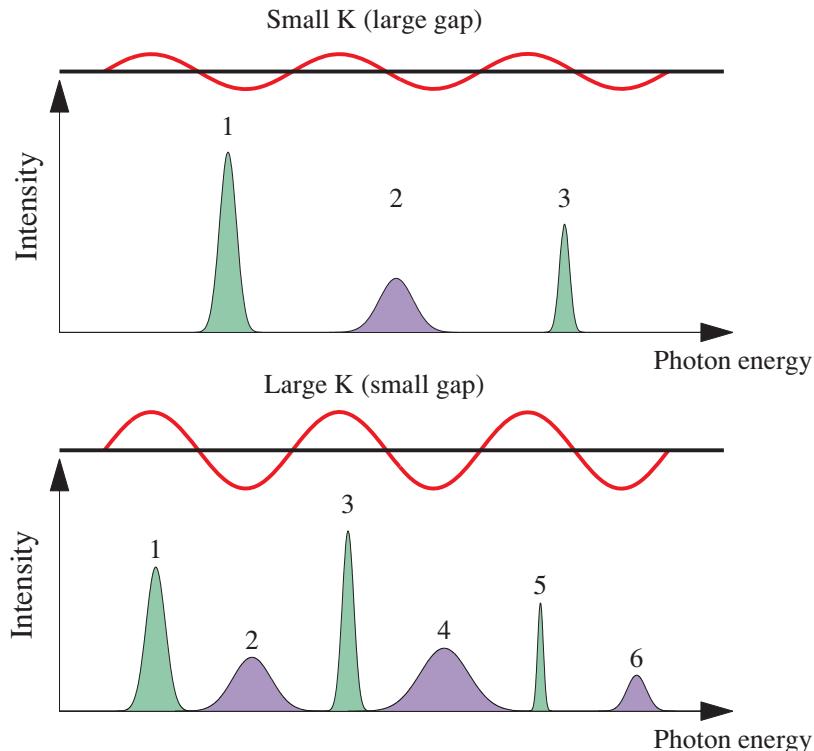
Fig. 2.14 Schematic of the spectrum from an undulator. The energy of the harmonics can be tuned by K so that a larger gap, implying a lower field and thereby a smaller K, gives a higher energy.

(b) The on-axis spectrum has a fundamental peak in wavelength given by Eq. (2.14), and has odd harmonics with a relative width of $1/nN$ (FWHM). The higher the K value, the higher is the relative proportion of the harmonics.

(c) The intrinsic angular divergence of the fundamental (and the odd harmonics) is much smaller than γ^{-1} and is given by Eq. (2.20).

(d) The finite divergence of the electron beam implies that the on-axis spectrum contains contributions from finite values of φ, and thus has intensity also at energies corresponding to the even harmonics.

(e) Undulator radiation has high intrinsic brilliance.

These properties are represented schematically in Fig. 2.14. The ideal X-ray source should be monochromatic with a tunable energy, and a selectable polarization. The angular divergence of the beam should be small, preferably in all directions. The main power of the source beam should be in a quasi-monochromatic band, so that the heat load on the first optical elements in the beamline is not unduly high. The undulator beam from a third-generation synchrotron storage ring has all of these desired properties.
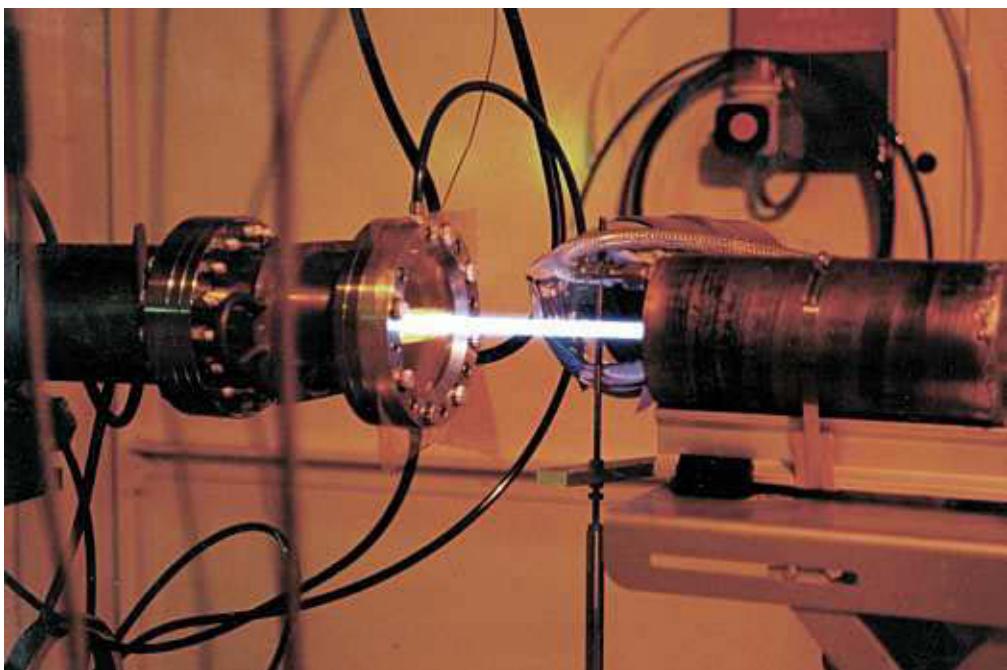
Fig. 2.15 The white X-ray beam from the wiggler at the ID11 beamline, ESRF. The X-ray beam emerges from an evacuated beam tube with an intensity that is high enough to ionize air. (Image courtesy of Åke Kvick, ESRF.)

2.5   Wiggler radiation

As far as the trajectory of an electron is concerned a wiggler can be viewed as a series of circular arcs, turning successively to the left and to the right, as shown in Fig. 2.7. This leads to an enhancement in the intensity of the observed radiation by a factor of $2N$, where N is the number of periods. The spectrum from a wiggler is the same as that from a bending magnet of the same field strength. The formula for the emitted power is similar to that given by Eq. (2.11), except for one important difference. In a bending magnet the field $\mathbf{B}$ is constant along the length L, whereas in a wiggler the average of the square of the field is $\langle B^2 \rangle = B_0^2/2$, where B_0 is the maximum field. As a consequence Eq. (2.11) is altered to read

$$\mathcal{P}[\text{kW}] = 0.633\,\mathcal{E}_e^2[\text{GeV}]\,B_0^2[\text{T}]\,L[\text{m}]\,I[\text{A}]$$

The observed path length L of the electron is approximately equal to the length of the wiggler, which is typically of order 1 m. The radiated power is then of order 1 kW or more. Such a high heat load would distort, if not destroy, the optical performance of the perfect crystals that are used to monochromate the X-ray beam, and various methods have had to be devised to retain the optical quality. A dramatic illustration of the power of the X-ray beam from a wiggler at a third-generation synchrotron source is shown in Fig. 2.15. Here the intensity of the beam is so high that it ionizes the air rendering the path of the beam visible.
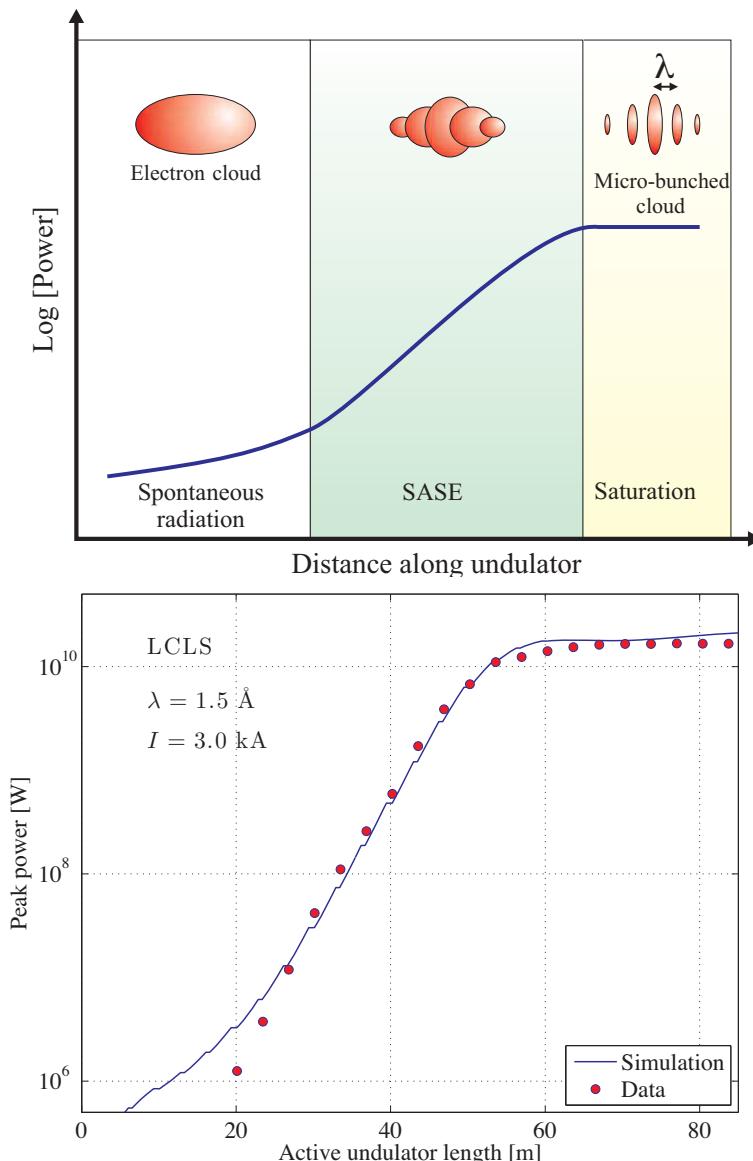
Fig. 2.16 Top panel: schematic of the power radiated by an electron cloud as it traverses through a long undulator. For short distances along the undulator there is no correlation between the radiation emitted by the different electrons in the cloud. Each electron emits as a coherent source, and the power of the 'spontaneous radiation' is proportional to the number of electrons in the cloud. Further downstream the electrons start to form micro-bunches and the SASE effect switches on, leading to an exponential growth in power. Eventually a train of micro-bunches forms with a spacing equal to the X-ray wavelength, and once this train is fully formed the intensity saturates. Each micro-bunch can be regarded as a point-like charge, so that in the ideal case the power is now proportional to the *square* of the number of electrons in a micro-bunch. Bottom panel: red points, the measured power emitted from the LCLS as a function of undulator length; blue line, the results of a simulation of the power expected from the known parameters of the electron beam. (Data courtesy of Paul Emma, LCLS.)

2.6   Free-electron lasers

Although an undulator at a synchrotron has many desirable properties as a source of radiation it could nonetheless be improved upon considerably. The reason is that although the radiation from a single electron is coherent, in the sense that the radiation from one oscillation is in phase with that from the subsequent ones, the radiation from different electrons is incoherent. This results from the fact that the electrons traverse the undulator in a bunch without any positional order, in other words as an electron gas. If somehow the electrons in the bunch (or macro-bunch) could be ordered spatially into smaller micro-bunches (containing an average of N_q electrons with $N_q \gg 1$), with a separation equal to the X-ray wavelength, then the radiation from one micro-bunch would be in phase with that from all of the following micro-bunches. It follows that the charge, eN_q, in a single micro-bunch would be much larger than e, and, since the micro-bunch is confined spatially within a distance shorter than the emitted wavelength, this charge can be considered as point like. In this case the brilliance would be enhanced by a factor of N_q^2 relative to a conventional undulator.

In an undulator the radiation field increases from zero at the entrance to its full value at the exit. An electron traversing through an undulator experiences a force from the magnetic lattice, and after a certain distance the electron also begins to respond to the radiation fields from the other electrons in the bunch. The interaction with the radiated field is spatially modulated with a period equal to the X-ray wavelength, and will hence tend to modulate the electron density within a bunch into micro-bunches. Once this effect occurs it will, through boot-strapping, enhance itself, as the radiation field increases rapidly as the electrons move downstream. The mechanism is called Self Amplified Stimulated Emission, or SASE for short, and an undulator designed to exploit the SASE principle is known as a free-electron laser [Derbenev et al., 1982, Murphy and Pellegrini, 1985]. A schematic representation of the SASE effect is shown in the top panel of Fig. 2.16.

Crucially, the boot-strapping mechanism described above requires that the radiation field acting on the electrons is sufficiently strong to produce micro-bunching, and the more localized the electron gas bunch, the stronger will be the radiation field. The electron gas density is therefore a decisive parameter for the SASE mechanism to be realised. Even in low-emittance, third-generation storage rings the electron density is not sufficiently high. This is primarily because the bunch length, of order 100 ps times the speed of light, or about 30 mm, turns out to be far too long. One solution to this problem is to use a linear accelerator, usually abbreviated to LINAC. In a LINAC it is possible to produce small electron beams, of order 100 μm (FWHM) in diameter, with a very small angular divergence, of order 1 μrad. Most importantly, with recently developed electron guns and LINAC bunch compression devices one can obtain the required high electron density, and bunch times as low as 0.1 ps, corresponding to a bunch length of 30 μm. With such a compressed electron gas volume the SASE principle can be realised even for radiation in the hard X-ray regime.

Estimating the expected flux from a free-electron laser requires detailed numerical calculations, as the SASE mechanism is more complicated than our description above suggests. As the electron bunch enters the undulator, the electrons are distributed like in a gas. There will be spontaneous fluctuations in the electron density within the bunch, and the region that happens to have a slightly higher density than the average will spontaneously act as the seed for SASE growth of a spatially modulated electron density with a wavelength equal to the first harmonic (or possibly the third harmonic) X-ray wavelength of the undulator. However, this region will *not* grow to extend over the entire macro-bunch: its size will be limited by the distance where the photon field will be in phase with the electrons that created it. Numerical estimates indicate that the length of an ordered region will be some hundred wavelengths. Within the total length of the bunch there will be many such partly ordered regions, but the radiation from different regions will be incoherent. Superimposed on this SASE radiation, which is extremely

brilliant, is the radiation from all of the electrons that remain spatially disordered, and this is like the ordinary undulator radiation that was discussed earlier in the chapter.

The LINAC coherent light source (LCLS) situated in California, USA, is the world's first operational hard X-ray free-electron laser. LCLS lased for the first time on 10 April 2009, and achieved SASE saturation at 1.5 Å just four days later (see Fig. 2.16, bottom panel [Emma, 2009]). The peak brilliance of LCLS is around 10^{32} (in the usual units), some 10 orders of magnitude more than the typical brilliance of undulator radiation from third-generation synchrotrons sources (Fig. 1.1). X-ray free-electron lasers not only produce radiation of unprecedented brilliance, but radiation that has full transverse coherence and is pulsed with typical pulse lengths of less than 100 fs. The first of these additional attributes can be exploited in imaging applications (see Chapter 9), while the second enables time-resolved experiments. When fully operational the LCLS, and other X-ray free-electron lasers that are being constructed, will revolutionise our ability to understand the structure and function of materials at the atomic level.

2.7 Compact light sources

The history of the development of ever more brilliant X-ray sources has largely been one of facilities of increasing scale and cost. One question that then naturally arises is whether it would be possible to produce a compact, laboratory scale, but brilliant source of X-ray radiation. Here we describe briefly one scheme that is currently being pursued to achieve this goal.

We have seen how the undulator has many features that make it an attractive source of radiation, most especially the fact that it is quasi-monochromatic and highly collimated. The on-axis wavelength of the radiation is

$$\lambda_1(\theta = 0) = \frac{\lambda_u}{2\gamma^2}\left(1 + K^2/2\right) \tag{2.22}$$

In practice, the undulator period λ_u is typically a few centimetres as determined by the array of permanent magnets in the undulator. Thus to produce hard X-rays an electron energy corresponding to $\gamma \approx 10^4$ is required, and this in turn implies a storage ring with a circumference of about a kilometre, in other words a large scale facility. Clearly, one way to reduce the scale and cost of the facility, but still produce X-ray photons, would be to significantly reduce the undulator period, which would concomitantly reduce the required electron energy. One way to achieve this is to replace the permanent magnet undulator with an effective undulator formed by the periodic electromagnetic field of an optical laser [Huang and Ruth, 1998, Bech et al., 2008]. The required electron energy can then be reduced by two orders of magnitude, since the effective undulator period is then given by the wavelength of the optical laser (around a micron), some four orders of magnitude smaller than the period of a permanent magnet undulator.

A schematic of a compact light source which combines an optical laser with a low energy electron storage ring is shown in Fig. 2.17. The operation of this type of compact light source can be understood from two distinct points of view. One may consider the interaction between a laser photon and an electron as the head-on collision between two particles. If the electron energy is sufficiently high, then in the impact the energy of the laser photon is increased to X-ray energies. This process is known as inverse Compton scattering, as in conventional Compton scattering an X-ray photon loses energy when it collides with a stationary electron. The alternative way of looking at the problem is to consider the electromagnetic field as providing an undulating force on the electron.

Following the second of these two approaches, we start by recalling that the Lorentz force exerted
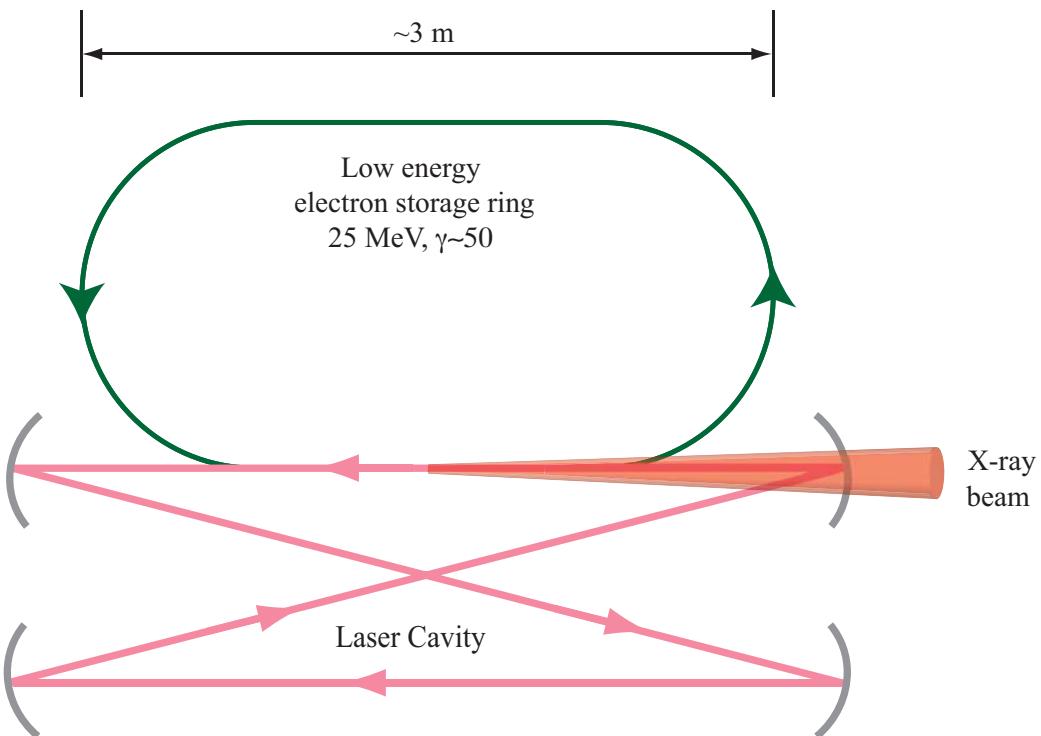
Fig. 2.17 Schematic layout of a compact light source in which a bunched low-energy (but still relativistic, $\gamma \sim 50$) electron beam makes a head-on collision with optical photons in a laser cavity. Viewed as a collision between two particles, the operation of the compact light source can be understood as an example of inverse Compton scattering, in which the optical photon is back scattered and emerges with a much shorter wavelength, i.e. it emerges as an X-ray photon. An alternative, but fully equivalent, description views the electromagnetic field of the optical photon bunch in the laser cavity as forming an effective undulator with a period equal to the laser wavelength.

on an electron due to combined effect of $\mathbf{E}$ and $\mathbf{B}$ fields is

$$\mathbf{F} = d\mathbf{p}/dt = -e\,(\mathbf{E} + \mathbf{v} \times \mathbf{B}) \tag{2.23}$$

Two cases will be compared: (a) a spatially alternating magnetic field produced by an array of permanent magnets in a conventional undulator, which we shall denote by the subscript 'u'. (b) a strong laser field in which both the electric field $\mathbf{E}$ and the magnetic field $\mathbf{B}$ provide a force on an electron, which we shall denote by superscript 'l'. The goal is to determine the laser power density, or equivalently the magnetic field B_l of the laser, which gives the same radiation as the permanent magnetic array described by the magnetic field B_u. We argue that if the force is the same in these two cases, then the acceleration and hence the radiation produced must also be the same, and that argument holds in any inertial system we may choose.

The simplest expression for the force is in an inertial system where the electron velocity is zero, because then the Lorentz force is simply $-e\mathbf{E}$. However, we start by expressing the electric and magnetic fields in the laboratory system, where the electron moves with velocity v along the x axis, and the permanent magnetic field alternates up and down along the z axis thus undulating the electron along the y axis.

To proceed we require the appropriate transformations from the lab (unprimed) to the electron rest (primed) frames[7]. For the (space, time) set of variables (x, t) to (x', t') the Lorentz transformations and their inverse are

$$
\begin{aligned}
x' &= \gamma (x - vt) & x &= \gamma (x' + vt') \\
t' &= \gamma (t - \beta x/c) & t &= \gamma (t' + \beta x'/c)
\end{aligned}
\tag{2.24}
$$

while for the components of the electric field the transformations are

$$
\begin{aligned}
E'_x &= E_x \\
E'_y &= \gamma \left(E_y - vB_z \right) \\
E'_z &= \gamma \left(E_z + vB_y \right)
\end{aligned}
\tag{2.25}
$$

In the case of a permanent magnet undulator, the y component of the electric field in the primed frame from Eq. (2.25) is

$$
E'_{y,u} = \gamma \left(0 - vB_u e^{ik_u x} \right) \approx -\gamma c B_u e^{ik_u \gamma ct'}
\tag{2.26}
$$

In the second equation we have used the fact that electron position in its rest frame is $x' = 0$, so $x = \gamma vt \approx \gamma ct$. The laser field expressed in the lab frame has a phase $\phi = k_l x + \omega_l t$ for propagation along the $-x$ direction. In the primed frame the phase becomes $\phi = k_l \gamma ct' + \omega_l \gamma t' = 2k_l \gamma ct'$ since $\omega_l = k_l c$. The magnetic and electric fields of the laser in the unprimed frame are therefore $B_l e^{i\phi}$ and $-E_l e^{i\phi}$, respectively, since the Poynting vector is along the $-x$ direction. As $|E_l| = c |B_l|$ we find from Eq. (2.25) that

$$
E'_{y,l} \approx -2\gamma c B_l e^{i2k_l \gamma ct'}
\tag{2.27}
$$

Comparison of Eqs. (2.26) and (2.27) establishes two important facts: (a) $k_u = 2k_l$, or equivalently[8] $\lambda_u = \lambda_l/2$; (b) $B_u = 2B_l$. The first allows us to calculate the X-ray wavelength expected for the compact light source from Eq. (2.22) using $\lambda_u = \lambda_l/2$. The second facilitates calculation of the expected performance of a compact light source (K parameter, flux, etc.) using the formulae pertaining to a permanent magnet undulator (see Eq. (2.21)) with $B_u = 2B_l$. In particular, it can be shown that with reasonable assumptions of electron beam current, laser power, etc., that a compact light source of the scale indicated in Fig. 2.17 should have a performance approaching that of a bending magnet at a synchrotron source.

2.8   Coherence volume and photon degeneracy

While source brilliance is one of the most useful figures of merit when comparing different sources, it is not by any means the whole story. Brilliance provides a measure of the raw photon power of a source, allowing for the effects of source size, and the collimation of the beam and its energy bandwidth. However, it does not convey information on the 'quality' of the photons in the sense of whether or not they are coherent. Increasing use is being made of coherent X-ray beams as explained in Chapter 9 on imaging. It is therefore of interest to determine the number of photons present in the volume of the

---

[7]Convention requires that we use primed coordinates for the rest frame of the electron. We hope that the reader is able to differentiate between this case, and our earlier use of t' which referred to the retarded, or emitter, time in the same inertial frame as the observer.

[8]We note that this result agrees with the analysis of the compact light source in terms of an inverse Compton process.

beam in which the photons are fully coherent, as defined by the transverse, L_T, and longitudinal, L_L coherence lengths (see Section 1.5). From a quantum mechanical point of view, photons are coherent with one another if they occupy the same eigenstate of the photon field. The number of photons in an eigenstate is known as the *photon degeneracy*. Thus the photon degeneracy is equal to the number of photons in the coherence volume.

We can derive an expression for the photon degeneracy from the source brilliance, $\mathcal{B}$, and the transverse and longitudinal coherence lengths. In the numerator of Eq. (2.1) we have the number of photons per unit time. The longitudinal coherence length, L_L, can be converted into a coherence time t_c by dividing by the speed of light, i.e. $t_c = L_L/c \equiv 1/\delta\nu$, where $\delta\nu$ is the frequency bandwidth. It follows that the photon degeneracy is proportional to the brilliance multiplied by $1/\delta\nu$. We also have to take account of the factors that appear in the denominator of Eq. (2.1). At a distance R from the source, the coherence volume subtends a solid angle $\Delta\Omega_{tr} = (L_T)^2/R^2$ which from Eq. (1.24) can be written as $\Delta\Omega_{tr} = \pi\lambda^2/(16A_s)$ where A_s is the area of the source. With a relative bandwidth of $\delta\nu/\nu$, the photon degeneracy, $\mathcal{D}_{photon}$, can be expressed as

$$\mathcal{D}_{photon} = \mathcal{B}\, t_c\, \Delta\Omega_{tr}\, A_s \left(\frac{\delta\nu}{\nu}\right) = \mathcal{B}\, \Delta\Omega_{tr}\, A_s\, \frac{\lambda}{c} = \mathcal{B}\frac{\pi}{16}\frac{\lambda^3}{c}$$

The photon degeneracy is a dimensionless quantity as it should be, although the pre-factor depends on the exact definitions of the longitudinal and transverse coherence lengths over which there is not universal agreement. Here we follow what we believe to be convention and write the photon degeneracy as

$$\mathcal{D}_{photon} = \frac{\mathcal{B}\lambda^3}{4c} \tag{2.28}$$

In practical units $\mathcal{B}$ is expressed in photons/s/mrad^2/mm^2/0.1%BW. With λ in Eq. (2.28) in Å, $\mathcal{B}$ in practical units must be multiplied by $(10^{-7})^2$ to convert the source area from mm^2 to Å^2, by $(10^3)^2$ to convert mrad^2, and finally by 10^3 for the 0.1%BW, i.e. altogether a prefactor of 10^{-5}. Since $\lambda/(4c) = 8.3 \times 10^{-20}\lambda$[Å] s, altogether one obtains

$$\boxed{\mathcal{D}_{photon} = 8.3 \times 10^{-25}\mathcal{B}[\text{photons/s/mrad}^2/\text{mm}^2/0.1\%\text{BW}]\lambda^3[\text{Å}]} \tag{2.29}$$

The scaling of photon degeneracy with wavelength cubed has the consequence that in moving from the optical to the X-ray regimes, say, the source brilliance source must increase rapidly to maintain the same coherent flux. This explains why X-ray free electron lasers are a much more potent source of radiation for experiments requiring a fully coherent beam than an undulator at a synchrotron source. For the latter, the maximum brilliance that can currently be realised at a third generation source is around 10^{22} photons/s/mrad^2/mm^2/0.1%BW, which gives a photon degeneracy at 1.5 Å of around 0.03, i.e. an average of much less than one photon in the coherence volume. An X-ray free-electron laser, such as the LCLS, operating at the same wavelength is expected to have a peak brilliance, and hence a peak photon degeneracy, approximately ten orders of magnitude higher.

In principle, since photons are bosons, there is no reason why the photon degeneracy cannot be increased without limit. However, it should be noted that the power delivered by current and planned free-electron lasers is enough to destroy most samples of interest, through a process known as 'Coulomb explosion', on the time scale of a few hundred femto-seconds[9]. In this sense, experiments for the

---

[9]A high flux X-ray beam will liberate a large number of photo electrons, leaving behind positively ionised atomic cores. Once the photo-ionisation passes a critical threshold, the mutual repulsion between the positive ion cores destabilises the material, and it disintegrates in a process known as Coulomb explosion.

foreseeable future will probably be limited as much by detector technology, and in particular the need to acquire data before the sample explodes, as it will be by innovations in the source.

2.9   Further reading

The Feynman Lectures on Physics, Vol. 1, Ch. 34, Richard P. Feynman, Robert B Leighton, and Matthew Sands (Addison-Wesley, 1977).

Characteristics of Synchrotron Radiation, K.-J. Kim, AIP Conference Proceedings, **184**, 565 (AIP, 1989).

Soft X-Rays and Extreme Ultraviolet Radiation: Principles and Applications, David Attwood (Cambridge University Press, 2007).

Synchrotron Radiation Made Simple, B.D. Patterson, Am. J. Phys. (2010) (In press).

2.10   Exercises

2.1   Show that to generate 1 W of photon power requires $5.04 \times 10^{14} \, \lambda \left[\text{Å} \right]$ photons per second.

2.2   Estimate the total power radiated by the ESRF. (Consider only the bending magnet radiation. The relevant parameters can be found in Section 2.3.4, and the total radiated power is given by $\mathcal{P} = e\gamma^4 I/(3\epsilon_0 \rho)$, where the symbols have their usual meaning.)

2.3   The Large Hadron Collider (LHC) at CERN in Switzerland circulates protons at an energy of 7 TeV. Assuming a bending magnet field strength of 8.3 T, and a current of 500 mA, calculate the total power radiated. How much power would be radiated if the protons were replaced by electrons of the same energy and bending radius?

2.4   Would the LHC make a useful source of hard X-rays?

2.5   Consider an electron moving through an undulator with period λ_u and with $K \ll 1$. In the rest frame of the electron the undulator period is relativistically contracted and appears as $\lambda' = \lambda_u/\gamma$. In this rest frame the electron radiates as a dipole with frequency $\nu' = c/\lambda'$, while in the lab the on-axis frequency is Doppler shifted to $\nu = \nu' / \left[\gamma (1 - \beta) \right]$. Show that this leads to the on-axis undulator radiation formula $\lambda = \lambda_u/(2\gamma^2)$ valid for $K \ll 1$.

2.6   Show that in practical units the on-axis wavelength of the first harmonic of an undulator may be written as $\lambda_1 \left[\text{Å} \right] = 13.056 \, \lambda_u \, [\text{cm}] \, (1+K^2/2)/ \mathcal{E}_e^2 \, [\text{GeV}]$.

2.7   Show that in an inverse Compton scattering event, in which a relativistic electron collides head on with an optical photon propagating along the x direction, the fractional energy change of the photon is given by

$$\frac{\Delta \mathcal{E}}{\mathcal{E}} = \frac{(\gamma_i \beta_i - \chi_i)(1 - \cos \psi)}{\gamma_i (1 + \beta_i \cos \psi) + \chi_i (1 - \cos \psi)}$$

where χ_i is the incident photon energy divided by the rest mass of the electron, ψ is the scattering angle of the photon, and all other symbols have their usual meaning. Establish

(a) that the maximum fractional change in the photons energy occurs when it is back scattered and (b) in the limit that the incident photon energy is small compared with that of the electron, the fractional change in energy is approximately $4\gamma^2$. Assuming an electron energy of 25 MeV, and an incident photon wavelength of 1 μm, calculate the minimum wavelength of the scattered photon produced by a compact light source.

2.8 Assuming an energy density of 4×10^7 Jm^{-3} in the laser cavity of a compact light source, calculate the equivalent magnetic field of a permanent magnet undulator, and use the result to calculate the undulator K parameter. Calculate the X-ray flux in the central cone for an electron beam current of 100 mA, a laser wavelength of 1 μm and an effective length of 1 cm over which the photon and electron beams interact.

Refraction and reflection from interfaces

A ray of light propagating in air changes direction when it enters glass, water or other transparent materials. This is the basis for the classical optics of lenses. Quantitatively, the phenomenon is described by Snell's law. For visible wavelengths the refractive index n of most transparent materials has a value in the range between 1.2 and 2. The refractive index depends on the frequency ω of the light, so that blue light is refracted more than red light, etc.

The index of refraction for electromagnetic waves displays resonant behaviour at frequencies corresponding to electronic transitions in atoms and molecules. On the low frequency side of a resonance, n increases with ω, and this is known as normal dispersion. Immediately above the resonance frequency it decreases, and as more and more resonances are passed, the magnitude of the index of refraction decreases. X-ray frequencies are usually higher than all transition frequencies, perhaps with the exception of those involving the inner K- or maybe L-shell electrons. As a result in the X-ray region n turns out to be *less* than unity. (See Fig. 1.8 and accompanying discussion.) This reflects the phase shift of π in the Thomson scattering of X-rays, as we shall see. Moreover, it leads to the phenomenon of total external reflection from a flat, sharp interface: for incident glancing angles α below a certain critical angle α_c the ray will no longer penetrate into the material but will be totally reflected from it. The deviation of n from unity is tiny, so the critical angle is small. The reader might wonder how n can be less than unity, since the velocity in the material is c/n, and this would seem to imply that the speed of light is higher in the material than in vacuum. However, c/n is the phase velocity, not the group velocity. The latter, evaluated as $d\omega/dk$, is indeed less than c.

In this chapter we shall see that the deviation of n from unity, δ, is related to the scattering properties of the medium. Each electron scatters the X-ray beam with the Thomson scattering amplitude r_0, and δ turns out to be proportional to the product of r_0 and the electron density ρ. With the explicit formula derived below, Eq. (3.1), one finds that δ is of order 10^{-5}. Snell's law evaluated at small glancing angles implies that the critical angle $\alpha_c = \sqrt{2\delta}$, and therefore is of order of a few milli-radians. Although this is small, it transpires that it is sufficient in practice to allow the production of highly reflecting X-ray mirrors, which can be shaped so as to focus an incident X-ray beam. The glancing angle geometry implies a long focal length, of order 10 metres, and rather long mirrors, since the 'footprint' of the beam on the mirror is the beam height divided by the sine of the glancing angle. This problem can be

Phase shift and scattering from a sharp interface
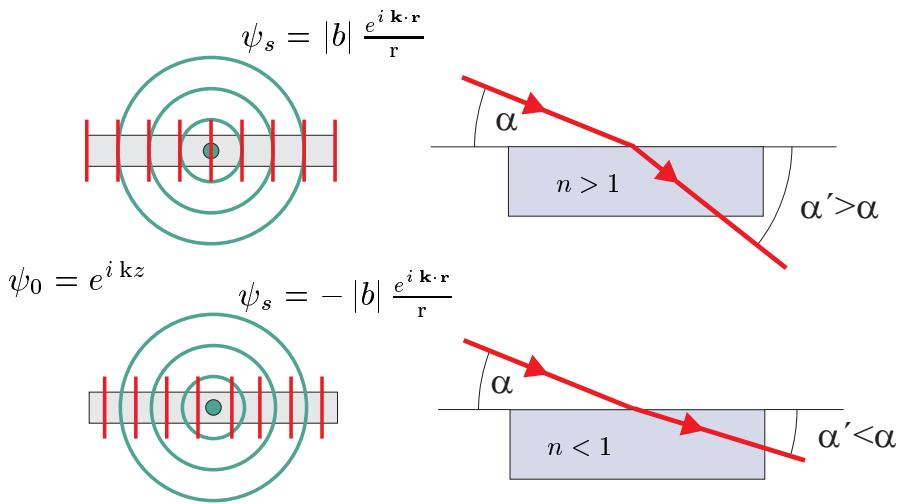
Fig. 3.1 The spherical wave ψ_s from a point scatterer can be in phase (top) or 180° out of phase with the incident plane wave ψ_0 (bottom). The refractive index is greater than unity in the first case, and smaller than unity in the second case.

overcome with a multilayer mirror, which has peaks in its reflectivity curve at angles well beyond the critical angle, allowing shorter mirrors to be used. The fact that δ is so small would seem to make the construction of refractive lenses in the X-ray region unfeasible. This turns out not to be the case, and we shall expand on this, and other aspects of X-ray optical elements, towards the end of this chapter.

In general X-ray reflectivity is a very powerful probe of the structure of interfaces. The reference interface is the sharp, flat interface for which the reflectivity is given by the Fresnel equations. Although these may be well known to the reader in the optical region, we shall derive them here and see how they are simplified in the X-ray region. Real interfaces are rarely sharp on a length scale of an Ångström, and neither are they ideally flat. Most importantly, one can determine deviations from the ideal sharp, flat interface by reflectivity studies. The ideally flat, but graded interface, and the ideally sharp, but roughened interface, will be considered in later sections, followed by examples of reflectivity experiments where these ideas have been an essential component of the models used to interpret the data. The interesting part of the spectrum of the reflected intensity versus incident glancing angles is often at reflectivities below 10^{-6}, so an intense beam from a synchrotron source is often of advantage.

3.1   Refraction and phase shift in scattering

To start with absorption processes will be neglected, and it will be assumed that the interface between vacuum and the medium of interest is both flat and sharp. Furthermore, the medium will be considered to have a homogeneous density of scatterers each giving rise to a spherical scattered wave of real amplitude b.

As shown in Fig. 3.1 there are two possibilities for the spherical wave emanating from a scattering

centre: either it is in phase with the incident wave (top), or there is a phase shift of π in the scattering process (bottom). A phase shift cannot be detected in an ordinary scattering experiment, since the intensity is proportional to the absolute square of the scattering length b. But, as we shall prove in the next section, there is a distinct difference in the refraction at an interface. With no phase shift the refractive index n is larger than unity, and the ray is therefore refracted as shown in the top, right part of Fig. 3.1. With a phase shift of π, the index of refraction becomes smaller than unity and the phenomena of *total external reflection* occurs at sufficiently small glancing angles α. The argument does not depend on the kind of radiation considered: for example, it also applies to beams of neutrons. This is the reason why the nomenclature of b has been used for the amplitude of the spherical wave, since the nuclear scattering length for neutrons is commonly denoted by b. Moreover, the sign of b varies from nucleus to nucleus. A well known example is the deuteron and the proton, which have nuclear scattering lengths of opposite sign. Here we are mainly interested in X-rays, and in that case the scattering length for each electron is r_0, and as was shown in Chapter 1 there is a phase shift of π between the incident and scattered waves. The refraction of neutrons is discussed further in Appendix F.

Below we derive the equation relating the index of refraction, n, to the scattering properties of the medium given by the number density of electrons, ρ, and the scattering amplitude per electron, r_0. The equation is

$$n = 1 - \delta \tag{3.1}$$

with

$$\delta = \frac{2\pi \rho \, r_0}{k^2} \tag{3.2}$$

and where the wavelength of the radiation, λ, is related to the wavevector, k, by $k = 2\pi/\lambda$. The electron density ρ in condensed matter is of order 1 electron/Å^3. This means that with $r_0 = 2.82\times 10^{-5}$ Å and k around 4 Å^{-1}, δ is of the order of 10^{-6}. This is very much smaller than unity and explains why refraction phenomena in the X-ray region are not completely trivial to observe[1]. Snell's law relates the glancing angles α and α' defined in Fig. 3.1 to each other through the equation

$$\cos \alpha = n \, \cos \alpha'$$

which is also derived below. The critical angle $\alpha = \alpha_c$ for total external reflection is obtained by setting $\alpha' = 0°$, and by expanding the cosines to yield

$$\alpha_c = \sqrt{2\delta} = \frac{\sqrt{4\pi \rho \, r_0}}{k} \tag{3.3}$$
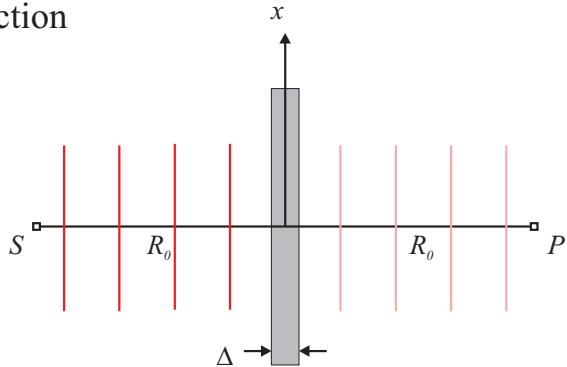
Using the values of the typical parameters given above, α_c is of order one milli-radian.

3.2 Refractive index and scattering length density

In order to derive the relationships stated in Eqs. (3.1) and (3.2) between the refractive index of a material and its scattering properties we consider in Fig. 3.2 a plane wave at normal incidence to a

---
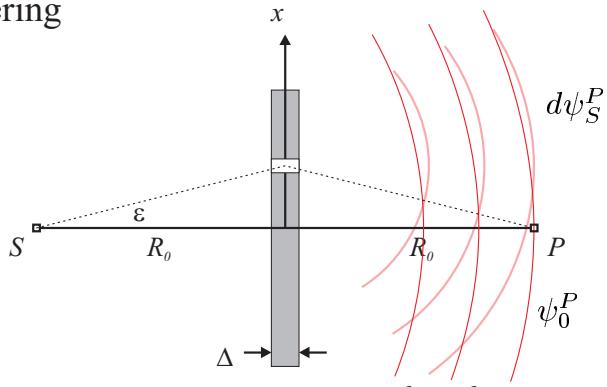
[1]W.C. Röntgen had a suspicion that X-rays were waves, and attempted to look for refraction phenomena, but without success.

Refraction

$$\psi^P_{tot} = \psi^P_0\, e^{i\,(n\mathrm{k}-\mathrm{k})\Delta} \approx \psi^P_0\left[1 + i\,(n-1)\mathrm{k}\Delta\right]$$

Scattering

$$\phi(x,y) = \mathrm{k}(2R - 2R_0) \approx \mathrm{k}(x^2 + y^2)/R_0$$

$$d\psi^P_S = \left(\frac{e^{i\,\mathrm{k}R_0}}{R_0}\right) \qquad \text{incident wave}$$

$$(\rho\,\Delta\,dxdy) \qquad \text{number of scatterers}$$

$$\left(-b\,\frac{e^{i\,\mathrm{k}R_0}}{R_0}\right) \qquad \text{spherical wave from one scatterer}$$

$$e^{i\,\phi(x,y)} \qquad \text{apart from this phase factor}$$

$$\psi^P_{tot} = \psi^P_0 + \int d\psi^P_s = \psi^P_0\left[1 - i\,\frac{2\pi\,\rho b\Delta}{\mathrm{k}}\right]$$

Fig. 3.2 The refractive description (top) implies that the thin plate introduces a small phase shift in the wave observed at point *P*. In the scattering description (bottom) the incident plane wave is approximated by a point source far away, and the perturbation of the plate is derived as a superposition of scattered spherical waves. (Absorption has been neglected in both treatments). The two descriptions are equivalent and lead to the relation between the refractive index and the scattering properties.

Evaluation of the integral in Eq. (3.4)

Here the integral

$$I = \int_{-\infty}^{\infty} e^{i(k/R_0)x^2}\, dx$$

is evaluated.

The starting point is the integral given in Eq. (D.3) on page 361 which we restate here for convenience:

$$f(a) = \int_{-\infty}^{\infty} e^{-ax^2}\, dx = \sqrt{\frac{\pi}{a}}$$

In evaluating this integral in Appendix D it is assumed that a is a real positive number. By utilizing the mathematical theory of complex functions (see, for example, *Methods of Theoretical Physics* by Morse and Feshbach, McGraw-Hill) one can generalize the function to complex values of a, in particular to values of a on the imaginary axis

$$a = -i\,\frac{k}{R_0}$$

since in this case $f(a) = I$.

Then one can invoke analytic continuation, which in the present case means that the result is still $f(a) = \sqrt{\pi/a}$ with a complex number substituted for a. We therefore find

$$I = \sqrt{\frac{\pi}{-i\,k/R_0}} = \sqrt{\frac{i\,\pi}{k/R_0}}$$

and thus

$$I^2 = i\left(\frac{\pi R_0}{k}\right)$$

thin plate[2]. The presence of the plate is sensed at the observation point P by a change in the wave ψ_{tot}^{P} compared to the situation without a plate. For X-rays ψ_{tot}^{P} describes the electric field, for neutrons it is the Schrödinger wavefunction. The notation of ψ is used to emphasize the similarity of X-ray and neutron optics. The derivation is simplified by considering normal incidence, since then the wave does not change direction when entering the material, and for a thin plate any phase difference between waves scattered from the front or the back of the plate can be neglected. There are then two equivalent descriptions: on the one hand a refractive description where the presence of the plate is taken into account by a phase difference of $(n-1)\,k\,\Delta$; and on the other hand a scattering description, where the wave at P is a superposition of the infinitesimal spherical waves emanating from each scattering centre in the plate, plus of course the incident wave. For the refractive description the total wave at P is

$$\psi_s^{P} = \psi_0^{P} e^{i(n-1)k\Delta} \cong \psi_0^{P}[1 + i(n-1)k\Delta]$$

[2]An alternative derivation is given in Section 8.1.3 on page 280 by relating the index of refraction to the polarizability of the medium. In Appendix F yet another derivation is given for neutrons by applying energy conservation.

A quantitative evaluation of the scattering description requires a little work. First of all, the incident plane wave is approximated by a train of spherical waves coming from a very distant source point S. For convenience, let the observation point P be the point symmetric to S on the other side of the plate. Next, let us consider the waves scattered from an element in the plate, lying within the plane of the drawing at a distance x from the axis. The distance to the source and to the observation point from this element, R, is a little longer than the closest distance R_0.

By expansion we find $R = (R_0^2 + x^2)^{1/2} \approx R_0 \left[1 + x^2/(2R_0^2)\right]$, and the phase difference compared to the direct path from S to P is $2kx^2/(2R_0)$, where the first factor of 2 accounts for equal phase lags on the source and observation sides of the plate. A similar expression is obtained for an element at coordinate $(0, y)$, so that the phase difference, $\phi(x, y)$, for rays emanating from the element at (x, y) is

$$e^{i\phi(x,y)} = e^{i(x^2+y^2)k/R_0} = e^{ix^2k/R_0}e^{iy^2k/R_0}$$

The number of scattering centres in that element is $\rho \Delta\, dxdy$, and each wave has the scattering amplitude r_0 with a phase shift of π. Altogether, the contribution $d\psi_s^P$ to the scattered wave at P from the volume element at (x, y) is

$$d\psi_s^P \approx \left(\frac{e^{ikR_0}}{R_0}\right)(\rho\Delta\, dxdy)\left(-b\frac{e^{ikR_0}}{R_0}\right)e^{i\phi(x,y)}$$

as indicated in Fig. 3.2. The subscript 's' stands for 'scattered' to remind ourselves that, after integration over all elements in the plate, we have to add the scattered wave to the incident wave in order to obtain the total. The scattered wave at P is found by integrating the above to yield

$$\psi_s^P = \int d\psi_s^P = -\rho b\Delta \left(\frac{e^{i\,2kR_0}}{R_0^2}\right)\int_{-\infty}^{\infty} e^{i\phi(x,y)}\, dxdy$$

$$= -\rho b\Delta \left(\frac{e^{i\,2kR_0}}{R_0^2}\right)I^2 \tag{3.4}$$

The integration over (x, y) is described in the box on the preceding page, and leads to the result

$$I^2 = \int_{-\infty}^{\infty} e^{i\phi(x,y)}\, dxdy = i\left(\frac{\pi R_0}{k}\right)$$

The incident wave at P, a distance of $2R_0$ from the source S, is

$$\psi_0^P = \frac{e^{ik2R_0}}{2R_0}$$

and the total wave at the observation point P becomes

$$\psi_{tot}^P = \psi_0^P + \psi_s^P = \psi_0^P\left[1 - i\frac{2\pi\rho b\Delta}{k}\right] \tag{3.5}$$

When the expression for ψ_{tot}^P from the scattering picture is identified with ψ_{tot}^P in the refractive description (compare the top and bottom panels in Fig. 3.2) one arrives at the result stated in Eq. (3.1).

Our discussion of the forward scattered wave shown in Fig. 3.2 can be extended to include a thin plate composed of atoms, instead of the uniform distribution of electrons that has been considered so far. All that needs to be done is to replace the electron number density ρ in Eq. (3.5) by the product of

the atomic number density, ρ_{at}, and the atomic scattering factor $f(\mathbf{Q})$ (see Eq. (1.12)). The expression for ψ_{tot}^P given in Eq. (3.5) can then be written as

$$\psi_{tot}^P = \psi_0^P \left[1 - i\, \frac{2\pi \rho_{at} f^0(0)\, r_0\, \Delta}{k} \right]$$

where for the forward direction $\mathbf{Q} = 0$, and the dispersion corrections to $f(\mathbf{Q})$ have been neglected. Later we shall consider the diffraction from atomic planes where the angle of incidence θ is not necessarily $90°$. This is taken into account by replacing Δ by $\Delta/\sin\theta$. To emphasize that the effect of a thin plate is to introduce a phase shift of the forward scattered wave the above is rewritten as

$$\psi_{tot}^P = \psi_0^P \left[1 - i\, g_0 \right] \cong \psi_0^P\, e^{-i\, g_0}$$

where g_0 is the phase shift given by

$$g_0 = \frac{\lambda \rho_{at} f^0(0) r_0 \Delta}{\sin\theta} \tag{3.6}$$

The factor of $\sin\theta$ has been introduced to allow for the change in thickness of material traversed as the incident angle is changed. In terms of the atomic density and atomic scattering length δ becomes

$$\delta = \frac{2\pi \rho_{at} f^0(0)\, r_0}{k^2}$$

3.3 Refractive index including absorption

Suppose now that in addition to scattering, absorption processes also take place in the medium. Absorption implies that the beam is attenuated in the material with a characteristic $1/e$ length which is denoted by μ^{-1}, where μ is known as the absorption coefficient. By definition, this length refers to the *intensity* attenuation, and not to the *amplitude* attenuation. After traversing a distance z in the material the intensity is attenuated by a factor $e^{-\mu z}$, but the amplitude only by a factor of $e^{-\mu z/2}$.

In the refractive description of a wave incident at normal angles to a plate (see Fig. 3.3) the wavevector changes from k in vacuum to nk in the medium. If the refractive index n is now allowed to be a complex number, $n = 1 - \delta + i\beta$, then the wave propagating in the medium is

$$e^{i n k z} = e^{i(1-\delta)k z}\, e^{-\beta k z}$$

From this equation for the amplitude it can be inferred that $\beta k = \mu/2$, or

$$n \equiv 1 - \delta + i\beta \tag{3.7}$$

with

$$\delta = \frac{2\pi \rho_{at} f^0(0)\, r_0}{k^2} \tag{3.8}$$
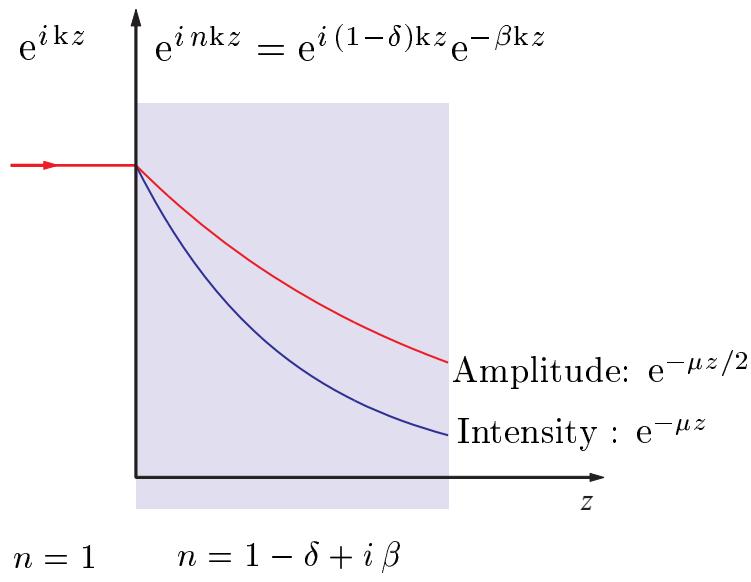
Fig. 3.3 A plane wave at normal incidence to a plate with absorption length $1/\mu$. The absorption is formally equivalent to an imaginary part of the refractive index.

and

$$\beta = \frac{\mu}{2k} \tag{3.9}$$

An alternative approach is to write the atomic scattering length $f(\mathbf{Q})$ as a complex number by including the dispersion corrections (see Chapter 8). The atomic scattering length is then $f(\mathbf{Q})=f^0(\mathbf{Q})+ f' + if''$, and the refractive index becomes

$$n \equiv 1 - \frac{2\pi \rho_{at} r_0}{k^2} \left\{ f^0(0) + f' + i f'' \right\}$$

with

$$-\left(\frac{2\pi \rho_{at} r_0}{k^2}\right) f'' = \beta$$

Using Eq. (1.18) and Eq. (3.9) this can be rearranged by writing

$$f'' = -\left(\frac{k^2}{2\pi \rho_{at} r_0}\right)\beta = -\left(\frac{k^2}{2\pi \rho_{at} r_0}\right)\frac{\mu}{2k}$$

to read

$$f'' = -\left(\frac{k}{4\pi r_0}\right)\sigma_a \tag{3.10}$$
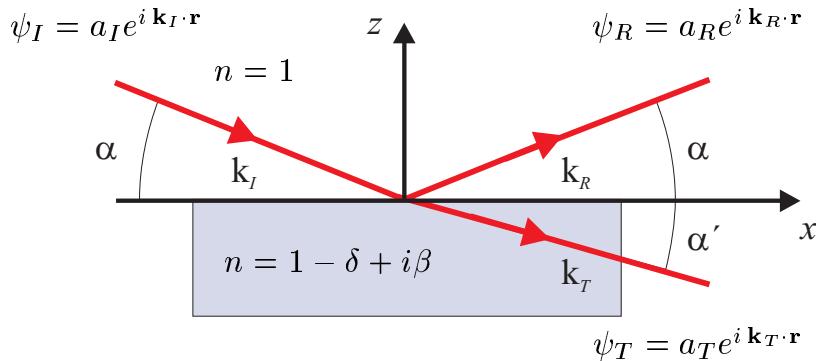
Fig. 3.4 Snell's law and the Fresnel equations can be derived by requiring continuity at the interface of the wave and its derivative.

Thus the absorption cross-section, σ_a, is proportional to the imaginary part of the atomic scattering length, f'', in the forward direction. This result is sometimes known as the Optical Theorem. It should be noted that f'' is negative since σ_a is a positive real number, and that in other texts the sign convention is sometimes such that f'' is positive.

3.4 Snell's law and the Fresnel equations in the X-ray region

In the X-ray wavelength region, both δ and β are very much smaller than unity. It follows that when considering refraction and reflection phenomena we can limit ourselves to small angles and take advantage of the appropriate expansions.

The incident wavevector is $\mathbf{k}_I$, and the amplitude is a_I, as indicated in Fig. 3.4. Similarly the reflected and the transmitted wavevectors (at angle α') are $\mathbf{k}_R$ and $\mathbf{k}_T$, respectively, and the amplitudes are a_R and a_T. Snell's law and the Fresnel equations are derived by imposing the boundary conditions that the wave and its derivative at the interface $z = 0$ must be continuous. These require that the amplitudes are related by

$$a_I + a_R = a_T \tag{3.11}$$

and

$$a_I \mathbf{k}_I + a_R \mathbf{k}_R = a_T \mathbf{k}_T \tag{3.12}$$

The wavenumber in vacuum is denoted by $k=|\mathbf{k}_I|=|\mathbf{k}_R|$ and in the material it is $nk=|\mathbf{k}_T|$. Taking components of $\mathbf{k}$ parallel and perpendicular to the surface yields respectively

$$a_I k \cos\alpha + a_R k \cos\alpha = a_T(nk)\cos\alpha' \tag{3.13}$$

$$-(a_I - a_R)k \sin\alpha = -a_T(nk)\sin\alpha' \tag{3.14}$$

From Eq. (3.11) together with the projection parallel to the interface (Eq. (3.13)) one readily derives

Snell's law:

$$\cos \alpha = n \cos \alpha'$$ (3.15)

As α and α' are small the cosines can be expanded to yield

$$\alpha^2 = \alpha'^2 + 2\delta - 2\,i\beta$$
$$= \alpha'^2 + \alpha_c^2 - 2\,i\beta$$ (3.16)

where the refractive index n has been taken from Eq. (3.7), and Eq. (3.3) has been used to relate δ to the critical angle, α_c, for total reflection.

From Eq. (3.11) together with the projection perpendicular to the interface (Eq. (3.14)) it follows that

$$\frac{a_I - a_R}{a_I + a_R} = n\frac{\sin \alpha'}{\sin \alpha} \cong \frac{\alpha'}{\alpha}$$

from which the Fresnel equations are derived as

$$r \equiv \frac{a_R}{a_I} = \frac{\alpha - \alpha'}{\alpha + \alpha'} \;;\;\; t \equiv \frac{a_T}{a_I} = \frac{2\alpha}{\alpha + \alpha'}$$ (3.17)

Here the *amplitude* reflectivity, r, and transmittivity, t, have been introduced. The corresponding *intensity* reflectivity (transmittivity), denoted by the capital letter R (T), is the absolute square of the amplitude reflectivity (transmittivity).

Note that α' is a complex number to be derived from Eq. (3.16) for a given incidence angle α. By decomposing α' into its real and imaginary parts

$$\alpha' \equiv Re(\alpha') + i\,Im(\alpha')$$

it can be seen that the transmitted wave falls off with increasing depth into the material as

$$a_T e^{i\,(k\alpha')z} = a_T e^{i\,k\,Re(\alpha')z}e^{-k\,Im(\alpha')z}$$

The *intensity* therefore falls off with a $1/e$ penetration depth Λ given by

$$\Lambda = \frac{1}{2k\,Im(\alpha')}.$$ (3.18)

The results for r, t and Λ depend on several parameters: the incident angle α, the density and absorption in the medium, as well as the wavevector. In order to get an overview of this multi-parameter problem, it is convenient to use suitable units. The normalization unit for angles is the critical angle α_c. However, in connection with diffraction and reflection phenomena, the wavevector transfers are more useful than angular variables:

$$Q \equiv 2\,k \sin \alpha \cong 2\,k\,\alpha \;\;;\;\; Q_c \equiv 2\,k \sin \alpha_c \cong 2\,k\,\alpha_c$$ (3.19)

and in particular their dimensionless counterparts

$$q \equiv \frac{Q}{Q_c} \cong \left(\frac{2\,k}{Q_c}\right)\alpha \;\;;\;\; q' \equiv \frac{Q'}{Q_c} \cong \left(\frac{2\,k}{Q_c}\right)\alpha'$$

Equation (3.16) can then be rewritten in terms of the dimensionless wavevectors q and q' by multiplying both sides of the equation by $(2k/Q_c)^2$ to yield

$$q^2 = q'^2 + 1 - 2 i b_\mu \qquad (3.20)$$

where from Eq. (3.9) the parameter b_μ is related to the absorption coefficient μ through

$$b_\mu = \left(\frac{2\,k}{Q_c}\right)^2 \beta = \left(\frac{4\,k^2}{Q_c^2}\right)\frac{\mu}{2k} = \frac{2k}{Q_c^2}\mu$$

The wavevector Q_c at the critical angle is

$$Q_c = 2k\alpha_c = 2k\,\sqrt{2\delta} = 4\,\sqrt{\pi\,\rho\,r_0\left(1 + \frac{f'}{Z}\right)} \qquad (3.21)$$

as can be seen from Eq. (3.3) and Eq. (3.8). For completeness the dispersion correction f' to f^0 has been included in the expression for Q_c (see Chapter 8 for a complete discussion of the dispersion corrections).

   Calculation of the reflectivity, transmittivity and penetration depth proceeds as follows. For the material in question values for the absorption length μ^{-1} (at the particular X-ray wavelength being used), the electron density ρ, and possibly the dispersion correction f', are obtained from standard sources, such as the International Tables of Crystallography. From these numbers the quantity b_μ is calculated. The complex number q' can then be derived from Eq. (3.20), and thereby the complex amplitude reflectivity (transmittivity) from the wavevector form of Eq. (3.17):

$$r(q) = \frac{q - q'}{q + q'} \quad ; \quad t(q) = \frac{2q}{q + q'} \quad ; \quad \Lambda(q) = \frac{1}{Q_c Im(q')} \qquad (3.22)$$

Let us consider the solutions to some limiting cases, recalling that $b_\mu \ll 1$ in all cases.

$q \gg 1$ The solution to Eq. (3.20) yields $Re(q') \cong q$ and $Im(q') \cong b_\mu/q$. From Eq. (3.22), $r(q)$ can be written as $r(q) = (q^2 - q'^2)/(q + q')^2$ so in the considered limit $r(q) \cong (2q)^{-2}$, i.e. the reflected wave is in phase with the incident wave. The intensity reflectivity falls off as $R(q) \cong (2q)^{-4}$, there is almost complete transmission, and the penetration depth is $\alpha\mu^{-1}$.

$q \ll 1$ In this case q' is almost completely imaginary with $Im(q') \cong 1$ and $r(q) \cong -1$, i.e. the reflected wave is out of phase with the incident wave, so the transmitted wave becomes very weak. It propagates along the surface with a minimal penetration depth of $1/Q_c$, independent of α as long as $\alpha \ll \alpha_c$. Due to the small penetration depth, it is called an *evanescent* wave.

$q = 1$ From Eq. (3.20) one finds $q' = \sqrt{b_\mu}(1 + i)$. The penetration depth is $b_\mu^{-1/2}$ times larger than the asymptotic value of $1/Q_c$. Since $b_\mu \ll 1$ the amplitude reflectivity is close to $+1$ so the reflected wave is in phase with the incident wave. This implies that the evanescent amplitude is almost twice that of the incident wave.
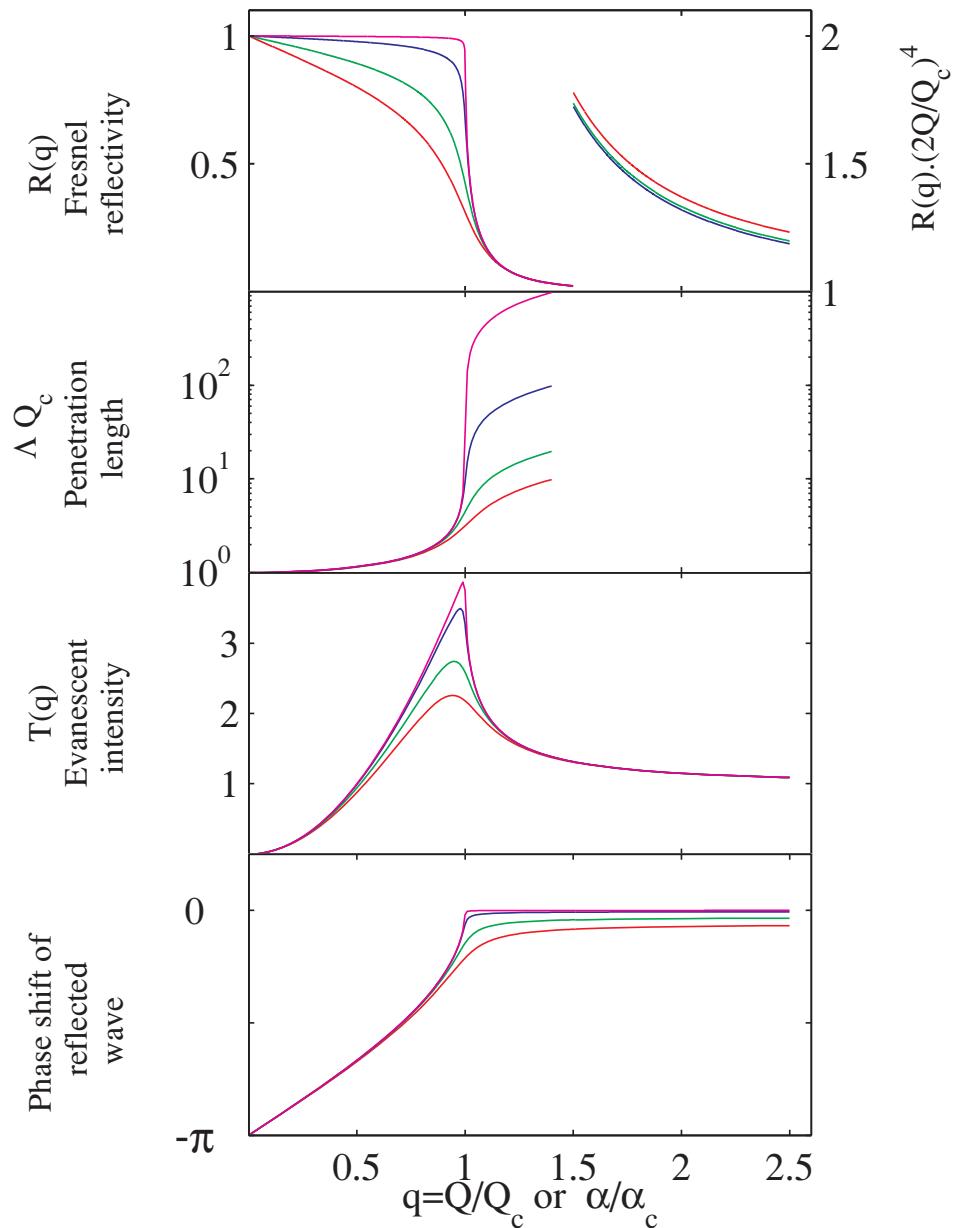
Fig. 3.5 ★ The intensity reflectivity $R(q)$, the penetration depth ΛQ_c, the intensity transmittivity $T(q)$ and the phase of the reflected wave, all versus Q/Q_c or α/α_c. In each case a family of curves is given corresponding to different values of the (small) parameter b_μ. The values of $b_\mu (= 2\mu k/Q_c^2)$ used were: 0.001, 0.01, 0.05, 0.1. The right hand side of the figure gives the asymptotic behaviour, scaled to the expressions in the text for $q \gg 1$, which by definition approaches unity as $q \gg 1$.

	Z	Molar density (g/mole)	Mass density (g/cm^3)	ρ (e/Å^3)	Q_c (1/Å)	$\mu \times 10^6$ (1/Å)	b_μ (1/Å)
C	6	12.01	2.26	0.680	0.031	0.104	0.0009
Si	14	28.09	2.33	0.699	0.032	1.399	0.0115
Ge	32	72.59	5.32	1.412	0.045	3.752	0.0153
Ag	47	107.87	10.50	2.755	0.063	22.128	0.0462
W	74	183.85	19.30	4.678	0.081	33.235	0.0409
Au	79	196.97	19.32	4.666	0.081	40.108	0.0495

Table 3.1 Reflectivity parameters for selected elements: electron density, ρ; critical wavevector, Q_c; linear absorption coefficient, μ, at $\lambda=1.54051$ Å.

An overview of the different quantities versus scattering vector or incident angle is given in Fig. 3.5$\star$. In Table 3.1 the parameters needed to compute the reflectivity for several elements are given.

It should be emphasized here that the Fresnel reflectivity is *specular*. This means that the reflected intensity is confined to the plane spanned by the incident wavevector and the interface normal, and that within this plane the angle of the reflected beam equals the angle of the incident beam. Non-specular reflectivity is produced by rough surfaces, as we shall explain later in this chapter.

3.5   Reflection from a homogeneous slab
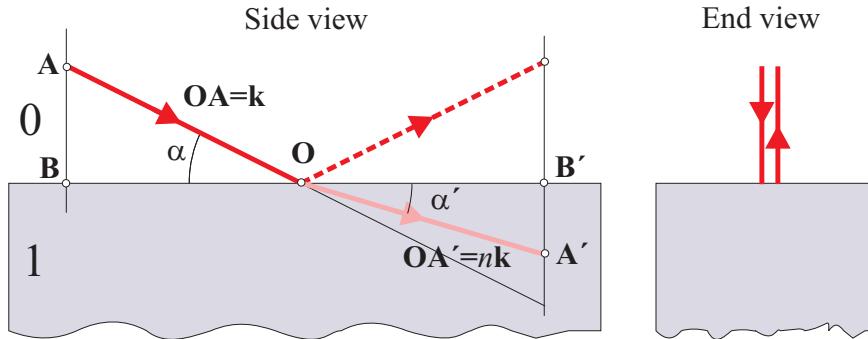
In this section the reflectivity from a slab of finite thickness is considered. This is shown schematically in Fig. 3.6 where it is compared with the case of the infinitely thick medium described in the previous section.

Consider first Fig. 3.6(a) where a wave propagating in medium 0 with refractive index 1 is incident on an infinitely thick medium of refractive index n. This part of the figure illustrates how Snell's law can be inferred directly from the boundary condition that the waves are continuous at the interface. The incident plane wave, $e^{i\mathbf{k}\cdot\mathbf{r}}$, with wavevector $\mathbf{OA}=\mathbf{k}$, can be decomposed into two plane waves with wavevectors along, k_x, and normal, k_z, to the interface: $e^{i\mathbf{k}\cdot\mathbf{r}}=e^{ik_x x}e^{ik_z z}$. Continuity at the interface implies that the component of k_x cannot change in going from medium 0 to medium 1, i.e. the waves propagating along x in medium 0 and medium 1 must necessarily have the same wavelength if a continuous transition is to be made on crossing the interface at any arbitrary point. The wavevector of the transmitted wave in medium 1 must therefore terminate on the vertical line through B$'$. The termination point A$'$ is determined by the condition that OA$'$=nk. Snell's law then follows immediately.

Next consider a slab of finite thickness shown in Fig. 3.6(b). The side view depicts only the transmitted wavevectors across the two interfaces from medium 0 to 1, and from 1 to 2, whereas the right panel shows the z components of the wavevectors. In contrast to the case of the infinite slab there is now an infinite series of possible reflections, and the first three of these are drawn in the figure:

(a) Reflection at interface 0 to 1, amplitude r_{01}.

(b) Transmission at interface 0 to 1, t_{01}, then reflection at interface 1 to 2, r_{12}, followed by transmission at interface 1 to 0, t_{10}. In adding this wave to the above it is necessary to include the phase factor $p^2 = e^{iQ\Delta}$.

(a) Infinitely thick slab

(b) Finite thickness slab
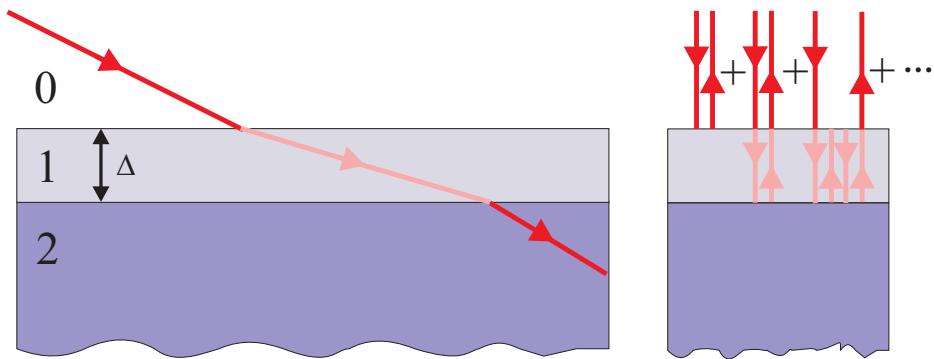
Fig. 3.6 Reflection and transmission from a slab of infinite (a) and finite (b) thickness. The finite slab is of thickness Δ and the total reflectivity is the sum of the infinite number of reflections, as indicated in the right panel of (b).

(c) Transmission at interface 0 to 1, t_{01}, then reflection at interface 1 to 2, r_{12}, followed by reflection at interface 1 to 0, r_{10}, then another reflection at interface 1 to 2, r_{12}, finally followed by transmission 1 to 0, t_{10}. The total phase factor for this wave is p^4.

The total amplitude reflectivity is therefore:

$$
\begin{aligned}
r_{\text{slab}} &= r_{01} + t_{01}t_{10}r_{12}\,p^2 + t_{01}t_{10}r_{10}r_{12}^2\,p^4 + t_{01}t_{10}r_{10}^2 r_{12}^3\,p^6\cdots \\
&= r_{01} + t_{01}t_{10}r_{12}\,p^2 \left\{1 + r_{10}r_{12}\,p^2 + r_{10}^2 r_{12}^2\,p^4\cdots\right\} \\
&= r_{01} + t_{01}t_{10}r_{12}\,p^2 \sum_{m=0}^{\infty}(r_{10}r_{12}p^2)^m
\end{aligned}
$$

This is a geometric series which may be evaluated as described on page 52 to give

$$
r_{\text{slab}} = r_{01} + t_{01}t_{10}r_{12}\,p^2\,\frac{1}{1 - r_{10}r_{12}p^2}
$$

This expression may be simplified using the Fresnel equations (Eq. (3.22)). Following the notation of
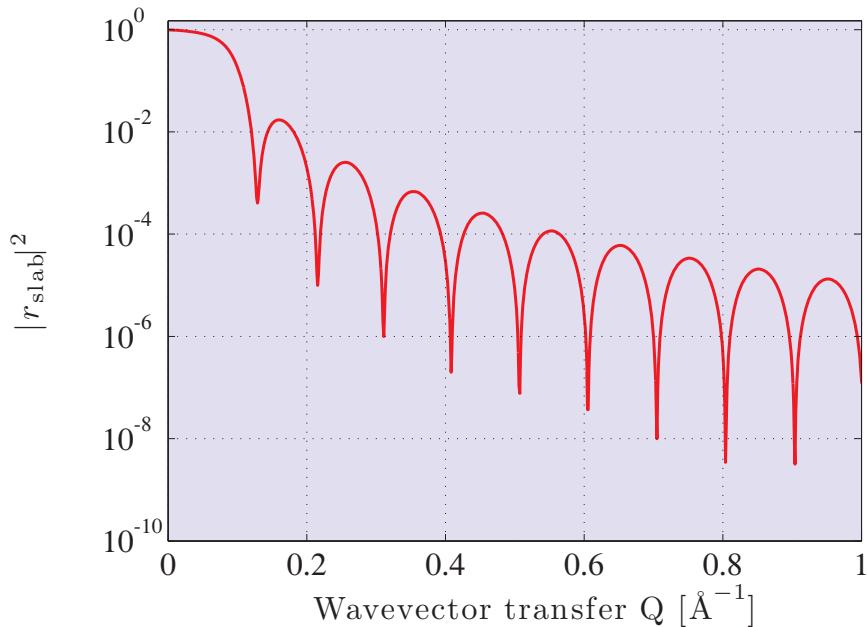
Fig. 3.7 ⋆ Kiessig fringes from a homogeneous slab of Tungsten. Solid curve: the calculated reflectivity $|r_{slab}|^2$ for a slab of thickness $10 \times 2\pi$ Å. The density of the film is 4.678 electrons per Å^3, Table 3.1.

Fig. 3.6 we have

$$r_{01} = \frac{Q_0 - Q_1}{Q_0 + Q_1} \quad \text{and} \quad t_{01} = \frac{2Q_0}{Q_0 + Q_1}$$

which in turn imply that

$$r_{01} = -r_{10}$$

and

$$r_{01}^2 + t_{01}t_{10} = \frac{(Q_0 - Q_1)^2}{(Q_0 + Q_1)^2} + \frac{2Q_0 \, 2Q_1}{(Q_0 + Q_1)^2} = \frac{(Q_0 + Q_1)^2}{(Q_0 + Q_1)^2} = 1$$

so that $t_{01}t_{10} = 1 - r_{01}^2$. The expression for r_{slab} thus becomes

$$\boxed{r_{slab} = \frac{r_{01} + r_{12}p^2}{1 + r_{01}r_{12}p^2}} \tag{3.23}$$

The phase factor, p^2, of the rays reflected from the top and bottom faces of the slab is $e^{iQ_1\Delta}$, where $Q_1 = 2k_1 \sin \alpha_1$.

For simplicity it is further assumed that the media on either side of the slab are the same, or in other words that $r_{01} = -r_{12}$. In this case the slab reflectivity becomes

$$r_{slab} = \frac{r_{01}(1 - p^2)}{1 - r_{01}^2 p^2}$$

The intensity reflectivity given by this formula is plotted in Fig. 3.7⋆, and displays oscillations known as Kiessig fringes [Kiessig, 1931] due to the interference of waves reflected from the top and bottom interfaces. The peaks in the oscillations correspond to the waves scattering in phase, and the dips to them scattering out of phase. In the figure Δ has been chosen to be equal to $10 \times 2\pi$ Å, which makes it clear that the oscillations occur with a period of $2\pi/\Delta$ in Q.

The expression for the reflectivity of a slab is exact, but it is instructive to consider some limiting cases. Assume first that the angles are sufficiently large that refraction effects can be neglected, with the result that $|r_{01}| \ll 1$. The reflectivity amplitude in this limit ($q \gg 1$) is derived on page 79 as $r(q) \cong (2q)^{-2}$ with $q = Q/Q_c$. In this case the slab reflectivity becomes

$$r_{\text{slab}} = \frac{r_{01}(1 - p^2)}{1 - r_{01}^2 p^2} \cong r_{01}(1 - p^2) \cong \left(\frac{Q_c}{2Q}\right)^2 (1 - e^{iQ\Delta})$$

This can be recast in a form that will be of use to us in the section on multilayers by rewriting it as

$$r_{\text{slab}} = -\frac{16\pi\rho r_0}{4Q^2} e^{iQ\Delta/2} (e^{iQ\Delta/2} - e^{-iQ\Delta/2})$$

$$= \left(\frac{16\pi\rho r_0\Delta}{2Q}\right) \frac{e^{iQ\Delta/2}}{2(Q\Delta/2)} (-i)\frac{(e^{iQ\Delta/2} - e^{-iQ\Delta/2})}{2i}$$

$$= -i\left(\frac{4\pi\rho r_0\Delta}{Q}\right) \left(\frac{\sin(Q\Delta/2)}{Q\Delta/2}\right) e^{iQ\Delta/2}$$

Second, in addition to neglecting refraction effects it is assumed that the slab is thin, i.e. $Q\Delta \ll 1$, with the result that the reflectivity becomes

$$r_{\text{thin slab}} \cong -i\frac{4\pi\rho r_0\Delta}{Q} = -i\frac{\lambda\rho r_0\Delta}{\sin\alpha} \tag{3.24}$$

This expression is valid for angles well above the critical angle, where the reflectivity is weak, and both multiple reflections and refraction effects can be neglected. This is referred to as the region of kinematical reflectivity.

An alternative way to derive the reflectivity from a thin film is to use the following heuristic argument. The amplitude of the reflected wave must be proportional to the density of electrons, ρ, as well as to the scattering length r_0, and to the thickness of sample traversed which is equal to $\Delta/\sin\alpha$. However, the product of these three variables has the dimension of inverse length, whereas the reflectivity is a dimensionless number. The only length remaining in the problem is the X-ray wavelength. Thus from a dimensional analysis the reflectivity from a thin slab is $r_{\text{thin slab}} = C(\rho r_0 \lambda\Delta/\sin\alpha)$, where C is a complex constant to be determined. The value of C can be found by imagining an infinitely thick medium as being formed from an infinite stack of thin slabs. In other words, by integrating the expression for $r_{\text{thin slab}}$ from 0 to ∞, taking into account of course the appropriate phase factor, we should obtain the Fresnel reflectivity, r_F:

$$r_F = C \int_0^\infty \left(\frac{\rho r_0\lambda}{\sin\alpha}\right) e^{iQz} dz = C\left(\frac{\rho r_0\lambda}{\sin\alpha}\right)\left(\frac{1}{iQ}\right) \int_0^\infty e^{iQz} d(iQz)$$

$$= -iC\left(\frac{\rho r_0 2\pi}{Qk\sin\alpha}\right)\left[e^{iQz}\right]_0^\infty = iC\left(\frac{Q_c}{2Q}\right)^2$$
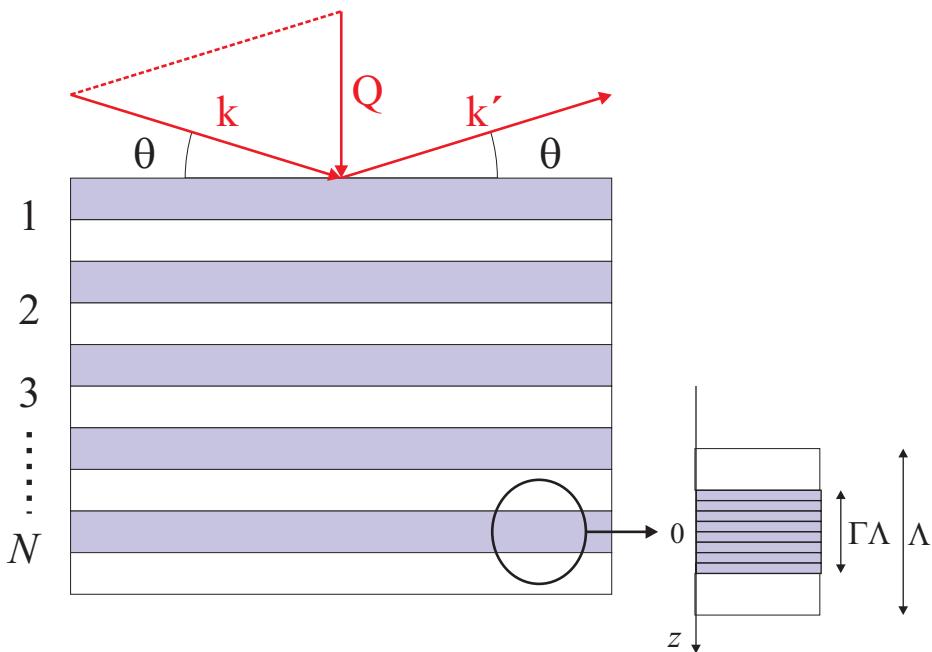
Fig. 3.8 Schematic of a multilayer which here is a stack of bilayers. Each bilayer, as shown to the right has a homogeneous high electron density region of thickness $\Gamma\Lambda$, and a low density region. The total thickness of a bilayer is Λ.

where the expression given in Eq. (3.21) for Q_c has been used. However, the Fresnel amplitude reflectivity is $r_F \approx (Q_c/2Q)^2$ in the limit that $\alpha \gg \alpha'$, which implies that $C = -i$. Thus the heuristic argument taken together with this determination of C is in accordance with Eq. (3.24).

3.6 Specular reflection from multilayers

The scattering from multilayer structures has assumed particular significance in recent years. Modern growth techniques allow materials to be designed and fabricated at the atomic or molecular level. Many technologically important materials are now produced in this way, as under favourable conditions it is possible to tailor make materials with desired physical properties. One particularly interesting and useful class of materials is the multilayer or superlattice. This is a system grown by depositing one material on top of another in a repetitive sequence as shown in Fig. 3.8.

Materials that are used to fabricate multilayers range from metallic or semiconducting elements, through to complex molecules such as are found in a Langmuir layer. In most cases a specific growth technique has been developed to produce the multilayer system of interest. What is common to all of these systems is that there is a need to characterize the resulting structure. X-ray and neutron reflectivity turns out to be an excellent tool for this task, as the contrast in scattering density between the two materials gives rise to scattering. However, from now on we consider X-ray reflectivity only, for which the scattering length density is simply ρr_0.

The most general approach is to extend what has been developed so far for the single slab, so as to obtain an expression that is valid at all scattering angles. It is more instructive, however, to start

by considering the kinematical reflectivity, where multiple reflections and refraction are assumed to be small. The resulting formulae are then valid only at angles well away from the critical angle, but have the advantage that the connection between the equations and the electron density profile is more transparent. The mathematical implication of restricting ourselves to the kinematical region is that we can deduce the amplitude reflectivity as a superposition of reflected waves from infinitesimal sheets, taking into account of course the phase factor e^{iQz} for the sheet at depth z. Unsurprisingly, the equations are very similar to those used to describe the scattering of light from an optical diffraction grating.

Kinematical approximation

For convenience we imagine the structure of the multilayer as being composed of N repetitions of a single bilayer of thickness Λ formed from one layer of material A followed by B, as shown in Fig. 3.8. No assumption is made about the detailed structure of A or B, so that the formulae apply equally well to amorphous or crystalline materials: all that matters is that there is an electron density contrast between A and B. Having decomposed the multilayer into a sum of bilayers it is then straightforward to write down an expression for the reflectivity. First the scattering amplitude from a single bilayer is calculated, and then a sum made over the N bilayers, making suitable allowance for the difference in phase factors for the waves scattered from each bilayer. Here it is assumed that the interfaces are flat, and the wavevector $\mathbf{Q}$ is parallel to the surface normal, so the reflectivity is specular, and the problem of summing the phases is then one dimensional.

If r_1 is the reflectivity from a single bilayer, then the reflectivity from N bilayers comprising the multilayer is

$$r_N(\zeta) = \sum_{\nu=0}^{N-1} r_1(\zeta)\, e^{i\,2\pi\zeta\nu} e^{-\beta\nu} = r_1(\zeta)\,\frac{1 - e^{i\,2\pi\zeta N} e^{-\beta N}}{1 - e^{i\,2\pi\zeta} e^{-\beta}} \tag{3.25}$$

where ζ is defined by $Q = 2\pi\zeta/\Lambda$, and β is the average absorption per bilayer. The bilayer reflectivity, r_1, is evaluated using the expression for the reflectivity of a thin slab given in Eq. (3.24). To apply this result to the bilayer two modifications need to be made. First, the electron density of the slab must be replaced by the difference in electron densities between A and B, where it is assumed that $\rho_A > \rho_B$. Second, as usual it is necessary to allow for the change in phase of waves reflected from different depths in the bilayer. To do so we imagine the high density material A to comprise a fraction Γ of the bilayer, and to be subdivided into thin sheets, each of which has the reflectivity of a thin slab, but with ρ replaced by $\rho_{AB} = \rho_A - \rho_B$.

From Eq. (3.24) the amplitude reflectivity from one bilayer may then be written as

$$\begin{aligned}
r_1(\zeta) &= -i\frac{\lambda r_0 \rho_{AB}}{\sin\theta} \int_{-\Gamma\Lambda/2}^{+\Gamma\Lambda/2} e^{i\,2\pi\zeta z/\Lambda}\, dz \\
&= 4\pi r_0 \rho_{AB}\frac{1}{iQ} \int_{-\Gamma\Lambda/2}^{+\Gamma\Lambda/2} e^{i\,2\pi\zeta z/\Lambda}\, dz \\
&= -2i r_0 \rho_{AB}\left(\frac{\Lambda^2 \Gamma}{\zeta}\right)\frac{\sin(\pi\Gamma\zeta)}{\pi\Gamma\zeta}
\end{aligned} \tag{3.26}$$

To evaluate the absorption parameter β for a bilayer we note that the incident X-ray has a path length $\Lambda/\sin\theta$ in the bilayer, of which a fraction Γ is through A and a fraction $(1-\Gamma)$ through B. Remembering that the absorption coefficient μ refers to intensity and not amplitude, the amplitude absorption for a

bilayer is $e^{-\beta}$ with

$$\beta = 2\left[\left(\frac{\mu_A}{2}\right)\left(\frac{\Gamma\Lambda}{\sin\theta}\right) + \left(\frac{\mu_B}{2}\right)\left(\frac{(1-\Gamma)\Lambda}{\sin\theta}\right)\right]$$

$$= \frac{\Lambda}{\sin\theta}\left[\mu_A\Gamma + \mu_B(1-\Gamma)\right]$$

where the factor of 2 in the first line allows for the path length of both the incident and reflected beam.

In Fig. 3.9(a)⋆ the reflectivity curve of a multilayer is shown. This serves to illustrate how the different factors in Eq. (3.25) combine to produce the resulting curve. A specific example has been chosen of a multilayer formed from 10 bilayers, where each bilayer has 10 Å of W and 40 Å of Si. (This or similar types of multilayers are useful optical components in X-ray beamlines, as we shall see in Section 3.10.) The main peaks in the reflectivity occur when ζ is an integer, as the denominator in Eq. (3.25) is then zero (at least if β may be assumed to be negligible). These correspond to the principal diffraction maxima from a diffraction grating. In between the principal maxima there are auxiliary maxima due to oscillations in the numerator. In real optical components for X-ray applications the number of bilayers is normally much larger than 10, so that the spacing between the auxiliary maxima becomes small and the reflectivity of the first principal maxima tends to 100%.

Parratt's exact recursive method

A method to extend the exact result for a single slab (Eq. (3.23)) to the case of a stratified medium has been described by Parratt [Parratt, 1954]. The medium is imagined as being composed of N strata, or layers, sitting on top of an infinitely thick substrate. By definition the N'th layer sits directly on the substrate. Each layer in the stack has a refractive index $n_j = 1 - \delta_j + i\beta_j$ and is of thickness Δ_j. It follows from Fig. 3.6 that the z component of the wavevector, $k_{z,j}$, in the slab labelled j is determined from the total wavevector $k_j = n_j k$ and the x component, $k_{x,j}$, which is conserved through all layers so $k_{x,j} = k_x$ for all j. The value of $k_{z,j}$ is found from

$$k_{z,j}^2 = (n_j k)^2 - k_x^2 = (1 - \delta_j + i\beta_j)^2 k^2 - k_x^2 \approx k_z^2 - 2\delta_j k^2 + i\,2\beta_j k^2$$

Noting that $Q_j = 2k_j \sin\alpha_j = 2k_{z,j}$, the wavevector transfer in the j'th layer is

$$Q_j = \sqrt{Q^2 - 8k^2\delta_j + i\,8k^2\beta_j}$$

In the absence of multiple reflections, the reflectivity (Eq. (3.22)) of each interface is obtained from the Fresnel relation

$$r'_{j,j+1} = \frac{Q_j - Q_{j+1}}{Q_j + Q_{j+1}}$$

where the prime is used to denote a reflectivity amplitude that does not include multiple scattering effects.

The first step is to calculate the reflectivity from the interface between the bottom of the N'th layer and the substrate. As the substrate is infinitely thick there are no multiple reflections to consider and

$$r'_{N,\infty} = \frac{Q_N - Q_\infty}{Q_N + Q_\infty}$$

The reflectivity from the top of the N'th layer is then evaluated using Eq. (3.23) as

$$r_{N-1,N} = \frac{r'_{N-1,N} + r'_{N,\infty}p_N^2}{1 + r'_{N-1,N}r'_{N,\infty}p_N^2}$$
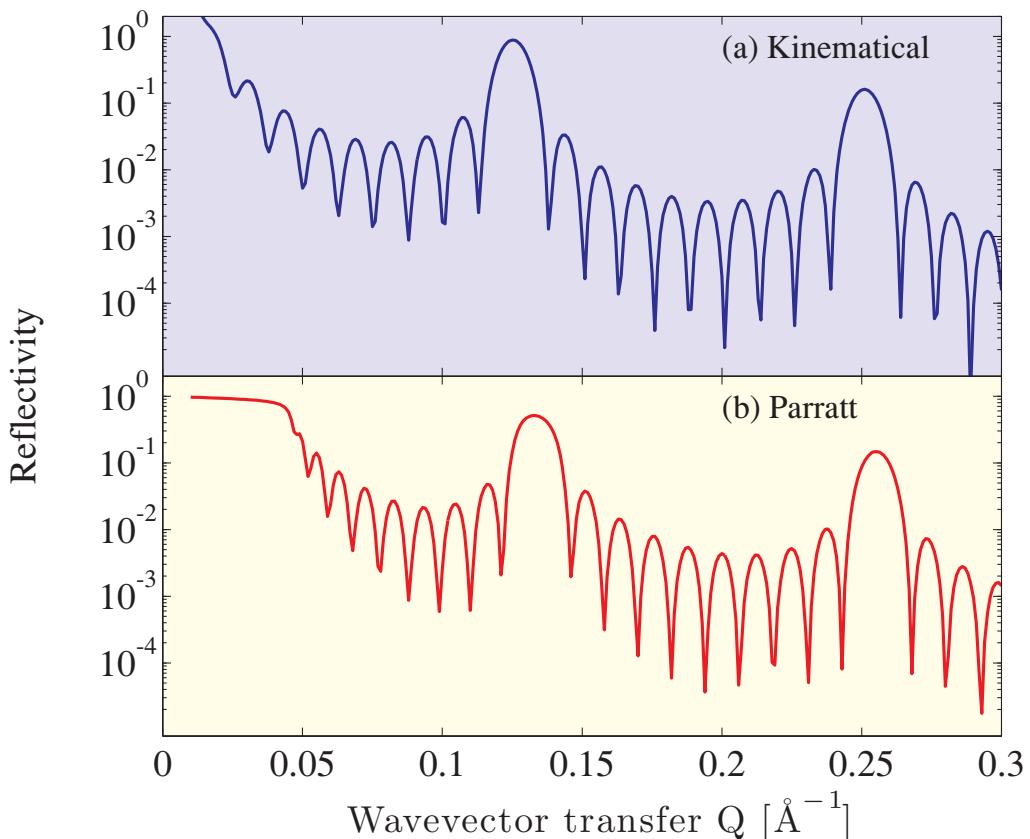
Fig. 3.9 ★ Specular reflectivity from a W/Si multilayer: 10 bilayers each being 10 Å (amorphous) W on 40 Å (amorphous) Si. (a) Kinematical reflectivity. (b) Reflectivity curve calculated using Parratt's method. The parameters used in the calculation were taken from Table 3.1.

which allows for the multiple scattering and refraction in the N'th layer, and where p_N^2 is the phase factor $e^{i\Delta_N Q_N}$, or in general $p_j^2 = e^{i\Delta_j Q_j}$. It follows that the reflectivity from the next interface up in the stack is

$$r_{N-2,N-1} = \frac{r'_{N-2,N-1} + r_{N-1,N} p_{N-1}^2}{1 + r'_{N-2,N-1} r_{N-1,N} p_{N-1}^2}$$

and it is clear that the process can be continued recursively until the total reflectivity amplitude, $r_{0,1}$, at the interface between the vacuum and first layer is obtained.

The reflectivity from the same W/Si multilayer discussed above has been calculated using Parratt's method and is plotted in Fig. 3.9(b)★. A comparison of the two curves shows that as expected there is little difference at high values of Q where the kinematical approximation is valid, but close to the critical wavevector $Q_c \approx 0.04$ Å^{-1} the approximation fails completely.
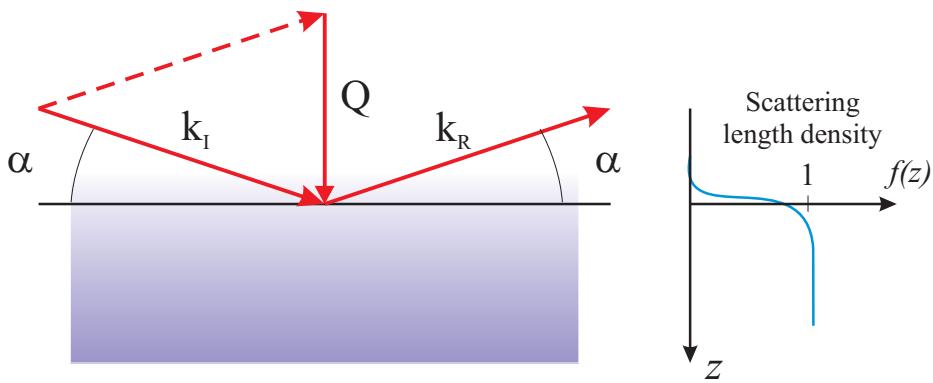
Fig. 3.10 A flat interface with a graded density given by the shape function $f(z)$, normalized to unity at large z. The Fourier transform of its derivative, $\phi(Q)$, can be considered to be the form factor of the density variation across the interface.

3.7   Reflectivity from a graded interface

So far we have considered the reflectivity from systems that have sharp, flat interfaces. Many interesting systems cannot be described in this way, and hence it is necessary to extend the formalism to include graded interfaces. For the sake of simplicity we shall limit ourselves to the kinematical region, where Q is much larger than Q_c. As with the example of reflectivity from a multilayer, this means that the reflectivity is derived by considering the contribution from a thin slab at a depth z, and then summing up all the contributions from the graded interface, making allowance for the change in phase e^{iQz}. The density profile of the interface is given by the function $f(z)$, which is normalized so that $f(z) \to 1$ as $z \to \infty$ as shown in Fig. 3.10. In addition since the density profile represents an interface it must obey the condition that $f(z) \to 0$ as $z \to -\infty$. From Eq. (3.24) the contribution to the reflectivity from an infinitesimal thin slab at depth z is

$$\delta r(Q) = -i \left(\frac{Q_c^2}{4Q} \right) f(z) \, dz$$

The amplitude reflectivity for the superposition of infinitesimal layers is thus

$$
\begin{aligned}
r(Q) &= -i \left(\frac{Q_c^2}{4Q} \right) \int_{-\infty}^{\infty} f(z) \, e^{iQz} dz \\
&= i \frac{1}{iQ} \left(\frac{Q_c^2}{4Q} \right) \int_{-\infty}^{\infty} f'(z) \, e^{iQz} dz \\
&= r_F(Q) \, \phi(Q)
\end{aligned}
\tag{3.27}
$$

where $r_F(Q)$ is the Fresnel reflectivity, and $\phi(Q)$ is defined by

$$\phi(Q) = \int_{-\infty}^{\infty} f'(z) \, e^{iQz} dz$$

In the second line of Eq. (3.27) we have used partial integration, and in the third we have used the expression from Eq. (3.22) for the Fresnel reflectivity of a sharp interface in the limit $q \gg 1$. The

measured reflectivity is the intensity reflectivity, obtained as the absolute square of $r(Q)$. The *master formula* for the intensity reflectivity of a graded interface is therefore

$$\frac{R(Q)}{R_F(Q)} = \left| \int_{-\infty}^{\infty} \left(\frac{df}{dz}\right) e^{iQz}\, dz \right|^2 \tag{3.28}$$

or expressed in words: the ratio between the actual reflectivity and that for an ideal sharp interface is the absolute square of the Fourier transform of the normalized gradient of the density across the interface. In Appendix E the reader is reminded of the definition of the Fourier transform.

The master formula is particularly useful as it allows analytical expressions to be used for the density gradient at an interface. One commonly used function in this context is the error function

$$f(z) = \text{erf}\left(\frac{z}{\sqrt{2}\sigma}\right)$$

where σ is a measure of the width of the graded region. The derivative of the error function is a Gaussian

$$\frac{df(z)}{dz} = \frac{1}{\sqrt{2\pi\sigma^2}}\, e^{-\frac{1}{2}\left(\frac{z}{\sigma}\right)^2}$$

and the Fourier transform of a Gaussian is another Gaussian, $e^{-Q^2\sigma^2/2}$ (see Appendix E). The intensity reflectivity for this model may then be written in the compact form

$$R(Q) = R_F(Q)\, e^{-Q^2\sigma^2} \tag{3.29}$$

It was pointed out by Névot and Croce [1980] that the reflectivity as given in Eq. (3.29) violates time reversal and therefore is incorrect. The correct solution as discussed also by Dosch [1992] is

$$R(Q) = R_F(Q)\, e^{-QQ'\sigma^2}$$

where $Q = k \sin\theta$ and $Q' = k' \sin\theta'$. In practice the difference seldom matters.

3.8   Rough interfaces and surfaces

Real interfaces are rarely, if ever, perfectly flat or uniformly graded. Instead it is expected that the height of an interface has a degree of randomness, in other words the interface is rough. In this section it is explained how the presence of roughness gives rise to distinctive features in the X-ray reflectivity. In keeping with the approach adopted in the preceding sections the reflectivity from a rough interface is treated within the kinematical approximation, where the scattering is assumed to be weak so that multiple reflections may be neglected. This approach has the advantage that it is possible to understand the effects of roughness by comparing directly the results for a rough interface with the limiting form of the Fresnel reflectivity from a flat interface, which varies as $(Q_c/2Q_z)^4$ at high angles.

The formalism in this section differs from what has gone before in that the interface is now described by a statistical distribution [Wong, 1985, Sinha et al., 1988, Cowley, 1994]. In addition the heights

of the interface (or surface) at different points on the rough interface are correlated in a way that is characteristic of the particular type of roughness. One important consequence of the existence of these correlations is that the reflectivity is no longer necessarily strictly specular, as is the case for the Fresnel reflectivity from a sharp interface or from a graded but flat interface. Instead it develops a diffuse component, which is also referred to as the off-specular reflectivity.

Figure 3.11(a) illustrates the reflection of an X-ray beam from a rough surface. A beam of intensity I_0 is incident at a glancing angle θ_1, and the reflected beam is observed at a glancing exit angle θ_2. The incident beam illuminates a volume V (indicated by the darker shading) to a depth determined by the absorption coefficient. Within the kinematical approximation the reflected amplitude of the beam is calculated by summing all of the beams scattered from volume elements $d\mathbf{r}$ within V, taking into account the appropriate phase factors. The scattering amplitude is

$$r_V = -r_0 \int_V (\rho d\mathbf{r}) \, e^{i\mathbf{Q}\cdot\mathbf{r}} \tag{3.30}$$

Here r_0 is the Thomson scattering length of a single electron, $(\rho d\mathbf{r})$ is the number of electrons in a volume element centred at position $\mathbf{r}$, and the last term in the integrand is the phase factor. The volume integral can be transformed to a surface integral using Gauss' theorem, which states that

$$\int_V (\nabla \cdot \mathbf{C}) \, d\mathbf{r} = \int_S \mathbf{C} \cdot d\mathbf{S}$$

where $\mathbf{C}$ is a vector field, S refers to the surface, and $d\mathbf{S}$ is normal to the surface at position (x, y) and has a magnitude equal to $dxdy$.

Gauss' theorem may be applied to transform Eq. (3.30) to a surface integral in the following way. Let $\mathbf{C}$ be the unit vector $\hat{\mathbf{z}}$ along the z axis multiplied by the function $e^{i\mathbf{Q}\cdot\mathbf{r}}/(iQ_z)$. The divergence of $\mathbf{C}$ is then $\nabla \cdot \mathbf{C} = e^{i\mathbf{Q}\cdot\mathbf{r}}/(iQ_z) \times (iQ_z) = e^{i\mathbf{Q}\cdot\mathbf{r}}$, which is the integrand in Eq. (3.30). Expressed as a surface integral the scattering amplitude becomes

$$r_S = -r_0 \int_V (\rho d\mathbf{r}) \, e^{i\mathbf{Q}\cdot\mathbf{r}}$$
$$= -r_0\rho \left(\frac{1}{iQ_z}\right) \int_S e^{i\mathbf{Q}\cdot\mathbf{r}} \, \hat{\mathbf{z}} \cdot d\mathbf{S}$$

The dot product $\hat{\mathbf{z}}\cdot d\mathbf{S}$ is the area element of the rough surface projected onto the $x-y$ plane, $\hat{\mathbf{z}}\cdot d\mathbf{S} = dxdy$, so that

$$r_S = -r_0\rho \left(\frac{1}{iQ_z}\right) \int_S e^{i\mathbf{Q}\cdot\mathbf{r}} \, dxdy$$

It should be noted that the rough surface is not the entire surface enclosing the volume V, as Gauss' formula assumes. However, the lower surface of V does not contribute, since the depth of V can be chosen such that, by the time the beam has penetrated to the lower surface, absorption reduces the beam intensity effectively to zero.

To proceed let the height variation of the rough surface be given by the function $h(x, y)$. Then the scalar product of $\mathbf{Q}$ and $\mathbf{r}$ is $\mathbf{Q} \cdot \mathbf{r} = Q_z h(x, y) + (Q_x x + Q_y y)$, so that the scattering amplitude from the surface is simply

$$r_S = -r_0\rho \left(\frac{1}{iQ_z}\right) \int_S e^{i Q_z h(x,y)} e^{i(Q_x x + Q_y y)} \, dxdy$$
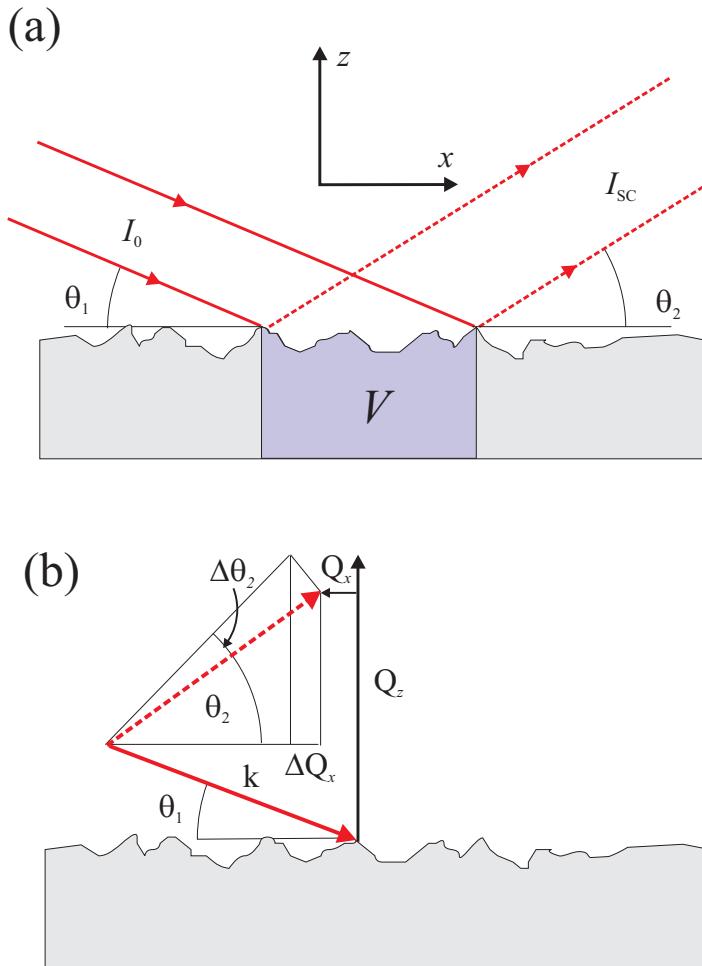
Fig. 3.11 (a) Scattering from a rough surface. (b) Definition of ΔQ_x.

The differential scattering cross-section, $(d\sigma/d\Omega)$, is the absolute square of the scattering amplitude (see Appendix A):

$$\left(\frac{d\sigma}{d\Omega}\right) = \left(\frac{r_0\rho}{Q_z}\right)^2 \int e^{iQ_z[h(x,y)-h(x',y')]} e^{iQ_x(x-x')} e^{iQ_y(y-y')} \, dx\,dx'\,dy\,dy'$$

It is now assumed that the difference in heights, $h(x,y)-h(x',y')$, depends only on the relative difference in position $(x-x', y-y')$. The four-dimensional integral above then reduces to the product of two two-dimensional integrals, one of which is simply $\int dx\,dy = A_0/\sin\theta_1$, the illuminated surface area, and we obtain

$$\left(\frac{d\sigma}{d\Omega}\right) = \left(\frac{r_0\rho}{Q_z}\right)^2 \left(\frac{A_0}{\sin\theta_1}\right) \int \langle e^{iQ_z[h(0,0)-h(x,y)]}\rangle e^{i(Q_x x + Q_y y)} \, dx\,dy$$

The angular brackets indicate an ensemble average: for a fixed (x', y') one evaluates the average value of the function for all possible choices of the origin within the illuminated area. (We note in passing

that the right hand side of the formula has the correct dimension of area.) One further assumption is now introduced, namely that the statistics of the height variations are Gaussian, with the consequence that the cross-section may be written as

$$\left(\frac{d\sigma}{d\Omega}\right) = \left(\frac{r_0\rho}{Q_z}\right)^2 \left(\frac{A_0}{\sin\theta_1}\right) \int e^{-Q_z^2\langle[h(0,0)-h(x,y)]^2\rangle/2}\, e^{i(Q_x x + Q_y y)}\, dxdy \qquad (3.31)$$

This follows from the Baker-Hausdorff theorem, which is proved in Appendix D. In the following the reflectivity is calculated for different models of the function $g(x, y)$ describing the ensemble average of height differences, where

$$g(x, y) = \langle[h(0, 0) - h(x, y)]^2\rangle$$

3.8.1   The limiting case of Fresnel reflectivity

It is instructive to first check Eq. (3.31) against the kinematical form of the Fresnel reflectivity from a flat interface. To do so we set $h(x, y) = 0$ for all (x, y) with the result that

$$\left(\frac{d\sigma}{d\Omega}\right)_{\text{Fresnel}} = \left(\frac{r_0\rho}{Q_z}\right)^2 \left(\frac{A_0}{\sin\theta_1}\right) \int e^{i(Q_x x + Q_y y)}\, dxdy \qquad (3.32)$$

From the definition of the Fourier transform (see Appendix E) it can be seen that if $F(q) = 2\pi\delta(q)$ then $f(x) = (1/2\pi)\int F(q)e^{-iqx}dq = 1$, and since also by definition $F(q) = \int f(x)e^{iqx}dx = \int 1\,e^{iqx}dx$, the double integral above is equal to $(2\pi)^2\delta(Q_x)\delta(Q_y)$, and thus

$$\left(\frac{d\sigma}{d\Omega}\right)_{\text{Fresnel}} = \left(\frac{2\pi r_0\rho}{Q_z}\right)^2 \left(\frac{A_0}{\sin\theta_1}\right)\delta(Q_x)\delta(Q_y)$$

In order to make a connection between the cross-section, which has been derived here, and the formula for the intensity reflectivity that was derived earlier, we recall that the scattered intensity is related to the differential cross-section through

$$I_{\text{sc}} = \left(\frac{I_0}{A_0}\right)\left(\frac{d\sigma}{d\Omega}\right)\Delta\Omega$$

(see Appendix A). The element of solid angle $\Delta\Omega$ is evaluated with the help of Fig. 3.11(b), which shows the relationship between the angular variables (θ_1, θ_2) and the wavevector variables $(\Delta Q_x, \Delta Q_y)$. It is clear from this figure that $k\Delta\theta_2 \sin\theta_2 = \Delta Q_x$, and as the y axis is perpendicular to the plane of the paper $k\Delta\varphi = \Delta Q_y$. Then since $\Delta\Omega = \Delta\theta_2\Delta\varphi$ the expression for the intensity becomes

$$I_{\text{sc}} = \left(\frac{I_0}{A_0}\right)\left(\frac{d\sigma}{d\Omega}\right)\frac{\Delta Q_x \Delta Q_y}{k^2 \sin\theta_2}$$

Inserting now the Fresnel scattering cross-section it can be seen that the delta functions in Q_x and Q_y imply that the Fresnel reflectivity is confined to the specular direction, $\theta_1 = \theta_2$. Furthermore we note that $k^2 \sin\theta_1 \sin\theta_2 = (Q_z/2)^2$, and recall from Eq. (3.21) that $2\pi r_0\rho = Q_c^2/8$, where the term f'/Z due

to the dispersion correction has been neglected. Collecting all of these factors together the intensity reflectivity is

$$R(Q_z) = \frac{I_{sc}}{I_0} = \left(\frac{Q_c^2/8}{Q_z}\right)^2 \left(\frac{1}{Q_z/2}\right)^2 = \left(\frac{Q_c}{2Q_z}\right)^4$$

which is the expected form of the Fresnel reflectivity in the kinematical limit.

3.8.2   Uncorrelated surfaces

It is now assumed that the heights at different points (x, y) vary without any correlation: the height at (x', y') is independent of the height at (x, y) no matter how close (x, y) is to (x', y'). For points close to each other this is clearly an unphysical assumption, but it is instructive to carry out the analysis of this model anyway. For an uncorrelated surface the ensemble average of height differences Eq. (3.31) is

$$\langle [h(0, 0) - h(x, y)]^2 \rangle = 2\langle h^2 \rangle - 2\langle h(0, 0)\rangle\langle h(x, y)\rangle = 2\langle h^2 \rangle$$

where the average value of h is defined to coincide with $z = 0$. The cross-section then has the form

$$\left(\frac{d\sigma}{d\Omega}\right) = \left(\frac{r_0\rho}{Q_z}\right)^2 \left(\frac{A_0}{\sin\theta_1}\right) e^{-Q_z^2\sigma^2} \int e^{i(Q_x x + Q_y y)} \, dx dy \tag{3.33}$$

which from Eq. (3.32) may be re-expressed as

$$\left(\frac{d\sigma}{d\Omega}\right) = \left(\frac{d\sigma}{d\Omega}\right)_{\text{Fresnel}} e^{-Q_z^2\sigma^2} \tag{3.34}$$

where $\sigma = \sqrt{\langle h^2 \rangle}$ is the rms roughness. From this the following points may be concluded:

(a) Fluctuations in height due to roughness diminish the Fresnel reflectivity. The **Q** dependence of this reduction, given in Eq. (3.34), is very much like the Debye-Waller factor we shall discuss in connection with thermal vibrations of atoms in a crystal in Chapter 5.

(b) Since the height fluctuations are uncorrelated, the scattering is confined to the specular direction, as for the perfectly sharp interface.

(c) The result is identical to Eq. (3.29) for the particular example of a graded, but flat, surface. This illustrates that different models may yield the same reflectivity curve. In other words, reflectivity experiments cannot *uniquely* reveal the true nature of an interface.

3.8.3   Correlated surfaces

Our starting point is again Eq. (3.31). The difference from the previous section is that now the height fluctuations are correlated. It is further assumed that the correlations are isotropic in the plane of the surface (or interface), or in other words that $g(x, y)$ depends only on $r = |r| = \sqrt{x^2 + y^2}$. For correlated surfaces it is possible to distinguish between two different cases, depending on the behaviour of $g(x, y)$ in the limit that $r \to \infty$.

The first case to consider is when $g(x, y)$ is given by

$$g(x, y) = \langle [h(0,0) - h(x, y)]^2 \rangle = \mathcal{A}r^{2h}$$

In this case the height fluctuations develop without limit as $r \to \infty$. This type of roughness is displayed by fractal surfaces, and the exponent h determines the morphology of the surface: if $h \ll 1$ the surface is jagged, while as $h \to 1$ it becomes smoother. To evaluate the reflectivity in this case we simplify the mathematics by setting $y = 0$ in Eq. (3.31). This is justified if the resolution in the Q_y direction is very broad, as the intensity is proportional to the integral

$$\int_{-\infty}^{\infty} e^{i Q_y y}\, dQ_y \propto \delta(y)$$

The problem then reduces to evaluating a one-dimensional integral, and as $g(x, y)$ depends on $|x|$ it is a symmetric function so that Eq. (3.31) becomes

$$\left(\frac{d\sigma}{d\Omega} \right) = \left(\frac{r_0 \rho}{Q_z} \right)^2 \left(\frac{A_0}{\sin \theta_1} \right) \int_0^{\infty} e^{-\mathcal{A}Q_z^2 |x|^{2h}/2} \, \cos(Q_x x)\, dx$$

In general the integral must be evaluated numerically, except for when $h = 1/2$ or $h = 1$, where it may be evaluated analytically using the results given in Appendix E to give

$$h = \frac{1}{2} \quad \Rightarrow \quad \left(\frac{d\sigma}{d\Omega} \right) = \left(\frac{A_0 r_0^2 \rho^2}{2 \sin \theta_1} \right) \frac{\mathcal{A}}{\left(Q_x^2 + (\mathcal{A}/2)^2 Q_z^4 \right)} \tag{3.35}$$

$$h = 1 \quad \Rightarrow \quad \left(\frac{d\sigma}{d\Omega} \right) = \left(\frac{2 \sqrt{\pi} A_0 r_0^2 \rho^2}{\sin \theta_1} \right) \frac{1}{Q_z^4} e^{-\frac{1}{2}\left(\frac{Q_x^2}{\mathcal{A}Q_z^2} \right)} \tag{3.36}$$

The first has a Lorentzian lineshape as a function of Q_x with a half width of $\mathcal{A}Q_z^2/2$, while the second has a Gaussian lineshape with the variance of $\mathcal{A}Q_z^2$. It is clear that the reflectivity from a surface where the height correlations are unbounded is completely diffuse, that is it lacks a delta function component in x (or y). This is contrast to the earlier cases of flat or uncorrelated surfaces, which have purely specular reflectivities. To illustrate this we show in Fig. 3.12 the reflectivity calculated using Eq. (3.35). Scans of Q_x at different fixed values of Q_z display a Lorentzian lineshape with a width that is proportional to Q_z^2.

The second case to consider is where the height fluctuations remain finite as $r \to \infty$. This is best explored by writing

$$g(x, y) = \langle [h(0,0) - h(x, y)]^2 \rangle = 2\langle h^2 \rangle - 2\langle h(0,0)h(x, y)\rangle$$
$$= 2\sigma^2 - 2\, C(x, y) \tag{3.37}$$

where $C(x, y) = \langle h(0,0)h(x, y)\rangle$ is known as the height-height correlation function. For example, if $C(x, y) = \sigma^2 e^{-(r/\xi)^{2h}}$ then it can be seen that for $r \ll \xi$, $g(x, y) \propto r^{2h}$, and that as $r \to \infty$, $g(x, y) \to 2\sigma^2$ as required. From Eqs. (3.31) and (3.37) the cross-section becomes

$$\left(\frac{d\sigma}{d\Omega} \right) = \left(\frac{r_0 \rho}{Q_z} \right)^2 \left(\frac{A_0}{\sin \theta_1} \right) e^{-Q_z^2 \sigma^2} \int e^{Q_z^2 C(x,y)} e^{i(Q_x x + Q_y y)} \, dxdy$$
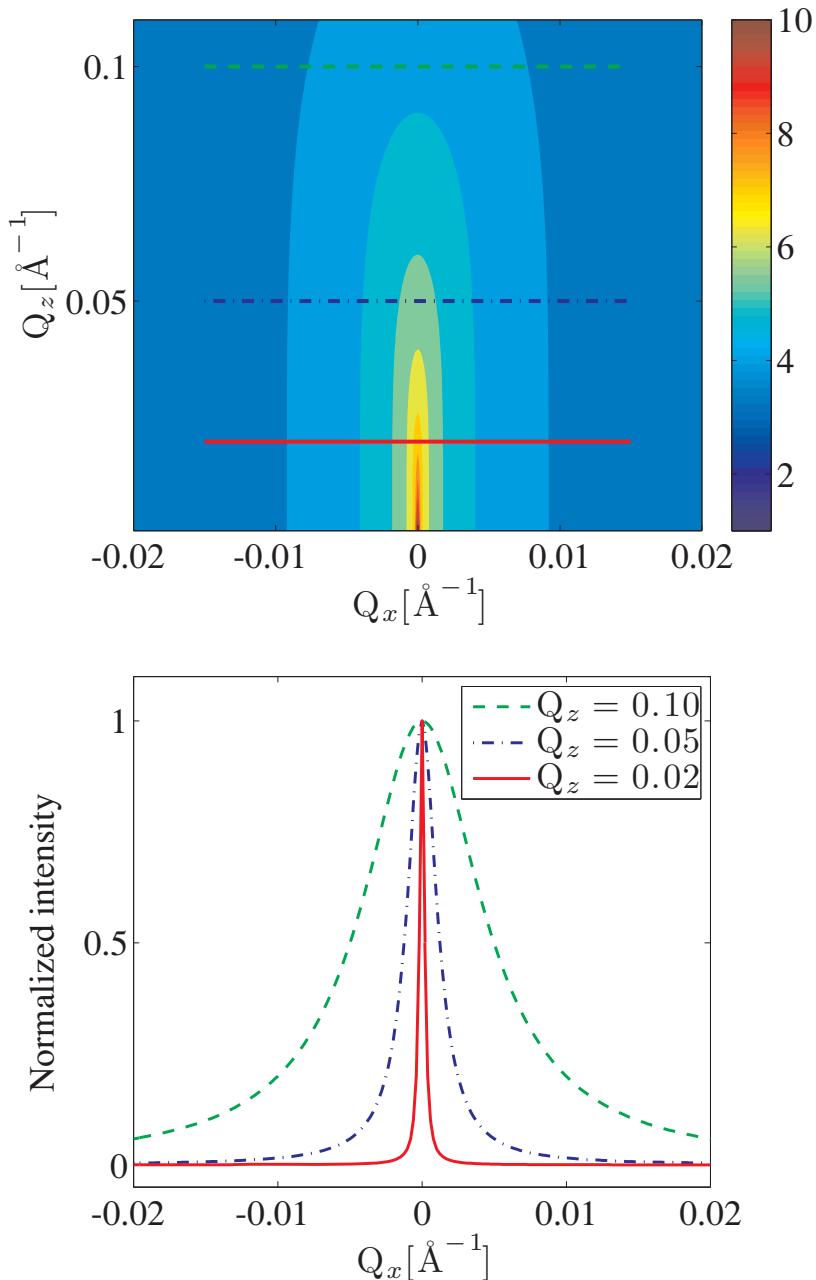
Fig. 3.12 Top: the diffuse scattering from a rough surface described by $g(x, y) = \mathcal{A}r^{2h}$ with $h = 1/2$ (see Eq. (3.35)). The coordinate system is such that Q_z is perpendicular to the surface, and Q_x lies in the surface plane. The intensity has been plotted on a logarithmic scale. Bottom: Q_x scans at different values of Q_z indicated by the dashed lines in the top part of the figure. For clarity, each of the scans has been normalized to unity. The lineshape is seen to be Lorentzian, with a width that broadens as a function of Q_z.

By rewriting it in the form

$$\left(\frac{r_0\rho}{Q_z}\right)^2 \left(\frac{A_0}{\sin\theta_1}\right) e^{-Q_z^2\sigma^2} \int \left[e^{Q_z^2 C(x,y)} - 1 + 1\right] e^{i(Q_x x + Q_y y)} \, dx dy$$

it is possible to separate it into a specular and diffuse (or off-specular) term, since the last term in the square brackets is evidently the specular reflectivity from an *uncorrelated* surface given by Eq. (3.33). The total cross-section then becomes

$$\left(\frac{d\sigma}{d\Omega}\right) = \left(\frac{d\sigma}{d\Omega}\right)_{\text{Fresnel}} e^{-Q_z^2\sigma^2} + \left(\frac{d\sigma}{d\Omega}\right)_{\text{diffuse}} \tag{3.38}$$

where the diffuse component is now given by

$$\left(\frac{d\sigma}{d\Omega}\right)_{\text{diffuse}} = \left(\frac{r_0\rho}{Q_z}\right)^2 \left(\frac{A_0}{\sin\theta_1}\right) e^{-Q_z^2\sigma^2} F_{\text{diffuse}}(\mathbf{Q})$$

with

$$F_{\text{diffuse}}(\mathbf{Q}) \equiv \int \left[e^{Q_z^2 C(x,y)} - 1\right] e^{i(Q_x x + Q_y y)} \, dx dy$$

The scattering from a surface where the height fluctuations are bounded therefore consists of two components. As a function of Q_x (or Q_y) the scattering has a sharp specular component superimposed on a diffuse component. In an experiment the ratio of the two will depend on the instrumental resolution. This takes us beyond the scope of this introduction, but it should be clear that X-ray reflectivity is a useful probe of the correlations displayed by rough surfaces.

3.9 Examples of reflectivity studies

Two examples of reflectivity studies are given. In the first the *specular* reflectivity from a Langmuir layer is considered. Although such a layer is a heterogeneous structure formed from complex organic molecules it turns out that X-ray reflectivity is an excellent tool for characterizing the overall morphology of such a layer. The second example concerns the reflectivity from liquid crystals. By studying the specular and *off-specular* reflectivities together it is shown how it is possible to understand the detailed nature of the critical fluctuations associated with the phase transitions in these systems.

3.9.1 Langmuir layers

X-ray reflectivity can be used to study heterogeneous structures with one or more atomic or molecular layers on a substrate. One such example is a so-called Langmuir layer. These are composed of insoluble amphiphilic molecules, with a hydrophilic chemical group at one end, and a hydrophobic chemical group at the other. When dissolved in a volatile solvent, for example chloroform, a drop of the resulting solution can be spread onto a water surface. The solvent quickly evaporates, and with the appropriate concentration one is left with a monolayer of amphiphilic molecules on top of the water surface: a Langmuir layer.

An example is shown in Fig. 3.13★. The hydrophobic part is a hydrocarbon chain $(CH_2)_n CH_3$ terminating in a methyl group, and the hydrophilic part is carboxylic acid COOH. When the pH of the

subphase is increased by adding a base like NH_3 or $Na(OH)$, the carboxylic acid is charged to COO^-. If in addition the subphase contains positive and negative ions from a salt, in the present case $CdCl_2$, the positive ions will be attracted to the negatively charged COO^- head groups.

We shall now discuss the modelling of the reflectivity data given in the upper right panel. As a first approximation the electron density of the molecules shown in the upper left panel can be modelled as a series of boxes: the upper box of the hydrocarbon tail is of length ℓ_t with a density ρ_t; then comes the head group, represented by a shorter box of length ℓ_h, but with a higher density ρ_h; finally a semi-infinite box corresponding to the water subphase of density ρ_w. The reflected waves from the different interfaces have different phases. Choosing the origin to be in the middle of the head-box, the phase from the upper interface of tail box is $\phi_1 = Q(\ell_t + \ell_h/2)$, the phase form the upper interface of the head-box is $\phi_2 = Q\ell_h/2$, and $-\phi_2$ from the lowest interface. We can readily allow for imperfectly sharp interfaces between the different boxes using the master formula of Eq. (3.28), and by assuming that the change in density between the different boxes can be represented adequately by an error function (see Eq. (3.29)). The density and its derivative are shown schematically in the lower panel of Fig. 3.13$\star$. The Fourier transform of the density gradient then assumes the simple form

$$\phi(Q) = \int \frac{\rho'(z)}{\rho_w} e^{iQz} dz$$

$$= e^{-Q^2\sigma^2/2} \frac{\left[\rho_t e^{-i\phi_1} + (\rho_h - \rho_t)e^{-i\phi_2} - (\rho_h - \rho_w)e^{i\phi_2} \right]}{\rho_w}$$

For this two-box model five parameters can be obtained by fitting it to the data; two for each box (length and density) plus a common smearing parameter. However, one can constrain the model from a knowledge of the molecular chemistry. For example, if there were no counter ions in the subphase, then the total number of electrons in the tail and head group together is known from the chemical formula CH_3-$(CH_2)_{18}$-COO^-. Least-squares fits of $|\phi(Q)|^2 \equiv R(Q)/R_F(Q)$ to the data are represented by the solid lines in the plot of the reflectivity data, and the values of the parameters deduced from the fits are given in the figure caption.

Dramatic differences in the reflectivity curve are apparent when the pH is altered. In (a) it was adjusted by adding NH_3, which resulted in singly charged $Cd(OH)^+$ ions being attracted to the COO^- head group in a 1:1 ratio. In (b) the base was $Na(OH)$ and in this case doubly charged Cd^{++} ions were attracted in the ratio 1:2.

3.9.2   Free surface of liquid crystals

Liquid crystals consist of long molecules with a typical length-to-diameter ratio of 5:1. In the upper part of Fig. 3.14 we show an example of a liquid crystal molecule, for brevity labelled nCB, consisting of a hydrocarbon chain C_nH_{2n+1} terminating in two aromatic rings. Two such molecules pair head-to-head, and this entity is considered as one rod-shaped building block of the structures that form at different temperatures. One must differentiate between the positional and the orientational order of such a building block. In the isotropic phase (I) both the position and orientation of the molecules are disordered, whereas in the nematic phase (N) the positions are disordered, but all molecules have a particular average direction. For the smectic-A phase (SmA) the common orientation is maintained, and in addition the molecules are ordered in layers perpendicular to their long axis with a well-defined repetition distance between the layers, but with positional disorder within the same layer. The smectic-A phase is a particularly interesting object from a structural point of view as it is like a solid crystal in one direction, and, in the plane perpendicular to it, it is like a liquid. Different sequences of transitions
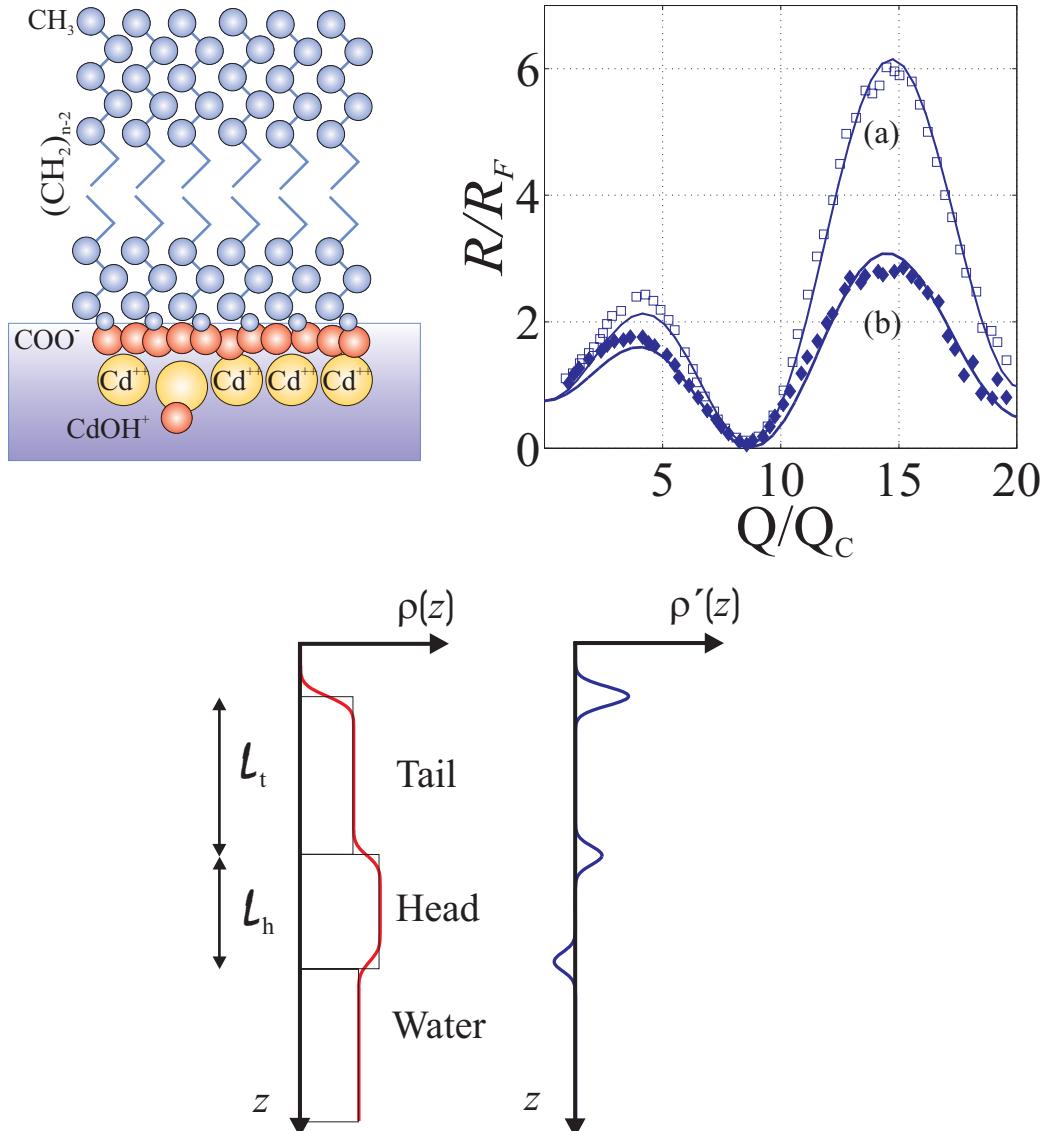
Fig. 3.13 ⋆ Top left: Langmuir layer of arachidic acid (n=20) on a salt solution of CdCl$_2$. Top right: the measured reflectivity data, normalized to the Fresnel reflectivity, and plotted as a function of Q/Q_c, where Q_c=0.0217 Å^{-1} is the critical wavevector of water. Curves (a) and (b) correspond to pH adjustments with NH$_3$ and Na(OH), respectively [Leveiller et al., 1994]. The dramatic difference shows that in the first case monovalent Cd(OH)$^+$ ions are bound to the monovalent COO$^-$ head group in approximately a 1:1 ratio, whereas in the second case divalent Cd^{++} ions are bound in approximately the ratio 1:2. Bottom: two-box model of the density variation across the interfaces of a Langmuir layer on water. Each interface is smeared by a common parameter σ. Parameters deduced from fits to data: (a) ρ_h/ρ_w = 2.28, ρ_t/ρ_w = 1.08, ℓ_h = 6.2 Å, ℓ_t = 22.0 Å, σ = 1.36 Å; (b) ρ_h/ρ_w = 3.35, ρ_t/ρ_w = 1.01, ℓ_h = 2.7 Å, ℓ_t = 23.4 Å, σ = 2.74 Å. The monolayer coverage was 75% in both cases.
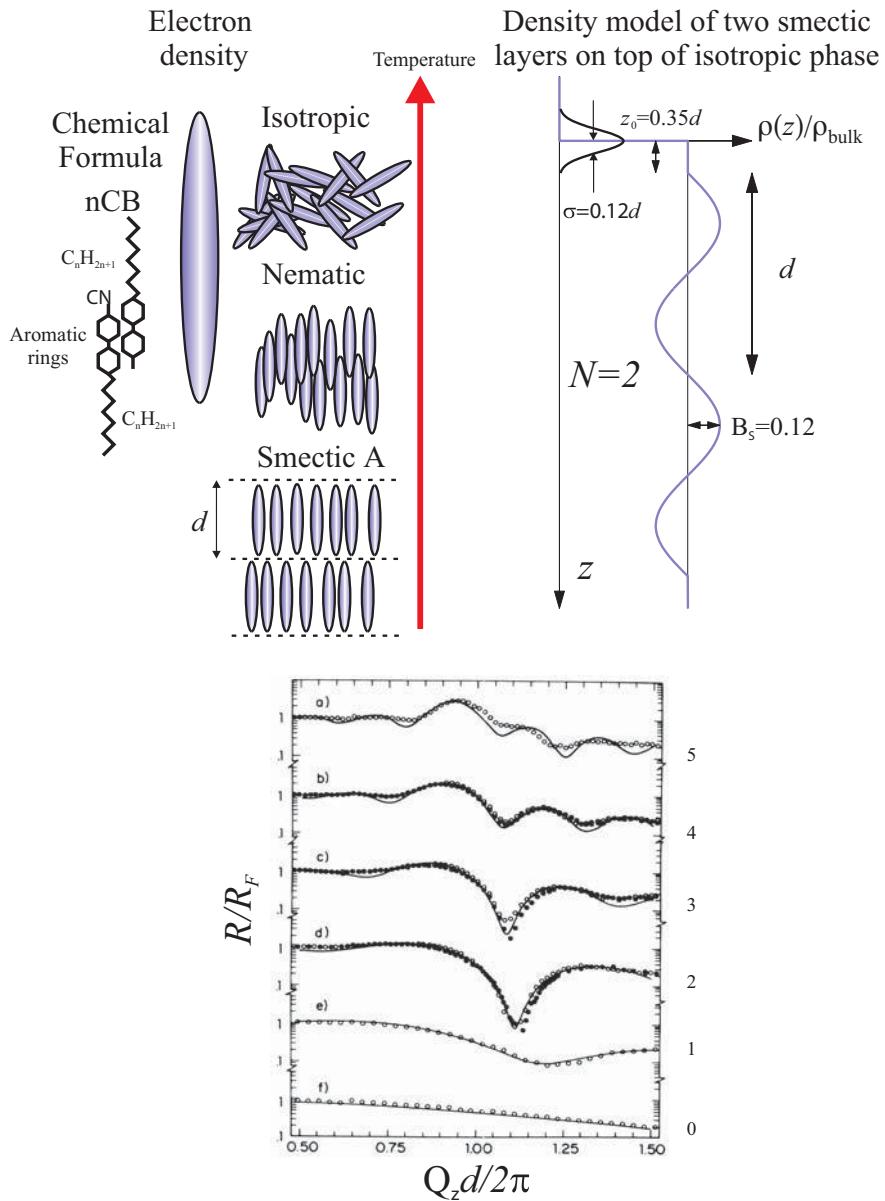
Fig. 3.14 Liquid crystals consist of long, rod-shaped molecules (top left). Different phases are characterized by both positional and orientational order of the molecules. In the isotropic phase both of these are disordered. In the nematic phase the position of the molecules is still random, but they all have a common average orientation, the so-called director field. In the smectic-A phase the position of the molecules along the director field is ordered in layers with a repeat distance d but within a given layer the positions are random: it is like a crystal in one direction and like a liquid in the two perpendicular directions. A density model of two smectic layers on top of the isotropic phase is shown top right. This model was used to interpret reflectivity data (lower panel) from the molecule 12CB, which with decreasing temperature goes from the isotropic phase directly to the smectic-A phase [Ocko et al., 1986]. As the transition is approached a distinct number of layers form at the surface. In the lower figure, f) corresponds to zero layers, e) to one layer, etc.

between these phases may occur. With decreasing temperature one may find I→SmA, or I→N→SmA. Here the I→N transition is first order, but the N→SmA transition may be discontinuous or continuous. In the latter case critical fluctuations of short-range ordered SmA regions in the N matrix become more and more extended as the N→SmA transition temperature is approached.

In the bottom part of Fig. 3.14 we show data at different temperatures in the isotropic phase for 12CB. This compound has no nematic phase but goes directly from the I phase to the SmA phase in a first-order transition. The reflectivity data shows that as the transition is approached by decreasing the temperature a discrete number of layers build up: the bottom curve corresponds to no layering, the next curve corresponds to one layer, the next to two layers and so on. Modelling of two layers is indicated in the upper right panel of Fig. 3.14. The smectic-A layering is a modulation of the density and may be modelled by a sine curve, which in the example shown has two repetitions, each of length d. Adjustable parameters used in fitting to the data are the amplitude B_S (best value is 0.12 of the bulk density), the phase displacement of the sine-curve with respect to the surface (best value $0.35d$) , and also a smearing of the surface (best r.m.s. value is $0.12d$). In fact, all of these parameters are the same for all of the full lines in the plot, except the number of layers N, i.e. the number of periods of the sine wave density.

All it takes to obtain a nematic phase between the I phase and the SmA phase is a shortening of the aliphatic tail of the nCB molecules from n=12 to say n=8. The surface layering is now quite different and so is the scattering and reflectivity data shown in Fig. 3.15.

Let us now consider the scattering from the schematic model shown in the bottom part of Fig. 3.15, and see that this is indeed consistent with the data shown in the top part of the figure. The surface layering has a well defined lattice spacing d, so as usual it must give a peak in the reflectivity curve when $Q_z = 2\pi/d$. If the layer structure is extended very far in the lateral directions, it means that the corresponding scattering must be very confined in reciprocal space, i.e. the surface layering as shown must show up in the specular reflecting direction, and be modulated with a peak at $Q_0 = 2\pi/d$, c.f. the open circles in the left data panel. A scan in the same direction, but slightly displaced from the specular line, looks very different (filled squares in the left data-panel). The intensity is much lower and the peak is symmetric, although it has about the same width as the specular peak. Finally a scan in the lateral direction at fixed $Q_z = 2\pi/d$ (right data panel) shows a superposition of a very narrow peak, corresponding to the surface layering as already discussed, on top of a much broader peak, which must reflect the bulk SmA clusters occurring in the nematic matrix. It is remarkable that one can in this case so clearly separate scattering from the bulk from scattering near the surface. The width of the central peak in the Q_x-scan is resolution limited and proves that the layering is perfect over macroscopic distances. That the width of the surface Q_z-scan coincides with that of the bulk Q_z-scan tells us that the penetration of the surface layering is identical to the extent of the critical fluctuations: another remarkable feature that was found at all temperatures in the nematic phase. The reader is referred to the original research article to explain why this is so.

3.10 X-ray optics

3.10.1 Refractive X-ray optics

The ability to manipulate beams of visible light with lenses is of fundamental importance for ordinary optics. Optical lenses made from glass or plastic work so effectively since their refractive index deviates considerably from unity, and this produces a significant change in the direction of light propagation at the air–lens interface. In addition they are transparent and hardly any losses take place in transmitting the beam through the lens. As we have seen, refraction at an interface also occurs for X-rays, but there
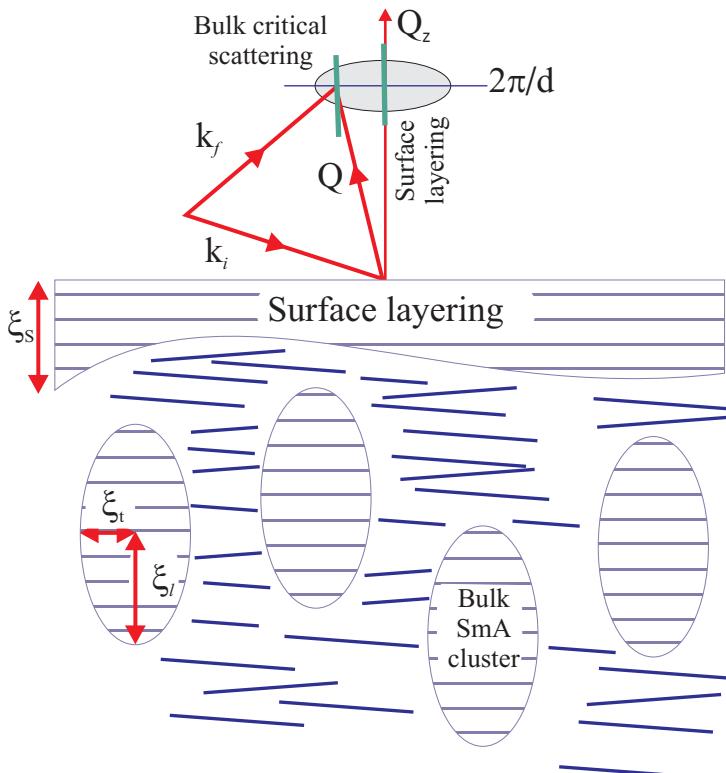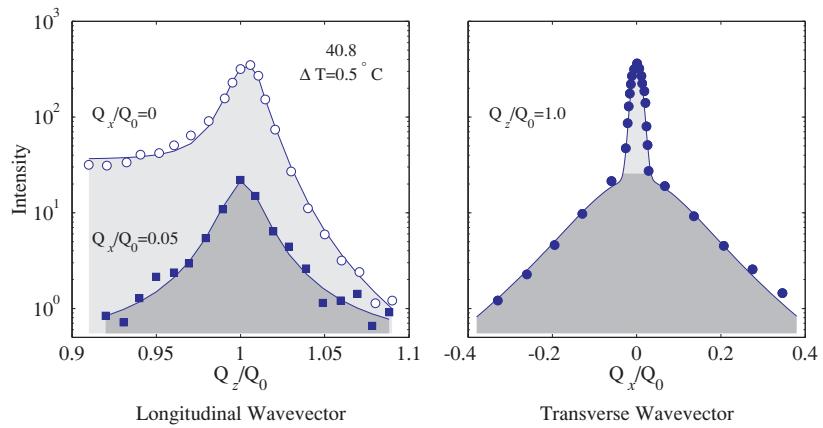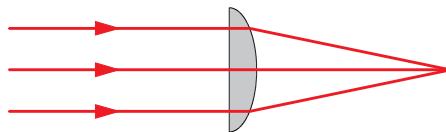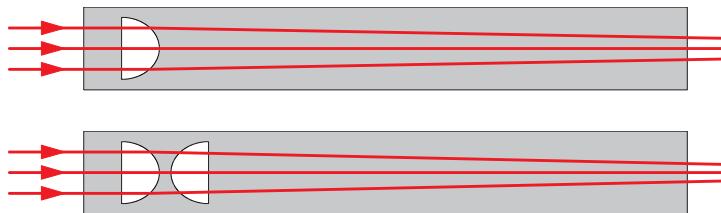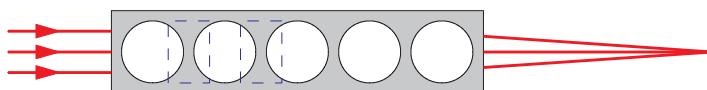
Fig. 3.15 Top: Intensity vs. wavevector transfer near the second-order phase transition N → SmA of the liquid crystal 8CB in a free-surface geometry. The left panel shows the longitudinal scans indicated by the two green lines in the scattering diagram, whereas the right panel is the transverse scan indicated by the blue line. Q_0 is $2\pi/d$, d being the lattice plane spacing [Pershan et al., 1987]. Middle: reciprocal space. Critical scattering from the bulk SmA clusters are indicated by the shaded ellipses. Scattering from the surface layering is confined to the Q_z-axis, peaking at $Q_z = Q_0$. Bottom: schematic model for the surface layering used to interpret the data. Horizontal lines indicate planes of SmA molecules. The two Q_z-scans show that the surface penetration depth ξ_s equals the bulk longitudinal correlation length ξ_l of the critical fluctuations.

(a) Visible light, $n > 1$

(b) X-rays, $n < 1$, single and double lenses

(c) X-rays, compound lens

(d) Silicon compound refractive lenses
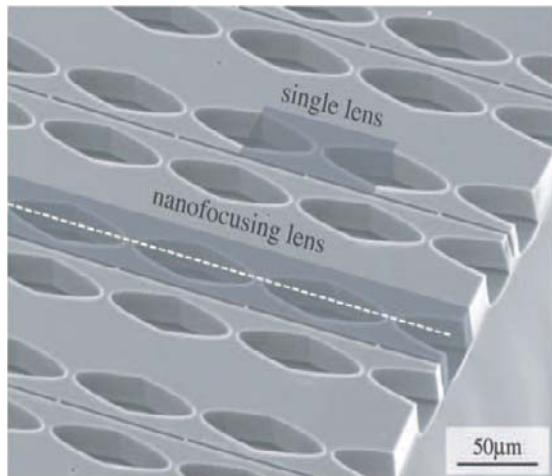
Fig. 3.16 A comparison of converging lenses for visible light (a) and X-rays ((b) and (c)). The shaded areas represent material, and the white areas cavities. In (c), the dashed lines indicate double lenses as shown in the bottom part of (b). The shape of a *converging* X-ray lens, is like that of a *diverging* lens for visible light. (d) Image of an array of X-ray lenses fabricated from silicon. In this example the lenses are parabolic, which is a better approximation to the ideal ellipse than a circle. (Image courtesy of Bruno Lengeler.)

are two basic differences from the case of visible light: the deviation in the index of refraction from unity is tiny, of order 10^{-5}; and the refractive index is less than one, not greater than one as it is for visible light. The latter implies that the shape of a converging X-ray lens must be the same as that of a diverging optical lens as illustrated in Fig. 3.16(a) and (b).

One consequence of the refractive index in the X-ray region being close to unity is that the focal length f of a single lens would be of order 100 m, which is impractically long for most applications. However, with a series of single lenses the combined focal length may be reduced in proportion to the number of lenses [Snigirev et al., 1996], see Fig. 3.16(c), making it compatible with the tens of metres or so available on a typical beam line at an X-ray synchrotron source.

In the context of imaging applications (see Chapter 9), one important figure of merit is the spatial resolution Δx perpendicular to the optical axis. For a perfect lens of diameter D the minimum resolvable feature is by convention taken to be given by the Rayleigh criterion:

$$\Delta x = 1.22 \left(\frac{\lambda f}{D} \right) \tag{3.39}$$

For fixed wavelength, the spatial resolution can therefore be improved by decreasing the focal length and/or increasing the aperture of the lens.

In the following section the ideal shape of the air–lens interface needed to achieve focusing is derived, along with the formulae for the focal length and the spatial resolution.

The ideal shape of an X-ray lens

Figure 3.17(a) illustrates the focusing of an incident X-ray beam by a lens. The incident beam is assumed to be a plane wave which can hence be represented by a series of parallel rays. The X-ray beam enters the material perpendicular to the lower flat interface, traverses the lens, and is refracted on exiting the material via a curved interface such that all of the incident rays are focused at point F. Our objective is to derive an expression for the shape of the curved interface. The most direct way of achieving this is to invoke Fermat's principle [Evans-Lutterodt et al., 2003]. In the current context we take this to mean that the optical path length (the product of the refractive index and the geometrical path length) of all of the rays shown in Fig. 3.17(a) are the same, since the transit of any of the rays then takes the same minimal time to reach the focal point. For example, the central ray on the optical axis, indicated by the dashed line, has the shortest total geometrical path length, and takes the shortest path through the material. Other rays have an increased geometrical path, but the same optical path length as the central ray since they traverse a longer distance in the material for which $n < 1$.

Now consider Fig. 3.17(b), in which we show just two rays: one on the optical axis which enters the lens at A, and one a distance x off of the optical axis which enters the lens at P'. The latter traverses the material along the geometrical distance $y(x)$ parallel to the optical axis, and thus has an optical path length of $P'P = ny = (1-\delta)y$. Applying Fermat's principle then requires that $AF = P'P + PF$. Inserting $AF = f$ and $(PF)^2 = x^2 + (f - y)^2$ leads to

$$x^2 + (2\delta - \delta^2)y^2 - 2f\delta y = 0 \tag{3.40}$$

This is recognizable as the equation of an ellipse:

$$\frac{x^2}{a^2} + \frac{(y - b)^2}{b^2} = 1$$

since it can be recast as

$$x^2 + (a/b)^2 y^2 - 2(a^2/b)y = 0 \tag{3.41}$$
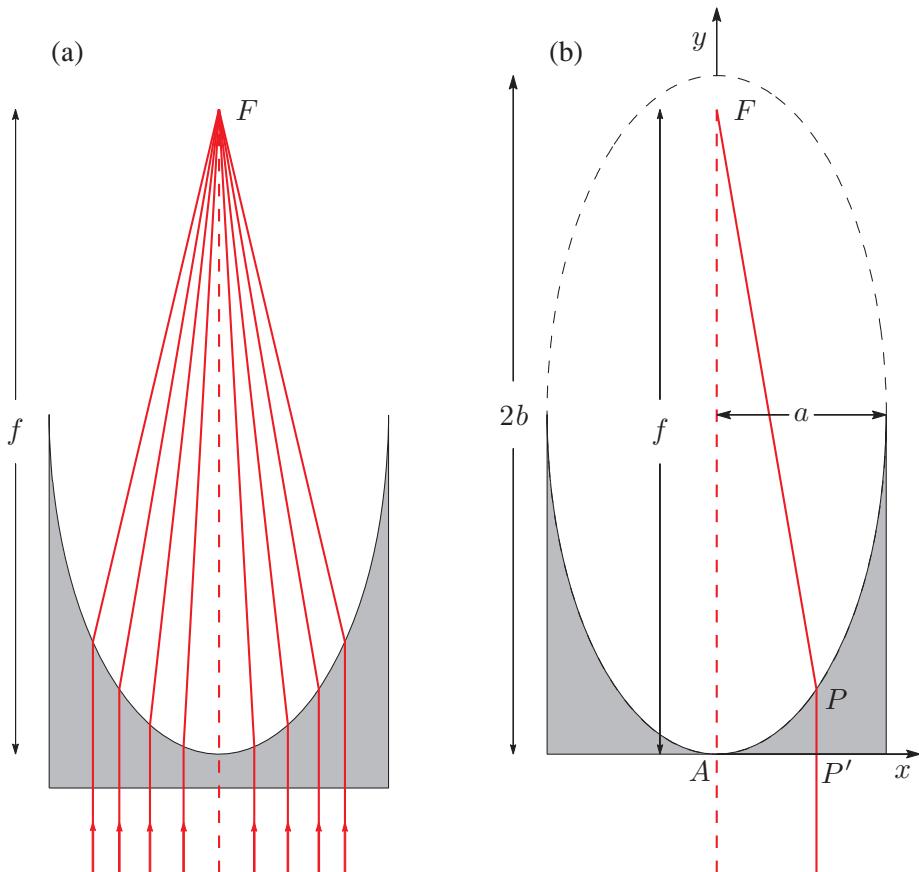
Fig. 3.17 The ideal shape of an X-ray lens. (a) A plane wave X-ray beam (represented by parallel rays) impinges at normal incidence to a solid material (grey region). Depending on the distance from the optical axis (dashed line), X-rays traverse varying thickness of material, before being refracted at a curved interface. If the curved interface is elliptical, then all of the exit rays are focused at point F. (b) Construction used to established that the ideal interface for a X-ray lens is an ellipse, where a and b are the semi-minor and semi-major axes of the ellipse, respectively.

where a and b are the semi-axes. By comparing Eqs. (3.40) with (3.41) we obtain the following expressions for the semi-axes of the ellipse:

$$b = \frac{f}{2 - \delta} \approx \frac{f}{2}$$

and

$$a = f \sqrt{\frac{\delta}{2 - \delta}} \approx f \sqrt{\frac{\delta}{2}}$$

This established that the ideal shape of a lens for focusing a beam of X-rays is an ellipse with axes given by the above formulae. From Eqs. (3.39) and the above expressions for a and b, the spatial resolution of an elliptical lens is

$$\Delta x = 1.22 \left(\frac{\lambda f}{2a} \right) = 1.22 \left(\frac{\lambda}{\sqrt{2\delta}} \right)$$

which depends on the X-ray wavelength and choice of lens material only.

It is useful to consider approximations to the ideal elliptical shape in the vicinity of A in Fig. 3.17(b). For example, it may be approximated by the circle $x^2 + (y - R)^2 = R^2$ where the radius R of the circle by comparison with Eq. (3.41) is

$$R = (a^2/b) = f\delta \tag{3.42}$$

Alternatively it may be approximated by a parabola

$$y = \frac{x^2}{2R} = \frac{x^2}{2f\delta}$$

Compound refractive lenses

Equation (3.42) implies that reducing the focal length of a single lens can only be achieved at the expense of limiting its aperture, and hence its efficiency as a focusing element in an optical system. The compound refractive lens sketched in Fig. 3.16(c) overcomes this conflict, as in this case the focal length is reduced in proportion to the number of lenses. In its simplest form, a compound refractive lens is formed by the simple expedience of drilling N holes into a solid block of material, thereby creating $2N$ lenses with a focal length of

$$f_{2N} = \frac{R}{2N\delta} \tag{3.43}$$

By way of a numerical example, consider an array of lenses formed by drilling a series of 30 holes of 2 mm diameter in Beryllium ($Z=4$), where the centre spacing of the holes is 2.1 mm. For a photon energy of 10 keV, $\delta = 3.41 \times 10^{-6}$ and the focal length is $f_N = 4.9$ m. While this may seem a little long, it is in fact well matched to the length of a typical synchrotron beamline, and arrays of lenses of the type illustrated in Fig. 3.16 have been used to successfully focus X-rays [Snigirev et al., 1996]. One potential problem with this type of lens is absorption. For Beryllium the absorption coefficient at 10 keV is $\mu = 1/(9589\,\mu\text{m})$, and the transmission is $\exp(-31 \times 0.1 \times 10^{-3}/9589 \times 10^{-6})$, or some 72%, more than sufficient for most applications. For an incident beam diameter of $R/2 = 0.5$ mm, the transmission would be 65%. Quadrupling the number of lenses, for example, to obtain a shorter focal length, and consequently higher spatial resolution, would diminish the transmission considerably.

An image of an array of compound refractive lenses fabricated from silicon is shown in Fig. 3.16(d). The lenses were designed to have a parabolic profile, rather than a paraboloidal shape, and hence produce a line focus. By deploying a crossed pair one obtains two-dimensional focusing. For the lenses shown, the spatial resolution achieved was 115×160 nm^2 [Lengeler et al., 2005].

Kinoform lenses and the Fresnel zone plate

An important observation to be made about the paths taken by the different rays shown in Fig. 3.17(a) is that the performance of the lens is insensitive to relative changes in the optical path length of the individual rays by an integer number of wavelengths. Here we define Λ to be the distance that a ray must travel in a material to be composed of one fewer wavelengths than a ray propagating in vacuum. It follows that Λ is determined by the condition

$$\Lambda = (N + 1)\lambda_0 = N\lambda = N(1 + \delta)\lambda_0$$

or in other words

$$\Lambda = \frac{\lambda_0}{\delta}$$

(a)

(b)

$$\Lambda = \frac{\lambda}{\delta}$$

(c)

AGERE   SEI   6.0kV   X850   10μm   WD 9.7mm
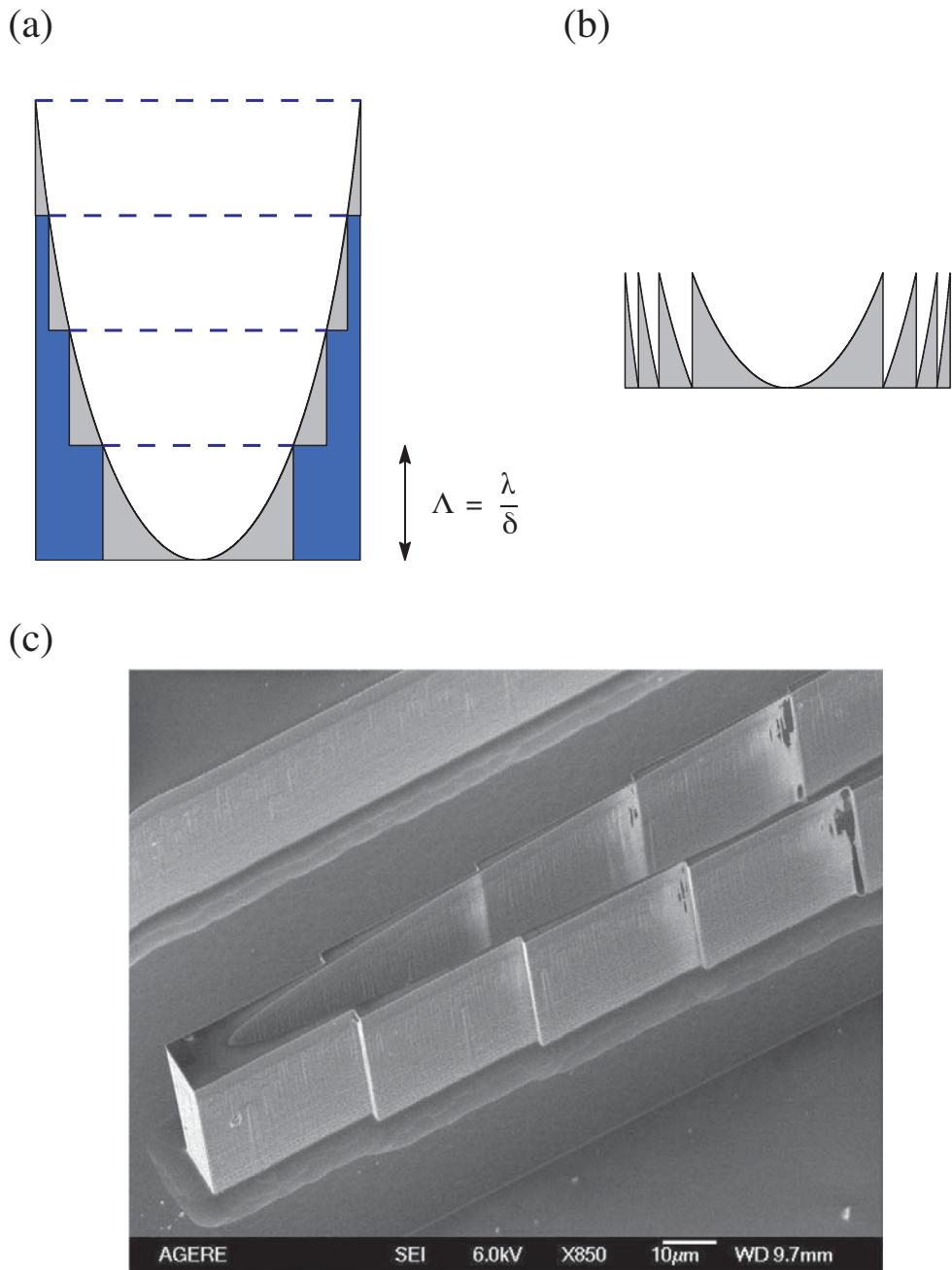
Fig. 3.18 (a) A kinoform lens formed by removing those regions of an elliptical lens that phase shift the wave in the material by an integer number of wavelengths relative to a wave propagating in vacuum. The length of these regions parallel to the optical axis is a multiple of the distance $\Lambda = \lambda/\delta$. (b) A kinoform Fresnel zone plate. (c) Scanning electron microscopy image of a kinoform lens fabricated from silicon designed to work at an X-ray wavelength of 1 Å. (Image courtesy of Kenneth Evans-Lutterodt.)

For hard X-rays, δ is of order $10^{-5} - 10^{-6}$, and so Λ is of order $10 - 100~\mu m$. Removing a length Λ of material from the appropriate section of a lens therefore does not adversely affect its function, but does have the beneficial consequence of reducing the absorption of the beam. This is the basic idea behind the design of the so-called kinoform lens shown schematically in Fig. 3.18(a). The horizontal lines indicate the depths where the central ray through $x = 0$ and the rays inside the material are in phase. Using electron beam lithographic techniques the feasibility of producing kinoform lenses for hard X-rays has been demonstrated [Evans-Lutterodt et al., 2003]. An example is shown in Fig. 3.18(c).

At optical wavelengths, it is straightforward to manufacture a more compact lens by removing all of the 2π phase shifting regions completely, as sketched in Fig. 3.18(b). This structure is known as a kinoform Fresnel zone plate (FZP). Manufacturing a FZP for X-rays with a profile that follows faithfully the kinoform shown in Fig. 3.18(b) is currently beyond the scope of what is possible with micro-fabrication techniques. Instead, for X-ray applications a binary approximation is employed when designing FZPs.

In Chapter 9 on imaging we consider further the properties and applications of X-ray lenses including binary FZPs.

3.10.2   Curved mirrors

One important application of X-ray reflectivity is the X-ray mirror. The mirror surface is often coated with a heavy material, like gold or platinum, in order to obtain a relatively large electron density. This produces a comparatively large critical angle for total reflection, thereby reducing the required length of the mirror. Such mirrors can be used to filter out the higher-order contamination from a beam monochromatized by Bragg reflection from a single crystal. This is rather obvious from the top part of Fig. 3.5$\star$: with a glancing angle $\alpha \leq \alpha_c$ for the fundamental wavevector k of the beam, one obtains close to 100% reflectivity, but the ν'th order wavevector transfer will be $\nu(2k \sin \alpha)$ and thus larger than Q_c by approximately a factor ν, so the reflectivity is reduced by approximately $(2\nu)^4$. In addition to serving as a low bandpass filter, a mirror may also be curved, and in this way one obtains a focusing optical element for X-rays.

In the ideal mirror device all rays from one particular point will be reflected by the mirror and focused into another point. We distinguish between two cases: in *tangential* focusing (also known *meridional* focusing) all the rays are in one and the same plane, spanned by the incident and reflected central rays; whereas in *sagittal* focusing it is the focusing of rays with a component perpendicular to this plane that is considered.

We shall first consider tangential focusing which is the simpler case since it only requires planar geometry. The ideal shape of a focusing mirror is an ellipse. An ellipse can be considered as the projection of a circle, where the projection angle, u, determines the ratio between the minor axis, b, and the major axis, a:

$$\frac{b}{a} = \cos u$$

A ray emitted from the centre of the circle is reflected back into itself. In an ellipse, the circle centre splits into two focal points, F_1 and F_2. A ray emitted in any arbitrary direction from one focal point will be reflected into the other focal point[3].

---

[3]Although this may be well known we shall give an elementary proof. Consider in Fig. 3.19 a point P on the ellipse at distance $p(q)$ from the focal point $F_1(F_2)$. The basic property of an ellipse is that $p + q$ is constant. Let us find a neighbouring point to P – neighbouring means that the point is on the tangent to the point P. Let point Q be a small amount δ further away from F_1
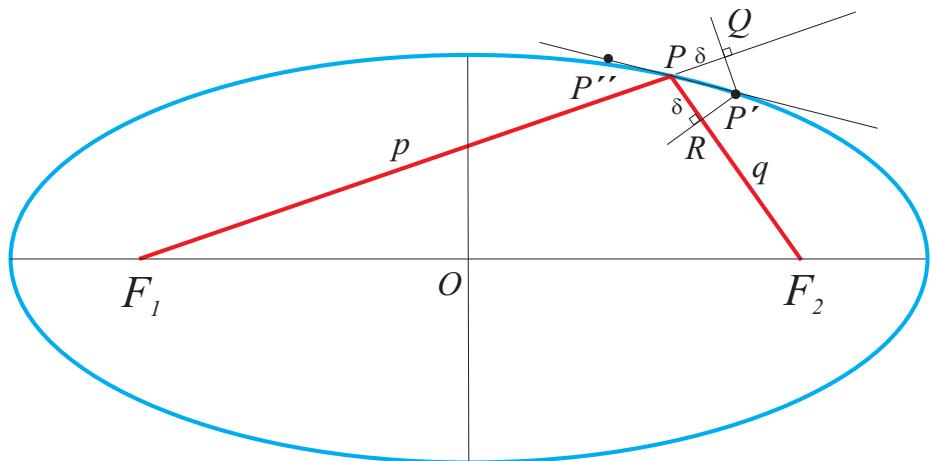
Fig. 3.19 Elementary proof that the tangent in a point of an ellipse bisects the angle of the rays from the two foci to the point. The angle RPP' is equal to the angle QPP' and hence a ray from F_1 will be focused at F_2.

For simplicity, we shall in the following restrict the point P to be the symmetric midpoint between F_1 and F_2, providing 1:1 focusing. As shown in Fig. 3.20, the constant sum of distances to the two focal points equals the major diameter $2a$ since $F_1A + F_2A = 2a$, and therefore $F_1B = F_2B = a$. From the general equation of optics:

$$\frac{1}{p} + \frac{1}{q} = \frac{1}{f}$$

where $p(q)$ is the distance from source (image) to the optical element having the focal length f, it follows that for $p = q = a$ one finds $f = a/2$.

Next we consider sagittal focusing. Imagine that the considered ellipse is rotated around the major axis forming an ellipsoid as shown in the bottom part of the figure. In an ellipsoid any ray from one focal point is focused on to the other focal point. In particular the sagittal rays from F_1 to anywhere on a line perpendicular to the plane of central rays through B will be focused in F_2 as indicated in the bottom part of the Fig. 3.20.

In the following we discuss the best approximation to tangential and sagittal cuts through the ellipsoid by circles. The reason is that it is much simpler and cheaper to produce a cylindrical or toroidal surface than it is to produce a true ellipsoidal surface. The issue is to determine the radius of curvature, ρ, of the best approximating circle.

The glancing angle, θ, at B equals the angle OF_1B, i.e.

$$\sin\theta = \frac{OB}{F_1B} = \frac{b}{a}$$

Furthermore we have just seen that $a = 2f$. The best sagittal circle is clearly the one with radius b as is

---

than P. Consider then all points where the distance from F_1 is increased by this small amount. They must be on the line through Q, perpendicular to F_1P. Similarly, all points with the distance to F_2 diminished by the same amount are on the line through R, perpendicular to PF_2. The intersection of these two lines is therefore the neighbouring point P' since the sum of distances to F_1 and F_2 is maintained constant. A ray from F_1 has an incident angle on the tangent which is $P'PQ$, but since triangles $P'PQ$ and $P'PR$ are congruent this incidence angle is also equal to angle $P'PR$, so the reflected ray will go through F_2.
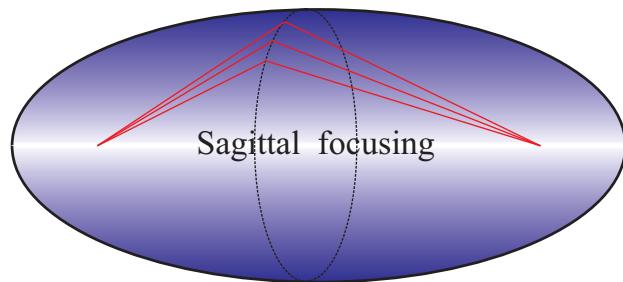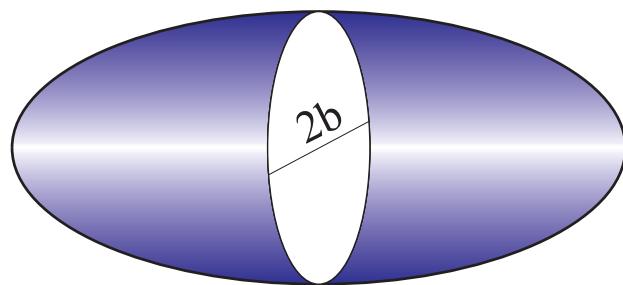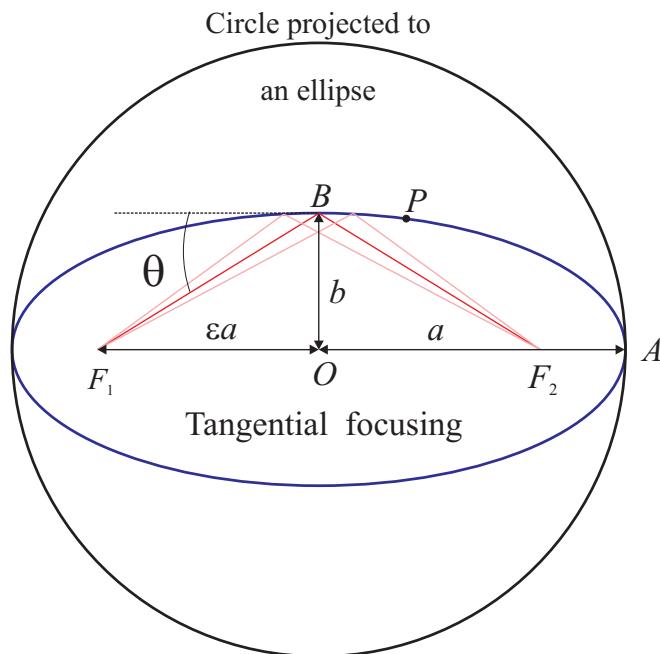
Fig. 3.20 By considering an ellipse as a projection of a circle (top), which is the same as a contraction of the vertical axis by the factor (b/a), one realizes that the radius of curvature at B must be the radius of the circle, a, divided by (b/a). Considering the ellipsoid (middle and bottom) it is clear that the best sagittal radius at B must be b.

evident from the middle part of the figure:

$$\rho_{\text{sagittal}} = b = 2f \sin \theta$$

The best tangential circle approximation of the ellipse at B requires a circular radius of

$$\rho_{\text{tangential}} = a\frac{a}{b} = \frac{2f}{\sin \theta}$$

This is clearly correct when $b = a$, and by considering the ellipse as a projection of a circle with radius a it is obvious that the radius at B becomes larger in the ratio of a:b.

As stated at the beginning of this section it is desirable to make the angle of incidence of the X-ray as large as possible, so as to reduce the overall length of the mirror, and hence its cost. One way to achieve this is to use a multilayer (as described in Section 3.6) as a mirror. The angle of incidence is then determined by the position of the first principal diffraction maxima, which may be chosen to be many times the critical angle of the materials that constitute the multilayer.

3.11   Further reading

X-ray Reflectivity Studies of Liquid Surfaces, J. Als-Nielsen, Handbook on Synchrotron Radiation (Eds. G.S. Brown and D.E. Moncton) **3**, 471 (1991).

X-ray and Neutron Reflectivity: Principles and Applications, Eds. J. Daillant and A. Gibaud (Springer-Verlag, 1999).

Critical Phenomena at Surfaces and Interfaces: Evanescent X-ray and Neutron, H. Dosch (Springer Tracts in Modern Physics 126, 1992).

Focus on Liquid Interfaces, Synchrotron Radiation News, **12** No. 2 (1999).

3.12   Exercises

3.1   Prove that when refraction effects are taken into account Bragg's law is modified to read

$$m\lambda \approx \left(1 - \frac{4d^2\delta}{m^2\lambda^2}\right)2d \sin \theta$$

where m is an integer and the other symbols have their usual meaning.

3.2   Show that the incident beam angle α required to achieve a given penetration depth Λ for the intensity is given by

$$\alpha = \sqrt{\alpha_c^2 - \left(\frac{1}{2k\Lambda}\right)^2}$$

Assume that $\alpha < \alpha_c$ and ignore the effects of absorption. Calculate the value of α required to obtain a value of $\Lambda = 50$ Å at the interface to Si for 10 keV photons. What is the minimum penetration length of the beam at this energy? (Take $\delta = 4.84 \times 10^{-6}$.)

3.3 By considering the condition for the constructive interference of waves scattered from the front and back surfaces of a freely supported thin film of thickness t show that Kiessig fringe maxima are observed when the angle of incidence is given by

$$\alpha^2 = \alpha_c^2 + m^2 \left(\frac{\lambda}{2t}\right)^2$$

Here m is the fringe order, other quantities have their usual meaning, and it has been assumed that $\lambda \ll t$. Hence explain how it is possible to obtain an accurate value of t from the observed positions of the Kiessig fringes.

3.4 One important application of X-ray mirrors is to remove unwanted high-energy photons from the incident beam. At fixed incident angle a mirror will reflect incident X-rays up to some critical photon energy $\mathcal{E}_c$, and the reflectivity curve as a function of energy can be calculated from the Fresnel equations since the dimensionless variable $q = Q/Q_c \equiv \mathcal{E}/\mathcal{E}_c$, etc. A crystal monochromator has been set to select a photon energy of $\mathcal{E} = 0.8\mathcal{E}_c$, while also diffracting higher-order contamination at energies of $m\mathcal{E}$. Calculate how much the mirror attenuates the higher order intensities for $m=2, 3$ and 4.

3.5 Show that the critical energy of a mirror at a fixed angle α to the incident beam may be written as

$$\mathcal{E}_c[\text{keV}] \approx \frac{12.398}{\alpha}\sqrt{\frac{\rho r_0}{\pi}}$$

For a 200 mm long Rhodium mirror and a beam height of 0.5 mm calculate the angle of incidence for full illumination of the mirror, and hence calculate the critical energy. Write a computer programme to calculate the reflectivity of the Rhodium mirror over the full range of energies of interest assuming a mirror roughness of 3 Å. (Rhodium ($Z = 45$) crystallizes in the fcc structure with a=3.8 Å, and an absorption coefficient of 2.4×10^{-5} Å^{-1} at 8 keV.)

3.6 The transmission of an X-ray beam through a compound refractive lens formed from N spherical holes may be approximately written as $e^{-2Nt_{av}\mu}$. In approximating the shape of one lens by a paraboloid determine the thickness $t(r)$ at beam position r away from the optical axis in terms of the hole diameter D. Evaluate the average thickness t_{av} as a function of the ratio between the beam diameter d and D, $\alpha = d/D$.

3.7 An X-ray lens can be used to de-magnify the source size so as to produce a finely focused beam for application in different forms of microscopy. If L_1 and L_2 are the source-lens and lens-sample distances, respectively, the demagnification is given by $M = L_1/L_2$. A beryllium compound refractive lens is required to focus a 10 keV X-ray beam down to 500 nm from a source of size 100 μm located at $L_1=100$ m. Estimate the number of lenses required assuming spherical lenses with a diameter of 800 μm and a geometrical aperture of 400 μm. Making reasonable assumptions, estimate the transmission of the lens system. (At 10 keV, Be has $\delta = 3.41 \times 10^{-6}$ and $\beta = 1.01 \times 10^{-9}$.)

3.8 Consider a double-focusing toroidal mirror, illuminated by a 1 mm high beam at a glancing angle of 5 mrad. The distances from the centre of the mirror to the source and to the image point are both 10 m. Determine the length of the footprint of the beam on the mirror, and the tangential as well as the sagittal radii of curvatures. Estimate how accurately the axis of the mirror must be aligned with the beam axis.

4

Kinematical scattering I: non-crystalline materials

One of the main uses of X-rays is in the determination of the atomic scale structure of materials using the principles of diffraction. In this chapter we introduce some of the key concepts underlying this subject and derive the essential equations. Our approach is to build on what has been learned already about the interaction of X-rays with a single electron, the Thomson scattering cross-section, and then to gradually add to the complexity, until we arrive at a description relevant to real materials.

An important approximation that often applies when an X-ray is diffracted by a material is that the scattering can be considered to be weak. This applies when multiple scattering effects can be neglected, and leads to considerable simplification of the theory. The weak-scattering limit is also known as the kinematical approximation. When multiple scattering effects cannot be neglected, which is most especially true in perfect crystals, then the resulting mathematics is necessarily more complex. The subject of so-called dynamical diffraction theory relevant to perfect crystals is covered in Chapter 6.

In describing the development and application of kinematical diffraction theory it proves convenient to divide the exposition into two parts. In this chapter we shall restrict ourselves to describing systems that may be loosely described as possessing short-range structural order: in the following chapter we will consider the scattering from systems displaying long-range crystalline order. While the definition of crystalline order can be stated rather precisely (albeit with an interesting twist associated with so-called quasicrystals), the same cannot be said to be true for materials displaying short-range order. Instead of striving to achieve such a definition, it will suffice to state that in this present chapter we focus our attention on non-crystalline materials including molecules, liquids, glasses, polymers, etc. Understanding the structure of such non-crystalline forms of matter is of considerable importance as not only are they abundant in nature, but they also arguably comprise the largest group of technologically significant materials.
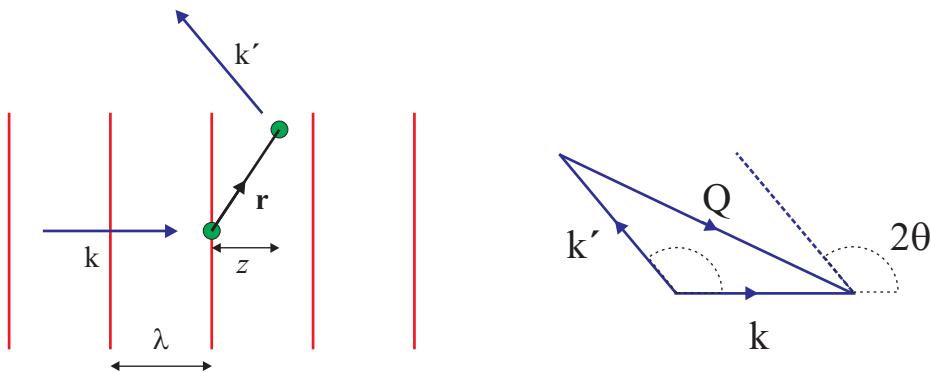
Fig. 4.1 The scattering of a monochromatic X-ray beam by a two-electron system. The incident X-ray is labelled by its wavevector **k**, and has wavefronts represented by the vertical lines. Scattered X-rays are observed in the direction **k′**. As the scattering is elastic $|\mathbf{k}| = |\mathbf{k'}|$. The phase difference between the incident and scattered X-rays is $\phi = (\mathbf{k} - \mathbf{k'}) \cdot \mathbf{r} = \mathbf{Q} \cdot \mathbf{r}$, where the wavevector transfer **Q** is defined as shown in the scattering triangle to the right.

4.1 Two electrons

The most elementary scattering unit that we shall consider is an electron, which is believed to be structureless. Consequently the simplest structure that can be conceived of must be comprised of two electrons. The origin is defined to coincide with one electron, and the second is at a position given by the vector **r**. Determining the structure of this system therefore amounts to determining **r**. To do so we imagine that the electrons are illuminated with a monochromatic X-ray beam, and that the *elastically* scattered radiation is observed along a direction **k′** as indicated in Fig. 4.1. We will further assume that the source and detector are sufficiently far from the origin that the incident and scattered X-rays may be represented as plane waves. This is the so-called far-field limit, and the resulting diffraction theory is associated with the name of Fraunhofer. In Chapter 9 we consider what happens when this approximation breaks down.

The incident wave is specified by its wavevector **k** and arrives at the electron at **r** *after* it has scattered from the electron at the origin. The phase lag for the incident wave, ϕ_{in}, is thus 2π times the ratio of z to the wavelength λ, where z is the projection of **r** onto the direction of the incident wave. Thus we can write $\phi_{\text{in}} = \mathbf{k} \cdot \mathbf{r}$. On the other hand, the wave scattered from the electron at **r** is *ahead* of the wave scattered from the one at the origin by an amount which in the Fraunhofer limit (see Chapter 9) is $|\phi_{\text{out}}| = \mathbf{k'} \cdot \mathbf{r}$. It follows that the resulting phase difference is $\phi = (\mathbf{k} - \mathbf{k'}) \cdot \mathbf{r} \equiv \mathbf{Q} \cdot \mathbf{r}$, which defines the wavevector transfer **Q**. For elastic scattering $|\mathbf{k}| = |\mathbf{k'}|$, and from the scattering triangle shown in Fig. 4.1 the magnitude of the scattering vector **Q** is related to the scattering angle 2θ by

$$|\mathbf{Q}| = 2k \sin \theta = \left(\frac{4\pi}{\lambda} \right) \sin \theta \tag{4.1}$$

The scattering amplitude[1] for the two-electron system may be written as

$$A(\mathbf{Q}) = -r_0(1 + e^{i\mathbf{Q}\cdot\mathbf{r}})$$

and it follows that the intensity is

$$I(\mathbf{Q}) = A(\mathbf{Q})A(\mathbf{Q})^* = r_0^2(1 + e^{i\mathbf{Q}\cdot\mathbf{r}})(1 + e^{-i\mathbf{Q}\cdot\mathbf{r}})$$
$$= 2r_0^2(1 + \cos(\mathbf{Q}\cdot\mathbf{r})) \tag{4.2}$$

In Fig. 4.2(a) the intensity $I(\mathbf{Q})$ is plotted for the *particular* case where $\mathbf{Q}$ is parallel to $\mathbf{r}$. The natural unit of $\mathbf{Q}$ is Å^{-1} if λ is in Å. However, it is often more convenient to express it in units of 2π divided by the characteristic length scale in the problem, in this case the bond length r. The periodic variation in intensity arises from the interference of waves scattered by the two electrons: it is a maximum when the waves are in phase, and a minimum when they are out of phase. Clearly by measuring $I(\mathbf{Q})$ as a function of $\mathbf{Q}$, that is the diffraction pattern, and fitting $\mathbf{r}$ in Eq. (4.2) to the data, the 'structure', i.e. $\mathbf{r}$, of the two-electron system can be determined.

These ideas can be extended to more than two electrons, with the result that the elastic scattering amplitude from any assembly of electrons may be written quite generally as

$$A(\mathbf{Q}) = -r_0 \sum_j e^{i\mathbf{Q}\cdot\mathbf{r}_j} \tag{4.3}$$

where $\mathbf{r}_j$ denotes the position of the j'th electron. Of course in the case that the electrons are continuously distributed the sum is replaced by an integral. In this way a model of the diffraction pattern of the sample can be built up gradually by first considering the scattering from all of the electrons in an atom, then all of the atoms in a molecule, etc., until we arrive at a description of the scattering from the material of interest.

It is important to realize that the procedure that we shall follow is valid only if the diffracting volume is small, and hence the scattering is weak. The problem then remains a linear one. In the language of quantum mechanics this means that the sample is only a perturbation on the incident beam, and that the Born approximation is valid. This weak-scattering requirement is also often referred to as the kinematical approximation, which contrasts to the more complicated dynamical one that is treated in Chapter 6. Fortunately the conditions for the validity of the kinematical approximation are met in many applications of X-ray diffraction. In practice this means that the results of an X-ray diffraction experiment are more readily interpreted than those obtained with a strongly interacting probe, such as the electron. Of course there is a price to be paid for this advantage: if the interaction is weak, so is the scattered signal. However, even this drawback is mostly overcome by the availability of intense X-ray beams from today's synchrotron sources.

Orientational averaging

In order to plot the scattered intensity of the two-electron system shown in Fig. 4.2(a) it was necessary to specify the angle between the wavevector transfer, $\mathbf{Q}$, and the position vector, $\mathbf{r}$. For many systems of interest, for example molecules or aggregates in solution, $\mathbf{r}$ is randomly oriented with respect to $\mathbf{Q}$. Here it is explained how the scattering from our simple, prototypical two-electron system is modified

---

[1]Here we are assuming that the polarization of the incident beam is perpendicular to the scattering plane spanned by $\mathbf{k}$ and $\mathbf{k}'$ so that the full Thomson acceleration of the electrons is observed at all scattering angles. If this is not the case then the expression for the intensity I must be multiplied by the appropriate polarization factor P, as given in Eq. (1.8).
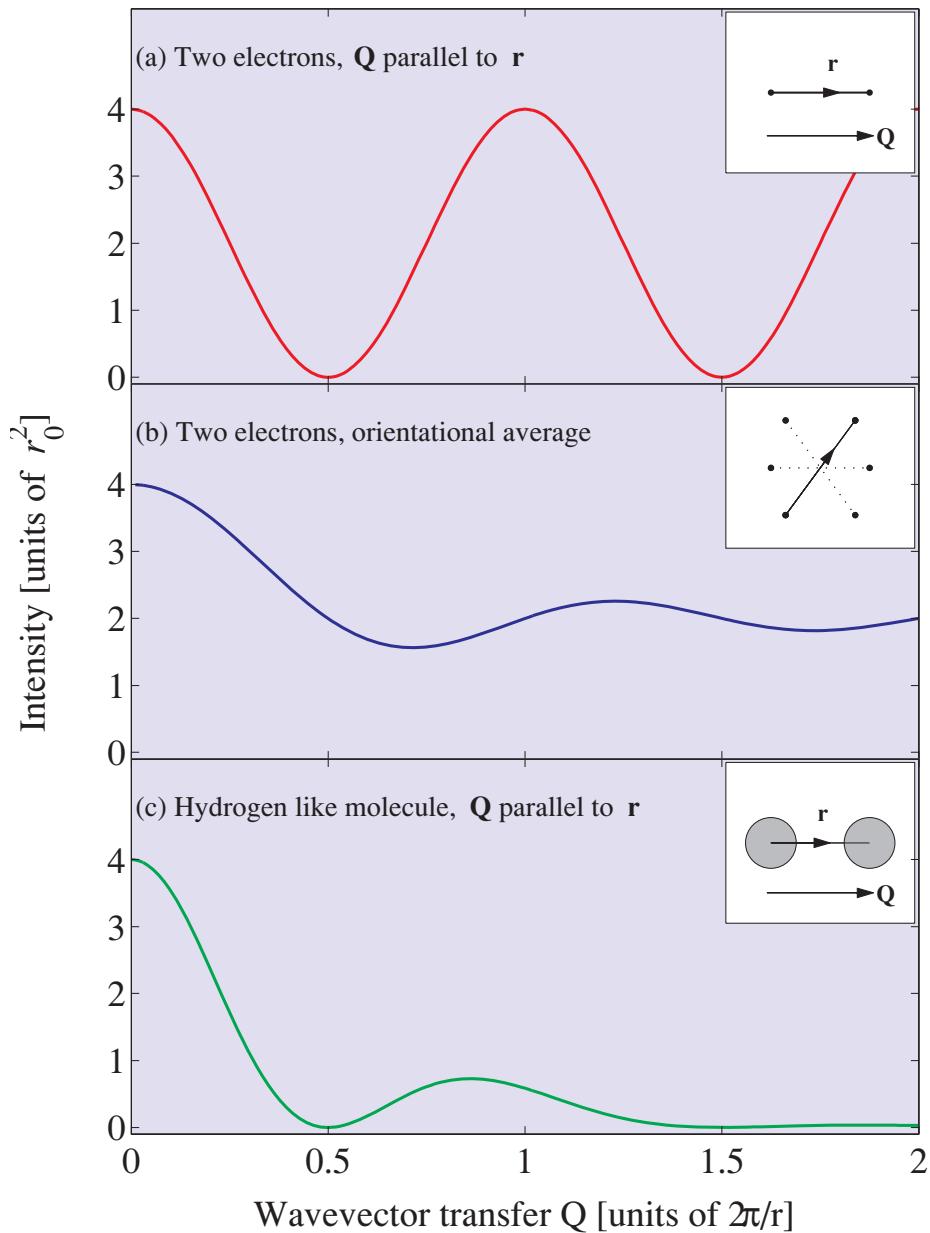
Fig. 4.2 The diffraction pattern from two electrons, assuming that they are distributed in various ways. (a) The two electrons are separated by a well-defined vector **r**. The intensity is given by Eq. (4.2), where for the sake of definiteness **r** has been taken parallel to the wavevector transfer **Q**. (b) The electrons are separated by a fixed distance r = |**r**|, but the direction of **r** is randomly oriented in space. In this case the intensity has been calculated from Eqs. (4.4) and (4.5), with $f_1 = f_2 = -r_0$. (c) The electrons are distributed in two charge clouds separated by a distance r = |**r**|, as they would be, for example, in a dumbbell like, diatomic molecule. The wavefunction of each electron has been taken to be the 1s state of the hydrogen atom (see Eq. (4.8)). The effective radius of the electron distribution is specified by the parameter a, and in this example $a/r=0.25$. Here **Q** has been taken to be parallel to the bond joining the two atoms.

by allowing the orientation of **r** to vary randomly. The equations derived will enable us to understand the scattering from more realistic systems, for example a gas of molecules, considered later in this chapter.

X-ray scattering is a 'fast' probe, in the sense that the time for the transit of the X-ray through the system is short compared to the characteristic time for the motion of the particles comprising the system. Thus in an X-ray experiment a series of snapshots are recorded, which are then averaged. To make the formalism a little more general, we will assume that there are two particles, one at the origin with a scattering amplitude of f_1, and one at a position **r** of scattering amplitude f_2, both taken to be real. The instantaneous scattering amplitude from a single snapshot is

$$A(\mathbf{Q}) = f_1 + f_2 e^{i\mathbf{Q}\cdot\mathbf{r}}$$

and the intensity is

$$I(\mathbf{Q}) = f_1^2 + f_2^2 + f_1 f_2 e^{i\mathbf{Q}\cdot\mathbf{r}} + f_1 f_2 e^{-i\mathbf{Q}\cdot\mathbf{r}}$$

If the length of **r** remains fixed, but its direction is randomly distributed, then the measured intensity is obtained by performing a spherical or orientational average. This is written as

$$\left\langle I(\mathbf{Q})\right\rangle_{\text{orient. av.}} = f_1^2 + f_2^2 + 2 f_1 f_2 \left\langle e^{i\mathbf{Q}\cdot\mathbf{r}}\right\rangle_{\text{orient. av.}} \tag{4.4}$$

The orientational average of the phase factor is

$$\left\langle e^{i\mathbf{Q}\cdot\mathbf{r}}\right\rangle_{\text{orient. av.}} = \frac{\int e^{i\,Qr\cos\theta}\,\sin\theta\,d\theta d\varphi}{\int \sin\theta\,d\theta d\varphi}$$

The denominator is equal to 4π, while the numerator is

$$\int e^{i\,Qr\cos\theta}\,\sin\theta\,d\theta d\varphi = 2\pi\int_0^\pi e^{i\,Qr\cos\theta}\,\sin\theta\,d\theta = 2\pi\left(\frac{-1}{iQr}\right)\int_{iQr}^{-iQr} e^x\,dx$$

$$= 4\pi\frac{\sin(Qr)}{Qr}$$

Thus the orientational average of the phase factor is

$$\boxed{\left\langle e^{i\mathbf{Q}\cdot\mathbf{r}}\right\rangle_{\text{orient. av.}} = \frac{\sin(Qr)}{Qr}} \tag{4.5}$$

It is straightforward to generalize this to a system comprising of N particles, with scattering amplitudes of $f_1 \cdots f_N$. The result is

$$\left\langle \left|\sum_{j=1}^N f_j\,e^{i\mathbf{Q}\cdot\mathbf{r}_j}\right|^2 \right\rangle_{\text{orient. av.}} = |f_1|^2 + |f_2|^2 + \cdots |f_N|^2$$

$$+ 2f_1 f_2 \frac{\sin(Qr_{12})}{Qr_{12}} + 2f_1 f_3 \frac{\sin(Qr_{13})}{Qr_{13}} + \cdots + 2f_1 f_N \frac{\sin(Qr_{1N})}{Qr_{1N}}$$

$$+ 2f_2 f_3 \frac{\sin(Qr_{23})}{Qr_{23}} + \cdots + 2f_2 f_N \frac{\sin(Qr_{2N})}{Qr_{2N}}$$

$$\cdots + 2f_{N-1} f_N \frac{\sin(Qr_{N-1,N})}{Qr_{N-1,N}}$$

$$\tag{4.6}$$

where $r_{12} = |\mathbf{r}_1 - \mathbf{r}_2|$, etc. This formalism was first derived in 1915 by Debye [Debye, 1915].

In a gas of N identical particles all the distances r_{nm} may be considered to be large enough that all of the cross terms in Eq. (4.6) can be neglected, and the intensity is then just N times the square of the scattering amplitude for a single particle. The scattering amplitude may still depend on Q if the particle is not point like as is the case of electrons.

In Fig. 4.2(b) the spherically averaged intensity for the two-electron system is plotted as a function of Q. The effect of the averaging is seen to wash out the oscillations in the diffraction pattern at high Q.

Mostly, however, we are interested in scattering of electrons bound in atoms, where they may no longer be regarded as point like, but are instead described by a distribution. The fact that atomic electrons have a finite spatial extent also leads to a damping of the diffraction pattern at high Q, as illustrated for a hydrogen like molecule in Fig. 4.2(c). This is the subject of the next section.

4.2   Scattering from an atom

As our first system of real interest we shall consider the X-ray scattering from an isolated, stationary atom. To begin with the electrons are described as a classical charge distribution, and the elastic scattering is calculated. This introduces the concept of an atomic form factor, which is nothing other than the atomic scattering amplitude. It is then explained, by way of a simple example, how the atomic form factor may be evaluated from a quantum mechanical description of the electrons.

Elastic scattering and the atomic form factor

Classically the atomic electrons are viewed as a charge cloud surrounding the nucleus with a number density $\rho(\mathbf{r})$. The charge in a volume element $d\mathbf{r}$, at a position $\mathbf{r}$ is then $-e\rho(\mathbf{r})d\mathbf{r}$, where the integral of $\rho(\mathbf{r})$ is equal to the total number of electrons Z in the atom. To evaluate the scattering amplitude we must weight the contribution in $d\mathbf{r}$ by the phase factor $e^{i\mathbf{Q}\cdot\mathbf{r}}$, and then integrate over $d\mathbf{r}$, which leads to

$$f^0(\mathbf{Q}) = \int \rho(\mathbf{r})\,e^{i\mathbf{Q}\cdot\mathbf{r}}d\mathbf{r} = \begin{cases} Z & \text{for } \mathbf{Q} \to 0 \\ 0 & \text{for } \mathbf{Q} \to \infty \end{cases} \tag{4.7}$$

where $f^0(\mathbf{Q})$ is the *atomic form factor* in units of the Thomson scattering length, $-r_0$. The limiting behaviour of $f^0(\mathbf{Q})$ for $\mathbf{Q} \to 0$ is obvious, as the phase factor then approaches unity and the total number of electrons is the integral of their number density. In the other limit we need to consider how the phases of the waves from the different electrons combine when the wavelength of the radiation becomes much smaller than the atom. The phase factor from any one electron can be represented as a point on the unit circle in the complex plane, since $e^{i\mathbf{Q}\cdot\mathbf{r}} = \cos(\mathbf{Q}\cdot\mathbf{r}) + i\sin(\mathbf{Q}\cdot\mathbf{r})$. Now, in limit of large $\mathbf{Q}$ the phase will be much larger than 2π and the phase factors for the different electrons will fluctuate rapidly around on the unit circle. Therefore the integral, even when weighted by the smoothly varying distribution $\rho(\mathbf{r})$, will tend to zero. In other words, when the wavelength of the radiation becomes small compared to the atom there is a destructive interference of the waves scattered from the different electrons in the atom.

In a quantum mechanical description, an atomic electron with principal quantum number n is described by its wavefunction $\psi_n(\mathbf{r})$. Here we shall take a simple example of the contribution made by the 1s electrons in the K-shell to the atomic form factor. The wavefunction of a K electron is similar

1s Wavefunction
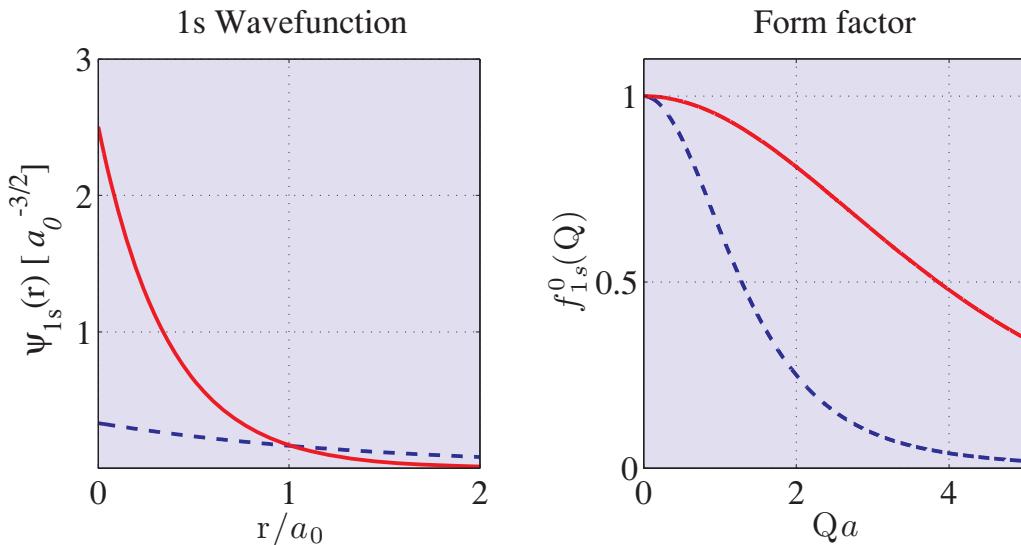
Form factor

Fig. 4.3 The wavefunction (Eq. (4.8)) and form factor (Eq. (4.9)) of the 1s state for $Z=1$ (dashed lines) and $Z=3$ (solid lines).

to that of the ground state of the hydrogen atom, and is given by

$$\psi_{1s}(r) = \frac{1}{\sqrt{\pi a^3}} e^{-r/a} \tag{4.8}$$

where

$$a = \frac{a_0}{Z - z_s}$$

and $a_0 = \hbar^2/me^2 = 0.53$ Å is the Bohr radius. If the nuclear charge Z is greater than one the effective radius a of the 1s electron is reduced compared with a_0 by the nuclear charge Z. This is itself partly screened by the other 1s electron, and typically $z_s \approx 0.3$. The density of a 1s electron is $|\psi_{1s}|^2$ so that the form factor is

$$f_{1s}^0(\mathbf{Q}) = \frac{1}{\pi a^3} \int e^{-2r/a} e^{i\mathbf{Q}\cdot\mathbf{r}} d\mathbf{r}$$

To evaluate this integral we use spherical polar coordinates (r, θ, ϕ) and note that the integrand is independent of the azimuthal angle ϕ so that the volume element becomes $d\mathbf{r} = 2\pi r^2 \sin\theta \, d\theta dr$. Writing $\mathbf{Q} \cdot \mathbf{r} = Q r \cos\theta$, the integral over θ is evaluated in the following way:

$$\begin{aligned} f_{1s}^0(\mathbf{Q}) &= \frac{1}{\pi a^3} \int_0^\infty 2\pi r^2 e^{-2r/a} \int_{\theta=0}^\pi e^{iQr\cos\theta} \sin\theta \, d\theta dr \\ &= \frac{1}{\pi a^3} \int_0^\infty 2\pi r^2 e^{-2r/a} \frac{1}{iQr} \left[e^{iQr} - e^{-iQr} \right] dr \\ &= \frac{1}{\pi a^3} \int_0^\infty 2\pi r^2 e^{-2r/a} \frac{2\sin(Qr)}{Qr} dr \end{aligned}$$

The next step is to write $\sin(Qr)$ as the imaginary part of a complex exponential, $\sin(Qr)=Im\left\{e^{iQr}\right\}$. The

	a_1	b_1	a_2	b_2	a_3	b_3	a_4	b_4	c
C	2.3100	20.8439	1.0200	10.2075	1.5886	0.5687	0.8650	51.6512	0.2156
O	3.0485	13.2771	2.2868	5.7011	1.5463	0.3239	0.8670	32.9089	0.2508
F	3.5392	10.2825	2.6412	4.2944	1.5170	0.2615	1.0243	26.1476	0.2776
Si	6.2915	2.4386	3.0353	32.333	1.9891	0.6785	1.5410	81.6937	1.1407
Cu	13.338	3.5828	7.1676	0.2470	5.6158	11.3966	1.6735	64.820	1.5910
Ge	16.0816	2.8509	6.3747	0.2516	3.7068	11.4468	3.683	54.7625	2.1313
Mo	3.7025	0.2772	17.236	1.0958	12.8876	11.004	3.7429	61.6584	4.3875

Table 4.1 Coefficients of the analytical approximation (Eq. (4.10)) to the atomic form factor f^0 for a selection of elements. (Source: *International Tables of Crystallography*.)

form factor then becomes

$$f_{1s}^0(\mathbf{Q}) = \frac{4}{a^3}\frac{1}{Q}\,Im\left\{\int_0^\infty \frac{r^2}{r}\,e^{-2r/a}\,e^{iQr}\,dr\right\}$$
$$= \frac{4}{a^3}\frac{1}{Q}\,Im\left\{\int_0^\infty r\,e^{-r(2/a-iQ)}\,dr\right\}$$

which may be integrated by parts to yield the final result[2]

$$f_{1s}^0(\mathbf{Q}) = \frac{1}{[1 + (Qa/2)^2]^2} \tag{4.9}$$

The wavefunction and form factor for two different values of the nuclear charge Z are plotted in Fig. 4.3. The wavefunction has been plotted against r in units of a_0, and the form factor plotted against the dimensionless quantity Qa. As Z is increased the wavefunction becomes more localized around the nucleus, and the form factor correspondingly more extended in Q. Because of this relationship between real space spanned by r and the space spanned by Q, the latter space is known as reciprocal space. Fig. 4.3 serves to illustrate the relationship between a description of objects in the two spaces: objects that are extended in real space, are localized in reciprocal space and vice versa. This should be obvious to those familiar with the properties of Fourier transforms, as it is evident from Eq. (4.7) that the atomic form factor is the Fourier transform of the electronic charge distribution.

Considerable effort has been devoted over the years to calculate the form factors of all free atoms (and most of the important ions) from the best available atomic wavefunctions. These are tabulated in the *International Tables of Crystallography* for different values[3] of $\sin\theta/\lambda = Q/4\pi$. For computational

---

[2]For a complex number $\alpha = (2/a - iQ)$ one obtains by partial integration

$$\int_0^\infty r\,e^{-\alpha r}dr = \left[r\frac{e^{-\alpha r}}{-\alpha}\right]_0^\infty + \frac{1}{\alpha}\int_0^\infty e^{-\alpha r}dr = 0 + \frac{1}{\alpha^2}$$

[3]Crystallographers tend to prefer to refer to the wavevector transfer as the scattering vector, and to define it without the leading factor of 4π in Eq. (4.1).
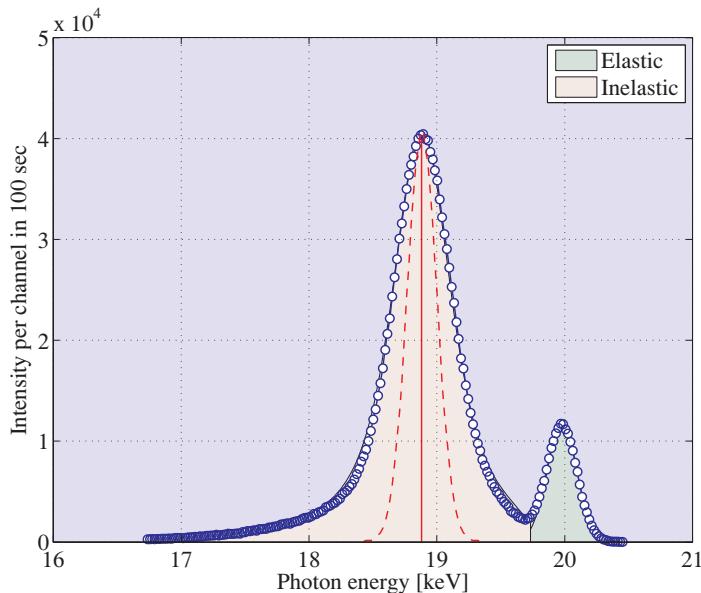
Fig. 4.4 The total scattering (circles) measured from a kapton foil is composed of elastic (green shading) and inelastic scattering (red shading). The energy resolution of the detector is given by the width of the elastic peak. The inelastic scattering is broadened beyond the resolution (red dashed line) by the momentum distribution of the electrons in the kapton foil. The incident energy was 20 keV corresponding to a photon wavevector of 10.13 Å^{-1}, and the scattering angle was 120°. At this energy and scattering angle the inelastic scattering is seen to dominate as a consequence of the fact that kapton is composed of low-Z elements (see Fig. 4.5).

convenience the calculated form factors have been fitted by the analytical approximation

$$f^0\left(\tfrac{Q}{4\pi}\right) = \sum_{j=1}^{4} a_j\, e^{-b_j \sin^2\theta/\lambda^2} + c = \sum_{j=1}^{4} a_j\, e^{-b_j\,(Q/4\pi)^2} + c \tag{4.10}$$

where a_j, b_j and c are fitting parameters. In Table 4.1 we tabulate their values for several of the elements that will be of interest to us later.

The total scattering length f of an atom is the sum of the energy independent part, f^0, and the dispersion correction factors $f' + if''$ that arise from the fact that electrons are bound in an atom. These dispersion corrections were introduced in Chapter 1 and are discussed further in Chapter 8.

Inelastic scattering

In Fig. 4.3 it is evident that as the wavevector transfer becomes large, the atomic form factor associated with elastic scattering tends to zero. However, it would be incorrect to infer that photon scattering is somehow being 'switched off' in the limit $Q \to \infty$. Instead, as the elastic, coherent scattering decreases, Compton scattering of the photon by the atomic electrons increases. Compton scattering is inelastic and is also incoherent, in the sense that it cannot give rise to interference effects since the wavelength of the photon is changed in the scattering event (see page 15).

As a first approximation in understanding the Compton scattering spectrum it might be assumed that all of the atomic electrons are initially at rest. The inelastic spectrum would then in principle
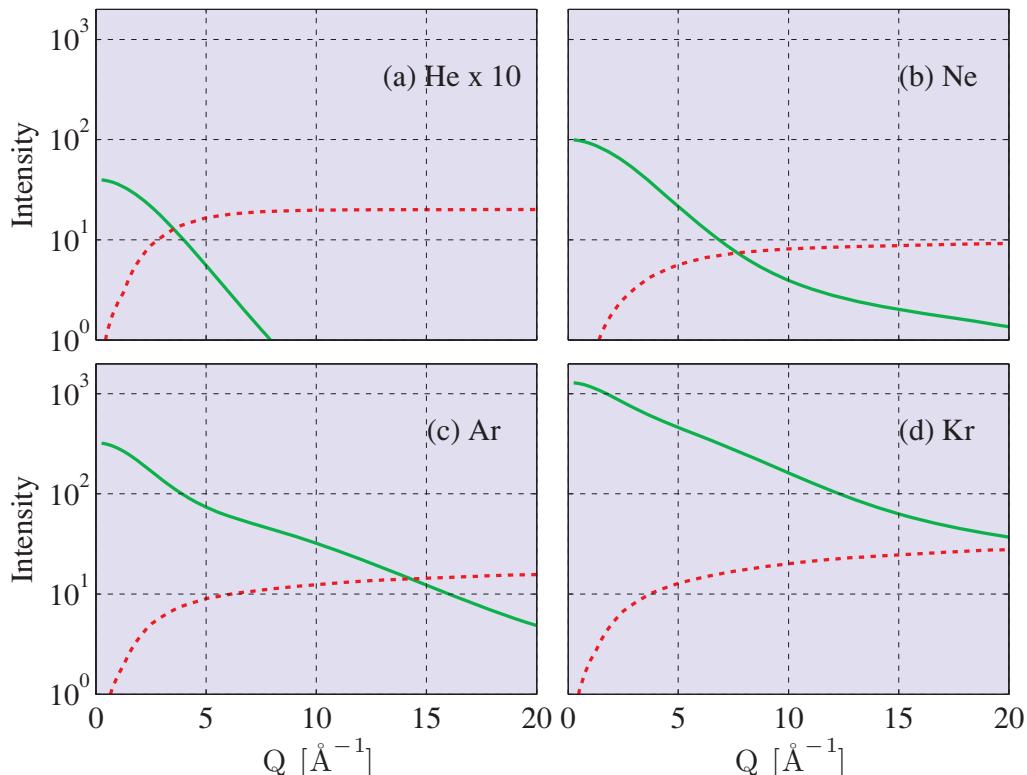
Fig. 4.5 The calculated scattered intensity separated into contributions from elastic (green line) and inelastic Compton scattering (red dashed line) from (a) He (b) Ne (c) Ar and (d) Kr . The cross over at which inelastic exceeds elastic scattering occurs at progressively higher Q as the atomic number increases. The calculations were performed using the information given in the *International Tables of Crystallography*. Note that the Thomson scattering approaches Z^2 as Q→0, whereas the Compton scattering approaches Z as Q→ ∞.

consist of a delta function response with a relative shift in energy from the elastic response given by Eq. (1.15). Atomic electrons of course carry a finite momentum in their groundstate. If the electronic momentum is distributed isotropically, then it can be shown that conservation of momentum leads to a broadening of the delta function response. Measurement of the Compton scattering spectrum therefore allows the groundstate electronic momentum distribution to be determined. A data set which illustrates the existence of both elastic and inelastic scattering components is shown in Fig. 4.4. Here a monochromatic X-ray beam is scattered by the electrons in a kapton foil. The scattering exhibits both an elastic line and a well-resolved, broadened inelastic response. The relative weights of the two components of the scattering can be specified by writing the total atomic scattering cross-section as the sum of an elastic $(d\sigma/d\Omega)_{el.} \sim r_0^2 |f(Q)|^2$ and an inelastic part $(d\sigma/d\Omega)_{inel.} \sim r_0^2 S(Z,Q)$.

From our opening remarks in this section it can be expected that the function $S(Z,Q)$ to approach Z as Q → ∞, as in this limit all of the Z atomic electrons scatter incoherently. Moreover, it might also be reasonably expected that the limiting form of $S(Z,Q)$ is reached at progressively larger values of Q as the atomic number Z increases, since the inner electrons become more and more tightly bound. The detailed calculation of $S(Z,Q)$, as with that of $f(Q)$, is beyond the scope of this book. The reader is again referred to the *International Tables of Crystallography*, where it has been tabulated in a useful
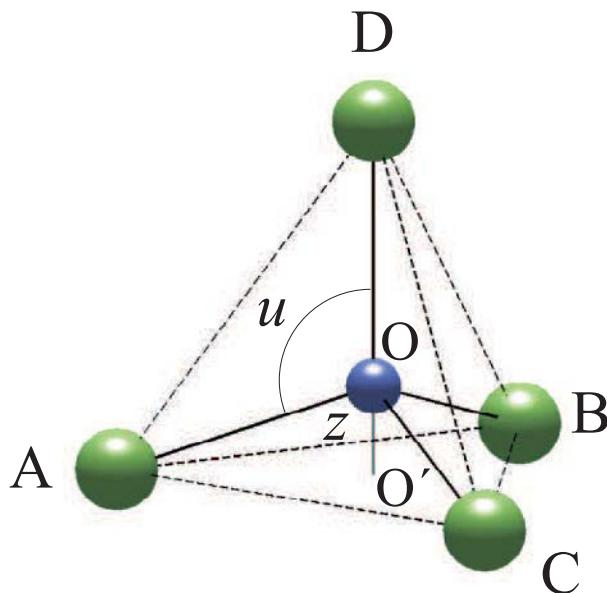
Fig. 4.6 The CF_4 molecule. The C-F bond length is 1.38 Å, and the geometry is such that the ratio of the length of OD to OO′ is 3:1.

form for all elements up to $Z < 55$. This enables the relative weight of elastic and inelastic scattering for any atom, and at any wavevector transfer Q, to be calculated. Examples for the rare gases are shown in Fig. 4.5, which underline the qualitative remarks regarding the dependence on Q and Z given above.

In the remainder of this chapter, and indeed most of the rest of the book, we shall be concerned predominantly with elastic scattering, as it is through exploiting this process that most of our understanding of the atomic scale structure of materials has been gained. The reader, however, should be aware of the existence of inelastic Compton scattering, and have an appreciation of under what conditions it might become a significant factor in their experiments.

4.3 Scattering from a molecule

The next level of complexity we might imagine is to consider the scattering from a group of atoms organized into a molecule. Let the atoms be labelled by j, so that we can write the scattering amplitude (again in units of $-r_0$) of the molecule as

$$F^{\text{mol}}(\mathbf{Q}) = \sum_j f_j(\mathbf{Q}) \, e^{i\mathbf{Q} \cdot \mathbf{r}_j} \tag{4.11}$$

To take a specific example, let us consider the molecule CF_4. The four fluorine atoms are tetrahedrally coordinated (at points A,B,C,D) around the central carbon atom (at O) as shown in Fig. 4.6.

The line from D to O intersects the plane spanned by A, B and C at the point O′. Assume that the dimensions are such that OA=OB=OC=OD=1. It is easy to show that OO′ $= z = \frac{1}{3}$ and that angle u between any of the lines from the centre to any of the four apices is given by $\cos u = -\frac{1}{3}$. The proof is
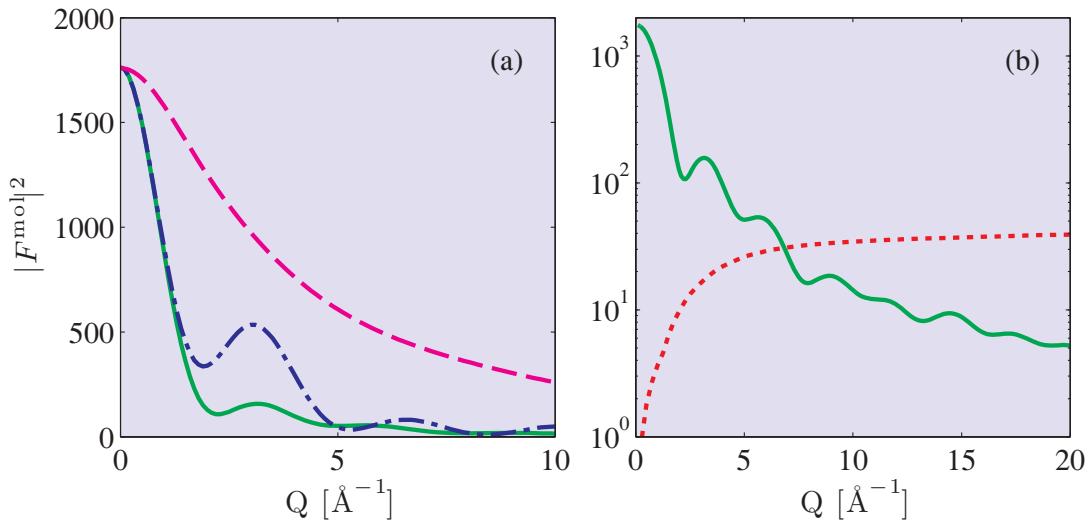
Fig. 4.7 The calculated molecular structure factor squared of the CF_4 molecule. (a) Dashed-dotted blue line is from Eq. (4.13); solid green line is calculated from a spherical average of the structure factor (Eq. (4.14)); magenta line is the square of the form factor of atomic molybdenum which has the same number of electrons as the CF_4 molecule. (b) Solid green line is the spherically averaged structure factor of CF_4; red dashed line is the Compton scattering calculated from the information given in the *International Tables of Crystallography*.

as follows. The scalar product of the vectors **OA** and **OD** is

$$\mathbf{OA} \cdot \mathbf{OD} = 1 \cdot 1 \cdot \cos u = -z$$

but by symmetry we also have

$$-z = \mathbf{OA} \cdot \mathbf{OD} = \mathbf{OA} \cdot \mathbf{OB} = (\mathbf{OO'} + \mathbf{O'A}) \cdot (\mathbf{OO'} + \mathbf{O'B})$$
$$= z^2 + \mathbf{O'A} \cdot \mathbf{O'B}$$
$$= z^2 + (\mathbf{O'A})^2 \cos(120^o).$$

From the right-angle triangle OO'A one immediately finds that $(O'A)^2 = 1 - z^2$, so that

$$-z = z^2 + (1 - z^2)\cos(120^o) = z^2 - \frac{1}{2}(1 - z^2) \tag{4.12}$$

from which it follows that $z = \frac{1}{3}$ and $u = \text{acos}(-OO'/OA) = 109.5^o$.

The molecular form factor of CF_4 is readily evaluated when the scattering vector **Q** is either parallel (+), or anti parallel (−), to a C-F bond:

$$F_{\pm}^{\text{mol}}(\mathbf{Q}) = f^C(Q) + f^F(Q)\left[3e^{\mp iQR/3} + e^{\pm iQR}\right] \tag{4.13}$$

where R is the C-F bond length (1.38 Å). In Fig. 4.7(a) $|F_{\pm}^{\text{mol}}|^2$ is plotted as a function of **Q**, where the values of the form factors $f^C(Q)$ and $f^F(Q)$ have been calculated from Eq. (4.10) using the coefficients in Table 4.1. The oscillations in the magnitude of $|F_{\pm}^{\text{mol}}|^2$ are characteristic features of the scattering from a molecule. They arise from the fact that there are distinct length scales, in this case the C-F

(1.38Å) and F-F (1.38 $\sqrt{8/3}$) bond lengths, and indeed the first peak in $|F_{\pm}^{mol}|^2$ near $Q = 2\pi/(1.38 \sqrt{8/3})$ can be identified with the latter. Clearly, $|F_+|^2 = |F_-|^2$, so that one should not expect too much deviation from the qualitative behaviour shown in Fig. 4.7(a) when **Q** is not parallel to a C-F bond. That this is indeed the case is evident in the same figure where the square of the spherical average of F^{mol} is also plotted. This has been calculated from Eq. (4.6) by noting that there are 4 C-F bonds of length $R =1.38$ Å and 6 F-F bonds of length $\sqrt{8/3}R$, so that altogether

$$\left|F^{mol}\right|^2 = \left|f^C\right|^2 + 4\left|f^F\right|^2 + 8 f^C f^F \frac{\sin(QR)}{QR} + 12\left|f^F\right|^2 \frac{\sin(Q\sqrt{8/3}R)}{Q\sqrt{8/3}R} \tag{4.14}$$

(For reference, the squared atomic form factor of molybdenum, the element that has the same number of electrons as CF_4, i.e. $Z =42$, is also plotted in Fig. 4.7(a).) In Fig. 4.7(b) the Q dependence of the elastic scattering from CF_4 is compared with the Compton scattering which is seen to dominate for Q greater than approximately 7 Å^{-1}.

4.4   Scattering from liquids and glasses

In Fig. 4.8(a) a schematic is shown of the configuration typically adopted by atoms in a crystalline material, where they exhibit long-range structural order. At this stage the details of the atomic coordination are irrelevant, as is the fact that the system shown is two dimensional. What is important is that the atoms sit on a regular array, known as the lattice, so that the exact location of all atoms, relative to the atom chosen to be at the origin, can be inferred. The defining structural characteristic of non-crystalline materials, on the other hand, is a degree of randomness in the position of the atoms as sketched in Fig. 4.8(b). The implication of this fact is that any structural order in non-crystalline material, if present at all, can only be described in a statistical sense. Indeed at first glance it might seem surprising to some to talk about structural order at all in the context of liquids, glasses and other forms of non-crystalline materials. However, well-defined, short-range structural correlations not only exist in these forms of matter, but as we shall see they can be studied in great detail using X-ray scattering techniques.

4.4.1   The radial distribution function

The position adopted by atoms in non-crystalline materials changes over an incredibly wide range of timescales, from a few nanoseconds in the case of liquids up to millennia and more in the case of glasses. As we have already noted in Section 4.1, X-rays are a fast probe, and hence we are justified in considering a snapshot of the structure as shown schematically in Fig. 4.8(b). The task then is to provide a statistical description of the structure frozen in time, and then to perform an average over all possible configurations. The first of these objectives is accomplished by introducing the radial distribution function, $g(r)$.

The radial distribution function is constructed by first choosing any one atom as the origin. The choice is of course arbitrary, as in an experiment an average is made over a series of snapshots. In the two-dimensional examples shown in Fig. 4.8, the radial density is calculated as $\rho(r) = N(r)/(2\pi r\, dr)$, where $N(r)$ is the average number of atoms in an annulus of radius r and thickness dr, and $2\pi r\, dr$ is the area of that annulus. The radial distribution function is then defined by $g(r)=\rho(r)/\rho_{at}$ where ρ_{at} is the average areal number density. The extension to three dimensions is straightforward, with the annulus being replaced by a shell of volume $4\pi r^2\, dr$.
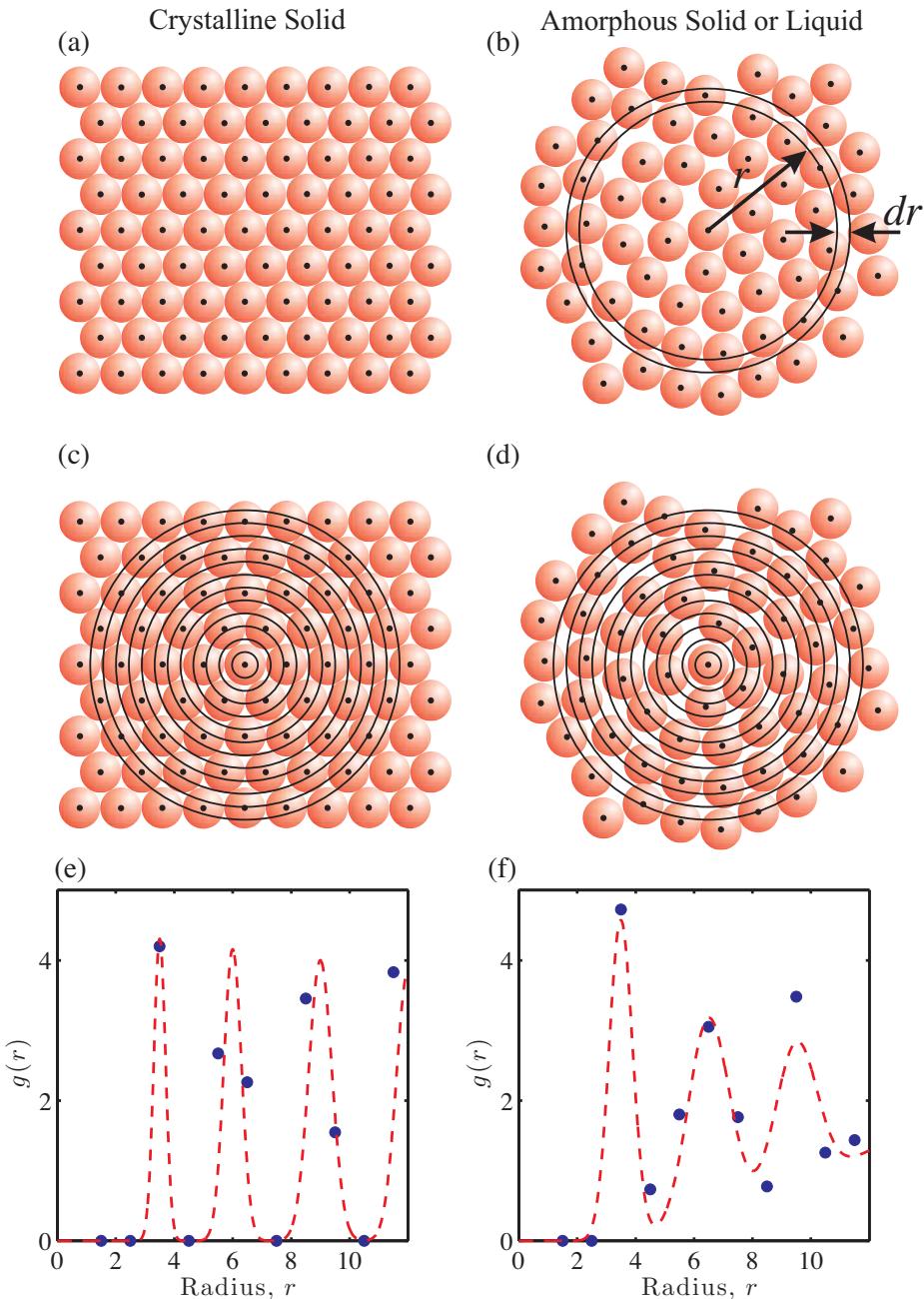
Fig. 4.8 Construction of the radial distribution function $g(r)$ for crystalline (left panels) and non-crystalline (right panels) materials in two dimensions. The radial distribution function is the probability density of finding two atoms separated by a distance r. It follows that in two dimensions, $g(r)$ $(2\pi r dr)\rho_{at}$ is the number of atoms in an annulus of radius r and thickness dr, where ρ_{at} is the average areal number density. The dashed lines in (e) and (f) are guides for the eye.

In Fig. 4.8(c)-(f) we compare the calculation of the radial distribution function for our two-dimensional models of crystalline and non-crystalline matter. In both cases, $g(r)$ is calculated by drawing a series of concentric circles of the same spacing centred on the origin. The number of atoms in each annulus is then added up to give $N(r)$, before dividing by the product of the area of the annulus and ρ_{at} to yield $g(r)$, which is plotted in Fig. 4.8(e) and (f). As the spacing of the shells tends to zero, the difference in $g(r)$ between a crystalline and a non-crystalline structure becomes evident. For the crystalline material, $g(r)$ exhibits sharp, non-overlapping peaks which form a series extending to indefinitely large r (Fig. 4.8(e)). The radial distribution function of the non-crystalline material is also seen to exhibit peaks, but in this case they dampen and broaden out, with $g(r)$ rapidly tending to unity as r increases (Fig. 4.8(f)). Although the 'toy model' we have constructed of a non-crystalline material should not be taken too seriously, the qualitative features of the resulting radial distribution function are in fact generic to those displayed by real non-crystalline forms of matter. For example, the position of the first peak in $g(r)$ is a measure of the minimal distance of approach between two atoms. In a liquid, mobile atoms or molecules are excluded from occupying the same volume (ultimately a consequence of quantum mechanics); in a glass there is a minimum (average) length of rigid chemical bonds.

Next we consider the salient features of the X-ray scattering from non-crystalline materials, and demonstrate how the radial distribution function can be obtained from the Fourier transform of the observed intensity as a function of wavevector transform.

4.4.2 The liquid structure factor

For simplicity, we start by considering a mono-atomic or mono-molecular system for which the scattered intensity in suitable dimensionless units may be written generally as

$$I(\mathbf{Q}) = f(\mathbf{Q})^2 \sum_n e^{i\mathbf{Q}\cdot\mathbf{r}_n} \sum_m e^{-i\mathbf{Q}\cdot\mathbf{r}_m} = f(\mathbf{Q})^2 \sum_n \sum_m e^{i\mathbf{Q}\cdot(\mathbf{r}_n-\mathbf{r}_m)}$$

Here $f(\mathbf{Q})$ represents the atomic or molecular form factor. To proceed the terms in the double summation with $n = m$ are separated from those with $n \neq m$ to yield

$$I(\mathbf{Q}) = Nf(\mathbf{Q})^2 + f(\mathbf{Q})^2 \sum_n \sum_{m\neq n} e^{i\mathbf{Q}\cdot(\mathbf{r}_n-\mathbf{r}_m)}$$

The next step is then to replace the sum over $m \neq n$ by an integral. In addition, as X-ray scattering ultimately arises from deviations in electron density from its average, we subtract and add a term proportional to the average density ρ_{at}. The expression for the scattered intensity then assumes the form

$$I(\mathbf{Q}) = \overbrace{Nf(\mathbf{Q})^2 + f(\mathbf{Q})^2 \sum_n \int_V \left[\rho_n(\mathbf{r}_{nm}) - \rho_{at}\right] e^{i\mathbf{Q}\cdot(\mathbf{r}_n-\mathbf{r}_m)} \, dV_m}^{I^{SRO}(\mathbf{Q})}$$

$$\underbrace{+ f(\mathbf{Q})^2 \rho_{at} \sum_n \int_V e^{i\mathbf{Q}\cdot(\mathbf{r}_n-\mathbf{r}_m)} \, dV_m}_{I^{SAXS}(\mathbf{Q})} \tag{4.15}$$

where $\rho_n(\mathbf{r}_{nm}) \, dV_m$ is the number of atoms or molecules in the volume element dV_m located at a position $\mathbf{r}_m - \mathbf{r}_n$ with respect to the reference atom at $\mathbf{r}_n$.

As illustrated in Fig. 4.8(f) for the dense non-crystalline materials of interest here, $g(r) \to 1$, or equivalently, $\rho_n(\mathbf{r}_{nm}) \to \rho_{at}$ after only a few inter-atomic spacings. The second term in the above equation is therefore sensitive to short range order (SRO), and is hence the term that contains structural information relevant to typical inter-atomic distances. The final term, on the other hand, only contributes to the scattering as $Q \to 0$, as for finite Q rapid oscillations of the phase factor lead to destructive interference. (This point is further discussed in the context of scattering from crystalline materials in Chapter 5.)

The limit $Q \to 0$ corresponds to long distances in real space, and since $Q \propto \sin(\theta)$, this limit occurs at small scattering angles close to the forward direction. This small angle X-ray scattering (SAXS) regime turns out to provide important and unique information on the size and morphology (as opposed to detailed positional information of the individual atoms) of large scale structures including polymers, micelles, etc., and is considered further in Section 4.5.   The remainder of this present section is concerned with understanding how to extract information on inter-particle correlations in disordered (non-crystalline) systems, and we proceed by first neglecting the small-angle scattering term in Eq. (4.15).

Further simplification of Eq. (4.15) is achieved in a number of steps. Firstly, an average is performed over different choices of origin, $\langle \rho_n(\mathbf{r}_{nm}) \rangle \to \rho(\mathbf{r})$, which allows us to write

$$I^{SRO}(\mathbf{Q}) = Nf(\mathbf{Q})^2 + Nf(\mathbf{Q})^2 \int_V [\rho(\mathbf{r}) - \rho_{at}] \, e^{i\mathbf{Q}\cdot\mathbf{r}} \, dV$$

Secondly, invoking the isotropy condition, expected to apply to a liquid or glass, allows us to make the replacement $\rho(\mathbf{r}) \to \rho(r)$, and facilitates calculation of the angular average of the phase factor, as described on page 115. The formula for the scattering intensity then becomes

$$I^{SRO}(Q) = Nf(Q)^2 + Nf(Q)^2 \int_0^\infty [\rho(r) - \rho_{at}] \, 4\pi r^2 \frac{\sin(Qr)}{Qr} \, dr$$

Rearranging this slightly leads to an expression for what is conventionally known as the liquid (or glass) structure factor[4]

$$\boxed{\mathcal{S}(Q) = \frac{I^{SRO}(Q)}{Nf(Q)^2} = 1 + \frac{4\pi}{Q} \int_0^\infty r \, [\rho(r) - \rho_{at}] \, \sin(Qr) \, dr} \qquad (4.16)$$

It is instructive to consider the limiting forms of the liquid structure factor $\mathcal{S}(Q)$. The limit $Q \to \infty$ is readily derived as the factor of $1/Q$ multiplying the integral means that $\mathcal{S}(Q) \to 1$, i.e. for short real space distances the scattering from a liquid or glass becomes independent of any inter-particle correlation effects. In the limit of long wavelengths, $Q \to 0$, the integrand of the right hand side becomes proportional to $[\rho(r) - \rho_{at}]$, since $\sin(Qr)/Q \to r$ as $Q \to 0$. The liquid structure factor in the long-wavelength limit thus depends on the density fluctuations in the system.

These become particularly strong when the compressibility is large, for the obvious reason that if it is easy to change the density by external forces, then thermal fluctuations can also do so spontaneously. At the critical point of a fluid the compressibility diverges, and the fluctuations extend over macroscopic distances. $\mathcal{S}(0)$ can in fact become so large that the fluid becomes opaque to visible light as well as for X-rays, and the phenomenon (first observed by Andrews [1869] and later explained by Einstein [1910])

---

[4]This nomenclature may be regarded as somewhat unfortunate, as the liquid structure factor is proportional to the intensity, whereas the molecular structure factor encountered earlier, and the structure factor used in crystallography refer to amplitude!

is known as critical opalescence. The isothermal compressibility, κ_T, is defined as the relative change in density when applying a pressure P at constant temperature T, or explicitly $\kappa_T = (\partial\rho/\partial P)_T /\rho$. For the ideal gas the equation of state is $P = \rho_{at}k_B T$, and the compressibility is $\kappa_T = 1/(\rho_{at}k_B T)$ which varies smoothly with density. For interacting gas particles, as phenomenological described by van der Waals, the compressibility diverges at a critical point in $P - T$ space. It can be shown rigorously that $\mathcal{S}(0) = \rho_{at}\kappa_T k_B T$, which is quantitatively consistent with the expected result for an ideal gas that $\mathcal{S}(Q)=1$ for all Q.

Equation (4.16) stated in words says that the structure factor depends on the sine Fourier transform of the deviation of the atomic density from its average. One way of making this clearer is to rewrite Eq. (4.16) as

$$Q\left[\mathcal{S}(Q) - 1\right] = \int_0^\infty \mathcal{H}(r)\sin(Qr)\,dr \tag{4.17}$$

with $\mathcal{H}(r)=4\pi r\left[\rho(r) - \rho_{at}\right] = 4\pi r\rho_{at}\left[g(r) - 1\right]$. Then from the definition of the Fourier transform (see Appendix E) $\mathcal{H}(r)$ is obtained from the inverse Fourier transform as

$$\mathcal{H}(r) = \frac{2}{\pi}\int_0^\infty Q\left[\mathcal{S}(Q) - 1\right]\sin(Qr)\,dQ \tag{4.18}$$

This can be rearranged to read

$$g(r) = 1 + \frac{1}{2\pi^2 r\rho_{at}}\int_0^\infty Q\left[\mathcal{S}(Q) - 1\right]\sin(Qr)\,dQ \tag{4.19}$$

Thus the radial distribution function of a liquid or glass − in other words the function that describes its structure − is obtained directly from the measured structure factor using the algorithm of Eq. (4.19).

In deriving the expression for the non-crystalline structure factor (Eq. (4.16)) it has been assumed implicitly that the scattering is dominated by elastic scattering events. For rigid systems, such as typical structural glasses, this turns out to be a reasonable assumption. For liquids it fails completely, as there is no strictly elastic scattering from a liquid. However, as the X-ray photon energy ($\sim$ 10 keV) is much higher than the energies of the relevant modes of excitation in a liquid ($\sim$ 10 meV for diffusion, sound modes (phonons), etc.), the change in the energy of the scattered photon is in most situations imperceptibly small[5]. Another way of looking at this is to say that an integration is performed in an X-ray scattering experiment over all possible excitation energies in the sample. In such a case the above equation is exact. When this does not hold, as in the case of neutron scattering where the energy of the incident neutron is comparable to the excitation, corrections have to be applied.

Although the formalism in this section has been developed for mono-particle systems, it can be readily extended to cover more complex, multi-component systems. The main conceptual step is to introduce a radial distribution function $g_{ij}(r)$ which now describes correlations between atoms of type i and j. This then leads to the concept of the so-called partial liquid structure factor $\mathcal{S}_{ij}(Q)$.

4.4.3   The structure of supercooled liquids

One of the most spectacular effects oberved when a liquid solidifies to form a crystalline solid is supercooling: it is possible to maintain the liquid state as a meta-stable phase well below the melting

---

[5]It is worth noting in passing, however, that X-ray spectrometers have been developed which are more than capable of resolving changes in photon energy of better than 1 part in 10^8, and indeed phonon dispersion relations can be routinely determined with such instruments.
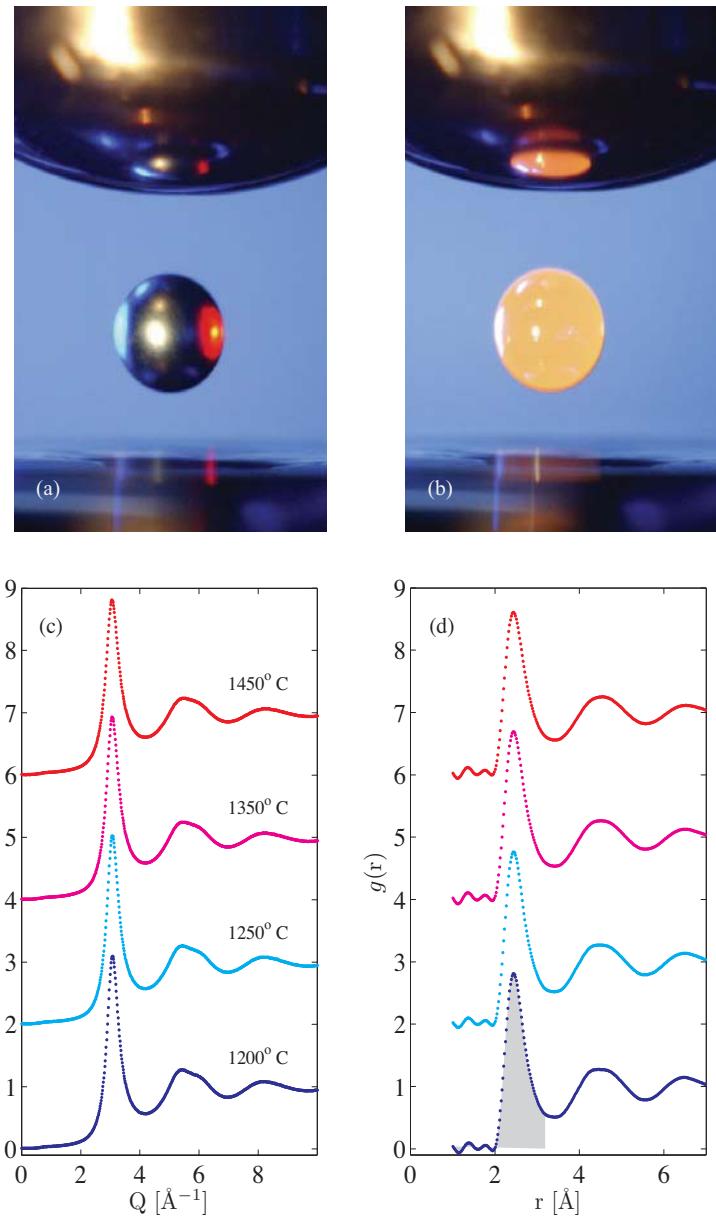
Fig. 4.9 X-ray scattering from liquid metals. (a) Image of a drop of a liquid metal (diameter approximately 2 mm) electrostatically levitated in an ultra-high vacuum chamber. (b) Drops levitated in this way can be heated with a laser, here causing the drop to glow. The metallic sample shown in (a) and (b) is $Ti_{39.5}Zr_{39.5}Ni_{21}$. (c) Wavevector dependence of the liquid X-ray structure factor of nickel for selected temperatures below its freezing point of 1455 °C. (d) The radial distribution function of liquid nickel evaluated using Eq. (4.19). The shaded area under the bottom most curve corresponds to a coordination number of 12 in the nearest neighbour shell. (Images courtesy Jan Rogers, NASA's Marshall Space Flight Center, Huntsville, AL; data from K. F. Kelton, Washington University in St. Louis.)

temperature. For an element like the transition metal nickel in its liquid phase the supercooling is several hundreds of degrees, for water it is tens of degrees. The explanation of this phenomenon was provided by Frank more than half a century ago (Frank [1952]). When approaching the melting temperature from the liquid state it can be expected that atoms in the liquid will form ordered clusters spontaneously. The structure of the clusters will obviously depend on the system under consideration. Here we focus on materials which in the solid phase form simple close packed structures such as the face centred cubic (*fcc*) or hexagonal close packed (*hcp*) structures (see Chapter 5). For these structures each atom has 12 nearest neighbours, and it would be reasonable to assume that clusters in the liquid would also be similarly coordinated. Frank's insight was that that apart from *fcc* or *hcp* packing there is an alternative way of forming a cluster with 12 neighbours, namely the icosahedron. This polyhedron, depicted in Fig. 4.10(a), consists of 20 equilateral triangles, which can be viewed as two pentagonal pyramids at the top and bottom, braced by a ring of 10 triangles.

It was argued by Frank that an icosahedron is the most likely configuration adopted by atoms in the liquid on the basis of its following properties. The Cartesian coordinates of the 12 vertices of an icosahedron are $(0, \pm 1, \pm \phi)$ and its two cyclic permutations, where ϕ is the golden mean number $\phi = (1 + \sqrt{5})/2$ (see Fig. 4.10(a)). With these coordinates the length of the side of each equilateral triangle is 2, as the reader can easily verify, but the distance from the origin to a vertex is only 1.9021. Visualizing the atoms as spheres, this calculation shows that the central atom touches its 12 neighbours, but the neighbours do not touch each other, in contrast to a *fcc* or an *hcp* cluster. The structure is therefore slightly more 'open' and thus a likely candidate for the arrangement of atoms forming a liquid cluster.

Although an icosahedral arrangement of atoms is permitted for an isolated cluster, it is impossible to form a regular crystal by attempting to stack icosahedral clusters in a three-dimensional, space-filling network. This is ultimately due to the five-fold symmetry displayed by the icosahedron, a point further discussed in Section 5.2 in the context of quasicrystals. The liquid-solid transition cannot therefore be thought of simply as the condensation of icosahedral clusters. Indeed there must be an energy barrier to overcome at the transition, arising from the different structures preferred by the liquid and solid, the existence of which explains the possibility of supercooling a liquid. In Frank's own words, '[if one assumes the atoms] *interact in pairs with attractive and repulsive energy terms proportional to r^{-6} and r^{-12}, one may calculate that the binding energy of the group of thirteen is 8.4% greater than for the two other packings. Thus freezing involves a substantial rearrangement, and not merely an extension of the same kind of order from short distances to long ones*'.

Here we describe two X-ray scattering studies of metallic liquids that have provided strong experimental support for Frank's proposal.

Scattering from bulk liquid nickel

In an experiment by Lee et al. [2004] using synchrotron X-ray diffraction sufficient accuracy was obtained to conclude that icosahedral clusters do indeed occur in the supecooled liquid phase of bulk Ni.

One of the main obstacles in obtaining accurate scattering data from a liquid is that the experiment has to be designed to minimize the scattering from the container in which the liquid is held. This is a far from trivial problem which has been overcome by the ingenious method of levitating the sample with electric or magnetic forces. In Fig. 4.9(a) and (b) we show images of a drop of metallic liquid levitated using electrostatic forces. This container-less technique also reduces any possible contamination of the sample, particularly if it is also held in ultra-high vacuum. Nucleation sites are therefore minimized which facilies studies of undercooled liquids. The temperature of the sample can be varied by heating
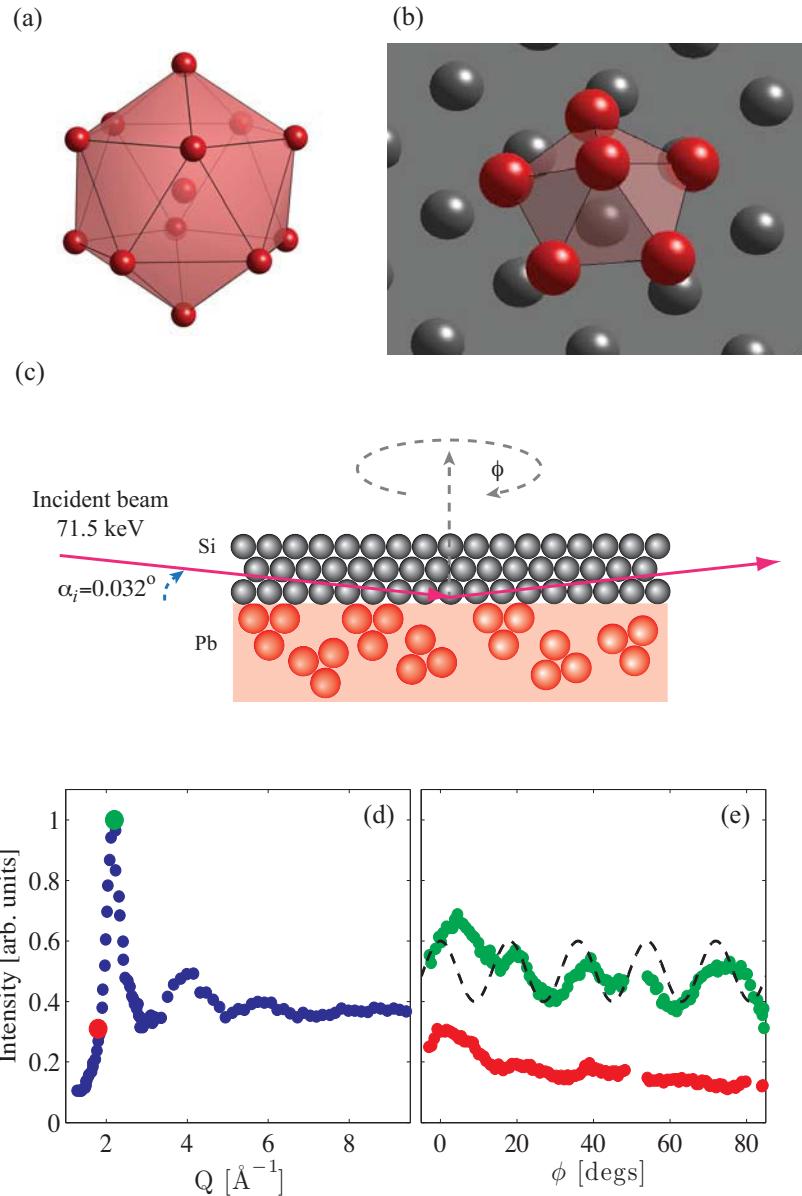
Fig. 4.10 Five-fold local symmetry in liquid lead. (a) An icosahedral atomic cluster, where the central atom is surrounded by 12 neighbours. (b) Instantaneous snapshot of a liquid fragment in proximity to the (100) surface of silicon. The fragment is formed from five, slightly distorted tetrahedra, and has five-fold symmetry for rotations around the (100) four-fold axis of silicon. For the case shown, the minimum overlap of the projected electron density between the fragment and the underlying silicon surface occurs for rotation angle $\phi_n = 2\pi n/20$, n integer. (c) Schematic of the scattering geometry used to measure the scattering from liquid lead in contact with a silicon surface. (d) Wavevector dependence of the structure factor of liquid lead measured with an X-ray angle of incidence of $\alpha_i = 0.0328°$ below the critical angle. The red and green symbols indicate the values of Q for which the anisotropy of the liquid structure factor was investigated by rotating the sample around ϕ. (d) Variation with ϕ of the liquid structure of liquid lead in contact with silicon. (Data courtesy of Harald Reichert.)

using a high-powered laser, as is evident in the images shown in Fig. 4.9(a) and (b).

In Fig. 4.9(c) we show the measured structure factor of an electrostatically levitated drop of liquid nickel as it is undercooled below its freezing point of 1455 °C [Lee et al., 2004]. It is apparent that the gross features of the scattering do not change even as the liquid is cooled to more than 200°C below its freezing point. Also apparent is the fact that this method produces data of extremely high quality.

The radial distribution functions calculated by transforming the data in Fig. 4.9(c) using Eq. (4.19) are plotted in Fig. 4.9(d). At a given temperature, the radial distribution function $g(r)$ exhibits a series of well-defined peaks as a function of r, tending to unity at large distances, as expected. The peaks in $g(r)$ directly reflect the existence of coordination shells in the liquid at characteristic distances, as shown schematically in Fig. 4.8. For example, the first main peak in $g(r)$ from the nearest-neighbour shell in Ni occurs[6] at r≈2.5 Å. Nickel crystallises in the face-centred-cubic structure (see Section 5.1) with the lattice parameter at room temperature of a=3.52 Å. The nearest-neighbour distance in the solid is therefore $a/\sqrt{2} \approx 2.5$ Å, close to the value found in the liquid. This illustrates the fact that although the solid and liquid are distinct phases, they nonetheless share some characteristics. For a *fcc* structure, the number of nearest neighbours is exactly equal to 12. The number of nearest neighbours in the first coordination shell of liquid nickel can be estimated by integrating the first peak in $g(r)$, as indicated by the grey area in the bottom most data set displayed in Fig. 4.9(d). Obviously, the choice of integration limits is arbitrary to some extent. The average number of atoms N_{nn} in the nearest neighbour shell is evaluated as

$$N_{nn} = \int_{r_1}^{r_2} \rho_{at} g(r) 4\pi r^2 \, dr$$

where ρ_{at} is the average number density. In Fig. 4.9(d), the lower limit r_1 has been set at 2, and the upper limit r_2 chosen such that N_{nn}=12, the number of nearest neighbours in the solid, or indeed in an icosahedron.

Closer inspection of the data shown in Fig. 4.9(c) reveals subtle but significant changes to the scattering on cooling. In particular, with decreasing temperature, a shoulder appears on the high Q side of the second peak in $\mathcal{S}(Q)$. By carefully comparing the data with structural model of the liquid it has been demonstrated [Lee et al., 2004] that this shoulder reflects the development of short-range icosahedral order in the undercooled liquid, as first proposed by Frank [1952].

Structure of liquid lead in contact with crystalline silicon

The smearing of the diffraction pattern produced by the orientational averaging of atomic clusters, as occurs in a bulk liquid, was overcome in an elegant way by Reichert et al. [2000]. The idea is that close to a crystalline interface a liquid will be subject to a modulated potential with the same symmetry as that of the crystalline surface. Reichert et al. [2000] investigated liquid lead in contact with the Si (100) surface, which imposes a potential of four-fold symmetry on any clusters localized close to the interface (see Fig. 4.10(b)). If, as expected for an icosahedron, or for a fragment of one, the cluster has five-fold symmetry, then the diffraction from the liquid in contact with the solid surface should exhibit a periodic variation when rotating around the four-fold axis. The period expected is $2\pi/(4 \cdot 5) = 2\pi/20$. The main challenge to realise such an experiment is to limit the diffraction so that it occurs only from the liquid in contact with the solid interface. This was achieved by Reichert et al. [2000] using a grazing incidence diffraction geometry to excite an evanescent wave in the liquid (see Chapter 3).

---

[6]The small oscillations evident in $g(r)$ for r< 2 Å are an artefact which arise from the fact that $\mathcal{S}(Q)$ is measured out to a finite value of Q only. As $\mathcal{S}(Q)$ is sampled out to a maximum Q, it follows from the properties of Fourier transforms, that $g(r)$ is not determined by the data for r less than 1/Q.

A schematic of the experimental geometry employed by Reichert et al. [2000] is shown in Fig. 4.10(c) where a narrow X-ray beam is incident at a glancing angle of 0.032° on a Si single crystal. The X-ray energy is chosen to be high enough so that the beam actually penetrates through the Si from the side before interacting with the liquid lead. According to Eq. (3.3) the critical angle α_c at the solid-liquid interface is proportional to the square root of the electron density difference between Si and Pb, *viz.* $\alpha_c = \sqrt{4\pi r_0(\rho_{Pb} - \rho_{Si})}/k = 0.705$ mrad $= 0.04°$. From Eq. (3.18), and neglecting for simplicity absorption effects, the penetration depth of the evanescent wave into the Pb is calculated to be $\Lambda = 32$ Å. This value pertains to the penetration of the incident beam. The actual penetration depth sampled in an experiment will be somewhat different from this value depending on the details of how the experiment is performed, as due allowance must be made for the exit wave. Of key importance is the fact that the X-ray beam samples the liquid lead only within a few nanometres from its interface with Si.

The diffraction pattern from the near-surface region of liquid lead in contact with crystalline silicon is shown in Fig. 4.10(d). The variation of intensity with wavevector follows that expected for the scattering from a liquid. With Q increasing from zero the intensity increases rapidly forming a well-defined peak around 2.18 Å^{-1}, close to the value found for the bulk liquid. Thereafter a number of oscillations are observed before the intensity saturates to a constant value at large wavevectors. The novel aspect of the experimental setup employed by Reichert et al. [2000] was the ability to rotate the ultra-high vacuum chamber containing the sample around a vertical axis (the axis marked ϕ in Fig. 4.10(c)). Data were then collected by scanning ϕ with the detector angle 2θ fixed. For a bulk liquid the intensity recorded in such a scan will be independent of ϕ. For lead in contact with silicon a very different result was obtained, with the intensity displaying five pronounced oscillations as a function of ϕ (Fig. 4.10(e)) in an interval of 90°. Modelling of the results proved that the data are fully consistent with the existence of liquid lead fragments similar to that shown in Fig. 4.10(b). Since the four-fold symmetry of the Si surface cannot possibly induce a Pb cluster with five-fold symmetry this study thus provided definite proof for the existence of poly-tetrahedral clusters of atoms in an elemental, metallic liquid.

4.5   Small-angle X-ray scattering (SAXS)

We now return to examine the third term on the right-hand side of Eq. (4.15) which we argued contributed to the scattering at small wavevector transfers, or equivalently small scattering angles, only. This term, giving the small angle scattering intensity in dimensionless form, can be recast as

$$I^{SAXS}(\mathbf{Q}) = f^2 \sum_n \int_V \rho_{at} e^{i\mathbf{Q}\cdot(\mathbf{r}_n - \mathbf{r}_m)} dV_m = f^2 \sum_n e^{i\mathbf{Q}\cdot\mathbf{r}_n} \int_V \rho_{at} e^{-i\mathbf{Q}\cdot\mathbf{r}_m} dV_m$$

Following earlier considerations on page 127, the sum on the right-hand side may be replaced by an integral to yield

$$I^{SAXS}(\mathbf{Q}) = f^2 \int_V \rho_{at} e^{i\mathbf{Q}\cdot\mathbf{r}_n} dV_n \int_V \rho_{at} e^{-i\mathbf{Q}\cdot\mathbf{r}_m} dV_m$$

which for sufficient averaging, as typically occurs in small-angle scattering, becomes

$$I^{SAXS}(\mathbf{Q}) = \left| \int_V \rho_{sl} e^{i\mathbf{Q}\cdot\mathbf{r}} dV \right|^2 \tag{4.20}$$
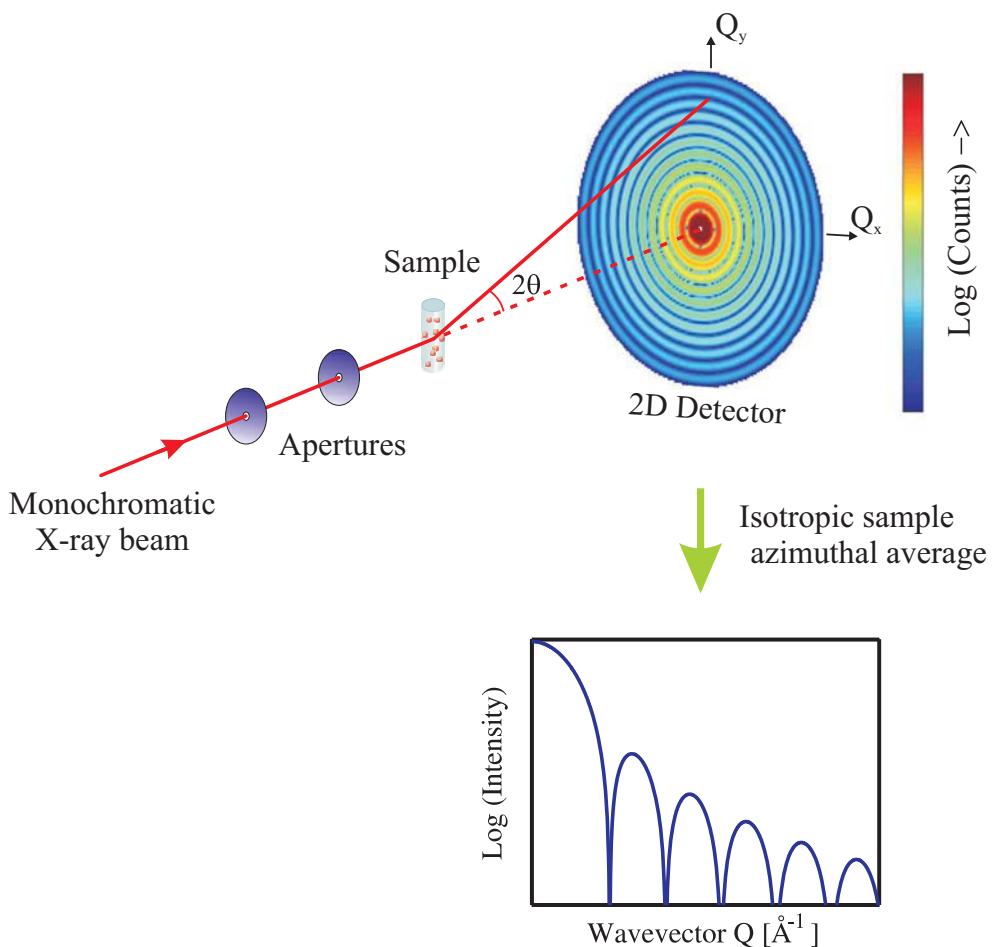
Fig. 4.11 Schematic layout of a small-angle X-ray scattering beamline. A monochromatic X-ray beam is collimated using a set of apertures and then impinges on the sample. The scattered beam is detected on a two-dimensional, position sensitive detector (PSD). For isotropic samples, the scattering can be azimuthally averaged to produce a plot of scattered intensity versus wavevector transfer.

Here we have introduced $\rho_{sl} = f\rho_{at}$ which when multiplied by r_0 gives the scattering length density.

The reader will hopefully recognize the form of Eq. (4.20) from our earlier consideration of the atomic form factor (see Section 4.2). Although the equations have identical formal structures − as is bound to be the case, as they are little more than general statements of the fact that the scattering amplitude is the Fourier transform of the charge density − the key difference is that here we are concerned with scattering from objects very large compared with typical inter-atomic distances. This confines the scattering of interest to small angles, and allows us to analyse the scattering through a number of simplifying assumptions.

The typical experimental layout of a beamline to determine the small-angle scattering from large-scale structures is appealingly simple, and is shown schematically in Fig. 4.11. The X-ray beam first passes through a monochromator (not shown) after which a series of apertures are used to control its
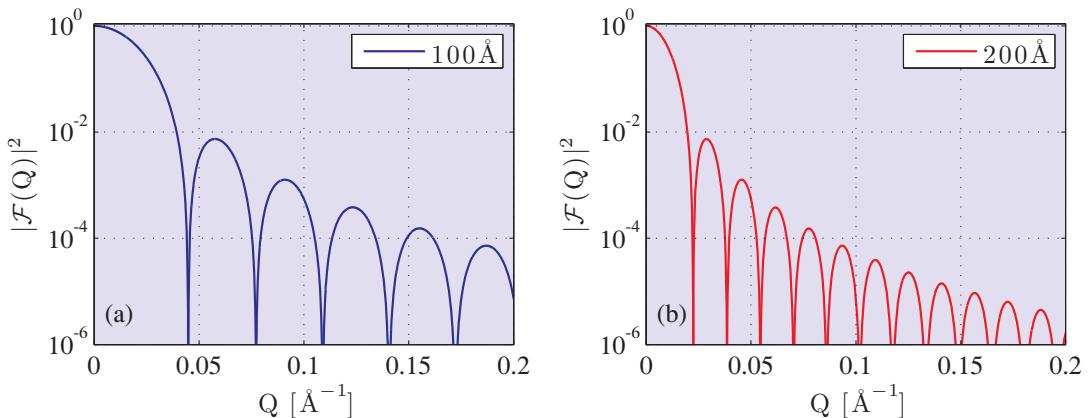
Fig. 4.12 Calculated small-angle scattering from a sphere (Eq. (4.23)). (a) Radius R=100 Å. (b) R=200 Å.

angular divergence. The X-ray beam then impinges on the sample, from which it is scattered at low angles into a detector. In modern small-angle X-ray scattering (SAXS) beamlines a two-dimensional, position-sensitive detector is invariably used. Each pixel of the detector records the number of scattered photons it receives in a given time, so that an image is built up of the scattered intensity as a function of the two components of the wavevector transfer which are approximately perpendicular to the incident beam.

4.5.1   The form factor of isolated particles

The simplest case to analyse is a dilute solution of molecules, or more generally particles, allowing inter-particle correlations to be be neglected, and where it is assumed that the particles are identical. If the scattering length density of each particle is uniform and represented by $\rho_{sl,p}$, and that of the solvent is $\rho_{sl,0}$, then from Eq. (4.20) the intensity scattered by a single particle is

$$I_1^{SAXS}(\mathbf{Q}) = (\rho_{sl,p} - \rho_{sl,0})^2 \left| \int_{V_p} e^{i\mathbf{Q}\cdot\mathbf{r}} \, dV_p \right|^2$$

where V_p is the volume of the particle. By introducing the single particle form factor[7],

$$\mathcal{F}(\mathbf{Q}) = \frac{1}{V_p} \int_{V_p} e^{i\mathbf{Q}\cdot\mathbf{r}} \, dV_p, \tag{4.21}$$

this becomes

$$\boxed{I_1^{SAXS}(\mathbf{Q}) = \Delta\rho^2 \, V_p^2 \, |\mathcal{F}(\mathbf{Q})|^2 .} \tag{4.22}$$

with $\Delta\rho = (\rho_{sl,p} - \rho_{sl,0})$.

The form factor depends on the morphology – *size and shape* – of the particle through the integral over its volume, V_p. Unfortunately, it can only be evaluated analytically in few cases. When this is

---

[7]In the small angle scattering literature the form factor is often defined as $\mathcal{P}(\mathbf{Q}) = |\mathcal{F}(\mathbf{Q})|^2$. In other words it refers to the intensity and not the amplitude.

not possible, the appropriate integrals have to be evaluated numerically. Probably the easiest case to consider is a sphere of radius R, for which the form factor can be readily calculated as

$$\mathcal{F}(Q) = \frac{1}{V_p} \int_0^R \int_0^{2\pi} \int_0^\pi e^{iQr\cos\theta}\, r^2 \sin\theta d\theta d\phi dr = \frac{1}{V_p} \int_0^R 4\pi \frac{\sin(Qr)}{Qr}\, r^2 dr$$

$$= 3\left[\frac{\sin(QR) - QR\cos(QR)}{Q^3 R^3}\right] \equiv \frac{3J_1(QR)}{QR} \tag{4.23}$$

where $J_1(x)$ is the Bessel function of the first kind. In Fig. 4.12(a)-(b) we illustrate the variation of $|\mathcal{F}(Q)|^2$ with particle size by plotting it for two different choices of sphere radius.

For $Q = 0$, $|\mathcal{F}(Q)|^2 = 1$, and from Eq. (4.22) the intensity from a single particle is given by $I_1^{SAXS}(0) = \Delta\rho^2 V_p^2$. This is the expected result as in the forward direction all electrons scatter in phase, and the intensity scattered from a particle embedded in a medium must then be proportional to the excess number of electrons squared. (See the discussion on atomic form factors on page 118.) If required, the intensity can of course be determined in absolute units which involves introducing an additional factor of r_0^2, as well as normalizing for the incident intensity I_0. At finite Q the intensity falls off rapidly, with strong oscillations evident in the SAXS intensity, where the period of the oscillations is inversely proportional to the radius of the sphere. An example of SAXS from spheres of silica is given in the figure on page 331, where oscillations in the observed intensity are clearly visible.

Greater insight into how information on the particle morphology is encoded in a SAXS experiment may be gleaned by considering the limiting forms of $\mathcal{F}(Q)$. In the first instance we will use the specific example of a sphere, and then indicate how the resulting concepts can be generalised to other particle shapes.

4.5.2   The long wavelength limit: Guinier analysis

In the long-wavelength limit, $QR \to 0$, and appropriate expansion of the trigonometric functions in Eq. (4.23) yields

$$\mathcal{F}(Q) \approx \frac{3}{Q^3 R^3}\left[QR - \frac{Q^3 R^3}{6} + \frac{Q^5 R^5}{120} - \cdots - QR\left(1 - \frac{Q^2 R^2}{2} + \frac{Q^4 R^4}{24} - \cdots\right)\right]$$

which simplifies to become

$$\mathcal{F}(Q) \approx 1 - \frac{Q^2 R^2}{10}$$

Therefore from Eq. (4.22) the intensity in the long-wavelength limit may be written as

$$I_1^{SAXS}(Q) \approx \Delta\rho^2 V_p^2 \left[1 - \frac{Q^2 R^2}{10}\right]^2 \approx \Delta\rho^2 V_p^2 \left[1 - \frac{Q^2 R^2}{5}\right]$$

This equation demonstrates that in the long-wavelength limit the variation of the scattered intensity with increasing wavevector can be used to determine the radius R of the particle. Often the right hand side of the above equation is written in exponential form[8], viz.,

$$I_1^{SAXS}(Q) \approx \Delta\rho^2 V_p^2 e^{-Q^2 R^2/5} \qquad QR \ll 1 \tag{4.24}$$

---

[8] $e^{-x} \approx 1 - x$
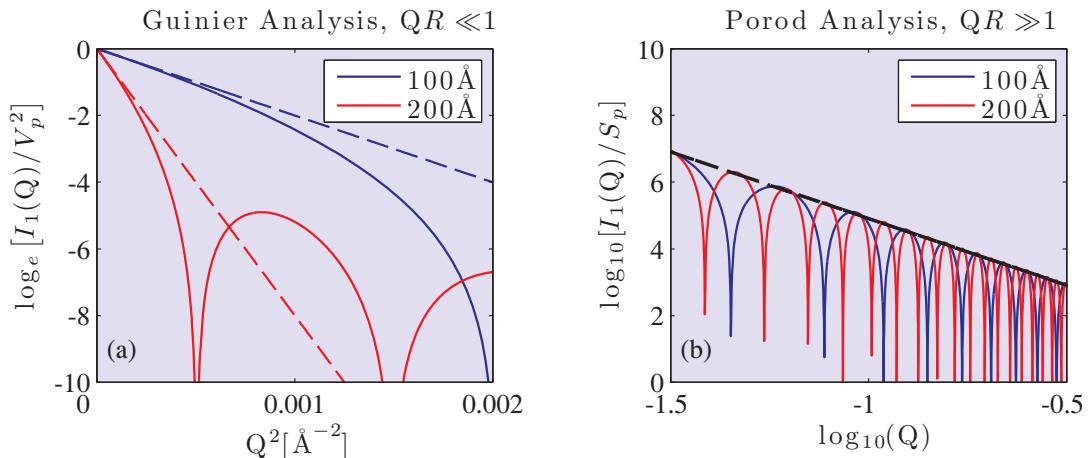
Fig. 4.13 Limiting forms of the small-angle scattering from a sphere (Eq. (4.23)). (a) Guinier analysis applicable in the long-wavelength limit ($QR \ll 1$) when the intensity $I_1(Q)$ is proportional to $\exp(-Q^2R^2/5)$ (Eq. (4.24)). A plot of $I_1(Q)$ versus Q^2 should therefore produce a line with a gradient of $-R^2/5$ as represented by the dashed lines. (b) At short wavelengths, $QR \gg 1$, in the Porod regime, the intensity falls off as $1/Q^4$ for a sphere (Eq. (4.27)). In a double log plot one decade in Q yields a decrease of four decades in the ordinate, i.e. a power of 4 in the power law. For simplicity in both (a) and (b) we have set $\Delta\rho$ equal to 1.

as then by plotting $\log_e(I_1^{SAXS}(Q))$ versus Q^2 a straight line should be obtained with a slope equal to $-R^2/5$ thus allowing the radius of the sphere to be determined. The above formula was first derived by Guinier, and in honour of this, analysis of small-angle scattering in the long-wavelength limit bears his name. In Fig. 4.13(a) we show Guinier plots for spheres of different radii, which confirm that when plotted appropriately the intensity recorded in a SAXS experiment in the long-wavelength limit tends asymptotically to a straight line with a slope proportional to the radius squared of the particle.

Guinier analysis can be applied not only to spheres but to the small-angle scattering from any dilute system containing particles of arbitrary shape. In this case, the radius of the sphere has to be replaced by a more general measure of the particle size, known as the radius of gyration.

Radius of gyration

The radius of gyration R_g of a particle is defined as the root-mean-squared distance from the particle's centre of gravity. If the scattering length density is uniformly distributed, and has spherical symmetry, the radius of gyration squared is given by

$$R_g^2 = \frac{1}{V_p} \int_{V_p} \mathrm{r}^2 dV_p$$

In general, the scattering length density is spatially dependent, and the radius of gyration is obtained by first evaluating

$$R_g^2 = \frac{\int_{V_p} \rho_{sl,p}(\mathbf{r})\, r^2\, dV_p}{\int_{V_p} \rho_{sl,p}(\mathbf{r})\, dV_p} \tag{4.25}$$

and then performing an orientational average. In most cases, the required integrals often can only be calculated using numerical techniques. One exception is the uniform sphere, for which it is straight forward to show that its radius of gyration is $R_g^2 = \frac{3}{5}R^2$. This allows us to re-write Eq. (4.24) as

$$I_1^{SAXS}(Q) \approx \Delta\rho^2 V_p^2 e^{-Q^2 R_g^2/3} \tag{4.26}$$

which can be used to extract the radius of gyration from a Guinier plot. Although Eq. (4.26) has been derived for the specific case of a spherical particle of uniform density, it can be shown to be generally true.

4.5.3   The short wavelength limit: Porod analysis

For wavelengths small compared with the particle size, i.e. $QR \gg 1$, but still large compared with inter-atomic spacings, the form factor for a sphere can be expanded as

$$\mathcal{F}(Q) = 3\left[\frac{\sin(QR)}{Q^3 R^3} - \frac{\cos(QR)}{Q^2 R^2}\right] \approx 3\left[-\frac{\cos(QR)}{Q^2 R^2}\right]$$

When $QR \gg 1$, $\cos^2(QR)$ oscillates rapidly as a function of Q with an average value of 1/2. The intensity may then be written as

$$I_1^{SAXS}(Q) = 9\Delta\rho^2 V_p^2 \frac{\langle\cos^2(QR)\rangle}{Q^4 R^4} = 9\Delta\rho^2 V_p^2 \frac{1}{2} \frac{1}{Q^4 R^4}$$

Noting the relation between the volume V_p and the surface S_p of a sphere, $V_p^2 = [(4\pi/3)R^3]^2 = (4\pi/9)R^4 S_p$, one finds

$$I_1^{SAXS}(Q) = \frac{2\pi\Delta\rho^2}{Q^4} S_p \tag{4.27}$$

Thus the SAXS intensity in the short-wavelength limit, the so-called Porod regime, is proportional to the surface area of the sphere and inversely proportional to the fourth power of Q. This is illustrated in Fig. 4.13(b) where we have scaled the calculated intensity by the surface area. While the oscillations for the two types of sphere occur with different periods, as they must, when plotted on a double logarithmic plot, the average of the two curves falls off with a gradient of -4, as represented by the dashed line.

In fact, the variation of scattered intensity with wavevector in the Porod regime turns out to depend sensitively on the shape of the particle, including its dimensionality. This dependence is examined in the following section.

4.5.4   Variation of the form factor with particle shape

In this section we examine how the single particle form factor depends on the shape of the particle. That the form factor has to vary with particle shape should be clear from the defining equation, Eq. (4.21), which for a three-dimensional particle involves an integral over the particle volume V_p. As indicated earlier, an analytic calculation of the orientationally averaged form factor can only be made for very

	$|\mathcal{F}(Q)|^2$	Radius of gyration R_g	Porod exponent n
Sphere ($d = 3$)	$\left(\frac{3J_1(QR)}{QR}\right)^2$	$\sqrt{\frac{3}{5}}\,R$	-4
Disc ($d = 2$)	$\frac{2}{Q^2R^2}\left(1 - \frac{J_1(2QR)}{QR}\right)$	$\sqrt{\frac{1}{2}}\,R$	-2
Rod ($d = 1$)	$\frac{2Si(QL)}{QL} - \frac{4\sin^2(QL/2)}{Q^2L^2}$	$\sqrt{\frac{1}{12}}\,L$	-1

Table 4.2 Variation with dimensionality d of the SAXS single-particle form factor, $\mathcal{F}(Q)$, radius of gyration, R_g, and Porod exponent. Results are given for a sphere of radius R, an infinitely thin disc of radius R, and an infinitely thin rod of length L. Here $Si(x)$ is the sine integral $\int_0^x \sin t/t\, dt$, and $J_1(x)=(\sin(x)-x\cos(x))/x^2$ is a Bessel function of the first kind.

few particle shapes. Beyond these cases, it is necessary to calculate the form factor using numerical integration methods. The form factors for various shaped particles have been compiled by Pedersen [2002].

The form factor can be shown to depend sensitively on particle dimensionality. An understanding of this fact can be gained without recourse to detailed calculation, but from examining how the element of integration, dV_p in three dimensions, itself varies with dimensionality. We have already considered an example of a three-dimensional object, the sphere, for which the element of integration is $dV_p=4\pi r^2 dr$, and therefore the integrand in Eq. (4.21) varies as r^2. An example of a two-dimensional object is an infinitesimally thin disk, radius R, for which the element of integration is an area $dA_p=2\pi r dr$. To complete the sequence, we consider an infinitesimally thin rod, of length L as an example of a one-dimensional object. In this case, the element of integration is a constant independent of r. Thus when sampled at length scales smaller than the particle itself, the form factor exhibits a characteristic power law r^α with an exponent that depends on the particle's dimensionality. It follows that in a scattering experiment performed as a function of wavevector (proportional to inverse length) one should expect to see power laws in Q from which it should be possible to determine the dimensionality of the particle.

In Table 4.2, we provide expressions for the form factors for the three representative objects of varying dimensions considered above. Derivations of the form factor of the infinitesimally disk and rod are not provided here as it suffices for our present purposes to quote the results. The form factors listed in this table are plotted and compared in Fig. 4.14★. The comparison is facilitated by plotting the form factors as a function of the product of Q and the radius of gyration R_g. When plotted on a linear scale (Fig. 4.14(a)★) significant differences are apparent in the form factors for values of QR_g greater than approximately two. These differences become even more pronounced when the form factors are shown over an extended range on a double logarithmic plot (Fig. 4.14(b)★). In the Porod regime the asymptotic Q dependence of the form factor is such that $|\mathcal{F}(Q)|^2 \propto Q^{-4}$, Q^{-2}, and in Q^{-1} in $d=3, 2$, and 1 dimensions, respectively.

It is important to appreciate that the apparent dimensionality inferred from experiment may change with the range of wavevector considered. The reason is that different wavevectors probe different real space length scales, and how an object appears will depend on the length scale at which it is investigated.
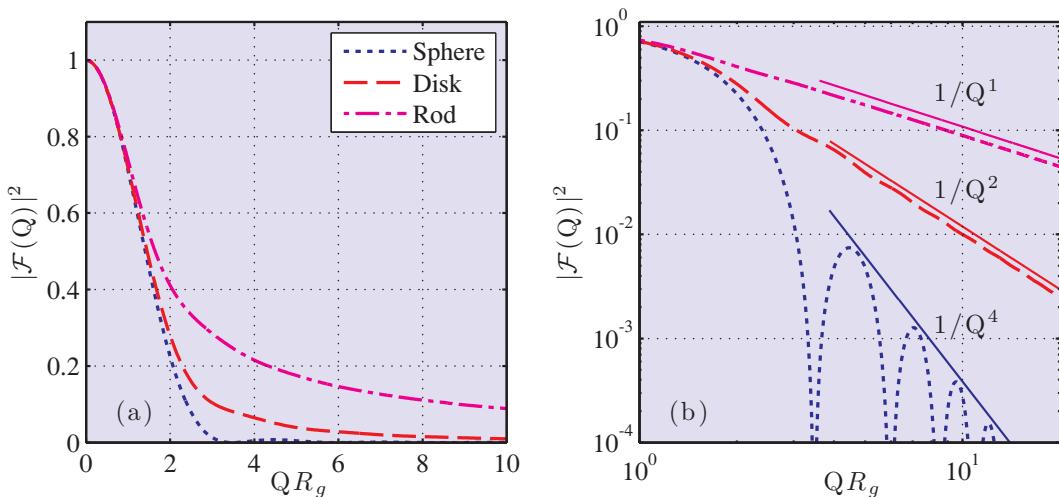
Fig. 4.14 ★ Illustration of the dependence of the small-angle scattering form factor on particle dimensionality. Here $|\mathcal{F}(Q)|^2$ is plotted as a function of the product of wavevector, Q, and the radius of gyration R_g. (a) The form factor for a sphere ($d = 3$), disk ($d = 2$) and rod ($d = 1$) (see Table 4.2). (b) The asymptotic behaviour at large Q of the form factor follows a power law with an exponent that depends on the dimensionality: $\mathcal{F}(Q) \propto Q^{-4}$, Q^{-2}, and Q^{-1} for $d = 3$, 2 and 1, respectively.

For example, polymers are extensively studied by small-angle scattering techniques. Simple polymers are composed of segments (monomers) bonded to form a long chain-like molecule. Depending on the solvent the chain can either be in an extended or collapsed state. For sufficiently large wavevectors the scattering from the former would fall off as $1/Q$, while for the latter as $1/Q^4$. At a critical concentration of solvent, the polymer structure is described as a random walk in three dimensions for which the intensity can be shown to vary as $1/Q^2$. Irrespective of the global structure assumed by the polymer, there is a minimum length scale in the problem set by the length of a monomer unit, and therefore at the highest wavevectors (shortest real space length scales) the scattering must fall off as $1/Q$, the characteristic behaviour of a rigid rod.

4.5.5   Polydispersivity

Up to now we have analysed the small-angle scattering from a dilute (i.e. non-interacting) ensemble of identical particles. In particular it has been assumed that all of the particles have the same size. Such an ensemble is said to be monodispersed. When this assumption no longer applies – as is most often the case when dealing with real systems, to a greater or lesser extent – the scattering system is said to be polydispersed. While it is undeniable that the existence of polydispersivity complicates the analysis of SAXS experiments, it is also true that one of the strengths of the technique is its ability to provide information on the statistical distribution of particle sizes.

If the distribution of particle sizes R is represented by the function $D(R)$, then in the presence of polydispersivity Eq. (4.20) must be amended to read

$$I(Q) = \Delta\rho^2 \int_0^\infty D(R)V_p(R)^2 |\mathcal{F}(Q,R)|^2 \, dR \tag{4.28}$$

The particle size distribution function is normalized such that $\int_0^\infty D(R)dR = 1$. Although it is possible

to use different functions to represent the particle size distribution according to the problem at hand, one particular function is particularly popular in the context of small angle scattering. The Schulz function is defined by

$$D(R) = \left[\frac{z+1}{\bar{R}}\right]^{z+1} \frac{R^z}{\Gamma(z+1)} \exp\left(-(z+1)\frac{R}{\bar{R}}\right) \tag{4.29}$$

where $\bar{R}$ is the mean particle size, and z is a measure of the spread in particle sizes, with $D(R)$ tending to a delta function as $z \to \infty$. The reason for the popularity of the Schulz function is that it is possible to obtain semi-analytic expressions for Eq. (4.28) for simple particle shapes such as rods, disks and spheres (see, for example, Kotlarchyk and Chen [1983] and references therein). For the Schulz distribution the percentage polydispersivity $p = 100/\sqrt{z+1}$.

Qualitatively, polydispersivity acts to smear out features in the SAXS curve. In Fig. 4.15★ we show the calculated effect of progressively increasing the polydispersivity of an ensemble of spheres. The solid blue line represents the familiar, well-defined intensity oscillations expected from a monodispersed system of spheres. Introducing a modest spread in particle size of $p=10\%$ ($z= 99$, dashed red line) leads to a rapid damping of the intensity oscillations. Doubling the spread to $p=20\%$ ($z = 24$, dot dashed green line), the intensity oscillations all but disappear.

4.5.6   Inter-particle interactions

We now consider briefly how to extend the theory that has been developed so far to describe the small-angle scattering from a concentrated system of particles. In analogy with the scattering from dense atomic liquids considered in Section 4.4, inter-particle correlations may be accounted for by introducing a structure factor $\mathcal{S}(Q)$ (Eq. (4.16)). Equation (4.22) then has to be amended to read

$$\boxed{I^{SAXS}(Q) = \Delta\rho^2 V_p^2 \, |\mathcal{F}(\mathbf{Q})|^2 \, \mathcal{S}(Q)} \tag{4.30}$$

Thus starting from the dilute limit, increasing the particle concentration will progressively lead to additional peaks in the intensity as a function of Q similar to those shown in Fig. 4.10 and Fig. 4.9.

Before considering an example of the application of SAXS it is worth remarking that very few of the formulae derived in this section are specific to this technique, in the sense that they also applicable to small-angle neutron scattering. One of the most significant changes occurs when converting the measured intensity to an absolute scale. In the SANS case it is necessary to use the appropriately weighted neutron scattering lengths b_i^2, instead of r_0^2.

4.5.7   Dynamics of the micelle to vesicle transition

Certain classes of organic molecules have the propensity to self organise into aggregates which assume a wide variety of ordered structures. Such behaviour is particularly prevalent amongst surface active molecules known as surfactants. The organic molecules forming a surfactant are amphiphilic, formed from a head group that is hydrophilic and a tail group that is hydrophobic. Structures exhibited by surfactants range from simple, particle-like structures, including micelles and vesicles, to extended objects such as bilayers and membranes, and even crystalline forms of matter. SAXS, and its sister technique small-angle neutron scattering, SANS, are ideally suited for studying these structures.

Here we consider the example of a time-resolved SAXS study of the micelle to vesicle transition which occurs when two different types of micelle are mixed (Weiss et al. [2005]). The experiment was
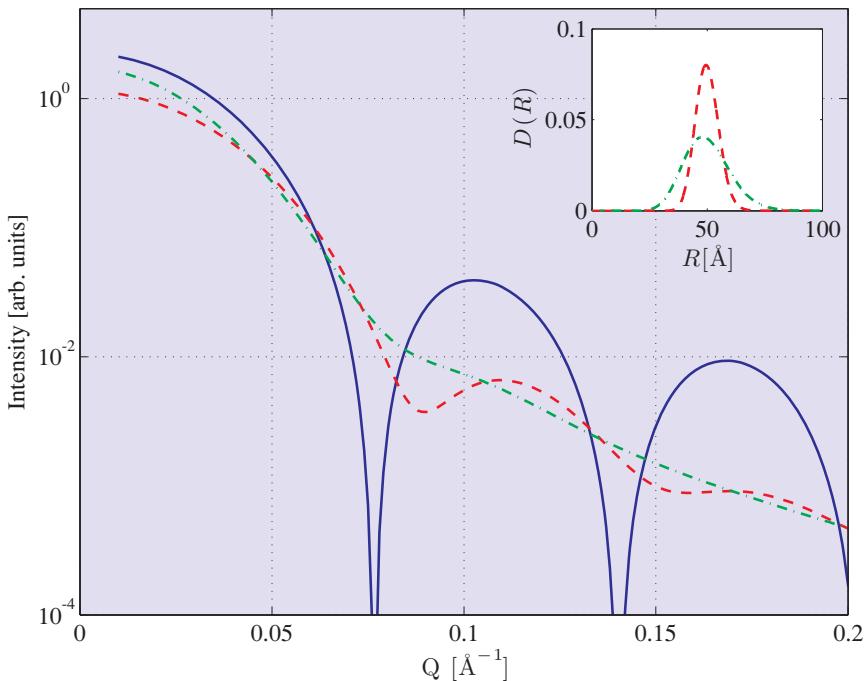
Fig. 4.15 ⋆ Effect of polydispersivity on the calculated SAXS curve. Solid blue line: form factor of a spherical particle, radius $R=50$ Å (Eq. (4.23)). Dashed red line: average form factor for particles described by a Schulz distribution (Eq. (4.29)) with $\bar{R}=50$ Å and a polydispersivity of $p=10$ % ($z=99$) (see inset). Dot-dashed green line: average form factor for particles described by $\bar{R}=50$ Å and $p=20$ % ($z=24$) (see inset).

performed on beamline ID2 at the ESRF in Grenoble, France. A remarkable feature of this experiment was that a combination of a fast, two-dimensional detector and the high intensity of the incident beam allowed a complete SAXS measurement to be made during an exposure lasting a few milliseconds.

A sketch of the structures of the micelles before mixing is given in the inset of Fig. 4.16(a). Micelles M_1 and M_2 are rod and sphere like, respectively. (Details on the chemical formulae of the micelles and other important information on the experiment can be found in Weiss et al. [2005].) Their morphologies are confirmed by the SAXS data shown in Fig. 4.16(a). The data for M_1 and M_2 studied separately are well accounted for by the expected small-angle scattering from a rod, and a sphere, respectively, as indicated by the solid lines through the data. Within 5 ms after mixing the SAXS curve M_1+M_2 shows that a drastic change to the structure has occurred. Analysis of the data establishes that a new, much larger disk-like micelle has formed. The small-angle scattering from a disk of radius R and height H is given by

$$I(Q) = V_p^2 \, \Delta\rho^2 \int_0^{\pi/2} \left[\frac{2J_1(QR\sin\phi)}{QR\sin\phi} \right]^2 \left[\frac{\sin(QH/2)\cos\phi}{(QH/2)\cos\phi} \right]^2 \sin\phi \, d\phi \qquad (4.31)$$

where J_1 is a Bessel function of the first kind. A good fit of the above expression to the M_1+M_2 data was obtained with $R=75$ Å and $H=48$ Å. Included in the fits shown in Fig. 4.16(a) was a small polydispersivity in the size of the micelles.

Figure 4.16(b) shows the time evolution of the SAXS data from the mixture of micelles. For times up to about 580 ms after mixing the SAXS data display a steady evolution. This is evident in Fig.
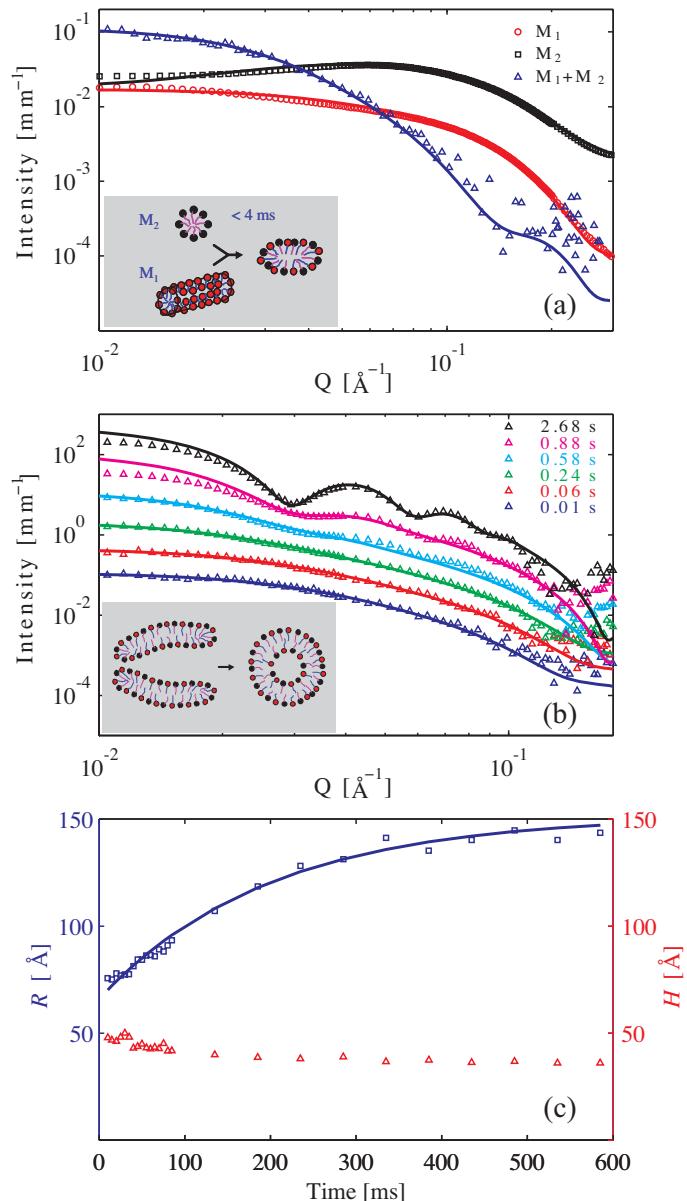
Fig. 4.16 Time resolved SAXS data of the micelle to vesicle transition in a surfactant mixture. (a) Comparison of SAXS data from solutions of micelle M_1 (red, rod of radius 18.5 Å and length 150 Å), M_2 (black, sphere of radius $10 - 12$ Å), and M_1+M_2 (blue) within 4 ms after they were mixed. The solid line through the M_1+M_2 data represents the scattering from a disk of radius $R=75$ Å and height $H=48$ Å (Eq. (4.31)). (b) Time dependence of SAXS from M_1+M_2. Offsets have been applied to the intensity scale for successive data sets. For times within roughly 580 ms the data continue to be well accounted for by Eq. (4.31) (solid lines). Beyond 580 ms the SAXS changes form and is instead described by the scattering from a spherical shell (Eq. (4.32)). (c) Temporal evolution of the disk parameters within 580 ms of mixing. The solid line represents the behaviour expected for exponential growth of the disk radius R with a time constant of $\tau=198$ ms. (Data courtesy of Theyencheri Narayan.)

4.16(c) which shows the results of an analysis of the data. Clearly, the main change to the morphology of the micelles in this time interval is a smooth increase in their radius. Beyond 580 ms, the SAXS data develops well-defined oscillations and can no longer be fitted by Eq. (4.31). Instead, the SAXS data reveals that the micelles have undergone a transition to form vesicles, as indicated in the schematic shown in the inset to Fig. 4.16(b). The expression for the small-angle scattering from a shell-like vesicle is given by

$$I(Q) = 16\pi^2 \Delta\rho^2 \left[R_2^2 \frac{J_1(QR_2)}{Q} - R_1^2 \frac{J_1(QR_1)}{Q} \right]^2 \tag{4.32}$$

This equation is obtained from a straightforward generalization of Eq. (4.23). Inspection of Fig. 4.16(b) shows that Eq. (4.32), appropriately modified to allow for the effects of polydispersivity, gives a good account of the data for $t > 580$ ms. In this time interval, the main structural change is an increase in the average radius of the vesicles, as can be seen directly from the data as a displacement in the intensity oscillations to lower Q. Deviations at low Q between data and theory are due to the growing importance of inter-particle correlations, which have not been included in the analysis. The growth of disk-like micelles immediately after mixing is driven by the unfavourable edge energy. At later times, once they are above a critical size, the bending energy of the bilayers favours closure of the disks to form vesicles.

This example therefore not only serves to illustrate the detailed nature of the structural information that can be obtained from SAXS experiments, but it also indicates the future direction of this field, where brighter sources will be able to provide data on ever shorter time scales, allowing the in situ study of chemical and biological processes.

4.6 Further reading

X-ray Diffraction, B.E. Warren (Dover Publications, 1990)

International Tables of Crystallography, (Kluwer Academic Publishers)

Introduction to the Theory of Thermal Neutron Scattering, G.L. Squires (Dover, 1996)

An Introduction to the Liquid State, P. A. Egelstaff (Oxford University Press, 1994)

Small-angle X-ray Scattering, O. Glatter amd O. Kratky (Academic Press, 1982)

Introduction to Polymer Physics, M. Doi (Oxford University Press, 1996)

4.7 Exercises

4.1 Account for the shift in energy of the inelastic component relative to the elastic one for the data shown in Fig. 4.4, and estimate the FWHM of the electronic momentum distribution in kapton.

4.2 The intensity of Compton scattering, I_C, from an atom can be estimated by assuming that the total scattered intensity, the sum of elastic and inelastic contributions, is constant and equal to r_0^2 per electron, i.e. in electron units $1 = I_C + |f_n(Q)|^2$ where $f_n(Q)$ is the contribution to the total atomic form factor from the n'th electron. Show that for the He atom $I_C = 2 - 2/(1 + (Qa/2)^2)^4$

with $a = a_0/(Z - z_s)$ where the symbols have their usual meaning. Compare this result with the calculation shown in Fig. 4.5(a).

4.3 Consider a diatomic molecule with two identical atoms separated by a distance a and each having the atomic form factor given by $Z/[1 + (Qa/20)^2]^2$. Calculate the scattered X-ray intensity as a function of Qa and determine the value of Qa for the first two intensity maxima.

4.4 Calculate the scattered X-ray intensity for a linear triatomic molecule where the central atom is distinct from its two neighbours. You may assume that the two outer atoms are identical, and take the total length of the molecule to be $2a$. Verify that in the limit that the central atom of a triatomic molecule has negligible scattering length the expression for the scattered intensity reduces to that of a diatomic molecule.

4.5 The difference between X-ray and neutron form factors (the latter being a constant because the nuclear interaction potential is delta-function like) is apparent in scattering from gas molecules, such as for example HgI_2. This triatomic, linear molecule as an Hg-I bond length of 2.65 Å. Calculate and plot the X-ray and neutron scattering intensities for Q up to 12 Å^{-1}, normalized to 1 at Q=0. Hint: the neutron scattering lengths for Hg and I are 12.7 fm and 5.3 fm, respectively. For X-rays, use the expansion given in Eq. (4.10) with the following parameters for I and Hg, respectively a=[20.1472 18.9949 7.5138 2.2735]; b=[4.3470 0.3814 27.76 66.8776]; c=4.0712; a=[20.6809 19.0417 21.6575 5.9676]; b=[0.545000 8.44840 1.57290 38.3246]; c= 12.6089.

4.6 The electronic density $\rho(r)$ of the buckyball molecule C_{60} may be approximated as a thin shell of charge of radius R with

$$\rho(r) = \frac{A}{4\pi R^2}\delta(R - r)$$

Determine the numerator A, and use this approximation to calculate the molecular form factor.

4.7 Show that the relative difference in intensity between the Guinier approximation and the exact solution for spherical particles is less than 1% for $QR<1.33$.

4.8 Prove numerically that the r.m.s. width of the Schulz distribution with $R = 1$ is 0.1 (0.2) when $p = 10\%(20\%)$.

4.9 Show that the small angle scattering form factor for a vesicle is given by Eq. (4.32).

4.10 Equation (4.26) was derived for the specific case of a spherical particle of uniform density. Establish its generality by considering the expansion in the small-angle scattering limit of the phase factor appearing in the definition of the form factor, Eq. (4.21).

Kinematical scattering II: crystalline order

It is by now universally appreciated that atoms in crystalline materials display long-range *positional* order. Indeed, the establishment of this fact by von Laue, the Braggs, and others, was one of the early triumphs of X-ray diffraction. The structural picture which emerged from these early studies of elements and simple compounds was of the regular, periodic stacking of atoms in three dimensions. Following on from this pioneering work, the power of X-ray diffraction techniques has developed enormously along a number of distinct lines. For example, it is now possible to routinely study the atomic arrangements in complex materials, including proteins and other biomolecules, or in lower dimensional objects, such as in two dimensions on surfaces. In addition, the brilliance of modern X-ray sources allows data to be taken in extremely short time intervals, currently less than 100 fs for a free-electron laser, opening up the possibility of studying chemical, biological and other time-dependent processes. X-ray diffraction has even led to a new definition of the crystalline state through the discovery of a new class of materials known as quasicrystals. These materials produce sharp diffraction spots and yet lack the usual translational symmetry associated with conventional, periodic crystal structures.

In this chapter we describe the scattering of X-rays from crystalline materials, and illustrate how different types of long-range order may be revealed through diffraction experiments. The underlying assumption employed throughout this chapter is that the X-ray is weakly scattered, allowing it to be analysed within the *kinematical approximation* (see the beginning of Chapter 4 where this approximation is discussed more fully).

5.1 Scattering from a crystal

Our exposition begins by considering the X-ray scattering from conventional crystalline materials where the atoms (or molecules) form periodic structures with translational symmetry. The detailed classification of crystals is described in many texts on solid state physics and crystallography and will not be repeated here. Instead we limit ourselves to reminding the reader of a few important facts that are made use of later.

5.1.1   Crystal structure: lattice and basis

A crystalline material may be constructed by regularly repeating a basic structural motif, known as the *unit cell*, so as to fill three-dimensional space. The points at which the origins of the unit cell are located form a hypothetical *lattice* which may exist in one, two, three and, in certain mathematical models, even higher dimensions. Thus a crystal is constructed by first specifying the lattice, and then associating a unit cells worth of atoms (or molecules) known as a *basis* with each point in the lattice.

Lattices and unit cells

For ease of illustration, we consider a two-dimensional (2D) lattice which can be specified by a set of vectors $\mathbf{R_n}$ with

$$\mathbf{R_n} = n_1\,\mathbf{a}_1 + n_2\,\mathbf{a}_2 \tag{5.1}$$

where $\mathbf{a}_1$ and $\mathbf{a}_2$ are the lattice vectors, and n_1 and n_2 are integers. The vectors $\mathbf{a}_1$ and $\mathbf{a}_2$ define the unit cell, as illustrated in Fig. 5.1(a) for the case of a 2D rectangular lattice. It is important to note that the choice of lattice vectors (including their origin) is to a large extent arbitrary. For example, in the case of our 2D rectangular lattice we could equally well have chosen $\mathbf{a}_2' = 2\mathbf{a}_2$ as shown in Fig. 5.1(b). For any lattice, however, we can always choose the lattice vectors such that the resulting area of the unit cell (or volume in three dimensions) is a minimum. This is known as the *primitive unit cell*, and is defined by the primitive lattice vectors. It follows that the primitive unit cell contains just a single lattice point. That this is the case can be seen by translating the origin by a small amount. When this is done to the unit cell drawn in Fig. 5.1(a) it is clear that it is primitive, whereas the unit cell of Fig. 5.1(b) is non-primitive. From these comments it may seem desirable to always work with a primitive unit cell, as that would seem to offer the best hope of minimizing any possible ambiguities. However, in many situations it turns out to be more convenient to work with a non-primitive unit cell, usually because it is easier to visualize the structure, and the unit cell that is mostly widely used for a given structure is known as the *conventional* unit cell. As an example, in Fig. 5.1(c) we show a cell that is indeed primitive, but one that does not readily reflect the rectangular symmetry of the lattice.

These considerations of course also apply in three dimensions where the lattice is specified by a set of vectors of the form

$$\boxed{\mathbf{R_n} = n_1\,\mathbf{a}_1 + n_2\,\mathbf{a}_2 + n_3\,\mathbf{a}_3} \tag{5.2}$$

A given lattice has characteristic symmetries, which not only include translations but also rotations, reflections, and compound symmetries formed by combining a translation with rotations and/or reflections. For example, the lattice shown in Fig. 5.1(a) has a two-fold rotation axis perpendicular to the plane of the paper through the origin. The lattice is also invariant if reflected in either of two orthogonal mirror planes. Lattices which have the property that each and every point in the lattice is identical are associated with the name of (Auguste) Bravais. He showed that in two dimensions there are five distinct types of lattice consistent with Eq. (5.1) (of which the rectangular lattice is but one), while in three dimensions there are 14.

To complete the description of a crystal structure we need to associate a basis worth of atoms (or molecules) with each and every lattice site. The construction of a two-dimensional crystal from a lattice and a basis is illustrated schematically in Fig. 5.1(d). When the possible symmetries of the basis (known as the *point group*) are combined with those of the lattice it turns out that all crystal structures can be classified into one of 230 possible *space groups*, as described in standard books on crystallography.

(a) primitive

a_2

a_1

(b) non-primitive

a_2'

a_1'

(c) non-conventional

a_2''

a_1''

(d) Crystal=lattice ⋆ basis

Lattice   Basis   Crystal
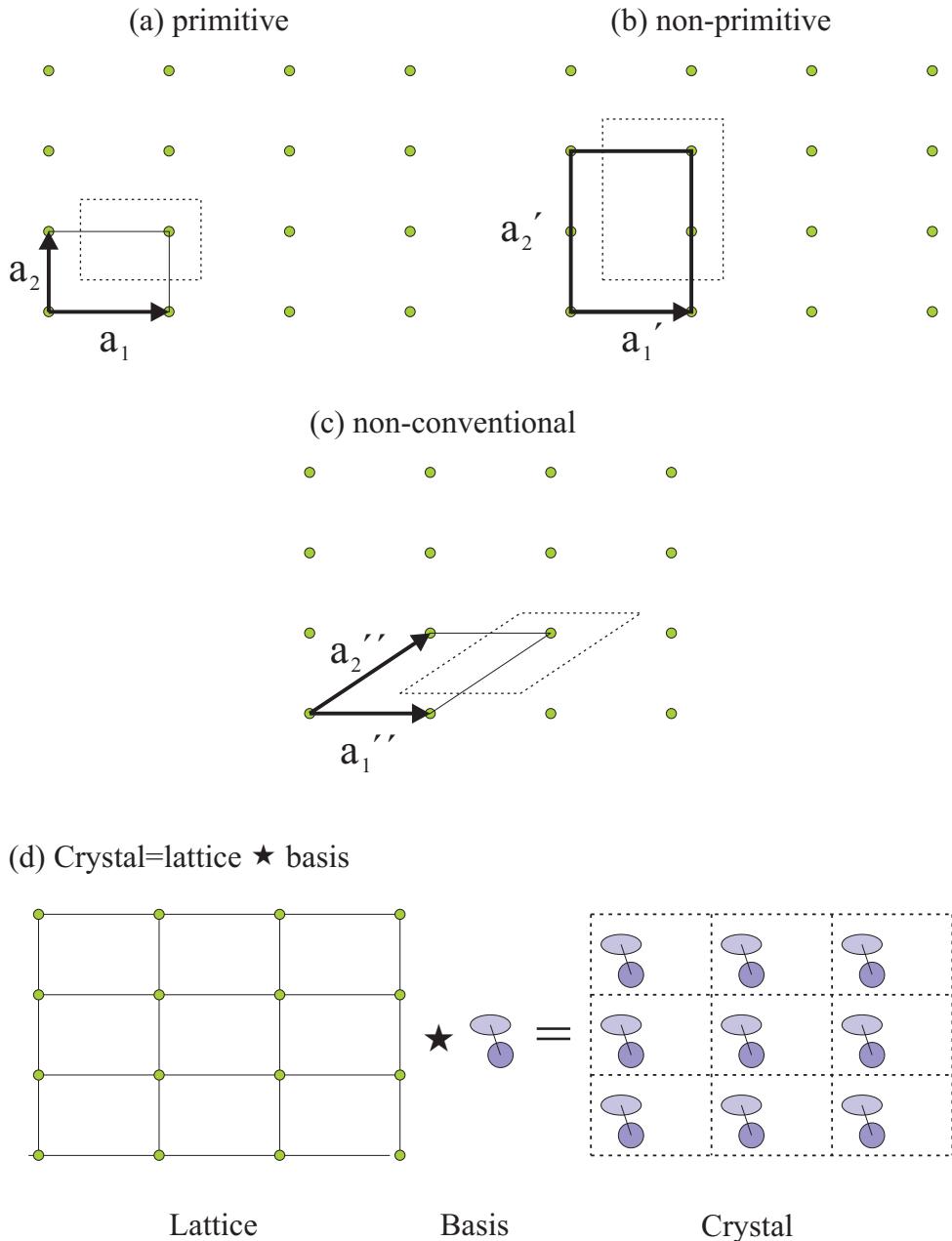
Fig. 5.1 Possible unit cells of the 2D rectangular lattice. (a) a primitive unit cell defined by $\mathbf{a}_1$ and $\mathbf{a}_2$. If we translate the origin and produce a new unit cell (indicated by the dotted line) then it is apparent that the unit cell contains one lattice point and is hence primitive. This is also the conventional cell of the 2D rectangular lattice. (b) non-primitive unit cell defined by $\mathbf{a}_1'$ and $\mathbf{a}_2'$, with $\mathbf{a}_2' = 2\mathbf{a}_2$. The unit cell produced by a shift of the origin is seen to contain two lattice points. (c) primitive, unconventional unit cell defined by $\mathbf{a}_1''$ and $\mathbf{a}_2''$. (d) The construction of a two-dimensional crystal structure from the convolution (designated by the symbol ⋆) of a lattice and a basis.
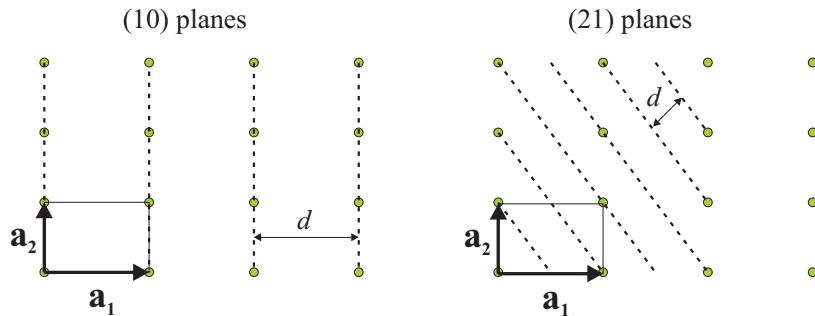
Fig. 5.2 Lattice planes and Miller indices for the 2D rectangular lattice: (a) the (10) planes; (b) the (21) planes. In both cases the d spacing of the planes is indicated.

Lattices that exist in the real space occupied by the crystal are sometimes referred to as *direct lattices* to distinguish them from ones that may be defined in other spaces.

Lattice planes and Miller indices

X-ray diffraction from a crystalline material is concerned with the scattering from atoms that may be thought of as lying within families of planes. Hence it is desirable to have some way to specify families of planes within a crystal. The *Miller indices* turn out to be the most convenient way to achieve this. For a given family of planes, the Miller indices (h, k, l) are defined such that the plane closest to the origin (but not including the origin) has intercepts $(a_1/h, a_2/k, a_3/l)$ on the axes $(\mathbf{a}_1, \mathbf{a}_2, \mathbf{a}_3)$. (We note that by convention a negative intercept is represented by writing a bar over the relevant Miller index.)

In Fig. 5.2 we indicate the (10) and (21) planes for the 2D rectangular lattice. This example serves to illustrate two important features of planes specified by their Miller indices. The first is that the density of lattice points in a given family of planes is the same, and that all lattice points are contained within each family. The second is that, again for a given family, the planes are equally spaced, so that it is possible to define a lattice spacing d_{hkl}. For example, the d spacings of a cubic lattice are given by

$$d_{hkl} = \frac{a}{\sqrt{h^2 + k^2 + l^2}} \tag{5.3}$$

where a is the lattice parameter, as we shall establish later.

Crystal structure as a convolution of lattice and basis

Mathematically, the synthesis of a crystal from a lattice and a basis is properly described as the convolution of two functions as defined in Appendix E. To establish this fact we consider a crystal in one dimension of lattice spacing a. Let the function $C(x)$ represent the crystal, and $\mathcal{L}(x)$ and $\mathcal{B}(x)$ describe the lattice and basis, respectively. Using this language, the crystal structure is represented by the function

$$C(x) = \sum_n \mathcal{B}(x - na)$$

which describes a series of copies of the basis $\mathcal{B}(x)$ separated by a distance a. The lattice is a purely mathematical construct comprised of a series of infinitely sharp points which can be written as

$$\mathcal{L}(x) = \sum_n \delta(x - na) \tag{5.4}$$

where $\delta(x - na)$ is the Dirac delta function. The reader is reminded of the definition and properties of the Dirac delta function in the box on the next page. The convolution of the functions representing the lattice and basis is then evaluated as

$$\mathcal{L}(x) \star \mathcal{B}(x) = \int_{-\infty}^{\infty} \mathcal{L}(x_1)\mathcal{B}(x - x_1)dx_1 = \int_{-\infty}^{\infty} \sum_n \delta(x_1 - na)\mathcal{B}(x - x_1)dx_1$$

$$= \sum_n \int_{-\infty}^{\infty} \delta(x_1 - na)\mathcal{B}(x - x_1)dx_1 = \sum_n \mathcal{B}(x - na)$$

$$= C(x)$$

This proof can be readily extended to higher dimensions.

5.1.2 Decomposition of the scattering amplitude

Having introduced a way of describing the structure of a crystal we can now proceed to calculate the scattering amplitude. Following Eq. (4.3), the scattering amplitude from a crystalline material comprised of atoms can be written in general as

$$F^{crystal}(\mathbf{Q}) = \sum_{\ell}^{\text{All atoms}} f_{\ell}(\mathbf{Q})e^{i\mathbf{Q}\cdot\mathbf{r}_{\ell}}$$

where $f_{\ell}(\mathbf{Q})$ is the atomic form factor of the atom situated at position $\mathbf{r}_{\ell}$, and the factor of $-r_0$ has been dropped. As indicated in Fig. 5.1(d), for a crystalline material $\mathbf{r}_{\ell} = \mathbf{R}_n + \mathbf{r}_j$, where $\mathbf{R}_n$ is a lattice vector and $\mathbf{r}_j$ labels the position of an atom within the unit cell. Writing the position vectors of the atoms in this way facilitates the decomposition of the scattering amplitude into the product of two terms:

$$F^{crystal}(\mathbf{Q}) = \sum_{\mathbf{R}_n + \mathbf{r}_j}^{\text{All atoms}} f_j(\mathbf{Q})e^{i\mathbf{Q}\cdot(\mathbf{R}_n + \mathbf{r}_j)} = \overbrace{\sum_n e^{i\mathbf{Q}\cdot\mathbf{R_n}}}^{\text{Lattice}} \overbrace{\sum_j f_j(\mathbf{Q})e^{i\mathbf{Q}\cdot\mathbf{r}_j}}^{\text{Unit cell}} \tag{5.5}$$

The first of these terms is a sum over the lattice, while the second is over the basis of atoms and is known as the *unit cell structure factor*,

$$F^{u.c.}(\mathbf{Q}) = \sum_j f_j(\mathbf{Q})e^{i\mathbf{Q}\cdot\mathbf{r}_j} \tag{5.6}$$

An alternative way to understand the decomposition of the scattering amplitude from a crystalline material into a product of a lattice and basis term is by invoking the convolution theorem. In real (or direct space) the crystal structure may be described as a convolution of a lattice and basis, as described earlier. Since the scattering amplitude is nothing other than the Fourier transform of the crystal structure, it follows from the convolution theorem that this must be equal to the product of the Fourier transforms of the functions describing the lattice and basis. These are, respectively, the lattice sum and the unit cell structure factor, which we consider separately in the following sections.

5.1.3 The Laue condition

Although conceptually the lattice sum is yet another step in building up the total scattering amplitude from a crystalline material, it is in practice quite different from all of the summations we have

The Dirac δ function

Usually a mathematical function such as $e^x, \sin(x)\cdots$, etc., can be tabulated and plotted. This is not the case for the Dirac δ function. It represents the limiting case for a number of functions with a peak, such as a box, triangle, Gaussian, or a Lorentzian, when the width tends towards zero while the area remains constant.

The Dirac δ function is used in connection with integration. When an arbitrary function, $f(x)$, is multiplied by the δ function and integrated, the result is by definition $f(x=0)$:

$$f(0) = \int f(x)\delta(x)\,dx$$

If the argument of the δ function is not x, but rather a function of x, $t(x)$ say, one can use the following procedure:

$$\int f(x)\delta(t(x))\,dx = \int f(t(x))\delta(t)\,(dt/dx)^{-1}\,dt$$
$$= \left[f(t)(dt/dx)^{-1}\right]_{t=0}$$

Suppose for example that $t(x) = x - a$. Then $dt/dx = 1$ and

$$\int f(x)\delta(x-a)\,dx = f(a)$$

Another linear function is $t(x) = x/a$:

$$\int f(x)\delta(x/a)\,dx = a\,f(0)$$

In connection with the derivation of the Lorentz factor we shall use and evaluate

$$F(\mathrm{k}) \equiv \int x^2\,\delta(x^2 - \mathrm{k}^2)\,dx \qquad \text{for}\quad \mathrm{k} > 0$$

With $t = x^2 - \mathrm{k}^2$ we obtain $dt/dx = 2x$ and therefore

$$F(\mathrm{k}) = \left[\frac{x^2}{2x}\right]_{t=0} = \frac{\mathrm{k}}{2}$$

or in other words

$$1 = \frac{2}{\mathrm{k}}\int x^2\,\delta(x^2 - \mathrm{k}^2)\,dx \qquad \text{for}\quad \mathrm{k} > 0$$

considered so far. The reason is that the number of terms in the lattice sum is enormous. A small crystallite may be of order of 1 micron on each side, which is of order 10^4 times the length of a basis vector, so that the number of terms is of order 10^{12} or more. Each of the terms is a complex number, $e^{i\phi_n}$, located somewhere on the unit circle. The sum of phase factors is of order unity, except when all phases are 2π or a multiple thereof, in which case the sum will be equal to the huge number of terms. The problem is then to solve

$$\mathbf{Q} \cdot \mathbf{R_n} = 2\pi \times \text{integer} \tag{5.7}$$

To find a solution, suppose that we now construct a lattice in the wavevector space (which has dimensions of reciprocal length) spanned by basis vectors $(\mathbf{a}_1^*, \mathbf{a}_2^*, \mathbf{a}_3^*)$ which fulfill

$$\boxed{\mathbf{a}_i \cdot \mathbf{a}_j^* = 2\pi \, \delta_{ij}} \tag{5.8}$$

where δ_{ij} is the Kronecker delta, defined so that $\delta_{ij} = 1$ if $i = j$ and is zero otherwise. The points on this *reciprocal lattice* are specified by vectors of the type

$$\boxed{\mathbf{G} = h\,\mathbf{a}_1^* + k\,\mathbf{a}_2^* + l\,\mathbf{a}_3^*} \tag{5.9}$$

where h, k, l are all integers. It is now apparent that the reciprocal lattice vectors $\mathbf{G}$ satisfy Eq. (5.7) since the scalar product of $\mathbf{G}$ and $\mathbf{R_n}$ is

$$\mathbf{G} \cdot \mathbf{R_n} = 2\pi(hn_1 + kn_2 + ln_3)$$

and as all of the variables in the parenthesis are integers, the sum of their product is also an integer. In other words, only if $\mathbf{Q}$ coincides with a reciprocal lattice vector will the scattered amplitude from a crystallite be non-vanishing. This is the Laue condition for the observation of X-ray diffraction:

$$\boxed{\mathbf{Q} = \mathbf{G}} \tag{5.10}$$

It is worth emphasizing that the Laue condition is a vector equation, requiring that each component of the wavevector transfer equals the corresponding component of the reciprocal lattice vector. Only when this condition is fulfilled will all of the phases of the scattered waves add up coherently to produce an intense signal. The Laue condition provides a mathematically elegant, but powerful way to visualize diffraction, as we shall see[1]. In order to calculate intensities it is of course necessary to explicitly evaluate the lattice sum, and we shall return to this in Section 5.1.6.

5.1.4 Reciprocal lattices

The reciprocal lattice vectors are generated through use of Eq. (5.8). In one dimension the construction of the reciprocal lattice is trivial, since $\mathbf{a}_1 \cdot \mathbf{a}_1^* = a_1 a_1^* = 2\pi$, which implies $a_1^* = 2\pi/a_1$ as shown in the top panel of Fig. 5.3. In two dimensions it is also reasonably straightforward to use Eq. (5.8). If we

---

[1]We have defined the wavevector transfer as $\mathbf{Q} = \mathbf{k} - \mathbf{k}'$, with the implication that $\mathbf{Q}$ points into the origin of reciprocal space. The Laue condition should then read $\mathbf{Q} = -\mathbf{G}$, but this change of sign does not affect any of the discussion.
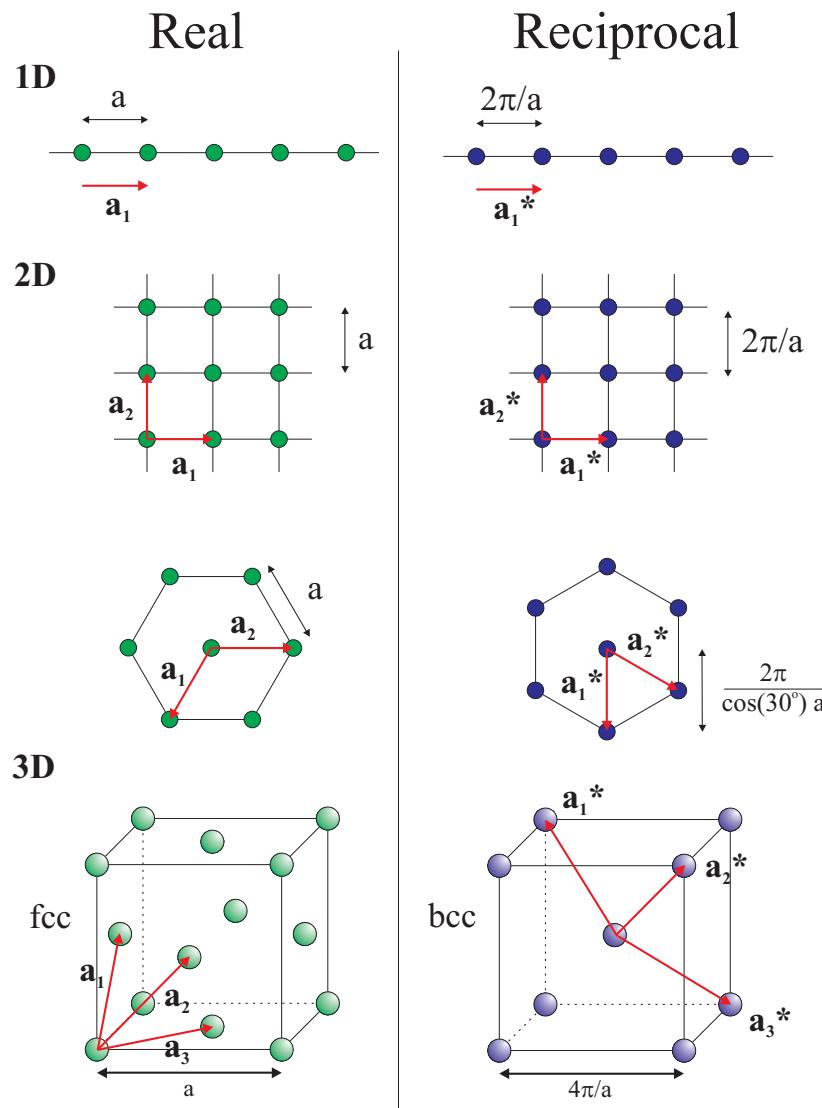
Fig. 5.3 Example of the construction of reciprocal lattices in one, two, and three dimensions.

write, in an appropriate coordinate system, $\mathbf{a}_1^* = (\alpha, \beta)$ and $\mathbf{a}_2^* = (\delta, \gamma)$, then substitution into Eq. (5.8) generates four equations from which the unknown parameters α, β, δ and γ can be determined. The second and third rows in Fig. 5.3, showing the reciprocal lattices of the two-dimensional square and hexagonal lattices were generated using this method. The hexagonal lattice serves to illustrate the point that if the axes in direct space are not orthogonal, then the basis vectors in real and reciprocal space are not necessarily parallel.

In three dimensions it proves to be more convenient to work with explicit expressions for the

reciprocal lattice basis vectors, given by

$$\mathbf{a}_1^* = \frac{2\pi}{v_c} \mathbf{a}_2 \times \mathbf{a}_3 \qquad \mathbf{a}_2^* = \frac{2\pi}{v_c} \mathbf{a}_3 \times \mathbf{a}_1 \qquad \mathbf{a}_3^* = \frac{2\pi}{v_c} \mathbf{a}_1 \times \mathbf{a}_2$$

where $v_c = \mathbf{a}_1 \cdot (\mathbf{a}_2 \times \mathbf{a}_3)$ is the volume of the unit cell. These may be verified by direct substitution into Eq. (5.8). In the bottom row of Fig. 5.3 we show the three-dimensional example of the face centred cubic lattice which has primitive lattice vectors of

$$\mathbf{a}_1 = \frac{a}{2}(\hat{\mathbf{y}} + \hat{\mathbf{z}}) \quad , \quad \mathbf{a}_2 = \frac{a}{2}(\hat{\mathbf{z}} + \hat{\mathbf{x}}) \quad , \quad \mathbf{a}_3 = \frac{a}{2}(\hat{\mathbf{x}} + \hat{\mathbf{y}})$$

where we have chosen a set of Cartesian axes parallel to the cube edges. The volume of the unit cell is $v_c = \mathbf{a}_1 \cdot (\mathbf{a}_2 \times \mathbf{a}_3)$, and the basis vectors of the reciprocal lattice are therefore

$$\mathbf{a}_1^* = \frac{4\pi}{a}(\frac{\hat{\mathbf{y}}}{2} + \frac{\hat{\mathbf{z}}}{2} - \frac{\hat{\mathbf{x}}}{2}) \quad , \quad \mathbf{a}_2^* = \frac{4\pi}{a}(\frac{\hat{\mathbf{z}}}{2} + \frac{\hat{\mathbf{x}}}{2} - \frac{\hat{\mathbf{y}}}{2}) \quad , \quad \mathbf{a}_3^* = \frac{4\pi}{a}(\frac{\hat{\mathbf{x}}}{2} + \frac{\hat{\mathbf{y}}}{2} - \frac{\hat{\mathbf{z}}}{2})$$

These are in fact the primitive basis vectors of a body centred cubic lattice with a cube edge of $4\pi/a$.

Reciprocal lattice: Fourier transform of the direct lattice

In Section 5.1.5 below we shall prove that the Laue condition for the constructive interference of waves scattered from a crystal is equivalent to Bragg's law. The proof of this equivalence relies on a particular aspect of the relationship between the direct and reciprocal lattices: a family of planes (h, k, l) in direct space is represented by the reciprocal lattice vector $\mathbf{G}_{hkl}$ in reciprocal space. The general relationship between the direct and reciprocal descriptions of a crystal lattice can be understood by considering the Fourier transform of the one-dimensional lattice function (Eq. (5.4)):
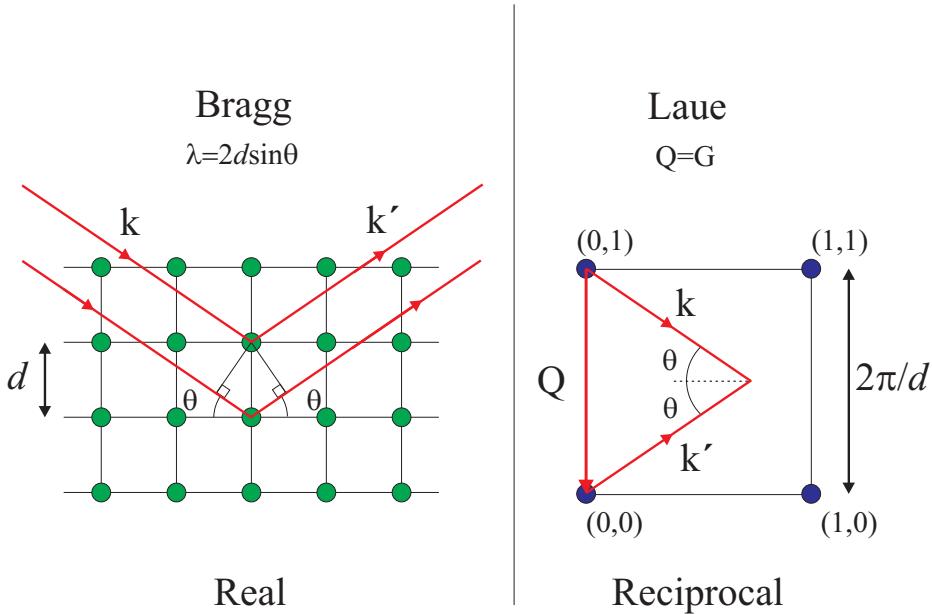
$$\int_{-\infty}^{\infty} \mathcal{L}(x)\, e^{iQx} dx = \int_{-\infty}^{\infty} \sum_n \delta(x - na)\, e^{iQx} dx = \sum_n \int_{-\infty}^{\infty} \delta(x - na)\, e^{iQx} dx$$
$$= \sum_n e^{iQna} = a^* \sum_h \delta(Q - ha^*)$$

where the last step makes use of a result which we shall derive in Section 5.1.6. Thus the Fourier transform of a one-dimensional direct lattice of spacing a is itself another lattice of spacing $a^* = 2\pi/a$ which we recognize as the reciprocal lattice. When extended to higher dimensions, the general result is obtained that the reciprocal lattice is nothing other than the Fourier transform of the direct lattice. (If required, the reader should refer to Appendix E where we define the Fourier transform and provide examples of its application to various functions.)

5.1.5   Equivalence of the Laue and Bragg conditions

It may be shown that the Laue condition is exactly equivalent to Bragg's Law. In Fig. 5.4(a) the proof of this equivalence is indicated for the specific case of a two-dimensional square lattice. The left hand part of the figure shows the construction normally used to derive Bragg's Law. X-rays are specularly reflected from atomic planes with a spacing of d, and the requirement that the path length difference is an integer multiple of the wavelength leads to the well-known statement of Bragg's law: $\lambda = 2d \sin\theta$. The same scattering event is drawn in reciprocal space in the right hand panel. The Laue condition requires that $\mathbf{Q} = \mathbf{G}$. The reciprocal lattice in this case is also square with a lattice spacing of $2\pi/d$,

(a) Equivalence of Bragg and Laue

(b) Miller indices and reciprocal lattice vectors
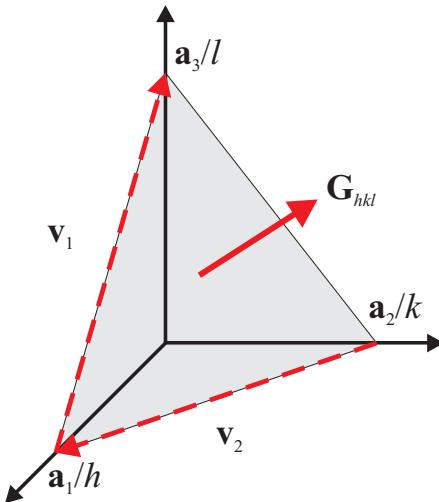
Fig. 5.4 (a) The equivalence of Bragg's Law and the Laue condition for the particular case of the 2D square lattice. (b) Construction to prove that the reciprocal lattice vector $\mathbf{G}_{hkl}$ is perpendicular to the (h, k, l) planes, and has a magnitude equal to $2\pi/d_{hkl}$.

and in the figure we have chosen $\mathbf{Q} = \frac{2\pi}{d}(0, 1)$. From the geometry $Q = 2k\sin\theta$, since $|\mathbf{k}| = |\mathbf{k}'|$, and we thus have $2\pi/d = 2k\sin\theta$ which can be rearranged to yield Bragg's Law.

The general proof of the equivalence of Laue's and Bragg formulations follows from the intimate relationship between *points* in reciprocal space and *planes* in the direct lattice. We shall now show that for each point of the reciprocal lattice given by Eq. (5.9) there exists a set of planes in the direct lattice such that

   (a) $\mathbf{G}_{hkl}$ is perpendicular to the planes with Miller indices (h, k, l).

   (b) $|\mathbf{G}_{hkl}| = \frac{2\pi}{d_{hkl}}$, where d_{hkl} is the lattice spacing of the (h, k, l) planes.

Consider the plane with Miller indices (h, k, l) shown in Fig. 5.4(b). Two vectors in this plane are given by

$$\mathbf{v}_1 = \frac{\mathbf{a}_3}{l} - \frac{\mathbf{a}_1}{h} \qquad \mathbf{v}_2 = \frac{\mathbf{a}_1}{h} - \frac{\mathbf{a}_2}{k}$$

Hence any point in this plane is specified by $\mathbf{v} = \epsilon_1 \mathbf{v}_1 + \epsilon_2 \mathbf{v}_2$, where ϵ_1 and ϵ_2 are parameters. From Eq. (5.8) the scalar product of $\mathbf{G}$ and $\mathbf{v}$ is

$$\mathbf{G} \cdot \mathbf{v} = (h\mathbf{a}_1^* + k\mathbf{a}_2^* + l\mathbf{a}_3^*) \cdot \left((\epsilon_2 - \epsilon_1)\frac{\mathbf{a}_1}{h} - \epsilon_2\frac{\mathbf{a}_2}{k} + \epsilon_1\frac{\mathbf{a}_3}{l} \right)$$

$$= 2\pi(\epsilon_2 - \epsilon_1 - \epsilon_2 + \epsilon_1) = 0$$

This establishes the first assertion. The plane spacing d is the distance from the origin to the plane, and is found by taking the scalar product of $\hat{\mathbf{G}} = \mathbf{G}/|\mathbf{G}|$, the unit vector along $\mathbf{G}$, and any vector connecting the origin to the plane, $\mathbf{a}_1/h$ say. The d spacing is thus

$$\boxed{d = \frac{\mathbf{a}_1}{h} \cdot \frac{\mathbf{G}}{|\mathbf{G}|} = \frac{2\pi}{|\mathbf{G}|}}$$

as required.

To complete the general proof of the equivalence we note that the Laue condition may be re-written in the form, $\mathbf{k} = \mathbf{G} + \mathbf{k}'$. Taking the square of both sides and using the fact that the scattering is elastic ($|\mathbf{k}| = |\mathbf{k}'|$) yields the result

$$G^2 = 2\mathbf{G} \cdot \mathbf{k} \tag{5.11}$$

where we have also utilized the fact that, if $\mathbf{G}$ is a reciprocal lattice vector, then so is $-\mathbf{G}$. From the scattering triangle (Fig. 5.4(a)) it is apparent that $\mathbf{G} \cdot \mathbf{k} = Gk\sin\theta$, and since we have already shown above that $G = 2\pi/d$, Eq. (5.11) can be rearranged as $\lambda = 2d\sin\theta$, thus completing the proof.

The relationship between $|\mathbf{G}|$ and d is an extremely useful one, as once $\mathbf{G}$ is known for the Bragg reflection of interest, d can be calculated. For example, for the simple cubic lattice $\mathbf{G} = \frac{2\pi}{a}(h, k, l)$, from which it follows that $|\mathbf{G}| = \frac{2\pi}{a}\sqrt{h^2 + k^2 + l^2}$, and hence $d = a/\sqrt{h^2 + k^2 + l^2}$ as stated in Eq. (5.3).

5.1.6 Lattice sums in one, two and three dimensions

A key ingredient that needs to be considered before the intensity of a given Bragg reflection can be calculated is the lattice sum defined in Eq. (5.5) as

$$S_N(\mathbf{Q}) = \sum_{\mathbf{n}} e^{i\mathbf{Q}\cdot\mathbf{R_n}}$$

In this section we evaluate the sum in one, two and three dimensions. The reader is reminded that the subscript **n** refers to the fact that the lattice vector $\mathbf{R_n}$ is specified by a set of integers that reflects the dimensionality of the lattice. In three dimensions we require a set of integers (n_1, n_2, n_3). As our main aim is to arrive at an expression for the intensity we will also evaluate the modulus squared of the lattice sum, $|S_N(\mathbf{Q})|^2$.

One dimension

In one dimension the lattice points are specified by $R_n = na$ where n is an integer and a is the lattice parameter. For a finite 1D lattice with N unit cells the sum may be written as

$$S_N(Q) = \sum_{n=0}^{N-1} e^{iQna}$$

Evaluation of this geometric series has already been considered on page 52, which allows us to write

$$|S_N(Q)| = \frac{\sin(NQa/2)}{\sin(Qa/2)}$$

For large N, $|S_N(Q)|$ exhibits a sharply defined peak whenever the denominator is equal to zero. This condition requires that $Qa/2 = h\pi$ (h integer), or in other words $Q = h(2\pi/a) = ha^\star = G_h$, where $\mathbf{G}_h$ is a reciprocal lattice vector. As expected, explicit evaluation of the lattice sum yields the Laue condition, which we had previously derived using plausibility arguments in Section 5.1.3.

In order to study the behaviour of the lattice sum when the Laue condition is almost fulfilled in the vicinity of a single reciprocal lattice point, a small parameter ξ is introduced which is defined by

$$Q = (h + \xi)a^*$$

The modulus of the lattice sum then becomes

$$|S_N(\xi)| = \frac{\sin(N\pi\xi)}{\sin(\pi\xi)} \to N \text{ as } \xi \to 0$$

Its width for large N may be estimated by setting $\xi = 1/(2N)$:

$$|S_N(\xi = \frac{1}{2N})| \approx \frac{1}{\pi/(2N)} = \left(\frac{2}{\pi}\right)N \approx \frac{N}{2}$$

With a peak height equal to N, and a full width at half maximum of approximately $1/N$, the peak area is approximately equal to unity. In fact it is possible to show that the area is exactly equal to unity, and in the limit that $N \to \infty$ we can write the modulus of the lattice sum as

$$|S_N(\xi)| \to \delta(\xi)$$

where $\delta(\xi)$ is the Dirac delta function. This result can be rewritten in a more general form in terms of the wavevector transfer Q as

$$|S_N(Q)| \to a^* \sum_{G_h} \delta(Q - G_h) \tag{5.12}$$

where the sum is over all reciprocal lattice points. The factor of a* arises since $\delta(Q - G_h) = \delta(\xi a^*)$ $= \delta(\xi)/a^*$ (see the box on page 152).

In a diffraction experiment it is the modulus squared of the lattice sum that is of interest. Using similar arguments to those given above it is straightforward to show that

$$|S_N(\mathbf{Q})|^2 \to N\,\mathrm{a}^* \sum_{G_h} \delta(\mathbf{Q} - \mathbf{G}_h) \tag{5.13}$$

which is plotted in the box on page 52.

Two and three dimensions

A two-dimensional lattice is shown in Fig. 5.1. The unit cell is spanned by the two basis vectors $\mathbf{a}_1$ and $\mathbf{a}_2$. A special case is when the macroscopic crystal has the shape of a parallelepiped, so that the number of unit cells along the $\mathbf{a}_1$ direction is always N_1, independent of the row number $1, 2, \cdots, N_2$. Following the same method outlined for the 1D case above it is obvious that

$$|S_N(\xi_1, \xi_2)|^2 \to N_1 N_2\, \delta(\xi_1)\, \delta(\xi_2)$$

for large (N_1, N_2). Again use is made of the Dirac delta function to write this in the form

$$|S_N(\mathbf{Q})|^2 \to (N_1 \mathbf{a}_1^*)(N_2 \mathbf{a}_2^*) \sum_{\mathbf{G}} \delta(\mathbf{Q} - \mathbf{G}) = NA^* \sum_{\mathbf{G}} \delta(\mathbf{Q} - \mathbf{G}) \tag{5.14}$$

where $\mathbf{G} = h\,\mathbf{a}_1^* + k\,\mathbf{a}_2^*$, A^* is the area of the unit cell in reciprocal space, and $N = N_1 N_2$ is the number of unit cells. In the general case, one cannot evaluate the sum analytically and afterwards square it to look at the limiting behaviour for large numbers of unit cells. However, the delta function character will be maintained for any crystal shape as long as the number of unit cells in both directions is large.

Generalization of the above result to three dimensions is straightforward. For a parallelepiped the summations can be carried out analytically, but for a general shape it cannot. When the number of unit cells in all three dimensions is large, then independently of the actual crystal shape

$$|S_N(\mathbf{Q})|^2 \to N\,v_c^* \sum_{\mathbf{G}} \delta(\mathbf{Q} - \mathbf{G}) \tag{5.15}$$

where $\mathbf{G} = h\,\mathbf{a}_1^* + k\,\mathbf{a}_2^* + l\,\mathbf{a}_3^*$, N is the total number of unit cells, and v_c^* is the volume of the unit cell in reciprocal space.

5.1.7 The unit cell structure factor

We now turn to the evaluation of the unit cell structure factor defined in Eq. (5.6). The starting point is to choose the lattice and hence the unit cell, as this in turn defines the basis of atoms within the unit cell. We illustrate this with a few simple examples.

The first example is the face centred cubic (fcc) structure shown in bottom panel of Fig. 5.3. Here the conventional cubic unit cell is chosen, as it reflects in a more obvious way the symmetry of the structure. With this choice of unit cell the lattice is simple cubic with a lattice spacing of a, and the basis consists of four atoms at

$$\mathbf{r}_1 = 0 \quad , \quad \mathbf{r}_2 = \frac{1}{2}(\mathbf{a}_1 + \mathbf{a}_2) \quad , \quad \mathbf{r}_3 = \frac{1}{2}(\mathbf{a}_2 + \mathbf{a}_3) \quad , \quad \mathbf{r}_4 = \frac{1}{2}(\mathbf{a}_3 + \mathbf{a}_1)$$
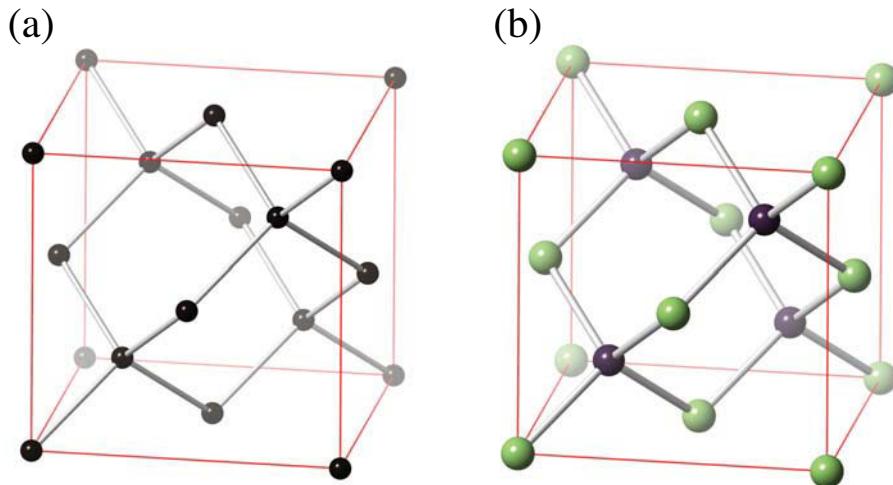
Fig. 5.5 The diamond lattice (a) can be formed from two inter-penetrating fcc lattices displaced by $(\frac{1}{4}\frac{1}{4}\frac{1}{4})$ with respect to each other. For the zinc sulfide (also known as zinc blende) structure (b) the two lattices are occupied by different types of atom.

Here $\mathbf{a}_1$, $\mathbf{a}_2$ and $\mathbf{a}_3$ are parallel to the cube edges. The choice of unit cell implies that the reciprocal lattice is also simple cubic with a lattice spacing of $2\pi/a$, and as a result a reciprocal lattice vector is of the form $\mathbf{G}=\left(\frac{2\pi}{a}\right)(h,k,l)$. For simplicity assume that all of the atoms in the unit cell are identical. The atomic scattering factor can then be taken outside the summation in Eq. (5.6), and the problem then is to sum the phase factors. The unit cell structure factor is evaluated as

$$
\begin{aligned}
F_{hkl}^{fcc} &= f(\mathbf{G}) \sum_j e^{i\mathbf{G}\cdot\mathbf{r}_j} \\
&= f(\mathbf{G})(1 + e^{i\pi(h+k)} + e^{i\pi(k+l)} + e^{i\pi(l+h)}) \\
&= f(\mathbf{G}) \times \begin{cases} 4 & \text{if } h,k,l \text{ are all even or all odd} \\ 0 & \text{otherwise} \end{cases}
\end{aligned}
$$

The $(1,0,0)$ reflection, which is the shortest reciprocal lattice vector, has a vanishing structure factor, since h is odd, but k and l are even: the reflection is said to be forbidden. The shortest reciprocal lattice vector of an allowed reflection is the $(1,1,1)$ reflection: all indices are odd. The next one is the $(2,0,0)$ reflection: here all indices are even.

The second example to consider is the diamond structure shown in Fig. 5.5(a). This is the structure adopted by elemental silicon and germanium, and of course of carbon in its diamond form. The diamond structure can be thought of in different ways. Choosing a conventional cubic unit cell implies that the basis would then be comprised of eight atoms (as the reader should be able to confirm). Alternatively, the diamond structure can be thought of as being formed from two interpenetrating fcc lattices, displaced $\frac{1}{4}$ of a body diagonal relative to each other. This suggests, following the discussion of the application of the convolution theorem in Section 5.1.2, to consider the diamond structure as a convolution of the fcc lattice and a two-atom basis, with one chosen to be at the origin, and the other at $(1/4,/1/4,1/4)a$. The advantage of this approach is that the structure factor of diamond can be written
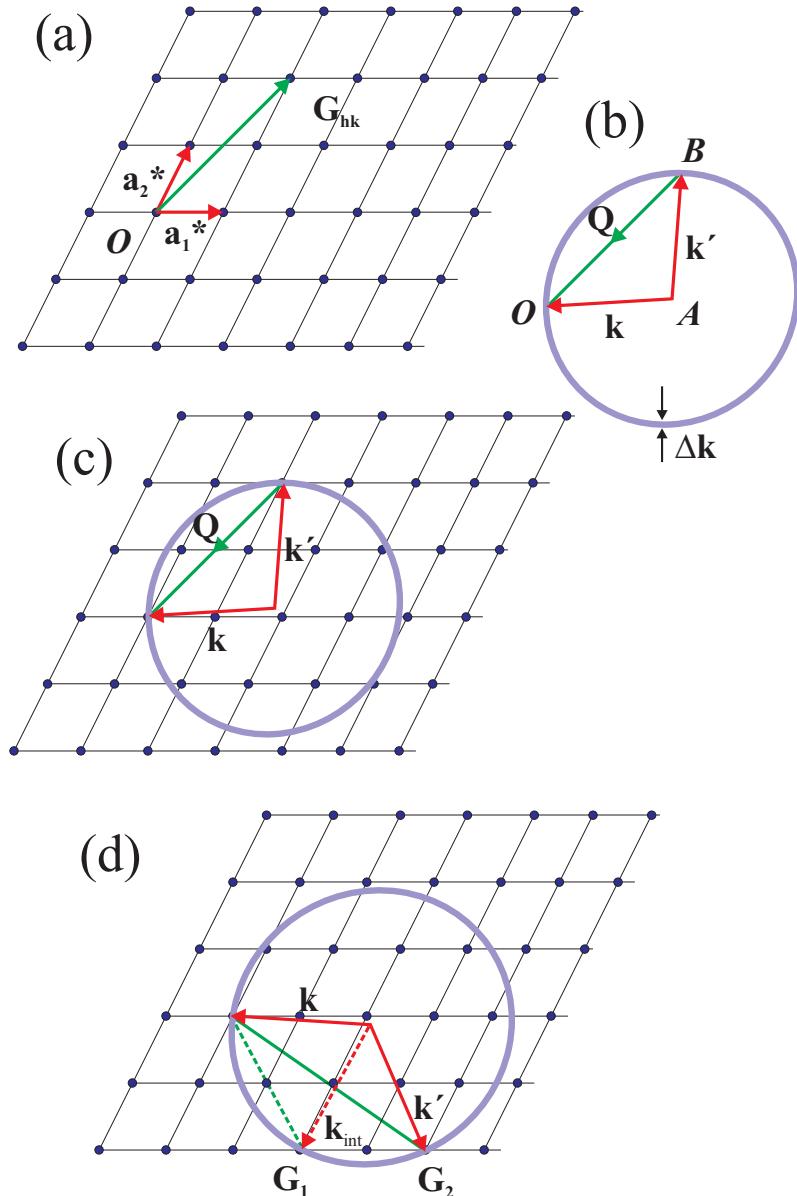
Fig. 5.6 The Ewald circle in two dimensions. (a) In 3D the reciprocal lattice is generated by integer coordinates (h, k, l) of the reciprocal basis vectors $(\mathbf{a}_1^*, \mathbf{a}_2^*, \mathbf{a}_3^*)$. For simplicity a 2D lattice at points given by $\mathbf{G} = h\mathbf{a}_1^* + k\mathbf{a}_2^*$ is shown. (b) The scattering triangle. Monochromatic incident radiation specified by $\mathbf{k} = \mathbf{AO}$ can be scattered to any wavevector $\mathbf{k}'=\mathbf{AB}$ terminating on the sphere of radius k. The bandwidth of the incident radiation Δk is indicated by the thickness of the circle. The scattering vector is defined as the vector $\mathbf{Q} = \mathbf{BO}$. (c) The Ewald circle (or Ewald sphere in 3D) is a superposition of (a) and (b) with $\mathbf{k}$ terminating on the origin of the reciprocal lattice. (d) Multiple scattering occurs if two or more reciprocal lattice points fall on the Ewald sphere. The rotation of the crystal and detector are set to record the $\mathbf{G}_2$ reflection, but as $\mathbf{G}_1$ is on the circle, the incident wave will also be scattered to $\mathbf{k}_{\text{int}}$. *Inside* the crystal $\mathbf{k}_{\text{int}}$ is scattered to $\mathbf{k}'$ by the reflection $\mathbf{G}_2 - \mathbf{G}_1$, and intensity may appear in the direction of $\mathbf{k}'$, even if the unit cell structure factor for this reflection vanishes.
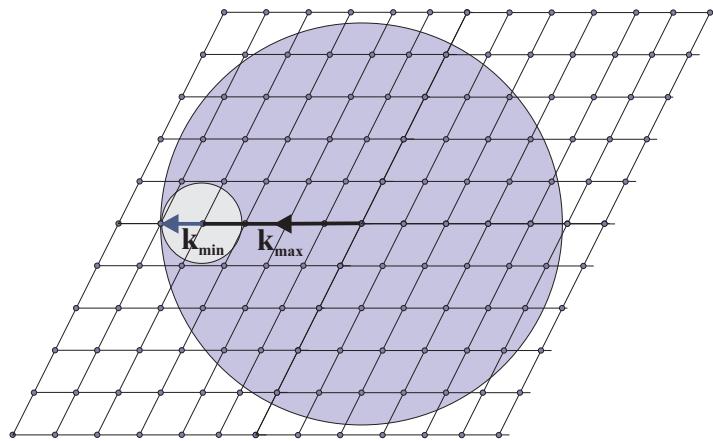
Fig. 5.7 The Ewald sphere construction for a white beam containing all wavevectors from k_{min} to k_{max}. All the reciprocal lattice points in the shaded area will Bragg reflect simultaneously. Knipping, Friderich and von Laue's discovery of the diffraction of X-rays from a single crystal of ZnS was performed in this way using the bremsstrahlung spectrum from an X-ray tube, and with a photographic film as detector. The exposure time was several hours. With today's third generation synchrotron sources one can register of order a 1000 reflections on an area detector within the duration of a single pulse from the electron bunch, i.e. about 100 ps.

Fig. 5.8 Pulsed Laue diffraction pattern from the photo-active yellow protein. The diffraction pattern was collected by averaging over 10 exposures, each of 100 ps duration. This image contains about 3700 usable reflections from which the structure could be obtained. (Data courtesy of Michael Wulff, European Radiation Facility, and Benjamin Perman, University of Chicago.)

as the product of the structure factors of an fcc lattice and the two atom basis, or in other words

$$F_{hkl}^{\text{diamond}} = (1 + e^{i\pi(h+k)} + e^{i\pi(k+l)} + e^{i\pi(l+h)})$$
$$\times (f^C(\mathbf{G}) + f^C(\mathbf{G})e^{i2\pi(h/4+k/4+l/4)})$$

By inspection, the $(1,1,1)$ reflection has a structure factor of $4(1-i)$, the $(2,0,0)$ reflection is forbidden, the $(4,0,0)$ reflection has a structure factor of 8, the $(2,2,2)$ reflection is forbidden[2], etc.

The final example to consider is the important variant of the diamond structure which forms when the two fcc lattices are occupied by different types of atom. This is known as the zinc sulfide (or zinc blende) structure, see Fig. 5.5(b), and is the structure adopted by many semiconducting materials such as GaAs, InSb, CdTe, etc. To take the specific case of GaAs, the structure factor is

$$F_{hkl}^{\text{GaAs}} = (1 + e^{i\pi(h+k)} + e^{i\pi(k+l)} + e^{i\pi(l+h)})$$
$$\times (f^{Ga}(\mathbf{G}) + f^{As}(\mathbf{G})e^{i2\pi(h/4+k/4+l/4)})$$

It can then be seen that the structure factor for the $(2,0,0)$ reflection, which is forbidden in the diamond structure, is

$$F_{200}^{\text{GaAs}} = 4(f^{Ga}(2,0,0) - f^{As}(2,0,0))$$

which is non-zero since Ga and As have different numbers of electrons and $f^{Ga}(\mathbf{G}) \neq f^{As}(\mathbf{G})$.

5.1.8 The Ewald sphere

A useful way to visualize diffraction events in reciprocal space is provided by the Ewald sphere, or in two dimensions the Ewald circle, construction. First consider the case where a monochromatic beam is incident on a sample. In Fig. 5.6(a) part of a 2D reciprocal lattice is shown. The Laue condition requires that the wavevector transfer $\mathbf{Q}$ is equal to a reciprocal lattice vector $\mathbf{G} = h\mathbf{a}_1^* + k\mathbf{a}_2^*$. In Fig. 5.6(b) the incident X-ray beam is labelled by $\mathbf{k}$ and originates at A and terminates at the origin O. A circle is now drawn centred at A with a length of k, and hence passes through the origin. As shown in Fig. 5.6(c), if any reciprocal lattice points fall on the circle, then the Laue condition is fulfilled, and a diffraction peak observed if the detector is set in the direction of $\mathbf{k}'$. The figure shows an example where we have chosen the point $h = 1$ and $k=2$ to lie on the circle. Rotating the crystal (equivalent to rotating the Ewald circle about the origin O) brings other reciprocal lattice points onto the Ewald circle. These ideas can be generalized to three dimensions and give rise to the concept of the Ewald sphere.

In certain settings it could occur that more than one reciprocal lattice point falls on the Ewald circle at the same time, giving rise to the simultaneous observation of several reflections (Fig. 5.6(d)). This is known as multiple scattering.
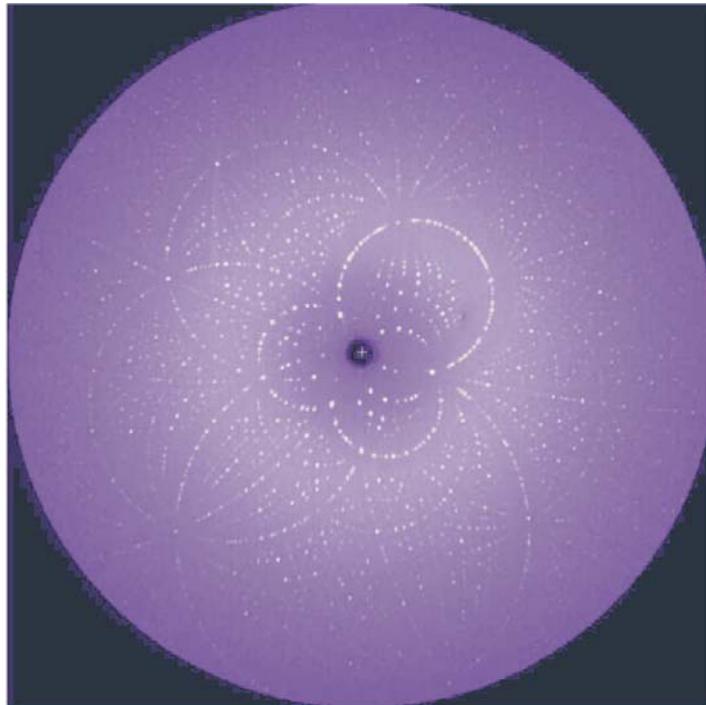
A beam that is not completely monochromatic may be represented by allowing the Ewald circle to have a finite width. Obviously, in the limit that the incident beam is 'white' all reflections will be observed within the circles of radius equal to the maximum and minimum $\mathbf{k}$ vector in the beam, as illustrated in Fig. 5.7. The discovery of X-ray diffraction by Knipping, Friderich and von Laue was performed in this way. They used the bremsstrahlung spectrum from an X-ray tube to record the diffraction pattern from a single crystal of ZnS. Diffraction data taken with a white beam are now known as Laue patterns. This method is particularly suited to the study of complex structures, such as

---

[2]However, as shown schematically in Fig. 5.6(d) one can accidentally observe intensity with the spectrometer set for a forbidden reflection such as $(2,2,2)$ through a multiple scattering event. For example, the forbidden $(2,2,2)$ reflection can be thought of as the sum of two allowed reflections, $(3,1,1)+ (\bar{1},1,1)$, and if both of these reciprocal lattice points happen to fall on the Ewald sphere, then scattered intensity is observed.

proteins, where it is necessary to record the intensity of perhaps thousands of Bragg reflections. It may also be desirable to follow the kinetics of a chemical or biological process by monitoring the changes to the structure that occur as the process proceeds. Using modern X-ray sources it is possible to collect a complete Laue pattern from the radiation produced by a single bunch of electrons in the storage ring (Fig. 5.8). This allows the kinetics to be studied on a time scale of 100 ps.

5.2 Quasiperiodic structures

The defining property of a crystal, in contrast to a liquid or gas, is that it displays long-range order at the atomic level. Up to this point long-range positional order of the atoms has been interpreted as meaning that the crystal structure is periodic. This allows it to be described in terms of a lattice of unit cells, with lattice vectors given by Eq. (5.2). The requirement of periodicity restricts the set of transformations which leave the properties of the lattice invariant. If we consider possible rotations, then a periodic lattice may be invariant under a n-fold rotation only if n is equal to 2, 3, 4, or 6. In two dimensions, for example, the fact that it is not possible to have a five-fold axis corresponds to the well-known problem of trying to tile a 2D surface with pentagons, which cannot be achieved without leaving holes.

It is no exaggeration to state that the whole edifice of crystallography was built on the assumption of periodicity, and it therefore came as a considerable shock when a new class of materials was discovered by Shechtman and co-workers in 1982 which displayed a sharp diffraction pattern with a 10-fold axis of rotation. This discovery was met with a large degree of disbelief, and indeed it took over two years for the results to be accepted for publication in a scientific journal [Shechtman et al., 1984]. The paradox posed by these materials was that they had a 10-fold axis of rotation, which is forbidden for periodic materials, while at the same time they produced sharp Bragg peaks, which can only occur if the system has long-range order at the atomic level. The materials are now known as quasicrystals, and the solution to the paradox is that they have long-range *quasiperiodic* order. The discovery of quasicrystals has led to a profound redefinition of what constitutes a crystal, as will be explained here.

Incommensurably modulated crystals

Before proceeding it is worth pointing out that even prior to the discovery of quasicrystals it had been known for a long time that certain crystalline materials are not periodic. In these materials the position of the atoms is modulated with a wavelength that is an irrational fraction of a lattice parameter. Such materials are said to be *incommensurate*, or *modulated*. This is illustrated in the upper panel of Fig. 5.9 for the case of a 1D lattice. The positions of the atoms are given by

$$x_n = \text{a}n + u \, \cos(\text{qa}n) \tag{5.16}$$

where a is the lattice parameter, n is a positive integer, u is the amplitude of the displacement, and q=$2\pi/\lambda_m$ is its wavevector. In the case of an incommensurate material the modulation wavelength is given by $\lambda_m = c\,\text{a}$, where c is an irrational number. If, as is sometimes found, the wavelength is expressible as a rational fraction, then the material is said to posses a *commensurate* modulation. Examples of commensurate and incommensurate modulations are shown in the upper panel of Fig. 5.9.

For incommensurate materials it is still possible to define an average, periodic lattice. The scattering then consists of Bragg peaks from the average lattice, plus additional Bragg peaks known as satellite reflections from the modulation. This can be verified by performing a numerical calculation of the intensity of the scattering from an incommensurate chain of N atoms with positions given by Eq. (5.16).

Commensurate, $\lambda_m = 5a$

Incommensurate, $\lambda_m = (2/\sqrt{3})\,a$
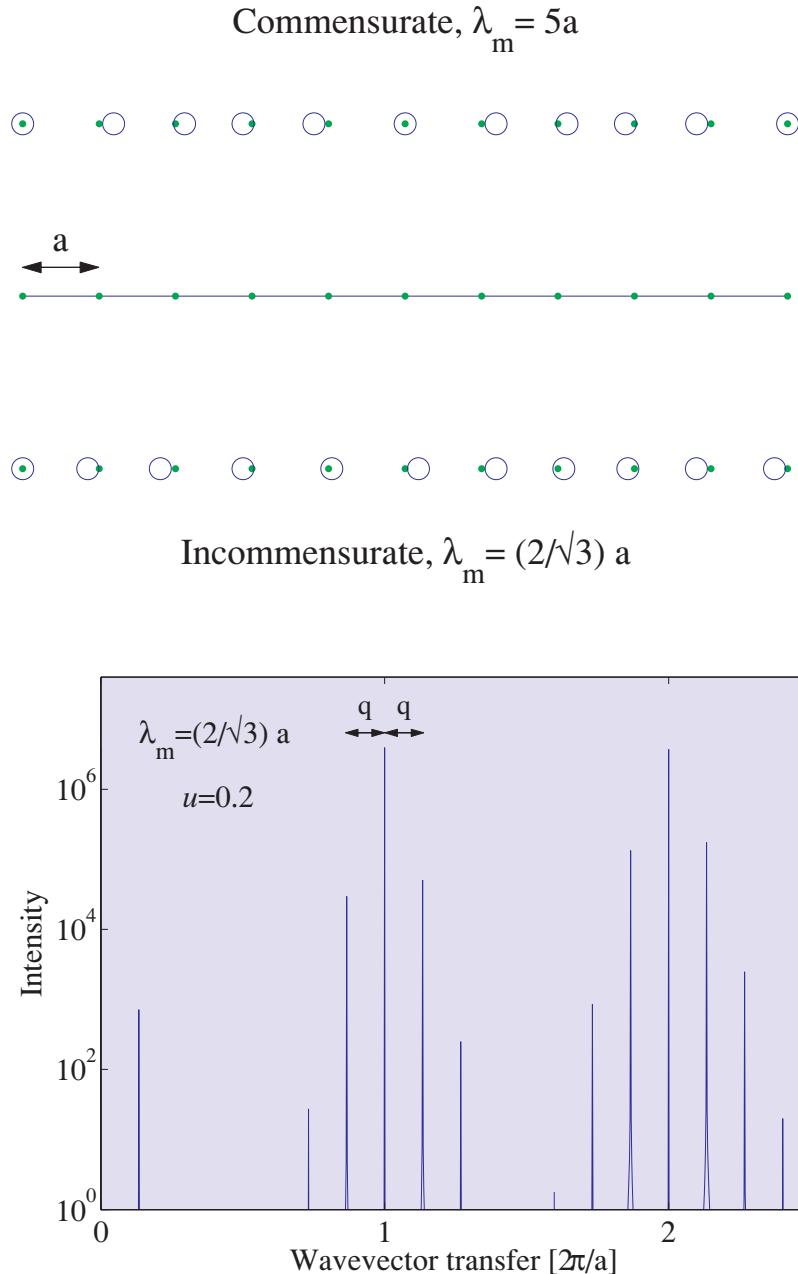
Fig. 5.9 Scattering from a 1D incommensurate chain. The top panel shows the position of atoms in a 1D chain with a commensurate, $\lambda_m = 5a$, and an incommensurate, $\lambda_m = (2/\sqrt{3})a$ modulation wavevector. The bottom panel is the calculated scattered intensity for a chain of $N=2000$ atoms, with positions given by Eq. (5.16), a modulation wavelength of $\lambda_m = (2/\sqrt{3})a$, and a displacement amplitude of $u=0.2$. For simplicity it has been assumed that the atomic scattering length is unity, and independent of wavevector transfer Q.

An example of such a calculation is shown in the lower panel of Fig. 5.9, where for simplicity the atomic scattering length has been set equal to unity. The main Bragg peaks occur at integer multiples of the modulus of the reciprocal lattice vector, $(2\pi/a)$, while the satellite peaks are displaced from the main peaks by multiples of the modulation wavevector $q=2\pi/\lambda_m$.

It is not a difficult exercise to show analytically that a modulation produces regularly spaced satellite peaks. The scattering amplitude for an incommensurate 1D chain is

$$A(Q) = \sum_{n=0}^{N-1} e^{i\,Qx_n} = \sum_{n=0}^{N-1} e^{i\,Q(an+u\,\cos(qan))} = \sum_{n=0}^{N-1} e^{i\,Qan} e^{i\,Qu\,\cos(qan)}$$

For simplicity the atomic scattering length has again been set equal to unity. The approximation is now made that the displacement u is small. This allows the second phase factor to be expanded, and the amplitude becomes

$$A(Q) \approx \sum_{n=0}^{N-1} e^{i\,Qan} \left(1 + iQu\,\cos(qan)\right) + \cdots)$$

$$= \sum_{n=0}^{N-1} e^{i\,Qan} + i\left(\tfrac{Qu}{2}\right) \sum_{n=0}^{N-1} \left[e^{i(Q+q)an} + e^{i(Q-q)an}\right]$$

In the limit that N becomes large, the scattered intensity is given by

$$I(Q) = N\left(\tfrac{2\pi}{a}\right) \sum_{h} \delta(Q - G_h) + N\left(\tfrac{Qu}{2}\right)^2 \left(\tfrac{2\pi}{a}\right) \sum_{h} \left[\delta(Q + q - G_h) + \delta(Q - q - G_h)\right] \qquad (5.17)$$

where $G_h = (2\pi/a)h$ is a reciprocal lattice vector, h the Miller index of the 1D lattice, and the results derived in Section 5.1.6 have been used to replace the squared sums by Dirac delta functions. The first term generates the main Bragg peaks at $Q=G_h$, while the second generates satellite reflections at $Q=G_h \pm q$. In the numerical example shown in Fig. 5.9 satellites are also evident at $\pm 2q$ and $\pm 3q$. These do not appear in the analytical calculation of Eq. (5.17), as the expansion of the exponential was truncated after the second term.

To index a given Bragg peak from an incommensurate system it is first necessary to specify the main Bragg peak with which it is associated. In three dimensions this requires the usual three Miller indices (h, k, l). The satellite peaks then require additional indices. In the example of a one dimensional modulation shown in Fig. 5.9 one extra index suffices. It turns out that incommensurate systems regain their periodicity if they are described in an abstract mathematical higher dimensional space. For a 1D modulation in a 3D crystal the dimension would be four, and the actual physical structure is obtained by making a particular three-dimensional cut through this 4D space.

Quasicrystals

Quasicrystals are fundamentally different from incommensurate crystals, as for one thing they lack anything that can be identified with an average, periodic lattice. To make this clear we shall discuss the properties of the Fibonacci chain or lattice. This is an example of a quasiperiodic system, and is often used as a 1D model of a quasicrystal.

There are several ways to obtain a Fibonacci chain. One method is to employ what is known as a substitution rule to generate a chain composed of two types of objects, or tiles, here labelled S for short and L for long. We create a pyramid of the letters L and S by the following iterative procedure: a new

<div align="center">

L

L S

L S L

L S L L S

L S L L S L S L

L S L L S L S L L S L L S

</div>

Fig. 5.10 Generation of the Fibonacci chain by a substitution rule described in the text.

row of letters is generated from the last row by substituting L for S, and the two letters L and S for L (see Fig. 5.10). Let the number of L's and the total number of elements in a row be denoted by n_L and N, respectively. As can be seen by inspection, the ratio of n_L/N has the following values in subsequent rows: 1/1, 1/2, 2/3, 3/5, 5/8, 8/13, 13/21, $\cdots$. This is obviously related to the Fibonacci series 1, 2, 3, 5, 8, 13, 21, $\cdots$ where any number is the sum of the two previous ones. It can be shown that the limiting value of the series of fractions is $\tau - 1$, where τ is the golden ratio, $(1 + \sqrt{5})/2$. By way of example a one-dimensional Fibonacci lattice of 21 elements could be constructed using the spacings in the seventh row of the pyramid with the lattice spacings of S and L.

Consider now the diffraction pattern of a one-dimensional Fibonacci lattice where N is large. The key question is whether or not its diffraction pattern exhibits sharp peaks, with a width proportional to $1/N$ as would be expected for a periodic lattice. The answer to this question is, yes, as indicated in Fig. 5.11$\star$. The top panel of Fig. 5.11$\star$ illustrates a method for generating a 1D Fibonacci lattice from a 2D square lattice. A strip of width $\Delta = 1 + \tau$ is drawn with a slope of $1/\tau$ on a square lattice of spacing $\sqrt{\tau^2 + 1}$. All lattice points that fall inside the strip are projected onto the line denoted x_n. The projected points then have a series of spacings identical to the Fibonacci chain. The reader can check the veracity of this statement by comparing the last row in the pyramid (Fig. 5.10) with the spacings from the second to the fourteenth points (Fig. 5.11$\star$, top panel). Since the two-dimensional lattice has sharp Bragg peaks, so will the projected points on the line as illustrated in the lower panel of Fig. 5.11$\star$. In general, a strip drawn at an irrational slope will generate a quasiperiodic lattice; the choice of the slope $1/\tau$ was made to obtain the Fibonacci chain.

The scattered intensity calculated for a Fibonacci chain derived from a 10x10 2D lattice is shown in Fig. 5.11$\star$. As the size of the lattice is increased the predominant peaks become sharper, but their positions remain fixed. It is therefore apparent that a quasiperiodic lattice, which lacks anything that may be identified with an average, periodic lattice, still produces a sharp diffraction pattern. Following the discovery of quasicrystals, the International Union of Crystallographers in 1991 decided to change the definition of a crystal to include the statement:

'...by crystal we mean any solid having an essentially discrete diffraction diagram.....'
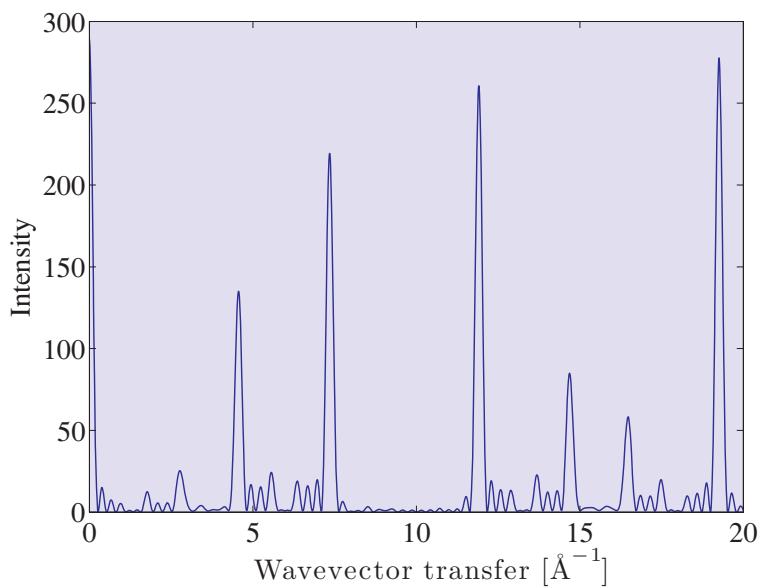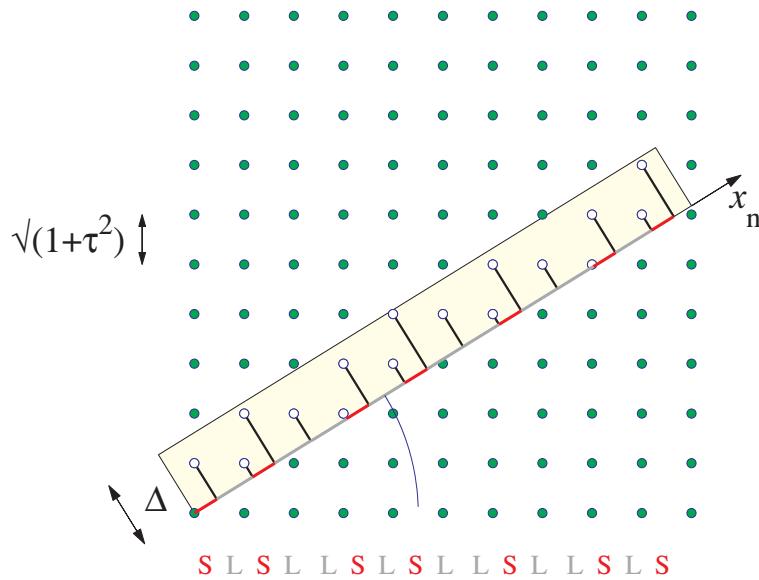
Fig. 5.11 ⋆ The Fibonacci chain. The top panel illustrates how the Fibonacci chain may be obtained from a 2D square lattice using the strip-projection method. The slope of the strip is irrational, equal to $1/\tau$, where $\tau=(1+\sqrt{5})/2$ is the golden ratio. Lattice points inside the strip are projected down onto the axis x_n, and the chain is then formed from two tiles S (short) and L (long) in the sequence shown. The bottom panel plots the calculated intensity from the Fibonacci chain derived from the lattice shown above. The predominant peaks are not regularly spaced, as would be the case for a periodic lattice. As the lattice size is increased the peaks become sharper, showing that long-range quasiperiodic order produces sharp Bragg peaks.
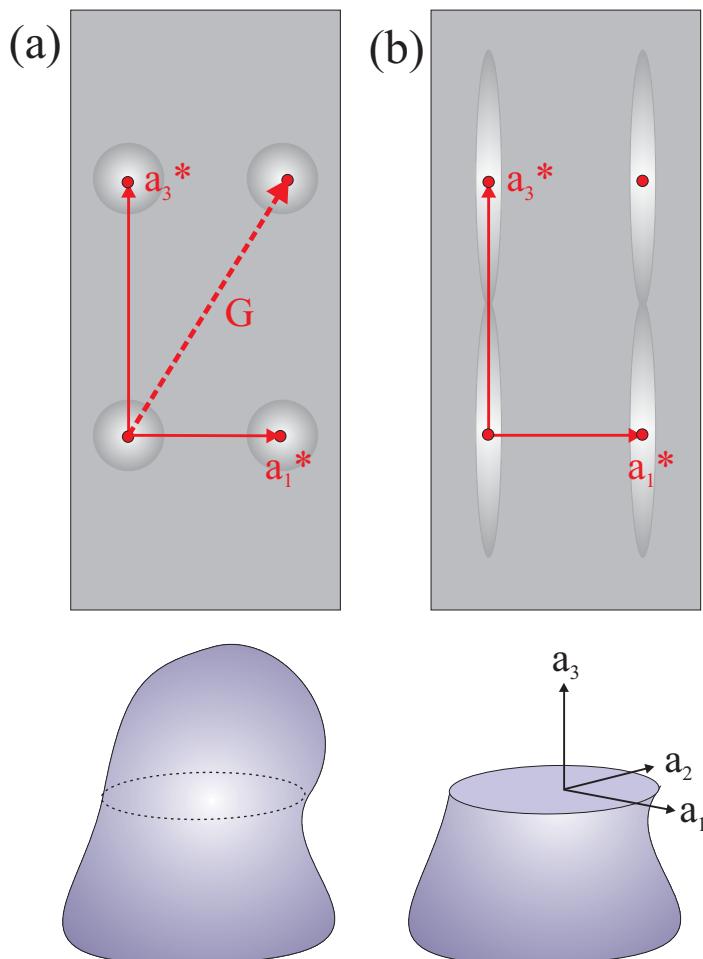
Fig. 5.12 (a) Top: a map of reciprocal space in the plane spanned by $\mathbf{a}_1^*$ and $\mathbf{a}_3^*$ for the crystal shown in the bottom part of the figure. (b) Same as (a) except that the crystal has been cleaved to produce a surface perpendicular to the $\mathbf{a}_3$ axis. This produces streaks of scattering – known as crystal truncation rods – through all Bragg peaks in a direction perpendicular to the surface.

The definition thus shifted emphasis from a crystal thought of as a periodic structure in real space, to one that produces sharp diffraction peaks in reciprocal space.

Quasicrystals have many fascinating properties, and the reader is referred to the book by Janot for further information [Janot, 1992].

5.3 Crystal truncation rods

In Section 5.1.6 it was shown that in the case of an infinite three-dimensional crystal the lattice sum produces a delta function. Scattering events are then restricted by the Laue condition such that $\mathbf{Q} = \mathbf{G}$, and as this is a vector equation it applies to all three components of $\mathbf{Q}$. For a *finite* size crystal

this condition is relaxed and the scattering then extends over a volume in reciprocal space inversely proportional to the size of the crystal. This is illustrated in Fig. 5.12(a). We now imagine that the crystal is cleaved, so as to produce a flat surface. The scattering will no longer be isotropic and streaks of scattering appear in the direction parallel to the surface normal as shown in in Fig. 5.12(b). These are the crystal truncation rods (CTR) [Andrews and Cowley, 1985, Robinson, 1986].

Insight into the origin of the CTR's follows once it is realized that the act of cleaving the crystal may be represented mathematically as a multiplication of the original density of the crystal, $\rho(z)$, by a step function, $h(z)$. (Here the coordinate system is chosen with z perpendicular to the surface.) The scattering *amplitude* is proportional to the Fourier transform of the product of the density $\rho(z)$ and $h(z)$. From the Convolution Theorem (see Appendix E) this is equivalent to the convolution of the Fourier transforms of $\rho(z)$ and $h(z)$. The Fourier transforms of $\rho(z)$ and $h(z)$ are a delta function and i/q_z respectively, as described in Appendix E. Away from a Bragg peak the scattering amplitude is thus proportional to $1/q_z$ and the intensity to $1/q_z^2$. The effect of the surface is therefore to produce streaks of scattering, known as crystal truncation rods, in the direction normal to the surface.

To develop an expression for the intensity distribution of the CTR we need only consider the lattice sum in the direction of the surface normal, $\mathbf{a}_3$; the sum over the other two directions leads to the usual product of delta functions $\delta(Q_x - ha_1^*)\,\delta(Q_y - ka_2^*)$. If $A(\mathbf{Q})$ is the scattering amplitude from a layer of atoms (here for simplicity assumed to be the same for all layers), then the scattering amplitude from an infinite stack of such layers is

$$F^{\mathrm{CTR}} = A(\mathbf{Q}) \sum_{j=0}^{\infty} e^{i\,Q_z a_3\, j} e^{-\beta j} = \frac{A(\mathbf{Q})}{1 - e^{i\,Q_z a_3} e^{-\beta}} \tag{5.18}$$

where $\beta = a_3 \mu / \sin\theta$ is the absorption parameter per layer. The intensity distribution along the crystal truncation rod is

$$I^{\mathrm{CTR}} = |F^{\mathrm{CTR}}|^2 = \frac{|A(\mathbf{Q})|^2}{(1 - e^{i\,Q_z a_3} e^{-\beta})(1 - e^{-i\,Q_z a_3} e^{-\beta})} \tag{5.19}$$

To examine how the intensity falls off close to a Bragg peak the wavevector transfer is written as $Q_z = q_z + 2\pi l/a_3$, where q_z is the deviation in wavevector from the Laue condition as l is an integer Miller index. Since q_z is small the above simplifies to

$$I^{\mathrm{CTR}} \approx \frac{|A(\mathbf{Q})|^2}{q_z^2 a_3^2 + \beta^2}$$

Thus I^{CTR} is proportional to $1/q_z^2$, as expected from the introductory remarks made at the beginning of this section. If we neglect for a moment the effect of absorption and write $Q_z = 2\pi l/a_3$, where now l is a continuous variable and not a integer Miller index, then Eq. (5.19) simplifies to read

$$I^{\mathrm{CTR}} = \frac{|A(\mathbf{Q})|^2}{4\sin^2(Q_z a_3/2)} = \frac{|A(\mathbf{Q})|^2}{4\sin^2(\pi l)}$$

The calculated intensity of the crystal truncation rod is plotted in the top panel of Fig. 5.13★ as a function of l in reciprocal lattice units (r.l.u.). The expression for I^{CTR} is clearly only valid away from the Bragg peaks when l is not an integer, otherwise $\sin(\pi l)$ is zero and the intensity diverges. The effect of absorption can be calculated from Eq. (5.19) and is also plotted in Fig. 5.13★, where it is evident that it mainly alters the intensity distribution in the vicinity of the Bragg peak.

The intensity distribution along the CTR depends on the exact way in which the surface is terminated, and measurements of CTR's have become a very useful probe of the structure of the surface
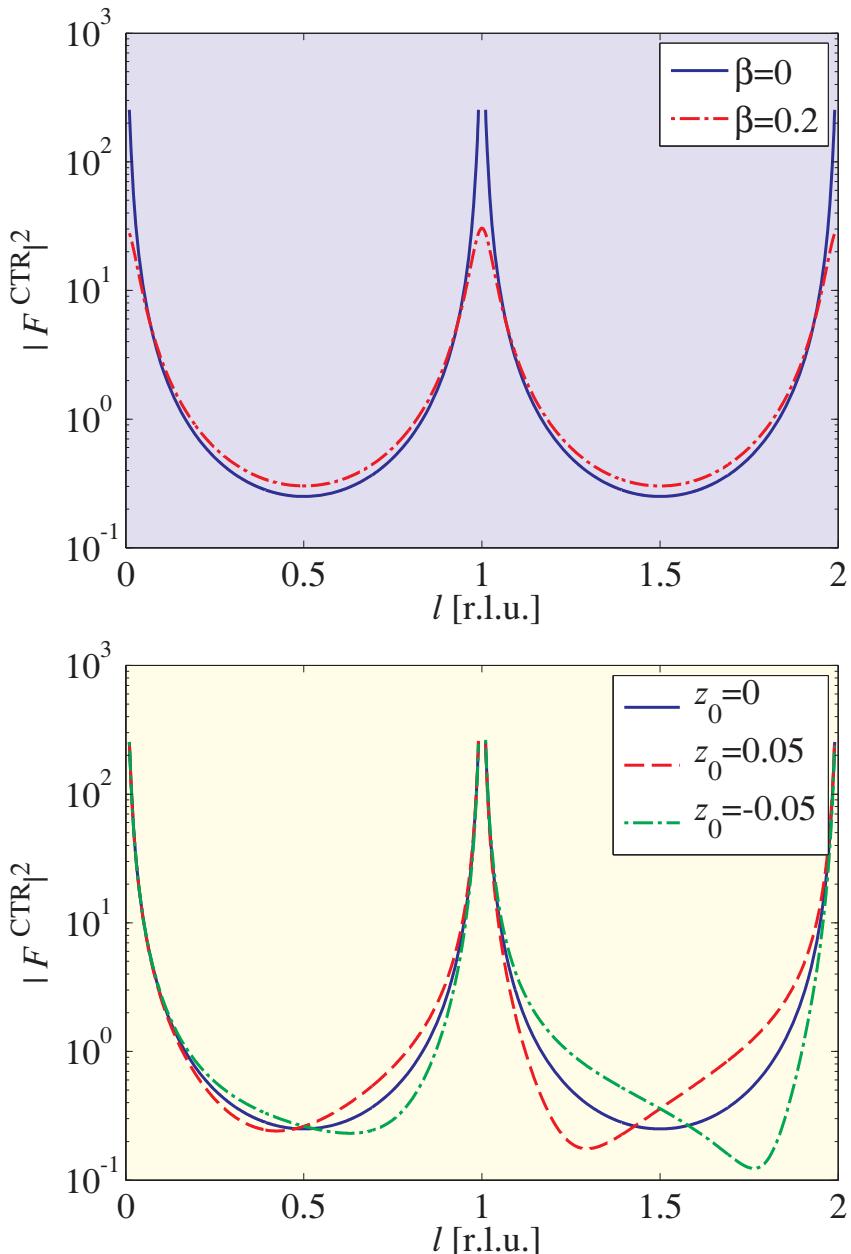
Fig. 5.13 ★ Top: Crystal truncation rod from a perfectly flat surface. Solid line, no absorption ($\beta = 0$); dashed-dotted line with absorption. Typically β is of order 10^{-5}, as may be seen from the values of the absorption coefficient μ listed in Table 3.1. Here β has been chosen to be 0.2, an unrealistically high value, but one that serves to illustrate the effects of absorption. For simplicity $A(\mathbf{Q})$ has been chosen to be unity. Bottom: Crystal truncation rod ($\beta = 0$) from a flat surface with an overlayer. The relative displacement of the overlayer from the bulk lattice spacing is given by z_0. The effect of the displacement of the layer is seen to become more pronounced at higher wavevector transfers.

and near-surface region of single crystals. This can be illustrated by imagining that the top most layer, having $j = -1$ in Eq. (5.18), of the crystal has a lattice spacing that is different from the bulk value. The total scattering amplitude is then

$$F^{\text{total}} = F^{\text{CTR}} + F^{\text{top layer}}$$

$$= \frac{A(\mathbf{Q})}{1 - e^{i\,2\pi l}} + A(\mathbf{Q})\, e^{-i\,2\pi(1+z_0)l} \tag{5.20}$$

where z_0 is the relative displacement of the top layer away from the bulk lattice spacing of a_3. For $z_0 = 0$ the same intensity distribution along the rod is found. If z_0 is non-zero then the interference between the scattering from the top layer and the rest of the crystal leads to characteristic features in the CTR, as shown in the bottom panel of Fig. 5.13$\star$. In Section 5.6.3 it is explained through the example of oxygen deposited on the copper (110) surface exactly how determination of the CTR helps in solving the surface structure.

In deriving Eq. (5.18) we assumed for simplicity a specular scattering geometry, so that the angle of incidence is equal to the angle of reflection. The argument presented here can be generalized to show that CTR's arise from all Bragg peaks, with the direction of the rods being parallel to the surface normal.

5.4 Lattice vibrations, the Debye-Waller factor and TDS

The lattices considered so far have been assumed to be perfectly rigid. Atoms arranged on a lattice in a crystal vibrate, and here we explore the effect of these vibrations on the scattered intensity. The vibrations are due to two distinct causes. The first is purely quantum mechanical in origin and arises from the uncertainty principle. These vibrations are independent of temperature, and occur even at the absolute zero of temperature. For this reason they are known as the zero-point fluctuations. At finite temperatures elastic waves (or phonons) are thermally excited in the crystal, thereby increasing the amplitude of the vibrations.

To start with we shall consider the scattering from a simple crystal structure in which there is one type of atom located at each lattice point. From Eq. (5.5) the scattering amplitude is then

$$F^{\text{crystal}} = \sum_{n} f(\mathbf{Q})\, e^{i\,\mathbf{Q}\cdot\mathbf{R}_n}$$

The effects of vibrations are allowed for by writing the *instantaneous* position of an atom as $\mathbf{R}_n + \mathbf{u}_n$, where $\mathbf{R}_n$ is the time-averaged mean position, and $\mathbf{u}_n$ is the displacement. By definition, $\langle \mathbf{u}_n \rangle = 0$, the angle brackets $\langle \cdots \rangle$ indicating a temporal average. The scattered intensity is calculated by taking the product of the scattering amplitude and its complex conjugate, and then evaluating the time average. The intensity is thus

$$I = \left\langle \sum_{m} f(\mathbf{Q})\, e^{i\,\mathbf{Q}\cdot(\mathbf{R}_m + \mathbf{u}_m)} \sum_{n} f^*(\mathbf{Q})\, e^{-i\,\mathbf{Q}\cdot(\mathbf{R}_n + \mathbf{u}_n)} \right\rangle$$

$$= \sum_{m} \sum_{n} f(\mathbf{Q}) f^*(\mathbf{Q})\, e^{i\,\mathbf{Q}\cdot(\mathbf{R}_m - \mathbf{R}_n)} \left\langle e^{i\,\mathbf{Q}\cdot(\mathbf{u}_m - \mathbf{u}_n)} \right\rangle \tag{5.21}$$

For convenience, the last term on the right hand side is rewritten as

$$\left\langle e^{i\,\mathbf{Q}\cdot(\mathbf{u}_m - \mathbf{u}_n)} \right\rangle = \left\langle e^{i\,Q(u_{Qm} - u_{Qn})} \right\rangle$$

where u_{Qn} is the component of the displacement parallel to the wavevector transfer $\mathbf{Q}$ for the n'th atom. This expression can be further simplified by using the Baker-Hausdorff theorem, which was introduced in the context of the scattering from rough surfaces in Section 3.8 on page 90. (The proof of the Baker-Hausdorff theorem is given in Appendix D.) This theorem states that if x is described by a Gaussian distribution then

$$\langle e^{ix} \rangle = e^{-\frac{1}{2}\langle x^2 \rangle}$$

Using this result the temporal average becomes

$$\left\langle e^{iQ(u_{Qm} - u_{Qn})} \right\rangle = e^{-\frac{1}{2}\langle Q^2(u_{Qm} - u_{Qn})^2 \rangle}$$

$$= e^{-\frac{1}{2}Q^2 \langle (u_{Qm} - u_{Qn})^2 \rangle}$$

$$= e^{-\frac{1}{2}Q^2 \langle u_{Qm}^2 \rangle} e^{-\frac{1}{2}Q^2 \langle u_{Qn}^2 \rangle} e^{Q^2 \langle u_{Qm} u_{Qn} \rangle}$$

Due to the translational symmetry $\langle u_{Qm}^2 \rangle = \langle u_{Qn}^2 \rangle$, and for brevity we shall denote it by $\langle u_Q^2 \rangle$ and write $e^{-Q^2 \langle u_Q^2 \rangle / 2}$ as e^{-M}. To proceed we write the last term in the above expression for the temporal average as

$$e^{Q^2 \langle u_{Qm} u_{Qn} \rangle} = 1 + \left\{ e^{Q^2 \langle u_{Qm} u_{Qn} \rangle} - 1 \right\} \tag{5.22}$$

This allows the scattered intensity to be separated into two terms:

$$I = \sum_m \sum_n f(\mathbf{Q}) \, e^{-M} e^{i\mathbf{Q}\cdot\mathbf{R}_m} \, f^*(\mathbf{Q}) \, e^{-M} e^{-i\mathbf{Q}\cdot\mathbf{R}_n}$$

$$+ \sum_m \sum_n f(\mathbf{Q}) \, e^{-M} e^{i\mathbf{Q}\cdot\mathbf{R}_m} \, f^*(\mathbf{Q}) \, e^{-M} e^{-i\mathbf{Q}\cdot\mathbf{R}_n} \left\{ e^{Q^2 \langle u_{Qm} u_{Qn} \rangle} - 1 \right\} \tag{5.23}$$

The first term is recognizable as the elastic scattering from a lattice except that the atomic form factor is replaced by

$$\boxed{f^{\text{atom}} = f(\mathbf{Q}) \, e^{-\frac{1}{2}Q^2 \langle u_Q^2 \rangle} \equiv f(\mathbf{Q}) \, e^{-M}} \tag{5.24}$$

where the exponential term in known as the Debye-Waller factor. As the first term contains contributions for large values of $|\mathbf{R}_m - \mathbf{R}_n|$ it still gives rise to a delta function in the scattering. This shows that the elastic Bragg scattering is reduced in intensity by atomic vibrations, but its width is not increased. The contribution from the last factor in Eq. (5.23) has a distinctly different character. It has an intensity that actually increases as the mean-squared displacement increases, and has a width determined by the correlations, $\langle u_{Qm} u_{Qn} \rangle$, between the displacements of different atoms. These turn out to be correlated significantly only over short distances, so that the lattice sum extends only over a few lattice sites, and the scattering has an appreciable width, much greater than the width of a Bragg peak. For these reasons this contribution is known as *thermal diffuse scattering*, or TDS for short. In crystallographic experiments TDS gives rise to a background signal which sometimes needs to be subtracted from the data. Alternatively, the study of TDS may also be of interest in its own right, as it provides information on the low-energy elastic waves in lattices. In this case the diffuse nature of TDS requires that the scattering is mapped out over large volumes of reciprocal space. To compare the experimental results with theory it is necessary to evaluate the second term in Eq. (5.23). This is achieved by performing a calculation of the lattice dynamics, which yields the atomic displacements $\mathbf{u}_n$, and hence the correlation term $\langle u_{Qm} u_{Qn} \rangle$.
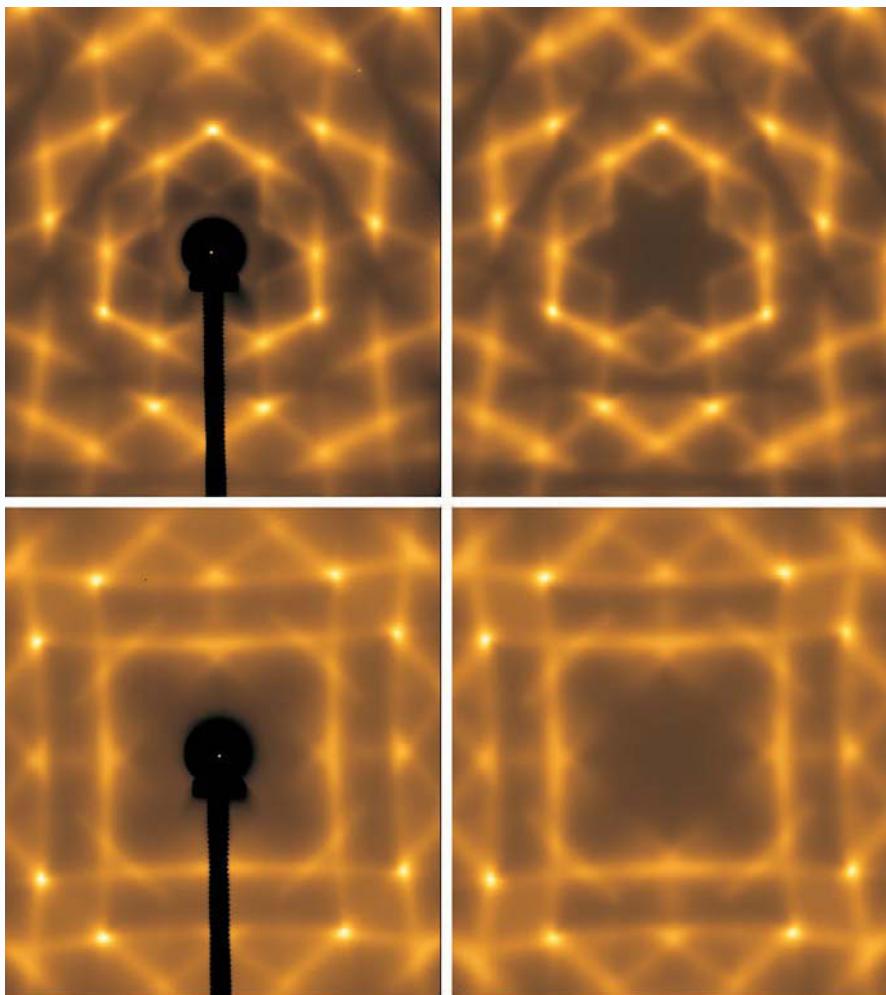
Fig. 5.14 Thermal diffuse scattering (TDS) from Si. The data were collected in a transmission geometry (photon energy 28 keV) using an image plate detector. The data were collected on the UNI-CAT beamline at the Advanced Photon Source in an exposure time of ~10 s. The top and bottom left panels show the data taken with a (111) and a (100) axis parallel to the incident beam respectively. The data are plotted on a logarithmic scale. The brighter spots are not Bragg peaks, as the Laue condition is never exactly fulfilled, but are due to the build up of TDS close to the position of where the Bragg peaks would occur. The right panels show the corresponding calculated images based on a simultaneous pixel-by-pixel fit to the data [Holt et al., 1999].

An example of TDS from Si is shown in Fig. 5.14 [Holt et al., 1999]. The data (left panels) were recorded in a transmission geometry with a (111) (top) and a (100) (bottom) axis parallel to the incident beam. The data are plotted on a logarithmic scale so that the weak diffuse scattering which peaks along high-symmetry directions connecting reciprocal lattice points is enhanced. In the right panels are shown the corresponding images obtained by fitting a model of the lattice dynamics to the data. Good agreement was found for the phonon dispersion curves derived from this model and earlier neutron scattering experiments.

(a) Transverse acoustic phonons

(b) Phonon dispersion

(c) Density of phonon states in 3D

$$g(\omega)d\omega = 3 \times \frac{V}{(2\pi)^3} 4\pi q^2 dq$$
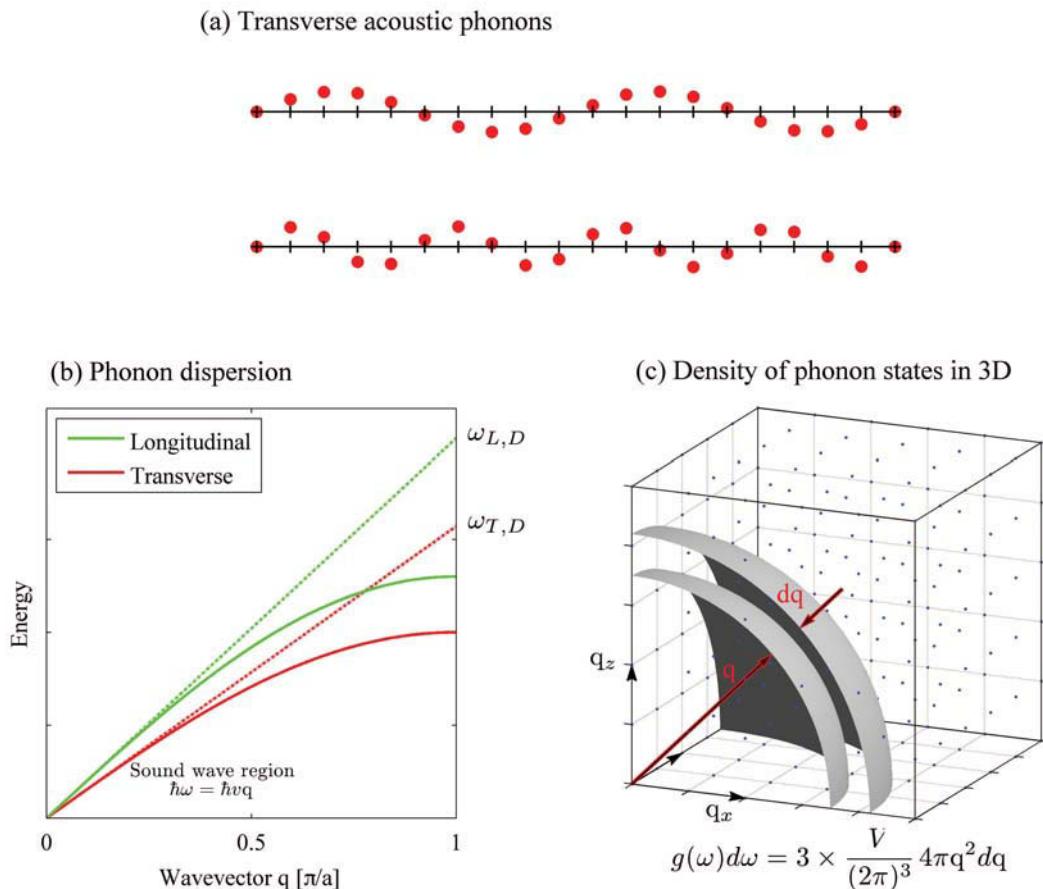
Fig. 5.15 (a) Representative snap shots of the atomic displacements associated with transverse acoustic phonons calculated for two different wavevectors. (b) Phonon dispersion relation for a monoatomic crystal. The phonons can have either a longitudinal or one of two transverse polarizations. In the Debye model the dispersion relation is assumed to be linear, $\omega = vq$, up to some cut off frequency ω_D. In three dimensions the cut off frequency is defined by $\int_0^{\omega_D} g(\omega)d\omega = 3N$, where $g(\omega)$ is the density of states and N is the number of atoms. (c) Periodic boundary conditions produce quantization of the allowed wavevectors, $\mathbf{q} = (2\pi/L)(l, m, n)$ with l, m and n integer, illustrated here in the positive octant. In general, the density of states taking into account the three possible polarizations is $g(\omega)d\omega = 3V/(2\pi)^3 4\pi q^2 dq$. For the Debye model $g(\omega) = 9N\omega^2/\omega_D^3$ with $\omega_D^3 = 6N\pi^2 v^3/V$.

The separation of the total diffracted intensity into a sharp Bragg and a diffuse component in the presence of thermal vibrations is analogous to the separation of the reflectivity from a rough interface into specular and diffuse components, as described in Section 3.8. Indeed this separation is useful whenever there are random atomic displacements, be they static or dynamic, from the lattice sites. Here we have considered the case of dynamic displacements by elastic waves, but static distortions, caused for example by lattice defects, can be studied through the diffuse scattering.

In the rest of this section we consider the properties of the Debye-Waller factor. It is straight forward to generalize the above results to the case of a crystal with several different types of atom in the unit

cell. In this case the unit cell structure factor (Eq. (5.6)) becomes

$$F^{\text{u.c.}} = \sum_j f_j(\mathbf{Q}) \, e^{-M_j} \, e^{i\mathbf{Q}\cdot\mathbf{r}_j}$$

where

$$M_j = \frac{1}{2}Q^2 \langle u_{Qj}^2 \rangle = \frac{1}{2}\left(\frac{4\pi}{\lambda}\right)^2 \sin^2\theta \, \langle u_{Qj}^2 \rangle = B_T^j \left(\frac{\sin\theta}{\lambda}\right)^2$$

refers to the j'th atom in the unit cell, and $B_T^j = 8\pi^2 \langle u_{Qj}^2 \rangle$. The reason for writing it in this form is that crystallographers prefer to express the wavevector transfer as $\sin\theta/\lambda$ instead of as $Q = 2k\sin\theta$. If the atom vibrates isotropically then $\langle u^2 \rangle = \langle u_x^2 + u_y^2 + u_z^2 \rangle = 3\langle u_x^2 \rangle = 3\langle u_Q^2 \rangle$, so that

$$B_{T,\text{isotropic}} = \frac{8\pi^2}{3}\langle u^2 \rangle \tag{5.25}$$

The effect of the vibrations can be viewed as being equivalent to a smearing of the electron distribution around the point at $\mathbf{R}$ with a Gaussian distribution of radius σ, with $\langle u^2 \rangle/6 = \sigma^2/2$. If the vibrations are anisotropic, they can be described by a 'vibrational ellipsoid' with three principal axes of different magnitude.

In a compound each type of atom will in general have a different Debye-Waller factor, as it should be obvious that lighter atoms will generally vibrate more than heavier ones. The Debye-Waller factors need not be isotropic, as the bonding will also restrict the vibrations along certain directions. For example, it usually costs less energy to change a bond angle than a bond length, so the vibrations of atoms at the ends of bonds will have a larger amplitude perpendicular to the bond than along it. These subtleties are usually taken into account by including extra fitting parameters in the data analysis. Here, however, we can simplify the discussion by restricting ourselves to consider only one type of atom in cubic symmetry so that the vibrations are isotropic. Then within the harmonic approximation the Debye-Waller factor depends on $\langle u^2 \rangle$ only. Excitation modes of such a monoatomic lattice can be visualized as shown in Fig. 5.15(a). A mode of given wavevector q and polarization (transverse or longitudinal) can only exist at a specific frequency ω with the two quantities connected by a dispersion relation as shown in Fig. 5.15(b). In a real lattice the longitudinal mode is stiffer than the transverse mode. This can be taken into account but for simplicity we shall neglect this detail.

The task is to calculate the mean-squared amplitude, $\langle u^2 \rangle$, averaged over all phonon modes, where the energy of the modes are those of an harmonic oscillator, i.e. equidistant with spacing $\hbar\omega$ and a ground state energy of $\hbar\omega/2$. For a harmonic oscillator, the average energy for a single mode is divided equally between the kinetic and potential energies, allowing us to write

$$\frac{1}{2}\mathcal{E}_{ph} = \frac{1}{2}Nm_A\omega^2 \langle u^2 \rangle$$

where $\mathcal{E}_{ph}$ is the phonon energy, and the right hand side is the kinetic energy of the mode for N atoms each of mass m_A. The phonon energy averaged over all modes, $\bar{\mathcal{E}}_{ph}$, is given by

$$\bar{\mathcal{E}}_{ph} = \int_0^\infty g(\omega)\left[\frac{\hbar\omega}{e^{\hbar\omega/k_BT} - 1} + \frac{\hbar\omega}{2}\right]d\omega$$

where $g(\omega)$ is the density of phonon states as a function of mode frequency. The mean-squared amplitude averaged over all modes is therefore given by

$$\langle u^2 \rangle = \frac{1}{Nm_A}\int_0^\infty \frac{g(\omega)}{\omega^2}\left[\frac{\hbar\omega}{e^{\hbar\omega/k_BT} - 1} + \frac{\hbar\omega}{2}\right]d\omega$$
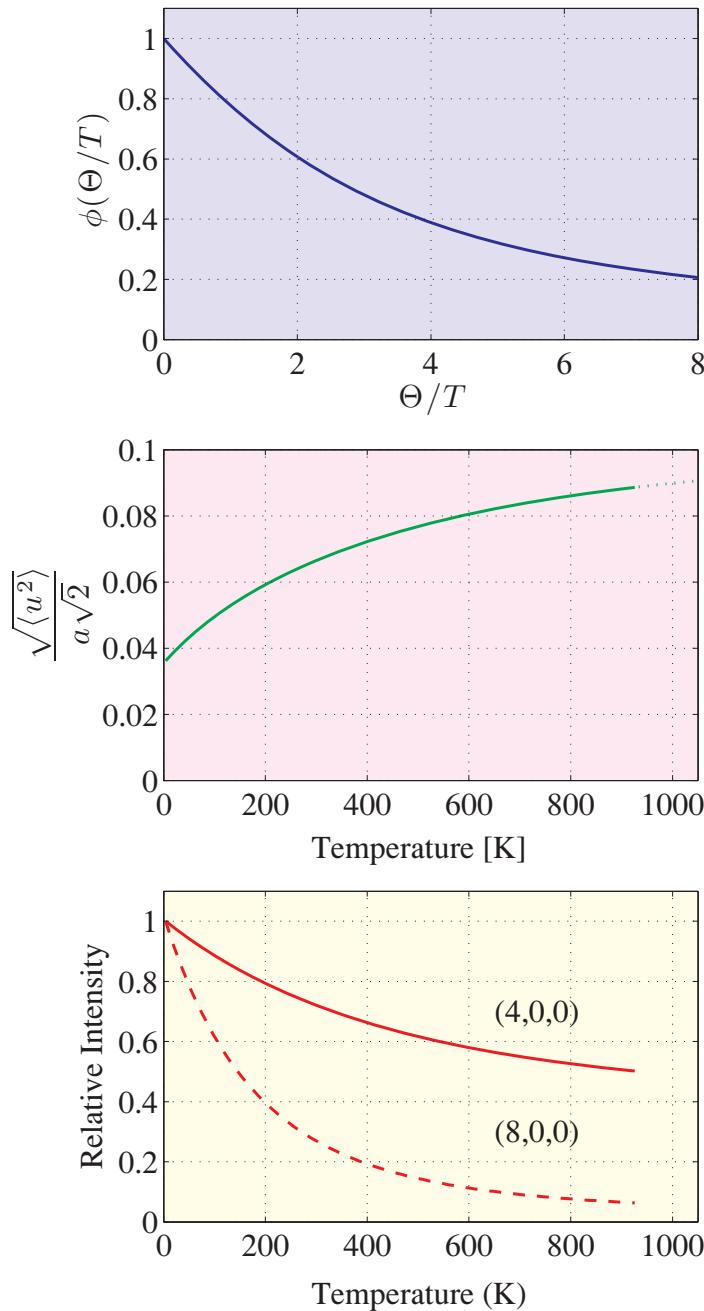
Fig. 5.16 ★ Top: plot of the value of the integral $\phi(x)$ versus $x = \Theta/T$. Middle: temperature dependence of the rms fluctuation **u** in units of $a/\sqrt{2}$ for Al. Bottom: the relative intensity of the scattered intensity from Al as a function of temperature. The curves were calculated for the (4,0,0) (solid line) and the (8,0,0) (dashed line) Bragg peaks respectively. The melting temperature of Al is 933 K.

	A	Θ	$B_{4.2}$	B_{77}	B_{293}
		(K)		($\mathring{A}^2$)	
Diamond	12	2230	0.11	0.11	0.12
Al	27	428	0.25	0.30	0.72
Si	28.1	645	0.17	0.18	0.33
Cu	63.5	343	0.13	0.17	0.47
Ge	72.6	374	0.11	0.13	0.35
Mo	96	450	0.06	0.08	0.18

Table 5.1 The Debye temperature Θ, and the Debye-Waller factor B_T at temperatures of 4.2, 77 and 293 K, for a selection of cubic elements. The Debye-Waller factors have been calculated from the stated Debye temperatures using Eq. (5.27).

It is convenient to calculate the density of states within the Debye model, in which the dispersion relation is assumed to be linear up to some cut off frequency ω_D (see Fig. 5.15(b)). The density of states for this model is

$$g(\omega) = 9N\frac{\omega^2}{\omega_D^3}$$

(see Fig. 5.15(c)) and hence the expression for the mean-squared displacement becomes

$$\left\langle u^2 \right\rangle = \frac{9\hbar^2 T^2}{m_A k_B \Theta^3} \int_0^{\Theta/T} \left[\frac{1}{e^\xi - 1} + \frac{1}{2} \right] \xi d\xi$$

where the Debye temperature $\Theta = \hbar\omega_D/k_B$. Combining this result with Eq. (5.25), the explicit expression for the thermal factor B_T calculated within the Debye model is

$$B_T = \frac{6\,h^2}{m_A k_B \Theta} \left\{ \frac{\phi(\Theta/T)}{\Theta/T} + \frac{1}{4} \right\} \tag{5.26}$$

with

$$\phi(x) \equiv \frac{1}{x} \int_0^x \frac{\xi}{e^\xi - 1}\, d\xi$$

where Θ and T are in degrees Kelvin. The thermal parameter B_T has dimension of length squared, which in practical units of $\mathring{A}^2$ is

$$B_T[\mathring{A}^2] = \frac{11492\,T[\mathrm{K}]}{A\Theta^2[\mathrm{K}^2]} \phi(\Theta/T) + \frac{2873}{A\Theta[\mathrm{K}]} \tag{5.27}$$

and A is the atomic mass number. The function $\phi(x)$ is shown in the top panel of Fig. 5.16⋆. At or close to absolute zero the first term in Eq. (5.26) is negligible, but B_T remains finite due to the second term of 1/4. This term arises from the zero-point motion, a purely quantum mechanical effect consistent with the uncertainty principle. With increasing temperature it can be seen from Eq. (5.26) that B_T increases once the temperature becomes comparable to Θ.

To illustrate how the Debye-Waller factor alters the scattering let us take the example of Al, which crystallizes in the face centred cubic structure (Fig. 5.3) with a cube edge of a=4.04 Å, and with Θ=428

K, A=27. It is interesting to compare the r.m.s. vibrational amplitude as the temperature is raised towards the melting temperature (933 K). This is shown in Fig. 5.16⋆ (middle panel) where we have normalized $\sqrt{\langle u^2 \rangle}$ by the nearest-neighbour distance a/$\sqrt{2}$. We note in passing that just below the melting temperature $\sqrt{\langle u^2 \rangle}$ divided by the nearest-neighbour distance is approximately 0.1, which is consistent with Lindemann's empirical criterion for the melting of a solid: when the thermal vibrations approach about 10% of the nearest-neighbour distance the solid melts. The lower part of Fig. 5.16⋆ shows that the Q^2 dependence of the Debye-Waller factor has a dramatic effect on the intensity when the scattering vector is increased in length. In Table 5.1 the Debye temperatures are given for a number of cubic elements, along with calculated values of B_T at different temperatures.

5.5   The measured intensity from a crystallite

In this section the integrated intensity of a Bragg reflection from a small crystal is evaluated, as this is the quantity that is readily determined in an experiment. This requires that we specify exactly how the integrated intensity is to be measured. The starting point is to assemble the various expressions that have been developed in the previous sections into a single formula for the intensity. However, instead of referring to the intensity we shall be a little more precise and use instead the *differential cross-section* $(d\sigma/d\Omega)$, which is discussed more fully in Appendix A. For the case considered here where the sample is fully illuminated by the beam the differential cross-section is defined by

$$\left(\frac{d\sigma}{d\Omega}\right) = \frac{\text{Number of X-rays scattered per second into } d\Omega}{(\text{Incident flux})(d\Omega)}$$

where $d\Omega$ is the solid angle. From Eqs. (1.8), (5.5), (5.6) and (5.15) we have that

$$\left(\frac{d\sigma}{d\Omega}\right) = r_0^2 P \, |F(\mathbf{Q})|^2 N \, v_c^* \, \delta(\mathbf{Q} - \mathbf{G}) \tag{5.28}$$

where the superscript on $F(\mathbf{Q})$, the unit cell structure factor, has been dropped, and P is the polarization factor (Eq. (1.9)).

   The experimental arrangement typically used for determining the integrated intensity of a Bragg peak is sketched in Fig. 5.17. The incident beam is assumed to be both perfectly monochromatic and collimated. The scattered beam will then also be perfectly monochromatic, since the scattering is elastic. However, it will not necessarily be perfectly collimated. In Section 5.1.6 it has been shown that the width of a Bragg peak is inversely proportional to N, the number of unit cells, and since N is not infinite, the Bragg peak has a finite width. This means that the Laue condition does not have to be exactly fulfilled for a measurable intensity to be recorded. This is represented in Fig. 5.18 by the existence of an elliptical contour: if $\mathbf{Q}$ falls within this contour then appreciable intensity is obtained, and the scattered beam will have some divergence. Let us assume that the geometry is such that all of the slightly divergent scattered rays hit the detector. Therefore, referring to Fig. 5.18, all of the scattering processes where $\mathbf{k}'$ terminates on the heavy red line will be recorded. However, we are interested in the sum of all the scattering processes where $\mathbf{Q}$ terminates within (or in the vicinity) of the smeared Bragg point contour. This means that the crystal has to be rotated (or rocked) a little with respect to the incident beam, and the measurement repeated, corresponding then to one of the other light red lines in Fig. 5.18, and in this way the integrated intensity is accumulated. (We note in passing,
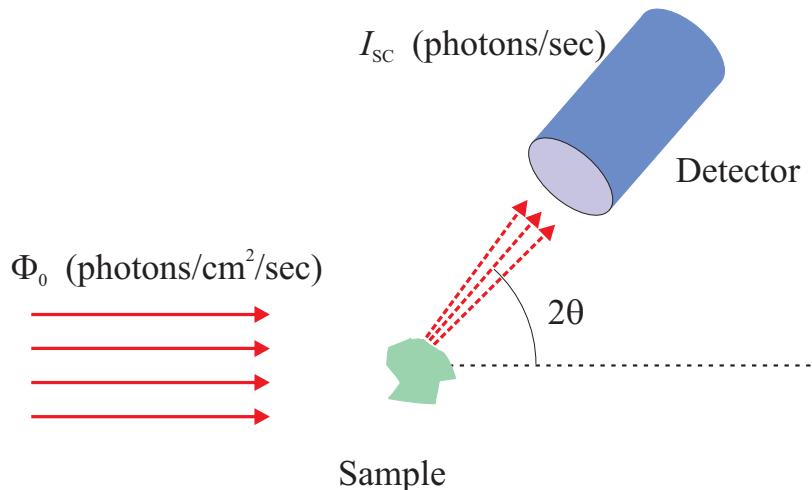
Fig. 5.17 Scattering from a small crystal. The incident beam is assumed to be perfectly collimated and monochromatic, and to fully illuminate the crystal. The scattered intensity I_{sc} is proportional to the flux Φ_0 and to the differential cross-section $(d\sigma/d\Omega)$ of the sample.

that the varying angle between **k** and **G** in the scan is equivalent to allowing the incident beam not to be perfectly collimated.)

Thus the integrated intensity is recorded by rotating the crystal so that the angle θ varies. The formula given in Eq. (5.28) applies to a single setting of the instrument, and in order to compare it with the integrated intensity that is measured in an experiment we have to allow for both the integration over **k**′ and over θ. This gives rise to an additional term known as the Lorentz factor, which is derived in the following section. It is important to appreciate that the Lorentz factor depends on exactly how the intensity is integrated and hence on the details of the experiment.

5.5.1   The Lorentz factor

Integration over **k**′

A unit vector along **k**′ is indicated by a hat. The element of solid angle $d\hat{\mathbf{k}}'$ is two-dimensional, and integration over the *directions* of **k**′ is therefore equivalent to integrating over $d\hat{\mathbf{k}}'$. Instead of **k**′ we introduce the vector $\mathbf{s} = k'\hat{\mathbf{s}}$, where $\hat{\mathbf{s}}$ is a unit vector (right panel Fig. 5.18). The problem then is to integrate the delta function in equation Eq. (5.28) over $d\hat{\mathbf{k}}'$, i.e.

$$\int d\hat{\mathbf{k}}' \, \delta(\mathbf{Q} - \mathbf{G}) = \int d\hat{\mathbf{k}}' \, \delta(\mathbf{k} - \mathbf{k}' - \mathbf{G})$$

The integral is rewritten as

$$\int d\hat{\mathbf{k}}' \, \delta(\mathbf{k} - \mathbf{k}' - \mathbf{G}) = \frac{2}{k'} \overbrace{\int s^2 \delta(s^2 - k'^2)\,ds}^{1} \int \delta(\mathbf{k} - \mathbf{s} - \mathbf{G})\,d\hat{\mathbf{s}}$$

since the first integral on the right hand side is unity, as proven in the delta function box on page 152, and in the second integral **k**′ has been replaced by **s**, as they are equal by definition. The point of this
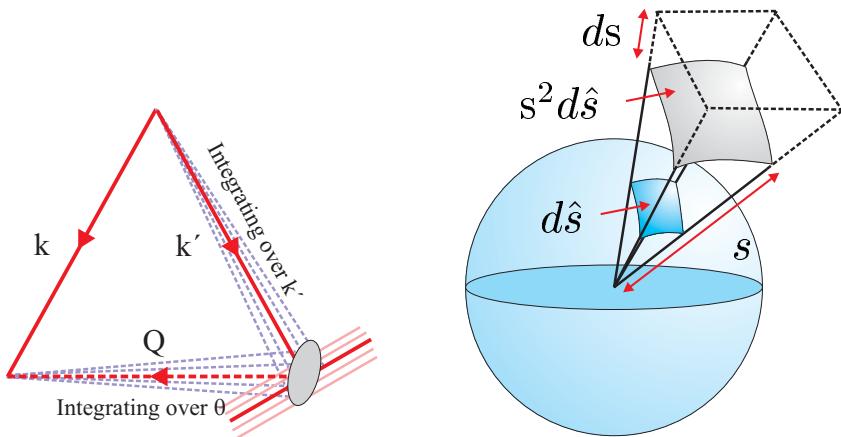
Fig. 5.18 Left: The scattering from a small crystallite is represented by the grey ellipse, which reflects the reciprocal of the shape of the crystal. For a given orientation of the crystal the detector accepts all of the scattered wavevectors $\mathbf{k}'$ which fall on the red line. As the crystal is rotated the integration corresponds to the other light red lines. Right: The solid angle element $d\hat{s}$ and the volume element $d\mathbf{s}$ are related by $d\mathbf{s}=s^2\,d\hat{s}\,ds$.

trick is to transform the two-dimensional integral into a three-dimensional one. This is made clear if the above is rearranged as

$$\int d\hat{\mathbf{k}}'\,\delta(\mathbf{k}-\mathbf{k}'-\mathbf{G}) = \frac{2}{k'}\int \delta(s^2-k'^2)\,\delta(\mathbf{k}-\mathbf{s}-\mathbf{G})\,s^2\,d\hat{s}\,ds$$

$$= \frac{2}{k'}\int \delta(s^2-k'^2)\,\delta(\mathbf{k}-\mathbf{s}-\mathbf{G})\,d^3\mathbf{s}$$

where $d^3\mathbf{s}=s^2\,d\hat{s}\,ds$ is the three-dimensional volume element. To proceed, the second delta function is used to require that $\mathbf{s} = \mathbf{k} - \mathbf{G}$, and this is then substituted into the first δ function, with the result that the integral becomes

$$\int d\hat{\mathbf{k}}'\,\delta(\mathbf{k}-\mathbf{k}'-\mathbf{G}) = \frac{2}{k'}\,\delta((\mathbf{k}-\mathbf{G})\cdot(\mathbf{k}-\mathbf{G})-k'^2)$$

$$= \frac{2}{k}\,\delta(G^2 - 2\,k\,G\,\sin\theta) \qquad (5.29)$$

In the second equation use has been made of the fact that the scattering is elastic, i.e. $k' = k$. When integrated over the directions of $\mathbf{k}'$ the cross-section is

$$\left(\frac{d\sigma}{d\Omega}\right)_{\text{int. over }\mathbf{k}'} = r_0^2 P\,|F(\mathbf{Q})|^2\,N\,v_c^*\,\frac{2}{k}\,\delta(G^2 - 2kG\,\sin\theta)$$

Integration over θ

Evaluation of the integrated intensity is completed by integrating over the angular variable θ. The remaining delta function is itself a function of θ, and using the results given in the box on page 152 the

integral is

$$\int \delta(G^2 - 2kG\sin\theta)\, d\theta = \int \delta(t(\theta))\, d\theta = \left[\left(\frac{dt}{d\theta}\right)^{-1}\right]_{t=0}$$

The derivative of the argument of the delta function is

$$\frac{d(G^2 - 2kG\sin\theta)}{d\theta} = -2kG\cos\theta$$

with the result that

$$\int \delta(G^2 - 2kG\sin\theta)\, d\theta = \left[\frac{-1}{2kG\cos\theta}\right]_{t=0} = \frac{-1}{2k^2\sin 2\theta}$$

Therefore the differential scattering cross-section integrated over both the directions of $\mathbf{k'}$ and over θ is

$$\left(\frac{d\sigma}{d\Omega}\right)_{\text{int. over }\mathbf{k'},\theta} = r_0^2 P\, |F(\mathbf{Q})|^2\, N\, v_c^* \frac{2}{k}\frac{1}{2k^2\sin 2\theta}$$

$$= r_0^2 P\, |F(\mathbf{Q})|^2\, N\, \frac{\lambda^3}{v_c}\frac{1}{\sin 2\theta}$$

In the second equation the volume v_c of the unit cell in real space has been introduced, rather than the volume v_c^* of the unit cell in reciprocal space, and we have utilized the fact that $2\pi/k = \lambda$.

The integrated intensity I_{sc} is then found by multiplying the above by the incident flux Φ_0 to yield the final result

$$I_{\text{sc}}\left(\frac{\text{photons}}{\text{sec}}\right) = \Phi_0\left(\frac{\text{photons}}{\text{unit area}\times\text{sec}}\right) r_0^2 P\, |F(\mathbf{Q})|^2\, N\, \frac{\lambda^3}{v_c}\frac{1}{\sin 2\theta} \tag{5.30}$$

Equation (5.30) is the master equation for crystallography, and we shall therefore pause briefly to discuss the various terms. Each electron in the unit cell has a differential scattering cross section of $r_0^2 P$, where P is a polarization factor. The differential scattering cross section of a unit cell is $r_0^2 P\, |F(\mathbf{Q})|^2$ where, in the limit $\mathbf{Q} \to 0$, $F(\mathbf{Q})=\sum_j Z_j$, the number of electrons in the unit cell. For general $\mathbf{Q} > 0$ the scattering is diminished due to different optical path lengths as given by $F(\mathbf{Q})$. The total scattering is proportional to the number of unit cells, N. Summation and proper integrations give rise to the last two factors, the last of which is sometimes called the Lorentz factor. Finally, we note with satisfaction that the dimensions are the same on the right and left hand sides, namely photons/s.

5.5.2 Extinction

The formula given in Eq. (5.30) applies to a single and idealized 'small' but otherwise perfect crystal, with all of the diffracting planes in exact registry. Real macroscopic crystals on the other hand are often imperfect, and may be thought of as being composed of small perfect blocks with a distribution of orientations around some average value. The crystal is then said to be mosaic, as it is considered to be composed of a mosaic of small blocks as shown in the left panel of Fig. 5.19. Typically the mosaic blocks may have orientations distributed over an angular range of between $0.01°$ and $0.1°$.

Each block is 'small' in the sense that there is a negligible chance of the diffracted beam being re-scattered before it exits the block, and the kinematical approximation applies. As the block size becomes larger this approximation breaks down, and instead it is necessary to allow for multiple
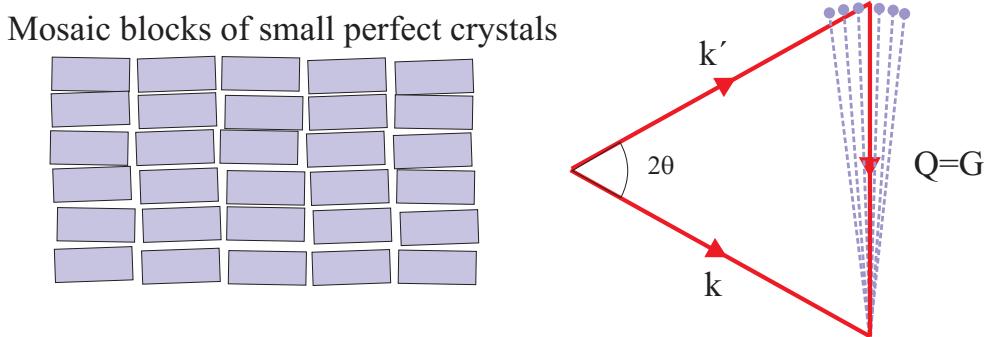
Fig. 5.19 Left: Real single crystals are often composed of small, ideal crystal grains, also called mosaic blocks which have a narrow distribution of orientations, the so-call mosaic distribution. Right: For a given (h, k, l) reflection the crystal is rotated, corresponding to rotating **G** about the origin. In this way the integrated intensity from each mosaic block is accumulated.

scattering effects. These are discussed in Chapter 6, where it is shown (Eq. (6.34)) that the integrated intensity from a macroscopic perfect crystal takes on a form very different from that given in Eq. (5.30). In fact, for reasons that will be discussed in Chapter 6, the integrated intensity from a macroscopic perfect crystal is in general lower than that of an imperfect one. Thus, if the mosaic blocks are not sufficiently small, then the measured integrated intensity of a given Bragg reflection will be less than predicted by Eq. (5.30). The reflection is then said to be reduced by *primary extinction* effects.

There is a second way that the scattering from a mosaic crystal may be less than given by Eq. (5.30). For a mosaic crystal it may happen that one or several mosaic blocks are shadowed by blocks which have an identical orientation. The beam incident on one of the shadowed blocks will then necessarily be weaker, since some of the beam has already been diffracted into the exit beam by the higher lying blocks. If this is the case, then *secondary extinction* is said to be present. In the event that both primary and secondary extinction are negligible, the crystal is said to be *ideally imperfect*.

The scattering diagram for an ideally imperfect crystal is shown in Fig. 5.19. Each mosaic block is indicated by a little dot in the fan of reciprocal lattice vectors denoted by **G**. The spectrometer is first set for a given (hkl) reflection at scattering angle $2\theta_{hkl}$. The crystal is then rotated or scanned through the Laue condition **Q** = **G**, over an angular range that is large enough to capture the entire mosaic fan and the integrated intensity recorded. Formula Eq. (5.30) can then be used to calculate the integrated intensity from the mosaic crystal. All that needs to be done is to replace N, the number of unit cells by $N'N_{mb}$, the product of the N', the number of unit cells in a single mosaic block and N_{mb}, the number of mosaic blocks. This follows from the fact that there is no definite phase relationship between waves scattered from different blocks and it suffices to add the intensities. This should be contrasted with the case of a single block where amplitudes are first added, and then the result multiplied by its complex conjugate to give the scattered intensity.

The idea that an imperfect crystal is composed of mosaic blocks is an oversimplification. Although it is true that dislocations and other defects produce a broadening of Bragg peaks, the micro-structure of an imperfect crystal rarely resembles that shown in the left panel of Fig. 5.19. It follows that the division of extinction effects into primary and secondary causes is not always valid. Indeed in many situations the use of a mosaic model to describe an imperfect crystal is an expediency, and is justified only in that it allows mathematical treatments of extinction effects, which can then be used to correct data. One way to avoid extinction effects altogether is to make a very fine powder of the sample, and powder diffraction is considered further in Section 5.6.1.
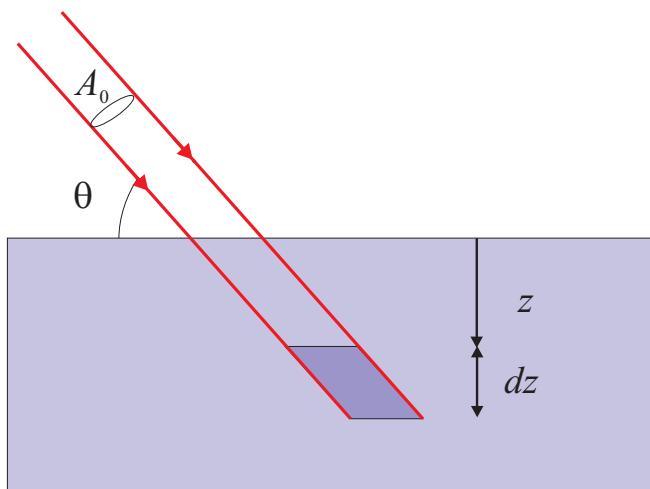
Fig. 5.20 Extended face geometry. A beam of X-rays is incident on the flat face of a crystal at an angle θ. The cross-sectional area of the beam is A_0, and the illuminated volume of sample at a depth of z from the surface is $(A_0/\sin\theta)dz$.

5.5.3   Absorption effects: extended face geometry

Equation (5.30) has been derived by neglecting absorption effects. It should be clear that in general these depend on the shape of the sample, and in practice various approximations are applied to correct the measured intensities. (The correction of integrated intensities for absorption effects is described in the *International Tables of Crystallography*.) One particularly useful and simple geometry for which an analytical solution can be found is the case of the diffraction from a crystal with an extended, flat face, as shown in Fig. 5.20, where it is assumed that the crystal is large enough to intercept the whole beam. If N is the total number of unit cells that are illuminated by the incident beam, then for a mosaic crystal we write $N = N' \times N_{\mathrm{mb}}$, where N' is the number of unit cells in a mosaic block, and N_{mb} is the number of mosaic blocks. The number of mosaic blocks illuminated by a beam of cross-sectional area A_0 in the interval from z to $z + dz$ is

$$N_{\mathrm{mb}} = \frac{A_0\, dz}{\sin\theta} \times \frac{1}{V'}$$

where V' is the volume of a mosaic block, and z is the depth of the beam in the crystal. At a depth z from the surface absorption reduces the intensity by $\mathrm{e}^{-2\mu z/\sin\theta}$, where the factor of 2 allows for the path length of the incident and exit beams through the crystal. The integrated intensity is found from

$$
\begin{aligned}
I_{\mathrm{sc}} &= \frac{\Phi_0 r_0^2 P\, |F(\mathbf{Q})|^2\, \lambda^3}{v_c \sin 2\theta}\, N' \int_0^\infty \mathrm{e}^{-2\mu z/\sin\theta}\, \frac{A_0\, dz}{V' \sin\theta} \\
&= \frac{\Phi_0 r_0^2 P\, |F(\mathbf{Q})|^2\, \lambda^3}{v_c \sin 2\theta}\, \frac{A_0 N'}{V'} \left[\frac{-1}{2\mu}\mathrm{e}^{-2\mu z/\sin\theta} \right]_0^\infty \\
&= \left(\frac{1}{2\mu} \right) \frac{\Phi_0 A_0 r_0^2 P\, |F(\mathbf{Q})|^2\, \lambda^3}{v_c^2 \sin 2\theta}
\end{aligned}
\tag{5.31}
$$

The fact the scattered intensity is now proportional to the intensity of the incident beam, i.e. the product of the flux Φ_0 and cross-sectional area of the incident beam A_0, arises from the fact that in deriving the
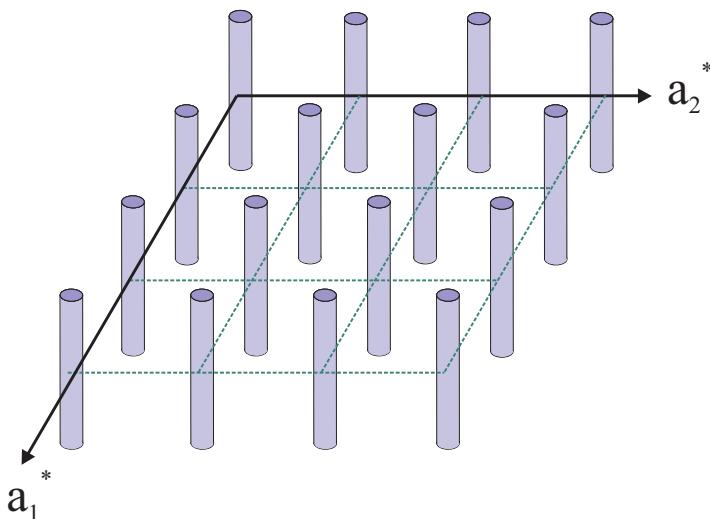
Fig. 5.21 Scattering cross-section from a two-dimensional crystal consists of rods of constant weight passing through the points of the 2D reciprocal lattice given by $\mathbf{G}_{hk} = ha_1^* + ka_2^*$.

above it has been assumed that the face of the crystal is extended enough that it intercepts the entire beam (see also Appendix A for a discussion of the definition of the differential cross-section). The above result for the integrated intensity from an extended face mosaic crystal with absorption effects included is compared in Chapter 6 with the case of the scattering from a perfect crystal with an extended face.

5.5.4   The Lorentz factor in 2D

In this section we consider briefly the two-dimensional (2D) equivalent of the Lorentz factor derived in the last section for a 3D crystal. The differential cross-section in 2D has the form

$$\left(\frac{d\sigma}{d\Omega}\right)^{2D} = r_0^2 \, P \, |F_{hk}|^2 \, N \, A^* \, \delta(Q_x - ha_1^*)\delta(Q_y - ka_2^*) \tag{5.32}$$

where N is the number of unit cells in the 2D lattice, A^* is the area of the unit cell in reciprocal space (see Eqs. (5.5), (5.6) and (5.14)). The Dirac delta functions restrict the scattering within the 2D plane to points forming the 2D reciprocal lattice given by $\mathbf{G}_{hk} = ha_1^* + ka_2^*$. The fact that there is no restriction on the scattering in the direction perpendicular to the 2D means that the scattering consists of rods of constant intensity passing through the points $\mathbf{G}_{hk}$, as illustrated in Fig. 5.21.

In the 3D case the delta function in Eq. (5.29) is three dimensional, and in order to derive the scattered intensity, Eq. (5.30), it was necessary to perform three integrations: one over the angle θ, and a two-dimensional integral over the element of solid angle. It is the latter integration which is different in the 2D case. Here it is only the in-plane part of the solid angle that involves an integration over a delta function; the out-of-plane part of the solid angle must be considered separately.

Let us first carry out the in-plane integrations, and in order to keep the notation simple let all vectors
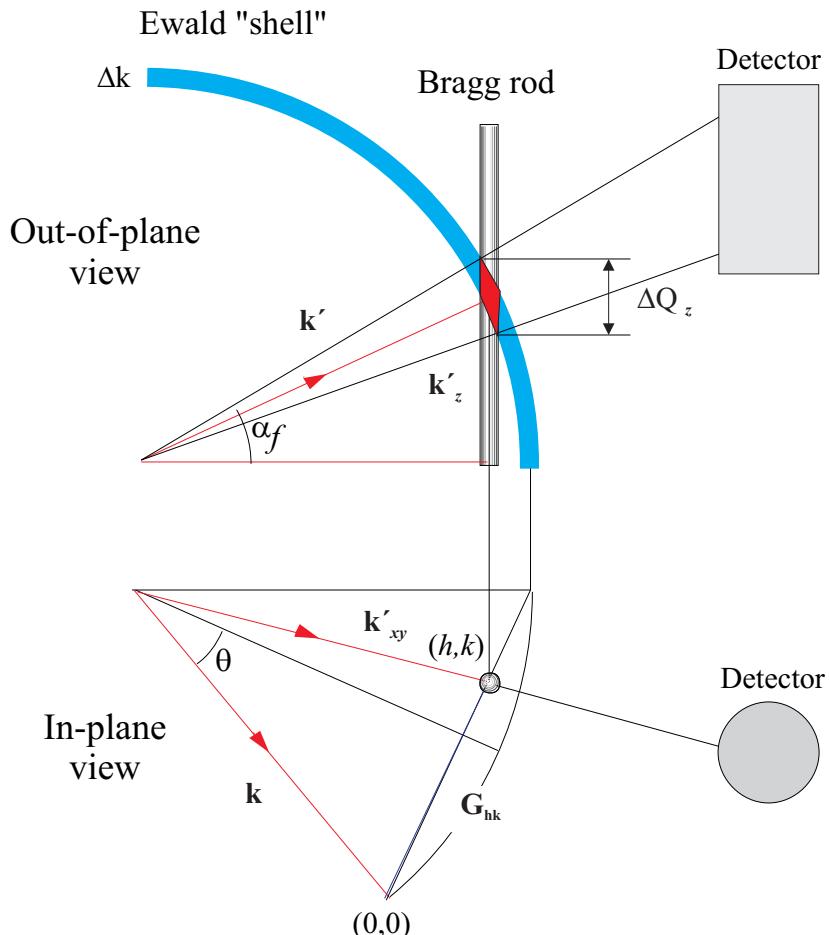
Fig. 5.22 Reciprocal space diagram for a 2D system showing the intersection of part of the Ewald sphere with the Bragg rod. The in-plane projection of reciprocal space is shown in the bottom part, and the out-of-plane projection in the top.

in the equations below be confined tacitly to the 2D plane. Utilizing the identity

$$\int x\,\delta(x^2 - \mathrm{k}^2)\,dx = \left[\frac{x}{2x}\right]_{x=\mathrm{k}} = \frac{1}{2}$$

we obtain

$$\int d\hat{\mathbf{k}}'\,\delta(\mathbf{k} - \mathbf{k}' - \mathbf{G}) = 2\overbrace{\int \mathrm{s}\,\delta(\mathrm{s}^2 - \mathrm{k}^2)\,d\mathrm{s}}^{1}\int \delta(\mathbf{k} - \mathrm{k}\hat{\mathbf{s}} - \mathbf{G})\,d\hat{\mathbf{s}}$$

$$= 2\int \delta(\mathrm{s}^2 - \mathrm{k}^2)\,\delta(\mathbf{k} - \mathbf{s} - \mathbf{G})\,d^2\mathbf{s}$$

$$= 2\,\delta((\mathbf{k} - \mathbf{G})\cdot(\mathbf{k} - \mathbf{G}) - \mathrm{k}^2)$$

$$= 2\,\delta(\mathrm{G}^2 - 2\,\mathrm{k}\,\mathrm{G}\,\sin\theta)$$

where $d^2\mathbf{s}=s\,d\hat{\mathbf{s}}\,ds$ is the two dimensional volume element. The integral over θ is performed in a similar way to the 3D case and yields

$$\int 2\delta(\mathrm{G}^2 - 2\mathrm{kG}\sin\theta)\,d\theta = \frac{-1}{\mathrm{k}^2\sin 2\theta}$$

leading to

$$\left(\frac{d\sigma}{d\Omega}\right)_{\text{int. over }\mathbf{k}'_{xy},\,\theta} = r_0^2 P\,|F_{hk}|^2\,N\,\frac{\lambda^2}{A}\,\frac{1}{\sin 2\theta}$$

Here A is the unit cell area in direct space, and N is the number of illuminated unit cells. The scattered wavevector has been written with the subscript xy to emphasize that it is the 2D part that has been considered so far.

Having performed the integration over the in-plane part of the scattered wavevector $\mathbf{k}'_{xy}$ it is now necessary to integrate over the out-of-plane part of the solid angle. This is illustrated in Fig. 5.22, which shows the in-plane and out-of-plane projections of reciprocal space. In contrast to the 3D case the *projected* scattering triangle is no longer isosceles as $|\mathbf{k}'_{xy}| \le |\mathbf{k}|$ since $\sqrt{(\mathbf{k}'_{xy})^2 + (\mathbf{k}'_z)^2} = |\mathbf{k}|$, where $\mathbf{k}'_{xy}$ and $\mathbf{k}'_z$ are the in-plane and out-of-plane components of the scattered wavevector respectively. The out-of-plane projection is shown in the top of the figure. As the scattering is elastic the projection of $\mathbf{k}'$ must lie within the circular band of the Ewald sphere. The finite thickness of the band represents the bandwidth $\Delta\mathrm{k}$ of the incident beam. Only scattered wavevectors with an out-of-plane component within the interval ΔQ_z are allowed. The corresponding component of the solid angle element is $\Delta\Omega_z=\Delta Q_z/\mathrm{k}$ and the scattered intensity is therefore

$$I_{\text{sc}}^{2D}\left(\frac{\text{photons}}{\text{sec}}\right) = \Phi_0\left(\frac{\text{photons}}{\text{unit area}\times\text{sec}}\right) r_0^2 P\,|F_{hk}|^2\,N\,\frac{\lambda^2}{A}\,\frac{1}{\sin 2\theta}\left(\frac{\Delta Q_z}{\mathrm{k}}\right) \tag{5.33}$$

5.6 Applications of kinematical diffraction

The objective of an X-ray diffraction experiment is to determine the structure, which for a crystalline material means determining the unit cell and basis. The formulae derived so far in this chapter apply mostly to the diffraction from a single crystal. Under favourable circumstances materials may indeed be available as single crystals. The three-dimensional structure of the material is then solved by measuring as many Bragg peaks as possible as a function of the Miller indices (h, k, l). In rough terms, the size and symmetry of the unit cell are found from the position of the Bragg peaks, while the nature of the basis and the position of the atoms (or molecules) within it determine the Bragg peak intensities. Sophisticated techniques have been developed for going from the measured intensities to the final structure, and for unit cells containing a modest number of atoms the whole process of structure solution using single crystals is now routine and highly automated.

Many important materials cannot be obtained in single-crystal form, and may instead be in the form of powders, or fibres. Alternatively, it may be that it is the two-dimensional structure of the crystal surface, and not the three-dimensional structure of the bulk that is of interest. Understanding the diffraction pattern in these situations requires further concepts to be developed. In this section these concepts are introduced, and examples are used to illustrate how they apply in practice.

5.6.1 Powder diffraction

A good crystalline powder consists of many thousands of tiny crystallites oriented at random. Let us focus our interest on a particular reciprocal lattice vector $\mathbf{G}_{hkl}$ specified by its Miller indices (h, k, l). In the ideal powder sample the directions of the $\mathbf{G}_{hkl}$ vectors are isotropically distributed over the sphere indicated in Fig. 5.23. Some of the grains have the correct orientation, relative to the incident wavevector $\mathbf{k}$, for Bragg scattering: in the figure they are represented by the circle, which is a cut through the sphere of the plane perpendicular to $\mathbf{k}$. The scattered wavevectors $\mathbf{k}'$ are thus distributed evenly on a cone with $\mathbf{k}$ as the axis and an apex half angle of 2θ. This cone is called the Debye-Scherrer cone after the two physicists who first correctly interpreted X-ray scattering from a powder.

At first sight it might appear to be an impossible task to solve a full three-dimensional crystal structure from a powder diffraction pattern, which is a two-dimensional projection. However, several methods for achieving this have been developed. Probably the most commonly one used is Rietveld refinement [Rietveld, 1969]. This seeks to use the entire diffraction profile, and not just the integrated intensities of the powder lines, to constrain or refine the parameters in the structural model. The Rietveld refinement which gives the method its name is in fact the last step in a process. The first step is known as indexing, and involves finding the size and symmetry of the unit cell so that the powder lines can be labelled with the appropriate values of (h, k, l). The second step is to extract the measured intensities and to convert them into structure factors. The third is to use the measured structure factors to build a structural model. Finally, the structural model is refined using the entire diffraction profile.

Here we restrict our discussion to showing how the measured intensity in a powder diffraction experiment is related to the structure factor. For a certain fixed (h, k, l) reflection the number of powder grains oriented to reflect is proportional to the circumference of the base-circle of the Debye-Scherrer cone shown in Fig. 5.23. The circumference is given by $\mathrm{G}_{hkl}\sin(\frac{\pi}{2} - \theta) = \mathrm{G}_{hkl}\cos\theta$. However, permutations of (h, k, l) may have the same sphere of $\mathbf{G}_{hkl}$ vectors, and this is taken into account by introducing the *multiplicity* of a reflection m_{hkl}. For example, for a cubic lattice the multiplicity of the $(h, 0, 0)$ reflections is 6 as the $(\pm h, 0, 0)$, $(0, \pm h, 0)$ and $(0, 0, \pm h)$ reflections will all Bragg reflect to the same 2θ. So for a given $\mathbf{G}_{hkl}$ the intensity must be proportional to $m_{hkl}\cos\theta$. At a *different* $\mathbf{G}_{hkl}$, and hence a different value of 2θ, the detector will see a different fraction of the base circle. Independent of $\mathbf{G}_{hkl}$, the circumference of the circle is $2\pi\mathrm{k}\sin 2\theta$. Thus the fraction seen by the detector is $\mathrm{k}\delta/(2\pi\mathrm{k}\sin 2\theta)$, which is proportional to $1/\sin 2\theta$. Finally, for a single crystallite the observed intensity will be proportional to the Lorentz factor we have already derived, $1/\sin 2\theta$. Altogether then the observed intensity will be proportional to

$$L_{\mathrm{powder}} = m_{hkl}\cos\theta\frac{1}{\sin 2\theta}\frac{1}{\sin 2\theta} = \frac{m_{hkl}}{2\sin\theta\sin 2\theta} \tag{5.34}$$

The structure factors squared can be derived on a relative scale from the observed diffraction intensities. Suppose, for example, that it is required to determine the ratio of squared structure factors for the $(1,1,1)$ and $(2,0,0)$ reflections from an fcc crystal. In addition to the combined Lorentz factor given above, it is also necessary to allow for the polarization factor P which depends on the scattering angle, so that the ratio of the intensities is

$$\frac{I_{111}}{I_{200}} = \frac{\left|F_{111}\right|^2}{\left|F_{200}\right|^2}\frac{L_{\mathrm{powder}}(\theta_{111})}{L_{\mathrm{powder}}(\theta_{200})}\frac{P(\cos 2\theta_{111})}{P(\cos 2\theta_{200})} \tag{5.35}$$

The assumption of an isotropic distribution of orientations of the crystallites is not fulfilled trivially in practice. When this condition is not fulfilled the powder is said to posses preferred orientations.
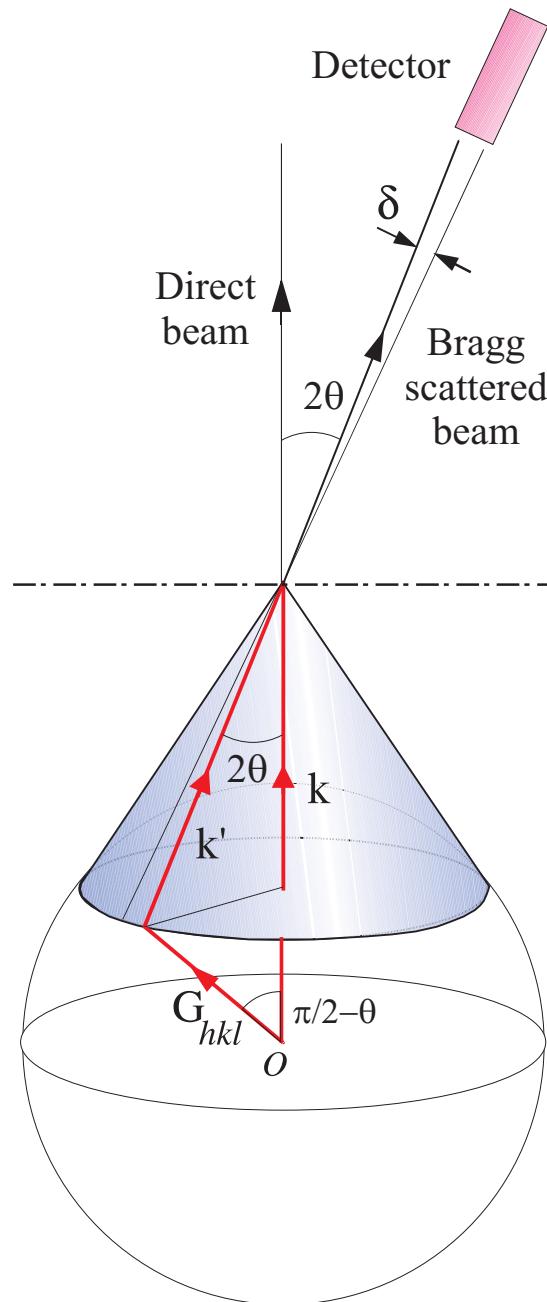
Fig. 5.23 In an ideal powder there is an isotropic distribution of crystal grain orientations, as indicated by the sphere which represents the terminal points of the reciprocal lattice vector **G** from all of the grains. For fixed incident wavevector **k** all of the **G** vectors terminating on the circle will Bragg reflect, so that the scattered wavevectors **k**′ span a cone, the so-called Debye-Scherrer cone. The angular acceptance of the detector is δ.

(a) Ambient pressure

(b) 4.9 GPa   (49 kbar)
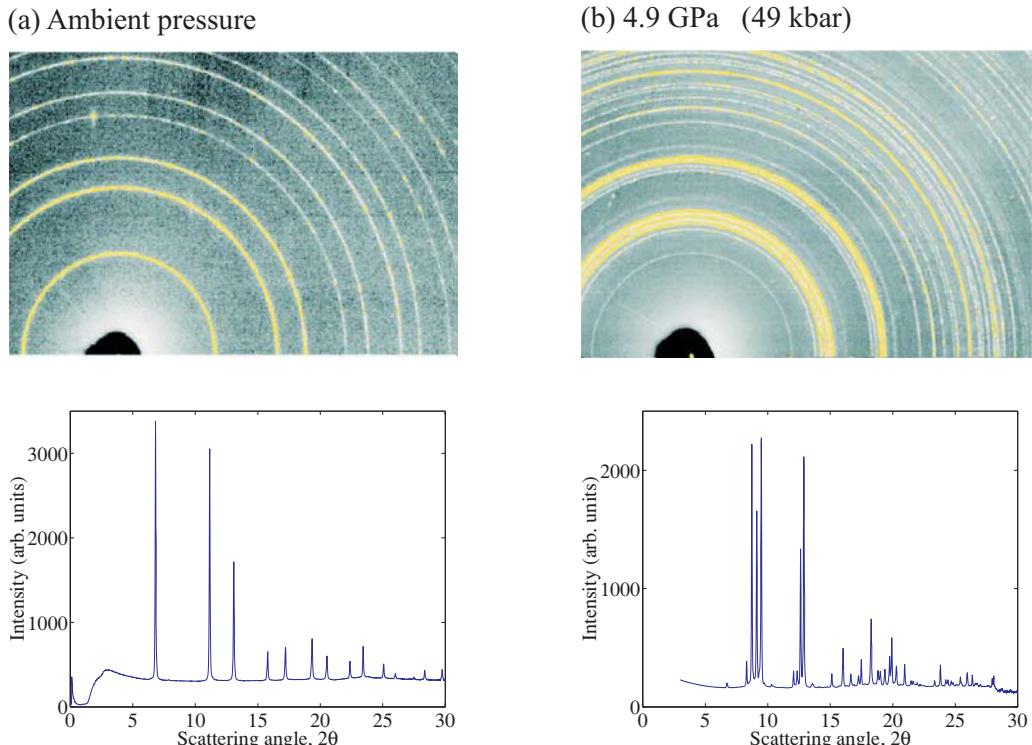
Fig. 5.24 Powder diffraction patterns from InSb at (a) ambient pressure, and (b) at a pressure of 4.9 GPa. The patterns recorded on an image plate detector are shown in the top row, and display rings where the detector intercepts the Debye-Scherrer cones. The data were recorded with an incident wavelength of $\lambda = 0.447$ Å. In the bottom row the radially averaged patterns as a function of 2θ are displayed. The results show that InSb undergoes a phase transition from the zinc sulfide structure to a phase with an orthorhombic structure at pressures above 4.9 GPa. (Data courtesy of Malcolm McMahon, University of Edinburgh.)

Grains in a metal ingot, for example, may be highly textured in orientation due to mechanical rolling. The texture is in fact of importance for the mechanical properties of the metal, and it can be determined by suitable rotation of the sample. In other cases a powdered sample is prepared by crushing the material into a powder and loading it into a glass capillary tube. An isotropic distribution is then ensured by rotating the capillary tube around its axis during exposure. Powder diffraction is particularly useful for studying the structure of materials under extreme conditions, such as the study of phase transitions as a function of applied pressure.

In Fig. 5.24 data are shown from a study of the semiconducting material InSb as a function of pressure. The data were obtained by loading a small quantity of powdered InSb into a diamond anvil pressure cell, and then recording the powder diffraction patterns with an image plate detector. The data shown in Fig. 5.24(a) were recorded at ambient pressure where InSb adopts the zinc sulfide structure (see Fig. 5.5(b)) with a lattice parameter of 6.48 Å. The X-ray wavelength was 0.447 Å, and Debye-Scherrer cones were observed at scattering angles of 2θ= 6.81°, 11.15°, 13.06°, 15.78°, 17.21°, $\cdots$, corresponding to the (1,1,1), (2,2,0), (3,1,1), (4,0,0), (3,3,1), $\cdots$, Bragg peaks respectively. When pressure is applied to the system a phase transition occurs, as shown in Fig. 5.24(b) for an applied

pressure of 4.9 GPa, and the crystal structure transforms to become orthorhombic.

5.6.2 Diffraction from a fibre

From a crystallographic point of view a fibre can be considered as an extreme limit of anisotropy in a powder: all the crystallites have one of their crystallographic axes, here denoted the c-axis, aligned along the fibre axis, whereas the azimuthal orientation of the $a - b$ plane is random. Fibres occur frequently in nature, for example, in muscles and in collagen, and artificial fibres are widely used in industry. The structure of fibres, as revealed by diffraction studies, is therefore of general interest and is the subject of this section.

In fibre diffraction geometry, the monochromatic incident beam with wavevector $\mathbf{k}$ is perpendicular to the vertical fibre axis, as shown in Fig. 5.25. Bragg reflections occur in the horizontal (equatorial) plane due to the fact that each individual fibre in the sample is formed from a bundle of thinner long filaments, which pack in a two-dimensional lattice perpendicular to the fibre axis. Each filament may also exhibit periodicity along the axis, thus giving rise to Bragg reflections in the vertical (meridional) plane.

The lower right part of Fig. 5.25 shows reciprocal space. The scattering vector $\mathbf{Q}$ is decomposed into the vertical component $\mathbf{Q}_z$ and the horizontal component $\mathbf{Q}_h$. For Bragg scattering $\mathbf{Q}$ must terminate in layers at $\mathbf{Q}_z = lc^*$ with $l = 0,\ \pm 1,\ \pm 2, \cdots$, etc., and $c^* = 2\pi/c$, where c is the period along the filament axis. Furthermore, if the filaments making up the fibre are arranged in a 2D lattice, Bragg reflections will occur in the different l-layers outside the meridional axis. The $l=0$ layer is called the equatorial layer. For a certain l-layer, the angle β is constant. The scattered wavevector $\mathbf{k}'$ must terminate on a circle in the l-layer since the scattering is elastic: the scattering angle 2θ varies with the azimuthal angle α according to $\cos 2\theta = \cos\alpha\,\cos\beta$, so for certain values of α the Bragg condition $\lambda = 2d_{hkl}\sin\theta$ will be fulfilled. In the bundle of many fibres making up the sample there will always be one with the correct (a^*, b^*) orientation for Bragg reflection. Independent of the fibre structure, symmetry implies that the Bragg spots occur symmetrically around the meridional plane at $\pm\alpha$.

Example: helices in biology and the structure of DNA

The primary structure of a protein is a polypeptide backbone, depicted in Fig. 5.26, onto which is attached a sequence of amino acids. Around 1950 Linus Pauling formulated a seminal idea on the structure of proteins which has had far reaching consequences [Pauling et al., 1951]. In Pauling's laboratory they had been studying the building blocks of polypeptide chains. As a result of this work Pauling became convinced that a protein was formed by structural units which could be considered to be rigid and planar, or at least approximately so. This is illustrated in Fig. 5.26 where the shaded parallelograms indicate that the carbonyl and amide groups are planar. It follows that when the polypeptide chain folds to form a protein the main degrees of structural freedom are the rotation angles around the links between these rigid structural units. One of Pauling's most important insights was that the formation of a hydrogen bond between the carbonyl C=O of one unit and the amino N-H group four units further along would cause the chain to curl up into a helix. This structure was christened the α-helix, and has 3.7 residues for one period of rotation. Subsequent experiments established that Pauling was indeed correct, and it is now known that α-helices are an important structural component of many proteins.

Inspired by Pauling's ideas, Cochran et al. calculated the generic diffraction pattern from a helix [Cochran et al., 1952]. As the scattering from helices has assumed such significance in structural biology an outline of this calculation is given here. The starting point is to imagine that a uniform and continuous distribution of material lies on an infinitely long helical string of period P. The problem
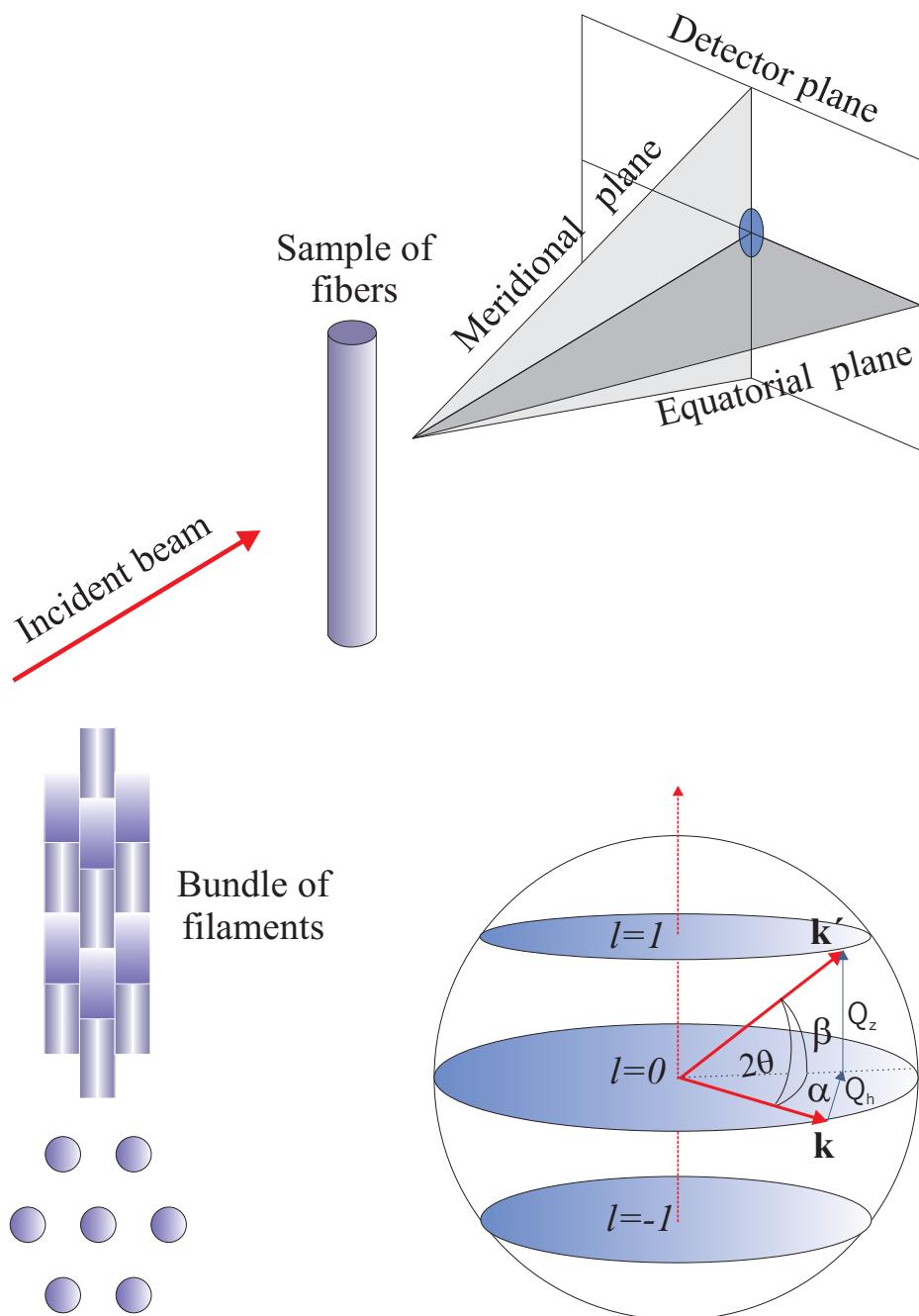
Fig. 5.25 Top: geometry of fibre diffraction. The fibre sample is perpendicular to the incident monochromatic beam. Bottom left: the fibre sample comprises a large number of filaments, randomly orientated in the azimuthal angle. Bottom right: periodicity along the fibre implies that Bragg reflections are restricted to layers.
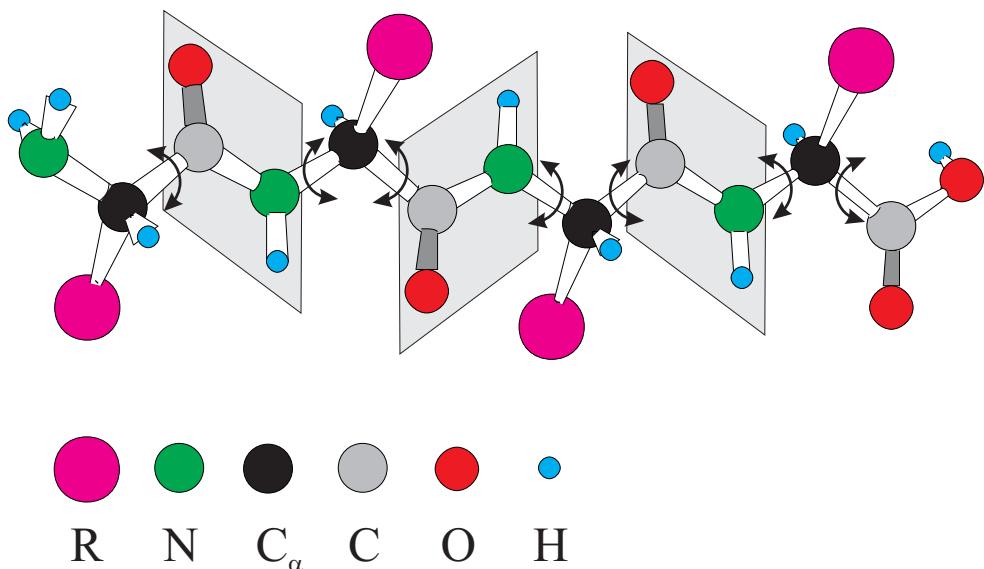
Fig. 5.26 A polypeptide chain is composed of planar moieties of carbonyl and amide groups. These planar moieties can be rotated around either the N-C$_\alpha$ or the C$_\alpha$-C bonds. Hydrogen bonding between the N-H and C=O groups causes the chain to fold into a helical structure known as the α-helix after Pauling. Here R stands for an amino acid residue.
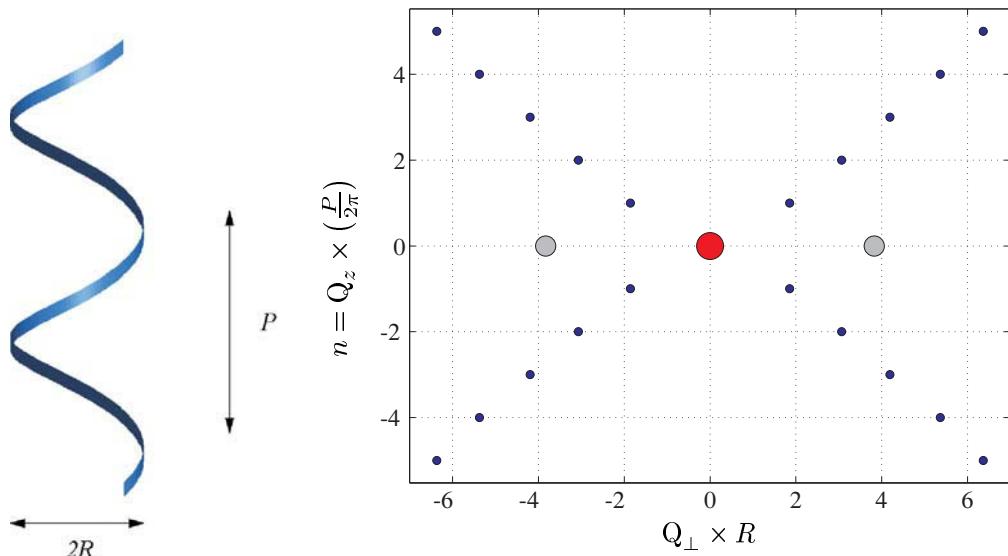
Fig. 5.27 Scattering from a single, infinitely long helix of radius R and period P. The structure factor squared has principle maxima arising from the peaks in the Bessel functions, and form a cross in reciprocal space as indicated by the blue circles. The grey circles on the equatorial axis are the secondary maxima from the zeroth-order Bessel function. Here Q_z and $Q_\perp$ are the components of the scattering vector parallel and perpendicular to the axis of the helix respectively.

in calculating the diffraction pattern is to add up the phase factor for each differential element along the helix. As the material is uniformly distributed the scattering amplitude is found by evaluating the integral

$$A(\mathbf{Q}) \propto \int e^{i\mathbf{Q}\cdot\mathbf{r}}\,dz$$

where z is taken to be along the axis of the helix. For a helix with a period of P and a radius of R, any point $\mathbf{r}$ on the helix is given by

$$\mathbf{r} = \left(R\cos(\tfrac{2\pi z}{P}),\ R\sin(\tfrac{2\pi z}{P}),\ z\right)$$

As the helix is periodic, the integral decomposes into a sum over all periods (or lattice sites) multiplied by the structure factor of a single period. The scattering amplitude then becomes

$$A(\mathbf{Q}) \propto \sum_{m=0}^{\infty} e^{i Q_z m P} \int_{z=0}^{z=P} e^{i\mathbf{Q}\cdot\mathbf{r}}\,dz$$

$$\propto \int_{z=0}^{z=P} \delta(Q_z - \tfrac{2\pi n}{P})\, e^{i\mathbf{Q}\cdot\mathbf{r}}\,dz \tag{5.36}$$

Here n is an integer, and use has been made of Eq. (5.12), which allows the sum over lattice sites to be written as a delta function.

To evaluate the phase $\mathbf{Q}\cdot\mathbf{r}$ it is convenient to use cylindrical coordinates and express the scattering vector as

$$\mathbf{Q} = \left(Q_\perp \cos(\Psi),\ Q_\perp \sin(\Psi),\ Q_z\right)$$
$$= \left(Q_\perp \cos(\Psi),\ Q_\perp \sin(\Psi),\ \tfrac{2\pi n}{P}\right)$$

where Q_z is the axial component, $Q_\perp$ is the radial component and Ψ is the azimuthal angle. The scattering amplitude from a helix then assumes the form

$$\boxed{A_1(Q_\perp, \Psi, Q_z) \propto e^{i n \Psi}\, J_n(Q_\perp R)}$$

where $J_n(Q_\perp R)$ is the n'th order Bessel function of the first kind, and $Q_\perp R$ is a dimensionless argument. The mathematics leading to this expression are explained in the box on the next page. The subscript '1' is used as a reminder of the fact that the expression refers to the scattering from a single helix. The scattered intensity given by the above equation is plotted in Fig. 5.27.

Perhaps the most celebrated helical structure in biology is the *double* helix of DNA (deoxyribose nucleic acid). The structure of DNA was first solved by James Watson and Francis Crick [Watson and Crick, 1953], who mainly used stereo-chemical arguments to build a model which helped them deduce the correct structure. They were assisted greatly in their work by the X-ray diffraction experiments performed around the same time by Wilkins et al. [Wilkins et al., 1953] and Franklin and Gosling [Franklin and Gosling, 1953]. These experiments established the helical nature of the DNA molecule, and provided decisive structural parameters, such as its period and radius. The discovery of the double helix probably ranks as one of the most important scientific advances of the twentieth century. As the authors note: *'It has not escaped our notice that the specific pairing we have postulated immediately suggests a possible copying mechanism for the genetic material'*.

Structure factor of a helix and the Bessel function $J_n(\xi)$

From Eq. (5.36) the scattering amplitude from a helix of period P and radius R is

$$A(\mathbf{Q}) \propto \int\limits_{z=0}^{z=P} \delta(Q_z - \tfrac{2\pi n}{P})\, e^{i\mathbf{Q}\cdot\mathbf{r}}\, dz$$

Using cylindrical coordinates the scalar product of the scattering vector $\mathbf{Q}$ and position $\mathbf{r}$ is

$$\mathbf{Q}\cdot\mathbf{r} = Q_\perp \cos(\Psi)\, R\cos(\tfrac{2\pi z}{P}) + Q_\perp \sin(\Psi)\, R\sin(\tfrac{2\pi z}{P}) + Q_z z$$
$$= Q_\perp R\cos(\tfrac{2\pi z}{P} - \Psi) + \left(\tfrac{2\pi z}{P}\right)n$$

It is convenient to rewrite this as

$$\mathbf{Q}\cdot\mathbf{r} = \xi\cos\varphi + n\varphi + n\Psi$$

with $\xi = Q_\perp R$ and $\varphi = (2\pi z/P - \Psi)$. The scattering amplitude can then be written in the form

$$A(\mathbf{Q}) \propto e^{in\Psi} \int\limits_{0}^{2\pi} e^{i\xi\cos\varphi + in\varphi}\, d\varphi$$

The n'th order Bessel function of the first kind is given in integral form by

$$J_n(\xi) = \frac{1}{2\pi i^n} \int\limits_{0}^{2\pi} e^{i\xi\cos\varphi + in\varphi}\, d\varphi$$

It is then apparent that the scattering amplitude from a single helix assumes the form

$$A_1(Q_\perp, \Psi, Q_z) \propto e^{in\Psi}\, J_n(Q_\perp R)$$

A photograph of the fibre diffraction pattern from DNA is shown in the top part of Fig. 5.28⋆. This is from the B phase, and is similar to one of the original patterns reported by Franklin and Gosling [Franklin and Gosling, 1953]. In contrast to the type of pattern recorded from a single crystal, this diffraction pattern arises from a large number of crystallites with random orientation about the chain axis. The reflections are spread into arcs because the alignment of the crystallites along the chain axis is not perfect. Although cylindrical averaging frequently occurs in fibres and results in overlap of systematically related reflections, the loss of information is not normally severe. This type of diffraction method has been used to determine the structures of four of the five principal DNA conformations. It is also used to study other biomolecules including filamentous viruses, cellulose, collagen, flagella, etc. The use of neutron diffraction in combination with X-ray methods is especially powerful since it allows important insights into hydration of these molecules.

It is evident that the diffraction pattern from DNA possesses some of the features predicted by
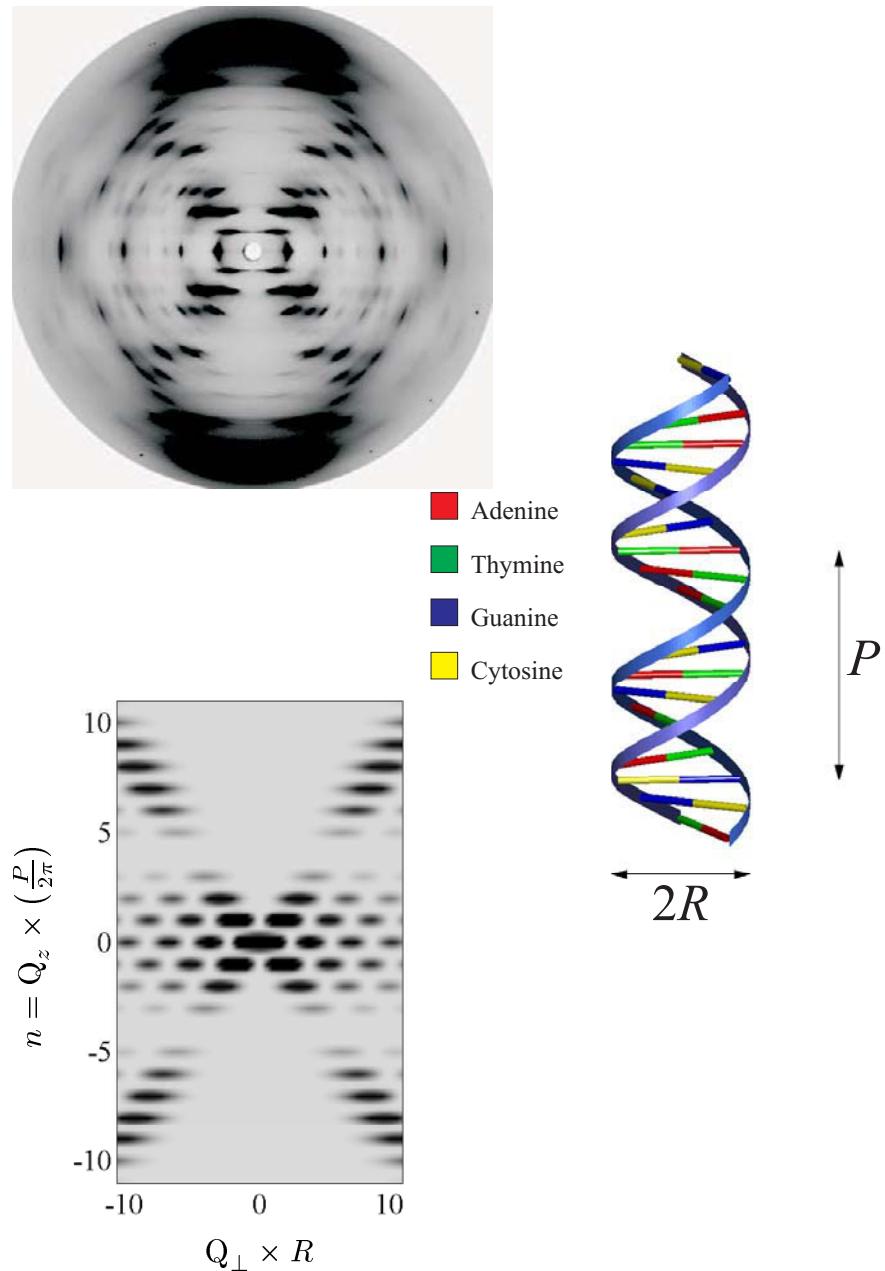
Cochran et al. for the scattering from a helix. In particular there is a characteristic cross of Bragg peaks. From the position of these peaks along the meridional (vertical) axis the period of the helix is found to be 34 Å, while from the angle of the cross it can be deduced that the radius of the helix is 10 Å. The double nature of the helix is only apparent from a detailed analysis of the pattern. Most tellingly the reflections from the 4'th order layer are missing on the film, although the 3'rd and 5'th order are clearly apparent. Indeed Rosalind Franklin herself was aware that this feature of the diffraction pattern could be explained naturally by assuming that DNA is formed from two intertwined helices as shown in the middle part of Fig. 5.28★. If the two helices are displaced along the common z axis by an amount Δ, then this corresponds to an azimuthal angle $\Psi = 2\pi(\Delta/P)$, and the scattering amplitude becomes

$$A_2(Q_\perp, \Psi, Q_z) \propto (1 + e^{in\left(\frac{2\pi}{P}\right)\Delta}) \, J_n(Q_\perp R) \qquad (5.37)$$

with $Q_z = n(2\pi/P)$. The waves scattered by the two helices interfere in such a way that the intensity of the 4'th layer reflections becomes vanishingly small when Δ/P=1/8, 3/8, 5/8, etc. In the bottom part of Fig. 5.28★ the intensity calculated from this equation is plotted. It can be seen that it accounts for most of the qualitative features of the central part of the diffraction pattern. To obtain better agreement it would obviously be necessary to specify the position of all the molecules in the structure and their scattering factors. One feature not accounted for by the simple model described here is the existence of strong, but diffuse reflections on the meridional axis close to the 10'th layer. These reflections arise from the fact that the double helix has 10 pairs of bases per period.

5.6.3   Two-dimensional crystallography

One area that has benefitted greatly from the high flux produced by synchrotron sources is the study of surfaces using X-ray scattering. Although X-rays are scattered only weakly by a monolayer of atoms or molecules, it transpires that the sensitivity is still high enough that it is possible to study the structure in great detail. Moreover, the fact that the scattering is weak simplifies the interpretation of the data considerably, as the kinematical approximation then applies. This contrasts with the case of strongly interacting probes, such as the electron, where the data analysis is complicated by the need to resort to a full multiple scattering theory.

X-ray scattering experiments from surfaces are usually performed with the angles of the incident and exit beams close to the critical angle, α_c, for total external reflection, as this limits the penetration depth of the beam which in turn reduces the background scattering from the bulk of the crystal. One consequence of this is that it is necessary to correct the above formula for refraction effects. In Section 3.4 it was shown that the transmittivity, $t(\alpha_i)$, of the incident beam is enhanced for angles close to α_c (Fig. 3.5). From Eq. (3.17) the amplitude transmittivity is

$$t(\alpha_i) = \frac{2\alpha_i}{\alpha_i + \alpha'}$$

where α' refers to the transmitted beam. By reversing the direction of the incident and transmitted rays one obtains a ray in the crystal at a glancing angle of α' that exits the crystal at a glancing angle of α_f. Clearly, the transmission coefficient for this process must be $t(\alpha_f) = 2\alpha_f/(\alpha_f + \alpha')$. Including these refraction effects, the integrated intensity given in Eq. (5.33) becomes

$$I_{sc}^{2D} \longrightarrow I_{sc}^{2D} \, |t(\alpha_i)|^2 \, |t(\alpha_f)|^2 \qquad (5.38)$$
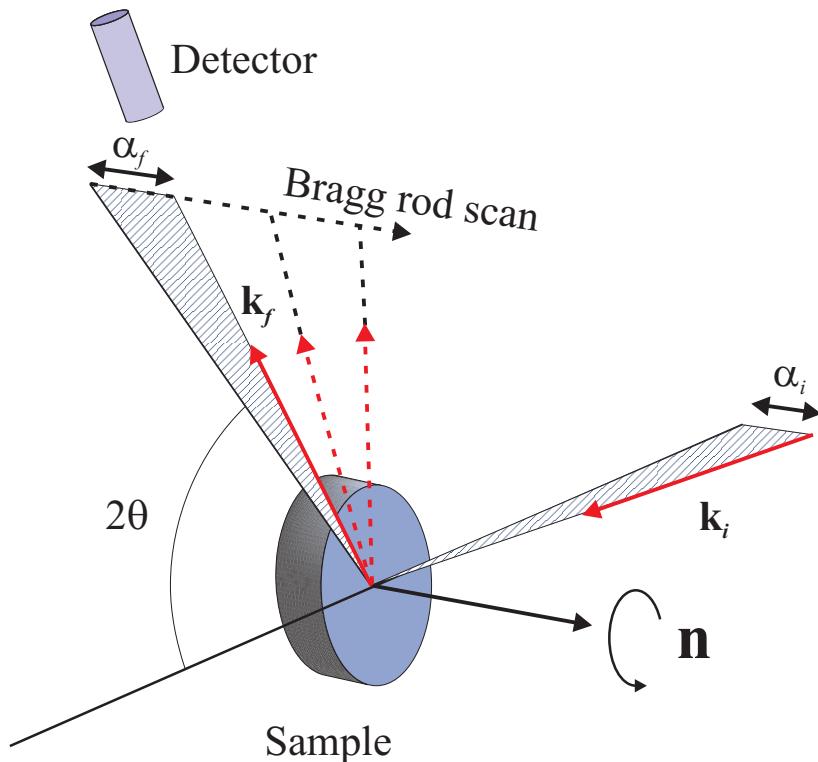
Fig. 5.29 Geometry of a grazing incidence diffraction (GID) experiment from a solid single crystal surface at a synchrotron. The surface can be rotated around the surface normal **n**, and the detector can be both rotated around **n** in the vertical plane, and moved perpendicular to it so as to scan along the crystal truncation rods.

A free standing two-dimensional crystal is difficult to realize in nature, and quasi two-dimensional structures are instead studied on crystal surfaces. The structure may of course be the surface of the crystal itself, as the difference in the bonding of the surface atoms often leads to a reconstruction of the surface. Alternatively it may be the structure of an absorbed layer of atoms or molecules. In either case, experiments on surfaces are performed in two distinct steps. The first is to study the *in-plane* structure of the surface, in other words the positional coordinates of the topmost atoms within the plane of the surface. To this end it may be convenient to define a new unit cell for the surface. For example, a unit cell may be defined with the (**a**, **b**) axes in surface plane, and the **c** axis perpendicular to it. Conventional crystallographic structure determination then requires that the structure factor $|F_{hk}|$ of as many Bragg peaks as possible are determined, with $l \approx 0$. These can then be compared with calculations of the structure factor for different models of the surface. The in-plane structure is most readily determined when the Bragg peaks from the surface layer appear at different positions from those of the bulk. In other words when the surface has a different in-plane periodicity to that of the bulk. This is often found to be the case for either reconstructed surfaces, or absorbed layers. The second step is to study the *out-of-plane* structure. Here the intensity distribution of the scattering is studied as a function of l with the values of h and k set to coincide with a 2D Bragg peak. We have seen already (Section 5.3) that for an ideally terminated surface the scattering is extended along l to form the crystal truncation rods (CTR), and that the observed intensity distribution along the rods is sensitive to any modifications of

the near-surface region.

A schematic of the experimental setup used to measure the scattering from a surface in grazing incidence geometry is shown in Fig. 5.29. The sample here is a disc with a surface normal $\mathbf{n}$ in the horizontal plane. The incident, monochromatic beam is horizontal and the incident wavevector $\mathbf{k}_i$ is at a glancing angle α_i to the surface. The incident glancing angle is close to the critical angle for total reflection, so that only a thin surface layer (thickness Λ) is exposed to the X-rays, as discussed in Section 3.4. When the sample is rotated around $\mathbf{n}$, the glancing incident angle should remain fixed which can be monitored by requiring a constant value of the specularly reflected beam. For a certain $(h, k, 0)$ Bragg reflection with reciprocal lattice vector $\mathbf{G}_{hk}$ the Bragg angle θ is calculated from $2k \sin \theta = G_{hk}$. The detector arm is turned around $\mathbf{n}$ to the angle 2θ, and for $l \cong 0$ the detector is then translated a small angle α_f (of order α_i) along the surface normal. The sample lattice can be turned around $\mathbf{n}$ so that the reflecting (h, k) planes bi-sect the angle between $\mathbf{k}_i$ and $\mathbf{k}_f$. To obtain the intensity along the CTR's the detector is translated along the surface normal so that α_f becomes much larger than α_i.

Example: absorption of O on the Cu(110) surface

The example we shall use to illustrate many of the concepts introduced above is the structure of the (110) copper surface with oxygen atoms chemisorbed onto it [Feidenhans'l et al., 1990].

Copper crystallizes in a face centred cubic structure as shown in the top part of Fig. 5.30. The Cu atoms are located at the corners and at the centres of the faces of a cube. The copper crystal has been cut so that a (110) plane forms the surface. A front-view of the truncated bulk (110) surface is shown in the middle panel of Fig. 5.30. Cu atoms in the top layer are shown as large filled circles, whereas Cu atoms in the second layer are represented by smaller ones. Cu atoms in the third layer sit directly below those in the top layer, etc.

The cubic unit cell is not convenient for describing the positions of atoms in the surface layer. For the surface we rather choose the unit cell as shown shaded in the middle panel. Clearly the length of $\mathbf{a}$ is $a_c / \sqrt{2}$ and the length of $\mathbf{b}$ is a_c. The third axis of the unit cell, $\mathbf{c}$, is perpendicular to the surface and has the length $a_c / \sqrt{2}$. With this choice there are two atoms per unit cell: one at $(0,0,0)$ and one at $(1/2,1/2,1/2)$. We define a full monolayer of Cu atoms as that of the top layer. Referring to this unit cell the reciprocal lattice $(\mathbf{a}^*, \mathbf{b}^*)$ is shown to the right. The length of $\mathbf{a}^*$ and $\mathbf{b}^*$ are $2\pi/(a_c / \sqrt{2})$ and $2\pi/a_c$ respectively, so that a general reciprocal lattice vector in the plane of the surface is $\mathbf{G}_{hk} = h\mathbf{a}^* + k\mathbf{b}^*$.

If the bare Cu(110) surface terminated as the bulk structure, allowed (hk) reflections would require an even sum of h and k since $F_{hk} \propto 1 + e^{i\pi(h+k)}$. These reflections are indicated by diamonds in the reciprocal lattice shown in Fig. 5.30. However, when exposed to oxygen the surface undergoes a reconstruction from that of the truncated bulk lattice. By LEED (Low Energy Electron Diffraction) one can immediately see the symmetry of the surface unit cell, or rather that of the reciprocal lattice cell. For a certain dosage of oxygen, it turns out to be exactly like the truncated unit cell along the k-axis, but only half as large along the h-axis as indicated in the right panel by the h' index. This means that the unit cell in direct space must have doubled along the $\mathbf{a}$ direction as shown in the lower, left panel, and one refers to the reconstructed cell as a (2×1) cell. Furthermore, one can by other surface techniques (such as Scanning Tunnelling Microscopy, STM) determine that there is only half a monolayer of Cu atoms in the top layer and half a monolayer of oxygen. Finally, one knows that in the bulk structure of Cu_2O, the oxygen is located midway between two Cu atoms with a Cu-O bond length of 1.852 Å, which is only slightly larger than $b/2 = a_c/2 = 1.8075$ Å. It is therefore a good starting point to assume a model where every second row of Cu atoms along the $\mathbf{b}$ direction is missing (as this gives half a monolayer), and where half a monolayer of oxygen atoms is formed by the oxygen atoms occupying positions midway between neighbouring Cu atoms along the $\mathbf{b}$ direction. As Cu-O-Cu bonds are slightly larger

Direct lattice

Reciprocal lattice
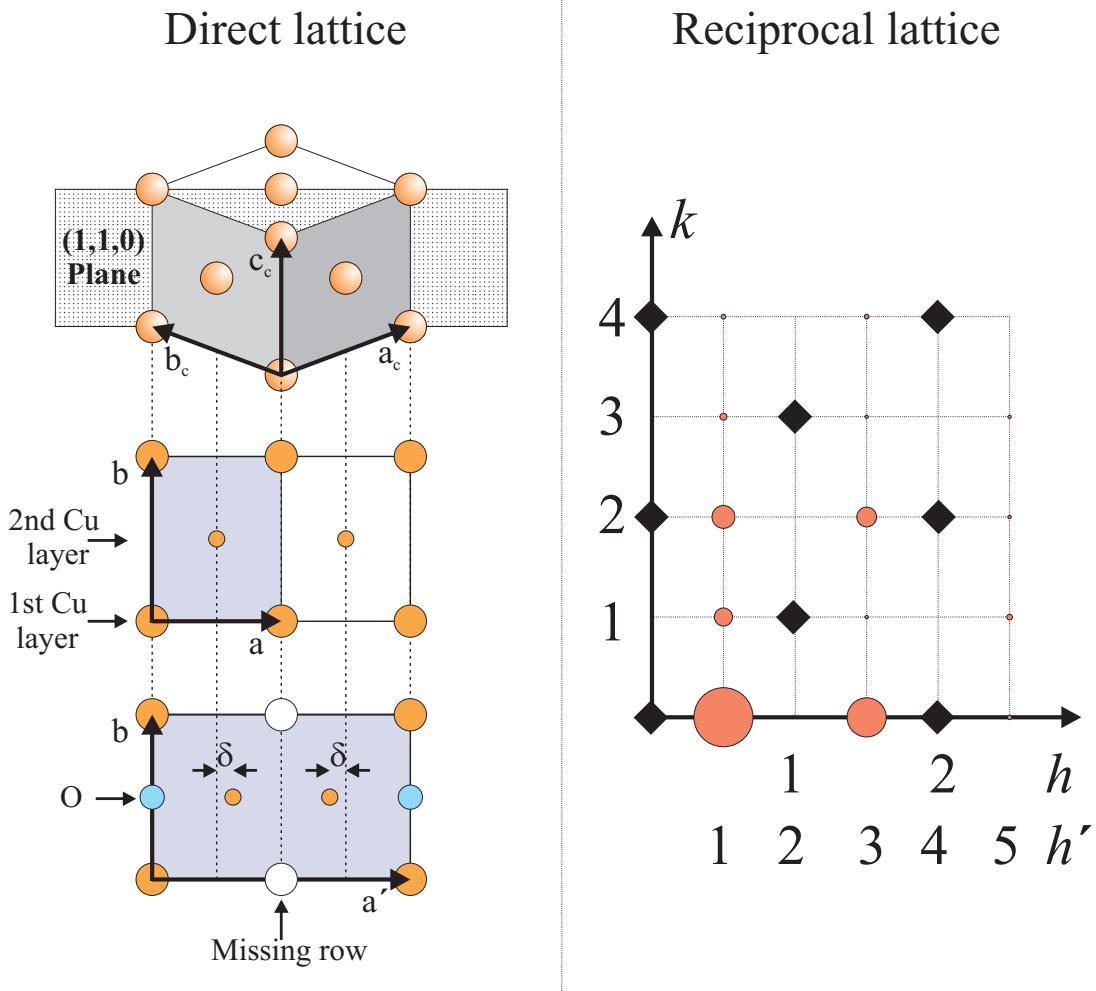
Fig. 5.30 Top, left: The face centred cubic structure of Cu with a (110) plane indicated. The lattice vectors $(\mathbf{a}_c, \mathbf{b}_c, \mathbf{c}_c)$ of the *conventional* unit cell are shown. Middle, left: The structure of the (110) surface layer, with the unit cell defined by **a** and **b**. Bottom, left: A model for the Cu surface exposed to O, with half of the Cu atoms in the surface layer missing along the **a** direction. Right: The reciprocal lattice of the Cu surface after exposure to O. The reflections arising from the doubling of the unit cell along the **a** direction (shown in the bottom, left panel) are represented by the filled circles, where their radius is proportional to the measured Bragg intensity. The diamonds indicate the allowed Bragg reflections from bulk Cu.

		k				
		0	1	2	3	4
	1	10.7 (10.7)	3.29 (3.85)	4.13 (4.23)	1.27 (1.01)	0.86 (0.75)
h'	3	7.09 (7.04)	0.39 (0.68)	3.58 (3.72)	0.32 (0.15)	0.84 (0.96)
	5	0.16 (0.52)	1.02 (1.23)	0.21 (0.23)	0.41 (0.48)	-

Table 5.2 ⋆ Observed intensities in arbitrary units for (h', k, l) reflections for O on Cu(110) with $l = 0$. The intensities from the model described in the text are given in the brackets.

than $a_c/2 = 1.8075$ Å it is also likely that the O is displaced an amount z Å above or below the Cu-plane, with z given by $(1.8075^2 + z^2) = 1.852^2$. As a refinement, one could further imagine that the Cu atoms in the next layer are pushed towards the missing row by an amount δ. This model unit cell is shown in the lower, left panel of Fig. 5.30.

The intensities observed in the experiment are given in Table 5.2⋆, where corrections have been made for the Lorentz factor $1/\sin 2\theta$ as well as for the crossed beam area, which is also proportional to $1/\sin 2\theta$. These data are also indicated in Fig. 5.30 as the shaded circles in reciprocal space. The area of each circle is proportional to the measured intensity when corrected for Lorentz factor and scattering area. In the reciprocal lattice the allowed bulk reflections are indicated by the diamonds.

Let us first discuss the in-plane data ($l \approx 0$) given in Table 5.2⋆. For h' odd and integer k, the structure factor for the first two layers (i.e. the top layer of unit cells) is the sum of three terms:

$$F_{h'k} = F^{Cu1} + F^{O} + F^{Cu2}$$

where Cu1 and O refer to the first layer, and Cu2 to the Cu in the second layer. Using the unit cell shown in the bottom panel on the left of Fig. 5.30 the structure factors are

$$F^{Cu1} = f^{Cu} e^{-M_{Cu1}}$$
$$F^{O} = f^{O} e^{i 2\pi(k/2)} e^{-M_O} = (-1)^k f^{O} e^{-M_O}$$
$$F^{Cu2} = f^{Cu} e^{i 2\pi(k/2)} e^{i 2\pi(h'/4)} \left[e^{i 2\pi h' \delta} - e^{-i 2\pi h' \delta} \right] e^{-M_{Cu2}}$$
$$= f^{Cu} e^{i \pi k} e^{i \pi h'/2} 2i \sin(2\pi h' \delta) e^{-M_{Cu2}}$$
$$= (-1)^{h'/2+k+1/2} f^{Cu} 2 \sin(2\pi h' \delta) e^{-M_{Cu2}}$$

In evaluating the contribution from the second layer with Cu atoms we have utilized that for odd h', which we are dealing with in the table, $e^{i 2\pi(3h'/4)} = -e^{-i 2\pi(h'/4)}$. We have also taken into account that the thermal vibration (Debye-Waller) factor e^{-M} may be different for Cu atoms in the first layer and in the second layer, where the atoms are more tightly bound than in the first layer. The best fit to the data are obtained for $\delta = 0.00606$, corresponding to a displacement of 0.031 Å, and Debye-Waller factors of $B_T^{Cu1} = 1.7 \pm 0.2$ Å^2, and $B_T^{O} = 0 \pm 0.4$ Å^2. (For the second Cu layer B_T^{Cu2} was set equal to the value of 0.55 Å^2 for bulk copper.) The Debye-Waller factor is discussed in Section 5.4, and for the present example the relationship between the parameters M_X and B_T^X for element X is

$$M_X = B_T^X \left(\frac{\sin \theta}{\lambda} \right)^2 = B_T^X \left(\frac{G_{h'k}}{4\pi} \right)^2 = B_T^X \left(\frac{1}{4\pi} \right)^2 \left\{ (h' a^*/2)^2 + (kb^*)^2 \right\}$$

With these parameters the observed and calculated intensities for the in-plane reflections (given in brackets in Table 5.2⋆) are seen to be in good agreement.

In addition to these measurements, CTR's along ($h = 1, k = 0, l$) and ($h = 1, k = 1, l$) were also measured with the results shown in Fig. 5.31⋆. The CTR data can be modelled by first considering the crystal to be ideally terminated, and then by adding to the complexity of the model until agreement with the data is reached. Successive layers along the surface normal direction have a phase factor of $e^{i\Psi}$, where $\Psi = \pi(h + k + l)$. The structure factor of the CTR from the ideally terminated surface is then given by

$$F_{hk}^{CTR}(l) = f^{Cu}e^{-M_{Cu2}} \sum_{n=0}^{\infty} e^{in\Psi}$$

$$= f^{Cu}e^{-M_{Cu2}} \frac{1}{1 - e^{i\Psi}} \tag{5.39}$$

This is plotted as the dashed-dotted curve in Fig. 5.31⋆, and is in poor agreement with the data. What is missing from the model is a description of the surface structure, here denoted by $F_{hk}^{S}(l)$, so that the
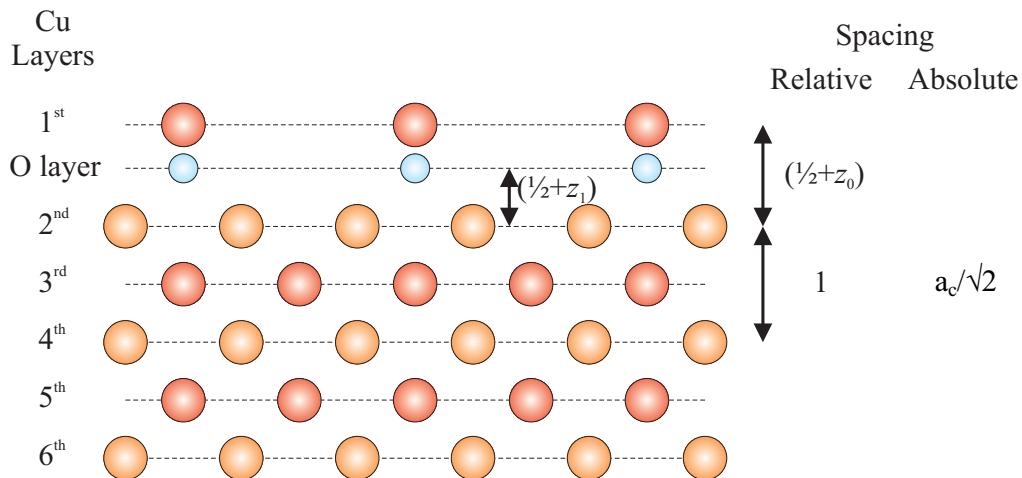
Fig. 5.32 Schematic of the side view of O on Cu(110) surface showing the possible displacements perpendicular to the surface of the oxygen and copper atoms z_1 and z_0 respectively. The view is along the **b** axis of Fig. 5.30, and the displacements are not to scale.

total structure factor is

$$F_{hk}^{\text{total}}(l) = F_{hk}^{\text{CTR}}(l) + F_{hk}^{\text{S}}(l)$$

The simplest modification to the model is to allow for the missing row structure by adding half a monolayer of Cu atoms by writing

$$F_{hk}^{\text{S}}(l) = \frac{1}{2} f^{\text{Cu}} \, e^{-M_{\text{Cu1}}} \, e^{i\pi(h+k)} \, e^{-i\pi l}$$

The last two phase factors arise because the origin in Eq. (5.39) was taken at $n = 0$, so that the next layer up is displaced in the negative z direction by half of a lattice unit, and is displaced in the plane by $(1/2, 1/2)$ (see middle left panel of Fig. 5.30). When this is added to F_{hk}^{CTR} it results in the dashed curve in Fig. 5.31$\star$. Better agreement with the data is achieved by allowing the topmost Cu layer to relax outwards, and by including the oxygen (Fig. 5.32). The surface structure factor then becomes

$$F_{hk}^{\text{S}}(l) = \frac{1}{2} \, e^{i\pi(h+k)} (f^{\text{Cu}} \, e^{-M_{\text{Cu1}}} \, e^{-i2\pi(1/2+z_0)l} + f^{\text{O}} \, e^{i\pi k} \, e^{-i2\pi(1/2+z_1)l})$$

The best fit to the data is found with $z_0 = 0.1445$ and $z_1 = 0.0115$.

5.7   Further reading

Crystallography

An Introduction to X-ray Crystallography, M.M. Wolfson (Cambridge University Press, 1997).

X-ray Diffraction, B.E. Warren (Dover Publications, 1990).

International Tables of Crystallography, (Kluwer Academic Publishers).

Solid State Physics

Solid State Physics, J.R. Hook and H.E. Hall (John Wiley & Sons, 1991).

Introduction to Solid State Physics, C. Kittel (John Wiley & Sons, 1996).

Surface Crystallography

Surface Structure Determination by X-ray Diffraction, R. Feidenhans'l, Surface Science Reports **10**, 105 (1989).

Surface X-ray Diffraction, I.K. Robinson and D.J. Tweet, Rep. Prog. Phys. **55**, 599 (1992).

Critical Phenomena at Surfaces and Interfaces: Evanescent X-ray and Neutron, H. Dosch (Springer Tracts in Modern Physics 126, 1992).

5.8   Exercises

5.1   The primitive lattice vectors of the two-dimensional hexagonal Bravais lattice may be written in Cartesian coordinates as $\mathbf{a}_1 = a(1,0)$ and $\mathbf{a}_2 = a(-1/2, \sqrt{3}/2)$ where a is the lattice constant.

(a)   Sketch the direct lattice, indicate the $(1,0)$ and $(1,1)$ planes and use the sketch to calculate their d spacings.

(b)   Show that a reciprocal lattice vector $\mathbf{G}$ of the two-dimensional Hexagonal Bravais lattice may be written as $\mathbf{G} = h(2\pi/a)(1, 1/\sqrt{3}) + k(2\pi/a)(0, 2/\sqrt{3})$ where (h, k) are the Miller indices.

(c)   Sketch the reciprocal lattice.

(d)   The Wigner-Seitz cell in two dimensions is defined to be the area enclosed by lines drawn as perpendicular bisectors between the lattice point at the origin and its nearest neighbours. Make sketches of the Wigner-Seitz cells of the direct and reciprocal lattices.

(e)   Use the result in (b) to find an expression for the d spacing, and from this calculate the d spacing of the $(1,0)$ and $(1,1)$ planes. (You should get the same answer as in (a).)

5.2   A diffraction experiment on a cubic crystal, using monochromatic X-rays with a wavelength of 1.0 Å, reveals the first eight powder lines at the following scattering angles: 19.2°, 27.3°, 33.6°, 38.9°, 43.8°, 48.2°, 56.3°, 60.0°. Deduce the Bravais lattice type.

5.3   Imagine that the data in the Exercise 5.2 were recorded with neutron rather than X-ray scattering. Make a sketch of the powder diffraction pattern expected, plotting the Bragg peaks with the correct relative intensities. Note: for neutrons the scattering length of a nucleus is a constant, and also there is no polarization factor P to consider. You may also neglect the effect of thermal vibrations.

5.4   NaH crystallizes in the NaCl structure. Experimentally it is found that when studied with X-rays reflections with (h, k, l) all odd or all even are visible, whereas when studied with neutrons reflections with (h, k, l) all even are negligibly weak. Explain this result.

5.5 The primitive lattice vectors of the hexagonal Bravais lattice in three dimensions may be written in Cartesian coordinates as $\mathbf{a}_1 = a(1,0,0)$, $\mathbf{a}_2 = a(1/2, \sqrt{3}/2,0)$ and $\mathbf{a}_3 = c(0,0,1)$. Show that the modulus of a general reciprocal lattice vector is

$$|\mathbf{G}| = 2\pi \left(\frac{4}{3a^2} \left(h^2 - hk + k^2 \right) + \frac{l^2}{c^2} \right)^{1/2}$$

and use this result to to derive the general expression for the lattice spacing d_{hkl}.

5.6 The hexagonal close packed structure is formed from convoluting a two atom basis with the hexagonal Bravais lattice. The coordinates of the atoms in the basis may be taken as $\mathbf{r}_1 = (0,0,0)$ and $\mathbf{r}_2 = (a/3, a/3, c/2)$, now written with respect to the direct lattice vectors $(\mathbf{a}_1, \mathbf{a}_2, \mathbf{a}_3)$ given above. Show that the unit cell structure factor is

$$F_{hkl} = 1 + e^{2\pi i(h/3 + k/3 + l/2)}$$

Holmium crystallizes in the hcp structure with lattice parameters of a=3.57 Å and c=5.61 Å. Assuming an X-ray wavelength of 1Å, calculate the scattering angles 2θ of the two observable Bragg reflections closet to the origin.

5.7 Show that for a cubic material the Debye-Waller factor can be written as

$$e^{-M} = e^{-B_T(h^2 + k^2 + l^2)/(4a^2)}$$

Silicon has a Debye temperature of 645 K and a lattice constant of 5.43 Å. On heating silicon from 0 K which is the first Bragg peak to lose 5% of its Bragg peak intensity at room temperature.

5.8 Show that for a one-dimensional crystal the mean squared atomic displacement diverges causing the Debye-Waller factor to vanish.

5.9 Consider a simple model of the surface roughness of a crystal in which all of the lattice sites of the $z = 0$ layer are fully occupied by atoms, but the next layer out ($z = -1$) has a site occupancy of η, with $\eta \leq 1$, the $z = -2$ layer an occupancy of η^2, etc. Show that midway between the Bragg points, the so-called anti-Bragg points, the intensity of the crystal truncation rods is given by

$$I^{CTR} = \frac{(1 - \eta)^2}{4 (1 + \eta)^2}$$

What effect does a small, but finite, value of the roughness parameter η have on I^{CTR}?

5.10 Half a monolayer is added randomly to the surface of a crystal, with the half-monolayer composed of the same material as the bulk crystal. Calculate the crystal truncation rod intensity for this situation, and determine the CTR intensity at the anti-Bragg position. What does this result suggest for an experimental method to monitor layer-by-layer growth of a crystal?

Diffraction by perfect crystals

The X-ray beam from a synchrotron source is polychromatic. Typical values for the bandwidth in energy vary between a fraction of a keV for an undulator, up to a few hundred keV or so in the case of a bending magnet. Many experiments require a monochromatic beam, where both the energy and energy bandwidth can be set to convenient values. By far the most common type of monochromator is a crystal that Bragg reflects an energy band, or equivalently wavelength band, out of the incident beam. The band is centred around a wavelength λ given by Bragg's Law, $m\lambda = 2d \sin\theta$, where d is the lattice spacing, θ is the angle between the incident beam and the lattice planes, and m is a positive integer.

One requirement of a monochromator crystal is that it preserves the inherently good angular collimation of the synchrotron beam, which is of order 0.1 mrad. For this reason, perfect crystals, which are essentially free from any defects or dislocations, are often used. However, even a perfect crystal does not have an infinitely sharp response, but instead has an intrinsic width. This width may be defined in various ways, depending on the type of experiment imagined. Here we shall start out by considering the relative wavelength band, $\zeta = (\Delta\lambda/\lambda)$, a perfect crystal reflects out of a white, parallel incident beam.

Candidate monochromator crystals must not only be perfect, but they should maintain their perfection when subjected to the large heat loads imposed by the incident white beam. In practice, few materials can meet these exacting requirements. Most monochromators are either fabricated from silicon, diamond or germanium, with each having its own advantages depending on the application, as discussed later.

To develop a theory of the diffraction of X-rays from perfect crystals it is necessary to go beyond the kinematical approximation used in Chapter 5. This approximation applies to imperfect crystals, formed from microscopic mosaic blocks (see Fig. 5.19 on page 183). The size of these blocks is taken to be small, in the sense that the magnitude of the X-ray wavefield does not change appreciably over the depth of the block[1]. The scattering amplitude is then evaluated by summing together the amplitude of the waves scattered by each unit cell, taking into account the appropriate phase factors. Diffraction from macroscopic perfect crystals is fundamentally different from this scenario. As the incident wave propagates down into the crystal its amplitude diminishes, as a small fraction is reflected into the exit

[1]The X-ray beam may of course be attenuated by absorption.

(a) symmetric Bragg

(b) symmetric Laue

$Q=mG(1+\zeta)$

$Q=mG$

Δk

k k'

k k'

d

d
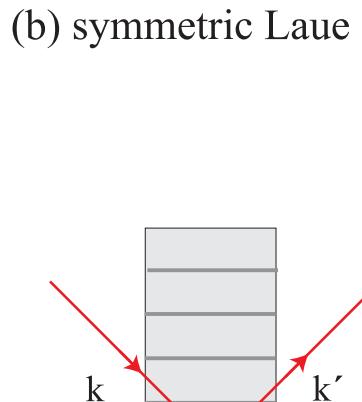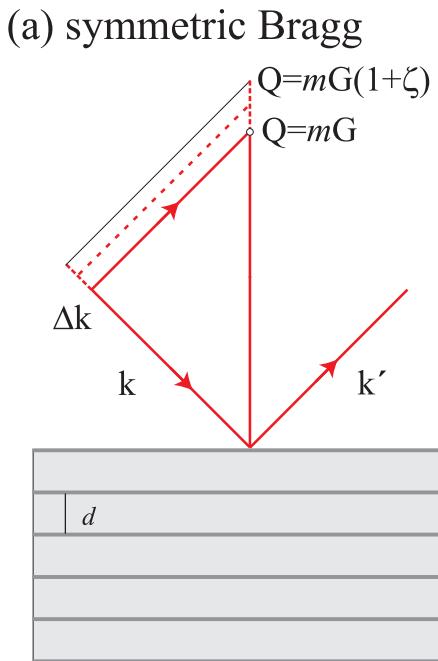
Fig. 6.1 Diffraction by a crystal with a lattice spacing of d in (a) Bragg reflection and (b) Laue transmission geometries. Both cases are symmetric since the incident and exit beams form the same angle with respect to the physical surface. The incident beam is assumed to be parallel and white. The crystal reflects a width in wavevector given by Δk. The small variable ζ is defined by $\zeta = \Delta G/G \equiv \Delta k/k$. The relative energy bandwidth or wavelength bandwidth is also equal to $\Delta k/k$.

beam as it passes through each atomic plane. In addition there is a chance that the reflected beam will be re-scattered into the direction of the incident beam before it has left the crystal. The theory which has been developed to allow for these multiple scattering effects is known as dynamical diffraction theory.

At the outset it is important to specify exactly the scattering geometry, as it transpires that this has a profound influence on the diffraction profile from a perfect crystal. Diffraction may occur either in reflection or transmission, which are known as Bragg and Laue geometries respectively, as shown in Fig. 6.1. The angle that the physical surface makes with respect to the reflecting atomic planes is also an important factor. The reflection is said to be symmetric if the surface normal is perpendicular (parallel) to the reflecting planes in the case of Bragg (Laue) geometry. Otherwise it is asymmetric. Within the kinematical approximation the scattering is independent of the geometry. To take one striking example of how the diffraction profile from a perfect crystal is affected by the geometry, consider the symmetric Bragg and Laue cases (Fig. 6.1), and imagine that the incident beam is perfectly collimated and white, in the sense that it contains a continuous distribution of wavelengths. As we shall see, in the Bragg case the collimation of the beam is preserved, whereas the Laue geometry imparts an angular divergence to the reflected beam even though the incident beam is perfectly collimated. To start with we shall examine the symmetric Bragg case, and later explain how the results are modified with the crystal set in an asymmetric Bragg or Laue geometry.

The approach followed here is essentially the same as the one first developed by C. G. Darwin in 1914. In his method, Darwin treated the crystal as an infinite stack of atomic planes, each of which gives rise to a weak reflected wave which may subsequently be re-scattered into the direction of the
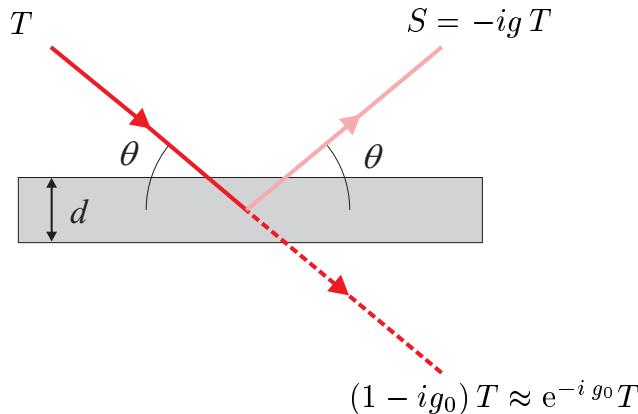
Fig. 6.2 A wave T incident on a sheet of unit cells will be partly reflected and partly transmitted. The reflected wave is $-i\,gT$, and the transmitted wave is $T(1 - ig_0)$, where g and g_0 are small parameters given in the text.

incident beam. An alternative approach was developed by Ewald (1916-1917), and later re-formulated by von Laue (1931). They treated the crystal as a medium with a periodic dielectric constant, and then solved Maxwell's equations to obtain results in agreement with those derived earlier by Darwin.

Before deriving the dynamical theory, the reader is reminded of a few important results concerning the reflectivity from a thin slab. The kinematical diffraction from a stack of thin slabs is then calculated. This differs from the discussion in Chapter 5 as effects due to refraction are now included. The kinematical approximation is of importance, as any dynamical theory must give the same results in the limit of weak scattering.

6.1   One atomic layer: reflection and transmission

Consider an X-ray beam incident on a thin layer of electrons of density ρ and with a thickness d, such that $d \ll \lambda$, as shown in Fig. 6.2. The incident wave, T, is partly reflected specularly from the layer, and partly transmitted through it. From Eq. (3.24) in Chapter 3 we know that the reflected wave is phase shifted by $-\frac{\pi}{2}$ (i.e. by a factor of $-i$) with respect to the incident wave, and has an amplitude equal to

$$g = \frac{\lambda r_0 \rho\, d}{\sin \theta}$$

To generalize this expression so that it is applicable to the scattering from a layer of unit cells, the density ρ is replaced by $|F|/v_c$, where F is the structure factor of the unit cell, and v_c is its volume. This is a necessary step, as it can no longer be assumed that d is small compared to the wavelength, and hence destructive interference will reduce the scattering at higher scattering angles (see Section 4.2). Using Bragg's law, $m\lambda = 2d \sin \theta$ the above becomes

$$g = \frac{[2d \sin \theta/m]\, r_0\, (|F|/v_c)\, d}{\sin \theta} = \frac{1}{m}\left(\frac{2d^2 r_0}{v_c}\right)|F| \tag{6.1}$$

Since v_c is of order d^3, g is of order $r_0/d \simeq 10^{-5}$, and the reflectivity of even a thousand layers is approximately 10^{-2} only[2]. For simplicity the incident wave has been assumed to be polarized with its electric field perpendicular to the plane containing the wavevectors of the incident and reflected beams, so that the polarization factor, P, is unity (see Eq. (1.8)).

The transmitted wave in Fig. 6.2 may be written as $(1 - ig_0)T \approx e^{-ig_0}T$, since g_0 is the small real number given by Eq. (3.6) on page 75. This equation may be recast in terms of g as

$$g_0 = \frac{|F_0|}{|F|} g \tag{6.2}$$

Here F_0 is the unit-cell structure factor in the forward direction, i.e. $Q = \theta = 0$. We note that for forward scattering the polarization factor is always equal to unity, independent of the polarization of the incident beam.

6.2   Kinematical reflection from a few layers

A single layer of atoms reflects an X-ray beam only very weakly. It is straightforward to derive the reflectivity from a stack of N layers as long as the product of N and the reflectivity per layer, g, is small, i.e. $Ng \ll 1$. In this case we simply add the amplitude of rays reflected from layers at different depths in the stack, taking into account the phase factor e^{iQdj}, where j labels the layer. This is the so-called kinematical approximation, and the *amplitude* reflectivity for N layers is

$$r_N(Q) = -ig \sum_{j=0}^{N-1} e^{iQdj} e^{-ig_0 j} e^{-ig_0 j}$$

$$= -ig \sum_{j=0}^{N-1} e^{i(Qd-2g_0)j} \tag{6.3}$$

The phase shift is $2g_0$ rather than just g_0 as each layer is traversed twice, once in the T direction, and once in the S direction.

The reciprocal lattice of a stack of layers with layer spacing d is a line of points in reciprocal space at multiples, m, of $G = 2\pi/d$. In general we are interested in small, relative deviations of the scattering vector Q away from mG, so that

$$Q = mG (1 + \zeta) \tag{6.4}$$

where ζ is then the small relative deviation (see Fig. 6.1). This is equivalent to the relative bandwidth in energy (or wavelength) since

$$\zeta = \frac{\Delta Q}{Q} = \frac{\Delta k}{k} = \frac{\Delta \mathcal{E}}{\mathcal{E}} = \frac{\Delta \lambda}{\lambda} \tag{6.5}$$

---

[2]Writing Bragg's law as $m\lambda = 2d \sin \theta$ implies that d is the longest lattice spacing for a given family of planes (h, k, l). For example, if one is considering the (220) reflection, say, then the d spacing is calculated for the (110) planes, and the appropriate value of m is 2.

The phase appearing in the exponential of Eq. (6.3) can thus be rewritten in terms of ζ as

$$Qd - 2g_0 = mG(1 + \zeta)\frac{2\pi}{G} - 2g_0$$
$$= 2\pi\left(m + m\zeta - \frac{g_0}{\pi}\right)$$

The sum then becomes

$$\sum_{j=0}^{N-1} e^{i(Qd-2g_0)j} = \sum_{j=0}^{N-1} e^{i\,2\pi m j} e^{i\,2\pi(m\zeta-g_0/\pi)j}$$
$$= \sum_{j=0}^{N-1} e^{i\,2\pi(m\zeta-g_0/\pi)j}$$

and this geometric series can be summed (see page 52) to yield

$$|r_N(\zeta)| = g\left|\frac{\sin(\pi N[m\zeta - \zeta_0])}{\sin(\pi[m\zeta - \zeta_0])}\right| \tag{6.6}$$

where ζ_0 is the displacement of the Bragg peak defined by

$$\zeta_0 = \frac{g_0}{\pi} = \frac{2d^2|F_0|}{\pi m v_c} r_0 \tag{6.7}$$

To derive the explicit expression for ζ_0 above we have used the defining expression for g_0 in Eq. (3.6) with $\Delta = d$, $\sin\theta = m\lambda/(2d)$ and $\rho_a f^0(0) = |F_0|/v_c$.

From Eq. (6.6) the maximum amplitude reflectivity is Ng, and occurs when $\zeta = \zeta_0/m$. Therefore the reflectivity does not have its maximum at the reciprocal lattice points, but is displaced by a *relative* amount ζ_0/m. It follows from Eq. (6.4) that the *absolute* displacement is $mG(\zeta_0/m) = G\zeta_0$ which according to Eq. (6.7) varies as $1/m$. This displacement arises from the refraction of the incident wave as it enters the crystal, an effect that is usually neglected in the derivation of Bragg's law. The index of refraction is less than unity for X-rays, and inside the crystal the modulus of the X-ray wavevector has a smaller value than outside. For a fixed incident angle, the value of k outside of the crystal must be larger than $mG/(2\sin\theta)$ in order to obtain maximal constructive interference, i.e. $\zeta_0 > 0$ as is also clear from Eq. (6.7).

For the kinematical approximation to be valid it is required that $Ng \ll 1$. Adding more and more layers with a reflectivity g per layer increases the peak reflectivity, but of course it can never exceed 100%. Close to $\zeta = \zeta_0/m$ the line shape starts to deviate from $|r_N(\zeta)|^2$ given by Eq. (6.6), and we enter into the dynamical diffraction as indicated by the shading in Fig. 6.3. However, when far enough away from the Bragg condition, i.e. when ζ is sufficiently different from ζ_0/m, the kinematical approximation is still valid, even for many layers. When N becomes large the side lobes of the function $|r_N(\zeta)|^2$ become closely spaced, and the rapidly varying numerator $\sin^2(N\pi[m\zeta-\zeta_0])$ can be approximated by its average value of $1/2$ to obtain

$$|r_N(\zeta)|^2 \to \frac{g^2}{2\sin^2(\pi[m\zeta - \zeta_0])} \approx \frac{g^2}{2(\pi[m\zeta - \zeta_0])^2} \tag{6.8}$$
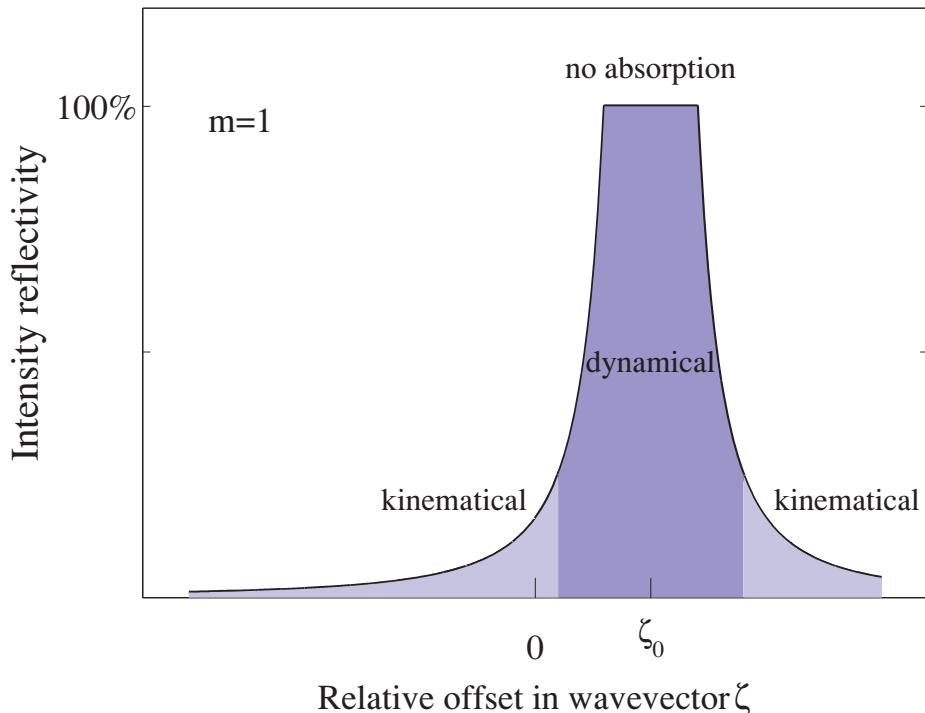
Fig. 6.3 The intensity reflectivity from a stack of N atomic layers. The relative deviation from the Bragg condition is given by the parameter ζ. The reflectivity is peaked not at $\zeta = 0$, but at $\zeta_0 = g_0/(m\pi)$ due to refraction of the X-ray beam inside of the crystal. When $|\zeta - \zeta_0|$ is large the reflectivity is small, and we are in the kinematical regime as indicated by the lighter shading. As $|\zeta - \zeta_0| \to 0$ the kinematical approximation breaks down, and the reflectivity is then described by dynamical theory.

The significance of this result is that a correct dynamical diffraction theory must attain this limiting form for large values of $|\zeta - \zeta_0|$. In Fig. 6.3 the kinematical region is indicated by the lighter shading.

Dynamical reflection takes place near a reciprocal lattice point, and must join the kinematic reflection regime in a continuous way. It has been shown in Section 5.3 that the surface gives rise to rods of scattering in a direction perpendicular to the physical surface. Continuity then requires that the region of dynamical diffraction and these so-called crystal truncations rods must be connected in a continuous manner. This has the somewhat surprising consequence that the reflection from an asymmetric cut crystal is no longer specular – specular reflection only occurs from a symmetrically cut crystal in Bragg geometry. We shall return to this issue at the end of this chapter.

6.3   Darwin theory and dynamical diffraction

We now turn our attention to the problem of how to calculate the scattering from an infinite stack of atomic planes, where each one reflects and transmits the incident wave according to the equations given in Section 6.1. The planes are labelled by the index j, with the surface plane defined by $j = 0$ (Fig. 6.4(a)). The objective is to calculate the amplitude reflectivity, which is the ratio of the total reflected wavefield S_0 to that of the incident field T_0.
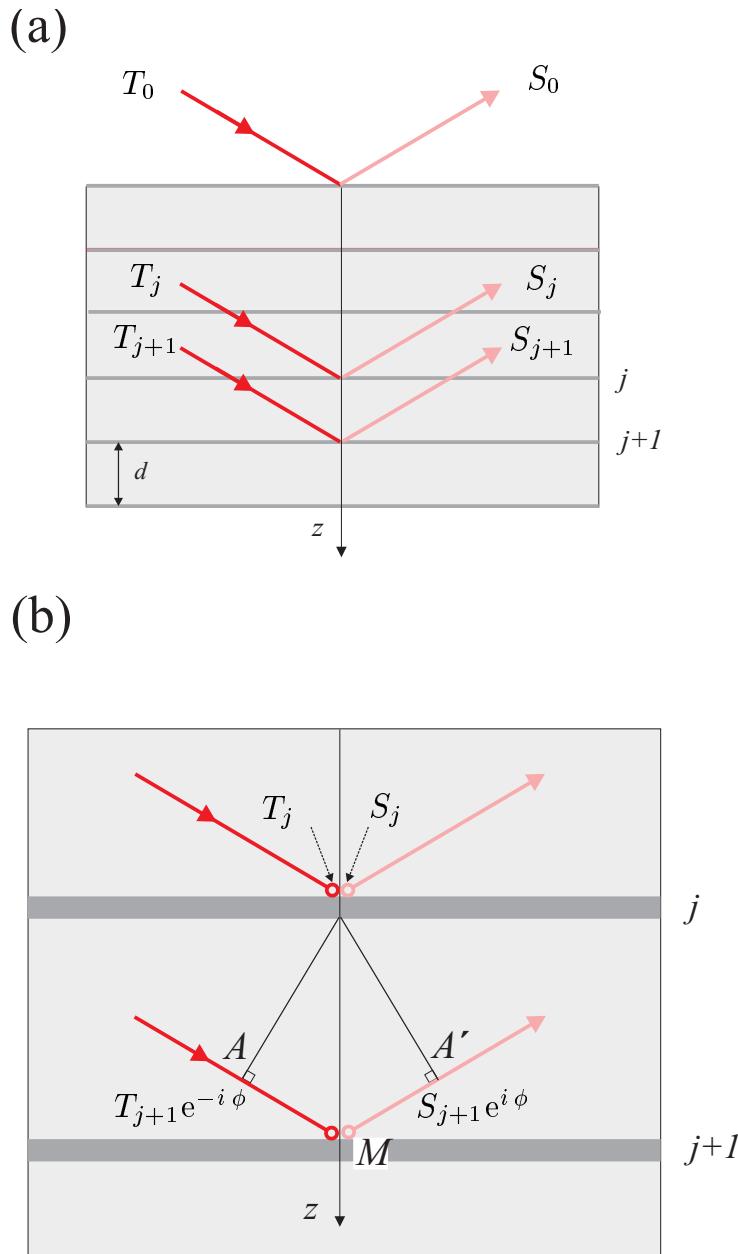
Fig. 6.4 Definition of the T and S wavefields. (a) The amplitude reflectivity is given by S_0/T_0. (b) Schematic used to derive the difference equations. The S field at A' is related to the S field just above the atomic plane at M by the phase factor $e^{i\phi}$. The field $S_{j+1}e^{i\phi}$ is then the same as the S_j field just below layer j. Above layer j it gets an extra contribution $(-igT_j)$, from reflection of the T field. Similar arguments apply to the T field.

Both outside and within the crystal there are two wavefields: the T field propagating in the direction of the incident beam, and the S field in the direction of the reflected beam. These fields change abruptly when they pass through the atomic planes for two reasons. First, a small fraction, equal to $-ig$, of the wave is reflected. Second, the transmitted wave is phase shifted by an amount $(1 - ig_0)$. The derivation of Bragg's law relies on the fact that the reflected wave from layer $j + 1$ is in phase with the one from layer j if the pathlength differs by an integer number of wavelengths. In Fig. 6.4(b) this corresponds to the requirement[3] that the distance AMA' is equal to $m\lambda$, or equivalently that the phase shift in going from A to M is $m\pi$. As we are interested in deriving the (small) bandwidth of the reflecting region, the phase is restricted to small deviations about $m\pi$, and the phase is then given by

$$\phi = m\pi + \Delta$$

where Δ is a small parameter. The relative deviation in phase is therefore $\Delta/(m\pi)$, which must be equal to the corresponding relative deviation in scattering vector, ζ (Eq. (6.4)), so that

$$\Delta = m\pi\, \zeta \tag{6.9}$$

In our development of Darwin's theory Δ will be used as the independent variable. We remind the reader that we are considering a perfectly collimated incident beam, so that the variation of Δ is through the variation of incident energy (or wavenumber), *c.f.* Eq. (6.5). Later when the algebra has been worked through, the results will be recast in terms of ζ, which is more useful for comparisons with experiment.

The fundamental difference equations

Let the T field just *above* layer j on the z axis be denoted T_j, and similarly for S_j. The S field just above layer $j + 1$ is S_{j+1} on the z axis, that is the point M in Fig. 6.4. At point A' it is $S_{j+1}e^{i\phi}$, and indeed it must have this value at any point on the wavefront through A', including the point on the z axis just below the j'th plane. On being transmitted through the j'th layer it changes its phase by the small amount $-ig_0$ so that the S field just above the j'th layer, which by definition is S_j, can be written as $(1 - ig_0)S_{j+1}e^{i\phi}$. To obtain the total field, we must also add the part due to the reflection of the wave T_j. In total then we have

$$S_j = -ig\, T_j + (1 - ig_0)S_{j+1}e^{i\phi} \tag{6.10}$$

Next consider the T field just below the j'th layer. This must be the same field that exits at M, except that its phase is shifted by an amount that corresponds to the distance from M to A, i.e. $T_{j+1}e^{-i\phi}$. This field is composed of contributions from the field T_j after it has been transmitted through the j'th layer, and from the wave $S_{j+1}e^{i\phi}$ after it has been reflected from the bottom of the j'th layer. This leads to the second difference equation

$$T_{j+1}e^{-i\phi} = (1 - ig_0)T_j - ig\, S_{j+1}e^{i\phi} \tag{6.11}$$

The coupled T to S fields in Eq. (6.11) and (6.10) are separated in the following way.

---

[3]Here it should be understood that λ is the wavelength inside the crystal, not the wavelength of the incident beam outside of the crystal.

Separating the T and S fields

We rewrite Eq. (6.11) as

$$ig\, S_{j+1} = (1 - ig_0)T_j e^{-i\phi} - T_{j+1} e^{-i2\phi} \tag{6.12}$$

The validity of this equation does not depend on the labelling, and in particular it must also hold for the field S_j. Replacing $j + 1$ by j, and j by $j - 1$ yields

$$ig\, S_j = (1 - ig_0)T_{j-1} e^{-i\phi} - T_j e^{-i2\phi} \tag{6.13}$$

The expressions for $ig\, S_{j+1}$ and $ig\, S_j$ given in Eq. (6.12) and (6.13) can now be substituted into Eq. (6.10) (after multiplying it by a factor of ig) to obtain an equation purely in terms of the T fields:

$$(1 - ig_0)T_{j-1} e^{-i\phi} - T_j e^{-i2\phi} = g^2 T_j + (1 - ig_0)[(1 - ig_0)T_j - T_{j+1} e^{-i\phi}]$$

Collecting the coefficients of T_{j+1}, T_j and T_{j-1} together one finds

$$(1 - ig_0)e^{-i\phi}[T_{j+1} + T_{j-1}] = [g^2 + (1 - ig_0)^2 + e^{-i2\phi}]T_j \tag{6.14}$$

Trial solution for the T and S fields

Possible solutions to the equation for the T fields are now considered. The fields T_j and T_{j+1} are almost out of phase, as is apparent from Eq. (6.11), since ϕ is approximately $m\pi$ and g_0 and g are small parameters. Moreover, it is expected that the T field is attenuated as it penetrates into the crystal, since a fraction of the incident beam is reflected out of the crystal when it passes through each atomic plane. A suitable trial solution therefore has the form

$$T_{j+1} = e^{-\eta} e^{im\pi} T_j \tag{6.15}$$

where η is in general complex. In order that the beam is attenuated only slightly from one plane to the next the real part of η must be small and positive. Inserting our trial solution into Eq. (6.14), and noting that $e^{-i\phi} = e^{-im\pi} e^{-i\Delta}$ and that $e^{\pm i2m\pi} = 1$ yields

$$(1 - ig_0)e^{-i\Delta}[e^{-\eta} + e^{\eta}] = g^2 + (1 - ig_0)^2 + e^{-i2\Delta}$$

Use is now made of the fact that all of the parameters in the above expression are small compared to unity. By expansion one finds cancellation of zero and first-order terms on the left and right hand sides. Equating second-order terms leads to the expression for η:

$$\eta^2 = g^2 - (\Delta - g_0)^2$$

which has the solution

$$\boxed{i\eta = \pm \sqrt{(\Delta - g_0)^2 - g^2}} \tag{6.16}$$

For the S fields the trial solution reads

$$S_{j+1} = e^{-\eta} e^{im\pi} S_j$$

and it can be shown that it yields the same equation for η.

Amplitude reflectivity, S_0/T_0

We are now in a position to calculate the amplitude reflectivity r, i.e. the ratio of S_0/T_0. First we set $j = 0$ in the above, and obtain $S_1 = e^{-\eta}e^{im\pi} S_0$. This is inserted into Eq. (6.10), also with $j = 0$, to give

$$S_0 = -ig\, T_0 + (1 - ig_0)S_0 e^{-\eta}e^{im\pi}e^{im\pi}e^{i\Delta} \tag{6.17}$$

This is then rearranged to read

$$\frac{S_0}{T_0} \cong \frac{-i\, g}{1 - (1 - i\, g_0)(1 - \eta)(1 + i\Delta)}$$

$$\cong \frac{-i\, g}{ig_0 + \eta - i\,\Delta} = \frac{g}{i\eta + (\Delta - g_0)}$$

Defining for convenience a new variable ϵ by

$$\epsilon = \Delta - g_0 = m\pi\zeta - \pi\zeta_0$$

and inserting the solution for $i\eta$ into the expression for S_0/T_0 leads to

$$\boxed{r = \frac{S_0}{T_0} = \frac{g}{i\eta + \epsilon} = \frac{g}{\epsilon \pm \sqrt{\epsilon^2 - g^2}}} \tag{6.18}$$

This completes our derivation of the Darwin reflectivity curve. There is, however, one point left to clarify, and that is the possible ambiguity over which sign to take with the square root in the above. To resolve this we note that if we choose the positive sign for ϵ positive, then in the limit of $\epsilon \gg g$ the intensity reflectivity decreases as $(g/(2\epsilon))^2$. For negative ϵ we choose the negative sign, as with this choice for $|\epsilon| \gg g$ the intensity reflectivity will again decrease as $(g/(2\epsilon))^2$. For $|\epsilon| < g$ the square root is purely imaginary, and the intensity reflectivity, evaluated as S_0/T_0 multiplied by its complex conjugate, is unity. This is the region of *total* reflection. In Fig. 6.5 we plot the intensity reflectivity as a function of ϵ/g. The many interesting aspects of this curve are discussed in the following section.

6.4   The Darwin reflectivity curve

In order to obtain explicit formulae for the Darwin reflectivity curve the variable x is introduced and defined by

$$x = \frac{\epsilon}{g}$$

This is related to the variable ζ through

$$x = \frac{\epsilon}{g} = \frac{\Delta - g_0}{g} = m\pi\frac{\zeta}{g} - \frac{g_0}{g} \tag{6.19}$$
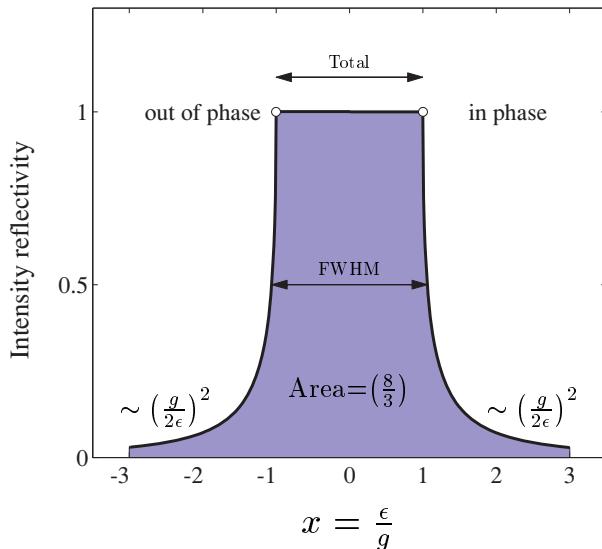
Fig. 6.5 The Darwin reflectivity curve calculated from Eq. (6.21). For values of x between -1 and 1 the reflectivity is 100%. This is known as the region of total reflection. For large values of $|x|$ the intensity decays as $1/(2x)^2$. At $x = 1$ the X-ray wavefield has its maxima on the atomic planes, whereas for $x = -1$ the nodes of the wavefield coincide with the atomic planes.

where m is the order of the reflection, i.e. $m = 1$ is the fundamental, $m = 2$ is the second-order, etc. From Eq. (6.18) the amplitude reflectivity curve in terms of x is

$$r(x) = \left(\frac{S_0}{T_0}\right) = \begin{cases} \dfrac{1}{x + \sqrt{x^2 - 1}} = x - \sqrt{x^2 - 1} & \text{for } x \geq 1 \\[2mm] \dfrac{1}{x + i\sqrt{1 - x^2}} = x - i\sqrt{1 - x^2} & \text{for } |x| \leq 1 \\[2mm] \dfrac{1}{x - \sqrt{x^2 - 1}} = x + \sqrt{x^2 - 1} & \text{for } x \leq -1 \end{cases} \qquad (6.20)$$

It follows that the intensity reflectivity is

$$R(x) = \left(\frac{S_0}{T_0}\right)\left(\frac{S_0}{T_0}\right)^* = \begin{cases} \left(x - \sqrt{x^2 - 1}\right)^2 & \text{for } x \geq 1 \\ 1 & \text{for } |x| \leq 1 \\ \left(x + \sqrt{x^2 - 1}\right)^2 & \text{for } x \leq -1 \end{cases} \qquad (6.21)$$

which is plotted in Fig. 6.5. A key feature of the Darwin reflectivity curve is that the phase shift between the T_0 and S_0 fields varies across it. This is illustrated in Fig. 6.6 where we plot the phase of the amplitude reflectivity r as a function of x. The two fields are exactly out of phase by $-\pi$ (or equivalently π) for $x \leq -1$, and in phase for $x \geq 1$.
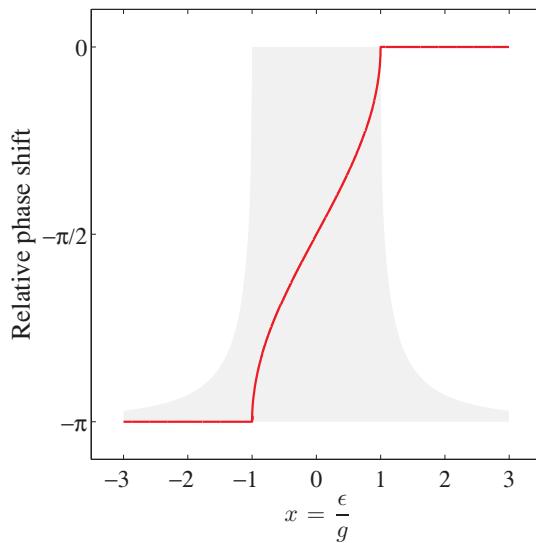
Fig. 6.6 The relative phase shift between the incident T_0 and reflected S_0 wavefields as calculated from Eq. (6.20). For reference, the Darwin curve is shown in shaded relief in the background. The two wavefileds are out of phase, here chosen to be $-\pi$, for $x \leq -1$, and in phase for $x \geq 1$.

The asymptotic form of $R(x)$ for $x \gg 1$ is

$$R(x) = \left(\sqrt{x^2(1 - \frac{1}{x^2})} - x \right)^2 \approx \left(x(1 - \frac{1}{2x^2}) - x \right)^2$$

$$= \frac{1}{4x^2} \qquad \text{for} \quad x \gg 1 \tag{6.22}$$

This should be compared to the expected asymptotic form for the kinematical region, discussed in Section 6.2. In terms of the variable x, Eq. (6.8) reads

$$|r_N(\zeta)|^2 \to \frac{1}{2x^2} \quad \text{for} \quad x \gg 1 \tag{6.23}$$

i.e. twice the result given by dynamical theory. The reason for this is subtle. In Section 6.2 the equations were derived on the assumption that the scattering arises from a finite stack of layers: the top and the bottom of the stack. Hence the wave encounters *two* interfaces. By contrast, Darwin's formalism assumes an infinite stack of layers, with only a single interface, the surface. The two asymptotic forms are therefore consistent.

6.4.1   Darwin width

One of the key parameters we are interested in obtaining is a measure of the width of the Darwin reflectivity curve. From Fig. 6.5 it is clear that there are several alternatives. First of all there is the region ($|x| < 1$) of total reflection itself, which has a width in x of 2. The relationship between x and the variable ζ is given in Eq. (6.19). This is rearranged to read

$$\zeta = \frac{gx + g_0}{m\pi} \tag{6.24}$$

	$\zeta_D^{\mathrm{FWHM}} \times 10^6$							
	(111)			(220)			(400)		
Diamond	61.0			20.9			8.5		
a= 3.5670 Å	3.03	0.018	-0.01	1.96	0.018	-0.01	1.59	0.018	-0.01
Silicon	139.8			61.1			26.3		
a= 5.4309 Å	10.54	0.25	-0.33	8.72	0.25	-0.33	7.51	0.25	-0.33
Germanium	347.2			160.0			68.8		
a= 5.6578 Å	27.36	-1.1	-0.89	23.79	-1.1	-0.89	20.46	-1.1	-0.89

Table 6.1 The calculated Darwin widths for the (111), (220) and (400) reflections in symmetric Bragg geometry from diamond, silicon, and germanium. For each reflection the values of $f^0(Q)$, f', f'' have also been listed. The values of $f^0(Q)$ have been calculated from the coefficients given in Table 4.1, and the values of f' and f'' are for a wavelength of 1.5405 Å, and have been taken from The International Tables of Crystallography. Here it has been assumed that the incident beam is polarized perpendicular to the scattering plane ($\hat{\sigma}$ polarization). For $\hat{\pi}$ polarization the widths have to be multiplied by a factor of $\cos(2\theta)$.

so that a width in x of 2 translates into a width in ζ of $2g/(m\pi)$. Thus the width ζ_D^{total} of the region of total reflectivity is

$$\zeta_D^{\mathrm{total}} = \frac{2g}{m\pi} = \frac{4}{\pi}\left(\frac{d}{m}\right)^2 \frac{r_0|F|}{v_c} \tag{6.25}$$

where g has been replaced by the expression given in Eq. (6.1). Alternatively, it is sometimes more convenient to work with the full width at half maximum (FWHM), and from Eq. (6.21) this is given by

$$\zeta_D^{\mathrm{FWHM}} = \left(\frac{3}{2\sqrt{2}}\right)\zeta_D^{\mathrm{total}} \tag{6.26}$$

For a given material and Bragg reflection the Darwin width ζ_D (Eq. (6.25)) is a constant, independent of the wavelength[4]. The same is not true for the *angular* Darwin width. The expression for the width ζ_D was derived by assuming a perfectly collimated, white incident beam. The other extreme is to consider the reflectivity of a crystal in a perfectly monochromatic beam as the incident angle is varied. It is quite straightforward to do this using the differential form of Bragg's equation:

$$\frac{\Delta\lambda}{\lambda} = \frac{\Delta\theta}{\tan\theta} \tag{6.27}$$

It follows immediately that the angular Darwin widths are

$$w_D^{\mathrm{total}} = \zeta_D^{\mathrm{total}} \tan\theta \tag{6.28}$$

---

[4]This is of course neglecting the small energy dependence of the dispersion corrections to the unit cell structure factor.

and

$$w_{\mathrm{D}}^{\mathrm{FWHM}} = \left(\frac{3}{2\sqrt{2}} \right) \zeta_{\mathrm{D}}^{\mathrm{total}} \tan \theta \tag{6.29}$$

The angular Darwin width thus varies with energy through its dependence on $\tan\theta$: as the wavelength is reduced the Bragg angle also becomes smaller, and hence so does the angular Darwin width.

Monochromators at synchrotron beamlines are most commonly fabricated from silicon. The reason is that the semiconductor industry has created a huge demand for defect-free, perfect single crystals, ensuring that the unit cost is low. In addition, silicon can be machined into complex optical elements (focusing monochromators, etc.). It also has the convenient property that the coefficient of thermal expansion passes through zero near the boiling temperature of liquid nitrogen, with the consequence that possible distortions arising from the heat deposited by the intense white beam from a synchrotron can be minimized by cryo-cooling. Silicon is by no means the only choice, and in recent years diamond has become a popular alternative, due to the fact that it has the highest thermal conductivity of any solid, and a low absorption. Both of these factors ensure that any thermal distortions produced by the incident white beam are minimized. In Table 6.1 the Darwin widths $\zeta_{\mathrm{D}}^{\mathrm{FWHM}}$ are listed for diamond, silicon, and germanium. The values have been calculated from Eq. (6.26), but by neglecting the dispersion corrections, f' and f''. The Darwin width is typically of order 100×10^{-6}, or 0.1 mrad for a wavelength 1 Å, and is well matched to the natural opening angle, $(1/\gamma)$, of a synchrotron source as described in Chapter 2.

6.4.2   Extinction depth

As an X-ray beam penetrates into a crystal it becomes weaker as part of it is scattered every time it passes through a plane of atoms. From Eq. (6.15) the incident beam is attenuated by an amount $\mathrm{e}^{-Re(\eta)}$ after passing through a single plane of atoms, where $Re(\eta)$ is the real part of the variable η. After N planes it is attenuated by an amount $\mathrm{e}^{-N\,Re(\eta)}$, and in this way it is possible to define a characteristic length for the attenuation of the incident beam. We define the effective number of reflecting layers, N_{eff}, by

$$\mathrm{e}^{-N_{\mathrm{eff}}\,Re(\eta)} = \mathrm{e}^{-1/2} \tag{6.30}$$

or

$$N_{\mathrm{eff}} = \frac{1}{2Re(\eta)} \tag{6.31}$$

The depth that the beam penetrates into the crystal, the so-called extinction depth, is given by the product of N_{eff} and the lattice plane spacing d. The extinction depth Λ_{ext} is given by

$$\Lambda_{\mathrm{ext}} = N_{\mathrm{eff}}\,d = \frac{d}{2Re(\eta)} \tag{6.32}$$

The value Λ_{ext} is not a constant, but varies across the Darwin reflectivity curve. This can be seen from Eq. (6.16) which is rewritten as

$$\eta = g\sqrt{1 - x^2}$$

As $x \to \pm 1$, $\eta \to 0$ and the extinction depth Λ_{ext} diverges to infinity. This means that for $|x| \geq 1$ the attenuation due to absorption processes, which we have so far neglected, solely determines how far the incident wave penetrates into the crystal. In any calculation of Λ_{ext} it is necessary to specify which

point on the Darwin reflectivity curve it refers to. Here the point $x = 0$ is chosen for which $\eta = g$, and the extinction depth is defined by

$$\Lambda_{\text{ext}}(x = 0) = \frac{d}{2g} = \frac{1}{4}\left(\frac{m}{d}\right)\frac{v_c}{r_0|F|} \tag{6.33}$$

where Λ_{ext} refers to the $1/e$ reduction of intensity, not amplitude.

The extinction depth defined in Eq. (6.33) is inversely proportional to the modulus of the structure factor $|F|$. For moderate or strong reflections it is much smaller than the absorption length. For example, the (4,0,0) reflection in GaAs has a unit cell structure structure factor of

$$\begin{aligned}
F_{\text{GaAs}}(4, 0, 0) &= 4 \times [f_{\text{Ga}}(4, 0, 0) + f_{\text{As}}(4, 0, 0)] \\
&= 4 \times [f_{\text{Ga}}^0(4, 0, 0) + f_{\text{Ga}}' + i f_{\text{Ga}}'' + (f_{\text{As}}^0(4, 0, 0) + f_{\text{As}}' + i f_{\text{As}}'')] \\
&= 4 \times [25.75 - 1.28 - i\,0.78 + (27.14 - 0.93 - i\,1.00)] \\
&= 154.0 - i\,7.1
\end{aligned}$$

(see Section 5.1.7 on page 159). Here the theoretical values of the dispersion corrections f' and f'' are given at an X-ray wavelength of $\lambda = 1.54056$ Å. The volume of the unit cell is $v_c = 180.7$ Å^3, and the (4,0,0) has a d spacing of 1.41335 Å. Using these values the extinction depth of the (4,0,0) reflection in GaAs is calculated to be 0.74 μm. The absorption depth is given by $\sin\theta/(2\mu)$=7.95 μm, where μ=0.0355 μm^{-1} is the absorption coefficient, and $\theta = 33.02°$ is the Bragg angle. It is evident that for this strong reflection the extinction depth is approximately 10 times smaller than the absorption depth. In contrast the (2,0,0) reflection is weak, as it corresponds to the Ga and As atoms scattering out of phase. The structure factor of the (2,0,0) is

$$\begin{aligned}
F_{\text{GaAs}}(2, 0, 0) &= 4 \times [f_{\text{Ga}}(2, 0, 0) - f_{\text{As}}(2, 0, 0)] \\
&= 4 \times [f_{\text{Ga}}^0(2, 0, 0) + f_{\text{Ga}}' + i f_{\text{Ga}}'' - (f_{\text{As}}^0(2, 0, 0) + f_{\text{As}}' + i f_{\text{As}}'')] \\
&= 4 \times [19.69 - 1.28 - i\,0.78 - (21.05 - 0.93 - i\,1.00)] \\
&= -6.96 + i\,0.91
\end{aligned}$$

and the extinction depth is 8.1 μm, more than a factor of two larger than the absorption depth of 3.9 μm.

6.4.3   The integrated intensity

It is also of interest to evaluate the integrated intensity of the Darwin reflectivity curve, and to compare it with the kinematical result given by Eq. (5.31) in Chapter 5. In terms of the variable x, from Eq. (6.21) the area under the Darwin curve shown in Fig. 6.5 is

$$2 + 2 \int_1^\infty \left(x - \sqrt{x^2 - 1}\right)^2 dx = \frac{8}{3}$$

Using Eq. (6.19) this can be converted into an integrated intensity in terms of the variable ζ, with the result that

$$I_\zeta = \frac{8}{3} \frac{g}{m\pi} = \frac{8}{3} \frac{1}{m\pi} \frac{2d^2|F|r_0}{mv_c}$$

$$= \frac{8}{3} \frac{1}{m\pi} 2 \left(\frac{m\lambda}{2\sin\theta} \right)^2 \frac{|F|r_0}{mv_c} = \left(\frac{8}{6\pi} \right) \frac{\lambda^2 r_0 |F|}{v_c \sin^2\theta}$$

The kinematical result was derived using the assumptions that the incident beam is monochromatic, and that the intensity is integrated by rotating the crystal through the Laue condition. It is thus necessary to multiply the expression above by a factor of $\tan\theta$ to convert from units of ζ to angle (see Eq. (6.28)). Here it is further assumed that the crystal is large enough that it intercepts the whole beam. The scattered intensity is then proportional to the product of the flux, Φ_0, and cross-sectional area, A_0, of the incident beam. Therefore the integrated intensity recorded by rocking a perfect crystal through the Laue condition is

$$I_{sc}^P = \Phi_0 A_0 I_\zeta \tan\theta$$

$$= \Phi_0 A_0 \left(\frac{8}{6\pi} \right) \frac{\lambda^2 r_0 |F|}{v_c \sin^2\theta} \tan\theta$$

$$= \left(\frac{8}{3\pi} \right) \frac{\Phi_0 A_0 \lambda^2 r_0 |F|}{v_c \sin 2\theta}$$

For completeness it is also necessary to allow for the polarization state of the incident beam. As the integrated intensity given by the above is proportional to $|F|$, the appropriate polarization factor assuming an unpolarized beam is $(1 + |\cos 2\theta|)/2$. Similarly the Debye-Waller factor is e^{-M}. Altogether the integrated intensity from a perfect crystal scattering in a symmetric Bragg geometry is

$$I_{sc}^P = \left(\frac{8}{3\pi} \right) \frac{\Phi_0 A_0 \lambda^2 r_0 |F|}{v_c \sin 2\theta} \left(\frac{1 + |\cos 2\theta|}{2} \right) e^{-M} \tag{6.34}$$

At first sight is might appear somewhat peculiar that the integrated intensity from a perfect crystal depends on $r_0|F|$, and not $r_0^2|F|^2$ as was the case for kinematical theory. The reason for this is apparent from an inspection of Fig. 6.5, and Eq. (6.25). The central region of the Darwin curve has a reflectivity of 100%, and as the width is proportional to $|F|$, so is the integrated area.

It is instructive to compare the expression for the integrated intensity from a perfect crystal with the corresponding one derived using the kinematical approximation. This comparison has already been discussed qualitatively in Chapter 5. There in the section on extinction (page 182) it was stated that crystals are rarely ideally imperfect as the model of a mosaic crystal requires, and that measured intensities are nearly always smaller than predicted by kinematical theory. One reason for this is that the mosaic blocks have a finite size, and dynamical (or multiple) scattering effects will be present at some level. The reduction of intensities from dynamical effects is known as primary extinction, and here a quantitative comparison is made between the intensities predicted by kinematical and dynamical theory.

We imagine that the reflection from a perfect crystal is measured where the extinction depth is much smaller than that due to absorption. The integrated intensity is then given by Eq. (6.34). The crystal is

now deformed to produce a mosaic structure. This can be done, for example, by heating it up to just below its melting temperature, and then plastically deforming it[5]. In the limit that the deformed crystal approaches the ideally imperfect mosaic crystal the penetration of the X-ray beam will be determined by absorption. For a mosaic crystal with an extended face the integrated intensity is given by Eq. (5.31) as

$$I_{sc}^M = \left(\frac{1}{2\mu}\right) \frac{\Phi_0 A_0 \lambda^3 r_0^2 |F|^2}{v_c^2 \sin 2\theta} \left(\frac{1 + \cos^2 2\theta}{2}\right) e^{-2M} \tag{6.35}$$

where μ is the absorption coefficient. The integrated intensity from a mosaic crystal is therefore larger than that from a perfect one by a factor of

$$\frac{I_{sc}^M}{I_{sc}^P} = \left(\frac{3\pi}{16}\right) \frac{\lambda r_0 |F|}{\mu v_c} \tag{6.36}$$

For clarity, the polarization and Debye-Waller factors have been neglected.

To take a definite example, we consider again the (4,0,0) reflection from GaAs. With the values of the parameters given in the section on the extinction depth above the ratio of integrated intensities is $I_{sc}^M/I_{sc}^P \approx 6$. This illustrates the fact that in general the integrated intensity from a mosaic crystal exceeds that from a perfect crystal, by a factor that is proportional to $|F|$. This presents the problem that when performing a crystallographic study to determine the structure of a material, it has to be determined whether it is appropriate to use kinematical or dynamical scattering theory. In practice most crystals are neither completely perfect nor ideally imperfect, but yield integrated intensities somewhere between the values predicted by the two theories. Data from crystallographic studies are nearly always analysed using the kinematical approximation, and then corrections to the data are made for extinction effects. (The reader is referred to the *International Tables of Crystallography* for a thorough discussion of applying extinction corrections.) To complete this discussion we also calculate the intensity ratio for the (2,0,0) reflection from GaAs. With the parameters given above the intensity ratio is $I_{sc}^M/I_{sc}^P \approx 0.2$. Somewhat surprising in this case of a very weak Bragg reflection the kinematical theory appears to predict a smaller intensity than the dynamical one. The reason is that so far absorption effects have been neglected in the dynamical theory. Once these are included it can be shown that in the limit of weak scattering (small $|F|$) the dynamical and kinematical theories yield the same result. Absorption effects are considered further in Section 6.4.6.

6.4.4 Standing waves

The total wavefield above a crystal is composed of the incident T wave, proportional to $e^{ik_y y}e^{ik_z z}$, and the diffracted S wave, proportional to $e^{ik_y y}e^{-ik_z z}$ as depicted in Fig. 6.4. Here the y-axis points to the right along the surface of the crystal, and the z-axis points vertically down. At $z = 0$ the two waves have amplitudes T_0 and S_0 in the complex ratio r as given by Eq. (6.20). Thus *above* the surface, $z < 0$, the total wave amplitude is

$$A_{total} = T_0\, e^{ik_y y}\left[e^{ik_z z} + re^{-ik_z z}\right]$$

In general $r = |r|e^{i\phi}$, where both the modulus $|r|$ and phase ϕ depend on the variable $x = \epsilon/g$, as plotted in Fig. 6.5 and 6.6. The intensity $I(z, x)$ normalized to $T_0=1$ above the crystal surface follows as

$$I(z, x) = |A_{total}|^2 = \left[e^{ik_z z} + |r|e^{i\phi}e^{-ik_z z}\right]\left[e^{-ik_z z} + |r|e^{-i\phi}e^{ik_z z}\right]$$
$$= 1 + |r|^2 + |r|e^{i\phi}e^{-i2k_z z} + |r|e^{-i\phi}e^{i2k_z z}$$

---

[5]Amongst other things this technique is used to produce monochromator crystals for neutron scattering instruments. Single crystal wafers of nearly perfect Ge are repeatedly deformed to produce a mosaic width of approximately 0.25°.

(a) in phase   (b) out of phase
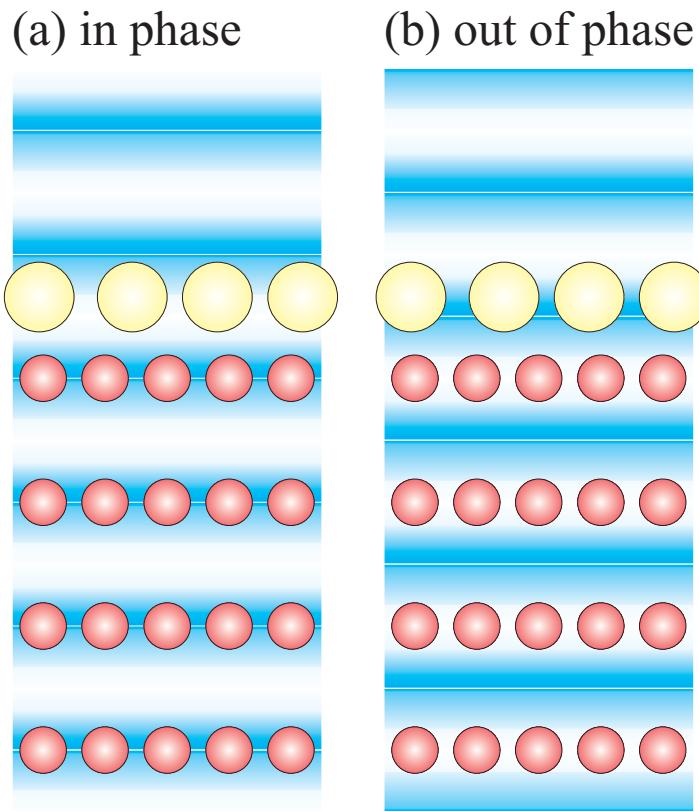
Fig. 6.7 The standing wavefield changes phase with respect to the lattice planes throughout the region of total reflectivity. (a) On one side ($x = 1$, Fig. 6.5) the standing wave has nodes between the lattice planes, and on the other side (b) ($x = -1$) at the lattice planes. The standing wavefield extends beyond the crystal surface, and the height of an absorbed layer (represented by larger circles) can be determined by their fluorescent yield vs the phase of the standing wave.

Here the reader should note that z is a spatial variable with dimension of length, while $x = \epsilon/g$ is the dimensionless independent variable we introduced to describe the Darwin reflectivity curve. Since the modulus of the wavevector transfer for the geometry considered is given by $Q=2k_z$, the above equation for $I(z, x)$ simplifies to become

$$I(z, x) = 1 + |r|^2 + 2|r|\cos(\phi - Qz) \qquad (6.37)$$

This equation describes the standing wave intensity above the surface of a crystal. For $x = 1$ the incident and diffracted waves are in phase ($\phi = 0$), and $I(z, x = 1)= 2(1 + \cos(Qz))$. For $x = -1$, the two wavefields are out of phase ($\phi = -\pi$), and $I(z, x = -1)= 2(1 - \cos(Qz))$. Thus as a function of Qz the standing wave intensities at $x = -1$ and $x = 1$ oscillate in quadrature. The standing wave intensity for $x = 1$ is a maximum when $Qz = 2p\pi$, p integer, i.e. when $z = pd$, whereas for $x = -1$ the intensity is a maximum when $z = (p + 1)d/2$. The wavefield inside the crystal is also a standing wave, but with an amplitude decaying with the penetration depth.

The existence of standing waves has some interesting consequences:

Fig. 6.8 Illustration of the sensitivity of the intensity of X-ray standing waves to Qz. The solid lines have been calculated from Eq. (6.37) using the phase ϕ and the modulus of the amplitude reflectivity $|r|$ obtained from Eq. (6.20).

(a) For the in-phase point the intensity is maximal at the atomic planes, i.e. where the density of absorbing electrons is high. For the out-of-phase point the opposite is true. The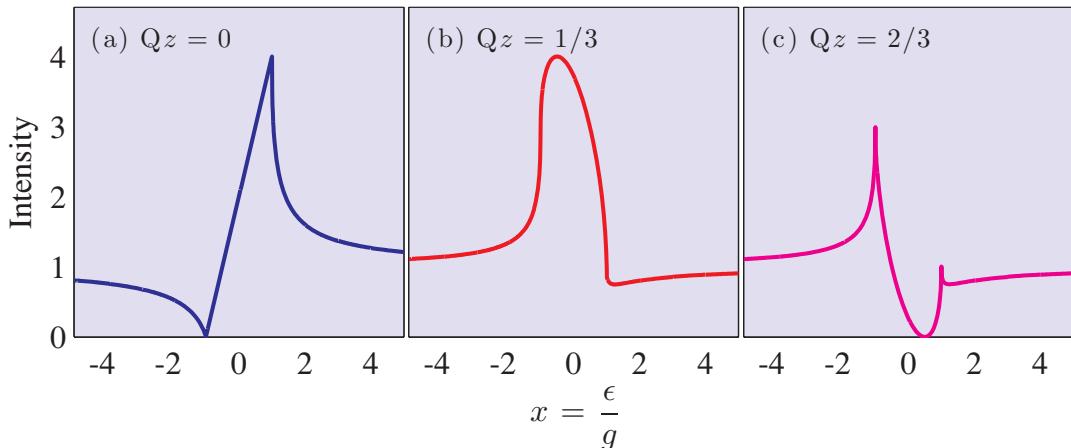refore the influence of absorption is more pronounced when the X-ray wavefields are in phase than when they are out of phase. When absorption is neglected the Darwin curve (Fig. 6.5) is symmetric, but this symmetry will be broken when absorption is taken into account: the right hand side of the curve will be more attenuated than the left hand side, i.e. the resulting reflectivity curve becomes progressively more depressed at higher scattering vectors.

(b) The standing wavefield continues of course outside the crystal as shown schematically in Fig. 6.7. As x is scanned through the Laue condition the maximum of $I(z, x)$ above the crystal moves by half a lattice spacing. It follows that if a layer of atoms different to those in the bulk crystal is absorbed on its surface then the atoms in the over layer will fluoresce as the maximum of $I(z, x)$ sweeps through them. To a first approximation it might reasonably be assumed that the fluorescent yield is proportional to $I(z, x)$. In Fig. 6.8 we plot $I(z, x)$ (Eq. (6.37)) for various values of Qz, from which it should be apparent that the fluorescent yield will depend sensitively on the distance z of the over layer above the crystal. In this way X-ray standing waves provide a sensitive method for measuring the spacing of layers deposited on perfect crystals [Batterman, 1964, Andersen et al., 1976].

6.4.5 Higher-order reflections

It has been shown in Section 6.2 that the centre of the Darwin reflectivity curve is offset from the reciprocal lattice points $G = m2\pi/d$ by an amount proportional to $1/m$ (Eq. (6.7)). While in Section 6.4.1 it was shown that the Darwin width varies faster than $1/m^2$ (Eq. (6.25)), since $|F|$ decreases with increasing m due to the reduction of the atomic form factor with increasing Q. This is illustrated in Fig. 6.9.

The variation of ζ_{D} and the displacement ζ_0 with m has some important implications when considering higher-order reflections from a monochromator crystal. According to Bragg's law a crystal illuminated by a collimated but white beam will not only reflect the desired wavelength $\lambda = 2d \sin\theta$,
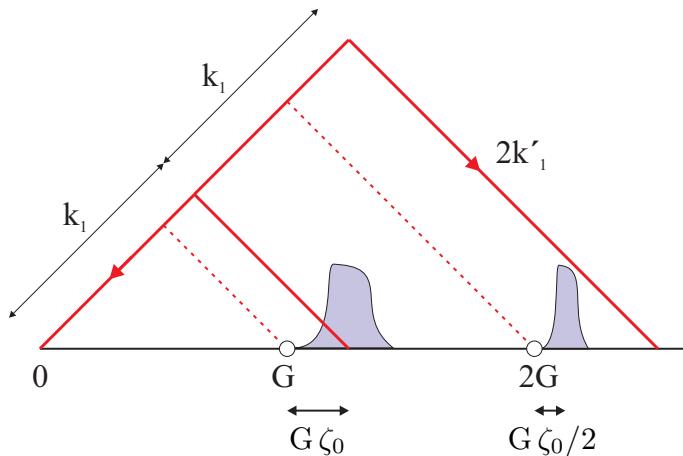
Fig. 6.9 The reciprocal lattice of a stack of atomic planes separated by a distance d is a line of points at positions given by $mG = m2\pi/d$, where m is an integer. The centres of the Darwin reflectivity curves are offset from these points by an amount $G\zeta_0$, varying with m as $1/m$, whereas the Darwin width ζ_D varies faster than $1/m^2$. (Note: the scale has been exaggerated.) The crystal is set to reflect a central wavelength of $\lambda_1 = 2\pi/k_1$. If the incident spectrum also contains $\lambda_1/2 \equiv 2k_1$, then the different dependences of ζ_D and $G\zeta_0$ on m ensures that the reflectivity from this component is small.

but also all multiples of λ/m. When performing experiments this can be a major source of irritation, and it is often necessary to take steps to reduce the higher-order contamination[6]. For perfect crystals the situation is not as bad as it may first appear, as illustrated in Fig. 6.9. The different dependences of ζ_D and ζ_0 with the reflection order m ensure that the contribution from the higher-order components is suppressed. One way to increase the suppression of higher-order contamination is to use a double crystal monochromator. Offsetting the angle of the second crystal by a small amount of order $g_0/(2\pi)$ will further reduce the reflectivity of the higher-order components without affecting significantly that of the fundamental wavelength.

From Eqs. (6.7) and (6.25) the explicit relationship between the refractive offset and the Darwin width is

$$\zeta^{\text{offset}} = \frac{\zeta_0}{m} = \frac{\zeta_D^{\text{total}}}{2} \frac{|F_0|}{|F|} \tag{6.38}$$

It follows that the angular offset $\Delta\theta$ in degrees is

$$\Delta\theta = \frac{\zeta_D^{\text{total}}}{2} \frac{|F_0|}{|F|} \tan\theta \frac{360°}{2\pi} \tag{6.39}$$

For example, the Si (111) reflection with $\lambda = 1.54056$ Å has a Darwin width of $w_D^{\text{total}} = 0.0020°$ (see Eq. (6.29)), and a refractive offset of $0.0018°$. An alternative expression for the offset $\Delta\theta$ in terms of δ, the difference of the refractive index from 1 (Eq. (3.1)), is

$$\Delta\theta = \frac{2\delta}{\sin 2\theta} \frac{360°}{2\pi} \tag{6.40}$$

which can be shown to be equivalent to Eq. (6.39).

---

[6]This can include the use of X-ray mirrors as explored in Chapter 3.

6.4.6   Effect of absorption

For a real crystal absorption has to be included in any calculation of the Darwin reflectivity curve. The way that this is achieved can be understood from a consideration of Fig. 6.2. If absorption is non negligible, then the transmitted wave not only undergoes a change in phase, proportional to g_0, but it is also attenuated. Thus absorption effects can be included by allowing g_0 to become complex, where the imaginary part of g_0 is proportional to the absorption cross-section. Similar considerations apply to the reflected wave. Equations (6.1) and (6.2) are therefore replaced by

$$g_0 = \left(\frac{2d^2 r_0}{m v_c} \right) F_0 \tag{6.41}$$

with

$$F_0 = \sum_j (Z_j + f_j' + i f_j'') \tag{6.42}$$

and

$$g = \left(\frac{2d^2 r_0}{m v_c} \right) F \tag{6.43}$$

with

$$F = \sum_j (f_j^0(\mathbf{Q}) + f_j' + i f_j'') e^{i \mathbf{Q} \cdot \mathbf{r}_j} \tag{6.44}$$

where f_j' and f_j'' are the real and imaginary parts of the dispersion correction to the atomic scattering length $f^0(\mathbf{Q})$, and j labels the atoms in the unit cell.

With these alterations the formulae for the reflectivity are essentially the same, except that the variable x in Eq. (6.19) is now a complex number, x_c, which is given by

$$x_c = m\pi \frac{\zeta}{g} - \frac{g_0}{g} \tag{6.45}$$

with g_0 and g complex. To calculate the reflectivity curves for a given value of ζ one can plot the result versus the real part of x_c, so that the amplitude reflectivity may be written as

$$r(Re(x_c)) = \left(\frac{S_0}{T_0} \right) = \begin{cases} \dfrac{1}{x_c + \sqrt{x_c^2 - 1}} = x_c - \sqrt{x_c^2 - 1} & \text{for } Re(x_c) \geq 1 \\[3mm] \dfrac{1}{x_c + i\sqrt{1 - x_c^2}} = x_c - i\sqrt{1 - x_c^2} & \text{for } |Re(x_c)| \leq 1 \\[3mm] \dfrac{1}{x_c - \sqrt{x_c^2 - 1}} = x_c + \sqrt{x_c^2 - 1} & \text{for } Re(x_c) \leq -1 \end{cases}$$

and as usual the intensity reflectivity is obtained by taking the absolute square of $r(Re(x_c))$.

The effects of absorption on the Darwin reflectivity curve are illustrated in Fig. 6.10(a)★, where the specific example of the Si (111) reflection has been taken. As expected the effect of absorption is more pronounced near $x \approx 1$ than at $x \approx -1$, because near $x \approx 1$ the X-ray wavefield is in phase with the position of the atomic planes. As the photon energy is increased the effect of absorption is diminished. In Fig. 6.10(b)★ the Darwin curves are plotted versus the rotation angle of the crystal in milli degrees at various energies. This part of the figure also serves to illustrate the point that, whereas the relative
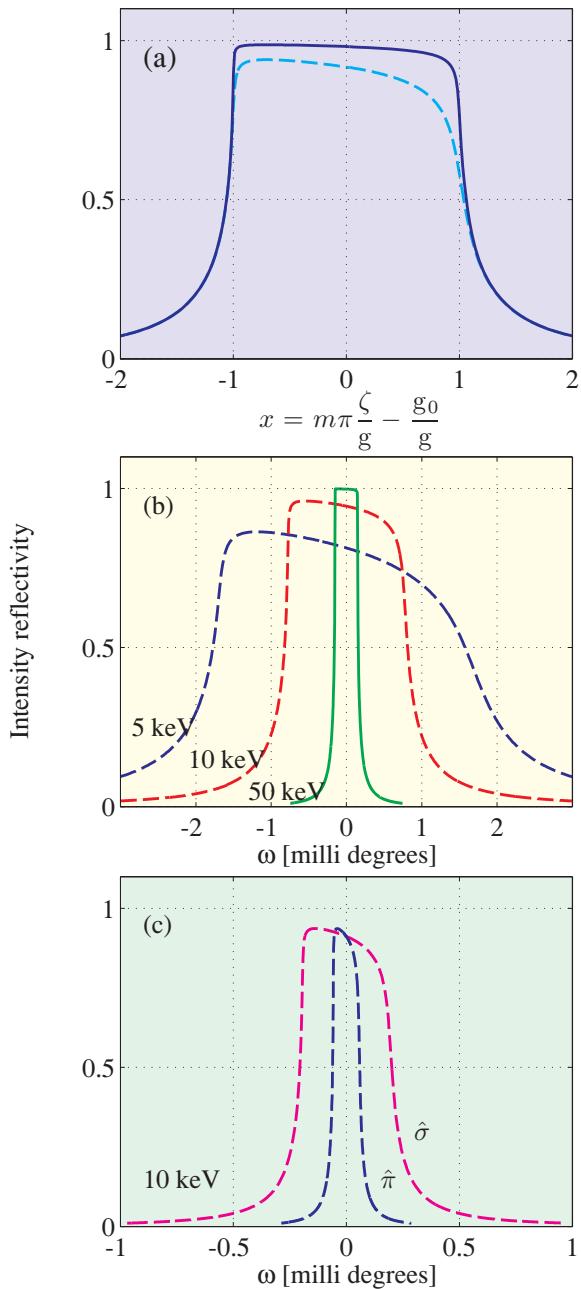
Fig. 6.10 ⋆ Effect of absorption and polarization on the Darwin curve of the Si (*hhh*) reflections. (a) Si (111) plotted as a function of the variable x (see Eq. (6.19)) for $\hat{\sigma}$ polarization. Solid line: λ=0.70926 Å, with $F_0 = 8\times(14+0.082-i\,0.071)$ and $F = 4|1-i|\times(10.54+0.082-i\,0.071)$. Dashed line: λ=1.5405 Å, with $F_0 = 8\times(14+0.25-i\,0.33)$ and $F = 4|1-i|\times(10.54+0.25-i\,0.33)$. (b) Si (111) plotted as a function of the rotation angle of the crystal in millidegrees (see Eq. (6.28)) at various energies for $\hat{\sigma}$ polarization. (c) Si (333) plotted with either $\hat{\sigma}$ (magenta) or $\hat{\pi}$ (blue) polarization.

Fig. 6.11 Asymmetric Bragg reflection. The surface of the crystal is at an angle α with respect to the reflecting atomic planes. The widths of the incident and scattered beams are then different. In this case the parameter b is greater than one.

bandwidth ζ (which is proportional to x from Eq. (6.45)) is independent of energy, the angular Darwin width is not.

In Fig. 6.10(c) we provide an example of how the Darwin width depends on the polarization of the incident beam. Up until now we have mostly assumed that the incident beam is polarized perpendicular to the scattering plane, so-called $\hat{\sigma}$ polarization, see Fig. 2.5, for which the polarization factor $P = 1$. With the polarization in the scattering plane $-\hat{\pi}$ polarization $-$ the scattering amplitude is reduced by a factor of $\cos(2\theta)$. In this latter case the primary beam therefore penetrates more deeply into the crystal producing a narrower Darwin width, as evidenced in Fig. 6.10(c). Another way of describing the polarization dependence of the reflectivity curve is to say that in the tails of the Darwin curve perfect crystals are birefringent, i.e. they exhibit a difference in the refractive index for waves polarized in orthogonal directions. This birefringence allows the construction of X-ray phase plates for manipulating the polarization of the beam. For example, a quarter-wave plate can be used to convert the polarization from linear to circular.
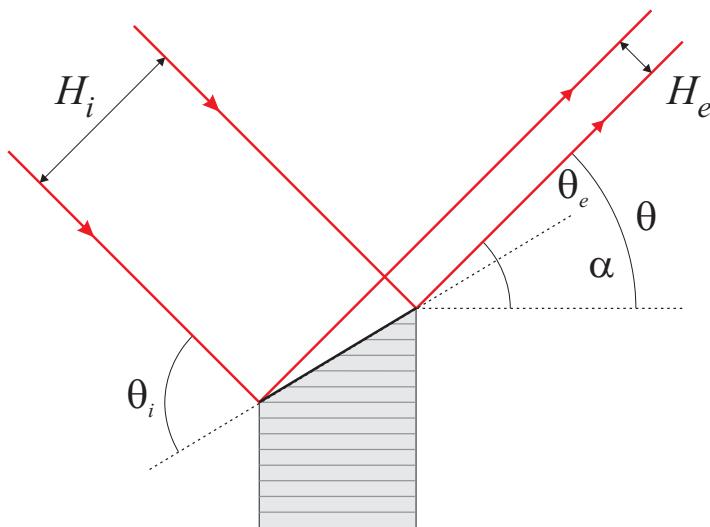
6.4.7   Asymmetric Bragg geometry

In general the surface of a crystal will not be parallel to the atomic planes which reflect the incident beam, as shown in Fig. 6.11. Let α be the angle between the surface and the reflecting planes. The incident, θ_i, and exit, θ_e, glancing angles are then given by $\theta_i = \theta + \alpha$ and $\theta_e = \theta - \alpha$. For a reflection geometry it is required that both θ_e and θ_i are greater than zero, or in other words that α fulfills the condition $0 < |\alpha| < \theta$. In Fig. 6.11 α has been chosen to be greater than zero. This implies a compression of the width of the exit beam. The asymmetry parameter, b, is defined by

$$b \equiv \frac{\sin \theta_i}{\sin \theta_e} = \frac{\sin(\theta + \alpha)}{\sin(\theta - \alpha)} \tag{6.46}$$

Symmetric Bragg diffraction corresponds to setting $b = 1$. For the particular case shown in the Fig. 6.11, $b > 1$. The widths of the incident, H_i, and exit, H_e, beams are related by the equation

$$H_i = b\, H_e$$

It turns out that a compression in the width of the exit beam implies an increase in its angular divergence. This is a consequence of Liouville's theorem[7]. By the same reasoning the acceptance angle of the incident beam must decrease to compensate for the increase in the incident beam width. Let the angular acceptance of the incident beam be $\delta\theta_i$, and the reflected beam divergence be $\delta\theta_e$. We now assert that $\delta\theta_i$ and $\delta\theta_e$ are given in terms of the asymmetry parameter b and the Darwin width ζ_D by the equations

$$\delta\theta_e = \sqrt{b}\,(\zeta_D \tan\theta) \tag{6.47}$$

and

$$\delta\theta_i = \frac{1}{\sqrt{b}}\,(\zeta_D \tan\theta) \tag{6.48}$$

These formulae are certainly correct in the symmetric case with $b = 1$ (see Eq. (6.28)). Moreover, since

$$\delta\theta_i\, H_i = \frac{1}{\sqrt{b}}\,(\zeta_D \tan\theta)\, b H_e = \sqrt{b}\,(\zeta_D \tan\theta)\, H_e = \delta\theta_e\, H_e$$

the product of beam width and divergence is the same for the incident and exit beams, as required by Liouville's theorem.

An interesting application of asymmetric crystals is in the measurement of Darwin reflectivity curves. The angular Darwin width is small, typically of order of $\sim 0.002°$, c.f. Fig. 6.10. Measurement of the reflectivity curve then requires a detector system that has a much better angular resolution than this value. This follows from the fact that the measured curve is the *convolution* of the Darwin reflectivity curve of the crystal and the angular resolution of the detector, or analyser, system. So if the angular divergence of the analyser is much smaller than that of the first crystal, then the measured curve is determined solely by the Darwin reflectivity of the first crystal. One way to achieve high angular resolution in the analyser is to use an asymmetric crystal. From Eq. (6.47), its angular acceptance can be made arbitrarily small by decreasing the value of b. Double crystal spectrometers with two perfect crystals are discussed further in the next section on DuMond diagrams.

In Fig. 6.12 we show data from a double crystal diffractometer composed of two perfect asymmetric silicon crystals. With two asymmetric crystals there are four possible ways of configuring the diffractometer. The narrowest curve is recorded when the first crystal is arranged with $b<1$, and the second with $b>1$. In this case the diffracted beam from the first crystal has the smallest possible angular divergence, which is matched to the narrow angular acceptance of the second.

6.5   DuMond diagrams

An optical element inserted into an X-ray beam is supposed to modify some property of the beam such as its width, its divergence, or its wavelength band. It is useful to describe the modification of the beam by a transfer function. The transfer function relates the input parameters of the beam upstream from the optical element to the output parameters of the beam after the beam has passed the optical element.

---

[7]Liouville's theorem states that for beams of particles, here photons, the product of beam width and divergence is a constant.
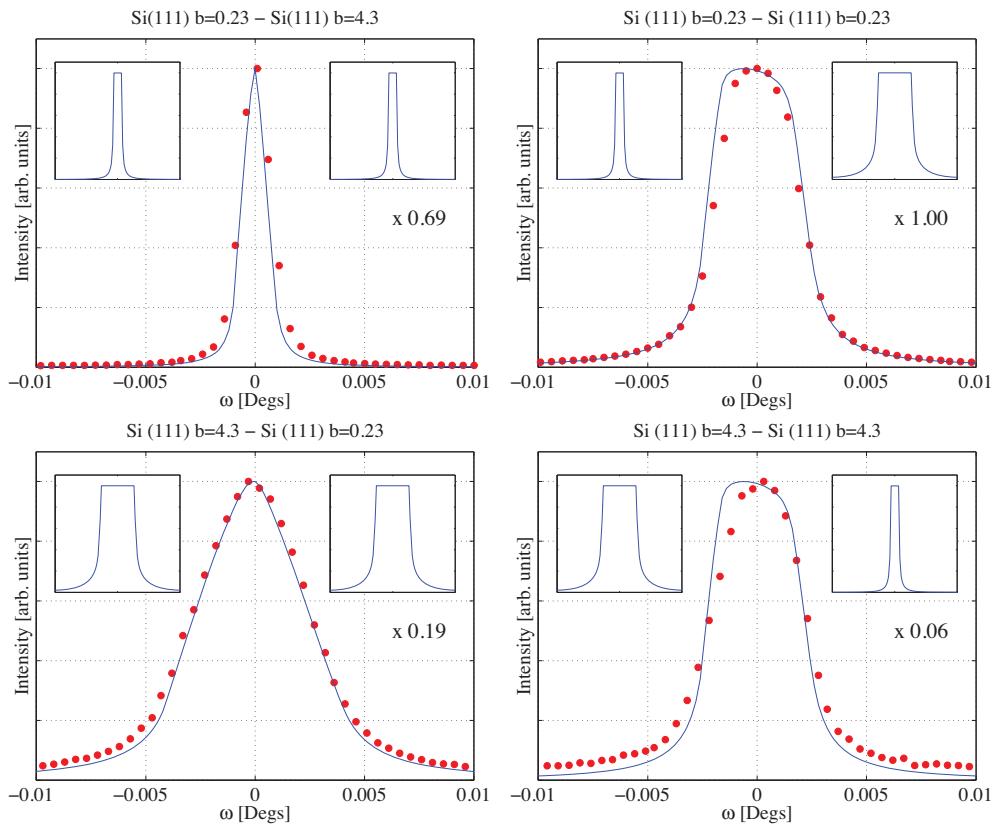
Fig. 6.12 Measured rocking curves for a double crystal diffractometer formed from two asymmetric perfect silicon crystals. The solid lines represent the calculated convolution of two Darwin curves with widths determined by how the asymmetric crystals were configured.

When the optical element is a perfect crystal the relevant beam parameters are amongst other things the beam divergence and the wavelength band. The DuMond diagram is a graphical representation of the transfer function. In the diagram the horizontal axes are the beam divergence, with the input beam to the left and the output beam to the right. The vertical axis is common and is $\lambda/2d$, the wavelength normalized by twice the lattice spacing d. In the crudest approximation, where the finite width of the Darwin curve and refraction effects are neglected, only the points of the incident parameter space in the $(\theta_i, \lambda/2d)$ plane which satisfy $\lambda/2d = \sin\theta_i$ will be reflected. For a white incident beam that falls within an angular window $\theta_{i,\min} < \theta_i < \theta_{i,\max}$ the output side of the DuMond diagram consists of a line given by $\lambda/2d = \sin\theta_e$ with $\theta_{i,\min} < \theta_e < \theta_{i,\max}$.

One crystal

According to Bragg's law, constructive interference of waves scattered from an infinite crystal occurs if the angle of incidence, θ_B, and the wavelength, λ, are related exactly by

$$m\lambda = 2d\sin\theta_B$$
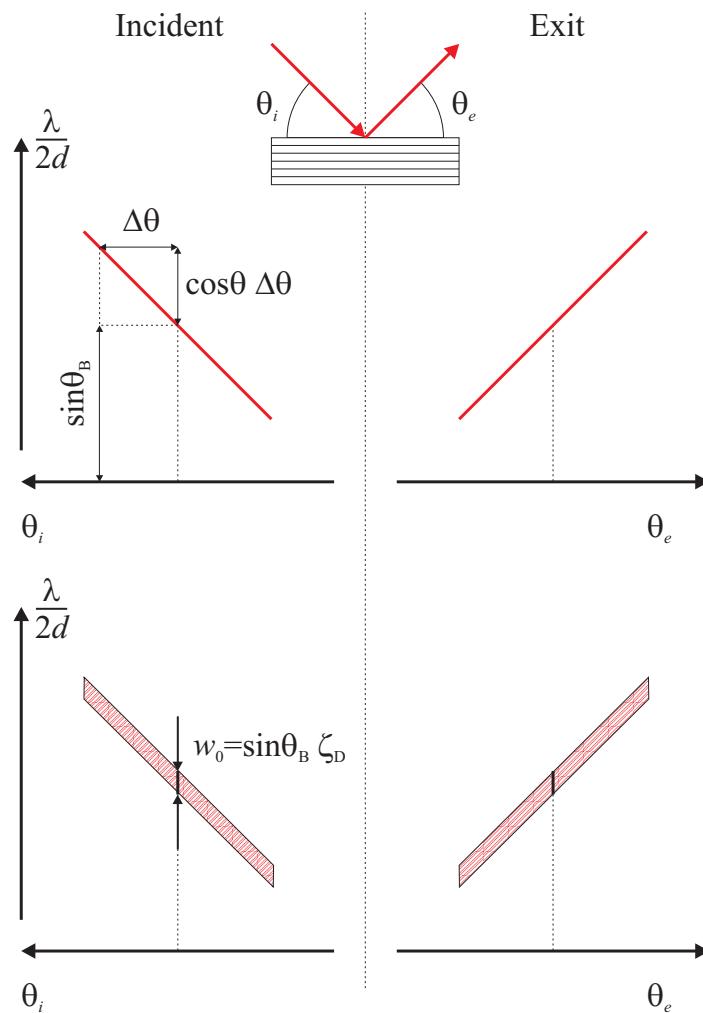
Fig. 6.13 DuMond diagram for symmetric Bragg geometry. In this case the angles of the incident, θ_i, and exit, θ_e, beams relative to the crystal surface are the same. The DuMond diagram is a graphical representation of the Bragg reflection condition, where the axes are angle, relative to the Bragg angle θ_B, and $\lambda/2d$. In (a) the Darwin width has been neglected. The intensity is non-zero for points on the line only. (b) The finite Darwin width broadens the line into a band with a width along the ordinate of $w_0 = \sin\theta_B\zeta_D$.

One way to represent this relationship is to plot a graph with $\lambda/2d$ on the ordinate and θ_B on the abscissa. Any point on the sinusoidal curve gives values of $\lambda/2d$ and θ_B that satisfy Bragg's law. Perfect crystals diffract over a small but finite range in angle and wavelength. When dealing with perfect crystals it is therefore necessary to consider deviations of the incident angle θ_i around θ_B, and deviations of wavelength around the value given by $2d\sin\theta_B$. For asymmetric crystals it is also necessary to consider the exit angle θ_e of the reflected beam.

The DuMond diagram is a graphical way to represent diffraction events, and is composed of two parts: one is a plot of $\lambda/2d$ against $\theta_i - \theta_B$, with θ_i increasing to the left; and the other is a plot of $\lambda/2d$ against $\theta_e - \theta_B$, with θ_e increasing to the right. For small deviations away from the Bragg condition
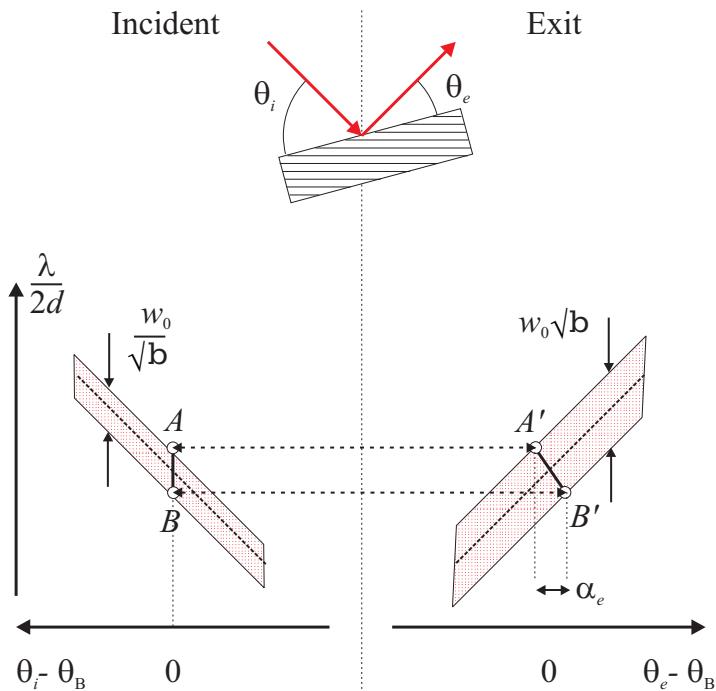
Fig. 6.14 DuMond diagram for asymmetric Bragg geometry. The ratio of the widths of the incident and exit beams is given by the parameter b. This implies that the angular acceptance of the incident beam is reduced by a factor of $1/\sqrt{b}$ while that of the exit beam is increased by the same amount. Thus in the DuMond diagram the incident bandwidth is reduced, and the exit one increased. Points A and B on the incident side are associated with points A' and B' on the exit side. This shows that an incident beam which is parallel and white acquires a finite angular divergence given by α_e when it has been diffracted by a crystal set in asymmetric Bragg geometry.

the sinusoidal dependence of $\lambda/2d$ approximates to a straight line with slope $\cos\theta$. The top part of Fig. 6.13 shows the DuMond diagram for a crystal diffracting according to Bragg's law in a symmetric reflection geometry. When neglecting the finite Darwin width, the reflectivity is non-vanishing only on the line indicated, and the relative change in wavelength $\Delta\lambda/\lambda$ and the deviation $\Delta\theta$ from the Bragg angle are related by

$$\frac{\Delta\lambda}{\lambda} = \frac{\Delta\theta}{\tan\theta}$$

For the symmetric Bragg geometry assumed here the surface coincides with the reflecting planes: the reflection is specular, and the wavelength and exit angle are linked by the same condition as the one above.

The lower part of Fig. 6.13 shows the DuMond diagram for symmetric Bragg geometry, but now including the finite Darwin bandwidth: all wavelengths from a perfectly collimated white source within a relative bandwidth ζ_D have a reflectivity of 100%. Outside of this band, the reflectivity falls off quickly as we move from the dynamical to the kinematical regimes (see Fig. 6.3 and 6.5). In the latter the scattering is located along the crystal truncation rods which run parallel to the surface normal (Section 5.3). In terms of the DuMond ordinate $\lambda/2d$ the width of the central band is

$$w_0 = \frac{\Delta\lambda}{2d} = \left(\frac{\lambda}{2d}\right)\left(\frac{\Delta\lambda}{\lambda}\right) = \left(\frac{\lambda}{2d}\right)\zeta_D = \sin\theta_B\,\zeta_D \tag{6.49}$$

where $\zeta_D = \Delta\lambda/\lambda$ is the Darwin width given by Eq. (6.25). As indicated, symmetry implies that a perfectly collimated incident beam is reflected to a perfectly collimated exit beam.

This is not the case for an asymmetric crystal, where the surface does not coincide with the reflecting planes, as is shown in Fig. 6.14. The exit beam width is now smaller than that of the incident beam. In Section 6.4.7 it has been shown that this implies that the bandwidth of the incident beam is reduced by a factor of $1/\sqrt{b}$, while the bandwidth of the exit beam is increased by a factor of $\sqrt{b}$. It is important to note that the crystal truncation rod is no longer parallel to the reciprocal lattice vector, since it runs perpendicular to the surface. The consequences of these considerations are illustrated in the lower part of Fig. 6.14. A perfectly collimated incident beam is reflected in the band AB. The scattering is elastic, so the point $A(B)$ is transferred to point $A'(B')$ on the exit part of the DuMond diagram. Since the points A' and B' have different abscissa, displaced by the amount α_e, a perfectly collimated incident beam acquires a finite divergence after Bragg reflection.

In the examples of the symmetric and asymmetric Bragg geometries there is an ambiguity left to resolve. This concerns the question of how to relate points on the DuMond diagram of the incident beam with those of the exit beam. For the asymmetric Bragg case, shown in the lower part Fig. 6.14, the point A on top of the incident band is shown connected to the point A' on top of the exit band. (The line runs at right angles to the $\lambda/2d$ axis since the scattering is elastic.) The reason for this is illustrated in Fig. 6.15, which should be compared with Fig. 6.1. The transition from the dynamical to the kinematical regimes must be continuous. In the kinematical regime the scattering lies along the crystal truncation rods (CTR's). If the incident beam is white and parallel then the crystal reflects a band Δk out of the incident beam. A given wavevector in the incident beam, $\mathbf{k}_1$ say, is scattered to a final wavevector $\mathbf{k}'_1$, with $|\mathbf{k}_1| = |\mathbf{k}'_1|$. The direction of $\mathbf{k}'_1$ is found from where the Ewald sphere, indicated by the circular arc, crosses the CTR. For the asymmetric Bragg case the truncation rod does not lie along the direction of the wavevector transfer: it runs perpendicular to the physical surface. From Fig. 6.15(b) this implies that the scattering angle of the exit beam must increase as $|\mathbf{k}'|$ increases. This is consistent with the choice of associating B with B'. Continuity between the dynamical and kinematical regime also implies that the central band of the former does not lie along the wavevector transfer. In other words the reflection is not specular.
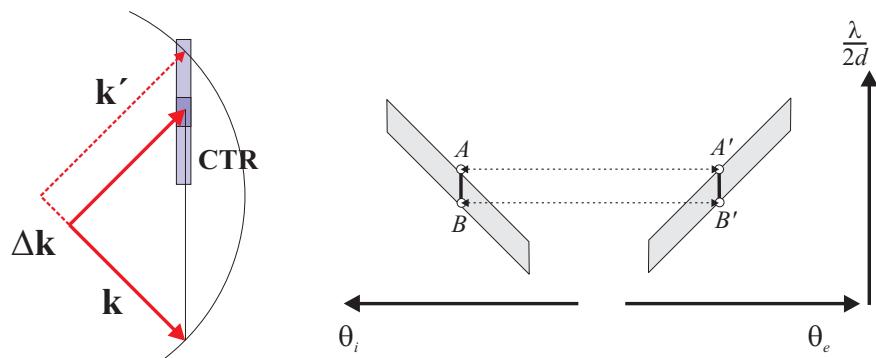
The same construction is shown for symmetric Laue geometry in Fig. 6.15(c). From this it is clear that a crystal diffracting in symmetric Laue geometry will impart a finite angular divergence to a parallel, white incident beam.

Two crystals in symmetric Bragg geometry
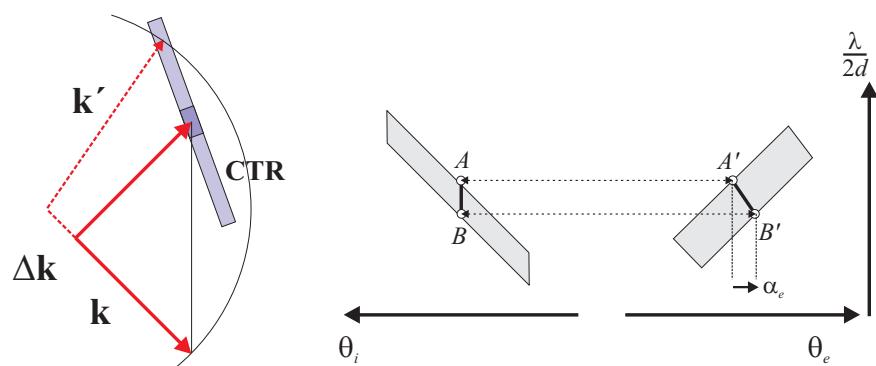
In Fig. 6.16 a white beam is incident on a crystal at a certain Bragg angle. To simplify the discussion it is assumed, as in the previous section, that the Darwin reflectivity curve may be approximated by a box function. The beam incident on the first crystal is thus the vertical, light shaded band with an angular width $2\Delta\theta_{in}$ in the DuMond diagrams in the lower part of the figure. A second crystal is set to reflect the central ray. This can be done in two ways.

If the Bragg planes in the second crystal are parallel to those in the first crystal, a ray deviating (dotted line) from the central ray by $\Delta\theta_{in}$ will be reflected at the same setting as the central ray. In a DuMond diagram this means that the response band of the second crystal is parallel to that of the first crystal. In scanning the angle of the second crystal there is no overlap with the intensity provided by the first crystal for any of the four settings shown. Only when the angular setting of the second crystal is in between those labelled 2 and 3 will there be scattered intensity after the second crystal. Since the bands are assumed to be box-like, the intensity versus angle will be triangular with a FWHM equal to the angular Darwin width w_1 of one crystal, independent of the incident angular bandwidth.

(a) symmetric Bragg

(b) asymmetric Bragg

(c) symmetric Laue
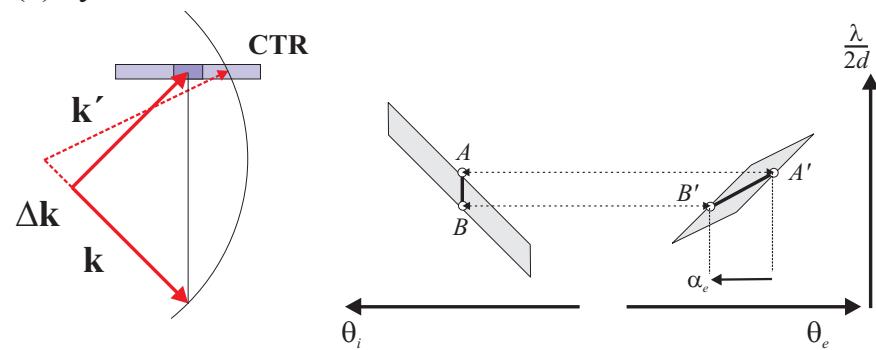
Fig. 6.15 Scattering triangles (left) and DuMond diagrams (right) for (a) symmetric Bragg, (b) asymmetric Bragg and (c) symmetric Laue geometries. In the scattering triangles the crystal truncation rod (CTR) is represented by the rectangular box, with the darker shaded part being the central dynamical band. Continuity between the kinematical and dynamical regimes allows points A, B and A', B' in the DuMond diagrams of the incident and exit beams to be associated with each other in an unambiguous way.
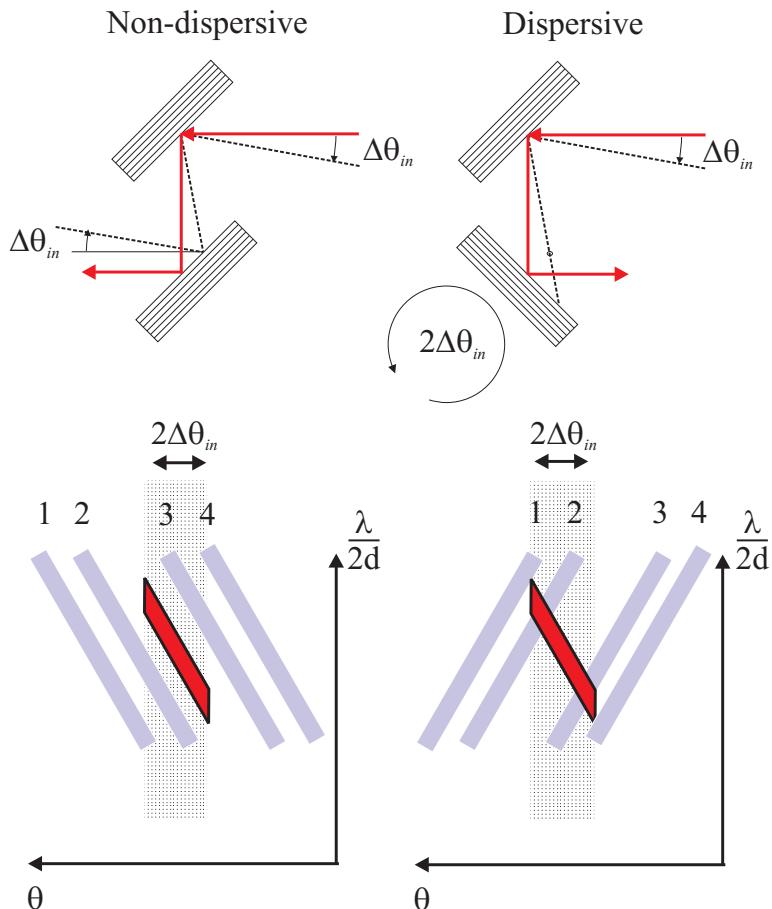
Fig. 6.16 Non-dispersive geometry (left): X-rays from a white source are incident on two crystals aligned in the same orientation. The central ray (full line) will be Bragg reflected by both crystals and will emerge parallel to the original ray. A ray incident at a higher angle than that of the central ray will only be Bragg reflected if it has a longer wavelength. The angle of incidence this ray makes with the second crystal is the same as that it made with the first, and will be Bragg reflected. The DuMond diagram in the lower part shows that a scan of the second crystal has a width equal to the convolution of the Darwin widths of the two crystals, independent of the incident angular divergence. Dispersive geometry (right): A ray incident at a higher angle than the central ray at the first crystal will be incident at a lower angle at the second crystal. The second crystal must be rotated by the amount $2\Delta\theta_{in}$ for Bragg's law to be fulfilled. The geometry is therefore wavelength dispersive.

Furthermore, the reflected wavelength band from the second crystal equals that after the first crystal and is determined by the angular spread $2\Delta\theta_{in}$. This orientation is therefore termed non-dispersive.

On the other hand, in the alternative orientation, the response band of the second crystal has the opposite slope to that of the first crystal. The angular width is now dependent of the incident width: in the limit of a very small Darwin width w_1 it is actually equal to that of the incident width. In the DuMond diagram there will be scattering after the second crystal in all of the positions 2 through 4. The wavelength bandwidth after the second crystal in position 3 is now much smaller than the wavelength bandwidth after the first crystal, and the orientation is termed dispersive. It is clear that this qualitative discussion of the dispersive setting can be sharpened to a quantitative estimate of both the angular and

wavelength bandwidths after scattering from the second crystal.

6.6 Further reading

X-ray Diffraction, B.E. Warren (Dover Publications, 1990) Chapter 14.

The Optical Principles of the Diffraction of X-rays, R.W. James (Ox Bow Press) Chapter 2.

Dynamical Theory of X-ray Diffraction, A. Authier (Oxford University Press, 2001).

X-ray Monochromators, T. Matsushita and H. Hashizume, in the Handbook of Synchrotron Radiation, Vol. 1b, Ed. E.E. Koch (North Holland, 1983) p.261.

6.7 Exercises

6.1 Consider a thick Si crystal where the normal to the surface is in the (100) direction.

  (a) What are the Miller indices in symmetric Bragg geometry of the reflection with the lowest Bragg angle?
  (b) What is the reflectivity per atomic layer of that reflection?
  (c) At a wavelength of 1.54 Å how far should one offset the rotation angle of the sample from the Bragg angle before the reflectivity is reduced by a factor of 100?

6.2 From Eq. (6.20) show that the phase of r is equal to $-\pi$ for $x \leq -1$; $-\mathrm{acos}(x)$ for $|x| \leq 1$, and 0 for $x \geq 1$.

6.3 Prove Eq. (6.26).

6.4 Explain why Eq. (6.33) for the extinction depth refers to the 1/e reduction of intensity rather than amplitude.

6.5 Prove Eq. (6.40).

6.6 Phonons energies are typically in the range 0−100 meV. Inelastic X-ray scattering offers the possibility of measuring phonon dispersion curves. However, as X-ray energies are of order 10 keV, this requires devising a spectrometer with very high energy resolution to detect the relatively small change in photon energy when it creates (or destroys) a phonon.

  (a) Starting from Bragg's law, derive a general expression for the resolution $\Delta \mathcal{E}/\mathcal{E}$ in terms of the Bragg angle θ. Under what conditions is the maximum resolution obtained?
  (b) Calculate the energy required to achieve the best resolution for a Si (12,12,12) monochromator.
  (c) By calculating the Darwin width at the appropriate energy calculate the resolution provided by a Si(12,12,12) monochromator.

6.7 Estimate the extinction depths of the (111) reflections from diamond, silicon and germanium by neglecting the Q and energy dependences of the atomic form factors.

6.8 Consider the (200) reflection from GaAs at 12.4 keV. Compare the extinction depth to the absorption depth. Discuss whether the integrated intensity in a rocking scan is proportional to $|F|$ or to $|F|^2$.

6.9 Evaluate and compare the ratio of widths of the (111) and (333) reflections shown in Fig. 6.10(b) and (c).

6.10 Consider the experimental arrangement in which a white beam is monochromated by a perfect crystal in symmetric Bragg geometry with a Bragg angle of $30°$. The monochromatic beam then impinges on a second, asymmetrically cut perfect crystal in which the lattice planes are at an angle of $15°$ with respect to the surface. The angle of incidence of the beam on the second crystal required to diffract the second beam is either (a) $15°$ or (b) $45°$ depending on its orientation. For the two cases make sketches of the expected variation of intensity of beam diffracted by the second crystal as its angle is rotated through the Bragg condition. (You may assume for simplicity that the Darwin curve may be represented by a top-hat function and ignore refraction effects.)

Photoelectric absorption

Almost everyone has benefitted in one way or another from the characteristics of the X-ray absorption cross-section. For example, most people have had the experience at the dentist of holding a piece of photographic film inside of their mouth during the fraction of a second it takes to record a shadow picture of a suspicious tooth. The ability to take shadow pictures, or radiographs, relies on two basic aspects of the absorption process. The first is that X-ray absorption has a pronounced dependence on the atomic number Z, varying approximately as the fourth power of Z. This feature provides the necessary contrast between materials of different densities, such as skin, bone, etc. The second relates to the penetrating power of the X-ray beam, which for a given element varies approximately as the reciprocal of the photon energy $\mathcal{E}$ to the third power. By adjusting the energy of the beam it is thus possible to obtain a suitable penetration depth into the material of interest.

The absorption cross-section per atom, σ_a, is in principle an easy quantity to measure. In a transmission experiment the ratio of beam intensities is recorded with (I) and without (I_0) the sample. For a sample of thickness z the transmission, T, is given by

$$T = \frac{I}{I_0} = e^{-\mu z} \tag{7.1}$$

The absorption coefficient μ is related to σ_a through

$$\mu = \left(\frac{\rho_m N_A}{M} \right) \sigma_a$$

where N_A, ρ_m and M are Avogadro's number, the mass density, and the molar mass, respectively (Eq. (1.18)). However, in practice careful corrections have to be applied for other processes that may attenuate the intensity of the beam. At X-ray energies, these comprise Thomson and Compton scattering, while for energies above twice the rest mass of the electron (1.02 MeV) the cross-section for pair production becomes significant.

An instructive way to illustrate the stated dependencies of σ_a on Z and $\mathcal{E}$ is shown in Fig. 7.1. Here the experimentally determined values of σ_a have been scaled by dividing by Z^4 and multiplying by $\mathcal{E}^3$. Five elements have been selected, with values of Z ranging between 13 and 82, providing a range of $(82/13)^4 \approx 1500$ for the dependence on Z. The energy range covered is one decade, so that altogether
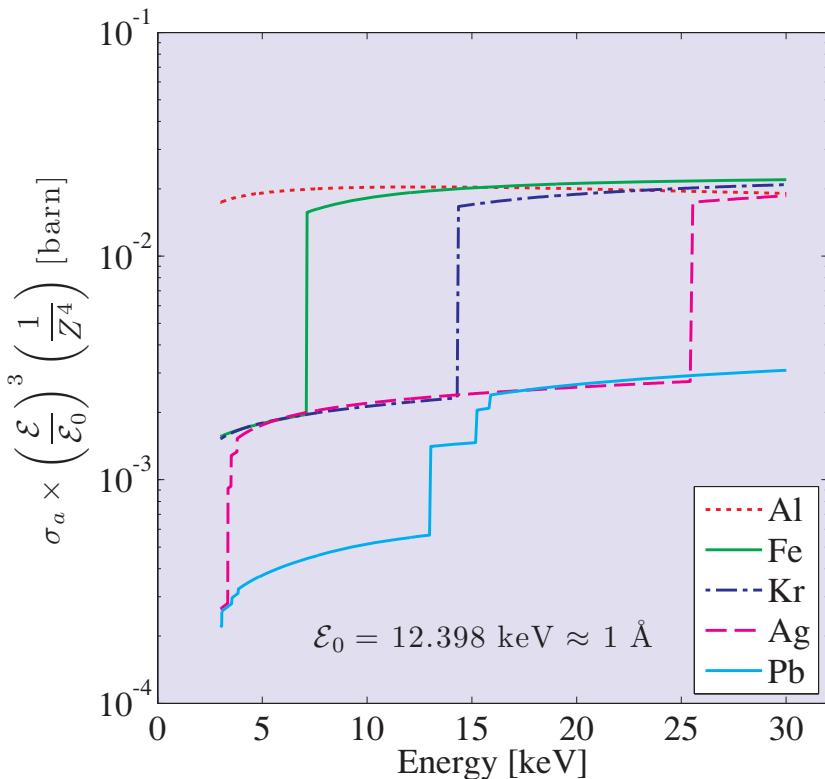
Fig. 7.1 The scaled absorption cross-section as a function of photon energy for a selection of elements. The absorption cross-section per atom, σ_a, has been scaled by dividing it by the atomic number Z to the fourth power, and multiplying it by the photon energy $\mathcal{E}$ to the third power.

the total span for the Z and $\mathcal{E}$ dependencies is more than six decades. For $Z < 47$ (Ag), and for $\mathcal{E} \geq 25$ keV, all of the scaled cross-sections collapse onto a single curve with a value of approximately 0.02 barn (1 barn $\equiv 10^{-24}$ cm^2). Below certain characteristic energies (approximately 25 keV for Ag, 14 keV for Kr, 7 keV for Fe) the scaled cross-section drops to another value, approximately one decade lower, where it joins the level that the heaviest element Pb has for $\mathcal{E} > 16$ keV. The element-specific energies of the discontinuous jumps in the absorption cross-section are called *absorption edges*, and the physical reason for their appearance is quite simple to understand. Electrons are bound in atoms with discrete energies. For example, the K electrons in Kr have a binding energy of 14.32 keV. At photon energies greater than 14.32 keV there is the possibility that the photon can interact with the atom, removing one of the K electrons in the process, with the photon being annihilated at the same time. This is known as *photoelectric absorption*. When the photon energy drops below the threshold value of 14.32 keV this particular process is no longer energetically possible, one of the channels for photoelectric absorption closes, and therefore the absorption cross-section falls by a certain amount.

The K edge for Pb is 88 keV, beyond the range of energies plotted in Fig. 7.1. However, three other discontinuities are apparent for Pb in the range 13-16 keV. These are the L edges, which correspond to the removal of electrons from the L shell. The structure evident in the L edges arises from the fact that the degeneracy of the electron energy in the L shell is lifted by two mechanisms. First, due to screening
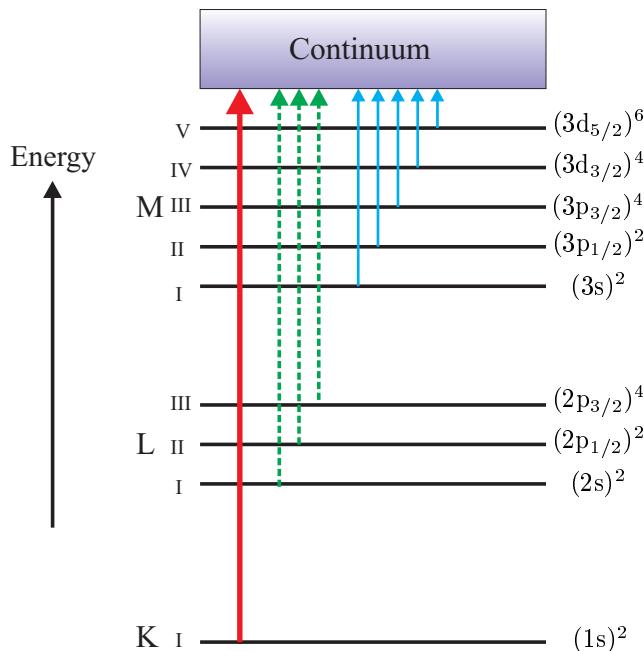
Fig. 7.2 A summary of the nomenclature used to label the absorption edges of the elements. The K edge corresponds to the energy required to remove an electron from the 1s shell to the continuum of free states, etc. The electronic shells are labelled as $(n\ell_j)^{2j+1}$, where n, ℓ and j are the principal, orbital angular momentum, and total angular momentum quantum numbers, respectively, of the single-electron states. The multiplicity is $2j + 1$.

of the nuclear charge by the inner K electrons, the self-consistent one-electron potential drops faster than the pure Coulomb potential, with the consequence that the energy of the 2s electrons is lower than that of the 2p electrons. By convention the 2s energy is labelled L_I. Furthermore the 2p level is split by spin-orbit coupling into levels denoted L_{II} and L_{III}. The nomenclature used to label the absorption edges is summarized in Fig. 7.2.

From a practical point of view the most useful way to quantify photoelectric absorption is not in terms of absorption cross-section but in terms of the mass absorption coefficient, μ/ρ_m. Since at fixed photon energy μ/ρ_m is a constant for a given element, independent of the form of matter being considered, the mass absorption coefficient of a mixture (including compounds, alloys, solutions, etc.) can be readily evaluated using

$$\left(\frac{\mu}{\rho_m}\right)_{mixture} = \sum_j w_j \left(\frac{\mu}{\rho_m}\right)_j \tag{7.2}$$

where w_j is the fraction by weight of the j'th component.

Photoelectric absorption is sometimes referred to as true absorption. This is to distinguish it from other processes that also act to reduce the intensity of a beam of photons. The photoelectric process

usually dominates the absorption cross-section for all but the lightest elements, except perhaps at the highest X-ray energies ($\gtrsim$ 100 keV) where it can weaken to become comparable to the cross-sections for Thomson and/or Compton scattering[1]. The initial objective of this chapter in Section 7.1 is to investigate whether from a first-principles calculation of the absorption cross-section, σ_a, it is possible to account not only for the observed dependences on Z and $\mathcal{E}$, but also for the absolute magnitude of the jump in σ_a at the K edge. We then proceed in Section 7.2 to outline the theoretical description of the oscillations in σ_a which are observed just above an absorption edge. These are known as Extended X-Ray Absorption Fine Structure (EXAFS), and in Chapter 1 the example was already given of crystalline Kr in Fig. 1.13 on page 21. Next, in Section 7.3 we provide an introduction to the use of X-ray dichroism − the differential absorption of orthogonally polarized photon states − in the study of magnetic materials. Finally, for completeness we discuss in Section 7.4 angle resolved photoemission, where the energy and momentum of photoelectrons are studied to deduce unique information on the electronic structure of materials.

In contrast to Thomson scattering, photoelectric absorption cannot be explained by classical physics, and instead it is necessary to invoke a quantum mechanical description of both the X-ray field and the photoelectron. Readers who are unfamiliar with this approach are referred to Appendix C. While reading this chapter it is probably also worthwhile to bear in mind the Optical Theorem which relates absorption to the imaginary part of the forward scattering amplitude (see Section 3.3, and in particular Eq. (3.10)). The consequences of this theorem will be more fully explored in Chapter 8 on resonant scattering.

7.1   X-ray absorption by an isolated atom

For the sake of definiteness an absorption process is chosen where a K electron is expelled from an absorbing atom, although the calculation would be essentially the same if an electron in another shell were to be considered.

Our starting point is the formula (Eq. (A.8)) for the absorption cross-section derived in Appendix A:

$$\sigma_a = \frac{2\pi}{\hbar c} \frac{V^2}{4\pi^3} \int \left| M_{if} \right|^2 \delta(\mathcal{E}_f - \mathcal{E}_i) \, \mathrm{q}^2 \sin\theta \, d\mathrm{q} d\theta d\varphi \tag{7.3}$$

This equation comes directly from first-order perturbation theory. In the absorption process an X-ray photon specified by $\mathbf{k}, \hat{\boldsymbol{\varepsilon}}$ (where $\mathbf{k}$ and $\hat{\boldsymbol{\varepsilon}}$ are the wavevector and polarization) is annihilated from the initial state $|i\rangle$, and a photoelectron is expelled into the continuum, where it ends in the final state $|f\rangle$ with a momentum $\mathbf{p} = \hbar\mathbf{q}$ and energy $\mathcal{E}_f = \hbar^2\mathrm{q}^2/2m$. As the photoelectron may be expelled into any direction, it is necessary to integrate over the entire solid angle, 4π, with the value of q^2 restricted to obey energy conservation by the introduction of the delta function in the integrand. The angles (θ, φ) relate the direction of $\mathbf{q}$ to $(\mathbf{k}, \hat{\boldsymbol{\varepsilon}})$ as shown in Fig. 7.3. It is also recalled that in order to normalize the wavefunctions the system is confined to a box of volume V.

The crucial quantity in the formula for σ_a is the matrix element $M_{if} = \langle f | \mathcal{H}_I | i \rangle$, where $\mathcal{H}_I$ is the interaction Hamiltonian that produces transitions between the initial $|i\rangle$ and final $|f\rangle$ states. Here we refer to Appendix C where it is shown that $\mathcal{H}_I$ is conveniently expressed in terms of the vector potential $\mathbf{A}$ of the incident photon field. Both the electric and magnetic fields may be derived directly from $\mathbf{A}$,

---

[1]The pair production cross-section only becomes significant for gamma rays with energies above $2mc^2$=1.02 MeV.
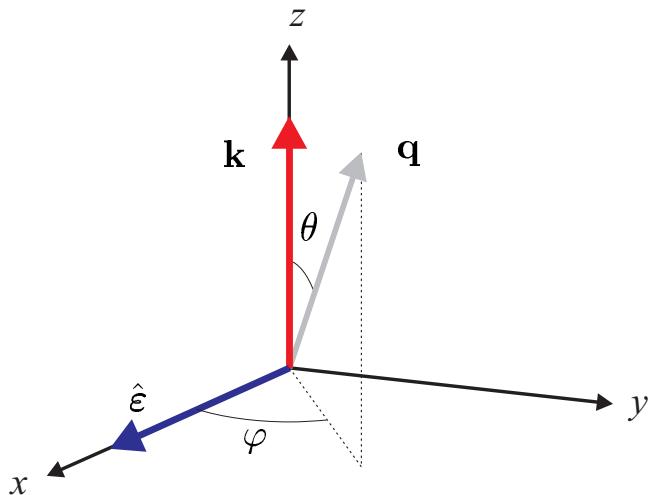
Fig. 7.3 The coordinate system relating the angles (θ, φ) to the wavevector of the photoelectron $\mathbf{q}$ and the wavevector and polarization of the incident photon $(\mathbf{k}, \hat{\boldsymbol{\varepsilon}})$. In this case the photon propagates along the z direction and has its electric field polarized along x.

and hence quantizing the electromagnetic field amounts to quantizing the vector potential $\mathbf{A}$. For a plane wave the time-independent operator representing the vector potential is

$$\mathbf{A} = \hat{\boldsymbol{\varepsilon}} \sqrt{\frac{\hbar}{2\epsilon_0 V \omega}} \left[a_{\mathbf{k}} \, e^{i\mathbf{k}\cdot\mathbf{r}} + a_{\mathbf{k}}^{\dagger} \, e^{-i\mathbf{k}\cdot\mathbf{r}} \right] \tag{7.4}$$

where $a_{\mathbf{k}}$ and $a_{\mathbf{k}}^{\dagger}$ are the annihilation and creation operators. They act on the eigenstates of the photon field, and either destroy or create a photon specified by $(\mathbf{k}, \hat{\boldsymbol{\varepsilon}})$.

Neglecting any magnetic interactions, the interaction Hamiltonian, $\mathcal{H}_I$, contains two terms, one linear in $\mathbf{A}$ and one that varies as A^2 (Eq. (C.7)). As shall now be shown, in first-order perturbation theory the linear term gives rise to absorption, whereas the squared term produces, amongst other things, Thomson scattering of the photon (see Appendix C). The explicit form of the matrix element of the linear term is

$$M_{if} = \langle f| \frac{e}{m} \mathbf{p} \cdot \mathbf{A} |i\rangle \tag{7.5}$$

This matrix element is evaluated by first neglecting the Coulomb interaction between the photoelectron and the positively charged ion that is left behind. In other words the photoelectron is assumed to be free. Its wavefunction must be normalized, and is thus proportional to $V^{-1/2}$. This together with the $V^{-1/2}$ dependence of $\mathbf{A}$ makes M_{if} proportional to V^{-1}, and hence, according to Eq. (7.3), σ_a is independent of V as required.

7.1.1   Free-electron approximation

In the initial state $|i\rangle$ there is one photon, specified by its wavevector and polarization, $(\mathbf{k}, \hat{\boldsymbol{\varepsilon}})$, and one K electron in its ground state. The initial state $|i\rangle$ is a product of the photon and electron states, and is

hence written as $|i\rangle = |1\rangle_x|0\rangle_e$. Similarly the final state is given by $|f\rangle = |0\rangle_x|1\rangle_e$, where the photon has been annihilated and the photoelectron expelled from the atom. From Eqs. (7.5) and (7.4) the matrix element for the absorption process is

$$M_{if} = \frac{e}{m}\sqrt{\frac{\hbar}{2\epsilon_0 V\omega}}\left[{}_e\langle 1|_x\langle 0| (\mathbf{p}\cdot\hat{\boldsymbol{\varepsilon}})\, a\, e^{i\mathbf{k}\cdot\mathbf{r}} + (\mathbf{p}\cdot\hat{\boldsymbol{\varepsilon}})\, a^\dagger\, e^{-i\mathbf{k}\cdot\mathbf{r}}|1\rangle_x|0\rangle_e\right]$$

To facilitate the evaluation of this matrix element the operators are allowed to act to the left on the final state. The advantage is that the final state of the electron is free, and is therefore an eigenfunction of the momentum operator of the electron, $\mathbf{p}$, with an eigenvalue $\hbar\mathbf{q}$. For the photon part it is recalled that when operating to the left an annihilation operator transforms to become a creation operator, etc., with the result that ${}_x\langle n|a = (\sqrt{n+1})\,{}_x\langle n+1|$ and ${}_x\langle n|a^\dagger = (\sqrt{n})\,{}_x\langle n-1|$, where n is the number of photons. The terms of interest are

$${}_e\langle 1|_x\langle 0|(\mathbf{p}\cdot\hat{\boldsymbol{\varepsilon}})\, a = \hbar(\mathbf{q}\cdot\hat{\boldsymbol{\varepsilon}})\,{}_e\langle 1|_x\langle 1|$$

and

$${}_e\langle 1|_x\langle 0|(\mathbf{p}\cdot\hat{\boldsymbol{\varepsilon}})\, a^\dagger = 0$$

since in the second case there are no photons in the final state to annihilate. It follows that the absorption matrix element simplifies to become

$$M_{if} = \frac{e}{m}\sqrt{\frac{\hbar}{2\epsilon_0 V\omega}}\left[(\hbar\,\mathbf{q}\cdot\hat{\boldsymbol{\varepsilon}})\,{}_e\langle 1|_x\langle 1| e^{i\mathbf{k}\cdot\mathbf{r}}|1\rangle_x|0\rangle_e + 0\right]$$

$$= \frac{e\hbar}{m}\sqrt{\frac{\hbar}{2\epsilon_0 V\omega}}(\mathbf{q}\cdot\hat{\boldsymbol{\varepsilon}})\,{}_e\langle 1| e^{i\mathbf{k}\cdot\mathbf{r}}|0\rangle_e$$

$$= \frac{e\hbar}{m}\sqrt{\frac{\hbar}{2\epsilon_0 V\omega}}(\mathbf{q}\cdot\hat{\boldsymbol{\varepsilon}})\int \psi_{e,f}^* e^{i\mathbf{k}\cdot\mathbf{r}}\psi_{e,i}\, d\mathbf{r}$$

The integral is over the position $\mathbf{r}$ of the photoelectron, and involves the plane wave $e^{i\mathbf{k}\cdot\mathbf{r}}$ of the incident photon field (Eq. (7.4)). Here the initial wavefunction of the electron, $\psi_{e,i}$, is taken to be that of the 1s bound state, while the final wavefunction, $\psi_{e,f}$, is assumed to be that of a free electron, which are written respectively as

$$\psi_{e,i} = \psi_{1s}(\mathbf{r})$$

and

$$\psi_{e,f} = \frac{1}{\sqrt{V}}\, e^{i\mathbf{q}\cdot\mathbf{r}}$$

The matrix element for the photoelectric absorption process is thus

$$M_{if} = \frac{e\hbar}{m}\sqrt{\frac{\hbar}{2\epsilon_0 V\omega}}(\mathbf{q}\cdot\hat{\boldsymbol{\varepsilon}})\int \frac{e^{-i\mathbf{q}\cdot\mathbf{r}}}{\sqrt{V}}\, e^{i\mathbf{k}\cdot\mathbf{r}}\psi_{1s}(\mathbf{r})\, d\mathbf{r} \tag{7.6}$$

With the wavevector transfer defined by $\mathbf{Q} = \mathbf{k} - \mathbf{q}$, the integral is written as

$$\phi(\mathbf{Q}) = \int \psi_{1s}(\mathbf{r})\, e^{i(\mathbf{k}-\mathbf{q})\cdot\mathbf{r}}\, d\mathbf{r} = \int \psi_{1s}(\mathbf{r})\, e^{i\mathbf{Q}\cdot\mathbf{r}}\, d\mathbf{r}$$

This is nothing other than the Fourier transform of the wavefunction of the electron in its initial state. The modulus squared of the matrix element for the particular process where the photoelectron is expelled into the direction specified by the polar angles (θ, φ) is

$$|M_{if}|^2 = \left(\frac{e\hbar}{m}\right)^2 \frac{\hbar}{2\epsilon_0 V^2 \omega} (q^2 \sin^2 \theta \cos^2 \varphi) \phi^2(\mathbf{Q})$$

since $(\mathbf{q} \cdot \hat{\boldsymbol{\varepsilon}}) = q \sin \theta \cos \varphi$, as can be seen from Fig. 7.3.

The absorption cross-section per K electron is found by substituting the above matrix element into Eq. (7.3) to obtain

$$\sigma_a = \frac{2\pi}{\hbar c} \frac{V^2}{4\pi^3} \left(\frac{e\hbar}{m}\right)^2 \frac{\hbar}{2\epsilon_0 V^2 \omega} I_3$$

$$= \left(\frac{e\hbar}{m}\right)^2 \frac{1}{4\pi^2 \epsilon_0 c \omega} I_3 \tag{7.7}$$

where the three-dimensional integral I_3 is defined by

$$I_3 = \int \phi^2(\mathbf{Q}) \, q^2 \sin^2 \theta \cos^2 \varphi \, \delta(\mathcal{E}_f - \mathcal{E}_i) \, q^2 \sin \theta \, dq d\theta d\varphi \tag{7.8}$$

To proceed it is required to specify an explicit form for $\phi(\mathbf{Q})$ and hence also for $\psi_{1s}(\mathbf{r})$. Here it is taken to be that of the 1s state of the hydrogen atom, but with a nuclear charge of Z. In this case the wavefunction is

$$\psi_{1s}(\mathbf{r}) = \frac{2}{\sqrt{4\pi}} \kappa^{\frac{3}{2}} e^{-\kappa r} \tag{7.9}$$

where $\kappa = Z/a_0$, and a_0 is the Bohr radius. The Fourier transform of ψ_{1s} may be evaluated using the method described on page 119 for the Fourier transform of $|\psi_{1s}|^2$. The result is

$$\phi(\mathbf{Q}) = \int \psi_{1s}(\mathbf{r}) e^{i\mathbf{Q}\cdot\mathbf{r}} \, d\mathbf{r} = \frac{4\sqrt{4\pi} \, \kappa^{\frac{5}{2}}}{[Q^2 + \kappa^2]^2} \tag{7.10}$$

We are now in a position to evaluate the integral I_3 defined in Eq. (7.8). The integration over φ is straightforward: the integral over one period of $\cos^2 \varphi$ is equal to π. Next, consider the integral over the delta function. The energy of the initial state is $\mathcal{E}_i = \hbar\omega - \hbar\omega_K$, i.e. equal to the difference between the incident photon energy and $\hbar\omega_K$, the binding energy of the K electron. The energy of the final state is equal to the kinetic energy of the photoelectron, $\mathcal{E}_f = \hbar^2 q^2 / 2m$. It is convenient to introduce $\tau = q^2$ as the integration variable, rather than to use q itself. The differential element dq then becomes $dq = d\tau/(2q) = d\tau/(2\sqrt{\tau})$. As far as the θ integration is concerned, the substitution $\mu = \cos\theta$ is made to obtain

$$I_3 = \pi \int \phi^2(\mathbf{Q}) \, \tau^2 \, (1 - \mu^2) \, \delta\left(\left(\frac{\hbar^2}{2m}\right)\tau - (\hbar\omega - \hbar\omega_K)\right) \frac{1}{2\sqrt{\tau}} \, d\tau d\mu$$

Integrating over τ is achieved using the properties of the delta function (see the box on page 152). This results in a factor of $(2m/\hbar^2)$, with the integrand evaluated at

$$\tau = \tau_0 = \left(\frac{2m}{\hbar^2}\right)\left[\hbar\omega - \hbar\omega_K\right] \tag{7.11}$$

Evaluation of integral I_1 and its limit when $\hbar\omega \gg \hbar\omega_K$

The integral I_1 given in Eq. (7.12) may be expressed in the form

$$I_1 = g \int_{-1}^{1} \frac{(1-\mu^2)}{(a\mu - b)^4} \, d\mu = \left(\frac{4}{3}\right) \frac{g}{(a^2 - b^2)^2}$$

with the parameters g, a and b defined as

$$g = \tau_0^{\frac{3}{2}} \kappa^5 \qquad = c^{-3} \left[\omega_c(\omega - \omega_K)\right]^{\frac{3}{2}} c^{-5} \omega_A^5 \qquad \to c^{-8} \omega_A^5 [\omega_c\omega]^{\frac{3}{2}}$$

$$a = 2k\sqrt{\tau_0} \qquad = 2c^{-2}\omega \left[\omega_c(\omega - \omega_K)\right]^{\frac{1}{2}} \qquad \to 2c^{-2}\omega[\omega_c\omega]^{\frac{1}{2}}$$

$$b = k^2 + \tau_0 + \kappa^2 = c^{-2}\left[\omega^2 + \omega_c(\omega - \omega_K) + \omega_A^2\right] \to c^{-2}[\omega_c\omega]$$

In the second equation we have introduced the following definitions of energies (or cyclic frequencies): $\tau_0 = \frac{2m}{\hbar}(\omega - \omega_K) = c^{-2}\omega_c(\omega - \omega_K)$, $\hbar\omega_c = 2mc^2$ and $\hbar\omega_A = \hbar c\kappa = Z\hbar c/a_0$ (see Fig. 7.4). Furthermore, the arrows indicate the limit when $\hbar\omega \gg \hbar\omega_K$, but still with $\hbar\omega \ll \hbar\omega_c$. In this limit $b \gg a$, and we find that

$$I_1 \to \left(\frac{4}{3}\right) \frac{g}{b^4} = \left(\frac{4}{3}\right) \left[\frac{\omega_A^2}{\omega\omega_c}\right]^{\frac{5}{2}}$$

In terms of the integration variables the square of $\phi(\mathbf{Q})$ is

$$\phi^2(\mathbf{Q}) = \frac{64\pi \kappa^5}{\left[k^2 + \tau - 2k\sqrt{\tau}\mu + \kappa^2\right]^4}$$

since $Q^2 = (\mathbf{k} - \mathbf{q}) \cdot (\mathbf{k} - \mathbf{q}) = k^2 + q^2 - 2\mathbf{k} \cdot \mathbf{q} = k^2 + \tau - 2k\sqrt{\tau}\mu$. The three-dimensional integral I_3 therefore reduces to a one-dimensional integral I_1, with

$$I_3 = 32\pi^2 \left(\frac{2m}{\hbar^2}\right) I_1(\tau_0, \kappa)$$

and

$$I_1(\tau_0, \kappa) = \int_{-1}^{1} \frac{\kappa^5(1 - \mu^2)\,\tau_0^{\frac{3}{2}}}{\left[k^2 + \tau_0 - 2k\sqrt{\tau_0}\mu + \kappa^2\right]^4} \, d\mu \tag{7.12}$$

Collecting the above results together the expression for the absorption cross-section given in Eq. (7.7) becomes

$$\sigma_a = \left(\frac{e\hbar}{m}\right)^2 \frac{1}{4\pi^2\epsilon_0 c\omega} 32\pi^2 \left(\frac{2m}{\hbar^2}\right) I_1(\tau_0, \kappa)$$

$$= \frac{e^2}{4\pi\epsilon_0 mc\omega} 32\,(2\pi)I_1(\tau_0, \kappa)$$

This can be simplified by noting that the Thomson scattering length is $r_0 = e^2/(4\pi\epsilon_0 mc^2)$, and that $\omega = 2\pi c/\lambda$. Hence the atomic absorption cross-section per K electron is

$$\sigma_a = 32\lambda r_0\, I_1(\tau_0, \kappa)$$

(7.13)

with τ_0 given by Eq. (7.11) and $\kappa = Z/a_0$. At this point it is interesting to note the following:

  (a) If the dimensionless integral I_1 turns out to be of order unity, as indeed it does at the edge, then the absorption cross-section per K electron is much larger than the scattering cross-section, which is of order r_0^2, since $\lambda \gg r_0$.

  (b) The dimension of the absorption cross-section is length squared, as expected.

  (c) The volume, V, of the box introduced for normalization purposes has disappeared from the final formula, also as expected.

The evaluation of the integral $I_1(\tau_0, \kappa)$ is given in the box on the facing page, along with its asymptotic behaviour in the limit that the photon energy is much greater than the binding energy of the K electron, but still much smaller than the rest mass energy of the electron. With energies as defined in Fig. 7.4 one finds

$$\sigma_a = 32\lambda r_0 \left(\frac{4}{3}\right)\left[\frac{\omega_A^2}{\omega\omega_c}\right]^{\frac{5}{2}} \quad \text{for } \hbar\omega_K \ll \hbar\omega \ll \hbar\omega_c$$

(7.14)

It is apparent that σ_a varies as Z^5 via ω_A, and as $\omega^{-7/2}$ via the dependence of I_1 on $\omega^{-5/2}$ and the factor of $\lambda = 2\pi c/\omega$. This behaviour is somewhat different from the experimental findings, summarized in Fig. 7.1, where σ_a is approximately proportional to Z^4 and ω^{-3}. The reason for this discrepancy is the approximation made at the beginning of this section, where we neglected the Coulomb interaction between the photoelectron and the positively charged ion. The benefit is that we have been able to obtain, with moderate effort, an analytical expression for σ_a. However, the price to be paid for this is apparently high, as the result is not sufficiently accurate. It is therefore necessary to consider a treatment of the problem beyond the free-electron approximation.

7.1.2   Beyond the free-electron approximation

Here the full calculation of the correct wavefunction of the photoelectron in the Coulomb field of the ion is not given. Instead the result which was derived in the 1930s by Stobbe is stated without proof [Stobbe, 1930]. Stobbe introduced the dimensionless photon energy variable

$$\xi = \sqrt{\frac{\omega_K}{\omega - \omega_K}}$$

and conveniently enough, his result can be written as a correction factor $f(\xi)$ to the asymptotic expression for the integral I_1 given above in Eq. (7.14). The absorption cross-section per K electron
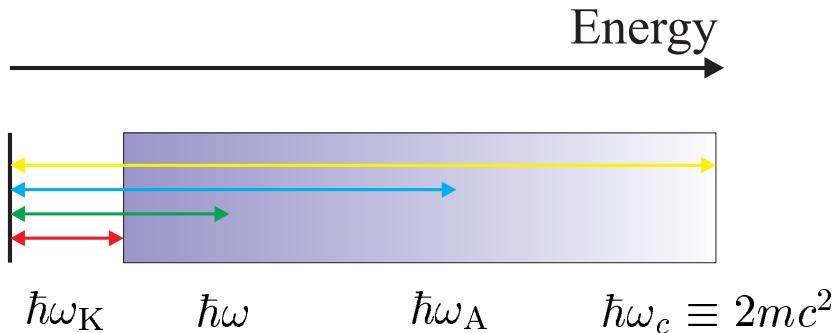
Fig. 7.4 A schematic of the different energy scales involved in calculating the absorption cross-section. The energy of the absorption edge is $\hbar\omega_K$, and is proportional to Z^2 in a simple hydrogen-like model of the atom. The energy $\hbar\omega_A$ is related to κ, the inverse length scale of the wavefunction ψ_{1s} (Eq. (7.9)). The relationship is $\hbar\omega_A \equiv \hbar c\kappa$, and thus $\hbar\omega_A$ is proportional to Z. The highest characteristic energy is $\hbar\omega_c$ and is defined to be twice the rest mass energy of the electron. i.e. 2×511 keV.

allowing for the Coulomb interaction between the photoelectron and the ion is then

$$\sigma_a = 32\lambda r_0 \left(\frac{4}{3}\right)\left[\frac{\omega_A^2}{\omega\omega_c}\right]^{\frac{5}{2}} f(\xi) \tag{7.15}$$

Stobbe's correction function, $f(\xi)$, depends on both Z and $\hbar\omega$. When it is included in the formula for σ_a it transpires that there is good agreement between the experimental and theoretical dependences on Z and $\hbar\omega$, and reasonable agreement with the absolute value of the cross-section. The explicit form of the correction function is

$$f(\xi) = 2\pi \sqrt{\frac{\omega_K}{\omega}} \left(\frac{e^{-4\xi \operatorname{arccot}\xi}}{1 - e^{-2\pi\xi}}\right)$$

Two limits are particularly illuminating to consider, namely when the photon energy is much greater than the binding energy, $\hbar\omega \gg \hbar\omega_K$ or equivalently $\xi \to 0$, and when the photon energy approaches the threshold energy from above, $\hbar\omega \to \hbar\omega_K^+$ or $\xi \to \infty$. At high photon energies we have $\operatorname{arccot}\xi \to \pi/2$, so that $e^{-4\xi \operatorname{arccot}\xi} \to e^{-2\pi\xi}$. Thus the high-energy limit of the correction factor is

$$f(\xi) \to 2\pi\xi \left(\frac{e^{-2\pi\xi}}{1 - e^{-2\pi\xi}}\right) \to 1 \qquad \text{for } \hbar\omega \gg \hbar\omega_K$$

This result makes physical sense. When the photon energy is high, so is the energy of the photoelectron, and it makes little difference whether the photoelectron is free or moves in the relatively weak attractive field of the positive ion. For photon energies approaching the threshold ($\hbar\omega \to \hbar\omega_K^+$, or $\xi \to \infty$) we have that $\operatorname{arccot}\xi \to 0$ as $1/\xi$, so that the product $\xi \operatorname{arccot}\xi \to 1$, and

$$f(\xi) \to \left(\frac{2\pi}{e^4}\right) \qquad \text{for } \hbar\omega \to \hbar\omega_K^+$$

At threshold we therefore find a discontinuous jump in the absorption cross-section *per* K electron of

$$\sigma_a = 32\lambda r_0 \left(\frac{4}{3}\right)\left[\frac{\omega_A^2}{\omega_K\omega_c}\right]^{\frac{5}{2}}\left(\frac{2\pi}{e^4}\right) \tag{7.16}$$

In order to evaluate either the energy dependence of σ_a (Eq. (7.15)) or the height of the step in σ_a at the K edge (Eq. (7.16)) it is necessary to know how to calculate ω_A and ω_K. The simplest approach is to take the model of a hydrogen atom as the starting point. The K shell ionization energy, $\hbar\omega_K$, of an atom with Z electrons is then approximately the binding energy of the hydrogen atom times Z^2. We thus can write $\hbar\omega_K = Z^2 e^2/(4\pi\epsilon_0 2a_0)$. The energy $\hbar\omega_A$ that we have introduced is given by $Z\hbar c/a_0$, and hence scales with Z. Within the model of the hydrogen-like atom the ratio $\omega_A^2/(\omega_K\omega_c)$ is independent of Z, and as $a_0 = 4\pi\hbar^2\epsilon_0/(me^2)$, the ratio is equal to unity. The edge jump per K electron is therefore

$$\sigma_a(\lambda_K) \cong 32\lambda_K r_0 \left(\frac{4}{3}\right)\left(\frac{2\pi}{e^4}\right)$$
$$= \left(\frac{256\pi}{3e^4}\right)\lambda_K r_0 \tag{7.17}$$

From Eq. (7.15), this approximation also allows the energy dependence of σ_a *per* K electron to be written in a particularly convenient form as

$$\sigma_a \cong 32\lambda r_0 \left(\frac{4}{3}\right)\left[\frac{\omega_K}{\omega}\right]^{\frac{5}{2}} f(\xi) \tag{7.18}$$

Comparison with experiment

As an example we have chosen the absorption cross-sections of the noble gas elements Ar ($Z = 18$), Kr ($Z = 36$) and Xe ($Z = 54$). The energy dependences of σ_a are shown in Fig. 7.5 in the vicinity of the K edges at 3.20, 14.32, and 34.56 keV for the three elements respectively. The dot-dashed lines are obtained from state-of-the-art calculations performed within the self-consistent Dirac-Hartree-Fock framework [Chantler, 1995] (See also Henke et al. [1993].).

Here a comparison is made of the absorption cross-sections shown in Fig. 7.5 with our simpler model given by Eq. (7.18). This was derived using the hydrogen-like model of the atom, and has only one free parameter, the energy of the K edge, $\hbar\omega_K$. For a hydrogen-like atom $\hbar\omega_K$ is given by Z^2 times the binding energy of the hydrogen atom, 13.60 eV. For the three elements chosen here the K edges are calculated to be 4.41, 17.63, and 39.66 keV. These are significantly greater than the experimental values. Slight adjustments to our approach, such as replacing Z by $(Z - 1)$, which allows for the shielding of the nuclear charge by one of the K electrons, brings little improvement to the estimate of $\hbar\omega_K$, although Moseley showed in 1913 that is does give good agreement with the K_α fluorescence energies, $\hbar(\omega_K - \omega_L)$ (see Eq. (1.20)). The hydrogen-like model probably works better in the case of fluorescence than absorption as the former involves differences in energies of the inner shell electrons, while the latter depends on being able to calculate the absolute value of the binding energy correctly. In either case the model is expected to become less appropriate as Z increases due to multi-electron and relativistic effects.
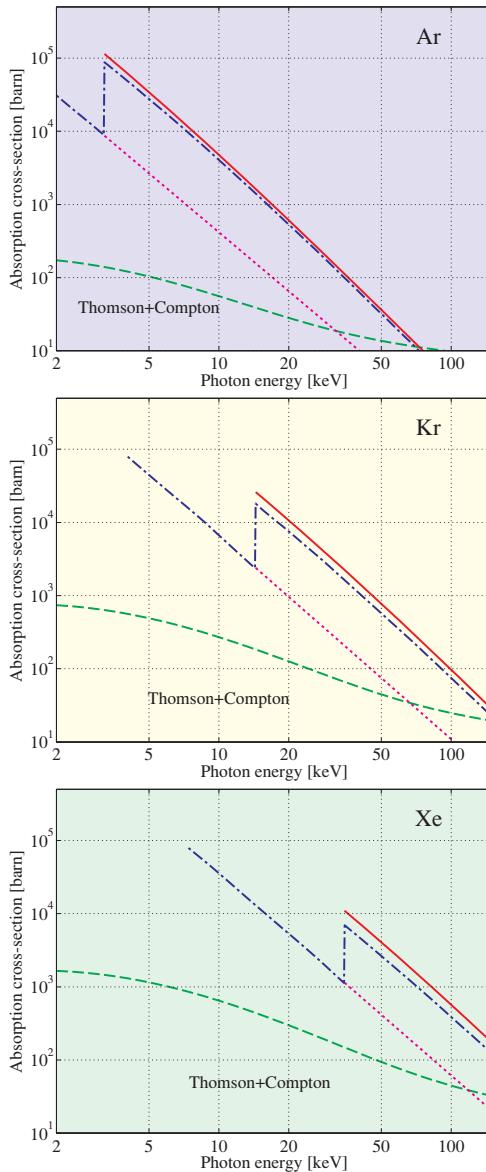
Fig. 7.5 The photoelectric absorption cross-sections of Ar, Kr and Xe plotted on a double logarithmic scale for energies in the vicinity of their K edges. The dot-dashed lines represent the results of calculations within the self-consistent Dirac-Hartree-Fock framework [Chantler, 1995]. The solid lines are calculated from Eq. (7.18) with $\hbar\omega_K$ equal to the experimentally observed values of 3.20, 14.32 and 34.56 keV respectively. In each case the result was multiplied by a factor of 2 to allow for the two K electrons, and then the extrapolated contribution from the L electrons (dotted lines) was added to it to produce the final result. For completeness the cross-sections for Thomson and Compton scattering are plotted as the dashed lines. The L edges of Kr ($\sim$ 2 keV) and Xe ($\sim$ 5 keV) have been omitted for clarity.

An alternative approach to calculating $\hbar\omega_K$ is to assume that Z scaling is approximately valid, and to treat $\hbar\omega_K$ as an experimentally determined parameter to be put into the theory. This approach has been adopted for Ar, Kr and Xe, and the photoelectron cross-section σ_a given by Eq. (7.18) with $\hbar\omega_K$ equal to the experimental values are represented by the solid lines in Fig. 7.5. In all three cases the theory developed here is seen to reproduce the energy dependence of σ_a very well. Agreement with the absolute value of σ_a is reasonable in the case of Ar, but becomes progressively worse for Kr and Xe. This is in line with the expectation that the hydrogen-like model becomes a poorer approximation the higher the value of Z. However, our intention here was not to derive exact values of σ_a, but rather to show how a relatively simple model of the photoelectron absorption process is capable of accounting for the main experimental features. Accurate methods for obtaining values of σ_a required for analysing experimental data are described and tabulated in a number of places, including the *International Tables of Crystallography*.

For completeness the cross-section from processes other than the photoelectric effect have also been included in Fig. 7.5. At the energies shown, these include Thomson and Compton scattering: at higher energies pair production becomes important. It is interesting to compare the limiting behaviour of the contribution made by these scattering processes for the different elements. In the case of Ar, the electrons can be considered to be effectively free for the highest photon energies shown, since the photon energy is much greater than that binding the electrons to the atom. The cross-section should then approach the value expected for a gas of Z electrons, i.e. $18 \times 0.667 = 12$ barn per atom, similar to the value shown in Fig. 7.5. (The total scattering cross-section per electron is 0.667 barn, see Eq. (B.5) on page 353.) The other extreme is Xe at low energies, where the electrons are tightly bound. The wavevector transfers, **Q**, accessible at these energies are small, and hence to a good approximation the atomic form factor squared is equal to Z^2 (Eq. (4.7)). The limiting cross-section in this case should therefore be $54 \times 54 \times 0.667 = 1945$ barn per atom, again close to the value shown.

7.2   EXAFS and near-edge structure

The simple step-like change in the X-ray absorption cross-section σ_a evident in Fig. 7.5 is the behaviour expected for isolated atoms only. For assemblies of atoms (molecules, crystals, etc.) the X-ray absorption cross-section develops structure for photon energies in the vicinity of an absorption edge. For example, in Fig. 1.13 the absorption cross-section is plotted for atomic Kr in various environments. Comparing the cross-section for Kr in its gaseous phase with its behaviour when bound to the surface of graphite it is clear that the absorption depends on the environment of the absorbing atom. The structure in σ_a results from a variety of physical processes which are referred to collectively as X-ray absorption fine structure (XAFS). The processes contributing to XAFS can be differentiated according to the photon energy relative to the edge. For energies within approximately ± 10eV of the edge the absorption cross-section may appear to overshoot the step-like behaviour. This is referred to as the X-ray absorption near edge structure (XANES) region. Physically it corresponds to transitions of core electrons to unfilled bound states just below the continuum of free electron states. As the density of such bound states close to the edge may be higher than the density of unbound states the absorption has a peak. (For historical reasons this is sometimes known as the 'white line' as this is the way that it appeared on photographic films used in early X-ray experiments.) For higher photon energies a photoelectron is liberated, which propagates from the source atom as a spherical wave. This outgoing wave may then be back scattered by neighbouring atoms producing oscillations in σ_a. Within 10–50 eV of the edge, the low energy of the photoelectron has the consequence that it undergoes multiple scattering. This is known as the near edge X-ray absorption fine structure (NEXAFS) regime. At

higher photon energies still, 50–1000 eV above the edge, the photoelectron acquires sufficient energy that single scattering events dominate. This is the extended X-ray absorption fine structure (EXAFS) region. A schematic of the origin of EXAFS oscillations in the interference between the outgoing and back scattered waves is given in Fig. 7.6. The EXAFS regime, dominated as it is by single photoelectron scattering events, is easier to analyse than the multiple scattering which is characteristic of NEXFAS. This explains why EXAFS has found wide utility in the determination of the local structure of materials, and also why it is the focus of this section.

7.2.1   Experimental considerations

In the analysis of EXAFS spectra it is customary to introduce the dimensionless quantity $\chi(q)$, defined by

$$\chi(q(\mathcal{E})) = \frac{\mu_\chi(\mathcal{E}) - \mu_0(\mathcal{E})}{\mu_0(\mathcal{E})} \tag{7.19}$$

Here $\mu_0(\mathcal{E})$ is the absorption coefficient of the isolated atom (which obviously does not display EXAFS), and $\mu_\chi(\mathcal{E})$ is the absorption coefficient of the atom in the material of interest. Rather than the photon energy $\mathcal{E}$, the photoelectron wavenumber q is used as the independent variable:

$$\frac{\hbar^2 q^2}{2m} = \mathcal{E} - \hbar\omega_K \tag{7.20}$$

The typical apparatus required for an EXAFS experiment is sketched in Fig. 7.7. A double crystal monochromator (as described in Chapter 6) is used to produce a monochromatic beam from the 'white' synchrotron beam. For relatively low X-ray energies it is found that the energy resolution provided by the Si(111) reflection is mostly adequate, whereas at higher energies the Si(311) or (511) may be needed. For all of these reflections, the second-order is forbidden, but it is important to ensure that higher orders in the beam are removed, either by offsetting slightly the angle of the second crystal as described on page 225, or by the use of mirrors.

The absorption spectrum can be measured in a transmission geometry, as indicated in Fig. 7.7. The transmission, defined as the ratio of intensities before, I_0, and after, I_1, the sample, is related to the absorption coefficient $\mu(\mathcal{E})$ at photon energy $\mathcal{E}$ by

$$T = \frac{I_1}{I_0} = e^{-\mu(\mathcal{E})d}$$

where d is the sample thickness (see Eq. (7.1)). The absorption coefficient $\mu(\mathcal{E})$ is then obtained from the measured transmission as a function of $\mathcal{E}$ from the above equation.

The measured absorption coefficient can be partitioned into contributions from the atoms of interest, $\mu_\chi(\mathcal{E})$, and that due to all the other atoms in the sample, $\mu_A(\mathcal{E})$, so that we may write

$$\mu(\mathcal{E}) = \mu_A(\mathcal{E}) + \mu_\chi(\mathcal{E}) = \mu_A(\mathcal{E}) + \mu_0(\mathcal{E})[1 + \chi(q)] \tag{7.21}$$

Both $\mu_A(\mathcal{E})$ and $\mu_0(\mathcal{E})$ vary smoothly as a function of $\mathcal{E}$ in the EXAFS region of interest, and can, by a combination of theoretical knowledge and numerical spline methods, be subtracted from the data in order to obtain $\chi(q)$. It is often of advantage to measure simultaneously a reference sample, as indicated in Fig. 7.7.
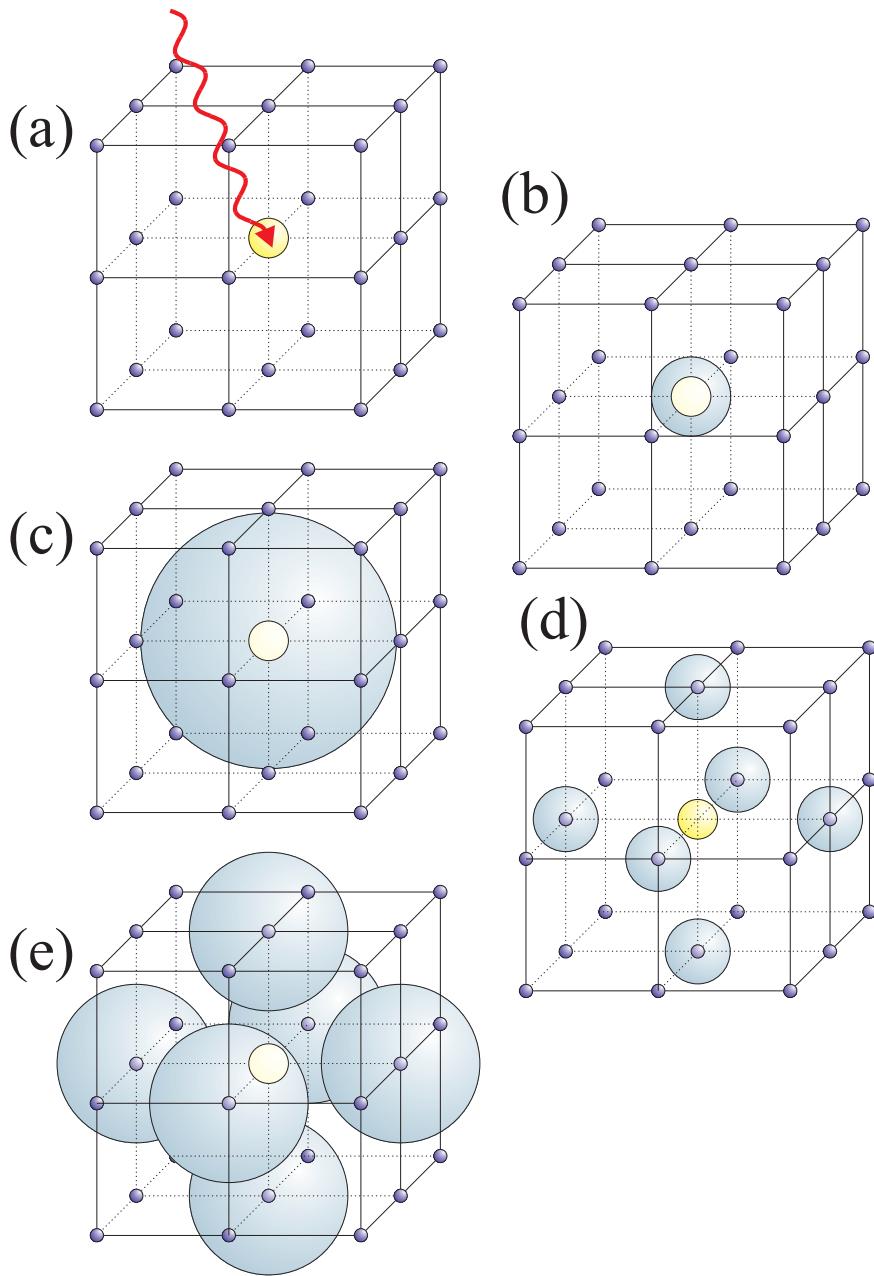
Fig. 7.6 Schematic of the EXAFS process. (a) An X-ray photon is incident on an atom located on a lattice. The energy of the photon is high enough that it liberates an electron from a core state in the atom, and the photon is absorbed in the process. (b)-(c) The outgoing wavefunction of the photoelectron propagates from the absorbing atom as a spherical wave until it reaches one of the neighbouring atoms. (d)-(e) The photoelectron wavefunction is scattered by the neighbouring atoms, which then gives rise to a back scattered wave. The interference between the outgoing and back scattered wavefunctions gives rise to EXAFS oscillations in the absorption cross-section [After Stern, 1976].

Plan view

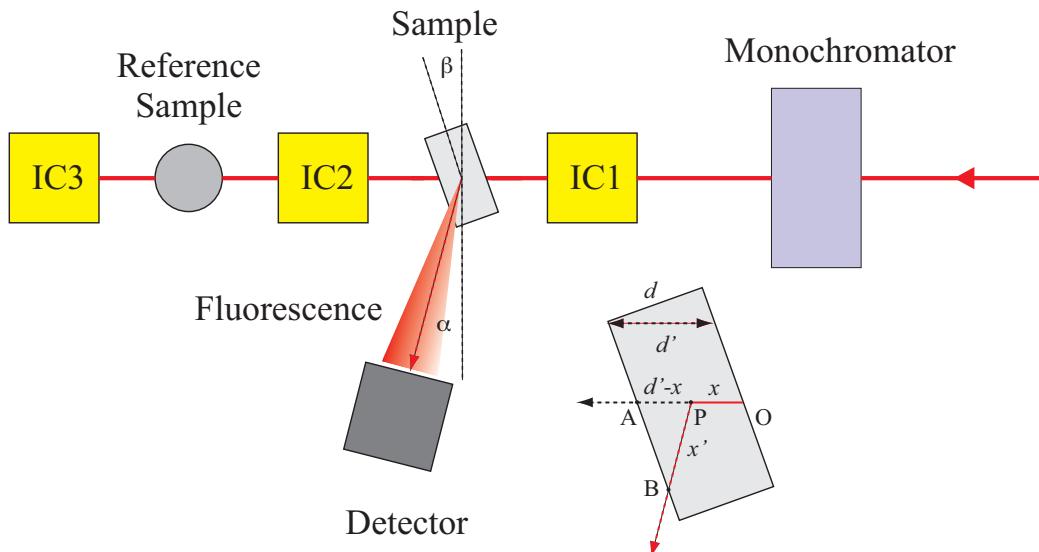**Fig. 7.7** Schematic layout of an EXAFS experiment in plan view. The energy of the incident beam is defined by a double-crystal monochromator. Incident and transmitted beam intensities are recorded by ionization chambers IC1 and IC2. It is also possible to measure the EXAFS signal by measuring the fluorescence yield with an energy sensitive detector. Also shown is an enlarged view of the sample. From the geometry it can be seen that angle ABP=$\alpha+\beta$ and angle BAP=$\pi/2-\beta$. Invoking the sine rule gives $x'/\sin(\pi/2-\beta) = (d'-x)/\sin(\alpha+\beta)$. The analysis assumes that the incident beam enters the sample through the face containing the point O, and that the beam exits the sample through the face containing the point A, i.e. effects arising from the ends of the sample can be ignored.

A second possible way to determine $\chi(q)$ is to measure the fluorescent radiation, which is emitted after the photoelectric absorption (Fig. 7.7). In this case an energy sensitive detector is preferred, as this allows the fluorescent radiation (which is monochromatic) to be isolated. The unwanted contribution from scattering processes can be further minimized by placing the detector at 90° to the incident beam in the horizontal plane since the polarization factor will then minimize the scattered radiation (see Eq. (1.8)). With a planar sample, as shown in Fig 7.7, having its normal tilted an angle β relative to the incident beam, and with the fluorescent detector axis at an angle α from 90°, we consider an absorption process at a distance in the interval x to $x + dx$ from the surface. The probability for the X-ray photon to reach this depth is $e^{-\mu x}$, and once the X-ray photon has reached this depth, the probability for an absorption process is μdx, so the resulting probability for this part of the process is $e^{-\mu x}\mu dx$. After the absorption the atom may expel an Auger electron or alternatively a fluorescent X-ray photon. The probability for the latter process is denoted ϵ. The fluorescent ray will then have to traverse the distance x' in the sample before reaching the detector which subtends a solid angle element $\Delta\Omega$. Therefore the total probability that a fluorescent X-ray is recorded in the detector is $e^{-\mu x}\mu dx\,e^{-\mu_f x'}(\Delta\Omega/4\pi)$. Here μ_f denotes the inverse absorption length at the fluorescent X-ray energy, $\mu_f = \mu(\mathcal{E}_f)$. To obtain the total fluorescent yield per incident photon, I_f/I_0, one must integrate over all depths, $d' > x > 0$, with d' being the sample thickness d divided by $\cos\beta$, i.e. $d' = d/\cos\beta$. In the caption to Fig. 7.7 it is shown

that $x' = a(d' - x)$ with $a = \cos\beta/\sin(\alpha + \beta)$. The final result is

$$
\begin{aligned}
\frac{I_f}{I_0} &= \mu\epsilon\left(\frac{\Delta\Omega}{4\pi}\right)\int_0^{d'} e^{-\mu x}dx\, e^{-\mu_f x'} \\
&= \epsilon\left(\frac{\Delta\Omega}{4\pi}\right)e^{-a\mu_f d'}\frac{\mu}{\mu - a\mu_f}\left[1 - e^{-(\mu - a\mu_f)d'}\right]
\end{aligned}
\tag{7.22}
$$

7.2.2 Theoretical outline

In this chapter it has been explained how a relatively simple model of the photoelectron process is capable of accounting for the main features of the absorption cross-section of an *isolated* atom. The key ingredient in this model was the matrix element $\langle f|\mathcal{H}_I|i\rangle$ of the interaction Hamiltonian, Eq. (7.5). The interaction Hamiltonian $\mathcal{H}_I$ is fundamental, and does not depend on the details of the neighbouring atoms. The initial state $|i\rangle$ describes the innermost electrons in the absorbing atom, and also cannot depend greatly on the environment of the atom. It follows that the EXAFS oscillations must arise from modification of the final state. This should come as no surprise. We have already seen that the assumption of a truly free photoelectron was only asymptotically correct in the high-energy limit: good agreement with experiment was found for a final state where the electron is *unbound*, moving in the attractive field of the ionized atom.

Let the relatively small modification to the final state $|f_0\rangle$ of the free atom due to neighbouring atoms be $|\Delta f\rangle$, so that the final state becomes $|f_0 + \Delta f\rangle$. The modulus squared of the matrix element is then

$$
\left|\langle f_0 + \Delta f|\mathcal{H}_I|i\rangle\right|^2 = \left[\langle f_0|\mathcal{H}_I|i\rangle + \langle\Delta f|\mathcal{H}_I|i\rangle\right]\left[\langle f_0|\mathcal{H}_I|i\rangle + \langle\Delta f|\mathcal{H}_I|i\rangle\right]^*
$$

$$
\approx \left|\langle f_0|\mathcal{H}_I|i\rangle\right|^2 + \left\{\langle f_0|\mathcal{H}_I|i\rangle^*\langle\Delta f|\mathcal{H}_I|i\rangle + \text{c.c.}\right\}
$$

$$
= \left|\langle f_0|\mathcal{H}_I|i\rangle\right|^2\left(1 + \left\{\frac{\langle f_0|\mathcal{H}_I|i\rangle^*\langle\Delta f|\mathcal{H}_I|i\rangle}{\left|\langle f_0|\mathcal{H}_I|i\rangle\right|^2} + \text{c.c.}\right\}\right)
$$

where c.c. refers to the complex conjugate. By comparison with Eq. (7.21) it can be seen that the first term describes the absorption coefficient of the free atom, $\mu_0(\mathcal{E})$. It can also be inferred that the second term must represent the EXAFS oscillations, with

$$
\chi(q) \propto \langle\Delta f|\mathcal{H}_I|i\rangle
\tag{7.23}
$$

The initial state wavefunction is strongly localized within the absorbing atom, with an extension given approximately by the Bohr radius, a_0=0.53 Å divided by Z. So as far as the modification is concerned, the initial wavefunction of the electron is highly localized and can be approximated by a delta function. We denote the change in the photoelectron wavefunction due to the neighbouring atoms by $\psi_{\text{back.sc.}}(\mathbf{r})$. Physically, the EXAFS modification is due to *back scattering* of the photoelectron by the neighbouring atoms, as sketched in Fig. 7.6. Referring back to Eq. (7.6) it can be seen that the appropriate form of the matrix element is

$$
\langle\Delta f|\mathcal{H}_I|i\rangle \propto \int\psi_{\text{back.sc.}}(\mathbf{r})e^{i\mathbf{k}\cdot\mathbf{r}}\delta(\mathbf{r})\,d\mathbf{r} = \psi_{\text{back.sc.}}(0)
$$

In comparison to Eq. (7.6) the plane wave of the photon field $e^{i\mathbf{k}\cdot\mathbf{r}}$ has been retained, but the wavefunction of the electron in its initial state, $\psi_{1s}(\mathbf{r})$, has been simplified to be a delta function $\delta(\mathbf{r})$, and $\psi_{\text{back.sc.}}$ has been inserted for the perturbation of the final state $\langle\Delta f|$. We thus assert that

$$\chi(q) \propto \psi_{\text{back.sc.}}(0)$$

and an expression for $\psi_{\text{back.sc.}}$ is now developed in a step-by-step procedure.

The wavefunction of the photoelectron emitted from the absorbing atom is an outgoing spherical wave, i.e. of the form (e^{iqr}/r), where r is measured from the centre of the absorbing atom. Let us first assume that there is only one neighbouring atom at a distance R from the absorbing atom. This neighbouring atom will scatter the incoming wave into a new spherical wave, with an amplitude proportional to the amplitude of the incident wave, and to a scattering length $t(q)$. Altogether then the back scattered wave at r=0 will be proportional to $t(q)$ $(e^{iqR}/R) \times (e^{iqR}/R)$, or $t(q)(e^{i2qR}/R^2)$. The free electron wavefunction, e^{iqr}/r, used in this argument neglects the electrostatic potential between the negatively charged electron and the ions of the lattice. Formally, such a potential can be taken into account by a phase shift $\delta(q)$, with the result that the wavefunction is modified to be of the form $e^{i[qr+\delta(q)]}/r$. The calculation of such a phase shift is a central problem in the branch of solid state physics which is concerned with electrons moving in the periodic potential of ions on a lattice, and we shall see an example of the result of such a calculation in the following section, Fig. 7.10. In the present context of EXAFS one must distinguish between the phase shift produced by the absorbing atom, $\delta_a(q)$, and that coming from the back scattering atoms, $\delta_{\text{back.sc.}}(q)$. The total phase shift, $\delta(q)$, is of course the sum of the two. Thus as a first step in obtaining an expression for the back-scattered wavefunction we write

$$\psi^{(1)}_{\text{back.sc.}}(0) = t(q)\frac{e^{i(2qR+\delta)} + \text{c.c.}}{qR^2}$$
$$\propto \frac{t(q)\sin(2qR + \delta)}{qR^2}$$

Following convention a factor of q has been included in the denominator, if for no other good reason than to obtain a dimensionless expression for $\psi^{(1)}_{\text{back.sc.}}(0)$.

The neighbouring atom is of course not stationary, but vibrates about its equilibrium position. If the r.m.s. value of the displacement parallel to $\mathbf{q}$ is σ, then the amplitude of the back scattered wave is reduced by the Debye-Waller factor of $e^{-Q^2\sigma^2/2}$ (see Section 5.4). For a scattering vector of $Q = 2q\sin 90° = 2q$ we have

$$\psi^{(2)}_{\text{back.sc.}}(0) \propto \frac{t(q)\sin(2qR + \delta(q))}{qR^2} e^{-2(q\sigma)^2}$$

It is the vibrations of the back scattering atom *relative* to that of the absorbing atom that is taken into account in this way. Since the two atoms are close neighbours, acoustic, long wavelength phonons will not contribute to σ, so it is smaller than determined from crystallography.

The state of a photoelectron and an atom left behind with a hole in its K shell is not a steady state: it has a finite lifetime. The discussion we have given so far tacitly assumed that the back scattered electron will find the atom in the initial state, but due to the lifetime there is a certain probability that the hole in the K shell has been filled in the meantime. In addition, the photoelectron may be scattered by other electrons in its round trip, so we introduce a phenomenological mean-free pathlength Λ to obtain

$$\psi^{(3)}_{\text{back.sc.}}(0) \propto \frac{t(q)\sin(2qR + \delta(q))}{qR^2} e^{-2(q\sigma)^2} e^{-2R/\Lambda}$$

Finally, we assume that the absorbing atom is surrounded by shells of neighbours, with N_j atoms in the j'th shell at a distance R_j. The shells may have different types of atoms, so the back scattering amplitude $t(q)$ also needs a suffix j, and we therefore write

$$q\chi(q) \propto \sum_j N_j \frac{t_j(q)\sin(2qR_j + \delta_j(q))}{R_j^2} \, e^{-2(q\sigma_j)^2} e^{-2R_j/\Lambda} \qquad (7.24)$$

This is the standard expression used for analysing EXAFS data. The goal is to extract the radii of the neighbouring shells, R_j, and their occupation number, N_j. The q dependence of the back scattering amplitude $t_j(q)$, and of the phase shift $\delta_j(q)$ is a subtlety that complicates the analysis. This is usually overcome by a combination of theory, and use of reference samples where R_j, N_j and σ_j are known.

7.2.3   Example: CdTe nano-crystals

EXAFS is now established as a powerful method for determining the structures of materials. It should be emphasized that EXAFS is a *local* probe, in the sense that information on only the first few neighbouring shells is obtained. This in itself should not be seen as a severe limitation of the technique, as it means that EXAFS can not only be used to study well-ordered single crystals, but also disordered materials such as glasses. Diffraction techniques discussed in Chapter 5 can also be applied to both ordered and disordered materials, and in this way EXAFS and diffraction are complementary to one another. In the example considered here this complementarity has been exploited in a study of very small crystals, so-called nano-crystals, of the semiconducting material CdTe. This example has been chosen for a number of reasons. First, the data turns out to be easier to interpret than most EXAFS data. The reason is that in this case only the EXAFS signal from the nearest-neighbour shell is significant, and the complication of the summation over neighbouring shells in Eq. (7.24) is avoided. Second, the solid state physics of CdTe nano-crystals is interesting, and may turn out to be of technological importance.

CdTe is a II-VI semiconductor compound. (The corresponding III-V compound is InSb.) The homologous compound CdS may be known to the reader from its use as photoelectric cells in cameras, and diodes in electronic circuitry. Perhaps the most important feature of CdTe nano-crystals is that the electronic band-gap, which determines the photo-sensitivity in the visible part of the electromagnetic spectrum, depends strongly on the size of the crystal when the size of the crystal is reduced to the nano-meter scale. This is simply due to quantum mechanical confinement of the electrons within the nano-crystal. The nano-crystal may be regarded as a large molecule with discrete electronic energy levels, rather than the continuous band of allowed electronic energies found in bulk crystals. Nano-crystals of CdTe with a well-defined size have been produced by chemical methods [Rogach et al., 1996]. The core of the nano-crystal is formed from a tetrahedron of Cd and Te atoms packed in the cubic zinc-blende structure, with an organic part, SCH_2CH_2OH, attached to the Cd atoms on the surface of the tetrahedra. The absorption spectrum of these CdTe nano-crystals in the UV part of the electromagnetic spectrum (see the original article for details) exhibits two distinct peaks at 2.9 eV (425 nm) and 2.7 eV (460 nm). In contrast the band-gap of the bulk CdTe is 1.5 eV (827 nm).

The powder diffraction spectrum from CdTe nano-crystals is shown in Fig. 7.8. Here, a slight digression from the main subject of this chapter is made to discuss this diffraction pattern. It serves to illustrate nicely several of the subjects that have already been treated in Chapter 5, and is relevant for
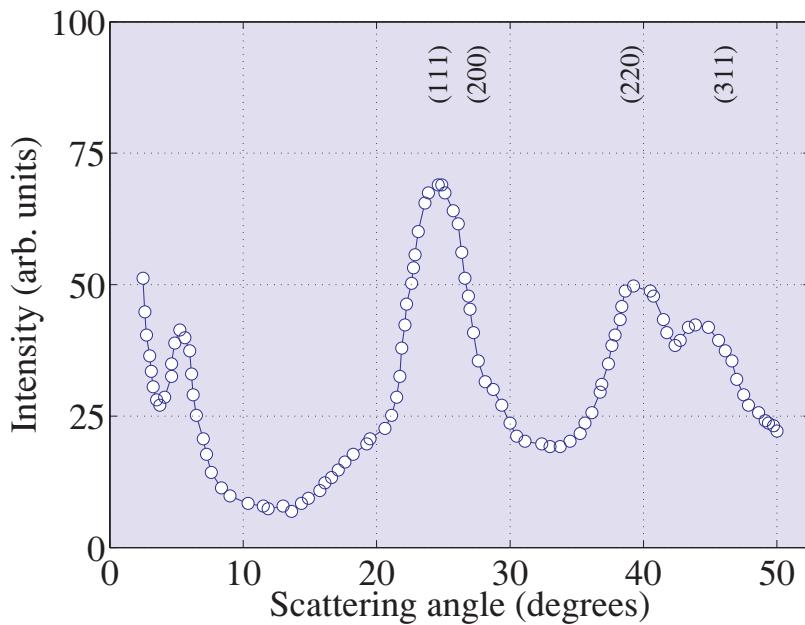
Fig. 7.8 Powder diffraction data for CdTe nano-crystals with an average diameter of around 15 Å. The X-ray wavelength was 1.54 Å. The graph was prepared by digitising the data of Rogach et al. [1996]

2θ (Degrees)	Relative intensity	Wavevector Q (Å^{-1})	Peak Width FWHM (Degrees)	No. of unit cells N	Miller indices (h, k, l)	$\dfrac{Q}{\sqrt{h^2 + k^2 + l^2}}$
5.2	–	0.37016	3.17	–	–	–
24.6	1	1.7383	6.3	3.5	(1,1,1)	1.0
39.0	0.7	2.7239	8.5	4	(2,2,0)	0.96
46.0	0.5	3.1884	9.5	4	(3,1,1)	0.96

Table 7.1 Analysis of the diffraction data shown in Fig. 7.8 for CdTe nano-crystals. The data were taken from Rogach et al. [1996].

interpreting the EXAFS spectra that will be considered a little later. The diffraction data were taken with an X-ray wavelength of 1.54 Å, and are tabulated in Table 7.1.

The first peak in the diffraction pattern occurs at a scattering angle of $2\theta = 5.2°$. This small-angle scattering feature is the interference peak from particles a distance R apart (see Section 4.1). The average distance R is given by $QR = 2\pi$. (Here recall that for elastic scattering the modulus of the wavevector transfer is related to the scattering angle by $Q=(4\pi/\lambda)\sin\theta$.) In this particular case with the peak at 5.2°, and for an X-ray wavelength of 1.54 Å, this means that the nano-crystals are approximately 17 Å apart. If the nano-particles are roughly spherical in morphology, then this is also the diameter of each sphere. Now consider the three peaks at higher scattering angles. These correspond to the powder diffraction peaks from randomly oriented CdTe nano-crystals. To establish this we first need to index the powder pattern, i.e. assign Miller indices to each of the high-angle diffraction peaks. Bulk CdTe

has the zinc blende structure, which in order of increasing scattering angle has strong Bragg reflections with Miller indices of (1,1,1), (2,2,0) and (3,1,1). The modulus of the wavevector transfer is related to the d spacing for a given set of (h, k, l) planes by $d = a/\sqrt{h^2 + k^2 + l^2}$, where a is the lattice parameter. As Q=$2\pi/d$, this means that the ratio of Q to $\sqrt{h^2 + k^2 + l^2}$ should be a constant, equal to $2\pi/a$, if the assignment of Miller indices given in Table 7.1 is correct. It is apparent that this ratio is indeed almost constant with a value of ≈ 1.0 within error. Thus the lattice parameter of the CdTe forming the nano-crystals is $a \approx 2\pi/1.0 \approx 6.3$ Å, somewhat smaller than the bulk value of 6.48 Å. It is also important to compare the intensities of the high-angle peaks with what would be expected for a powder of bulk CdTe. Using Eq. (5.35) the relative intensities of the peaks from bulk CdTe are evaluated to be in the ratios 1:0.78:0.42, similar to the ratios given in Table 7.1.

It is apparent from the data shown in Fig. 7.8 that the diffraction peaks appear to be broad. They are in fact much broader than the instrumental resolution. The width results from the fact that each nano-crystal is built up from so few Cd and Te atoms. The width of a diffraction peak is inversely proportional to the number N of unit cells that scatter coherently. From the box on page 52 we know that the relative width (FWHM) is equal to $0.88/N$, and thus from Table 7.1 the number of unit cells in the nano-crystal is ≈ 4. From this it can be expected that the size of the nano-crystal is about four times the unit cell length, i.e. 4×6.3=25.2 Å, a value reasonably close to the size of the nano-crystal estimated from the interference peak at small scattering angles.

Now to the EXAFS data. The absorption spectra, in the vicinity of the K edge of Te, for bulk and nano-crystalline CdTe are shown in the top row of Fig. 7.9. The first step in the data analysis is to obtain the EXAFS part of the signal, $\chi(q)$, from its definition in Eq. (7.19). The smooth part of the absorption coefficient, μ_0, is derived from the inverse transmission curve in the top row, and is represented by the dotted lines. The next step is to locate the energy of the K edge (here 31.813 keV) which allows the photon energy scale in keV to be converted into electron wavenumber in Å^{-1} using Eq. (7.20). It is then possible to generate $\chi(q)$ from Eq. (7.19). The result is shown in the second row of Fig. 7.9, where it has been weighted somewhat arbitrarily by q^3. Without performing any further analysis it is clear that there is a difference between the nano-crystal and the bulk forms of CdTe. The nano-crystal has one dominant frequency (or wavelength) which means that the EXAFS is dominated by the distance to the nearest-neighbour shell. In contrast, the bulk data for $q^3\chi(q)$ have a superposition of at least two frequencies. Clearly to understand the bulk data it is necessary to take into account more than the nearest-neighbour shell. These observations can be placed on a more quantitative footing by taking the Fourier transform of $q^3\chi(q)$. This is shown in the bottom panel of Fig. 7.9. These radial distribution functions have peaks corresponding to the position of the shells neighbouring a Te atom. The nano-crystal has one shell at a distance of 2.79 Å. This should be compared to the Te-Cd distance in bulk CdTe of 6.48×$\sqrt{3}/4$=2.806 Å. The small contraction of the nano-crystal is presumably due to the epitaxial strain from the interaction between the Cd ions on the surface of the tetrahedra and the S ions of the organic shell.

Using Eq. (7.24) it is possible to extract more information from the EXAFS spectra than just the distance from the absorbing Te atom to the nearest-neighbour shell. This is achieved by fitting Eq. (7.24) to the data. To this end we need to know the q dependence of the phase shift $\delta(q)$, and of the scattering length $t(q)$ of the back-scattered wave. These can be calculated reliably using sophisticated and accurate methods developed in solid state physics. The results for CdTe are given in Fig. 7.10. The remaining ingredient is the Debye-Waller factor which is usually treated as a parameter to be determined from fitting the full model to the data. In the present example data were recorded at several temperatures down to 8 K. This enabled the Debye-Waller factor to be separated into a temperature dependent part (12.6×10^{-3} Å^2) corresponding to a Debye temperature of 260 K (see Section 5.4), a zero point motion (3.5×10^{-3} Å^2), and a static strain field ($\langle u^2 \rangle = 1\times10^{-3}$ Å^2).
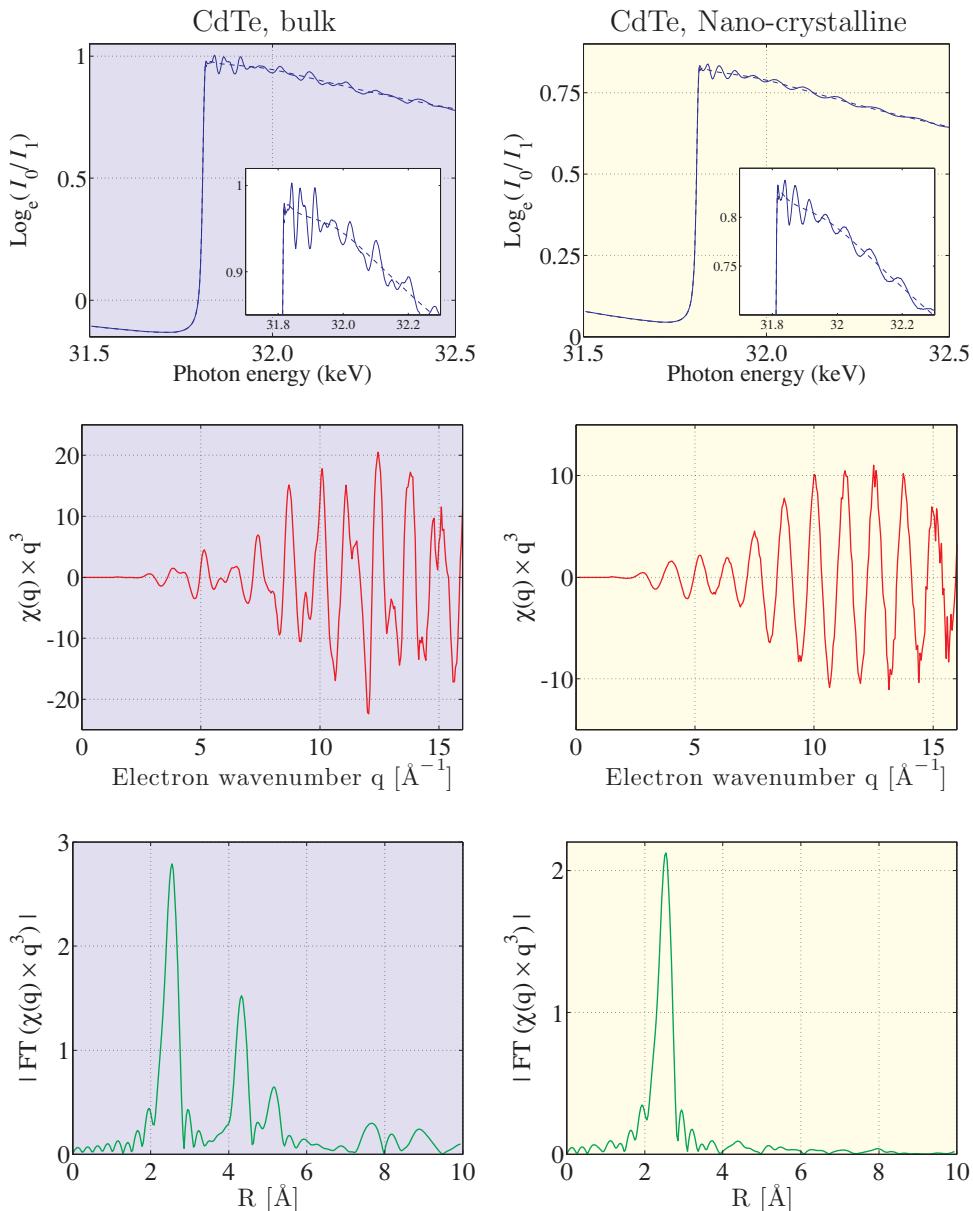
Fig. 7.9 A comparison of the EXAFS spectra from bulk and nano-crystalline CdTe. The data were taken near the K edge of Te (31.813 keV) at a temperature of 8K. Top row: The absorption spectra. The dotted line indicates the smooth signal that would be obtained from an isolated Te atom. Middle row: $\chi(q)$ multiplied by q^3 as a function of the electron wavenumber q. Bottom row: The Fourier transform of the data shown in the row above. The resulting radial distribution function has peaks corresponding to the position of successive shells of atoms centred on a Te atom. The nano-crystal has one such shell at 2.79 Å. (Data supplied by J. Rockengerger, L. Tröger, A.L Rogach, M. Tischer, M. Grundmann, A. Eychmüller, and H. Weller [Rockengerger et al., 1998]).
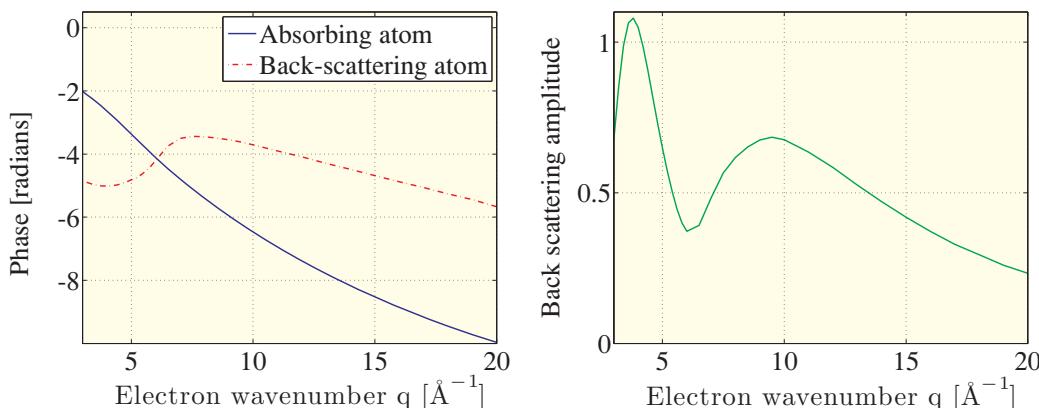
Fig. 7.10 Calculated phase and amplitude of the photoelectron at the Te K edge in CdTe.

By fitting the model to the data it could be deduced that the nearest neighbour shell to a Te atom on average contains 3.55 Cd atoms, somewhat smaller than the coordination number of four in bulk crystals. This number can be compared to a simple model of the nano-crystal, and it was found that the following description gave reasonable agreement with the known experimental facts. The nano-crystal is composed of a CdTe core with an organic shell. The core is modelled as a tetrahedron of Cd and Te atoms coordinated as in the bulk. The tetrahedron is complete only for a certain sequence of 'magic' numbers, for example 54 Cd atoms and 32 Te atoms. The organic part is $S-CH_2-CH_2-OH$, and is bound to the Cd sites on the surface of the core by the S atom. The nano-crystal can thus be visualized as a large molecule with the chemical formula $Cd_{54}Te_{32}(SCH_2CH_2OH)_{52}^{8-}$. This model yields an average coordination number to a Te atom of 3.63 in good agreement with the EXAFS data.

7.3   X-ray dichroism

Linear dichroism is defined as the preferential absorption of one of two orthogonal photon polarization states. This is a well known phenomenon for wavelengths in the optical part of the spectrum. Perhaps the most familiar example is Polaroid sheet, which is used to make sunglasses, amongst other things. Polaroid contains long polymeric molecules aligned along a specific direction. When illuminated with linearly polarized light it is found that light polarized parallel to the molecules is more strongly absorbed than light polarized in the orthogonal direction. Polaroid sheet therefore displays *linear dichroism* by virtue of a charge anisotropy. Dichroism is also produced whenever there is a magnetic anisotropy in a material. Of particular interest is the *circular dichroism* exhibited by ferromagnetic materials which is the difference in absorption of right and left handed circularly polarized light.

It is now established that materials also exhibit dichroism at X-ray wavelengths [Erskine and Stern, 1975, Thole et al., 1985, van der Laan et al., 1986, Schütz et al., 1987]. In recent years this has been exploited to develop several very powerful techniques for the study of magnetic materials. In this section a short introduction is given to one of the most popular of these techniques, X-ray magnetic circular dichroism (XMCD), which is used to study *ferromagnetic* materials. As the name suggests, an XMCD experiment consists of measuring the difference in absorption of left- and right-handed circularly polarized X-rays. The difference, the magnetic dichroic signal, can then be used to deduce
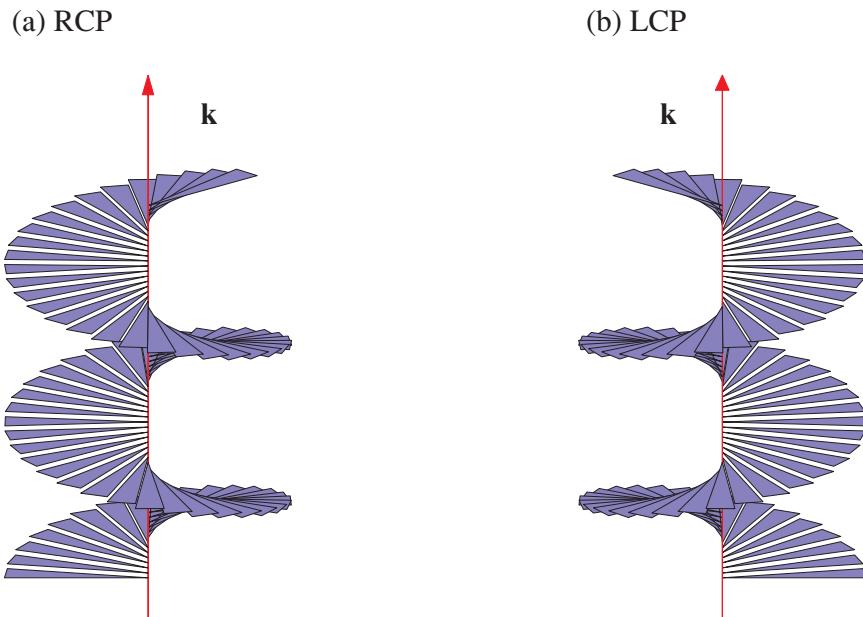
(a) RCP   (b) LCP

Fig. 7.11 Circular polarized X-rays can be depicted as a helical staircase where the steps in the staircase represent the electric field vector. The two possible polarization states correspond to the staircase turning clockwise along the direction of propagation **k** (right circularly polarized, RCP), or anticlockwise (left circularly polarized, LCP).

the magnetization in the material. In comparison with other techniques XMCD has several attractive features. The first is that XMCD experiments provide information on the spin and orbital magnetizations separately: most other methods (bulk magnetization, neutron scattering, etc.) are sensitive to the *total* magnetization only. Second, by studying the dichroism around absorption edges, as is in fact usual practice, the technique is element specific. Lastly, XMCD is very sensitive which allows it to be used to determine extremely small magnetic moments, and to study small quantities of materials. For example, one of the most important applications of XMCD is in the study of nano-scale structures, such as multilayers and thin films, which are the basis of modern data storage devices. In fact the sensitivity of XMCD is such that magnetic magnetic moments of $0.001\,\mu_{\mathrm{B}}$ per atom can be detected.

The departure point for our discussion of the physics underlying XMCD is a description of a circularly polarized electromagnetic wave. In a circularly polarized state the electric field of an electromagnetic wave describes a helical path around the propagation direction, **k**, and rotates once in each wavelength. The sense of rotation can either be clockwise or anticlockwise, as indicated in Fig. 7.11. By definition, a right circularly polarized (RCP) electromagnetic wave has an electric field which rotates in a clockwise sense as viewed along **k**, while for a left circularly polarized (LCP) electromagnetic wave the sense of rotation is anticlockwise. A circularly polarized electromagnetic wave in a quantum mechanical description is still composed of photons, but in this case the photon is in an definite eigenstate of the angular momentum operator, J_z, where z is the direction of propagation **k**. For RCP (LCP) photons the eigenvalue of J_z is $+\hbar$ ($-\hbar$). Linearly polarized photons have the expectation value of $\langle J_z \rangle = 0$, since they are an equally weighted superposition of RCP and LCP photons. The fact that a circularly polarized photon is in an eigenstate of J_z means that the selection rules for the conservation of angular momentum in electronic transitions becomes particularly simple.

The origin of the XMCD signal is easiest to understand by taking an atomic model as the starting point, and to consider an electronic transition from a core state to a bound one at higher energy. It is known from atomic physics that the probability of electronic transitions is controlled by selection rules for the change in the quantum numbers describing the initial and final states. The main mechanism driving electronic transitions is through the interaction of the electric field of the photon and the electric dipole moment operator. This operator is the product of charge times distance and is therefore an odd function. As the parity of the initial and final states is given by their respective orbital quantum numbers ℓ, a non-vanishing matrix element is obtained only if

$$\Delta\ell = \pm 1$$

This is the dipole transition selection rule[2]. Since the photon is annihilated in the absorption process, its angular momentum J_z must be transferred to the sample, so for circularly polarized photons one has

$$\Delta m = \begin{cases} +1 & \text{, RCP photons} \\ -1 & \text{, LCP photons} \end{cases}$$

To illustrate how these selection rules produce a difference in the absorption of left and right circularly polarized light, consider Fig. 7.12(a). Here the energy level scheme is shown of an atom containing eight electrons: two in the 1s state, two in the 2s state, and four in the 2p state, leaving two unoccupied states in the 2p level. A magnetic field has been applied parallel to the direction of photon propagation $\mathbf{k}$ as shown in Fig. 7.12(b); this is the normal XMCD geometry. Through the Zeeman effect, the field lifts the orbital degeneracy of the 2p state into the separate states $|\ell, m\rangle = |1, -1\rangle$, $|1, 0\rangle$ and $|1, 1\rangle$. To simplify things as much as possible only the orbital quantum numbers are shown, and the spin-orbit interaction has been neglected. The origin of XMCD in the selection rules is now apparent. When illuminated with RCP radiation the transition satisfies both selection rules in making the transition from the 1s core state $|0, 0\rangle$ to the unoccupied state $|1, 1\rangle$. In contrast, for LCP photons, the transition is forbidden as the only allowed final state $|1, -1\rangle$ is already occupied[3].

The magnetic field in the above example served to provide a splitting of the final state. In a typical ferromagnetic material the internal field from the magnetic moments is much greater than the applied field, which then serves merely to define the magnetization direction.

In Fig. 7.13 a schematic is shown of the key components needed to perform an XMCD experiment. After passing through the sample of thickness d the intensity of the two polarization states, indicated by $+$ or $-$, are

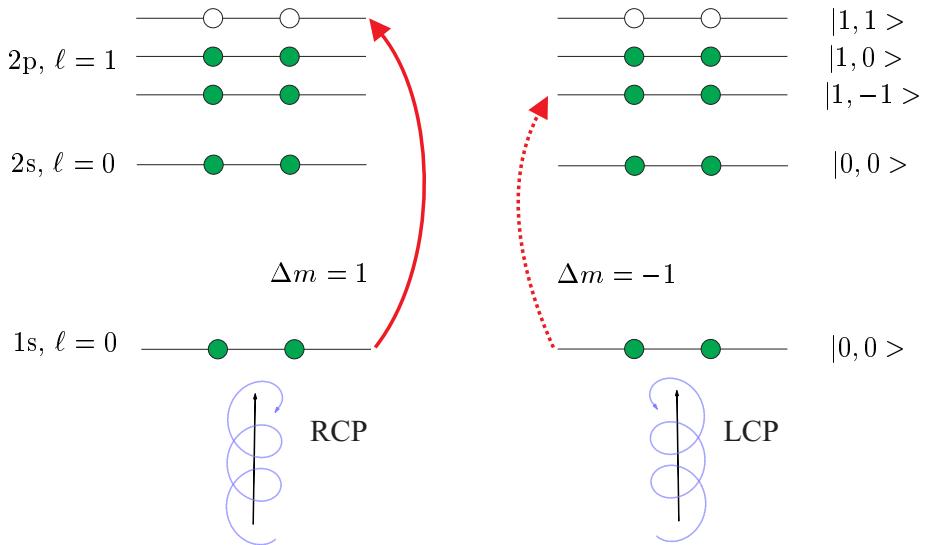$$I_1^+(\mathcal{E}) = I_0^+(\mathcal{E})\, e^{-\mu^+(\mathcal{E})d}$$

and

$$I_1^-(\mathcal{E}) = I_0^-(\mathcal{E})\, e^{-\mu^-(\mathcal{E})d}$$

---

[2]One example of the application of this selection rule is the ratio of intensities of the $K_{\alpha 1}$ and $K_{\alpha 2}$ fluorescence lines. The K_α fluorescence is created by an electron making the transition from the L to K shell. The degeneracy of the L shell is split into three sub-levels as indicated in Fig. 7.2. The dipole selection rule then limits the allowed transitions to $2p_{3/2} \to 1s$ ($K_{\alpha 1}$) and $2p_{1/2} \to 1s$ ($K_{\alpha 2}$), whereas 2s→1s is forbidden. As the $2p_{3/2}$ level has twice as many states as $2p_{1/2}$, it follows that the $K_{\alpha 1}$ fluorescence should be twice as large $K_{\alpha 2}$, in accord with observations.

[3]It should not be thought that all absorption processes involving LCP are forbidden. For example, a transition from 2s to the continuum is allowed.

(a) Simplified energy level diagram
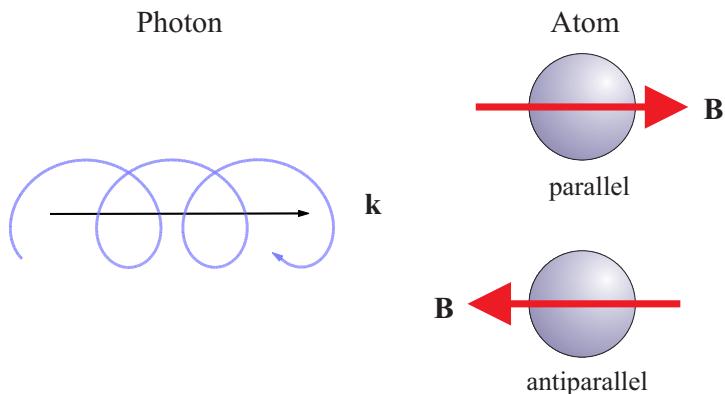

(b) Normal XMCD geometry

Fig. 7.12 (a) Simplified energy level diagram of an atom containing eight electrons. The Pauli exclusion principle limits the occupation of each state to two electrons. Possible transitions are restricted by the dipole selection rule $\Delta \ell = \pm 1$, and the selection rule $\Delta m = +1$ for RCP photons, and $\Delta m = -1$ for LCP photons. In the latter case the transition cannot proceed because the $m = -1$ state is already fully occupied, and hence a large XMCD signal results [After Lovesey and Collins, 1996]. (b) The normal geometry for XMCD experiments. A circularly photon interacts with an atom which has the magnetic symmetry axis parallel or antiparallel to **k**. The XMCD signal is the difference in the absorption when either the handedness of the X-ray or the direction of the field is reversed.
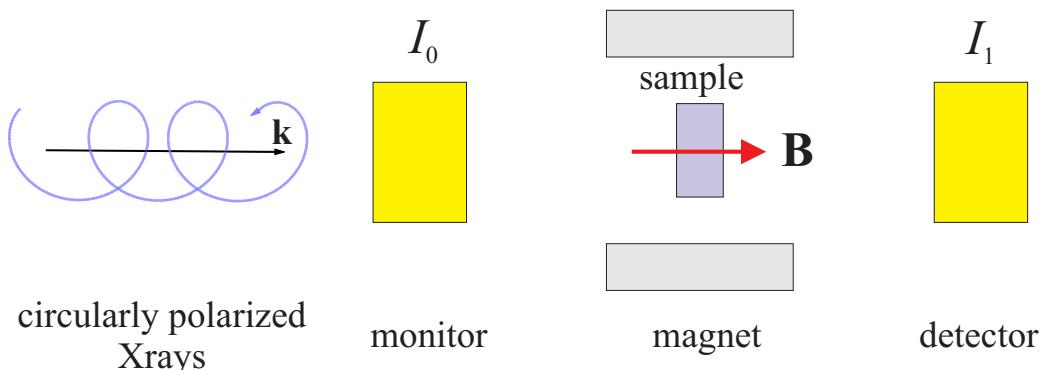
XMCD experimental layout

Fig. 7.13 Schematic layout of an XMCD experiment performed in a transmission geometry. The intensity I_0 of the incident circularly polarized beam is recorded by a monitor. A magnetic field is used to polarize the ferromagnetic sample in a direction either parallel or antiparallel to the propagation direction of the photon. After passage of the beam through the sample the intensity I_1 is measured a detector. The XMCD is the difference in absorption on either reversing the handedness of the incident radiation or by flipping the direction of the magnetic field.

where $\mu^{\pm}$ is the absorption coefficient. The absorption coefficient is deduced from the measured intensities using

$$\mu^+(\mathcal{E}) = \left(\frac{1}{d}\right)\log_e\left(\frac{I_0^+(\mathcal{E})}{I_1^+(\mathcal{E})}\right) \qquad (7.25)$$

with a similar expression for the other polarization state. The sensitivity of an XMCD experiment is greatly enhanced when the photon energy is in the vicinity of an absorption edge. This is particularly true if the photon produces an electronic excitation to a final state which is strongly magnetically polarized. For the first series of transition metals this requires that the photon excites an electron to a 3d state, while for the rare earths it should be a 4f state. The edges which couple into these states for a dipole transition ($\Delta\ell = \pm 1$) are L_{II} ($2p_{1/2} \rightarrow 3d$) and L_{III} ($2p_{3/2} \rightarrow 3d$) in the case of the transition metals, and M_{IV} ($3d_{3/2} \rightarrow 4f$) and M_V ($3d_{5/2} \rightarrow 4f$) in the case of the rare earths. (The reader is referred back to Fig. 7.2 for a summary of the nomenclature used to label absorption edges.)

XMCD experiments are performed in one of several different ways depending on both the nature of the X-ray source, and the energy of the edges under consideration. As explained on page 38 in Chapter 2, circularly polarized radiation can be obtained from a bending magnet by viewing the source out of the orbital plane. Depending on whether the source is viewed above or below the orbital plane the electrons will be seen to rotate in a clockwise or anticlockwise sense. This circular rotation imparts an angular momentum to the photons, which can then be used for XMCD measurements. Alternatively, helical undulators are now available which produce very intense beams with circular polarization, as described on page 53. In either case the dichroic signal can either be obtained by reversing the helicity of the photons, or by reversing the polarization direction of the magnetization. The two are entirely equivalent, and both are used in practice. At high photon energies XMCD experiments are usually performed in a transmission geometry, while for soft X-rays the XMCD signal is normally inferred by recording either the fluorescent radiation or by measuring the photoelectron yield.

One of the reasons that XMCD has become such a popular technique is that it has been established that the orbital, m_{orb}, and spin, m_{spin}, moments can be obtained from sum rules, which relate integrals
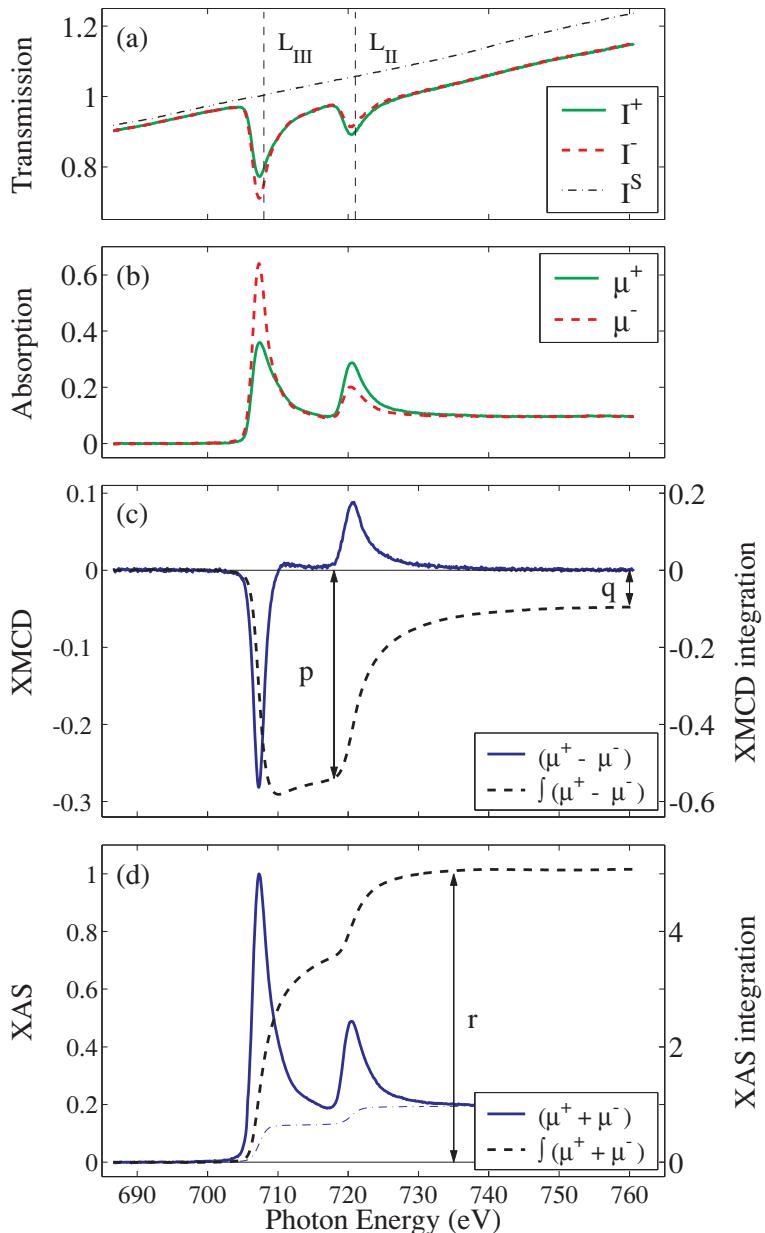
Fig. 7.14 X-ray absorption spectra from iron in the vicinity of the L edges. Circularly polarized light was used, and the spectra were recorded with the spin of the incident photon parallel (I^+, solid curve) and antiparallel (I^-, dashed curve) to the spin of the Fe 3d electrons. (a) Transmission spectra of Fe/parylene thin films, and of the parylene substrate alone, taken at opposite saturation magnetizations; (b) the X-ray absorption spectra calculated from the transmission data shown in (a); (c) the XMCD spectra; (d) the summed X-ray absorption spectra. In (c) and (d) the values of the integrals p, q and r which appear in the sum rules are given by the dashed lines. The dot-dashed line in (d) indicates two steps in the absorption cross-section at the L_{III} and L_{II} edges. These were removed from the data before integration of the spectra. (Taken from Chen et al. [1995].)

of the dichroic signal over the relevant absorption edges directly to m_{orb} and m_{spin} [Thole et al., 1992, Carra et al., 1993]. Following Chen et al. [Chen et al., 1995], we write the sum rules in the case of the 3d metals as

$$m_{\text{orb}}[\mu_B/\text{atom}] = -\frac{4q(10 - n_{3\text{d}})}{r} \qquad (7.26)$$

and

$$m_{\text{spin}}[\mu_B/\text{atom}] \approx -\frac{(6p - 4q)(10 - n_{3\text{d}})}{r} \qquad (7.27)$$

where $n_{3\text{d}}$ is the number of electrons in the 3d state, and p, q and r are given by

$$p = \int_{L_{III}} (\mu^+ - \mu^-)\, d\mathcal{E}$$

$$q = \int_{L_{III}+L_{II}} (\mu^+ - \mu^-)\, d\mathcal{E}$$

$$r = \int_{L_{III}+L_{II}} (\mu^+ + \mu^-)\, d\mathcal{E} \qquad (7.28)$$

For the spin sum rule the expression given in Eq. (7.27) is only approximate as we have neglected the so-called $\langle T_z \rangle$ term, which in the case of the 3d metals introduces an error of a few %.

The validity of the sum rules has been established through a number of experiments. In Fig. 7.14 we show the data for iron obtained by Chen et al. [Chen et al., 1995], who have performed one of the most exacting tests of the sum rules to date. The L edges for the 3d elements fall in the soft part of the X-ray spectrum. This usually means that the dichroic signal has to be inferred by measuring either the fluorescent radiation or the photoelectron yield. Both of these approaches introduce systematic errors which are difficult to correct for properly. By studying iron thin films grown on a parylene substrate, Chen et al. were able to perform their experiments in a transmission geometry, hence avoiding these complications. The absorption spectra for the parallel, μ^+, and antiparallel, μ^-, configurations are shown in part (b). Strong white lines are evident at the positions of the L_{III} and L_{II} edges, corresponding to the transitions $(2p_{3/2} \to 3d)$ and $(2p_{1/2} \to 3d)$, respectively. The dichroism signal is shown in part (c), which also indicates the values of the integrals p, q and r appearing in the sum rules, Eqs. (7.26) and (7.27). In part (d) the X-ray absorption spectra for the sum of the μ^+ and μ^- is plotted. With the values of p, q and r indicated, and with $n_{3\text{d}}=6.61$ taken from theory, good agreement (within 7%) was found with other experimental techniques and theory for the values of the spin and orbital moments.

In addition to XMCD, materials may also exhibit X-ray magnetic linear dichroism (XMLD) [van der Laan et al., 1986]. This is the analogue of the Faraday rotation effect in the X-ray region. Although in principle it can be used to extract similar information to XMCD it is somewhat more demanding from an experimental point of view, and has not yet gained widespread use.

It is worthwhile to consider briefly what implications follow from the optical theorem and the observation of XMCD. The optical theorem states that absorption is proportional to the imaginary part of the scattering length in the forward direction (Eq. (3.10)). This can of course be turned on its head, so that a particular type of absorption must imply an imaginary component to the scattering length: scattering and absorption are two sides of the same coin. As explained in the next chapter, the Kramers-Kronig relations state that there then must also be a contribution to the real part of the scattering length. Thus XMCD implies that there exists enhanced or resonant magnetic scattering at certain absorption edges. This takes us beyond the scope of this book, although a few remarks on resonant magnetic scattering are made at the end of the next chapter.

7.4 ARPES

At the most fundamental level, the physical properties of a given material can be understood and classified according to how electrons propagate within it. Electron band theory shows that electron motion in crystals is described by a dispersion relation for which the electronic binding energy $\mathcal{E}_B(\mathbf{q})$ is a function of the wavevector $\mathbf{q}$ of the electron within the material. It is now established that the most powerful technique for mapping electronic dispersion relations in solids is *angle resolved photoemission spectroscopy* (ARPES). In this section we provide a brief description of the ARPES technique. (The interested reader is referred to the review article by Damascelli et al. [2003] for a more complete description.) ARPES is included here in spite of the fact that in most (but not all) implementations it exploits photons with wavelengths (100-600 Å) lying just outside the X-ray band. Apart from its pivotal role in the determination of electronic structure, the reasons for its inclusion here are that ARPES beamlines can be found at most synchrotron facilities, and that ARPES is described by the same theory of the photoelectron absorption cross-section developed in Section 7.1. The essential idea of ARPES is that by measuring the energy and momentum of photoelectrons propagating freely in the vacuum outside of a solid it is possible to deduce the dispersion relation $\mathcal{E}_B(\mathbf{q})$ within the solid, simply by applying conservation laws to energy and momentum.

A schematic of the energetics of the photoemission process is given in Fig. 7.15. Here both tightly bound localized atomic states and more loosely bound valence electron band states in a crystal are represented. The minimum energy required to remove an electron from the uppermost occupied state to the vacuum is known as the *work function*, ϕ, which is characteristic of a particular material[4]. The left hand panel in Fig. 7.15(a) illustrates the situation for a metal where the uppermost occupied state is known as the Fermi level. In general, electrons can be removed from any state below the Fermi energy. By applying conservation of energy to the process, the kinetic energy $\mathcal{E}_{kin}$ of the photoelectron follows as

$$\mathcal{E}_{kin} = \frac{\hbar^2 q_v^2}{2m} = \hbar\omega - \phi - \mathcal{E}_B \qquad (7.29)$$

where $\mathbf{q}_v$ is the wavevector of the liberated electron in vacuum, $\hbar\omega$ is the photon energy and $\mathcal{E}_B$ is the electron binding energy relative to $\mathcal{E}_F$, i.e. $\mathcal{E}_B = \mathcal{E}_F - \mathcal{E}_i$ (see Fig. 7.15(b)).

Thus armed with a knowledge of $\hbar\omega$ and ϕ, $\mathcal{E}_B$ can be deduced by measuring $\mathcal{E}_{kin}$. For the localized core states, the determination of $\mathcal{E}_B$ alone is enough to provide a fingerprint of the chemical composition of the near surface region of the sample. This is the basis of *X-ray photoelectron spectroscopy* (XPS) which is widely used in various analytical techniques in surface science. In an ARPES experiment both the energy and momentum of the photoelectron are determined. The momentum of the photoelectron in vacuum $\hbar\mathbf{q}_v$ for convenience can be decomposed into components perpendicular and parallel to the surface

$$\hbar q_{\perp,v} = \sqrt{2m\mathcal{E}_{kin}}\cos\theta \ \text{ and } \ \hbar q_{\parallel,v} = \sqrt{2m\mathcal{E}_{kin}}\sin\theta \qquad (7.30)$$

(see the coordinate system in Fig. 7.3, but note that the same restriction on the propagation direction of the photon does not apply here.) Measurement of the kinetic energy of the photoelectron and its propagation direction therefore is enough to fully specify its kinematics. On modern ARPES beamlines this is accomplished using an angle-mapping electron lens system combined with a hemispherical electron energy analyser, as shown schematically in Fig. 7.16(a).

---

[4]In the simplest approach it is assumed that the photoemission process is completed before the system relaxes, and by ignoring many-body interaction effects between the electrons in the solid. These are known as the sudden and independent electron approximations, respectively.
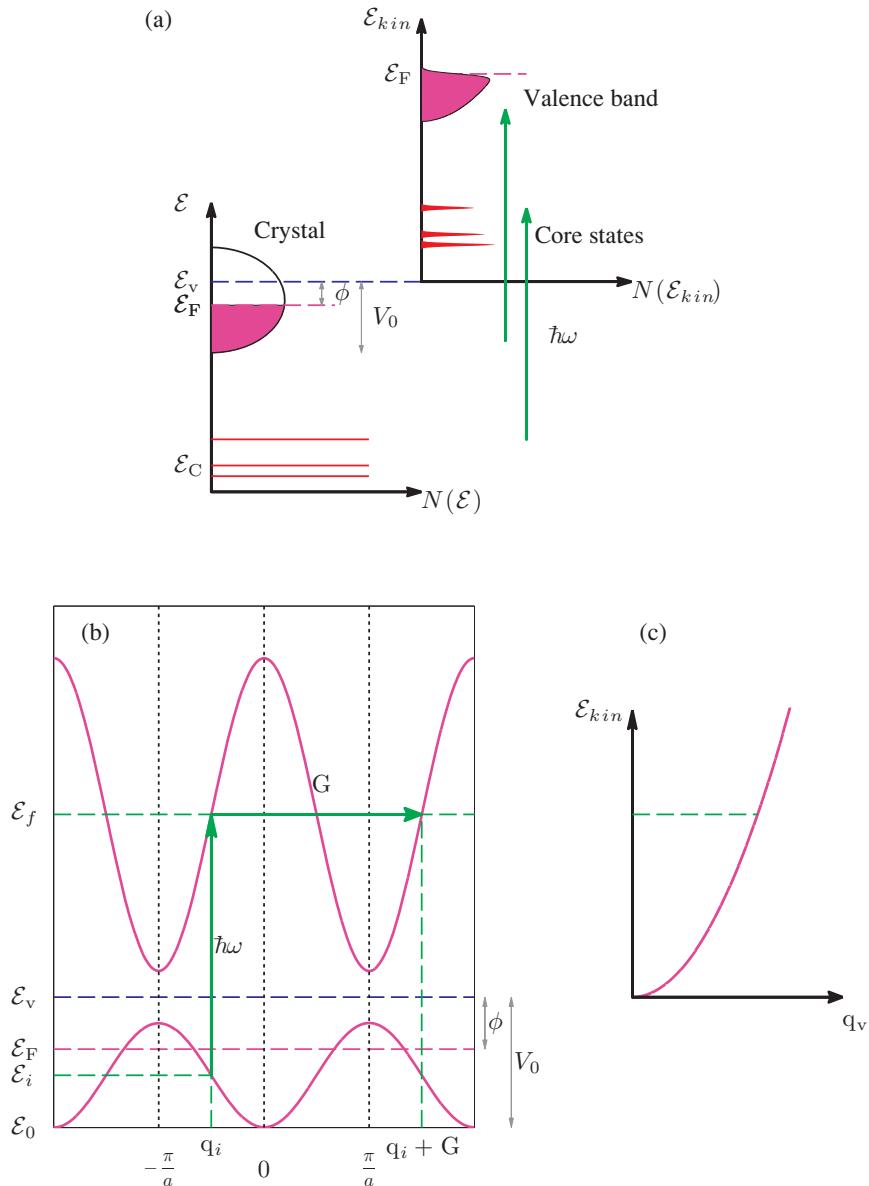
Fig. 7.15 (a) Left: schematic energy level diagram of a solid, indicating tightly bound localized atomic core states ($\mathcal{E}_C$) and more loosely bound valence band states filled up to the Fermi energy $\mathcal{E}_F$. The work function ϕ is the minimum energy required to remove an electron from the top of the filled band to the vacuum with an energy $\mathcal{E}_v$. The inner potential V_0 corresponds to the binding energy of the bottom of the valence band relative to $\mathcal{E}_v$. Right: the photoemission process in which a photon of energy $\hbar\omega$ removes an electron from a solid. The kinetic energy $\mathcal{E}_{kin}$ of the photoelectron depends on the difference between $\hbar\omega$ and the total binding energy of the state from which the electron is removed. (Adapted from Hüfner [1995].) (b) Photoelectron emission process for a band electron, showing a direct transition with the momentum supplied by the crytsal. (c) Corresponding free-electron dispersion relation of the photoelectron. (Adapted from Pilo [1999].)
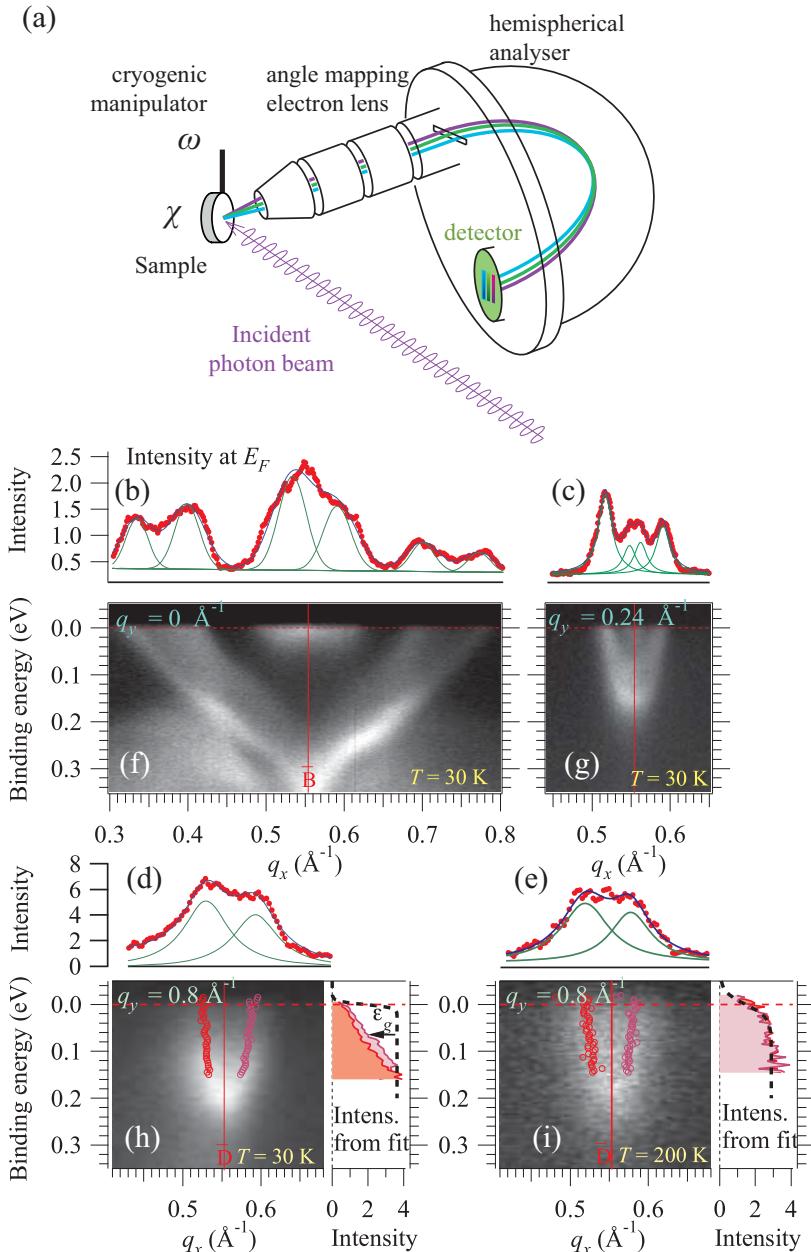
Fig. 7.16 (a) Schematic of an ARPES experiment in which electrons are liberated from a solid by the absorption of a photon. Both the energy and momentum of the photoelectrons are analysed from which it is possible to deduce the electronic dispersion within the solid by applying conservation laws. (b)-(i) ARPES data on the opening of a charge density wave (CDW) gap in ZrTe$_3$ [Hoesch et al., 2009]. Dispersion maps at three different position along the Brillouin zone boundary from $\bar{B}$ to $\bar{D}$ at T = 30 K (f-h) and T = 200 K (i). (b)-(e) Momentum dependent cuts (MDC) at the Fermi energy $\mathcal{E}_F$. In panels (h)-(i) the dispersion is determined by fits to the MDCs by two Lorentzians of equal width. The intensities of these fits are shown to the right of the panel together with a Fermi occupation function (dashed line) at the corresponding temperature. The energy of the gap opened by the CDW is indicated by the arrow in (h). (Image courtesy of Moritz Hoesch.)

As a conceptual aid, the photoemission process is often broken down into three discrete steps, although in reality no such division is possible: a photon excites an electron from the initial to the final state; the electron propagates to the surface; the electron is liberated to the vacuum by passing through the surface potential. The first of these steps for an electron confined to a band is illustrated in Fig. 7.15(b). The photoemission process in this case can either be described as a direct transition ($q_f = q_i$) in a reduced zone scheme, or as an indirect transition ($q_f = q_i + G$) in an extended zone scheme for which the process is enabled by the crystal providing the momentum $\hbar G$. Figure 7.15(c) indicates how, after the third step, the energy of the photoelectron propagating as a free particle in vacuum is related to the final energy $\mathcal{E}_f$ of the electron in the solid.

The determination of the electronic dispersion requires knowledge of both $\mathcal{E}_B$ and $\mathbf{q}$. The former can be inferred from the measured kinetic energy of the photoelectron (Eq. (7.29)), while the latter follows by applying conservation of momentum to the ARPES process. The first thing to note in this context is that since the photon wavelength in a typical ARPES experiment is much longer than the size of the unit cell, a, the photon momentum is small compared with that carried by band electrons (of order $\hbar(2\pi/a)$) and can be ignored. Secondly, the component of electron momentum parallel to the surface is rigorously conserved, and hence $\hbar q_\parallel = \hbar q_{\parallel,v}$. Lastly, the existence of the surface potential means that $\hbar q_\perp$ is not conserved. Further approximations are then required, or an appeal made to the results of calculations, in order to deduce its value. For example, if the final electronic states in the solid can be approximated by a free-electron model then

$$\hbar q_\perp = \sqrt{2m(\mathcal{E}_{kin}\cos^2\theta + V_0)} \tag{7.31}$$

where V_0 is the *inner potential*, which is the energy of the bottom of the valence band relative to the vacuum (Fig. 7.15(b)).

An example of the type of detailed information on the electronic structure that can be obtained with modern ARPES techniques is shown in Fig. 7.16(b)-(i) [Yokoya et al., 2005, Hoesch et al., 2009]. The material in this example is ZrTe$_3$ which is of interest because it undergoes a charge density wave (CDW) transition at $T_{CDW} = 63$ K, before becoming a superconductor at much lower temperatures below 2 K. CDW transitions are typically found in low-dimensional metallic systems, where a periodic lattice distortion opens a gap in the electronic structure at the Fermi energy $\mathcal{E}_F$ thereby reducing the electronic energy which more than offsets any increase in lattice energy. One of the key challenges in materials of this type is to understand how the observed phase transitions emerge from the underlying electronic structure. In Fig. 7.16(f)-(i) a selection of data is shown of the electronic dispersion as a function of q_x in this case for various slices near the Brillouin zone boundary. By comparing data taken above (200 K) and below (30 K) the CDW transition (Fig. 7.16(h)-(i)) is seen to result from the partial opening of a gap near the $\bar{D}$ point on the Brillouin zone boundary.

7.5 Further reading

The Analysis of Materials by X-ray Absorption, E.A. Stern, Scientific American **234** No. 4, p. 96 (1976).

The Quantum Theory of Light, R. Loudon (Oxford University Press, 1983).

The Quantum Theory of Radiation, W. Heitler (Dover Publications, 1984).

X-ray Scattering and Absorption by Magnetic Materials, S.W. Lovesey and S.P. Collins (Oxford University Press, 1996).

Angle-resolved Photoemission Studies of the Cuprate Superconductors, A. Damascelli, Z. Hussain and Z.-X. Shen, Rev. Mod. Phys. **75** 473 (2003).

7.6 Exercises

7.1 Prove Eq. (7.2).

7.2 Calculate the absorption length of a 10 keV X-ray beam in the compound GaAs. (Ga: μ/ρ_m(10 keV) = 34.21 cm^2/g and M=69.723 g/mol; As: μ/ρ_m(10 keV) = 41.15 cm^2/g and M=74.922 g/mol.)

7.3 Revaluate the absorption length in GaAs now for an X-ray energy of 15 keV, and explain why it is shorter than at 10 keV. (Ga: μ/ρ_m(15 keV) = 85.37 cm^2/g; As: μ/ρ_m(15 keV) = 98.56 cm^2/g)

7.4 Estimate the absorption length of a 10 keV X-ray beam in air at STP (ρ_m= 1.29 × 10^{-3} g/cm^3) using the following data: Weight%=76.7, 23.3, 1.29; M= 28, 32, 40 g/mole; ρ_m=1.3 × 10^{-3}, 1.4 × 10^{-3}, 1.8 × 10^{-3}; f''= 0.0224, 0.0414, 0.585, respectively, for N$_2$, O$_2$ and Ar.

7.5 Using the result above, estimate the absorption length of a 1 keV X-ray beam in air at STP.

7.6 Show that

$$\sigma_a \,[\text{barns/atom}] = 1.66\, M \,[\text{g/mol}] \left(\frac{\mu}{\rho_m}\right) \left[\text{cm}^2/\text{g}\right]$$

7.7 Prove the relationship stated in Eq. (7.10).

7.8 Show that the energy $\mathcal{E}$ at which the cross-sections for absorption and Thomson scattering are equal is given by

$$\mathcal{E}^{7/2} = 32 \left(\frac{12.398}{Z\pi r_0}\right) \mathcal{E}_K^{5/2}$$

where $\mathcal{E}_K$ is the energy of the K edge. Here energies are expressed in keV, and r_0 is in Å. Estimate the value of this energy for beryllium (K edge energy equal to 0.11 keV).

7.9 An ion chamber is often used to monitor the intensity of the incident beam. Show that the transmission T of a chamber of length L holding a gas of pressure P (in atmospheres) at room temperature can be written as

$$T = e^{-\mathcal{N}\sigma_a} \ \text{ with } \ \mathcal{N} = \frac{PLN_A}{24.0 \times 10^3}$$

where $\mathcal{N}$ is the number of atoms per unit area, and σ_A is the absorption cross-section in units of cm^2. What pressure of Ar gas should be used in an ion chamber with L =5 cm if it is to transmit 99% of the incident beam at a photon energy of 10 keV. (σ_a(10keV)= 3.71 × 10^3 barns/atom.)

7.10 Referring to Section 7.2.3 on CdTe, determine the radius of the second neighbour shell of a Te atom in the bulk, and compare the result to the data in the lower left panel in Fig. 7.9.

7.11 Moseley's law relates the energy of fluorescent radiation to the atomic number Z (see Eq. (1.20)). An analogous relationship can be established for the dependence of absorption edge energies on Z. In a hydrogen-like ion the electronic binding energy scales like $\mathcal{E}_H Z^2$ where $\mathcal{E}_H$=13.6 eV. A rough estimate of the binding energy $\mathcal{E}_K$ of a K electron is therefore $\mathcal{E}_K \approx \mathcal{E}_H(Z-1)^2$, since the other K-electron screens the nuclear charge of Z by one unit. Defining the relative error in the estimate of $\mathcal{E}_K$ as $\epsilon(Z)$, i.e.,

$$\mathcal{E}_K = \mathcal{E}_H(Z-1)^2 \left[1 + \epsilon(Z)\right]$$

(a) find a semi-empirical expression for $\epsilon(Z)$ in the region of $20 < Z < 90$ using the following data: Z= 26, 36, 47, 57, 69, 79; $\mathcal{E}_K$[eV]=7111, 14324, 25516, 38924, 59390, 80725.

(b) use the result from (a) to estimate the K edges of Ga ($Z = 31$) and As ($Z = 33$) (see Exercise 7.2).

Resonant scattering

In earlier chapters the scattering of X-rays has been discussed in terms of the classical Thomson scattering from an extended distribution of free electrons. Within this approximation the scattering length of an atom is written as $-r_0 f^0(\mathbf{Q})$, where $f^0(\mathbf{Q})$ is the atomic form factor, and r_0 is the Thomson scattering length of a single electron. The atomic form factor is nothing other than the Fourier transform of the charge distribution, and is hence a real number. We have also seen in Chapter 3 that with absorption processes included, the atomic scattering length must be generalized to be complex, the imaginary part being proportional to the absorption cross-section, σ_a (see Section 3.3 on page 75). It seems clear therefore that in order to pursue a classical model for the scattering, and at the same time require a complex scattering amplitude, a more elaborate model than that of a cloud of free electrons must be invoked. An obvious extension is to allow for the fact that electrons may be bound in atoms. In a classical picture they will respond to the driving field of the X-ray as damped harmonic oscillators, with an associated resonant frequency ω_s and a damping constant Γ.

As we shall see, the forced oscillator model does indeed give an imaginary component to the atomic scattering length, and in addition produces a correction to the real part. Altogether the scattering amplitude of the atom, in units of $-r_0$, can be written in the form

$$f(\mathbf{Q}, \omega) = f^0(\mathbf{Q}) + f'(\omega) + i\,f''(\omega) \tag{8.1}$$

where f' and f'' are the real and imaginary parts of the *dispersion corrections*. It should be clear that the dispersion corrections are energy (or equivalently frequency) dependent. As they take on their extremal values at the absorption edges they are also known as the *resonant scattering terms*. At one time it was also common to refer to them as the anomalous scattering corrections, but since they are now mostly understood, it is generally agreed that there is nothing really anomalous about them. The dispersion corrections are dominated by electrons in the K shell, except perhaps for the heavier elements, where the L and M shells become important. The electrons in these shells are so spatially confined that the $\mathbf{Q}$ dependence can be neglected, and this explains why it has been omitted in Eq. (8.1). The Thomson term, $f^0(\mathbf{Q})$, on the other hand, does not depend on the photon energy, but only on the scattering vector
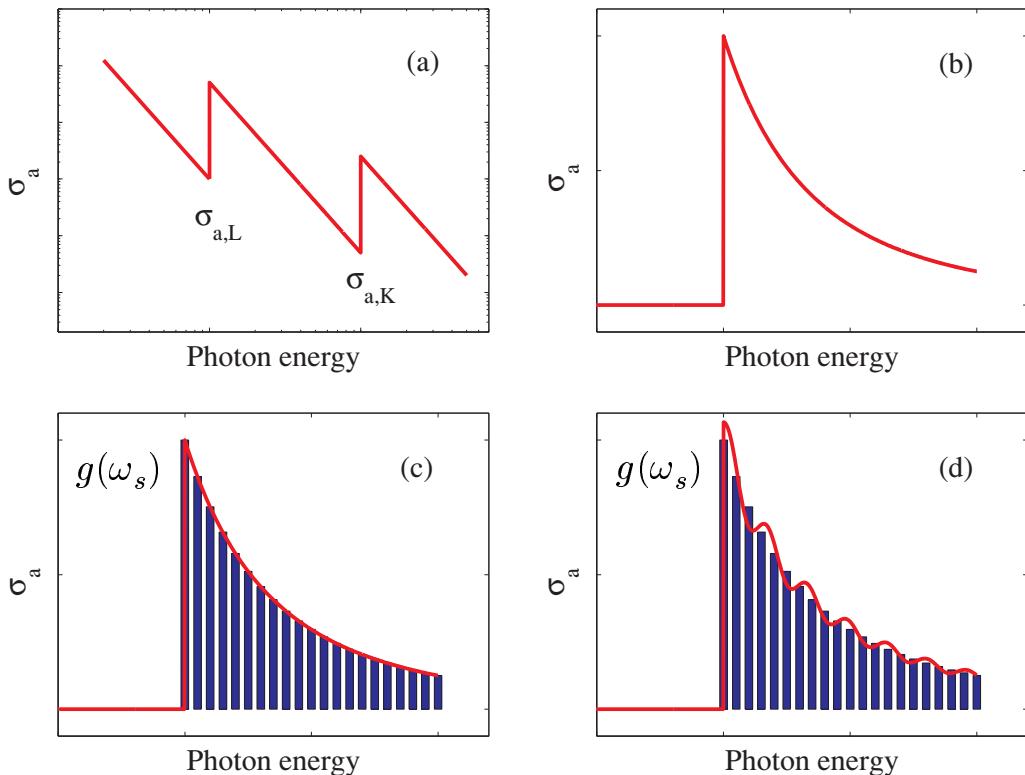
Fig. 8.1 (a) Double logarithmic plot of the absorption cross-section as a function of photon energy. The absorption cross-section σ_a has characteristic edges. In between these edges σ_a varies approximately as the inverse cube of the energy. (b) The absorption cross-section for a K electron on a linear scale. (c) The absorption cross-section for an isolated atom may be modelled by a series of harmonic oscillators described by a smooth weighting function $g(\omega_s)$. (d) This often is not an adequate approach, as it does not take into account near-edge structure, such as the white line, or EXAFS oscillations produced by neighbouring atoms.

Q. The **Q** dependence is due to the fact that the non-resonant scattering is produced by *all* atomic electrons, which have a spatial extent of the same order of magnitude as the X-ray wavelength (see the discussion of the atomic form factor on page 120).

It is important to emphasize that the resonant scattering considered here is elastic. That is, the scattered X-ray has the same energy as that of the incident one. In a quantum mechanical picture of resonant scattering the incident photon excites an electron to a higher lying level. The electron then decays back to the initial state by emitting a photon of the same energy as the incident one. This type of process, emission via some intermediate state, requires second-order perturbation theory to describe it, and the resonant behaviour then arises from the energy denominator present in the theory.

At this stage it is worth pausing to anticipate one of the limitations of the single oscillator model. The imaginary part of the dispersion correction f'' represents the dissipation in the system, or in other words the absorption. Indeed the explicit relationship between f'' and σ_a has already been given in Eq. (3.10) on page 76. It is known from elementary considerations that the imaginary part of the response of a forced harmonic oscillator displays a resonance when the driving frequency is close to

the natural frequency, and that the width of this resonance is small for light damping. It follows that the single oscillator model can be expected to yield at best a peak in f'', and hence one also in σ_a. This clearly does not resemble the absorption cross-section of an atom sketched in Fig. 8.1(a). This has a discontinuous jump at an absorption edge, followed by a ω^{-3} fall-off, as discussed in Chapter 7 on absorption. In order to model this behaviour, one must instead assume a superposition of oscillators with relative weights, so-called oscillator strengths, $g(\omega_s)$, proportional to $\sigma_a(\omega = \omega_s)$.

The resonant scattering terms are of particular importance in the crystallography of complex systems, such as in the determination of the structure of macromolecules. The reason is that in a diffraction experiment it is the modulus squared of the unit cell structure factor that is measured, and hence information on the relative phases of the scattering from different atoms in the unit cell is lost. This is known as the phase problem in crystallography. This makes it difficult, if not impossible, to solve uniquely the structure of a unit cell that may contain thousands of atoms. It turns out that a solution to the phase problem may be found by recording data sets at several photon energies around the absorption edge of one of the atoms (usually a heavy atom) in the structure. The technique that exploits this approach is known as MAD, for Multi-wavelength Anomalous Diffraction. The success of this technique depends on an accurate knowledge of the dispersion corrections.

In this chapter we shall explain the basic principles behind how f' and f'' are determined. In the following section expressions for the dispersion corrections are derived by treating atomic electrons as harmonic oscillators. This is obviously a crude approximation, but one that nonetheless allows us to explore more general aspects of the relationship of f' and f'' to each other, and to the absorption cross-section.

8.1   The forced charged oscillator model

Consider a classical model of an electron bound in an atom. Let the electron be subject to the electric field of an incident X-ray beam, $\mathbf{E}_{in} = \hat{\mathbf{x}} E_0 e^{-i\omega t}$, linearly polarized along the x axis, with amplitude E_0 and frequency ω. The equation of motion of the electron is

$$\ddot{x} + \Gamma \dot{x} + \omega_s^2 x = -\left(\frac{e E_0}{m}\right) e^{-i\omega t}$$

The velocity-dependent damping term, $\Gamma \dot{x}$, represents dissipation of energy from the applied field, primarily due to re-radiation. The damping constant, Γ, which has the dimension of frequency, is usually much smaller than the resonant frequency, ω_s. By substituting the trial solution $x(t) = x_0 e^{-i\omega t}$ into the above we obtain the following expression for x_0, the amplitude of the forced oscillation:

$$x_0 = -\left(\frac{e E_0}{m}\right) \frac{1}{(\omega_s^2 - \omega^2 - i\omega\Gamma)} \tag{8.2}$$

8.1.1   Dispersion corrections: real and imaginary parts

Explicit expressions for the frequency dependence of the dispersion corrections can be obtained using similar arguments to those given in Section 1.2, where we evaluated the scattering cross-section from a single, free electron. Here we are dealing with bound electrons; in both cases the derivation hinges on the strength of the radiated field. For an observer at a distance R and at time t the radiated field is

proportional to the acceleration $\ddot{x}(t - R/c)$ at the earlier time $t' = t - R/c$:

$$E_{rad}(R, t) = \left(\frac{e}{4\pi\epsilon_0 R c^2} \right) \ddot{x}(t - R/c)$$

where for convenience we have set the polarization factor $\hat{\varepsilon} \cdot \hat{\varepsilon}' = 1$. Inserting $\ddot{x}(t - R/c) = -\omega^2 x_0 e^{-i\omega t} e^{i(\omega/c)R}$, with x_0 given by Eq. (8.2), leads to

$$E_{rad}(R, t) = \frac{\omega^2}{(\omega_s^2 - \omega^2 - i\omega\Gamma)} \left(\frac{e^2}{4\pi\epsilon_0 mc^2} \right) E_0 e^{-i\omega t} \left(\frac{e^{ikR}}{R} \right)$$

or equivalently

$$\frac{E_{rad}(R, t)}{E_{in}} = -r_0 \frac{\omega^2}{(\omega^2 - \omega_s^2 + i\omega\Gamma)} \left(\frac{e^{ikR}}{R} \right)$$

The atomic scattering length, f_s, is defined to be the amplitude of the outgoing spherical wave, (e^{ikR}/R). In units of $-r_0$ this is

$$f_s = \frac{\omega^2}{(\omega^2 - \omega_s^2 + i\omega\Gamma)} \tag{8.3}$$

where the subscript 's' is there to remind us that the result is for a single oscillator. For frequencies large compared to the resonant frequency, $\omega \gg \omega_s$, the electron can be considered to be free, and the Thomson scattering expression is recovered, i.e. $f_s = 1$.

The expression for f_s given in Eq. (8.3) can be rearranged in the following way:

$$f_s = \frac{\omega^2 - \omega_s^2 + i\omega\Gamma + \omega_s^2 - i\omega\Gamma}{(\omega^2 - \omega_s^2 + i\omega\Gamma)} = 1 + \frac{\omega_s^2 - i\omega\Gamma}{(\omega^2 - \omega_s^2 + i\omega\Gamma)}$$

$$\approx 1 + \frac{\omega_s^2}{(\omega^2 - \omega_s^2 + i\omega\Gamma)} \tag{8.4}$$

where the last line follows from the fact that Γ is usually much less than ω_s. By writing it in this form it is clear that the second term is the dispersion correction to the scattering factor. The dispersion correction is then written as $\chi(\omega) = f_s' + if_s''$, so that

$$\chi(\omega) = f_s' + if_s'' = \frac{\omega_s^2}{(\omega^2 - \omega_s^2 + i\omega\Gamma)} \tag{8.5}$$

with the real part given by

$$f_s' = \frac{\omega_s^2(\omega^2 - \omega_s^2)}{(\omega^2 - \omega_s^2)^2 + (\omega\Gamma)^2} \tag{8.6}$$

and the imaginary part by

$$f_s'' = -\frac{\omega_s^2\omega\Gamma}{(\omega^2 - \omega_s^2)^2 + (\omega\Gamma)^2} \tag{8.7}$$

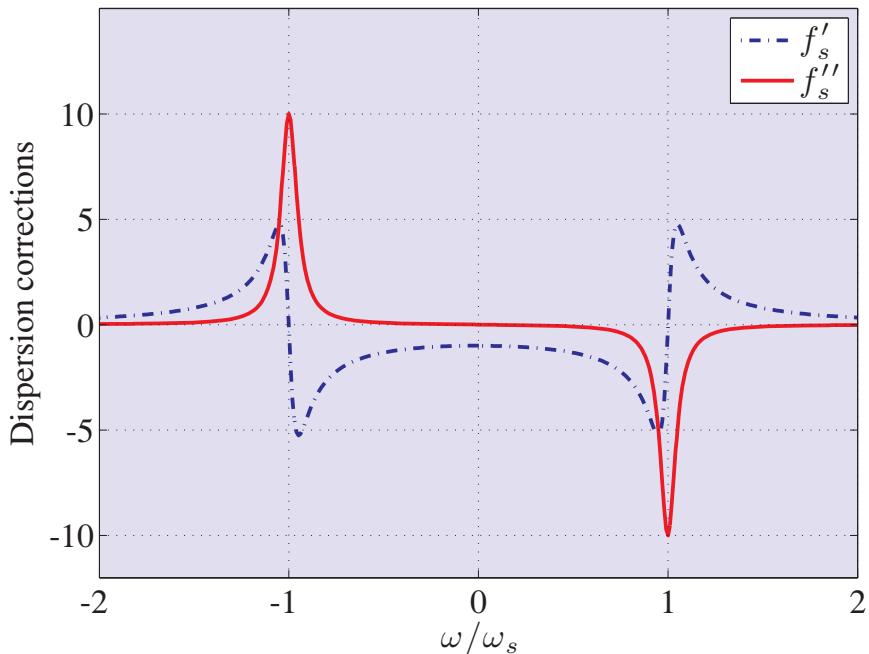The frequency dependence of the dispersion corrections for the single oscillator model are shown in Fig. 8.2.

Fig. 8.2 The real, f'_s, and imaginary, f''_s, parts of the dispersion corrections as a function of the driving frequency ω relative to the resonant frequency ω_s calculated for a single oscillator model. In the example shown here the damping Γ has been chosen to be equal to $0.1\,\omega_s$.

8.1.2   The total scattering cross-section

Here we recall that the *total* cross-section for the scattering of an electromagnetic wave by a single, free electron is

$$\sigma_{\mathrm{T}} = \left(\frac{8\pi}{3}\right) r_0^2$$

as derived in Section 1.2 on page 5 (see also Appendix B). It follows from Eq. (8.3) that the free electron result can be generalized to the case of a bound electron by writing

$$\sigma_{\mathrm{T}} = \left(\frac{8\pi}{3}\right) \frac{\omega^4}{(\omega^2 - \omega_s^2)^2 + (\omega\Gamma)^2}\, r_0^2 \tag{8.8}$$

The frequency dependence of the total scattering cross-section is plotted in Fig. 1.8(a), where it is seen to exhibit a peak when $\omega \approx \omega_s$.

In the limit that $\omega \ll \omega_s$ and $\Gamma \to 0$ the cross-section becomes

$$\sigma_{\mathrm{T}} = \left(\frac{8\pi}{3}\right) \left(\frac{\omega}{\omega_s}\right)^4 r_0^2$$

This is the limiting form appropriate for the scattering of electromagnetic radiation in the visible part of the spectrum, and is known as Rayleigh's law[1]. For this reason the scattering of X-rays from atoms is also sometimes referred to as Rayleigh scattering. In the opposite limit, $\omega \gg \omega_s$ the total scattering length approaches the value expected for the scattering from a free electron.

8.1.3   Dispersion corrections and the refractive index

It has been emphasized in earlier chapters (see, for example, Section 3.1) how scattering and refraction are alternative ways to view the same physical phenomenon. The existence of resonant scattering terms arising from the dispersion corrections can therefore be expected to lead to a frequency dependence of the refractive index, n.

To understand the form that this takes we consider the response of a medium, described by an electric susceptibility, $\chi = (\epsilon/\epsilon_0 - 1)$, to a time dependent electric field $\mathbf{E}(t)$. We assume that the effect of the applied electric field is to induce an electric polarization $\mathbf{P}(t)$ of the medium given by

$$\mathbf{P}(t) = \epsilon_0 \chi \, \mathbf{E}(t) = (\epsilon - \epsilon_0) \, \mathbf{E}(t)$$

By definition the polarization density $\mathbf{P}(t)$ from N electrons contained in a volume V and all displaced by the amount $x(t)$ is

$$\mathbf{P}(t) = \frac{-Nex(t)}{V} \equiv -e\rho x(t)$$

From Eq. (8.2) this can be rewritten as

$$\mathbf{P}(t) = -e\rho \left(-\frac{e}{m} \right) \frac{E_0 e^{-i\omega t}}{(\omega_s^2 - \omega^2 - i\,\omega\Gamma)}$$

which can be rearranged to read

$$\frac{\mathbf{P}(t)}{\mathbf{E}(t)} = \epsilon - \epsilon_0 = \left(\frac{e^2 \rho}{m} \right) \frac{1}{(\omega_s^2 - \omega^2 - i\,\omega\Gamma)} \tag{8.9}$$

The connection to the refractive index can then be made since it is defined by

$$n^2 = \frac{c^2}{v^2} = \frac{\epsilon}{\epsilon_0}$$

which on making use of Eq. (8.9) yields

$$n^2 = 1 + \left(\frac{e^2 \rho}{\epsilon_0 m} \right) \frac{1}{(\omega_s^2 - \omega^2 - i\,\omega\Gamma)} \tag{8.10}$$

The real and imaginary parts of the refractive index are plotted in Fig. 1.8(b) and (c), respectively. The imaginary part, which represents absorption or dissipation, peaks at $\omega = \omega_s$. For frequencies less than

---

[1]The ω^4 dependence of the cross-section explains, amongst other things, why the sky is blue in the middle of the day, and turns red at sunrise and sunset. Blue light has a shorter wavelength than red, and is more strongly scattered. Light from the sun is scattered from particles in the atmosphere. During the day the light reaching an observer comes partly from diffuse scattering, and is hence dominated by the blue part of the spectrum. When the sun is viewed close to the horizon the blue light is scattered out of the direct sun light, producing a red hue to the sky.

ω_s, $n > 1$, as is typically found in the optical part of the electromagnetic spectrum. Once the frequency exceeds ω_s, $n < 1$, as applies in the X-ray regime. In this limit, where $\omega \gg \omega_s \gg \Gamma$, the expression for the refractive index simplifies to read

$$n \approx 1 - \frac{1}{2} \frac{e^2 \rho}{\epsilon_0 m \omega^2} = 1 - \frac{2\pi \rho r_0}{k^2}$$

in agreement with Eq. (3.2).

8.1.4 The absorption cross-section

An expression for the frequency dependence of the absorption cross-section can be obtained by substituting the expression for f_s'' given in Eq. (8.7) into Eq. (3.10). Noting that $\omega/k = c$, the absorption cross-section for a single oscillator model becomes

$$\sigma_{\text{a,s}}(\omega) = 4\pi r_0 c \frac{\omega_s^2 \Gamma}{(\omega^2 - \omega_s^2)^2 + (\omega\Gamma)^2} \tag{8.11}$$

As the damping constant Γ is typically small compared to the resonance frequency ω_s, the absorption cross-section has a sharp peak at $\omega = \omega_s$, the peak width being $\Delta\omega_{\text{FWHM}} \approx \Gamma$. The effective absorption cross-section may thus be represented by a delta function centred at $\omega = \omega_s$:

$$\sigma_{\text{a,s}}(\omega) = 4\pi r_0 c \frac{\pi}{2} \delta(\omega - \omega_s) \tag{8.12}$$

The factor of $\frac{\pi}{2}$ ensures that when Eq. (8.12) is integrated over ω it gives the same result as integrating Eq. (8.11); the region of integration in both cases being from 0 to ∞.

8.2 The atom as an assembly of oscillators

In Fig. 8.1(a) a schematic plot is shown of the atomic X-ray absorption cross-section as a function of photon energy, where it is seen to exhibit characteristic absorption edges. For example, an X-ray photon with energy greater than the K edge energy can expel an electron from the K shell of the atom. This opens up a new channel for absorption, and produces an abrupt increase in the cross-section. In Chapter 7 on absorption we have shown how the magnitude of the absorption edge may be calculated from first principles, and also how the absorption between the edges varies approximately as ω^{-3}. The K absorption edge shown on a linear plot in Fig. 8.1(b) is clearly not the simple line spectrum of a single oscillator predicted by Eq. (8.12), and instead a more elaborate model is required.

If there was only one discrete quantum state that the electron could be excited into, then the classical line spectrum of a single oscillator would be an adequate description of the re-radiation. However, there is a continuum of free states above the absorption edge that the electron can be excited into. A different characteristic frequency ω_s can be associated with each of these states. Explicitly, the absorption cross-section given in Eq. (8.12) is generalized to

$$\sigma_{\text{a}}(\omega) = 2\pi^2 r_0 c \sum_s g(\omega_s) \delta(\omega - \omega_s)$$
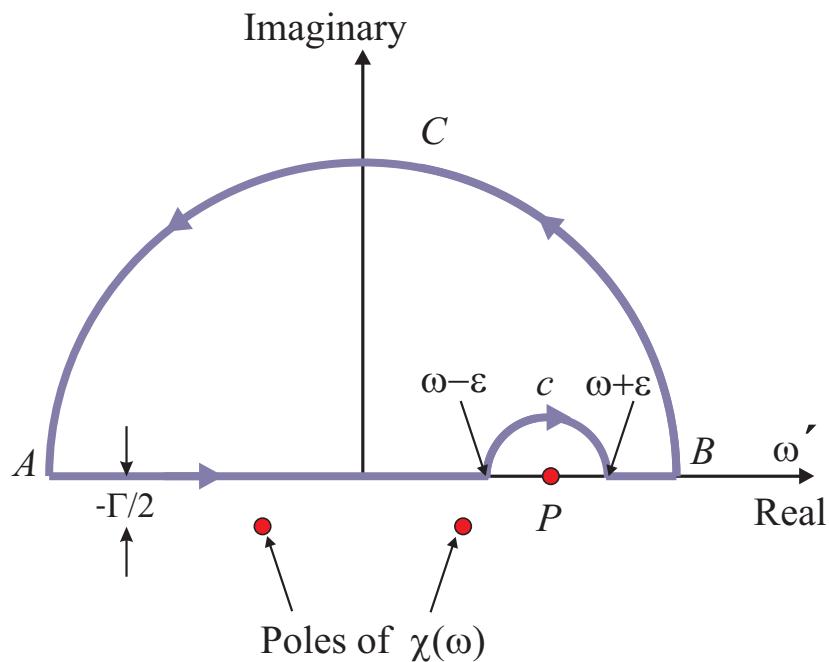
Fig. 8.3 The Kramers-Kronig relation can be derived from Cauchy's theorem using the contour integral in the complex plane shown here.

where $g(\omega_s)$ is the relative weight of each transition, and where the narrow absorption lines have been approximated by delta functions (Fig. 8.1(c) and (d)). The expression for the real part of the dispersion correction, f', then also becomes the weighted superposition of single oscillators:

$$f'(\omega) = \sum_s g(\omega_s) f'_s(\omega_s, \omega)$$

8.3 The Kramers-Kronig relations

When trying to interpret experimental data it is sometimes better not to rely on theoretical values of the dispersion corrections. The reason is simply that they may not be accurate enough. A more serious difficulty is that it is not straight forward to allow for effects, such as the existence of a white line, or EXAFS oscillations in σ_a which depend on the particular environment of the resonantly scattering atom (see Fig. 8.1(d)). Instead a method has been developed for obtaining $f'(\omega)$ indirectly from the absorption cross-section $\sigma_a(\omega)$. The starting point is to determine $\sigma_a(\omega)$ experimentally, from which it

Kramers-Kronig relations

The derivation of the Kramers-Kronig relations is based on Cauchy's theorem concerning the contour integral taken in the counter clockwise direction of an analytic function $F(z)$ in the complex plane, z. If $F(z)$ has a *simple* pole at z_0 which is encompassed by the contour, then the value of the contour integral is equal to $2\pi i$ times the *residue*, which for a simple pole is equal to $(z - z_0)F(z_0)$.

Let us apply this theorem to the function $\chi(z)/(z - \omega)$ with $\chi(z) = \omega_s^2/(z^2 - \omega_s^2 + iz\Gamma)$ given by Eq. (8.5). It is straightforward to show that the poles of $\chi(z)$ are in the lower half of the complex plane at $Im(z) = -\Gamma/2$ as shown in Fig. 8.3. We shall then consider the contour comprising the path with $z = \omega'$ on the real axis from $A(\to -\infty)$ to $(\omega - \epsilon)$, then clockwise along the semi-circle c, then again along the real axis from $(\omega + \epsilon)$ to $B(\to +\infty)$, and then finally back to A along the large semi-circle C.

On the real axis, our function $\chi(z)/(z - \omega)$ has a pole at $\omega' = \omega$ with a residue equal to $\chi(\omega)$. As the path did not encompass this pole, the entire contour integral must be equal to zero. The contribution from the large semi-circle C is also zero, because for large z our function decays as $|z|^{-3}$, whereas the path length is only proportional to $|z|$. Altogether then, the sum of the principal integral, $\mathcal{P} \int \chi(z)/(z - \omega)d\omega'$, and the integral along c, $\int_c \chi(z)/(z - \omega)d\omega'$, is zero.

The clockwise integral along the small *half* circle is $-\pi i \chi(\omega)$, since a contour integral counter clockwise along the *full* circle around the pole P must, according to Cauchy's theorem, be equal to $+2\pi i \chi(\omega)$. Splitting $\chi(z)$ into its real and imaginary components (Eqs. (8.6) and (8.7)) finally yields

$$i\pi \left(f_s'(\omega) + if_s''(\omega)\right) = \mathcal{P} \int_{-\infty}^{\infty} \frac{f_s'(\omega') + if_s''(\omega')}{\omega' - \omega}d\omega'$$

Identifying the real and imaginary parts on the left and right hand sides leads to the Kramers-Kronig relations for a single oscillator.

Since $f'(\omega)$ and $f''(\omega)$ are linear superpositions of single oscillators, the Kramers-Kronig relations also apply to them.

is possible to obtain $f''(\omega)$ through[2]

$$\boxed{f''(\omega) = -\left(\frac{\omega}{4\pi\, r_0\, c}\right)\sigma_a(\omega)}$$

(8.13)

(see Eq. (3.10)). The next step is to exploit the general relationships that exist between f' and f''. These are written as

$$f'(\omega) = \frac{1}{\pi}\mathcal{P}\int_{-\infty}^{+\infty}\frac{f''(\omega')}{(\omega'-\omega)}d\omega' = \frac{2}{\pi}\mathcal{P}\int_{0}^{+\infty}\frac{\omega' f''(\omega')}{(\omega'^2-\omega^2)}d\omega'$$

(8.14)

$$f''(\omega) = -\frac{1}{\pi}\mathcal{P}\int_{-\infty}^{+\infty}\frac{f'(\omega')}{(\omega'-\omega)}d\omega' = -\frac{2\omega}{\pi}\mathcal{P}\int_{0}^{+\infty}\frac{f'(\omega')}{(\omega'^2-\omega^2)}d\omega'$$

(8.15)

and are known as the Kramers-Kronig relations. The meaning of these relations is that if the energy dependence of the absorption cross-section is known, then $f''(\omega)$ can be found from Eq. (8.13), and with this substituted into Eq. (8.14) it is possible to derive the associated real part of the dispersion correction to the scattering amplitude. This method of obtaining f' from σ_a is illustrated in the next section by considering the simple model introduced in Chapter 7 for the variation of σ_a in the vicinity of a K edge.

The Kramers-Kronig equations relating f' to f'' require further comment. First, the $\mathcal{P}$ in front of the integral stands for 'principal value'. This means that the integration over ω' is actually performed by integrating from $-\infty$ to $(\omega-\epsilon)$ and from $(\omega+\epsilon)$ to $+\infty$, and then the limit $\epsilon \to 0$ is taken. Second, the alternative form of the expressions for $f'(\omega)$ and $f''(\omega)$ have been obtained by multiplying the numerator and denominator by $(\omega'+\omega)$, and by utilizing the fact that $f'(\omega')$ is an even function, and $f''(\omega')$ an odd function according to Eq. (8.6) and Eq. (8.7) (see Fig. 8.2). The validity of the Kramers-Kronig relations for the single oscillator expression given in Eqs. (8.6) and (8.7) may be established either by direct substitution, or by the more general derivation given in the box on the preceding page.

8.4 Numerical estimate of f'

8.4.1 Simple model

In this section an estimate is made of f', the real part of the dispersion correction, for photon energies near the K absorption edge. Equation (8.14) can be used together with (8.13) to relate f' to the energy dependence of the absorption cross-section:

$$\begin{aligned}
f'(\omega) &= \frac{2}{\pi}\mathcal{P}\int_{0}^{+\infty}\frac{\omega' f''(\omega')}{(\omega'^2-\omega^2)}d\omega' \\
&= -\frac{2}{\pi}\frac{1}{(4\pi\, r_0\, c)}\mathcal{P}\int_{0}^{+\infty}\frac{\omega'^2\,\sigma_a(\omega')}{(\omega'^2-\omega^2)}d\omega'
\end{aligned}$$

(8.16)

---

[2] f'' is negative since σ_a is a positive real number. In other texts the sign convention is sometimes such that f'' is positive.
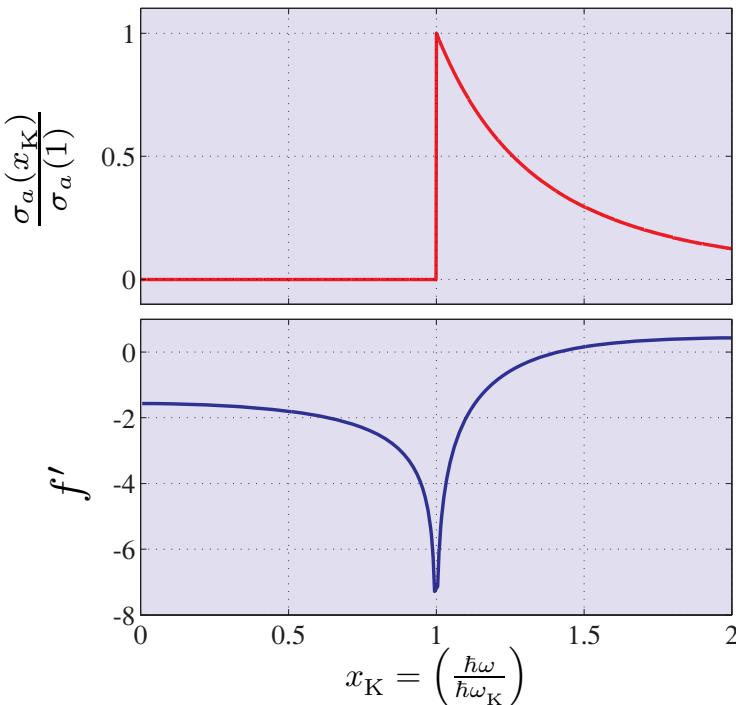
Fig. 8.4 Estimate of the dispersion corrections around the K edge. Top panel: The imaginary part of the dispersion correction f'' is proportional to the absorption cross-section σ_a, here assumed to vary as $1/\omega^3$ above the edge. In reality the discontinuity at $x_K = 1$ is broadened by the lifetime of the excited state in the presence of the hole created in the core electronic state (the so-called core-hole lifetime, as discussed in the text). The broadening in energy, which is inversely proportional to the core-hole lifetime, is represented by the parameter η in the text. Bottom panel: Numerical estimate of the real part of the dispersion correction f' for two K shell electrons in an atom. The curve for f' is given by Eq. (8.18) which has been derived from the Kramers-Kronig transform of f''. The behaviour of f' in the vicinity of the resonance at $x_K = 1$ is also determined by core-hole lifetime effects. Here for illustrative purposes we have set the energy broadening parameter η to be equal to 0.004.

To evaluate this integral the frequency ω is normalized to that of the K edge by introducing $x_K = \omega/\omega_K$ as the independent variable, so that the integration variable becomes $x=\omega'/\omega_K$. The energy dependence of the absorption cross-section was discussed in Chapter 7, and this allows us to write $\sigma_a(\omega')$ in the form

$$\sigma_a\left(\frac{\omega'}{\omega_K}\right) \approx \begin{cases} \sigma_a\left(\frac{\omega'}{\omega_K} = 1\right)\left(\frac{\omega'}{\omega_K}\right)^{-3} & \text{for } \left(\frac{\omega'}{\omega_K}\right) \geq 1, \\ 0 & \text{for } \left(\frac{\omega'}{\omega_K}\right) < 1 \end{cases}$$

This is plotted in the top panel of Fig. 8.4. With this functional form for $\sigma_a(\omega')$ the principal value

integral given in Eq. (8.16) is

$$P \int_0^\infty \frac{\omega'^2 \sigma_a(\omega')}{(\omega'^2 - \omega^2)} \, d\omega' \cong \sigma_a(1) \, P \int_1^\infty \frac{x^2 x^{-3}}{(x^2 - x_K^2)} \omega_K \, dx$$

$$= \sigma_a(1) \, \omega_K \, P \int_1^\infty \frac{1}{x(x^2 - x_K^2)} \, dx$$

$$= \sigma_a(1) \, \omega_K \, I(x_K)$$

where the integral $I(x_K)$ is defined by

$$I(x_K) = P \int_1^\infty \frac{1}{x(x + x_K)(x - x_K)} \, dx \tag{8.17}$$

Collecting these results together, the expression for the real part of the dispersion correction becomes

$$f'(\omega) = -\frac{2}{\pi} \frac{1}{(4\pi r_0 c)} \sigma_a(1) \, \omega_K \, I(x_K)$$

$$= -\frac{1}{\pi \lambda_K r_0} \sigma_a(1) \, I(x_K)$$

The magnitude of the discontinuity in the absorption cross-section at the edge, $\sigma_a(1)$, can be found from Eq. (7.17), which for *two* K electrons reads

$$\sigma_a(1) = 2 \times \left(\frac{256\pi}{3e^4}\right) \lambda_K r_0$$

In order to obtain a numerical value for f' it is necessary to perform the principal value integration given in Eq. (8.17). The evaluation of this integral is outlined in the box on the next page. The real part of the dispersion correction close to the K edge is therefore given by

$$f'(\omega) = -\left(\frac{512}{3e^4}\right) I(x_K, \eta) = -3.13 \, I(x_K, \eta) = \frac{3.13}{2x_K^2} \Re \log(1 - z^2) \tag{8.18}$$

with $z = x_K + i\eta$ which is plotted in Fig. 8.4. It can be verified that the energy dependence of f' has the correct asymptotic behaviour. From Eq. (8.17), for $x_K \to \infty$ the integral $I(x_K \to \infty) \to 0$, in accordance with the vanishing dispersion corrections at high photon energies. In the limit $x_K \to 0$ we have $I(x_K \to 0) = \int_1^\infty x^{-3} \, dx = 1/2$, and at low energies $f'(\omega \ll \omega_K)$ tends to the value -1.565. In other words the contribution of the two K electrons to the Thomson scattering is partly quenched. Thus the curve of $f'(x_K)$ versus x_K is not expected to be symmetric around $x_K = 1$, as indeed is evident in Fig. 8.4.

It should be appreciated that our simple model is incapable of capturing the behaviour of the resonant scattering terms in the vicinity of the discontinuity at $x_K = 1$. The reason is that close to resonance the excited state, produced by removing an electron from a core state to create a hole, has a finite lifetime. This leads to a broadening in energy of both f' and f'' which is inversely proportional to the core-hole lifetime. The core-hole lifetime itself depends on the detailed nature of the electronic states, and is thus affected by changes to the atomic environment from chemical bonding, etc. In our treatment we have represented these important complexities by introducing a broadening parameter η. In Fig. 8.4 we have chosen $\eta = 0.004$. In an experiment one would in addition have to convolute with the experimental band width.

Evaluation of the integral $I(x_K)$, Eq. (8.17)

First the integrand $f(x)$ is decomposed using the following method:

$$f(x) = \frac{1}{x} \frac{1}{(x + x_K)} \frac{1}{(x - x_K)}$$

$$= \frac{1}{2x_K^2} \left[\left(\frac{1}{(x + x_K)} - \frac{1}{x} \right) + \left(\frac{1}{(x - x_K)} - \frac{1}{x} \right) \right]$$

which can be verified by inspection. With the integrand decomposed in this way, we proceed to evaluate the limiting form of integrals of the type

$$\lim_{\Lambda \to \infty} \int_1^\Lambda \left(\frac{1}{(x + x_K)} - \frac{1}{x} \right) dx = \log \frac{(\Lambda + x_K)}{(1 + x_K)} - \log \Lambda$$

$$= \log(1 + x_K/\Lambda) - \log(1 + x_K)$$

$$\xrightarrow[\Lambda \to \infty]{} -\log(1 + x_K)$$

In other words, ignoring for a moment the prescription 'principal value', the integral in Eq. (8.17) can be evaluated as

$$2x_K^2 I(x_K) = -\log \left[(1 + x_K)(1 - x_K) \right] = -\log(1 - x_K^2)$$

However, the integral $I(x_K)$ is singular for $x_K = 1$. This can be circumvented by taking the principal value which amounts to adding a small imaginary number to x_K and then taking the real part. Thus we let $z = x_K + i\eta$ from which we obtain

$$2x_K^2 I(x_K, \eta) = -\Re \log(1 - z^2)$$

8.4.2 More realistic approaches

It is of course desirable to perform more accurate calculations of the dispersion corrections than described here. Accurate values of the dispersion corrections are needed in several branches of crystallography, including, for example, the derivation of electron density maps. In Fig. 8.5 examples of the energy dependence of the dispersion corrections for the noble gases Ar and Kr are shown. These have been calculated within the self-consistent Dirac-Hartree-Fock framework [Chantler, 1995]. (See also Henke et al. [1993].) For Ar the K edge occurs at 3.203 keV. By comparing the curves shown in the left panel of Fig. 8.5 with Fig. 8.4 it can be seen that our simpler model captures the essential features of the energy dependence of the dispersion corrections.

In fact, even the most sophisticated theoretical methods are not always adequate. The reason is that close to an absorption edge the dispersion corrections become sensitive to the details of the environment of the resonantly scattering atom. For example, it has already been described in Chapter 7 how the absorption cross-section is modified by EXAFS oscillations. Under these circumstances the best that can be done is to measure the absorption cross-section of the atom of interest in the particular crystal being investigated over a range of energies around the edge, and then use the general Kramers-Kronig relation to derive $f'(\hbar\omega)$ from $\sigma_a(\omega)$. In this way the effects of core-hole lifetime, as
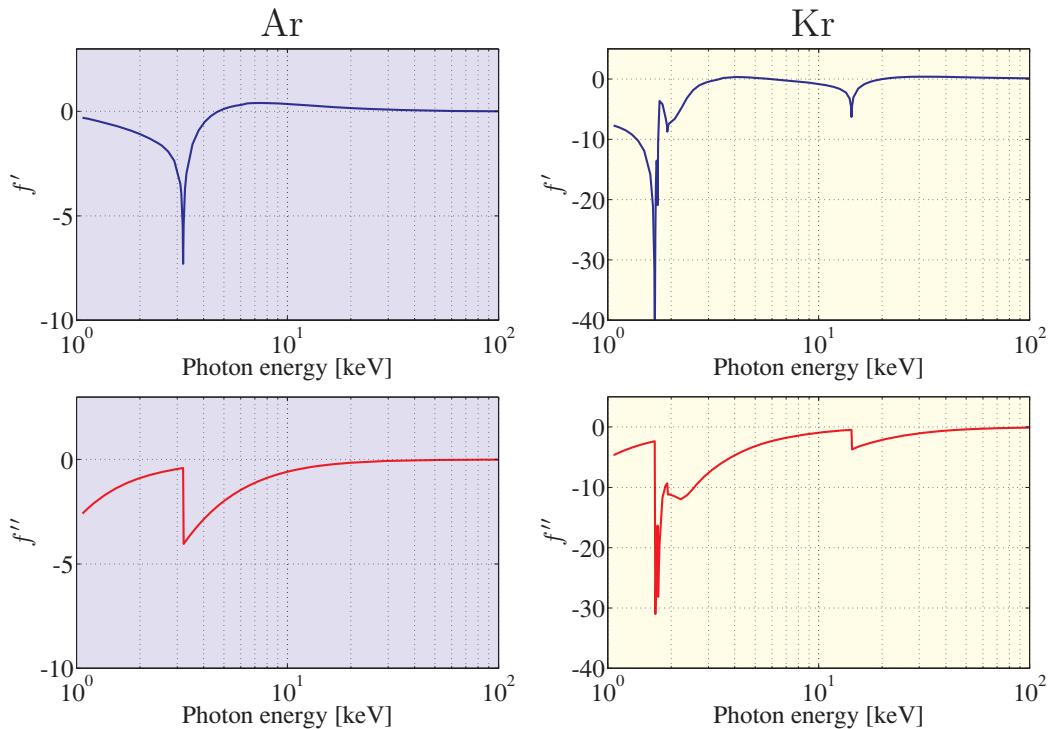
Fig. 8.5 The calculated energy dependence of the real, f', and imaginary, f'', parts of the dispersion corrections (in units of r_0) for Ar and Kr. The calculations were performed within the self-consistent Dirac-Hartree-Fock framework, and are discussed in the text. The K edge of Ar is evident at 3.203 keV. For Kr the K edge occurs at 14.32 keV, while the L edges are centred around 1.8 keV.

well as experimental resolution, are also included automatically.

In summary, the total atomic scattering amplitude is

$$f(\mathbf{Q}, \hbar\omega) = f^0(\mathbf{Q}) + f'(\hbar\omega) + i \, f''(\hbar\omega)$$

where $f^0(\mathbf{Q})$ is the form factor for *all* Z electrons in the atom, K electrons included, and the two extra terms are the dispersion corrections. As $f^0(\mathbf{Q})$ is the Fourier transform of the electrons density in the atom, normalized to Z at $\mathbf{Q} = 0$, it is independent of the photon energy. On the other hand, in our model the dispersion corrections are due to the K electrons only. These are localized close to the nucleus so that the Fourier transform of their wavefunction is essentially constant. This explains why to a good approximation the dispersion corrections are independent of the scattering vector $\mathbf{Q}$. For photon energies below the K edge, the K electrons are so tightly bound that the electromagnetic field of the incident X-ray cannot set them into full vibrations. In other words the scattering amplitude of the entire atom is reduced compared to the Thomson value, and it follows that $f'(\hbar\omega)$ must be negative. Since $f(\mathbf{Q})$ decreases with increasing $\mathbf{Q}$, whereas $f'(\hbar\omega)$ remains constant, the relative contribution of $f'(\hbar\omega)$ to the total atomic scattering amplitude increases with increasing $\mathbf{Q}$. Thus the relative importance of
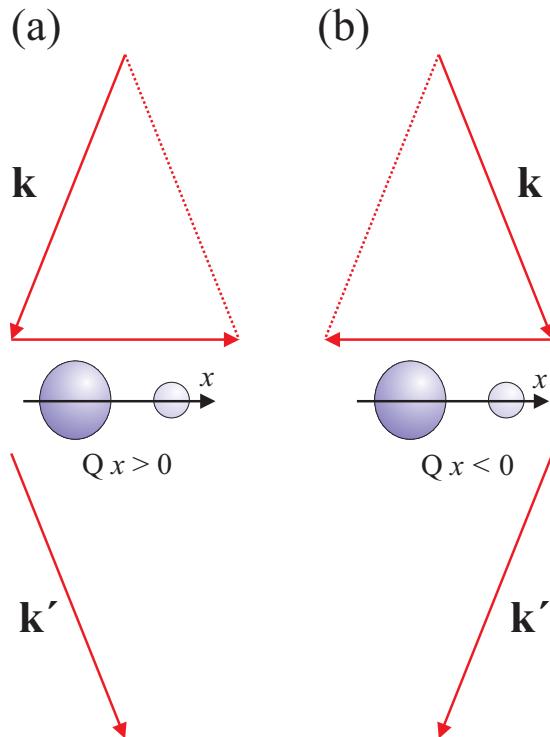
Fig. 8.6 Diffraction by two non-identical atoms. Analysis of the scattered intensities when the scattering vector is parallel to the direction connecting the large and small atoms, or when it is in the opposite direction, shows that with the dispersion corrections taken into account it is possible to tell whether the large atom is to the right or left of the smaller one.

the dispersion corrections increases at large scattering angles.

For heavier elements (La and beyond) the L edges fall in the X-ray region. Since the L shell contains six $2p$ electrons compared to the two electrons in the K shell, the dispersion corrections are larger by a factor of approximately three.

8.5   Breakdown of Friedel's law and Bijvoet pairs

At the start of Chapter 4 it was shown that several important concepts in diffraction from materials could be understood by considering the interference of waves scattered by a simple two electron system. Here a similar approach is adopted to explain some of the important consequences that the existence of dispersion corrections have for diffraction experiments. Instead of two electrons, the scattering system is formed from two non-identical atoms, as indicated in Fig. 8.6.

The first issue to consider is whether it is possible in a diffraction experiment to determine the absolute configuration of a system. For the present discussion this boils down to the question of whether it is possible to deduce which atom sits to left, and which one to the right. One obvious way to attempt this is to perform two different scattering experiments: one with the wavevector transfer to the right (a), and one where it is to the left (b). Let the scattering amplitudes be f_1 and f_2, as indicated, in units of the Thomson scattering length $-r_0$. To start with the dispersion corrections are neglected, so that the

scattering amplitudes are real, positive numbers. Further, let the distance between the two atoms be x, and the scattering vector component along this direction between the atoms be $+Q$ in case (a) and $-Q$ in (b). For case (a) the total scattered amplitude is

$$A(Q) = f_1 + f_2\, e^{i\,Qx}$$

and the intensity is

$$\begin{aligned} I(Q) &= (f_1 + f_2 e^{i\,Qx})(f_1 + f_2 e^{-i\,Qx}) \\ &= f_1^2 + f_2^2 + 2f_1 f_2 \cos(Qx) \end{aligned} \tag{8.19}$$

Under the stated assumptions it is obvious that for the wavevector $-Q$, case (b), the same scattered intensity is obtained, since $\cos(Qx) = \cos(-Qx)$. Therefore it is not possible from a diffraction experiment to determine the absolute position of the atoms. This argument can be generalized by letting the pair of atoms form the basis in a unit cell of a three-dimensional crystal. In this case the result is written as

$$\boxed{I(\mathbf{Q}) = I(-\mathbf{Q})} \tag{8.20}$$

which is known as Friedel's law.

The assumption that the scattering amplitudes of the individual atoms are real positive numbers is now lifted; in other words we allow for the effect of the dispersion corrections. The scattering length of the two atoms is then written in the form

$$f_j = f_j^0 + f_j' + i\,f_j'' \qquad j = 1, 2$$

This can be re-expressed more conveniently as

$$f_j = r_j e^{i\phi_j}$$

where $r_j = |f_j|$. The amplitude $A(Q)$ in case (a) then becomes

$$A(Q) = r_1\, e^{i\phi_1} + r_2\, e^{i\phi_2}\, e^{i\,Qx}$$

and Eq. (8.19) takes the form

$$I(Q*) = |f_1|^2 + |f_2|^2 + 2|f_1||f_2| \cos(Qx + \phi_2 - \phi_1)$$

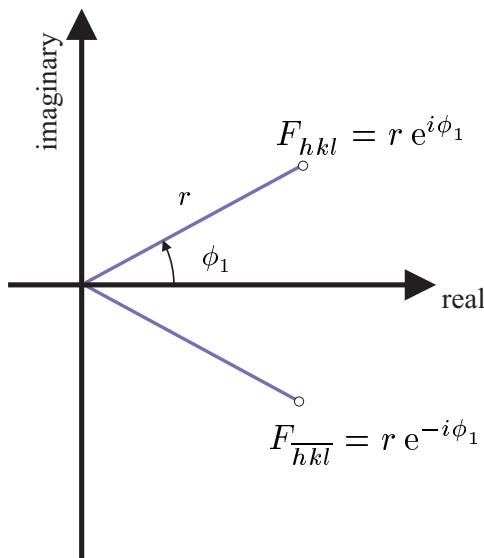As in general $\phi_1 \neq \phi_2$ it follows that

$$I(Q) \neq I(-Q)$$

since $\cos(Qx + \phi_2 - \phi_1) \neq \cos(-Qx + \phi_2 - \phi_1)$. In other words Friedel's law breaks down when dispersion corrections are taken into account. Thus by measuring whether $I(Q)$ is larger or smaller than $I(-Q)$ it is possible to determine which atom is to the left and which atom to the right in Fig. 8.6 once the sign of $(\phi_2 - \phi_1)$ can be inferred independently.

It would, however, be wrong to conclude from this that Friedel's law is never fulfilled. If the unit cell is centrosymmetric, consisting for example of atoms of type 1 at $\pm x_1$, and atoms of type 2 at $\pm x_2$, then the unit cell structure factor is

$$\begin{aligned} F &= r_1\, e^{i(\phi_1 + Qx_1)} + r_1\, e^{i(\phi_1 - Qx_1)} + r_2\, e^{i(\phi_2 + Qx_2)} + r_2\, e^{i(\phi_2 - Qx_2)} \\ &= [r_1\, 2\cos(Qx_1)]\, e^{i\phi_1} + [r_2\, 2\cos(Qx_2)]\, e^{i\phi_2} \end{aligned} \tag{8.21}$$

(a) no dispersion corrections
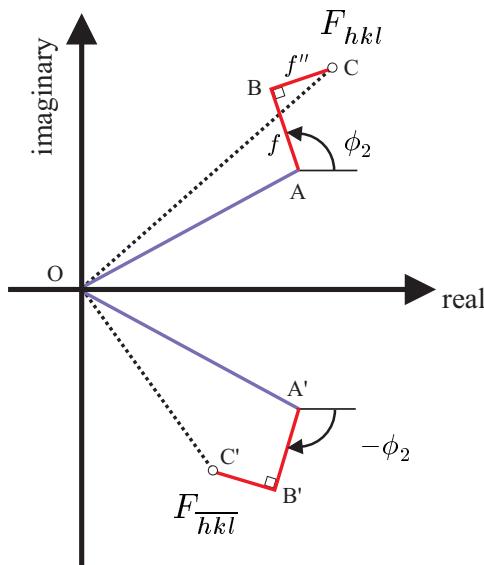

(b) with dispersion corrections

Fig. 8.7 Argand diagram for a unit cell structure factor. (a) One atom per unit cell neglecting dispersion corrections. In this case $|F_{hkl}|=|F_{\overline{hkl}}|$. (b) Adding one more atom, with dispersion corrections, to the unit cell will change the structure factors to be F_{hkl}=OC and $F_{\overline{hkl}}$=OC′. In this case $|F_{hkl}| \neq |F_{\overline{hkl}}|$.

and the intensity is

$$
\begin{aligned}
I(Q) &= |F|^2 \\
&= 4|f_1|^2 \cos^2(Qx_1) \\
&\quad + 4|f_2|^2 \cos^2(Qx_2) \\
&\quad + 8|f_1||f_2| \cos(Qx_1) \cos(Qx_2) \cos(\phi_2 - \phi_1)
\end{aligned}
\tag{8.22}
$$

The intensity in this case is evidently an *even* function of Q, or in other words Friedel's law is reestablished for centrosymmetric structures.

The algebra presented here may appear to be a little complicated. If one is content with a qualitative discussion, then it often suffices to plot the scattering amplitudes in a so-called Argand diagram. An Argand diagram is a graphical representation of a complex number, where the real and imaginary parts are plotted on the x and y axes respectively. We start by assuming that there is one atom in the unit cell, and by neglecting dispersion corrections. The unit cell structure factor F_{hkl} is a complex number, $r\,e^{i\phi_1}$, as shown in Fig. 8.7(a). The operation $\mathbf{Q} \to -\mathbf{Q}$ is equivalent to $\phi_1 \to -\phi_1$. It is obvious from the figure that the structure factor of the $(\bar{h}, \bar{k}, \bar{l})$ reflection is found by reflecting F_{hkl} about the real axis. The length of $|F_{hkl}|$ is unaffected by this operation, or in other words $|F_{hkl}| = |F_{\overline{hkl}}|$. Now imagine that an atom is added to the structure which has significant dispersion corrections due to the presence of resonant scattering terms. Let the scattering length of the atom be $f + if''$, where the real part of the scattering length is $f = f^0 + f'$ and the imaginary part is f''. When placed in the unit cell it acquires a phase factor $e^{i\mathbf{Q} \cdot \mathbf{r}_2}$, or for brevity $e^{i\phi_2}$. The construction of the total structure factor of the unit cell is shown in Fig. 8.7(b). Consider first the contribution from f. This is added as a line of length f originating from A at an angle ϕ_2 with respect to the real axis. In adding the contribution from if'', BC, it must be remembered that f'' is negative so that BC is turned $\pi/2$ in the clockwise direction with respect to AB. The total structure factor F_{hkl} is then OC. $F_{\overline{hkl}}$ is constructed in a similar manner, remembering that $\phi_2 \to -\phi_2$. From this geometrical structure it is clear that $|F_{hkl}| \neq |F_{\overline{hkl}}|$.

Example: the absolute polar direction in ZnS

A striking and simple experimental example of these considerations was obtained around 1930 independently by two groups [Nishikawa and Matsukawa, 1928, Coster et al., 1930]. In a crystal of ZnS with [111] faces they were able to determine which one of two opposite faces was terminated by Zn and which one by S. ZnS has the zinc-blende structure as shown in Fig. 5.5: it consists of two inter-penetrating fcc lattices, with one being occupied by Zn atoms and the other by S atoms. The displacement of the two lattices is $\frac{1}{4}$ of a cube diagonal, so that along a diagonal the structure can be considered as double layers of Zn and S as depicted in the Fig. 8.8. This structure obviously is not centro-symmetric, Friedel's law does not hold, and there will be a difference between the intensities $I_{(111)}$ and $I_{(\overline{111})}$. From this one can conclude which side of the crystal is the Zn side and which one is terminated by a plane of S atoms. The conclusions from such X-ray experiments have been confirmed by other means, such as ion scattering.

8.5.1   Bijvoet's experiment on chiral crystals

Having shown that it is possible to determine the absolute direction in a polar crystal, such as ZnS, by comparing the intensities of Friedel pairs of reflections, a question naturally arises: is it also possible to determine the absolute chirality of a molecule? It took approximately 20 years from the experiments on
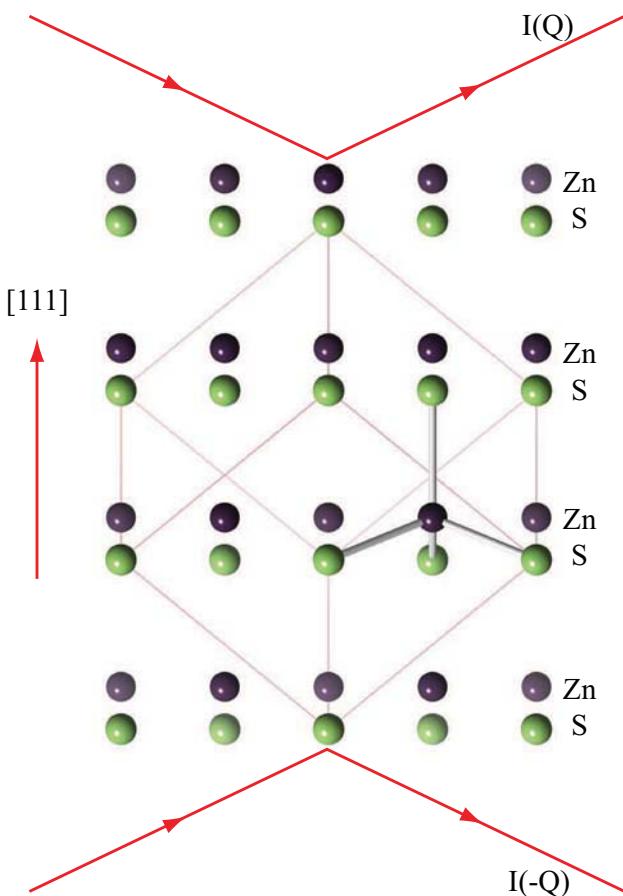
Fig. 8.8 The magnitude of intensity in symmetric Bragg reflection from a {111} ZnS crystal depends on whether one reflects from the 'Zn' (top) or the 'S' side (bottom). In this way the absolute sense of the polar direction can be determined.

ZnS until around 1950 before Bijvoet and co-workers [Bijvoet et al., 1951] proved that this was indeed possible. Before describing this important experiment a few comments are appropriate on the concept chirality. The precise mathematical definition of a chiral structure reads: '*A structure whose mirror image cannot be made to coincide with the original structure by rotation and translation is chiral.*' A familiar example from daily life is your hand: if you make a mirror image of a right-hand glove, say, it becomes a left-hand glove, and no matter how you try to twist and slide it, it will not fit on your right hand. Another comprehensible description is the comparison to a screw. A screw is characterized by a direction ('into or out of the wall') and a rotation direction. For example if a screw for going 'in' has to be rotated clockwise, it is called a right-hand screw.

The screw picture can be applied to a very common kind of chiral molecule, which is based on a central carbon atom with four tetrahedrally bound moieties (see Fig. 4.6). The 'direction' is then defined as the bond from the central carbon atom towards the lightest atom, often hydrogen. Figure 8.9(a) shows the tetrahedron looking along that direction, with the light atom and the central carbon in that particular projection coinciding at the point O. Imagine now that the carbon atom has bonds to three different atoms: O*l*, O*m*, O*s* in Fig. 8.9(a)), or equivalently OA, OB and OC in Fig. 4.6. Here *l*
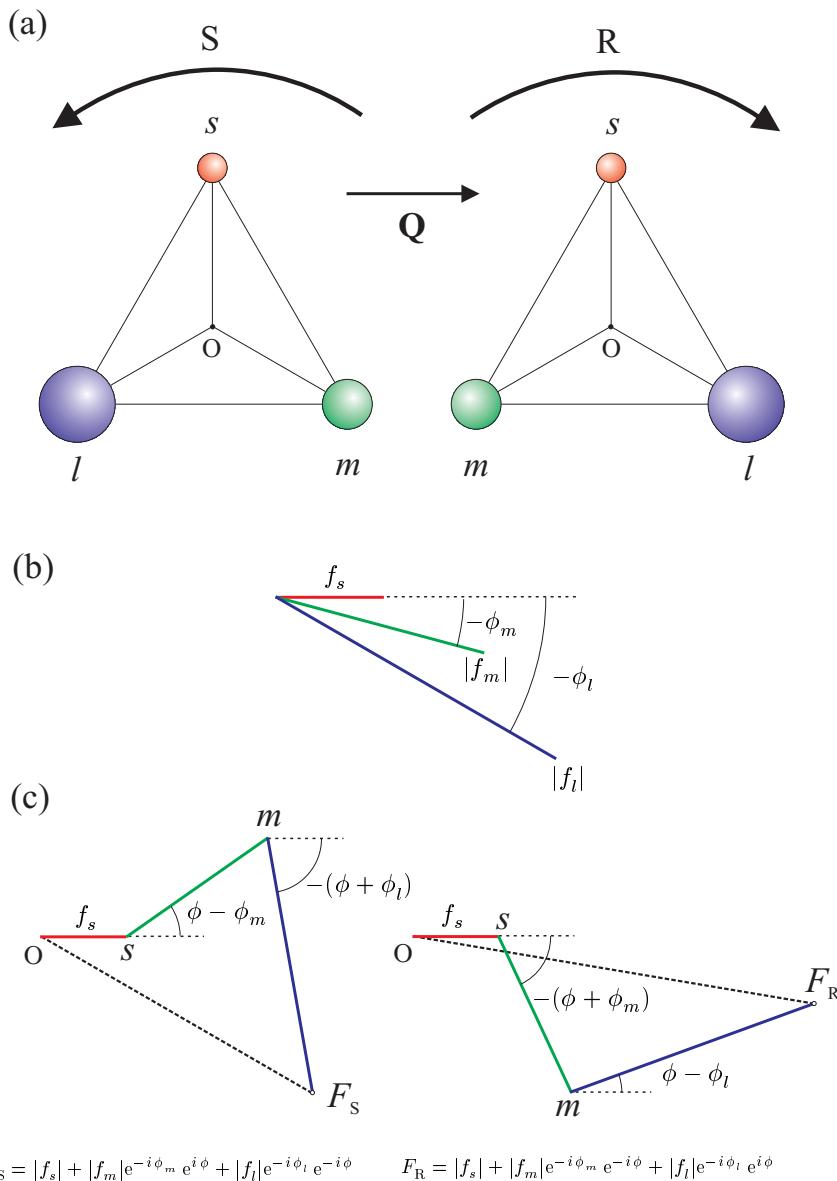
Fig. 8.9 The effect of the dispersion corrections on the scattering from chiral molecules. (a) Definition of the chirality for a molecule of type S and its enantiomer, a R molecule. (b) Argand diagram for the individual atomic scattering lengths of the small (f_s), medium (f_m), and large atoms (f_l). (c) Construction of the total scattering lengths for the R and S molecules. It is evident that $|F_S| < |F_R|$, and hence by measuring Friedel pairs of reflections it is possible to determine the absolute chirality of a molecule.

stands for large, m for medium, and s for small. There are then two different possible rotation directions in going in the sequence $l - m - s$, namely clockwise or anti-clockwise. The normal convention is to refer to the first case as an R molecule and the second case as an S molecule.

The issue that Bijvoet considered was whether for a given chirality of molecule (R or S) there would be any difference in the diffracted intensity when scattering to the right (scattering vector +Q) or to the left (−Q), or equivalently whether for a given scattering sense (+Q, say) R and S molecules would produce different intensities. Instead of trying to answer this question by writing down the appropriate formulae, we shall use a geometrical construction, as it serves to further illustrate the usefulness of plotting structure factors in an Argand diagram.

The Argand diagrams for the S and R forms of the molecule are plotted in Fig. 8.9. To simplify things as much as possible, it is assumed that the scattering vector $\mathbf{Q}$ is parallel to the direction lm. The phase factor $e^{i\mathbf{Q}\cdot\mathbf{r}}$ is then unity for atom s, as Os is perpendicular to $\mathbf{Q}$. With this assumption there are also symmetric phase factors $e^{i\mathbf{Q}\cdot\mathbf{r}} = e^{\pm i\phi}$ associated with atoms l and m. The scattering lengths of the three atoms s, m and l are drawn in part (b). They are all complex, as all atoms are assumed to have a finite absorption cross-section. Furthermore, to go from the real part to the full complex value, one has to go clockwise in the complex plane, since $-f''$ is proportional to the absorption cross-section, which is itself positive (Eq. (3.10)). The angle one has to go clockwise increases with increasing atomic number Z, as, f^0, the dominant contribution to the real part varies in proportion to Z, but the imaginary part varies in proportion to Z^4. The three complex scattering lengths must therefore appear as shown in Fig. 8.9(b), i.e. turning clockwise with increasing magnitude in the sequence $s - m - l$. The absolute phase of this set of scattering lengths is irrelevant, and f_s has been chosen to be parallel to the real axis in the complex plane. With these pieces in place, we are now ready to construct the Argand diagrams for the S and R variants of the molecular structure, and these are shown in Fig. 8.9(c).

The scattering length of the 's' atom is represented by the line Os of length $|f_s|$. This line is along the real axis since the scattering vector $\mathbf{Q}$ is perpendicular to Os, and hence the phase factor associated with the scattering from atom 's' for either variant is unity. Next consider the scattering from the m type atoms, which has a scattering length of $|f_m|e^{-i\phi_m}$. In case S the appropriate phase factor is $Qx > 0 = +\phi$, as the scalar product of Om and $\mathbf{Q}$ is positive. This means that f_m must be turned counter-clockwise by an amount $+\phi$. In the R case, it is the other way around, i.e. f_m must be turned clockwise by the same amount. The resulting scattering amplitude including the contributions from both 's' and 'm' type atoms is Om in Fig. 8.9(c). To the point m it is now necessary to add the scattering length of atom 'l' with the appropriate phase factor included. First consider case S. The phase is less than zero as the scalar product of Ol and $\mathbf{Q}$ is negative. This means that the line mF_S makes an angle $-(\phi + \phi_l)$ with the real axis. For case R the phase is greater than zero and the line mF_R makes an angle $(\phi - \phi_l)$ with the real axis. From this construction it is evident that $|F_S| < |F_R|$, or in other words the total scattering length from the three atoms is therefore different for the R and S molecules. It follows that by analysing the systematic difference of pairs of reflections it is possible to determine the absolute chirality of molecules. Pairs of reflections for which Friedel's law does not hold are known as Bijvoet pairs.

8.6   The phase problem in crystallography

In this section an outline is given of how the resonant scattering terms may be exploited to solve the phase problem in crystallography. Although the methods described here could be applied to solve the structure of any unit cell, they find their greatest utility in the crystallography of macromolecules, such as proteins, where there may be thousands of atoms in the unit cell.

The goal of macromolecular crystallography is to determine the structure of large molecules on an atomic length scale. This is accomplished by diffraction techniques. The amplitude of the diffracted X-ray beam is proportional to the molecular structure factor:

$$\begin{aligned}
F^{\mathrm{mol}}(\mathbf{Q}) &= \sum_j f_j(\mathbf{Q}) \, \mathrm{e}^{-M_j} \, \mathrm{e}^{i\mathbf{Q}\cdot\mathbf{r}_j} \\
&= \sum_j (f_j^0 + f_j' + i f_j'') \, \mathrm{e}^{-M_j} \, \mathrm{e}^{i\mathbf{Q}\cdot\mathbf{r}_j} \\
&= \left| F^{\mathrm{mol}}(\mathbf{Q}) \right| \mathrm{e}^{i\phi}
\end{aligned} \tag{8.23}$$

Here as before $\mathbf{Q}$ is the wavevector transfer (also known as the scattering vector), $f_j(\mathbf{Q})$ is the atomic form factor, and e^{-M_j} is the Debye-Waller temperature factor for the jth atom at position $\mathbf{r}_j$ in the molecule (see Chapter 5). In the last equation above we have emphasized that the molecular structure factor is a complex number specified by a modulus, $|F^{\mathrm{mol}}(\mathbf{Q})|$, and a phase, ϕ. With a knowledge of the molecular structure factor one can determine the position vectors of the atoms in the molecule, or in other words the structure of the molecule.

Even in the strongest X-ray beams the diffracting power of a single molecule is insufficient to obtain a measurable diffraction pattern[3]. However, when molecules are assembled into an array in a crystal, the diffracted waves from each molecule will interfere constructively whenever the scattering vector $\mathbf{Q}$ coincides with a reciprocal lattice vector $\mathbf{G}$: in other words the crystal acts as a diffraction amplifier for certain values of the scattering vector. For simplicity, let us assume a crystal structure with only one molecule per unit cell. The integrated intensity of a Bragg spot at $\mathbf{Q}$ around $\mathbf{G}$ is then

$$I(\mathbf{G}) \propto \left| F_{\mathrm{mol}}(\mathbf{G}) \right|^2$$

so the phase information of the molecular structure factor is lost by measuring the intensity rather than the amplitude of the diffracted ray. In the case of small molecules, a direct solution of the phase problem is possible from statistical relations among the intensities. However, these so-called direct methods do not work for the large number of atoms in a typical macromolecule.

8.6.1   The MAD method

It transpires that one way to solve the phase problem is to utilize the dispersion corrections by measuring the diffraction pattern at several wavelengths around the absorption edge of one of the types of atom in the molecule. The method that uses this technique is known as Multi-wavelength Anomalous Diffraction, or MAD for short [Karle, 1980, Hendrickson, 1985]. One obvious requirement for this technique is that the resonant scatterer should have its K edge or L edge in the X-ray region, and it thus needs to be a moderately heavy atom. For example, it could be a metal ion in a metalloprotein, or an isomorphous replacement atom, such as selenium for sulfur, in a derivative of the native molecule, or even a heavy rare earth metal replacing a calcium atom. In any eventuality it is likely that the number of resonantly scattering atoms in the molecule is much smaller than the total number of atoms in the molecule. Nevertheless, as the scattering power of the resonant atom(s) can be varied in a controlled manner near an absorption edge, it will modulate the total scattering power of the molecule in such a way that the phase can be determined. Here it will be shown how this is possible by performing some relatively simple algebraic manipulations.

---

[3]It is hoped that the advent of free-electron sources will enable diffraction experiments on single molecules to be performed.

The summation in Eq. (8.23) is split into a sum over the resonantly (or anomalously) scattering atoms, A, and a sum over all the other atoms, B, which produce a non-resonant structure factor $F_B(\mathbf{G})$. The sum over the resonant scatterers, assumed to be identical, can be written as

$$\sum_{j'} \left(f_A^0 + f_A' + i f_A'' \right) e^{i\mathbf{G}\cdot\mathbf{r}_{j'}} = \left(f_A^0 + f_A' + i f_A'' \right) \sum_{j'} e^{i\mathbf{G}\cdot\mathbf{r}_{j'}}$$

$$= f_A^0 \sum_{j'} e^{i\mathbf{G}\cdot\mathbf{r}_{j'}} + (f_A' + i f_A'') \sum_{j'} e^{i\mathbf{G}\cdot\mathbf{r}_{j'}}$$

$$= F_A(\mathbf{G}) + F_A(\mathbf{G}) \left[\frac{f_A'(\lambda)}{f_A^0} + i \frac{f_A''(\lambda)}{f_A^0} \right]$$

The second term on the right hand side is the resonant contribution from the atoms A, while the first term is the non-resonant contribution from the anomalous scatterers A. The latter can be added to $F_B(\mathbf{G})$ to give the total non-resonant structure factor

$$F_T(\mathbf{G}) = F_A(\mathbf{G}) + F_B(\mathbf{G})$$

The molecular structure factor including both the resonant and non-resonant contributions becomes

$$F^{\text{mol}}(\mathbf{G}) = \left| F_T \right| e^{i\phi_T} + \left| F_A \right| e^{i\phi_A} \left[\frac{f_A'(\lambda)}{f_A^0} + i \frac{f_A''(\lambda)}{f_A^0} \right]$$

The squared structure factor, determined by the measured intensity, is therefore

$$\begin{aligned} \left| F^{\text{mol}}(\mathbf{G}) \right|^2 = &\left| F_T \right|^2 \\ &+ a(\lambda) \left| F_A \right|^2 \\ &+ b(\lambda) \left| F_A \right| \left| F_T \right| \cos(\phi_T - \phi_A) \\ &+ c(\lambda) \left| F_A \right| \left| F_T \right| \sin(\phi_T - \phi_A) \end{aligned}$$

with

$$a(\lambda) = \frac{(f_A')^2 + (f_A'')^2}{(f_A^0)^2} ; \qquad b(\lambda) = \frac{2 f_A'}{f_A^0} ; \qquad c(\lambda) = \frac{2 f_A''}{f_A^0}$$

The three coefficients $a(\lambda)$, $b(\lambda)$ and $c(\lambda)$ are determined in the following way. First, $f_A''(\lambda)$ is determined by assuming that it is proportional to the fluorescent yield. This allows $f_A'(\lambda)$ to be computed from $f_A''(\lambda)$ using the Kramers-Kronig relations. With this knowledge the three coefficients $a(\lambda)$, $b(\lambda)$ and $c(\lambda)$ may be evaluated, since the values of $f_A^0(\mathbf{G})$ are tabulated in many places. There are then three unknowns in the problem: $|F_T|$, $|F_A|$ and $(\phi_T - \phi_A)$. A complete data set of reflections is then recorded for at least three wavelengths, allowing the three unknowns to be determined. One can then proceed to solve the structure. From the values of $|F_A|$ one can find the positions of the few A atoms in the unit cell using the direct methods applicable to small molecules. This then allows the phases ϕ_A to be calculated. Since $|F_T|$ and $(\phi_T - \phi_A)$ have already been derived, the entire complex molecular structure factor can then be determined, thus facilitating the solving of the molecular structure.

A schematic representation of the MAD method is given in Fig. 8.10 where the energy dependence is shown of the structure factor Argand diagrams just below, at, and above an absorption edge. Figure 8.11 illustrates the type of beautiful and complex protein structure that can be solved using the MAD method.
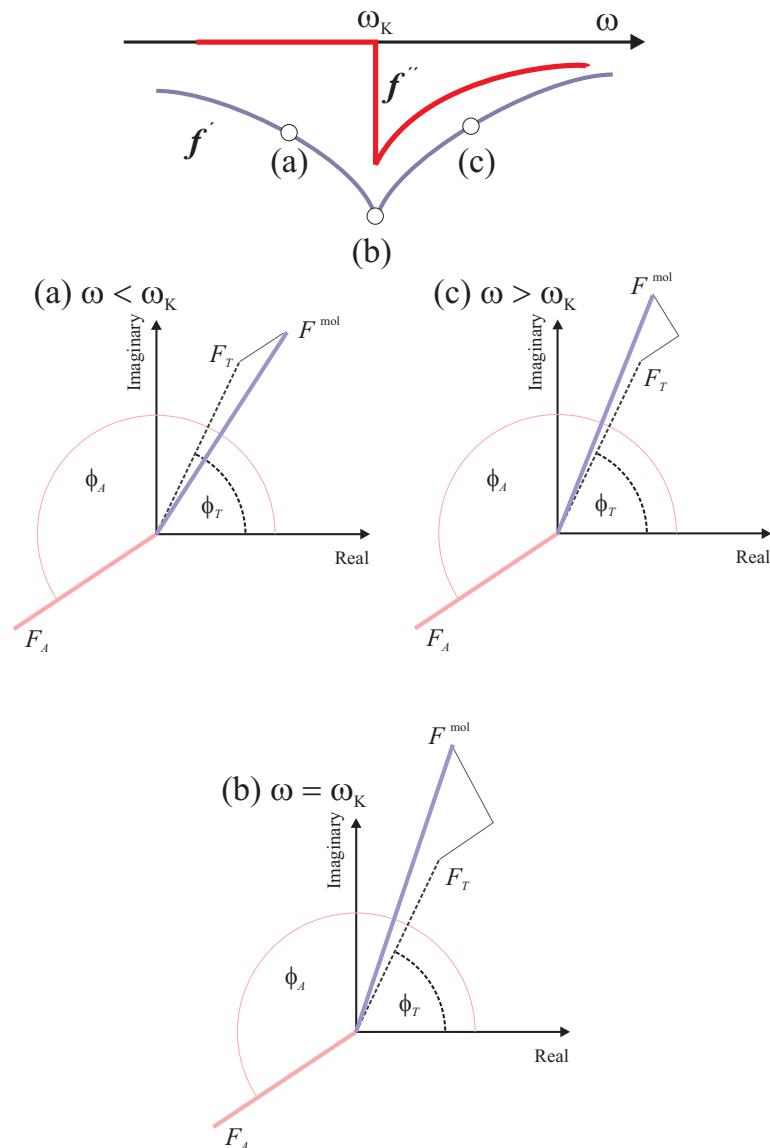
Fig. 8.10 A summary of the MAD method where the structure factors are plotted in the complex plane. The atoms in the crystal are divided into two groups: the A atoms which produce the resonant, or anomalous, scattering, and all the other atoms. The non-anomalous contribution from the A atoms has a structure factor F_A (solid line) and phase ϕ_A. When the structure factor of all the other atoms are added to F_A the total non-resonant scattering structure factor F_T is obtained (dashed line) with phase ϕ_T. To obtain the molecular scattering factor the anomalous contribution from the A atoms must be added to F_T. The anomalous contribution has a component parallel to F_A of magnitude $|F_A|(f'/f^0)$, and a component perpendicular to F_A of magnitude $|F_A|(f''/f^0)$. (Note that both f' and f'' are negative.) Here it is illustrated what happens to the resulting molecular structure factor for three choices of the incident energy. (a) First, the energy of the photon is below the edge, so that f'' is zero, and F^{mol} is obtained from F_T by subtracting an amount $|F_A||f'/f^0|$ from F_T. (b) Second, the photon energy equals the edge energy, and the magnitude of both f' and f'' is a maximum, with the result that F^{mol} differs considerably from F_T. (c) Third, the photon energy is above the edge, and f' and f'' have a reduced, but still significant effect on F^{mol}.
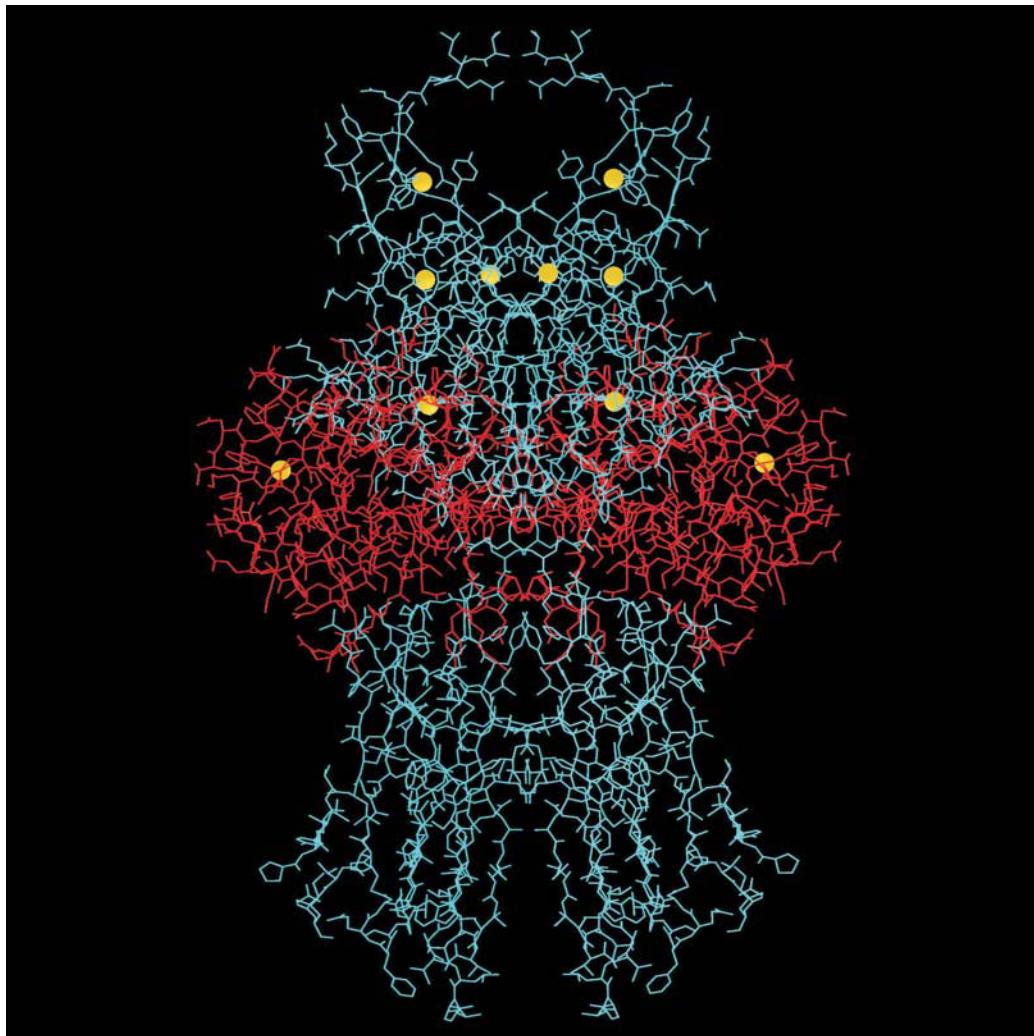
Fig. 8.11 Atomic model of a protein complex determined by the MAD method. The structure is a dimeric complex between fibroblast growth factor (FGF1) and the ligand-binding portion of the receptor tyrosine kinase FGFR2. Crystals were grown from the complex between variant proteins in which the methionine residues were all replaced by selenomethionine, and diffraction data were measured at four wavelengths near the Se K absorption edge. These MAD data were first used to find the positions of the selenium atoms (five per asymmetric unit) and then to evaluate phases and produce an image used to locate all 6,162 non-hydrogen atoms of the dimeric complex (D.J. Stauber, A.D. DiGabriele, and W.A. Hendrickson, Proc. Natl. Acad. Sci. USA 97, 49, 2000). The selenium atoms are drawn as yellow spheres, the FGF ligand is represented by inter-atomic covalent bonds drawn in red, and the receptor is shown with bonds drawn in blue.

8.7   Quantum mechanical description

In this section a short introduction is given to the subject of the quantum mechanical description of resonant scattering. The intention here is to explain how resonant scattering fits into the general framework of the interaction of X-rays with matter that has been described in this book, and to give an idea of the additional possibilities that resonant scattering offers for studying ordering phenomena in condensed matter systems.

   In a quantum mechanical derivation of the cross-section the quantity of interest is the transition rate probability, W, which in *first-order* perturbation theory is given by

$$W = \frac{2\pi}{\hbar} \left| \langle f | \mathcal{H}_I | i \rangle \right|^2 \rho(\mathcal{E}_f) \tag{8.24}$$

where $|i\rangle$ and $|f\rangle$ are the initial and final states of the combined system of X-ray photon plus target electron (Eq. (A.3)). The Hamiltonian, $\mathcal{H}_I$, describes the interaction between the photon and the electron. Neglecting the spin of the electron, the interaction Hamiltonian is given by

$$\mathcal{H}_I = \frac{e\mathbf{A} \cdot \mathbf{p}}{m} + \frac{e^2 \mathbf{A}^2}{2m} \tag{8.25}$$

as described in Appendix C. The vector potential $\mathbf{A}$ of the photon field is *linear* in photon creation and annihilation operators (Eq. (C.6)). The first contribution to $\mathcal{H}_I$ is linear in $\mathbf{A}$, and it follows that it can either create or destroy a photon, but not both. It was shown in Chapter 7 that this term gives rise to photoelectric absorption. The second contribution to $\mathcal{H}_I$ is quadratic in $\mathbf{A}$, and as such can first destroy and then create a photon, while leaving the electron in the same state, $|a\rangle$ say. (Here it is important to note that $|a\rangle$ is the initial state of the electron, while $|i\rangle$ is the ground state of the combined system, photon plus electron.) This term therefore describes elastic Thomson scattering. These first-order processes are represented schematically in Fig. 8.12(a) and (b).
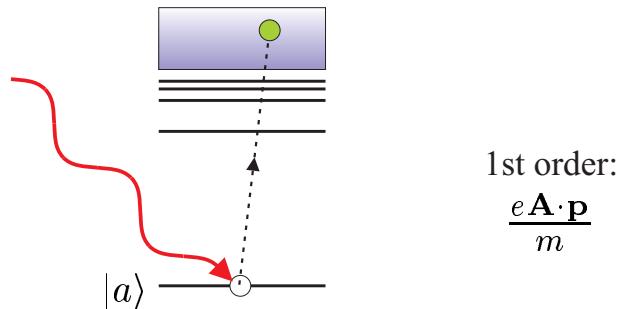
   To obtain resonant scattering terms it is necessary to take the calculation to higher-order. In *second-order* perturbation theory the transition probability is given by

$$W = \frac{2\pi}{\hbar} \left| \langle f | \mathcal{H}_I | i \rangle + \sum_{n=1}^{\infty} \frac{\langle f | \mathcal{H}_I | n \rangle \langle n | \mathcal{H}_I | i \rangle}{E_i - E_n} \right|^2 \rho(\mathcal{E}_f) \tag{8.26}$$
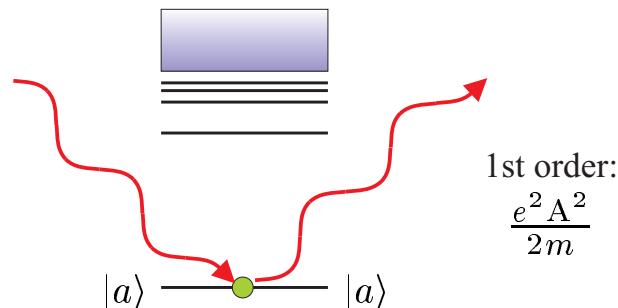
where the sum is over all possible states with energy E_n. It can now be seen that the $\mathbf{A} \cdot \mathbf{p}$ term, which is linear in creation and annihilation operators, can produce scattering via an intermediate state. Reading the matrix element that appears in the numerator of the second term from right to left the scattering process can be described in the following way: the incident photon is first destroyed, and the electron makes a transition from the ground state, $|a\rangle$, to an intermediate state, $|n\rangle$. In an elastic scattering event the electron then makes a transition from $|n\rangle$ to $|a\rangle$ with the creation of the scattered photon. The resonant behaviour arises when the denominator tends to zero. This occurs when the total incident energy, $E_i = \hbar\omega + E_a$, is equal to the energy of the intermediate state E_n, or in other words when the energy of the incident photon is equal to the difference in energy between the intermediate and ground states, $\hbar\omega = E_n - E_a$. The resonant scattering process is shown schematically in Fig. 8.12(c).

   Resonant scattering may be thought of as a probe of the intermediate atomic states. Transitions to the intermediate states are controlled by two considerations. The Pauli exclusion principle requires that only unoccupied intermediate states can be accessed, while the usual quantum mechanical selection rules imply that electric dipole transitions dominate (as described on page 263). Interesting effects
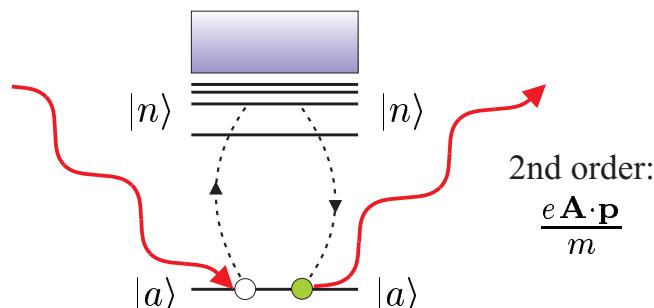
Fig. 8.12 Summary of the quantum mechanical description of the interaction of a photon with an atomic electron. Photoelectric absorption (a) and Thomson scattering (b) can be explained by applying first-order perturbation theory to the terms in the interaction Hamiltonian which depend on $\mathbf{A} \cdot \mathbf{p}$ and A^2 respectively. Resonant scattering (c) is a second-order process and occurs via an intermediate electronic state. This picture should not be taken too literally, however, as resonant scattering is a virtual process, and does not occur in the two discrete steps suggested here.

occur when the nature of the intermediate state is altered when atoms combine to form molecules, solids, etc. For example, the symmetry of the intermediate state may be lowered if it is involved in chemical bonding. Under this condition the dispersion corrections become dependent on the polarization geometry used in the experiment, and forbidden Bragg reflections may become observable which provide information on the phases of atoms in the unit cell [Templeton and Templeton, 1982]. Alternatively, the intermediate state may be split by magnetic interactions. Resonant scattering then becomes a probe of the magnetic order in the solid [Namikawa et al., 1985, Blume, 1985, Gibbs et al., 1988]. These and other aspects of resonant scattering, including inelastic processes, are presently at the forefront of experimental and theoretical X-ray science, and are still in a phase of rapid development [see, for example, Lovesey and Collins, 1996].

8.8 Further reading

Resonant Anomalous X-ray Scattering: Theory and Applications, Eds. G. Materlik, C.J. Sparks, and K. Fischer (Elsevier, 1994).

Determination of Macromolecular Structures from Anomalous Diffraction of Synchrotron Radiation, W.A. Hendrickson, Science **254**, 51 (1991).

A Link Between Macroscopic Phenomena and Molecular Chirality: Crystals as Probes for the Direct Assignment of Absolute Configuration of Chiral Molecules, L. Addadi, Z. Berkovitch-Yellin, I. Weissbuch, M. Lahav, and L. Leiserowitz, Topics in Stereochemistry **16**, 1 (1986).

8.9 Exercises

In all of these exercises the kinematical approximation should be invoked when calculating scattering intensities.

8.1 Show that

$$\mu\left[\mu\mathrm{m}^{-1}\right] \approx 4.214 \left(\frac{\rho_m\left[\mathrm{g/cm^3}\right]}{M\,[\mathrm{g/mol}]\ \mathcal{E}[\mathrm{keV}]} \right) \left| f'' \right|$$

8.2 The alloy β−brass contains equal amounts of Cu and Zn. At room temperature the alloy is ordered and the structure may be thought of as being formed from two inter-penetrating simple cubic lattices, exclusively populated by either Cu or Zn atoms, respectively, displaced by half a cube diagonal. At high temperature the alloy is disordered and the Cu and Zn atoms are randomly distributed across the two lattices forming on average a *bcc* lattice.

(a) Calculate the structure factor F_{hkl} of the high-temperature disordered phase in terms of f_{Cu} and f_{Zn}, and hence derive the selection rule in terms of the Miller indices (h, k, l) for allowed Bragg peaks.

(b) Evaluate the structure factor F_{hkl} of the room temperature structure and investigate its dependence on (h, k, l).

(c) Neglecting resonant scattering terms, estimate the intensity of the (100) peak relative to the (200). (You may also ignore the Q dependence of f_{Cu} and f_{Zn}.)

8.3 This exercise explores the change in the intensity of the weak (100) Bragg reflection from β−brass when the photon energy is tuned to be close to the energy of the Cu K edge (8.9789 keV). To simplify the calculation we shall assume that the atomic scattering form factor of Zn is constant over the energy interval of interest, and is equal to $(f^0 + f', f'')$= (23.223,-0.568). For energies -100, -1, 1, and 100 eV relative to the Cu K edge energy, the atomic scattering factors of Cu at the (100) reflection are: (20.580,-0.493); (15.666,-0.483); (15.645,-3.902); and (20.749,0.545). The lattice parameter of β−brass is 2.96 Å.

(a) Calculate the absorption coefficient for the four energies in the dimensionless form $a\mu$, where a is the lattice constant.
(b) Assuming that the intensity of the (100) reflection is measured in symmetric Bragg geometry from an extended face sample, calculate the structure factors and intensity in arbitrary units for the four photon energies,
(c) Sketch the energy spectrum observed using an energy resolving detector for energies of -100 and 100 eV relative to the Cu K edge.

8.4 Here we consider the problem of the separation of elastic scattering from X-ray fluorescence when the photon energy is tuned close to an absorption edge (Excercise 8.3(c)). This separation requires the use of an energy resolving detector which we assume has an aperture of 1 mm diameter. Imagine also that in the experiment the incident has a divergence of 1 mrad in both the vertical and horizontal directions, and is focused to a 0.1×0.1 mm^2 spot size on the sample.

(a) What is the maximum distance L that the detector can be placed from the sample for which it is still possible to integrate fully the (100) Bragg peak?
(b) What is the solid angle of the detector subtended at distance L?
(c) Estimate the ratio of scattered to fluorescent intensities recorded in the detector at a distance L for an incident photon energy 100 eV above the Cu K edge. Assume that the fluorescent relative to total yield is approximately 0.3.

8.5 Referring to the ZnS structure in Fig. 8.8, show that the ratio of the structure factors for the Friedel pair F_{111} and $F_{\bar{1}\bar{1}\bar{1}}$ is given by

$$\frac{F_{111}}{F_{\bar{1}\bar{1}\bar{1}}} = \frac{(f'_{Zn} + f''_S) - i(f'_S - f''_{Zn})}{(f'_S + f''_{Zn}) - i(f'_{Zn} - f''_S)}$$

where the atomic form factors of Zn and S have been written in terms of their real (f') and imaginary (f'') components.

8.6 Show that the difference $\Delta I_{111-\bar{1}\bar{1}\bar{1}}$ in the intensities of the (111) and $(\bar{1}\bar{1}\bar{1})$ reflections is proportional to $4(f'_{Zn}f''_S - f''_{Zn}f'_S)$.

8.7 Derive expressions for the ratios $F_{222}/F_{\bar{2}\bar{2}\bar{2}}$ and $F_{333}/F_{\bar{3}\bar{3}\bar{3}}$, and show that $\Delta I_{222-\bar{2}\bar{2}\bar{2}}= 0$, and that $\Delta I_{333-\bar{3}\bar{3}\bar{3}}= -\Delta I_{111-\bar{1}\bar{1}\bar{1}}$.

8.8 γ−CuI crystallizes in the zinc-blende structure with a lattice parameter of 5.4 Å. The breakdown of Friedel's law in this compound has been investigated by Bhalla and White [1971] using an X-ray energy of 5.4147 keV. The ratios of the integrated intensities of the (111), (222), and (333) type reflections were found to be 1.51, 0.983, and 0.470, respectively. Determine whether these observations are consistent with theory. (The atomic form factors for copper at the three types of reflection are (24.25,−1.19), (18.40, −1.19), and (13.42, −1.19); for iodine they are (39.21,−12.54), (29.90,−12.54), and (23.05,−12.54).)

Imaging

9.1 Introduction

X-ray imaging encompasses many fields of endeavour, although it is sometimes difficult to see what, if anything, they have in common. That is apart from the obvious desire to produce an image in real space of an object that would otherwise be invisible to the naked eye. They also all of course make use of the special properties of X-rays, but do so in a variety of ways. Compared with optical imaging, the two obvious advantages of X-rays are the fact that they are capable of penetrating through matter, and the fact that they have a much shorter wavelength and hence the potential to produce images with higher spatial resolution. The former combined with an imaging contrast due to absorption varying as Z^4 (see Chapter 7) endows X-ray radiography with its usefulness, and explains its wide-spread utility from medicine to materials science. The wave properties of X-rays on the other hand give rise to a number of advanced imaging techniques which allow the visualization of structures via their ability to scatter (or equivalently refract) an X-ray beam. In particular, it should at least seem like a reasonable proposition that imaging based on analysing the amplitude *and* phase of X-rays scattered from materials may hold some advantages over conventional radiography. This indeed proves to be the case as we shall describe in this chapter. Although X-ray imaging dates back to the discovery of X-rays themselves, many of these newer imaging techniques rely on the high-brightness and tunability of modern synchrotron sources and consequently have been developed only in recent years.

To understand the great versatility of X-rays in the context of imaging it is necessary to recall the nature of their interactions with matter. In the simplest approach X-rays can either be scattered or absorbed. These effects are enshrined in the expression for the refractive index $n = 1 - \delta + i\beta$, where δ is proportional to the scattering length density, and β to the absorption cross-section (see Chapter 3). As in general the imaging contrast depends on the spatial variation of n within the sample, it can be made element specific by tuning to an absorption edge around which both δ and β may vary rapidly. Beyond imaging electronic charge densities with X-rays, it is also possible to exploit the terms in the interaction Hamiltonian that depend on the spin and orbital magnetization densities, allowing imaging
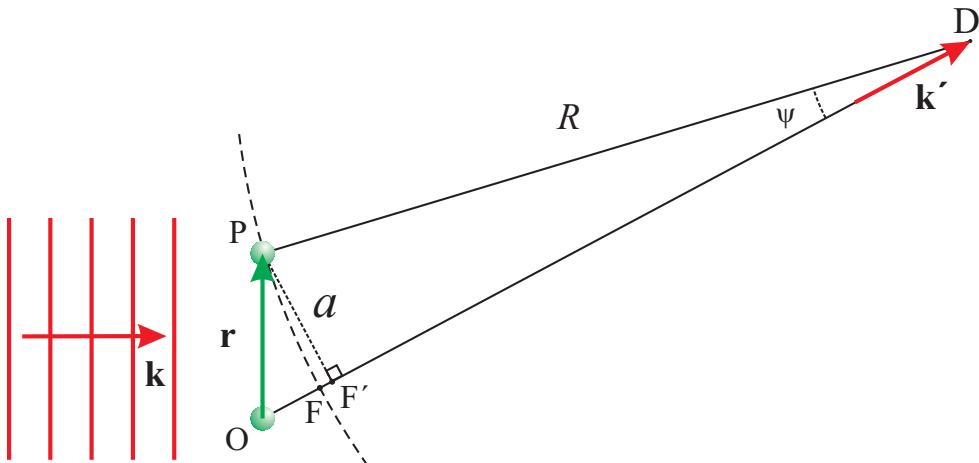
Fig. 9.1 Two expressions of progressively higher accuracy can be derived for the phase difference between two spherical waves originating from points O and P when they arrive at the detection point D. In the far-field limit (also known as the Fraunhofer region) the two waves are approximated as plane waves, and the phase difference between the waves scattered from O and from P is $\mathbf{Q} \cdot \mathbf{r}$, where $\mathbf{Q}$ is the wavevector difference $(\mathbf{k} - \mathbf{k}')$. For simplicity, $\mathbf{k}$ is taken to be perpendicular to $\mathbf{r}$, so that the phase difference in the far-field approximation is $\mathbf{k}' \cdot \mathbf{r}$, corresponding to the path length difference $OF' = \hat{\mathbf{k}}' \cdot \mathbf{r}$, the hat designating a unit vector. However, the true path length difference is OF. The error in the path length difference, Δ, is OF'-OF which is given by $\Delta = R - R \cos \psi \approx R(1 - (1 - \psi^2/2)) = a^2/(2R)$. When Δ is comparable to the wavelength λ, the so-called Fresnel region, there is a significant error in the far-field approximation. If $R \ll a^2/\lambda$ – the contact regime – an image of the objects is formed only from differences in absorption between O and P.

of magnetic domains to be performed.

Much of our discussion will turn on the phase of a scattered wave, and it turns out that in order to understand certain modern imaging methods we need to re-examine two assumptions that have been used more or less tacitly throughout this book. First, that the irradiated sample volume is smaller than the coherence volume of the beam, so that amplitudes from different parts of the structure should be added before squaring to obtain the intensity. Second, that the distance from object to detector is large enough allowing the diffracted beam to be approximated by a plane wave.

The question of beam coherence will be deferred to later in the chapter. Let us begin instead by considering the issue of the distance from object to detector, as this proves to be helpful in developing a general classification of imaging techniques. Figure 9.1 depicts an incident coherent plane wave interacting with two objects at P and O. The objects might be distinct, or they could be infinitesimal volumes that one later may integrate up to the full sample size. Each of these objects acts as a point source for a spherical wave. At the detection point D there will exist a phase difference due to the different path lengths experienced by the spherical waves. In the far-field limit both spherical waves can be approximated as plane waves of wavevector $\mathbf{k}'$. As we have discussed at length in previous chapters, the phase difference in this case is simply $\mathbf{Q} \cdot \mathbf{r}$, where $\mathbf{Q} = \mathbf{k}' - \mathbf{k}$, and $\mathbf{r}$ is the vector connecting the two points. In Fig. 9.1, $\mathbf{k}$ is perpendicular to $\mathbf{r}$, so that the phase difference in the far-field limit is $\mathbf{k}' \cdot \mathbf{r}$. The far-field limit is also called the Fraunhofer regime. If the detection point is closer to the scattering objects, a more accurate algorithm is required to calculate the phase difference. This is because the path length difference is shortened by an amount given by $\Delta = OF' - OF$ in Fig. 9.1,

with $\Delta \approx a^2/(2R)$. If Δ is of order λ then the far-field approximation breaks down and we are in the so-called Fresnel or near-field regime. As the detector is brought closer to the sample it becomes meaningless to consider the phase difference between the scattered waves. This is the contact regime where imaging contrast arises from differences in absorption between O and P only.

In terms of the three length scales in the problem a, R and λ, we have

$$\text{Fraunhofer region}: \ R \gg a^2/\lambda$$
$$\text{Fresnel region}: \ R \approx a^2/\lambda$$
$$\text{Contact region}: \ R \ll a^2/\lambda$$

Where the detector is placed clearly has a bearing on the type of image that one may expect to observe. Imagine, for example, that we wish to image objects separated by $a=1$ Å with X-rays for which we shall take $\lambda=1$ Å. The ratio a^2/λ is then also equal to 1 Å, and for all practical purposes imaging of objects at atomic resolution is restricted to the far-field limit. Now consider what happens if we set $a=1\ \mu$m. The ratio a^2/λ becomes equal to 10 mm, allowing the experimenter the possibility of selecting the imaging mode by the appropriate positioning of the detector. Finally, if $a=1$ mm, the ratio is equal to 10 km. Clearly in this case it would be difficult to escape the contact region.

These ideas are put on a more concrete footing in Fig. 9.2 where we show an example of the scattering calculated from a simple model of discs of diameter 5 μm. As described in the figure caption, two types of idealised discs are considered: perfect absorbers (red), and perfect phase objects (blue). In the contact region imaging arises from absorption contrast only. As we move to the near field (Fresnel regime) and beyond the phase objects become visible. Once the distance from object to detector is well beyond the Fresnel region, the shape of the diffraction image does not change any more, although of course it gets weaker in intensity per unit area of detector as the inverse square of the distance and correspondingly covers more detector area.

9.2 Absorption contrast imaging

9.2.1 Radiography and tomography

The first revolution in medical imaging with X-rays began in Roentgen's laboratory in 1895. The second had to wait until the 1970's when Godfrey Hounsfield invented the technique of Computer Axial Tomography, now commonly referred to as CAT or CT scanning. The theory underlying CT had been worked out independently in the previous decade by Allan McLeod Cormack, and in 1979 Hounsfield and Cormack were awarded the Nobel Prize in Medicine[1]. In common with Roentgen's original discovery, the diagnostic benefits of CT scanning were immediately recognized by clinicians so that by the time Hounsfield and Cormack delivered their Nobel Lectures in 1979 there were already more than a thousand CT systems operating in hospitals worldwide.

CT scanning overcomes the obvious main limitation of conventional radiography which measures a projection of any three-dimensional object onto a two-dimensional plane with a concomitant loss of spatial information. It does this by recording radiographic projections of the object over a wide range of projection angles, from which it is then possible to reconstruct the full three-dimensional structure. To understand how this works we consider the absorption of a perfectly narrow X-ray beam in the plane

---

[1]Here the reader is referred to the transcripts of Cormack's and Hounsfield's Nobel Prize lectures avaialable at http://nobelprize.org.
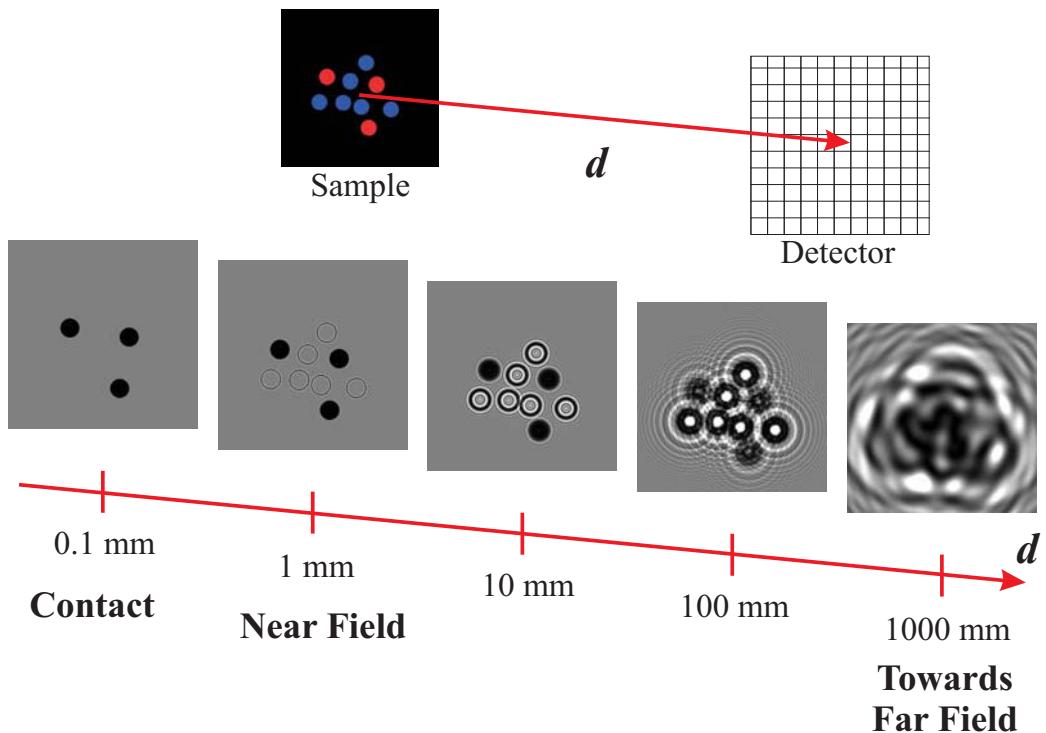
Fig. 9.2 X-ray radiographs simulated to illustrate the transition from pure absorption contrast (in the contact regime) via edge-enhancing in-line phase contrast (near field) to stronger phase contrast (Fresnel region) and towards the far-field regime (although the Fraunhofer image is not given). The phantom object used in this simulation is an ensemble of small disk-like objects, some of which are taken to be ideal absorbers (red: zero transmission) and the rest ideal phase objects (blue: no absorption, phase shift π). The diameter of each disk was 5 μm. The gray scale images show simulated radiographs of the phantom, for illumination by a monochromatic X-ray plane wave of wavelength 1 Å, at different distances between sample and detector (0.1, 1, 10, 100, and 1000 mm). The simulation of the wavefront propagation was performed with the XWFP propagation code (Weitkamp [2004]) using a pixel size of 100 nm. (Image courtesy of Timm Weitkamp.)

of a two-dimensional object as sketched in Fig. 9.3. The beam along the y' axis views the object at an angle θ with respect to the fixed $x - y$ coordinate system. For generality we assume that the absorption coefficient $\mu(x, y)$ of the object is non-uniform. The intensity recorded in a detector located behind the sample is

$$I = I_0 \, e^{-\int \mu(x,y)dy'}$$

which can be rearranged to read

$$log_e \left(\frac{I_0}{I}\right) = \int \mu(x, y)dy'$$

It is thus possible to deduce the line integral of the absorption coefficient, which defines the function $R(\theta, x' = 0)$, from the ratio of the intensity of the primary beam to that measured in the detector. Imagine now that the beam is scanned parallel to x' for fixed θ. This process will produce an intensity distribution $R(\theta, x')$ which depends on x' and the viewing angle θ. The function $R(\theta, x')$ is known as the Radon transform. The CT scan may therefore be thought of as a series of Radon transforms collected at a set of viewing angles.
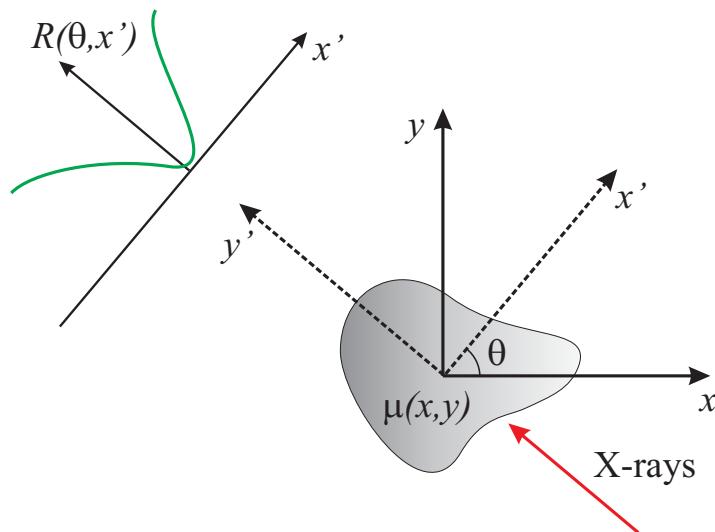
Fig. 9.3 In a radiography experiment an object is represented by a distribution of absorption coefficients which in two dimensions is $\mu(x, y)$. When a narrow X-ray beam is incident on the object the intensity recorded in the detector is a measure of the line integral of the absorption coefficient along the propagation direction of the beam. The line integral $R(\theta, x')$ is known as the Radon transform and is a function of the viewing angle θ and the coordinate x' perpendicular to the direction along which the line integral is performed.

The reconstruction of the two-dimensional image of the object from the Radon transform can be accomplished either algebraically, which is computationally inefficient, or using Fourier analysis techniques. The latter is the most widely adopted approach. It utilizes the Fourier slice theorem, which is derived in the next section.

Fourier slice theorem

Consider a general two-dimensional function $f(x, y)$ which is projected, or more precisely integrated, along the y axis to generate a new function of x only, defined by

$$p(x) = \int f(x, y)\, dy$$

The Fourier transform of $p(x)$ is

$$P(q_x) = \int p(x)\, e^{iq_x x}\, dx$$

It is then natural to ask what relationship does the Fourier transform of the projected function have to the Fourier transform of the original function $f(x, y)$. Again, by definition, the Fourier transform of $f(x, y)$ is

$$F(q_x, q_y) = \iint f(x, y)\, e^{i(q_x x + q_y y)}\, dxdy$$

Now we examine what happens when we set $q_y = 0$. This defines a slice through $F(q_x, q_y)$ given by

$$F(q_x, q_y = 0) = \int \left[\int f(x, y)\, dy \right] e^{iq_x x}\, dx$$
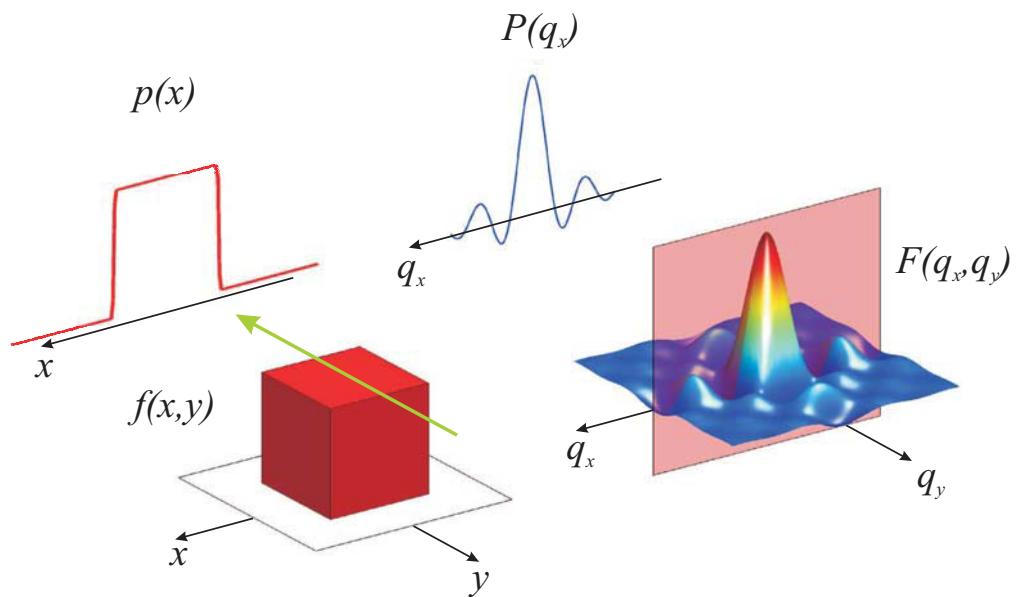
Fig. 9.4 Illustration of the Fourier slice theorem. Here the function in real space $f(x, y)$ is taken to be a two-dimensional top hat function which has a Fourier transform given by $F(q_x, q_y) = [\sin(q_x x)/(q_x x)][\sin(q_y y)/(q_y y)]$. When $f(x, y)$ is projected (integrated) down the y axis this generates a one-dimensional top hat function, $p(x)$, which depends on x only. The Fourier transform of the projected function $p(x)$ is $P(q_x) = \sin(q_x x)/(q_x x)$, which is nothing other than the $q_y = 0$ slice through $F(q_x, q_y)$. These considerations can be readily generalized for arbitrary rotation of $f(x, y)$ around the axis perpendicular to the $x - y$ plane. For example, for a rotation angle of $45°$, $p(x)$ becomes triangular, with a Fourier transform $P(q_x) = [\sin(q_x x)/(q_x x)]^2$ which by inspection indeed is the equation of a slice taken at $45°$ through $F(q_x, q_y)$.

The integral in the square brackets can then be readily identified as $p(x)$, allowing us to write

$$F(q_x, q_y = 0) = \int p(x)\, e^{iq_x x}\, dx = P(q_x)$$

In other words the Fourier transform of the projection along a particular line of a two-dimensional function $f(x, y)$ is equal to a slice through the Fourier transform of $f(x, y)$ taken along a line passing through the origin in the propagation direction. This is known as the Fourier slice theorem, which we illustrate in Fig. 9.4 for the particular case where $f(x, y)$ is a two-dimensional top hat function.

Implementing the Radon transform and its inverse

From the above considerations, the process of CT scanning can be thought of as comprising three key steps. The first is the acquisition of the data as a series of radiographs. In mathematical terms, the data are described as a set of Radon transforms $R(\theta, x')$ taken at different viewing angles. Second, the data $R(\theta, x')$ are Fourier transformed. From the Fourier slice theorem the Fourier transform of the object can be constructed. Finally, an inverse Fourier transform is performed to obtain the reconstructed image of the object. In Fig. 9.5⋆ we show a numerical example of this procedure for a test object, which in imaging is often referred to as a phantom. In panels (a) and (b) the results of a calculation of the Radon transform are shown for two particular viewing angles θ. The Radon transform for the full range of viewing angles is plotted in (d) as a function of the two variables θ and x', the latter being the position on the detector. When plotted in this way, strongly absorbing features in the object
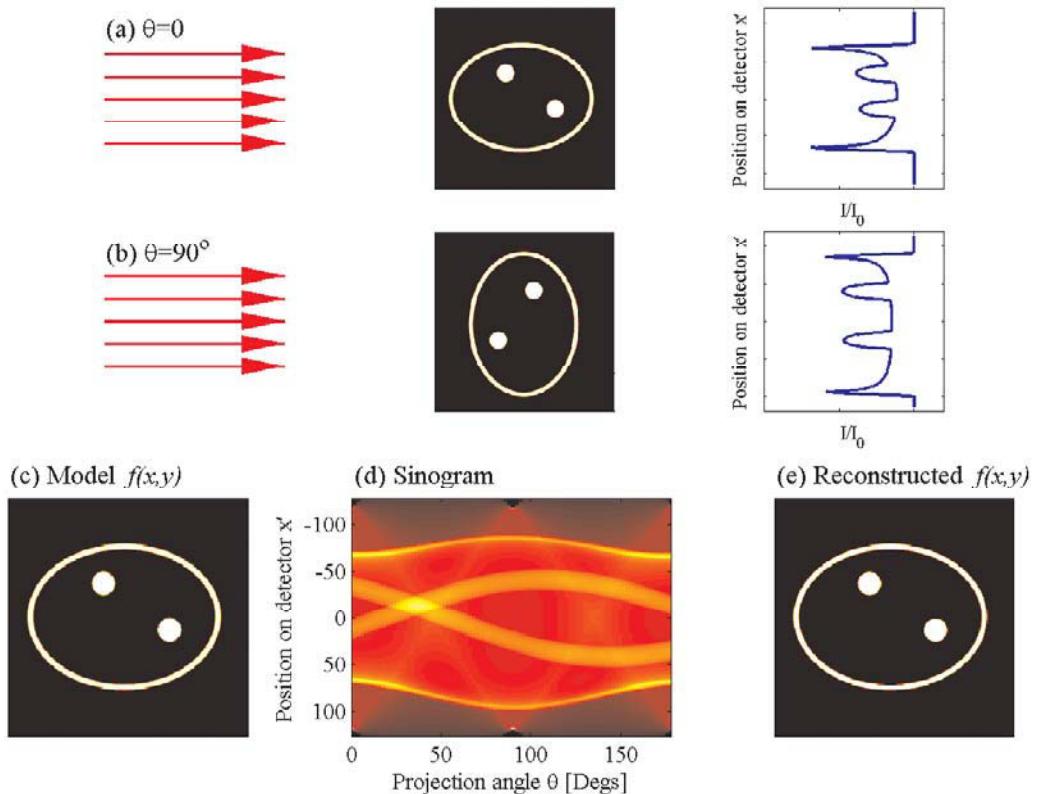
Fig. 9.5 ★ Numerical example of the reconstruction of a two-dimensional object from its Radon transform. The object is plotted in (c). In (a) and (b) the Radon transforms have been calculated and are plotted in the right most columns for two particular choices of viewing angle. (d) The sinogram for θ in the range 0 to $180°$. (e) The reconstructed image. This numerical example was computed using the functions **radon.m** and **iradon.m** which are part of MATLAB's image processing toolbox.

produce sinusoidal trajectories in the Radon transform. For this reason the plot is known as a sinogram. From the Radon transform, the two dimensional Fourier transform of the object is constructed, and the reconstructed image is then obtained via an inverse Fourier transform. In this simple example there is excellent correspondence between the original object and the reconstructed image. For the analysis of real-life data, sophisticated smoothing and filtering algorithms are required to improve the fidelity of the reconstructed image.

Medical CT scanning

A schematic of the type of CT scanner commonly found in hospitals is shown in Fig. 9.6 along with a series of images of a patient's head taken using the CT technique. The patient sits at the centre of a rotation axis around which the X-ray source and detector rotate. The simplest implementation of CT to consider (one in fact close to the one originally used by Hounsfield) is where for a fixed rotation the X-ray source produces a series of parallel X-ray beams. These impinge on the patient at a particular height, and the Radon transform is recorded on a position sensitive detector. The source-detector carousel then rotates to its next setting and the process repeated until the whole sinogram is collected. A two-dimensional image of the internal structure of the irradiated sheet of the body is then
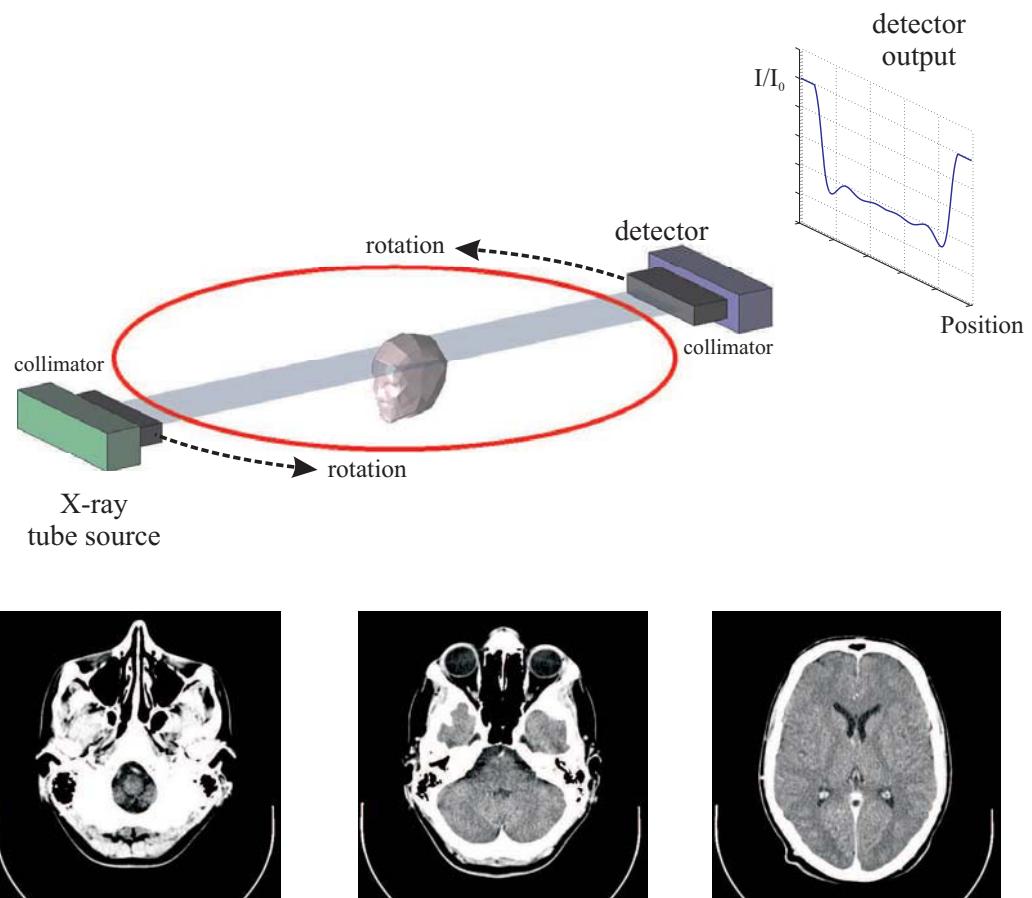
Fig. 9.6 Schematic of the medical application of CT scanning. The X-ray tube source and detector are configured to sit at diametrically opposite points on a circle with the patient at its centre. At fixed angle of rotation, the source produces a series of beams, which are collimated to be parallel. The beams intersect the patient at a particular height (here the upper part of the cranium) and the intensity of the beams passing through the patient is collected as a function of detector position. The combined source-detector system then rotates and another measurement performed. Once the full sinogram has been collected it can be processed as described in the text to produce a two-dimensional map of the absorption coefficient. Examples of CT scans of a patient's head taken at three different heights are shown in the bottom three panels. (CT images supplied courtesy of Mikael Häggström.)

computed using numerical methods similar to those described above. The patient's height relative to the X-ray beam is then adjusted, and a new sheet image is obtained, with the process iterated until a full three-dimensional image is obtained as a stack of two dimensional images.

Many improvements to the basic CT scheme have been introduced in the years since the first scanner was unveiled in 1972. These include innovations such as high-resolution medical CT scanning capable of resolving anatomical details down to 0.5 mm, the ability to collect volumetric data on internal organs in a single rotation, helical CT scanning, etc. A key driver for these developments is to improve the data quality while minimizing the radiation dose given to the patient[2].

---

[2]In a medical CT scan the patient receives a radiation dose in the range 1-10 mSv depending on the type of scan. This can be

The use of CT scanning methods is not restricted to the clinical environment. In fact X-ray tomography is widely applied to many problems in the materials and biological sciences to the extent that it has now become an indispensable analytical tool. An example of a three-dimensional CT reconstruction of a human vetebral bone is shown in Fig. 1.14. Indeed commercial micro-CT scanners are available, optimized for various types of application, which provide a spatial resolution of better than 10 μm.

9.2.2 Microscopy

In general terms, X-ray microscopy allows the imaging of structures on length scales that are intermediate between those probed by optical (<1 μm) and electron (~1 Å) based techniques. Common to all microscopies is the need for efficient focusing optics[3]. For X-rays we have seen in Chapter 3 that focusing can be achieved using either mirrors or lenses, even though the refractive index differs only slightly from one. An important milestone in the field of X-ray microscopy was the pioneering work by Patrick Kirkpatrick and Albert Baez in 1948 who demonstrated a system based on a pair of curved mirrors arranged to focus successively in orthogonal planes (Kirkpatrick and Baez [1948]). The 'KB' mirror system as it is commonly known has endured to the present day where it is routinely deployed in microscopes with a focused beam of around 100×100 nm^2 or so.

For lens based systems, focusing of the X-ray beam can be achieved either using a compound refractive lens (Snigirev et al. [1996]) or a Fresnel zone plate, as discussed on page 101. Due to absorption, compound refractive lenses work best at photon energies above about 10 keV, where a lateral resolution below 100 nm can be achieved. The performance of Fresnel zone plates, on the other hand, is much less compromised by attenuation of the primary beam, and can be designed to work over a very wide range of photon energies, including into the soft-part of the X-ray spectrum which facilitates the imaging of biological tissue. In this section we describe the use of Fresnel zone plates applied to X-ray microscopy.

The principles underlying the operation of the Fresnel zone plate were described on page 106 in terms of refraction. It was remarked that while a kinoform zone plate has certain attractive characteristics, in many situations a binary approximation is a more practicable solution. In Fig. 9.7(a) a schematic is shown of how a binary Fresnel zone plate acts on an incident parallel beam to focus it to a point. The radius r_m of a Fresnel zone is defined such that the waves radiated from that zone and arriving at f have an integrated phase shift of $m\pi$, equivalent to $m\lambda/2$, relative to the incident beam. Waves radiated from successive zones therefore tend to interfere destructively. It follows that a large increase in the radiation arriving at f can be achieved by introducing material into alternate zones that either completely absorbs the incident beam, or introduces a phase shift of π. These two alternative approaches are sometimes referred to as absorption and phase Fresnel zone plates, respectively.

From Fig. 9.7(a), we have

$$r_m^2 + f^2 = \left(f + \frac{m\lambda}{2}\right)^2$$

from which it follows that for X-rays the expression for the radius of the m'th Fresnel zone is

$$r_m \approx \sqrt{m\lambda f}$$

---

compared with the dose received in a conventional X-ray radiograph of approximately 0.1 mSv.

[3]Here we set aside simple microscopies based on pin holes and shadow projection methods. The latter has in fact been of important historical significance to the field of X-ray microscopy, although in a modern context its capabilities are somewhat limited. Diffraction based microscopy is an emerging type of 'lensless' imaging which will be dealt with later in the chapter.
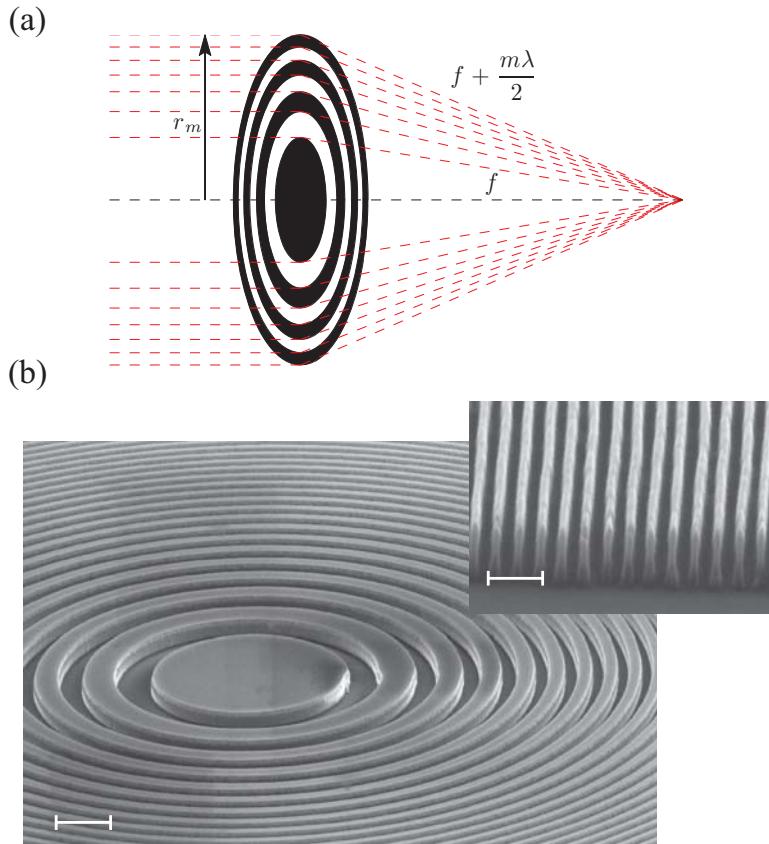
(a)

(b)

Fig. 9.7 (a) Schematic of the focusing of a parallel beam by a Fresnel absorption zone plate which is formed from a series of concentric rings, with the zones between the rings alternating from being transparent to opaque. The m'th ring has a radius given by $r_m \approx \sqrt{m\lambda f}$ where f is the focal length of the lens. (b) Scanning electron microscope (SEM) images of a Fresnel zone plate fabricated using electron beam lithography. The white horizontal lines correspond to a length scale of 1 μm in the main image, and 150 nm in the detail showing the outermost region of the zone plate. The Fresnel zone plate was designed to be used in a soft X-ray microscope operating at photon energies below 1 keV. The Fresnel zone plate was manufactured from a single crystal silicon membrane. The outermost zone has a width of $\Delta r_M = 30$ nm which determines its spatial resolution. The zone plate has a diameter of $D=4M\Delta r_M=100$ μm, and a focal length of $f=2400$ μm for 1 keV photons. (SEM images courtesy of Christian David and Joan Vila-Comamala.)

A critical parameter of the binary zone plate is the width Δr_M of the outermost zone:

$$\Delta r_M = \sqrt{\lambda f}\left(\sqrt{M} - \sqrt{M-1}\right) \approx \sqrt{\lambda f}\left(\sqrt{M} - \sqrt{M}\sqrt{\left(1 - \frac{1}{M}\right)}\right) \approx \frac{\sqrt{\lambda f}}{2\sqrt{M}}$$

In terms of Δr_M, the focal length of the zone plate is given by

$$f = 4M\frac{(\Delta r_M)^2}{\lambda}$$

and its diameter D is

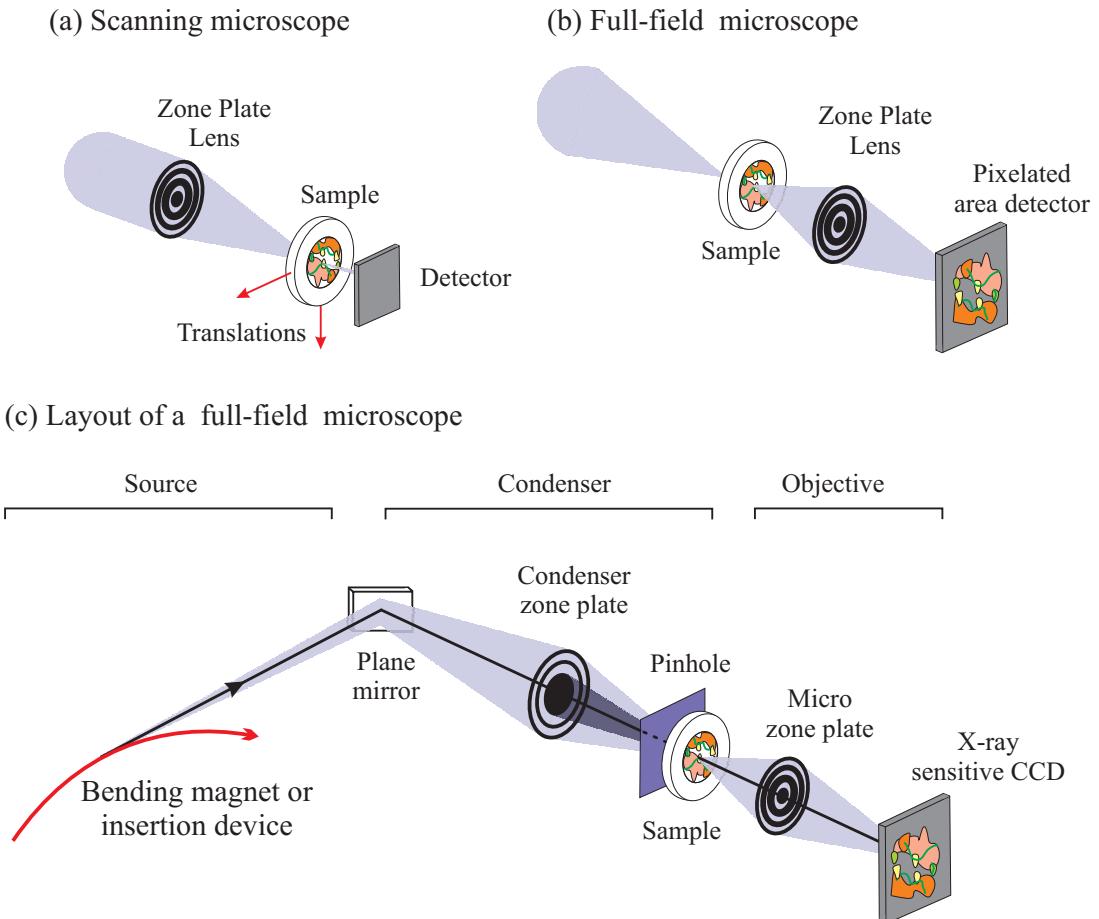$$D = 2r_M = 2\sqrt{M\lambda f} = 2\sqrt{M}\sqrt{\lambda f} = 4M\Delta r_M$$

(a) Scanning microscope

(b) Full-field microscope

Zone Plate
Lens

Zone Plate
Lens

Sample

Pixelated
area detector

Detector

Sample

Translations

(c) Layout of a full-field microscope

Source   Condenser   Objective

Condenser
zone plate

Plane
mirror

Pinhole

Micro
zone plate

X-ray
sensitive CCD

Bending magnet or
insertion device

Sample

Fig. 9.8 Fresnel zone plate based X-ray microscopes. (a) In the scanning transmission X-ray microscope (STXM) a zone plate is used to focus an incident parallel beam down to a small focal spot and the sample is then rastered through the beam to produce the image. (b) The full-field transmission X-ray microscope (TXM) utilizes a zone plate as an objective lens which projects a magnified image on a two-dimensional, pixelated detector. The magnification is determined by the ratio of the objective-detector to sample-objective distances, a ratio which can exceed 1000. (c) Schematic layout of a TXM. The schematic is based on the XM-1 soft X-ray microscope at the Advanced Light Source, Lawrence Berkeley National Laboratory, although the basic layout may be regarded as being generic to modern TXMs, including those designed to operate with hard X-rays. (After an image created by David Attwood.) The beam emanating from the source is first deflected by a plane mirror, after which it impinges on a condenser zone plate which fulfills several functions. Not only does it focus the beam down to a spot size on the sample of several microns, but in combination with a pin hole it serves as a monochromator. The beam transmitted by the sample is then collected by the micro zone plate which projects it onto a two dimensional, pixelated detector, normally based on charge-coupled device (CCD) technology.

Recalling the Rayleigh criterion, which states that the minimum detail resolvable by a perfect lens is given by

$$\Delta x = 1.22 \frac{\lambda f}{D},$$

we see that for a binary Fresnel zone plate operating at X-ray wavelengths the resolution is given by

$$\Delta x = 1.22 \, \Delta r_M$$

Therefore the best resolution is achieved by minimizing the width of the outermost zone. In practice, X-ray zone plates are manufactured using electron beam lithographic techniques. Figure 9.7(b) shows an example of a binary Fresnel zone plate fabricated in this way which has a 30 nm outermost zone width. The highest spatial resolution that has been demonstrated to date for a binary Fresnel zone plate based X-ray microscope is 15 nm (Chao et al. [2005]); it is believed that this can be reduced further down to the nanometre level.

A binary Fresnel zone plate can also be thought of as a variable period diffraction grating. The formula derived above refer to the first, positive diffraction order only. Other diffraction orders exist which have to be taken into account in any practical implementation of a binary zone plate. In Fig. 9.15⋆ we compare the full calculated wavefields produced by binary Fresnel zone plates that either use absorption or a phase shift of π in alternate zones to produce the focused beam.

Fresnel zone plates can be deployed in X-ray microscopes in two distinct ways. Either the zone plate can be used to focus a parallel beam down to a small focus, or it can be used to magnify an image. The former is the basis for the scanning transmission X-ray microscope (STXM). In an STXM the sample sits on a mechanical stage which allows it to be raster scanned through the focused beam to build up the image (see Fig. 9.8(a)). The image in an STXM can be formed either from absorption contrast in a transmission geometry, or more usually by collecting the fluorescence, in which case the image from an STXM acquires element specificity.

The alternative geometry of using the zone plate as a magnifying lens leads to the transmission X-ray microscope (TXM) as shown in Fig. 9.8(b). In a TXM a full-field image of the sample is collected in a single exposure on a two-dimensional, pixelated X-ray detector. The full-field TXM thus has the advantage of speed over the STXM, and does not require a highly parallel (i.e. transversely coherent) incident beam. The scanning microscope on the other hand allows element specific imaging via fluorescence, including the analysis of bulk samples in reflection geometry, and has a field of view that is less constrained by the optical components.

Example: X-ray transmission microscopy

In Fig. 9.8(c) we show the typical layout of a full-field TXM beamline at a synchrotron source. An example of data taken with this microscope is shown in Fig. 9.9(a). The image captures the moment of cell division in the unicellular yeast Schizosaccharomyces pombe. Captured clearly in exquisite detail is the organisation of organelles, and their duplication on either side of the septum that will eventually close to produce two daughter cells. Compared with electron microscopy, TXM applied to biological materials has the advantage that no sectioning is required to expose intra-cellular structure, indeed no sample preparation is required apart from flash freezing of the sample prior to imaging.

An example of data taken with an STXM is shown in Fig. 9.9(b). The sample in this case is a Co/Pt multilayer, where the ferromagnetic order of the Co breaks up into a series of worm-like domains in which the magnetic moments point either 'up' or 'down'. Contrast between these two possible types of domains is obtained by tuning to the Co L_3 edge, and measuring the XMCD signal (see Section 7.3). Several other techniques exist for visualizing magnetic domains, but STXM combined with XMCD is
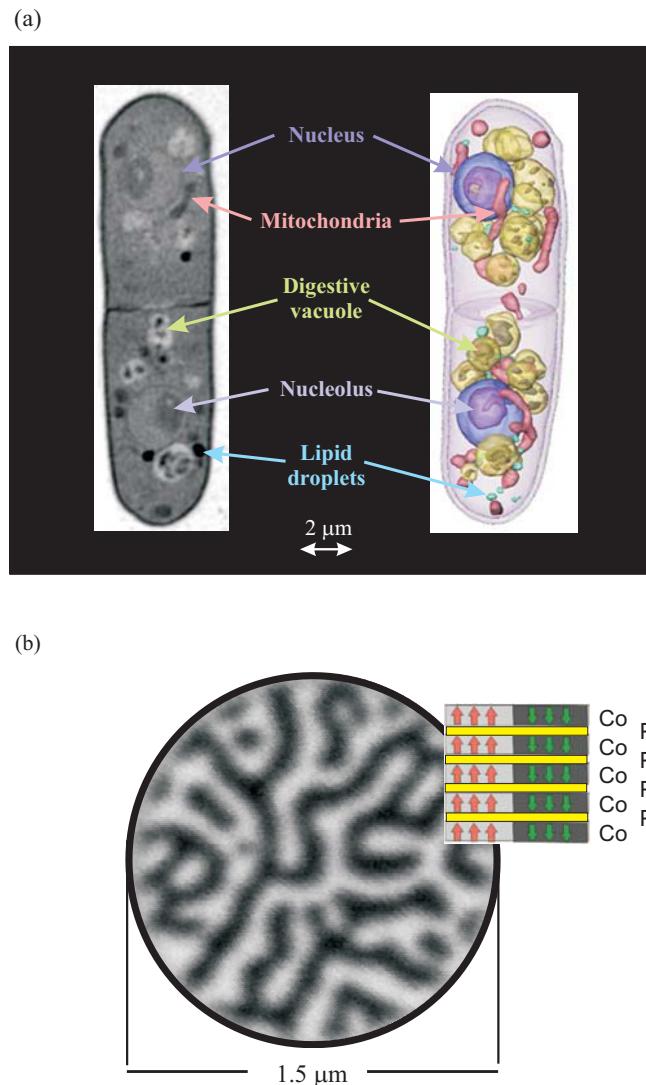
(a)

(b)

Fig. 9.9 X-ray microscopy images. (a) Transmission X-ray microscopy (TXM) image of cell division in the unicellular yeast Schizosaccharomyces pombe. The data were collected using the X-ray microscope XM-1, Advanced Light Source (ALS), at a wavelength of λ=24.0 Å. This wavelength was chosen as it lies in the middle of the 'water window' in which the X-ray absorption by organic material exceeds that of water by approximately an order of magnitude, thereby considerably increasing the imaging contrast. Left: single radiographic projection image revealing detailed, sub-micron information on the organization of organelles within the dividing cell. Right: Three-dimensional image of the cell from tomographic reconstruction. Typical exposure time for a single projection is of order one second, while a tomographic data sets takes three minutes or less. (Image courtesy of Carolyn Larabell.) (b) Scanning X-ray microscopy image of a Co/Pt multilayer film. The image was recorded on beamline 11, ALS, and reveals a pattern of worm-like magnetic domains. Imaging of the magnetic domains was achieved by utilizing the contrast provide by XMCD (see Section 7.3). The image shown is the difference between images recorded with opposite photon helicities with the photon energy tuned to the Co L_3 edge (λ=15.9 Å). The black and white areas correspond to domains in which the magnetic moments point either parallel or anitparallel to the incident beam. The spatial resolution is less than 50 nm. (Image courtesy of Joachim Stöhr.)
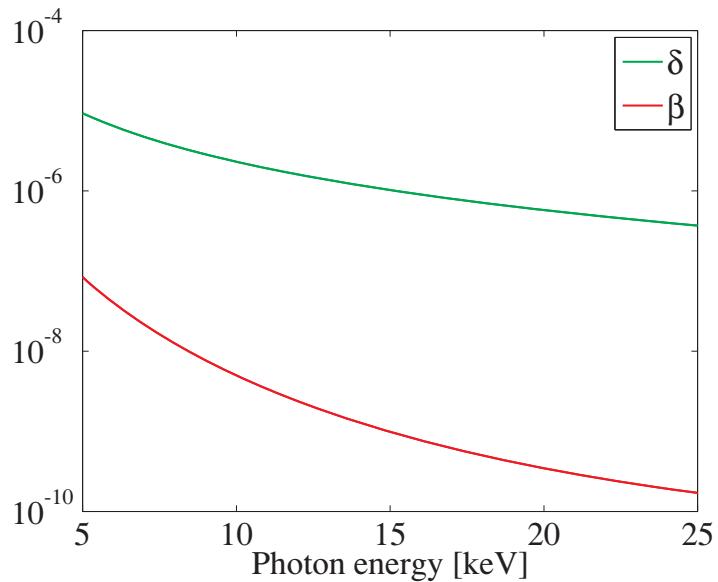
Fig. 9.10 The energy dependence of the real (δ) and imaginary (β) contributions to the refractive index of water. Although it might be expected that β of water is low − due to the weakness of the absorption cross-section − it turns out that in the hard part of the X-ray spectrum, above 5 keV or so, δ exceeds β in all materials.

the only one that combines extremely high spatial resolution (tens of nanometers) along with elemental specificity.

9.3   Phase contrast imaging

An important family of imaging methods that relies not on the absorption or diffraction of X-rays but on the fact that they are refracted when they impinge on a material. Although X-rays undergo only an extremely small angular deviation α when they are refracted, since the amount δ by which the refractive index n differs from one is tiny, it proves possible to determine α with great accuracy using a variety of methods, as we shall describe in this section. Imaging methods that exploit the refractive properties of materials are normally known as phase contrast imaging, as the angular deviation α is directly proportional to the gradient of the phase $\phi(\mathbf{r}) = \mathbf{k}' \cdot \mathbf{r}$ of the refracted beam. This can be readily seen by considering the direction of the refracted beam which is specified by the unit vector $\hat{\mathbf{n}} = \mathbf{k}'/k' = (\lambda/2\pi)\nabla\phi(\mathbf{r})$. It follows that the angular deviation as a function of the coordinates (x, y) in the plane perpendicular to the direction of propagation of the incident beam is

$$\alpha_x = \frac{\lambda}{2\pi}\frac{\partial\phi(x, y)}{\partial x} \quad \text{and} \quad \alpha_y = \frac{\lambda}{2\pi}\frac{\partial\phi(x, y)}{\partial y}$$

Thus by measuring α as a function of (x, y) the gradient of the phase can be determined from which $\phi(x, y)$ can be calculated by integration.

The fact that refraction is capable of providing sufficient imaging contrast for X-rays can be seen by inspecting Fig. 9.10 where we plot the energy dependence of the real (δ) and imaginary (β) deviations
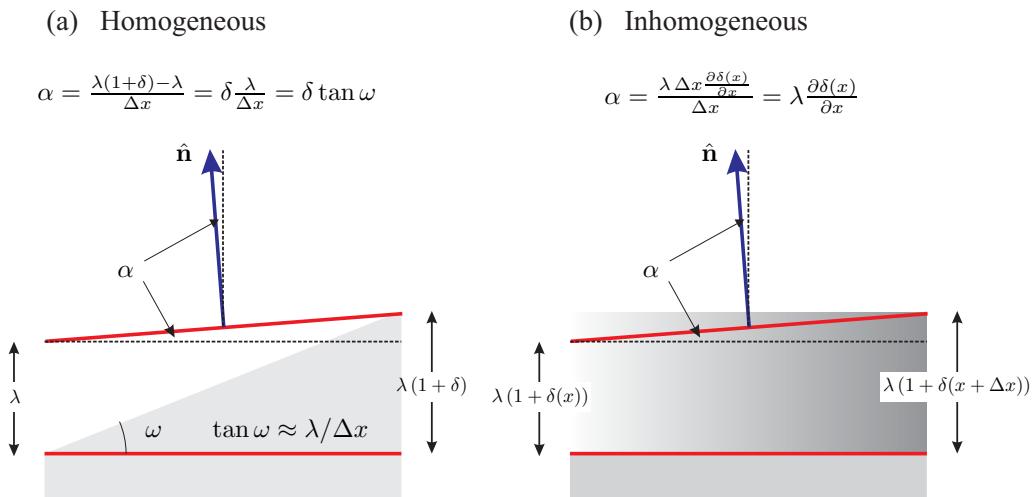
(a) Homogeneous

$$\alpha = \frac{\lambda(1+\delta)-\lambda}{\Delta x} = \delta\frac{\lambda}{\Delta x} = \delta\tan\omega$$

(b) Inhomogeneous

$$\alpha = \frac{\lambda\,\Delta x\frac{\partial\delta(x)}{\partial x}}{\Delta x} = \lambda\frac{\partial\delta(x)}{\partial x}$$

$\hat{\mathbf{n}}$

α

λ

$\lambda(1+\delta)$

ω $\tan\omega \approx \lambda/\Delta x$

$\hat{\mathbf{n}}$

α

$\lambda(1+\delta(x))$

$\lambda(1+\delta(x+\Delta x))$

Fig. 9.11 Relationship between angular deviation α due to refraction and δ. An X-ray beam incident in the vertical direction passes through a wedge shaped sample of uniform density (a) or a plate where the density steadily increases towards the right (b). X-ray wave-crest are indicated by the red lines. The wavelength λ in vacuum increases its magnitude to $\lambda(1 + \delta(x))$ in the material at position x, and therefore the wavecrest after passing the material is no longer horizontal.

of n from unity. The data in Fig. 9.10 are for water, for which it is evident that δ greatly exceeds β. Hence for weakly absorbing biological samples, imaging via refraction would seem to be more efficient than imaging via absorption. In fact even for heavy elements, δ is usually greater than β for hard X-rays, indicating that phase contrast imaging is viable in principle for all materials.

In Fig. 9.11 we consider the angular change due to refraction in more detail. To the left is shown a wedge of material of uniform electron density. The angle of the wedge is denoted ω. At the left corner of the wedge the wavefront (red) passes from material to vacuum. The wedge width Δx is chosen so that also at the right corner a wavefront passes into vacuum. (Here we use the term wavefront to denote a certain phase of the wave, say a wavecrest with the phase being some integer multiple of 2π.) A little geometry as indicated in the figure shows that the exit ray has changed its direction by an amount $\alpha = \delta\tan\omega$ in passing through the wedge. To the right is shown a piece of material with a constant thickness, but with varying density as indicated by the shading. As the density increases towards the right, the wavelength also increases towards the right, and the transmitted ray is refracted by an angle $\alpha = \lambda\partial\delta(x)/\partial x$. Thus in general the angular deviation α is directly related to the spatial derivative of δ, which is itself proportional to the number density of electrons.

It should be clear that the essential requirement of phase contrast imaging is to determine α accurately. Most methods of accomplishing this can be classified into one of three categories: free-space propagation; interferometric based techniques or analyser systems. The last of these methods uses an analyser crystal (often based on perfect crystal optics as described in Chapter 6) with a small acceptance angle to select rays refracted at a specified angle. Here we consider first imaging via free-space propagation, followed by grating interferometry.
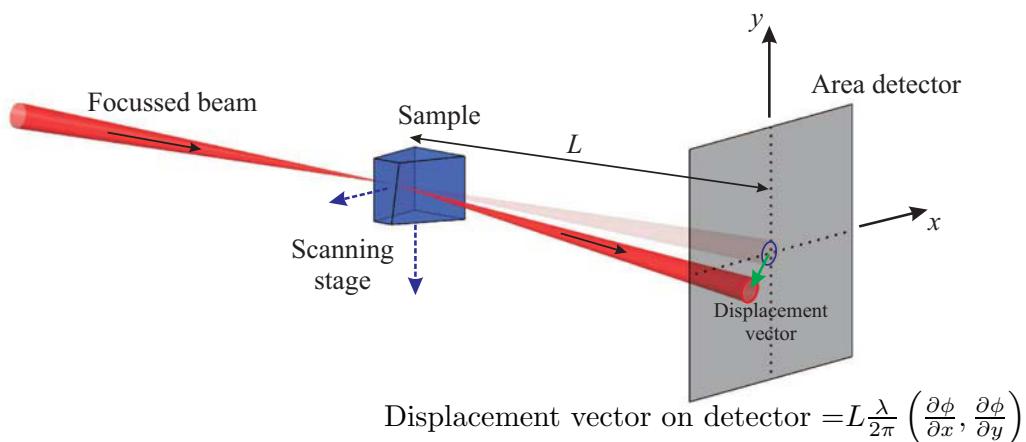
$$\text{Displacement vector on detector} = L\frac{\lambda}{2\pi}\left(\frac{\partial\phi}{\partial x}, \frac{\partial\phi}{\partial y}\right)$$

Fig. 9.12 Phase contrast imaging via free-space propagation. A finely focused X-ray beam is incident on a sample which has negligible absorption. Refraction causes the X-ray beam to be deflected by an angle $\alpha_x = (\lambda/2\pi)\partial\phi(x,y)/\partial x$, etc., where $\phi(x,y)$ is the phase of the refracted ray in the plane perpendicular to the direction of the incident beam. The deflection of the refracted ray recorded on a position sensitive area detector situated a distance L downstream of the sample is αL. In the figure the blue spot on the area detector corresponds to the direct beam without a sample in place, and the red spot to the deflected beam when the sample is at a fixed position (x,y) relative to the focal point of the incident beam. Scanning the sample in the (x,y) plane allows a map of the phase gradient to be built up, from which an image of $\delta(x,y)$ can be computed.

9.3.1   Free-space propagation

Perhaps the simplest realization of a phase contrast imaging method is when the refracted ray is allowed to propagate freely after exiting a thin (negligibly absorbing) sample, as shown schematically in Fig. 9.12. Here an incident beam of X-rays is focused to a small spot so as to impinge on the sample of interest at a selected point in the (x,y) plane. The beam traverses the sample and is refracted so that it exits the sample at a small angle α relative to the direction of the incident beam. A two-dimensional, pixelated detector positioned a distance L downstream from the sample is then used to record the deflection of the refracted beam. The translation (x,y) of the sample perpendicular to the incident beam is then adjusted and the experiment repeated so as to determine the deflection as a function of x and y. As indicated in the figure, the deflection is proportional to α times L, allowing an image of $\delta(x,y)$, and hence the number density of electrons $\rho(x,y)$ to be obtained.

Two examples of phase contrast imaging via free-space propagation are now considered. The first example is a sample fabricated from an etched Si wafer as shown in cross section in the bottom left panel of Fig. 9.13(a). The 350 μm thick (100) wafer has been etched in a central region, so as to remove the part indicated by the hatched region. The etching process is very anisotropic in single crystal Si with the result that slanted (111)-type faces form at an angle ω fulfilling $\tan\omega = d_{100}/d_{110} = \sqrt{2}$. A Si wafer etched in this way forms a convenient substrate, since the frame is thick and robust, while the bottom can be made very thin (typically 10 μm) and therefore, in terms of absorption, essentially transparent to the X-ray beam. The perfect single crystal structure means that the scattering is predominantly confined within a Darwin width or so of a reciprocal lattice vector (see Chapter 6), plus much weaker thermal diffuse scattering. Thus in terms of scattering the substrate may be thought of as being essentially transparent. In the second example the sample was placed on such a Si wafer, but first let us have a look at the refractive imaging of the wafer itself. In scanning the sample in the x direction, the narrow
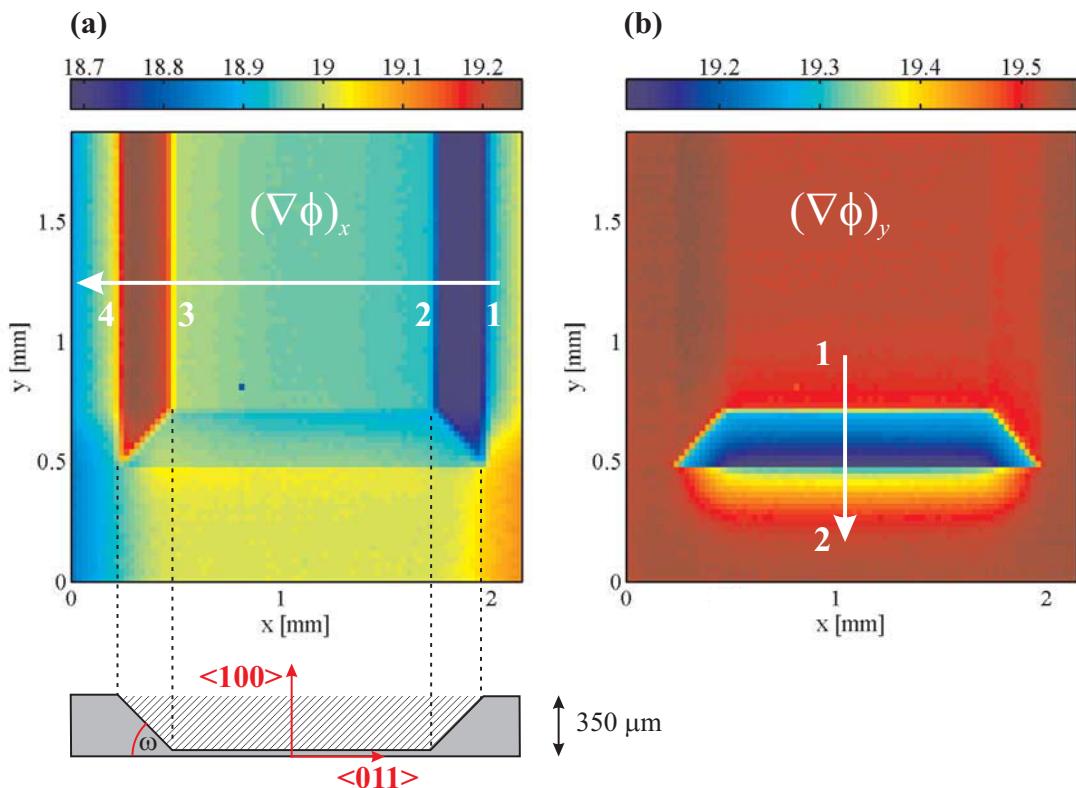
Fig. 9.13 Phase contrast imaging of a trough etched in a Si wafer as described in the text. (a) The cross section of the wafer is shown in bottom part of panel (a) in grey outline. The X-ray beam is refracted at a constant angle α after impinging on the sloped parts of the trough, where the α is proportional to the phase gradient in the scan direction. When the wafer is scanned along the x direction, (a), the slopes occur between points 1 and 2, and 3 and 4. The false colour scale encodes the average pixel position at which the beam was recorded in a detector placed 7.15 m downstream from the sample. The pixel size was 172 μm. When the beam impinges anywhere between point 2 and 3, the beam is detected in pixel position 19.00, c.f. the colour bar scale. When it traverses the sloped sides of the trough it is refracted so that the beam is detected at a slightly higher or lower average pixel number depending on the sign of the gradient of the slope. The angle α may be readily evaluated from the geometry, from which the slope angle ω may be deduced (see Fig. 9.11) (b) Shows the results of scanning the sample in the y direction, where only the sloped end of the trough is imaged. (Data courtesy of Martin Bech and Torben Jensen.)

X-ray beam traverses the line indicated in white in Fig. 9.13(a). From point 1 towards point 2 the beam encounters a negative sloping face, as indicated by the colour bar as blue. From point 2 to point 3 the X-ray beam traverses the thin part part of the sample with constant thickness, as indicated by the colour bar as green. Then from point 3 to point 4 there is an upward sloping face, indicated by red. In a scan parallel to the white line but on the north-south slope there is no colour change because the incident beam does not hit the north-south slope in the scanning direction. On the other hand, as shown in Fig. 9.13(b), in scanning in the north-south direction (the y direction) one indeed images the slope of that face. So the etched Si wafer represents a very simple example of imaging by observing the slight change in direction of the incident beam: this is usually not done because one conventionally puts up a beam stop to block the incident beam.

The second example shown in Fig. 9.14 illustrates the potential of this technique for analysing the structure of samples of biological importance. The images here are of single red blood cells, contrasting
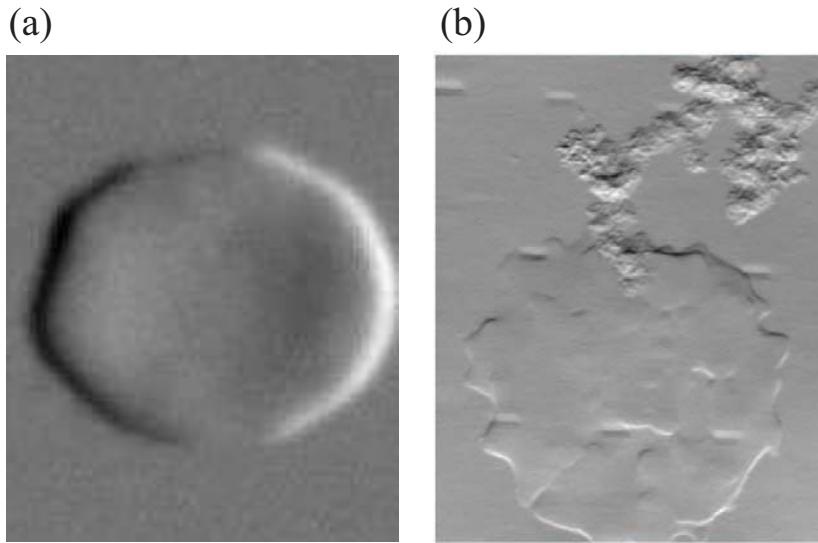
(a)   (b)

Fig. 9.14 Differential phase contrast images of human red blood cells. (a) A normal, healthy cell imaged on a Si substrate (see Fig. 9.13). (b) A red blood cell infected by a malaria parasite. The parasite consumes the haemoglobin in the cell, apart from the central heme molecule which in free form is toxic, but harmless in the crystalline form known as hemozoin. After the parasite has replicated several times in the cell, the red blood cell ruptures, liberating the parasites and leaving a number of sub-micron sized hemozoin crystals outside of the cell (upper right). The field of view is approximately $10{\times}10~\mu m^2$ in both images. The images were recorded by stepping the sample in increments of 20 nm, with each image taking around 12 hours to record. (Images courtesy of Martin Dierolf, Martin Bech and Torben Jensen.)

a healthy cell with one that has been infected by a malaria parasite.

The mathematics of wavefield propagation

Here we outline a mathematical approach to the description of wavefield propagation. Apart from providing an insight into a more rigorous approach to the problem, direct use will be made of the results derived here when we consider the grating interferometer.

Consider a monochromatic, plane wave propagating along the z-axis, e^{ikz}. The wavefronts are planes perpendicular to the z-axis with a separation of $\lambda = 2\pi/k$. Let this plane wave pass through a sample, or an optical element, for example, a grating. The wavefront is then distorted, and the wavefield in a plane perpendicular to the z-axis, say at $z=0$, is now a function of x and y, $\psi_0(x, y)$. We wish to evaluate the wavefield at a distance z further downstream by constructing a propagation operator $\hat{D}_z$ defined such that $\psi_z(x, y) = \hat{D}_z \psi_0(x, y)$. To accomplish this it is convenient to use the Fourier transform of $\psi_0(x, y)$. For the sake of simplicity of notation, let us keep explicitly the dependence of the x-coordinate only, when needed we can always revert to the full dependence on (x, y). Then by definition

$$\psi_0(x) = \frac{1}{2\pi} \int \tilde{\psi}_0(k_x) \, e^{-i k_x x} \, dk_x \qquad (9.1)$$

This equation states that at $z=0$ the wavefield is a superposition of plane waves each of which is a

Fresnel Zone Phase Plate

Fresnel Zone Absorption Plate

Wave Propagation

Wave Propagation

Amplitude profile
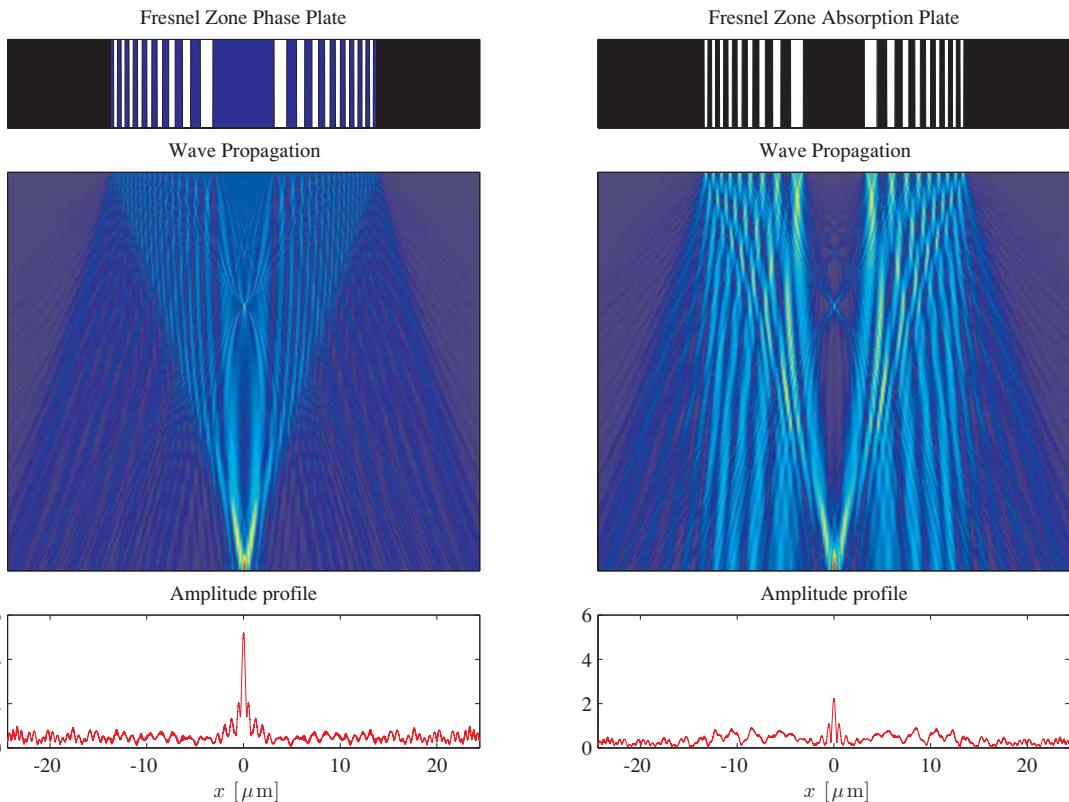
Amplitude profile

Fig. 9.15 ⋆ Example of the wavefield propagation method (see Eq. (9.2)). The images show the wavefield calculated for Fresnel zone plates illuminated with incident plane waves from above. The left hand column refers to a Fresnel zone phase plate while the righthand column refers to a Fresnel zone absorption plate. The parameters used in the calculations are: focal length, $f = 10$ cm, X-ray wavelength, $\lambda = 1$ Å and lens width equal to $100\,\mu$m. Both the convergent $m = 3$ and the divergent $m = -1$ wavefields are evident as weak features.

function of the wavevector $\mathbf{k}=(k_x, k_z)$, with $k_z = \sqrt{k^2 - k_x^2}$. We shall now make the assumption that $k_x \ll k$, so that $k_z \approx k - k_x^2/(2k)$. Each of the plane waves $\tilde{\psi}_0(k_x)e^{-ik_x x}$ propagates to z by multiplication with the phase factor $e^{ik_z z}$, or by using the expansion of k_z, by the phase factor $e^{i\left[kz - k_x^2 z/(2k)\right]}$ (see footnote[4]). We can thus understand the action of the operator as proceeding in a number of steps:

(a) Fourier transform the wavefield at $z=0$ to obtain a single, plane-wave component

$$\tilde{\psi}_0(k_x) = \mathcal{FT}\left[\psi_0(x)\right] = \int \psi_0(x)\,e^{ik_x x}\,dx$$

(b) Multiply the plane-wave component $\tilde{\psi}_0(k_x)$ by the propagator $e^{ikz}e^{-ik_x^2 z/(2k)}$ to obtain $\tilde{\psi}_z(k_x)$

[4]For a periodic structure like a grating of period p, k_x will be an integer multiple of $2\pi/p$. In that case the incident wavefield is repeated downstream at z values fulfilling $(z/2k)(2\pi/p)^2 = 2\pi m$ where m is an integer, i.e. $z = m(2p^2/\lambda)$, where $2p^2/\lambda$ is the so-called Talbot length of the grating. If the grating has a period of 1 μm, and the X-ray wavelength is 1 Å then the Talbot length is 20 mm.

(c) Construct the full propagated wave from inverse Fourier transformation as

$$\psi_z(x) = \mathcal{FT}^{-1}\left[\tilde{\psi}_z(\mathbf{k}_x)\right] = \frac{1}{2\pi}\int \tilde{\psi}_z(\mathbf{k}_x)\,e^{-i\,\mathbf{k}_x x}\,d\mathbf{k}_x$$

The propagated wavefield, now back to the full two-dimensional notation, is therefore given explicitly as

$$\psi_z(x,y) = \hat{D}_z\,\psi_0(x,y) = e^{i\,kz}\,\mathcal{FT}^{-1}\left[e^{-iz(\mathbf{k}_x^2+\mathbf{k}_y^2)/(2k)}\,\mathcal{FT}\left[\psi_0(x,y)\right]\right]$$

Note that the final Fourier transformation, $\mathcal{FT}^{-1}$, involves the product of two functions in k-space, namely $e^{-iz(\mathbf{k}_x^2+\mathbf{k}_y^2)/(2k)}$ and $\mathcal{FT}\left[\psi_0(x,y)\right]$, so by the convolution theorem the result is the convolution of the Fourier transform of the two functions in (x,y) space. The latter is in fact the input function $\psi_0(x,y)$ itself. The Fourier transform of the first function, $e^{-iz(\mathbf{k}_x^2+\mathbf{k}_y^2)/(2k)}$, can be evaluated as follows. For the simplified one-dimensional form, we write the Fourier transform as

$$P(x) = \frac{1}{2\pi}\int_{-\infty}^{\infty} e^{-i\mathbf{k}_x^2 z/(2\mathbf{k})}\,e^{-i\,\mathbf{k}_x x}\,d\mathbf{k}_x$$

$$\equiv \frac{1}{2\pi}\,e^{-i\,x^2(2\mathbf{k}/z)/4}\int_{-\infty}^{\infty} e^{-i(\mathbf{k}_x/(2\mathbf{k}/z)^{\frac{1}{2}}+x(2\mathbf{k}/z)^{\frac{1}{2}}/2)^2}\,d\mathbf{k}_x$$

This integral is of the form already considered in the box on page 73, viz.,

$$I(a) = \int_{-\infty}^{\infty} e^{-iat^2}\,dt = e^{-i\pi/4}\sqrt{\frac{\pi}{a}}$$

where in the present context $a = z/(2\mathbf{k})$. In two dimensions the Fourier transform may be written as

$$P(x,y) = P(x)\,P(y) = \frac{1}{4\pi^2}\frac{-i\pi}{a}\,e^{-ik(x^2+y^2)/(2z)} = -i\frac{k}{2\pi z}e^{-ik(x^2+y^2)/(2z)}$$

Thus the propagated wavefield is found by convolution (designated by the symbol $\star$)

$$\boxed{\psi_z(x,y) = -i\frac{e^{ikz}}{\lambda z}\left[e^{-ik(x^2+y^2)/(2z)}\right]\star\psi_0(x,y)} \tag{9.2}$$

An example of a calculation performed using the wavefield propagation method is given in Fig. 9.15$\star$, which compares the wavefields created by two different types of binary Fresnel zone plates when illuminated by incident plane waves. The fundamental operating principles of binary Fresnel zone plates and examples of their application in X-ray microscopy are presented in Section 9.2.2. The left-hand and right-hand columns in Fig. 9.15$\star$ refer to phase and absorption zone plates, respectively. For the phase zone plate the thickness of the phase plate parallel to the optical axis has been chosen so that the dark blue stripes introduce a phase shift of π relative to the white stripes. The action of the binary Fresnel zone phase plate on the incident beam can be described in terms of a diffraction grating: the first, positive diffraction order focuses the beam at the primary focal length, f; higher positive orders have focal lengths progressively shorter than f; negative orders are divergent. Focusing of the beam is still evident in the case of the absorption zone plate (with the various different diffraction orders exhibiting qualitatively similar behaviour to the phase zone plate), but in this case the efficiency is seen to be approximately one half of that of the phase zone plate.

9.3.2 Grating interferometry

In contrast to the method described in the previous section – scanning phase contrast imaging – interferometric based imaging systems are capable of producing full-field images.   Various types of interferometer have been developed for phase contrast X-ray imaging. In Fig. 9.16(a) we show the schematic layout of an X-ray interferometer based on gratings. The basic idea behind its operation is that it can be configured such that the lateral positions (i.e. perpendicular to the optical axis) of the interference fringes established behind a grating (G_1) are extremely sensitive to any angular perturbations of the incident X-ray wavefield produced by refraction from a sample placed in front of G_1. Changes in the positions of the fringes are analysed using a second grating (G_2) thus providing information on the phase gradient of the X-ray wavefield. This particular type of interferometer is often associated with the name of Talbot who in the 19th century made some important observations on Fresnel diffraction from an optical grating. The first demonstration of a Talbot interferometer for phase contrast X-ray imaging occurred only in the early years of this century (David et al. [2002], Momose et al. [2003], Weitkamp et al. [2005]). Here we have chosen to focus on this particular type of interferometer due to its relative simplicity and mechanical robustness. These attributes open the benefits of phase contrast imaging to a much wider community of users than has hitherto been the case, including most especially clinicians.

To understand in detail the operation of the Talbot interferometer we return to consideration of Fig. 9.16(a), where we shall first neglect the perturbation of the wavefront by the sample. An incident plane wave impinging on a grating (G_1) with period p_1 is diffracted into distinct orders at different directions, symmetric around the optical axis. The angular splitting of the first order is $\pm\lambda/p_1$, and is small since $\lambda \sim 1$ Å and $p_1 \sim 1\ \mu$m. Hence these beams overlap and interfere. As Talbot discovered, the resulting lateral pattern is repeated downstream at any multiple of the length $d_T = 2p_1^2/\lambda$ which is known as the Talbot length (see footnote on page 323). The repetition of the pattern over one Talbot length is illustrated in Fig. 9.16(c) for three different kinds of gratings: an absorption grating (top) and phase shift gratings (middle and bottom). It turns out that for particular phase shifts, the patterns are reproduced at rational fractions of the Talbot length. In addition, for a π-phase grating the lateral period becomes half of the period of the incident grating. For this type of grating the intensity pattern at a particular distance downstream from grating G_1 may be represented schematically by the pink box pattern in the top part of Fig. 9.17. An absorption grating with period $p_1/2$ placed at this distance will therefore occlude the intensity completely when the absorption stripes are in registry with the box pattern, or transmit the intensity completely when in anti-registry, and partly transmit the intensity pattern when in between these two extremes. The transmission versus the lateral position x_g of the absorption grating is thus a triangular pattern as indicated in the bottom part of Fig. 9.17.

In practice, a position sensitive area detector is placed behind the absorption grating G_2, which is scanned, or sheared, in the direction x_g perpendicular to the optical axis over a period p_2. (In this type of shearing interferometer, as it is more generally known, the action of scanning G_2 is referred to as phase scanning, since it provides information on the phase of the fringe pattern.) The spatial resolution of this type of imaging is ultimately determined by the size of a pixel, which at the time of writing can be as small as $10\ \mu$m.

The triangular variation of intensity with x_g drawn in Fig. 9.17 represents the ideal case of a point source and perfectly sharp gratings. The latter is in fact pretty well achievable in practice since the gratings are etched out of a Si single crystal (Fig. 9.16(b)). The finite source size on the other hand limits the transverse coherence length of the incident beam as discussed in Sec. 1.5. Suppose that the ideal point source, located at a distance R, is displaced a distance D (see Fig. 1.16). The intensity pattern at the grating G_2, a distance d from the first grating, is then translated by $d(D/R)$, which typically at a
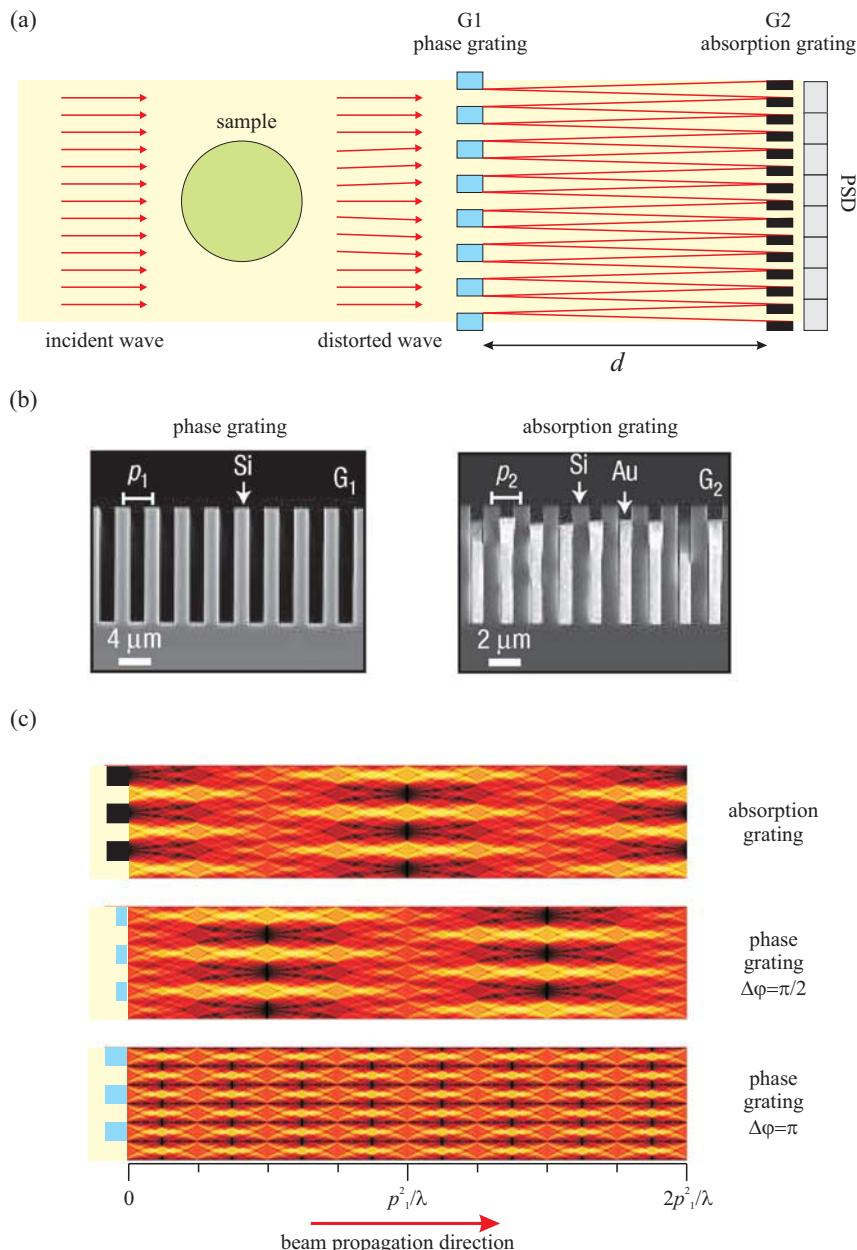
Fig. 9.16 (a) Schematic layout of a Talbot X-ray interferometer. (b) Scanning electron microscopy (SEM) images of gratings designed for use in a Talbot interferometer. The gratings were fabricated from Silicon using photo-lithography. Silicon is chosen partly as it can be processed with great accuracy, but also due to its low absorption of hard X-rays. This means that in practice G_1 is a good approximation to a pure phase grating; the absorption grating G_2 has to be formed by depositing gold in the grating channels. (Images courtesy of Franz Pfeiffer.) (c) Calculated wavefields for an ideal absorption grating (top), an ideal $\pi/2$ phase grating (middle), and an ideal π phase grating (bottom). The wavefields were calculated following the formalism outlined on page 322. (After an image by Weitkamp et al. [2006].)

Intensity

After π
beam splitter

absorption grating

x_g

Intensity

After absorption
grating

x_g

Detector pixel
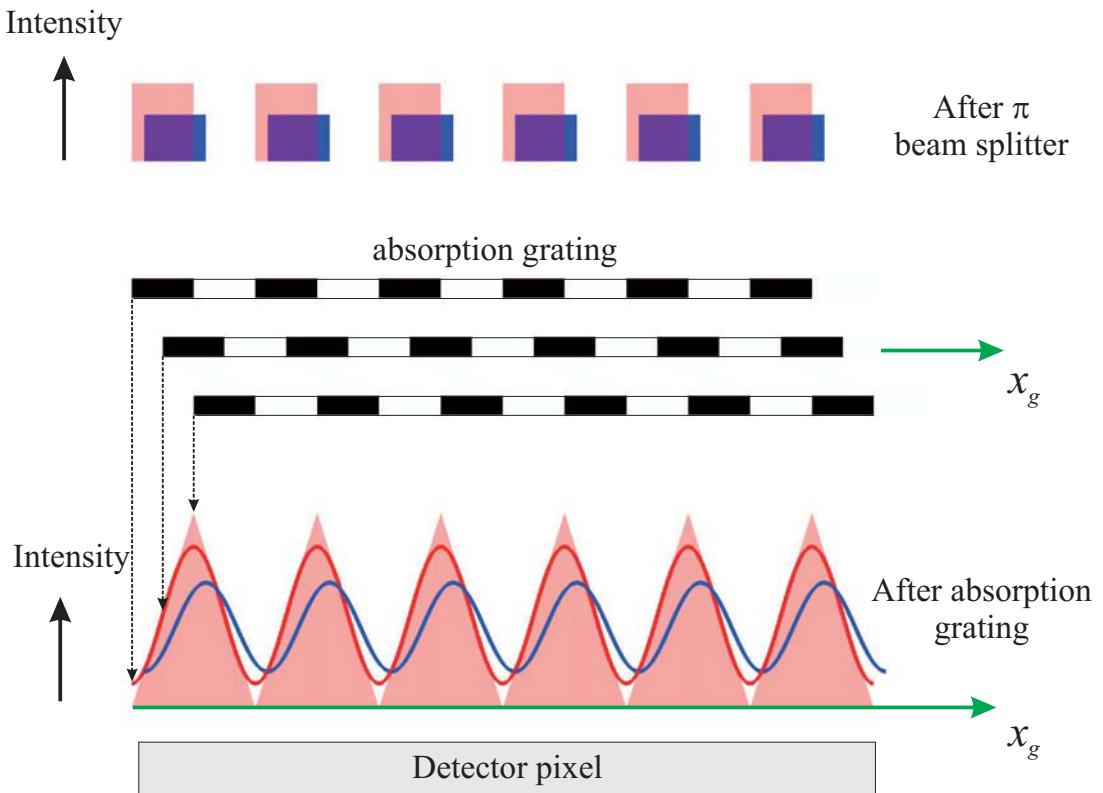
Fig. 9.17 Illustration of phase stepping of the analyser grating G_2 in a Talbot shearing interferometer. The topmost row represents the box-like intensity pattern at a distance $d = p_1^2/8\lambda$ downstream of a π phase grating as a function of the lateral coordinate x_g perpendicular to the optical axis. Pink (blue) refers to the wavefield without (with) a sample. The absorption grating is represented in the middle section by the black (no transmission) and white (no absorption) rectangles. The absorption grating is drawn at three lateral positions. (It is also translated parallel to the optical axis, but this is for illustrative purposes only.) The intensity pattern behind the absorption grating but immediately above the detector pixel is triangular in the ideal case, becoming sinusoidal-like when effects such as grating imperfection, finite coherence length of beam, etc., are included.

synchrotron source is small compared with the period p_1. A real source may be thought of as a Gaussian superposition of point sources, so the ideal box distribution should be folded with a Gaussian of root mean squared (r.m.s) width $\sigma = d(D/R)$, D being the r.m.s. size of the source. The ideal triangular transmission curve is concomitantly modified to a sinusoidal-like curve, represented as a red full line in Fig. 9.17. In particular the maximum intensity is reduced, and the minimum intensity will exceed the ideal value of zero. Quantitatively, one introduces the visibility V, defined as

$$V = \frac{I_{max} - I_{min}}{I_{max} + I_{min}}$$

which obviously is unity for the ideal, triangular shearing pattern. For the Gaussian smearing model discussed above it is left as an exercise to establish that at small smearing, $\sigma/p_1 \ll 1$,

$$V \approx 1 - \frac{8}{\sqrt{2\pi}} \frac{\sigma}{p_1}$$
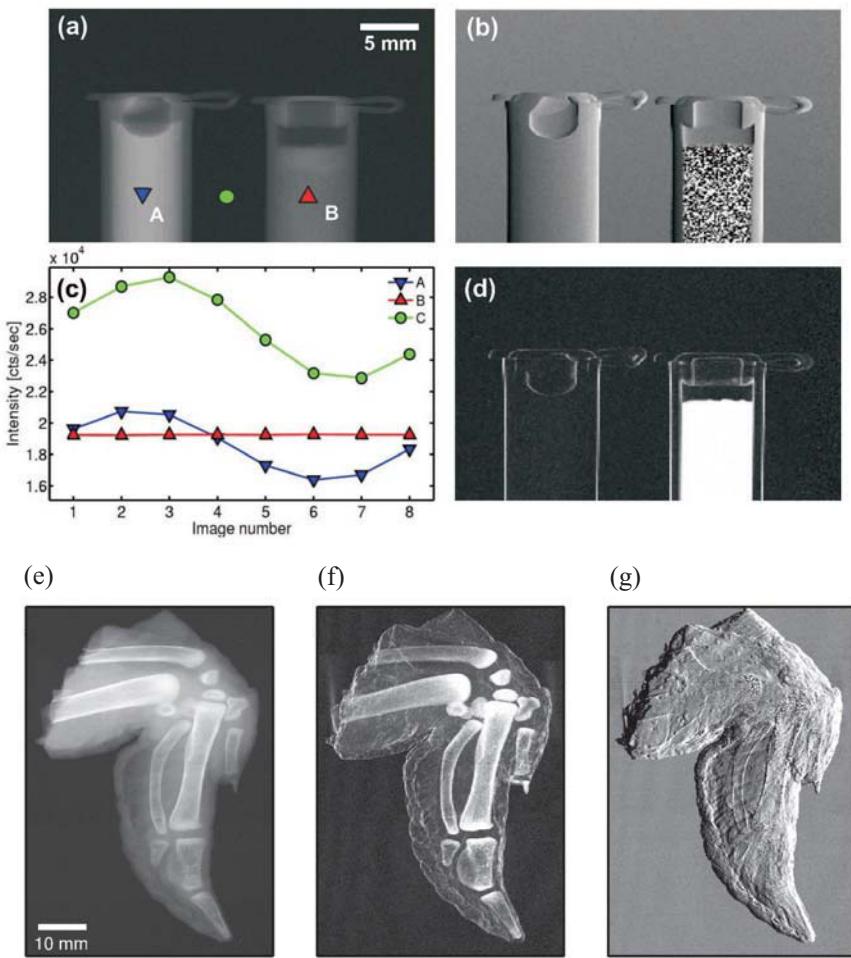
Fig. 9.18 Examples of images acquired with a Talbot X-ray interferometer. (a)-(d) are of a test sample containing two plastic containers filled with a liquid (water, left, A) and a powder (sugar, right, B). (a) Conventional X-ray transmission image, (b) differential phase-contrast image, (d) dark-field image. (c) Intensity oscillations observed in detector pixels corresponding to the three indicated regions of the sample, extracted from a series of eight images taken at different values of x_g (averaged over 50 pixels). (e)-(g) Imaging of a biological (and culinary!) specimen: a chicken wing. (e) X-ray transmission image, (f) dark-field image and (g) differential phase contrast image. The photon energy was 28 keV, pixel size is 172 micron, and eight images each of 5 seconds exposure time were used for these results. In (b) the image of the inside of the right-hand container (B) appears as a random array of black and white pixels. This is due to the fact that the visibility of the intensity oscillations is zero for this part of the sample, as shown by the red line in (c). (Images courtesy of Martin Bech and Franz Pfeiffer.)

So much for the shearing pattern with no sample in the beam. Now we consider how an absorbing and refracting sample modifies the shearing pattern, thereby enabling several imaging modes of the sample. First consider a part of the sample as small as one detector pixel of the detector. This part of the sample will attenuate the beam by a certain factor due to absorption, and it will refract the incident beam direction by a certain angle. Consequently the beam profile at the second grating will ideally look

like the blue boxes in the top part of Fig. 9.17: reduced in height due to absorption, and displaced due to refraction. Including smearing effects of the box pattern, the shearing pattern will resemble the blue curve in the bottom of Fig. 9.17. It is fully determined by the intensity obtained in the detector pixel for just three settings of x_g, thus by a simple algorithm (in practice a Fast Fourier Transform analysis) one obtains the absorption (a), the phase shift (b), and the visibility shift (c) of the pattern. This applies to every detector pixel, therefore producing three types of image: absorption, phase gradient, and what has been termed 'dark field' from the change in visibility. The last of these refers to optical microscopy. In the Talbot X-ray interferometer the reduced visibility is due to the third effect the beam undergoes in passing through the sample, namely scattering which in the shearing pattern shows up as a general background level. In other words the reduced visibility is a measure of the scattering, just as for dark field images in optical microscopy.

From what we have discussed so far, it should be clear that the Talbot interferometer has many features that make it attractive as an X-ray imaging system. The grating length can be made several inches long, thereby providing a large field of view which is particularly useful in medical applications. To add to the list of features, we note that it is possible, by taking a series of images as the sample is rotated, to operate it in a tomographic mode (see Sec. 9.2.1). This allows three-dimensional images of both the real and imaginary parts of a sample's refractive index to be determined from a single data set. Finally, we note that by placing a third grating in front of the sample means that the Talbot interferometer can even be used to produce high-quality phase contrast images using a conventional X-ray tube source (Pfeiffer et al. [2006]).

Examples of the three imaging modes recorded with a grating interferometer are shown in Fig. 9.18.

9.4 Coherent diffraction imaging

We have seen in earlier chapters how the diffraction pattern collected in the far-field (Fraunhofer) limit is directly related to the Fourier transform of a sample's electron density[5]. It should be clear that under normal circumstances it is not possible to recover an image of the electron density by performing an inverse Fourier transform of the diffraction pattern because of the phase problem. If, however, a small but finite sized object is illuminated with coherent radiation, then it turns out that the phases can be retrieved and a real space image of the sample reconstructed by Fourier inversion. This type of imaging is known as coherent X-ray diffraction imaging (CXDI, or simply CDI). It is an example of a 'lensless' imaging technique with the obvious benefit of obviating the need to fabricate complex optical elements. Another benefit includes the fact that it has been demonstrated to work on imaging both crystalline and non-crystalline materials.

Before describing the phase retrieval methods we first consider the effect of illuminating an object with coherent radiation.

9.4.1 Coherent beams and speckle patterns

When developing the expression for the diffracted intensity from a collection of point-like objects as $I = \left| \sum_j e^{i\mathbf{Q}\cdot\mathbf{r}_j} \right|^2$ an implicit assumption is that the incident beam is fully coherent over the volume spanned by the position of the objects. In the opposite limit, where the beam is fully incoherent, the scattered intensity from each object has to be first evaluated, with the individual contributions being

---

[5]This statement applies strictly only to a non-absorbing, weak phase object. More accurately speaking, the diffraction amplitude is proportional to the Fourier transform of the complex X-ray optical transmission function of the specimen.
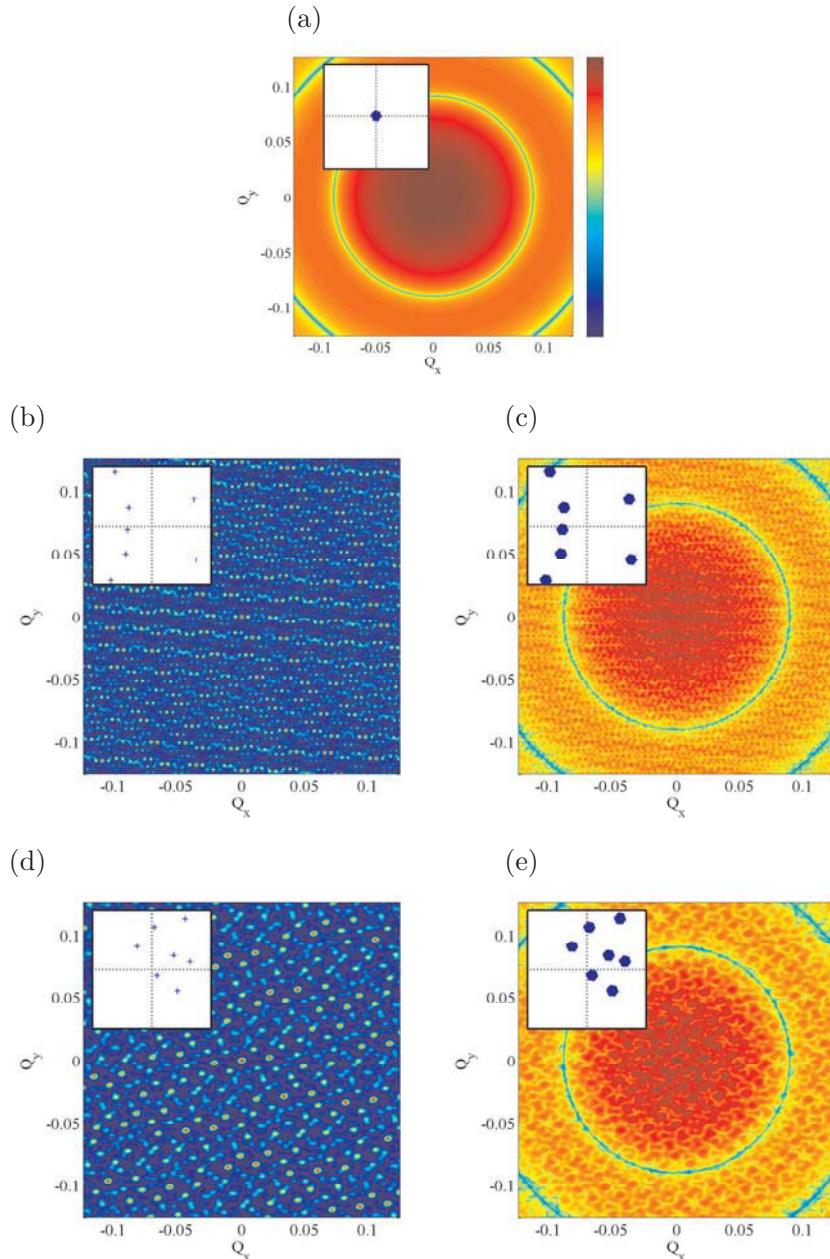
Fig. 9.19 Coherent X-rays beams and speckle. (a) shows the SAXS pattern calculated for an isolated sphere. (b)-(c) scattering from seven randomly positioned spheres. In (b) the scattering intensity I has been calculated from the spheres' centre-of-mass coordinates $\mathbf{r}_j$ where for a fully coherent X-ray beam $I = \left|\sum_j e^{i\mathbf{Q}\cdot\mathbf{r}_j}\right|^2$. A finely textured, but non-random, diffraction pattern results, known as the speckle pattern. (c) The total diffraction pattern is obtained by multiplying the speckle pattern by the square of the form factor of a single sphere. (d)-(e) same as (b)-(c) except for a different arrangement of spheres. The simulated data in panels (a), (c) and (e) are plotted on a logarithmic scale.
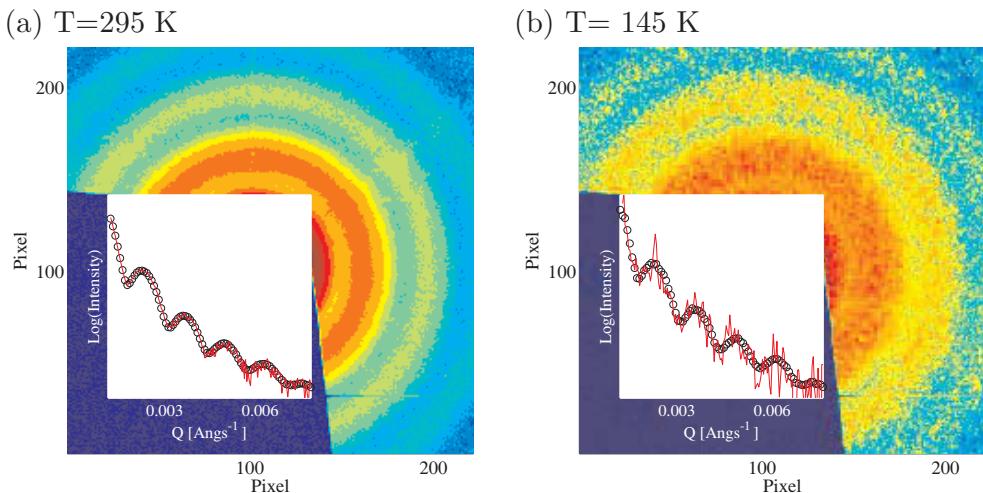
Fig. 9.20 Small angle X-ray scattering data from silica spheres of 500 nm diameter, 2% vol. in a H_2O/glycerol mixture. The measurements were performed at ID10C, ESRF using a coherent beam ($10 \times 10~\mu m^2$) at a photon energy of 8.02 keV. The images are averages of 200 exposures each of 0.7 s duration, i.e. 140 seconds in total. Insets: circles show the azimuthally averaged intensity; the red line a single representative radial cut. The CCD detector was 2.41 m downstream from the sample, with a pixel size of 22.5 micron. Image (a) was recorded above the glass transition where the movement of the silica spheres produces a dynamic speckle pattern, which when averaged over 200 exposures produces the same result as if the sample had been illuminated with an incoherent beam. (b) was recorded below the glass transition where the motion of the silica spheres is frozen, and the speckle pattern is correspondingly static. (Data courtesy of Anders Madsen.)

added to obtain the total intensity. In many experimental situations the coherence of the beam lies somewhere between the two extremes, and the beam is said to be partially coherent. Experimentally one can control the degree of transverse coherence by an aperture situated upstream from the sample, and this has been the approach used to date in coherent X-ray diffraction imaging. While the longitudinal coherence length can be controlled through the choice of monochromator crystal.

In Fig. 9.19 we depict the small-angle X-ray scattering (SAXS) pattern calculated from spheres under the condition of coherent illumination. SAXS from a single sphere was discussed at length in Chapter 4 and is plotted in Fig. 9.19(a) where it is seen to consist of a series of intensity maxima lying on rings with a spacing inversely proportional to the diameter of the sphere. In Fig. 9.19(b) and (c) we show the scattering from seven randomly positioned spheres. Frame (b) is calculated purely from the spheres' centre-of-mass coordinate (indicated by the crosses), where the diffraction pattern is seen to consist of a multitude of 'speckles'. The speckle pattern is not completely random, however, but reflects the location of the scattering centres. This is clear by comparing (b) with (e) which was calculated for a different configuration of spheres: the speckle patterns are quite distinct. Panels (c) and (e) show the full diffraction patterns calculated by multiplying (a) with the appropriate speckle pattern[6]. These two sets of patterns can be contrasted with the outcome of illumination with a beam coherent only across the width of a sphere, where the average pattern in (a) would be observed.

An example of a speckle pattern measured in a SAXS experiment is given in Fig. 9.20. The sample consisted of a dilute suspension of silica spheres (500 nm diameter) which was illuminated with a coherent beam created by passing an X-ray from an undulator through a $10 \times 10~\mu m^2$ aperture. A

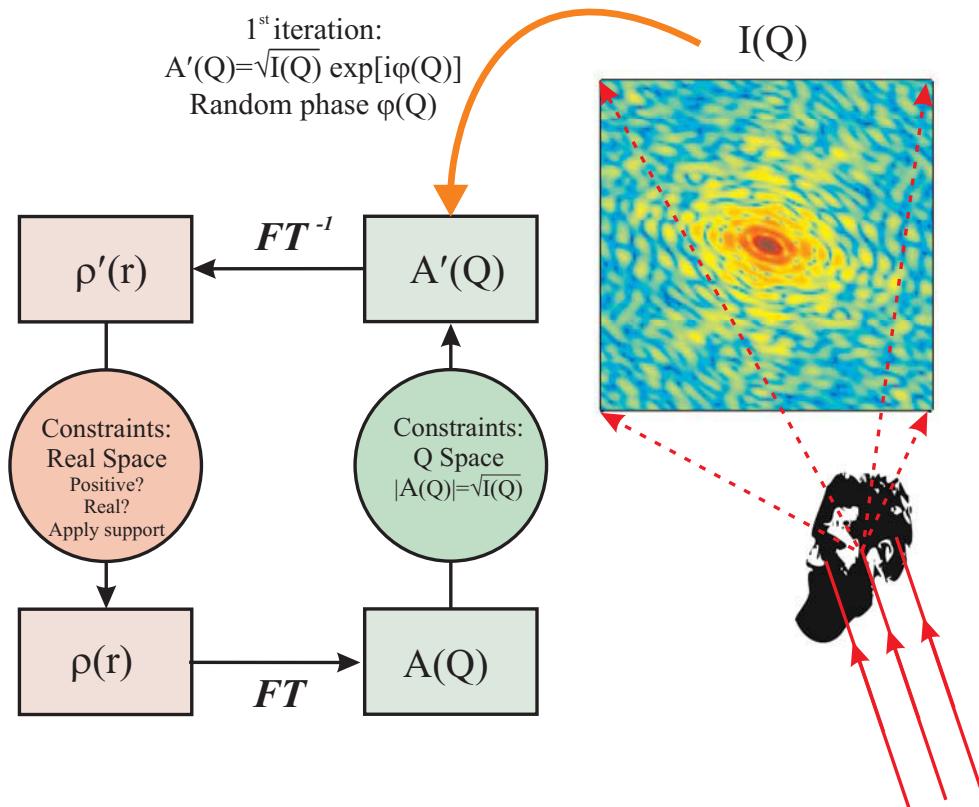[6]Another example of the convolution theorem.

Fig. 9.21 Schematic of the iterative, phase retrieval algorithm used to reconstruct real space images from coherent X-ray diffraction images. In the right hand panel a test object is illuminated by a coherent X-ray beam and the diffracted intensity, $I(\mathbf{Q})$, is recorded on a position sensitive area detector placed in the far-field. The diffraction pattern in this case is that of a portrait of W.C. Röntgen.

two-dimensional detector was used to record the diffraction pattern. In both (a) and (b) 200 exposures, each 0.7 s long, were averaged to produce the detector images. Around room temperature Fig. 9.20(a), the silica beads diffuse more or less freely through the suspension. Although there might be a speckle pattern in each exposure, the averaging over different sphere configurations results in a smoothly varying signal. This is made clear by plotting in the inset a radial cut averaged over all radial directions (open circles), where the intensity is seen to follow closely the form factor expected for an isolated sphere. On cooling the sample, Fig. 9.20(b), the suspension and the position of the spheres freeze. The speckle pattern is now completely static, and is easily visible directly in the detector images and in the radial cuts, even when averaging over a number of exposures.

|Amplitude|^2 Phase   Reconstructed object

(a) Loop 1

From data   Random

(b) Loop 10   Partial Retrieval

(c) Loop 374   Full Retrieval
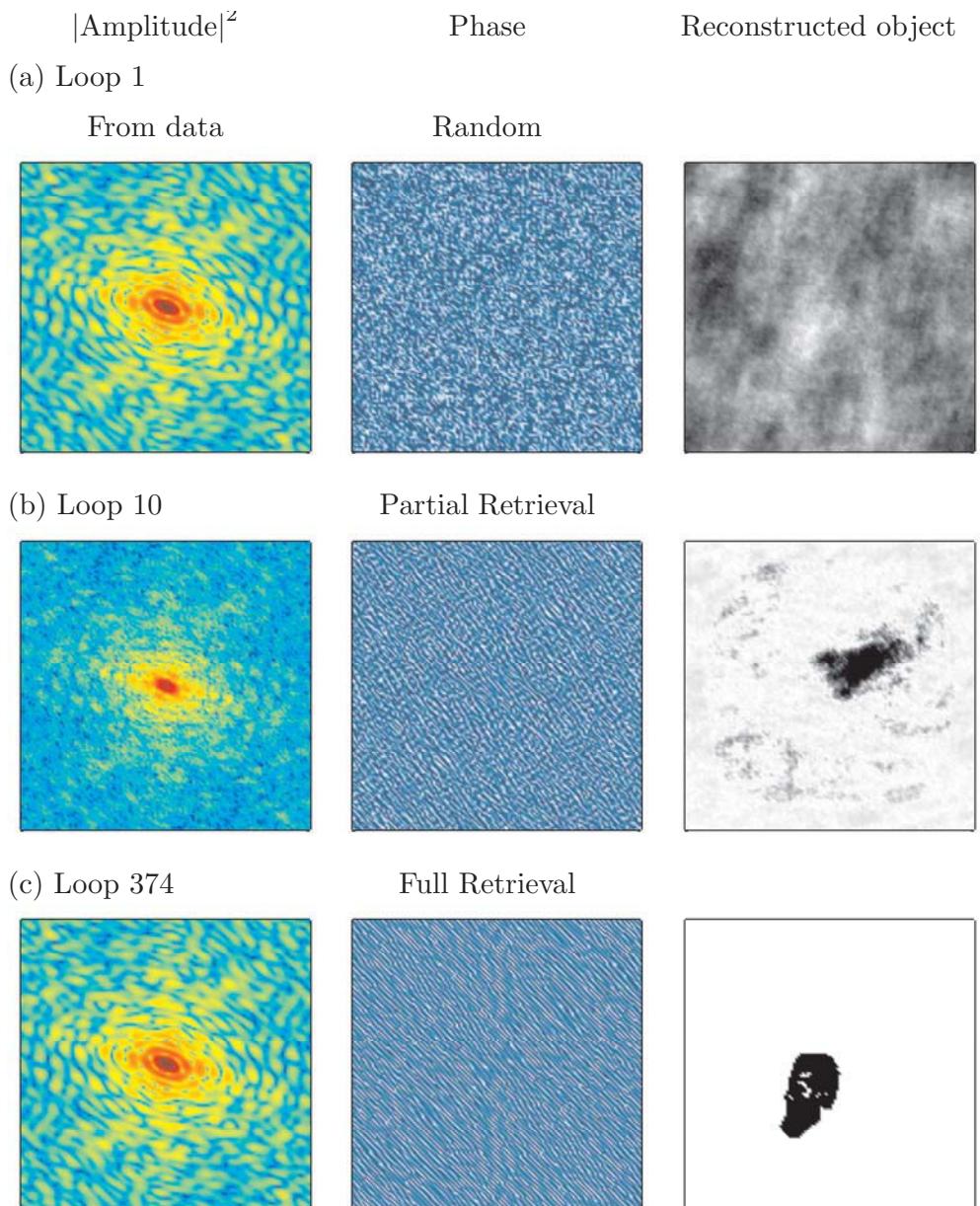
Fig. 9.22 Numerical example of phase retrieval using an iterative, phase retrieval algorithm that proceeds in a number of loops. The test object and its calculated diffraction pattern are given in Fig. 9.21.

9.4.2 Phase retrieval via oversampling

Solving the phase problem using coherent X-ray diffraction imaging relies first and foremost on the concept of oversampling of a diffraction pattern.

We know from the Laue condition that the diffraction pattern from an extended, three-dimensional crystal consists in essence of a series of delta functions, $\delta(\mathbf{Q} - \mathbf{G})$, in reciprocal space. It can therefore be measured, or sampled, when $\mathbf{Q} = \mathbf{G}$ only. The frequency of the sampling in reciprocal space is $|\mathbf{G}| = 2\pi/d$, proportional to the inverse of the unit cell parameter. In signal processing language sampling at a frequency equal to the inverse system size is associated with the name of Nyquist. When sampled at the Nyquist frequency, the diffraction pattern thus provides only half of the possible information: $|A(\mathbf{Q})|$ from the square root of the measured intensity but not the phases. Sayre [Sayre, 1952, 1980] building on earlier work of Shannon [Shannon, 1949] showed that if a diffraction pattern could be sampled at half of the Nyquist frequency, in other words oversampled, then it would be possible to retrieve information on both $|A(\mathbf{Q})|$ and the phases, thus allowing the electron density to be reconstructed. One interpretation of oversampling for the case of spatially limited objects (i.e. rather than crystals) was provided by Miao *et al.* [Miao et al., 1998] who proposed that it corresponds to surrounding the sample with a no-density region, and that once this exceeds the volume of the region in which the electron density is non-zero then the phases can be retrieved.

For oversampling to be possible, the diffraction pattern itself must be extended in reciprocal space. This occurs naturally when dealing with any finite-sized single object, be it non-crystalline or crystalline in nature. For example, in the case of a single molecule, there are no Bragg peaks and the diffraction pattern is a continuous function (as discussed in Chapter 4) which can hence be sampled at any $\mathbf{Q}$. Oversampling of the diffraction pattern from a crystalline material is also possible if the crystal itself is finite, as a crystal of volume L^3 in direct space, produces a diffraction pattern occupying a volume in reciprocal space proportional to $1/L^3$ surrounding each Bragg peak.

While oversampling provides for an unambiguous solution (in 2D or 3D, at least), it does not suggest a practical method of finding it. Formulation as a computer algorithm elegantly incorporates the oversampling as real-space constraints. Fienup (Fienup [1982]) described the numerical implementation of phase retrieval algorithms that apply constraints in different ways. Here we outline the principles and application of one of these, the error-reduction algorithm.

The schematic operation of the error-reducion, iterative algorithm used to retrieve the phases from an oversampled diffraction pattern is shown in Fig. 9.21. The algorithm works by successively Fourier transforming the data between real and reciprocal space, with constraints being applied in both spaces at each step in the iteration. As this requires the processing of numerical data, the appropriate transforms are most efficiently performed using a fast Fourier transform (FFT) protocol (and its inverse the IFFT). The effect of applying the constraints is to gradually reduce the errors in the estimate of the phases. To start the algorithm it is necessary to form an initial guess $\rho'(\mathrm{r})$ of the electron density[7]. This is accomplished by performing an inverse Fourier transform of the scattering amplitude estimated by multiplying the square root of the measured intensities with a random phase factor. Real-space constraints are then applied to $\rho'(\mathrm{r})$. These might include requiring $\rho'(\mathrm{r})$ to be real and positive (although not always), and the application of a mask known as the 'support' which sets $\rho'(\mathrm{r})$ to be zero outside of a region estimated from the spatial distribution of the auto-correlation function of the intensity. The new estimate of electron density $\rho(\mathrm{r})$ is then Fourier transformed to obtain an updated estimate of the complex scattering amplitude. However, only the phase information is retained, as the reciprocal space constraint is applied that the modulus of the complex scattering amplitude must be equal to the square

---

[7]The prime here does not refer to the derivative; rather it signifies an estimate of the electron density before the application of real-space constraints.

root of the measured intensity. The next loop of the iterative procedure then begins and continues until convergence is achieved.

Various loops in the progressive retrieval of the phases of a test object (Fig. 9.21) are summarized in the example shown in Fig. 9.22. In the first step, the complex scattering amplitude is estimated by multiplying the square root of the measured intensity by random phase factors. An inverse Fourier transform is next applied to yield a reconstructed image of the object's electron density. Unsurprisingly at this stage the electron density does not resemble that of the test object. The iterative, phase retrieval algorithm is then executed. Already by loop 10, the phases have been partly retrieved as is evidenced by the correspondence between the simulated and measured intensities, and the emergence of structure in the reconstructed image that begins to resemble the test object. Convergence in this example is achieved after 374 loops of the algorithm.

Example: Imaging of gold nanoparticles

The first demonstration of coherent X-ray diffraction imaging with the phases retrieved using the oversampling method was reported by Miao et al. [1999] who employed a SAXS geometry to image a micron sized non-crystalline sample.

The technique was later extended to crystalline materials by Robinson et al. [2001] who illuminated a gold, nanometre sized crystal with coherent radiation, and then oversampled the extended diffraction pattern emanating from a Bragg peak with a finite reciprocal lattice vector, i.e. not in a SAXS geometry. The application of coherent X-ray diffraction imaging to crystalline materials is illustrated in Fig. 9.23. In real space a finite size crystal can be described mathematically as the multiplication of a function representing the infinite direct lattice and a function, $S(\mathbf{r})$, describing the crystal's morphology. From the convolution theorem, the scattering is the convolution of the Fourier transform of the infinite direct lattice, i.e. the reciprocal lattice, and the Fourier transform of $S(\mathbf{r})$. It follows that each reciprocal lattice point is decorated with a copy of the Fourier transform of $S(\mathbf{r})$, as indicated in Fig. 9.23(a). In this type of imaging, data are usually collected using a two-dimensional, position-sensitive detector which is set to record maps of the extended diffraction pattern in the vicinity of a particular Bragg peak. By taking a series of maps as the sample angle is rotated through the Bragg condition, a three-dimensional data set may be acquired as shown in Fig. 9.23(c). This data set is then processed using the phase retrieval algorithm described above to produce the full electron density in three dimensions. A rendering of the electron density of the nanoparticle is given in Fig. 9.23(b) by showing a number of two-dimensional slices at different heights. For comparison we also show an image taken with a conventional scanning electron microscope of a gold nanoparticle from the same batch as the one analysed with X-rays. This serves to emphasise the fact that coherent X-ray diffraction imaging probes the electron density throughout the entire volume of the sample, whereas an SEM is mostly sensitive to its surface.

Like all forms of microscopy, the spatial resolution achievable with coherent X-ray diffraction imaging is ultimately limited in principle by the wavelength. In practice it is determined by the inverse of the maximum wavevector transfer at which the diffraction pattern can be sampled[8]. This in turn is currently limited by the low coherent flux delivered by synchrotron sources. The image shown in Fig. 9.23(b) is close to the state of the art at the time of writing, and has a spatial resolution of around 30 nm. It is hoped that the future availability of ultra-brilliant, fully (transversely) coherent radiation from free-electron lasers, will allow the resolution of coherent X-ray diffraction imaging to approach the atomic scale.

---

[8]Here the wavevector transfer is measured relative relative to the straight through beam or relative to the Bragg peak of interest, depending on the geometry of the experiment.

(a)

Real Space

Reciprocal Space

(b)

+30 nm   0 nm

-30 nm   SEM
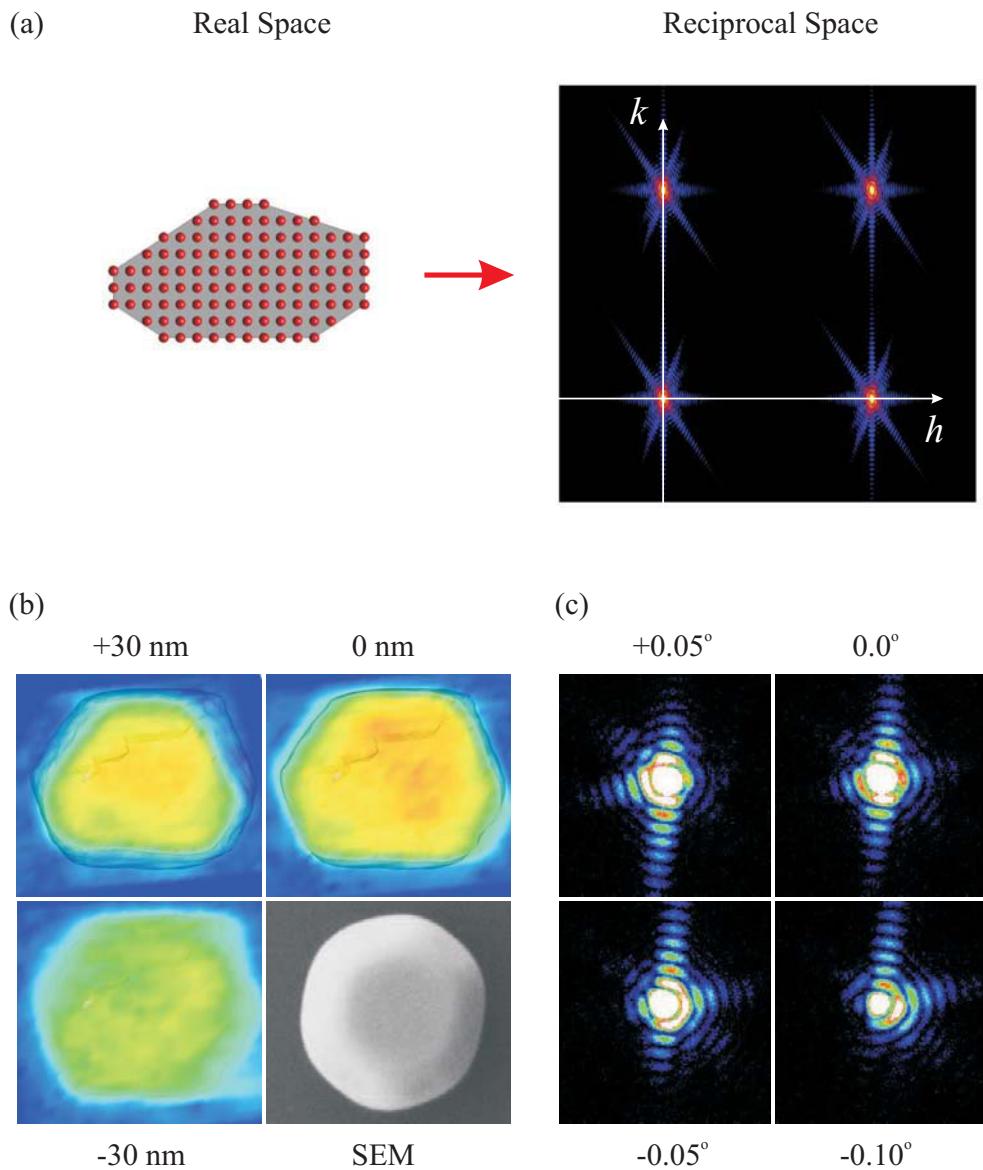
(c)

+0.05°   0.0°

-0.05°   -0.10°

Fig. 9.23 (a) Schematic of a finite sized crystal (left) and its diffraction pattern (right). (c) Coherent X-ray diffraction from a gold nanoparticle. The data were collected on beamline 34-ID-C at the Advanced Photon Source. The four images were collected in a rocking scan through the (111) reflection which is identified by the label 0.0°. Data collected in this way provides information on the three-dimensional structure of the crystal. The field of view of each diffraction pattern is approximately 0.07×0.07 Å^{-2}, and the intensity scale in both (a) and (c) is logarithmic. (b) Colour panels: real space images of the gold nanoparticle reconstructed from the diffraction data shown in (c). The individual images show planes of electron density, plotted on a false colour scale, at different heights through the nanoparticle. These are superimposed with a translucent isosurface (3D contour) of the crystal. The nanoparticle is approximately 180 nm across, and 70 nm deep. Grey-scale panel: SEM image of a gold nanoparticle taken from the same batch as the one used for the diffraction experiments. (Data courtesy of Ian Robinson.)
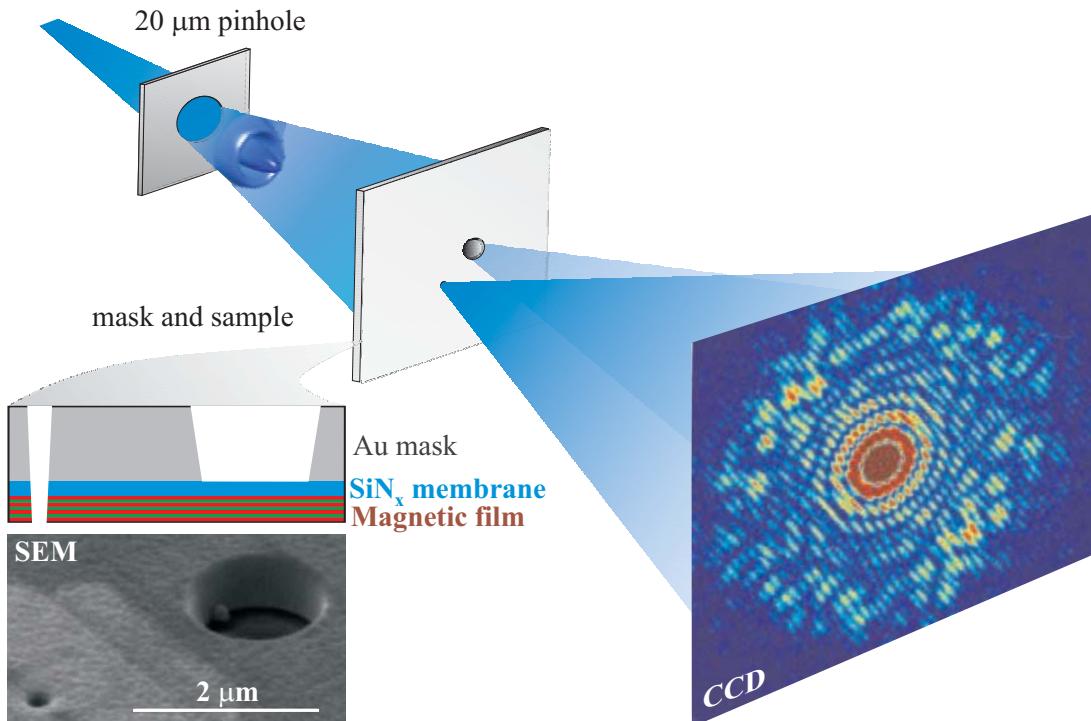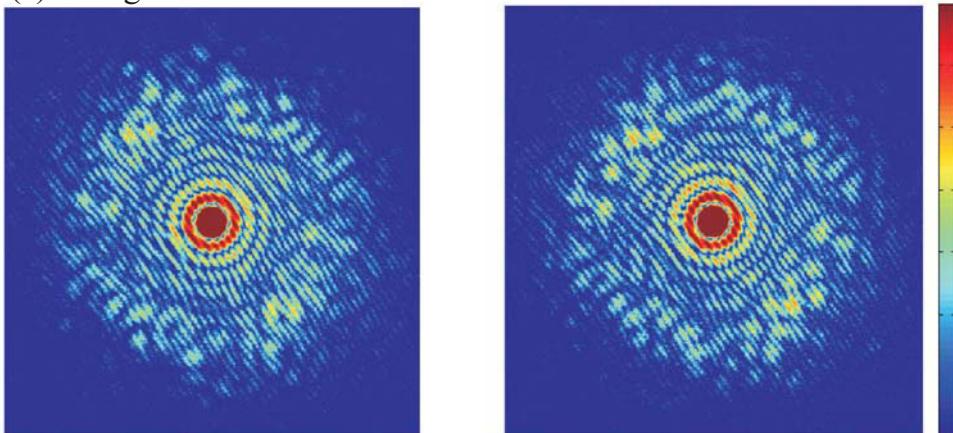
Fig. 9.24 Schematic layout of the experimental setup used to record Fourier transform holograms of magnetic domains on beamline 56 SGM at BESSY-II. Circularly polarized X-rays from an undulator were monochromated by a grating (not shown) and impinged on a 20 μm pin hole which served to define the transverse coherence length of the beam. The X-ray beam illuminated the combined mask and sample which had been grown on a Si_3Ni_4 membrane. The sample was the same Co/Pt multilayer for which an STXM image is shown in Fig. 9.9. The diameter of the sample aperture in the Au mask was 1.5 μm and defined the field of view of the object beam. The reference beam was defined by a conical shaped aperture which tappered down to 100 nm. The holograms were recorded on a CCD camera with the photon energy tuned to the Co L_3 edge (λ=15.9 Å). (Image courtesy of Joachim Stöhr.)

9.5   Holography

X-ray holography has some features in common with coherent diffraction imaging (CDI): it is also a lensless imaging technique that requires coherent radiation. The key difference is that in holography the phase problem is overcome by arranging for a reference beam to interfere with the object beam, i.e. the beam scattered by the sample. X-ray holography has been developed over many years by various groups. The first synchrotron radiation study was performed by Aoki and co-workers in 1972 (Aoki et al. [1972]) who produced holographic images using radiation at λ=6 nm. The great potential of X-ray holography was demonstrated later in 1992 by McNulty et al. (McNulty et al. [1992]), who working at λ=3.4 nm imaged gold nanoparticles with a resolution of around 60 nm.

In Fourier transform holography the interference between the reference and object beams is recorded in the far-field limit. The total scattering amplitude $A_T(\mathbf{Q})$ of the Fraunhofer diffraction pattern is simply the sum of the scattering amplitudes associated with the reference, $A_R(\mathbf{Q})$, and object beams,

Left Circular Polarization   Right Circular Polarization

(a) Holograms

(b) Fourier transform reconstruction
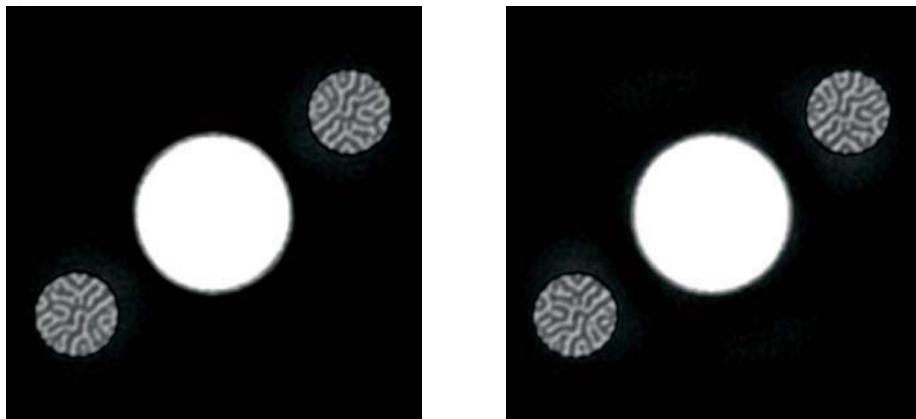
Fig. 9.25 (a) Fourier transform holograms of a Co/Pt multilayer using the setup shown in Fig. 9.24. The holograms were recorded using photons with either left circular polarization (left panel) or right circular polarization (right panel). Typical exposure times were 500 seconds. The images correspond to an area in reciprocal space of 0.067×0.067 nm^{-2}. The series of narrow concentric rings in the centre of the images arise from Fraunhofer diffraction by the sample aperture. A broader ring with a radius of approximately 0.036 nm^{-1} is due to small angle scattering from the domains in the Co/Pt multilayer and is broken up into a series of speckles. (b) Fast Fourier transforms of the holograms shown in (a) where real space images of the magnetic domain pattern in the Co/Pt multilayer appear symmetrically around the central region. Close inspection of the domain images obtained with RCP and LCP reveals that the images are negatives of each other: dark becomes light, and light becomes dark. The reason is that X-ray resonant magnetic scattering measures a projection of the magnetization, which is reversed for RCP and LCP. (Images courtesy of Joachim Stöhr.)

$A_O(\mathbf{Q})$. It follows that the intensity recorded in the hologram is

$$|A(\mathbf{Q})_T|^2 = |A(\mathbf{Q})_R + A(\mathbf{Q})_O|^2$$
$$= |A(\mathbf{Q})_R|^2 + |A(\mathbf{Q})_O|^2 + A(\mathbf{Q})_R A(\mathbf{Q})_O^* + A(\mathbf{Q})_O A(\mathbf{Q})_R^*$$

Thus in addition to encoding information on the contributions from the object and reference beams

(a) Reconstruction from holography   (b) STXM

(c) Comparison of line profiles
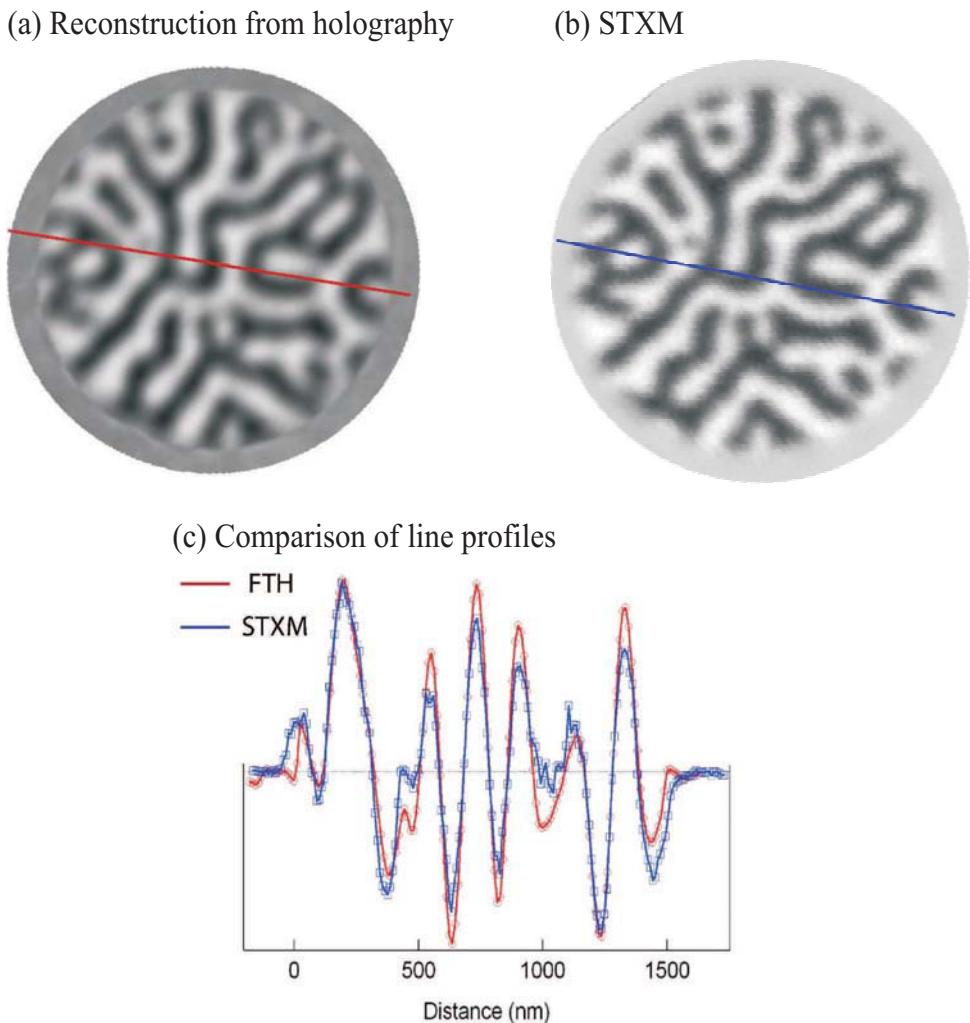
Fig. 9.26 Comparison of images of the magnetic domain structure in a Co/Pt multilayer obtained with Fourier transform holography (a) and STXM (b). (c) Shows the results of taking a line cut through the images and demonstrates that the two techniques have comparable spatial resolution. (Images courtesy of Joachim Stöhr.)

separately (the first two 'auto-correlation' terms in the above), the hologram also records information on the cross correlation between the reference and object beams and its conjugate (the last two terms).

To illustrate how an image of the real space structure is obtained in practice from a recorded hologram, we consider the example shown in Fig. 9.24 due to Eisebitt et al. [2004]. In this example the sample is a Co/Pt magnetic multilayer. It is in fact the same sample for which the image recorded with STXM is shown in Fig. 9.9(b). Contrast with sensitivity to magnetism for the STXM image is provided by XMCD. As noted in Section 7.3, resonant absorption implies resonant scattering (the two sides of the same coin), and the hologram in the present example is formed from resonant scattering which includes a magnetic component. To isolate the purely magnetic scattering, holograms are recorded with both right-circularly and left-circularly polarized light as shown in Fig. 9.25(a), and then their difference

taken. As the reference beam is provided by a hole drilled through the sample, it does not experience a phase shift and hence $A(\mathbf{Q})_R$ is real. The fact that it is also offset laterally from the object beam has the consequence that the cross-correlation terms $A(\mathbf{Q})_R A(\mathbf{Q})_O^*$ and $A(\mathbf{Q})_O A(\mathbf{Q})_R$ produce features that are spatially separated from the auto-correlation terms when the hologram is Fourier transformed into real space. This is clear from inspection of Fig. 9.25(b) which shows the Fast Fourier Transforms (FFT) of the images shown in Fig. 9.25(a). The bright central region of the FFT arises from the auto-correlation terms, while the twin diagonal features arise from the cross terms. Finally, since the reference hole is much smaller than the object hole, the former may be approximated by a delta function, which means that to a good approximation the twin diagonal features then represent real space images of the magnetic scattering amplitude[9].

In Fig. 9.26 we show a comparison of the magnetic domain patterns of the Co/Pt multilayer obtained with STXM and Fourier transform holography, where it is apparent that the data from the two techniques are in good agreement with comparable resolution. In both cases the ultimate resolution is of course determined by the wavelength of the X-rays, but in practice for STXM it is limited by the outer zone width of the Fresnel zone plate, while for Fourier transform holography it is the finite size of the reference beam.

9.6 Further reading

Soft X-rays and Extreme Ultraviolet Radiation: Principles and Applications, David Attwood (Cambridge University Press, 2007).

Optics, Eugene Hecht (Addison Wesley, 2001).

Coherent X-ray Optics, David Paganin (Oxford University Press, 2006).

Magnetism: From Fundamentals to Nanoscale Dynamics, J. Stöhr and H.C. Siegmann (Springer, 2006).

9.7 Exercises

9.1 In conventional projection radiography the subject contrast is defined by $C = (I_A - I_B)/I_A$ where A and B refer to two parallel paths that the X-ray takes through the patient, and where $I_A > I_B$. Calculate C for the situation where path A is of length z_1 with absorption coefficient μ_1, and path B comprises first a length of $(z_1 - z_2)$ with absorption coefficient μ_1 followed by a length z_2 with absorption coefficient μ_2.

9.2 The human femur has a diameter of around 3 cm. Calculate the energy dependence of the contrast C expected in a projection radiograph of the human femur. (μ (bone,muscle) in units of cm^{-1}: 30 keV (1.7, 0.38); 50 keV (0.57, 0.23); 100 keV (0.30, 0.17); 150 keV (0.24, 0.15).)

---

[9]From the convolution theorem, the Fourier transform of the cross term $A(\mathbf{Q})_O A(\mathbf{Q})_R$ becomes a convolution of the Fourier transforms of the two amplitudes. If the Fourier transform of $A(\mathbf{Q})_R$ is a delta function, then the convolution integral yields the Fourier transform of $A(\mathbf{Q})_O$, which in the example considered is a real space image of the projection of the magnetic moment along the incident beam direction.

9.3 Estimate the contrast C of the rib bones expected in a projection radiograph of the human chest. Estimate the contrast for a lung tumour of 5 cm thickness. (At 50 keV, μ in units of cm^{-1}: chest wall, 0.15; rib bone, 0.57; lung, 0.06; tumour, 0.13.)

9.4 X-ray imaging of cells can be performed using the absorption contrast between water and organic matter in the so-called 'water window' at energies below the oxygen K edge but above the carbon K edge. (a) Estimate the limits in energy of the water window using the solution to Exercise 7.11. (b) Very roughly speaking, the elemental composition of proteins is 53% carbon, 23% oxygen, 17% Nitrogen and 7% Hydrogen. Estimate the X-ray absorption lengths of water and protein at 500 eV. You may neglect the contribution from hydrogen. (μ/ρ_m [cm^2/g] at 500 eV: 1.37×10^4, C; 1.85×10^4, N; 1.36×10^3, O.)

9.5 The MATLAB function given below is designed to retrieve the phases of a one-dimensional density distribution rho_in using the error-correcting algorithm described in the text.

    (a)   Study the code with the aim of understanding how it works.

    (b)   Incorporate the function in a MATLAB programme (or convert the function to an alternative computing language) to explore the robustness of the algorithm in recovering different density distributions.

    (c)   Explore possible improvements to the algorithm.

```
1  function [rho]=phaseret(rho_in,n_iter)
2  %
3  % Retrieves phases and reconstucts rho
4  %
5  In=abs(fft(rho_in)).^2;                % calculate intensities from input electron density
6  pha=2*pi*(rand(1,length(In))-0.5);     % random phases
7  rho=ifft(sqrt(In).*exp(sqrt(-1)*pha)); % initialise: use sqrt(In) and random phases
8
9  rho=abs(rho);                          % real space constraints: rho real and positive
10 s=log(conv(fftshift(In),fftshift(In)));% form mask from autocorrelation function
11 mask=s(1:2:end)./max(s(1:2:end)); mask(find(mask<0.5))=0; mask(find(mask>0.5))=1;
12
13 for ii=1:n_iter;
14
15     % mask rho
16     rho=rho.*mask;
17
18     % improved amplitude from sqr(In) and new phases
19     A=sqrt(In).*exp(sqrt(-1)*angle(fft(rho)));
20
21     % back into real space and apply constraints
22     rho=ifft(A); rho=abs(rho);
23
24 end
```

9.6 Referring to the silicon wafer depicted in Fig. 9.13, calculate the transmission and the refracted angle versus the beam position across the wedge. Take the X-ray wavelength as 1.12 Å, for which the attenuation length of silicon is 184 μm.

9.7 This exercise deals with the smearing of the triangular intensity pattern of the lower panel in Fig. 9.17. The intensity after smearing is indicated in the figure by the red line, which represents the folding of the triangular pattern of period p with a Gaussian of r.m.s. width σ.

    (a)   Show that the maximal intensity is reduced by a factor $[1 - (4/\sqrt{2})(\sigma/p)]$, and discuss why this result is valid only when $(\sigma/p) \ll 1$.

(b)   Using the result from part (a), show that the visibility V varies linearly with (σ/p) when $(\sigma/p) \ll 1$, and sketch the entire dependence of V versus (σ/p).

9.8   In this exercise you are required to estimate the spatial resolution achievable in a coherent diffraction imaging experiment of a gold nanoparticle (see Fig. 9.23). You may assume that the particle has a diameter of around 200 nm, a unit cell parameter of 0.4 nm, and is illuminated with a coherent beam of intensity 10^{10} photons/s and area $10 \times 10 \, \mu m^2$.

9.9   A binary, $\pi-$phase Fresnel zone plate has an outer zone width of 50 nm and a depth 20 times the width, filled with Au. The diameter D of the lens is 100 μm. Determine the wavelength λ and the first order focal length f. Estimate the depth of focus.

A

Scattering and absorption cross-sections

Basic definitions

In this section the basic definitions of the cross-section are recalled for processes that involve either the scattering or absorption of an X-ray photon. The cross-section is an important quantity, as it is the meeting point of experiment and theory. Although its definition is straightforward, confusion sometimes arises as there are several, but essentially equivalent, definitions. As illustrated in Fig. A.1 the definition depends on the situation considered, and in particular on whether or not the cross-sectional area of the beam is larger or smaller than that of the sample.

We start by considering the *scattering* event shown in Fig. A.1(a) in which an X-ray beam of intensity I_0 photons per second is incident on a sample, and where the sample is large enough that it intercepts the entire beam. Our objective is to calculate the number of X-ray photons, I_{sc}, scattered per second into a detector that subtends a solid angle $\Delta\Omega$. If there are N particles in the sample per unit area seen along the beam direction, then I_{sc} will be proportional to N and to I_0. It will of course also be proportional to $\Delta\Omega$. Most importantly it will depend on how efficiently the particles in the sample scatter the radiation. This is given by the *differential cross-section*, $(d\sigma/d\Omega)$, so that we may write

$$I_{sc} = I_0 \, N \, \Delta\Omega \left(\frac{d\sigma}{d\Omega} \right)$$

Thus the differential cross-section per scattering particle is defined by

$$\left(\frac{d\sigma}{d\Omega} \right) = \frac{\text{No. of X-ray photons scattered per second into } \Delta\Omega}{I_0 \, N \Delta\Omega} \tag{A.1}$$

Here no restriction has yet been placed on whether or not the scattering event is elastic or inelastic.

The corresponding absorption experiment is simpler to analyse, as the detector is placed directly in the incident beam, and the change in intensity recorded when a sample is introduced into the beam.
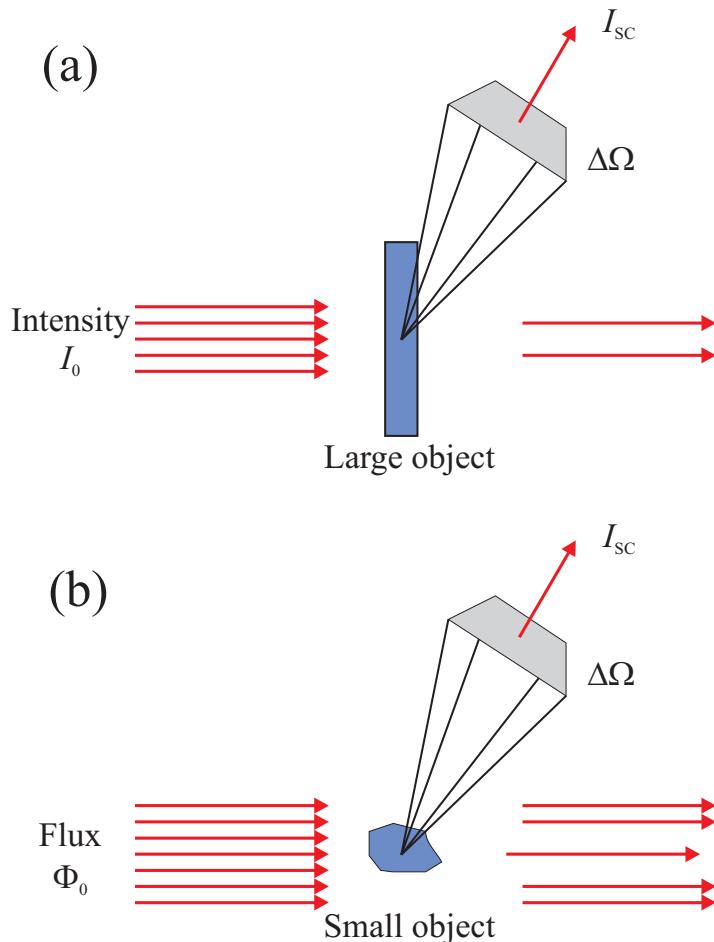
Fig. A.1 (a) A beam is incident on a sample with a larger cross-sectional area. In this case the intensity I_{sc} scattered into a solid angle $\Delta\Omega$ is proportional to the incident *intensity* I_0 of the beam, i.e. the number of photons per second. (b) A beam is incident on a sample with a smaller cross-sectional area. Now the scattered intensity I_{sc} is proportional to the incident *flux* Φ_0 of the beam, i.e. the number of photons per second per unit area.

The number of absorption events, $W_{4\pi}$, per second is proportional to I_0 and N as before. The subscript is used to remind us that the photoelectron liberated from the atom in the absorption process may be emitted into any direction in 4π steradians. The *absorption cross-section*, σ_a, is defined by

$$W_{4\pi} = I_0 N \sigma_a$$

so that

$$\sigma_a = \frac{W_{4\pi}}{I_0 N}$$

Alternatively a different situation could have been imagined in which the incident beam is larger than the sample, as shown in Fig. A.1(b). It should be clear that in this case it is necessary to consider

the *flux* of the incident beam, i.e. the number of photons per second per unit area, and not its intensity. The scattered intensity is now given by

$$I_{sc} = \Phi_0 \, \Delta\Omega \left(\frac{d\sigma}{d\Omega} \right) \tag{A.2}$$

where Φ_0 is the flux of the incident beam, and the differential cross-section refers to the whole sample. The absorption cross-section for this geometry is

$$\sigma_a = \frac{W_{4\pi}}{\Phi_0}$$

These are the definitions of the cross-sections which are operational for analysis of an experiment. Having defined what exactly is meant by the cross-section the next question is how it may be calculated. The classical description of the scattering of an electromagnetic wave by a single electron is used in Chapter 1 and Appendix B to derive the Thomson scattering cross-section. This description is usually sufficient in many fields such as reflectivity, crystallography, etc. In contrast there is no classical model of the absorption process, and instead a quantum mechanical approach must be taken.

Quantum mechanical treatment

In a quantum mechanical treatment the scattering process is described by time-dependent perturbation theory. The interaction between the incident radiation and sample is specified by an Hamiltonian $\mathcal{H}_I$, which produces transitions between the initial $|i\rangle$ and final $|f\rangle$ states. Here $|i\rangle$ and $|f\rangle$ refer to the *combined* states of the X-ray field and sample. The number of transitions, W, per second between $|i\rangle$ and $|f\rangle$ is given in first-order perturbation theory by Fermi's Golden Rule as

$$W = \frac{2\pi}{\hbar} \left| M_{if} \right|^2 \rho(\mathcal{E}_f) \tag{A.3}$$

where the matrix element $M_{if} = \langle f | \mathcal{H}_I | i \rangle$, and $\rho(\mathcal{E}_f)$ is the density of states, defined such that $\rho(\mathcal{E}_f) d\mathcal{E}_f$ is the number of final states with energy in the interval $d\mathcal{E}_f$ centered around $\mathcal{E}_f$. (The correct dimensions of 1/[time] for W can be confirmed by inspection.)
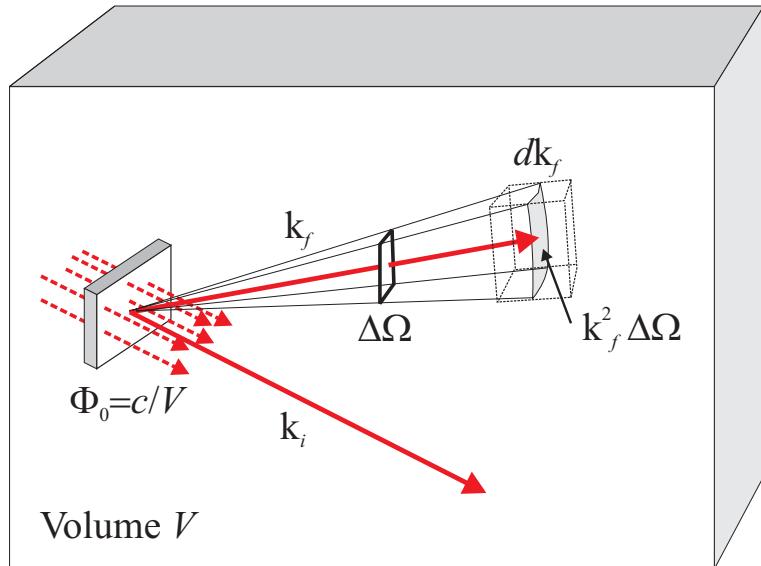
Scattering

To evaluate the differential cross-section for scattering the number of transitions per second into the solid angle $\Delta\Omega$ needs to be found, and as we are mostly interested in elastic scattering, the restriction $\mathcal{E}_f = \mathcal{E}_i$ needs to be placed.

Here we follow the standard method to calculate the density of states $\rho(\mathcal{E}_f)$, where it is assumed that the total system (X-rays + sample) occupies a box of volume V. Periodic boundary conditions are applied to the X-ray wavefunctions, resulting in a uniform density of states in wavevector of $V/(2\pi)^3$. By definition $\rho(\mathcal{E}_f) d\mathcal{E}_f$ is the number of states with energy between $\mathcal{E}_f$ and $\mathcal{E}_f + d\mathcal{E}_f$, which is equal to the number of states with wavevectors between k_f and $k_f + dk_f$. We can therefore write

$$\rho(\mathcal{E}_f) d\mathcal{E}_f = \left(\frac{V}{8\pi^3} \right) d\mathbf{k}_f$$

(a) Scattering

(b) Absorption
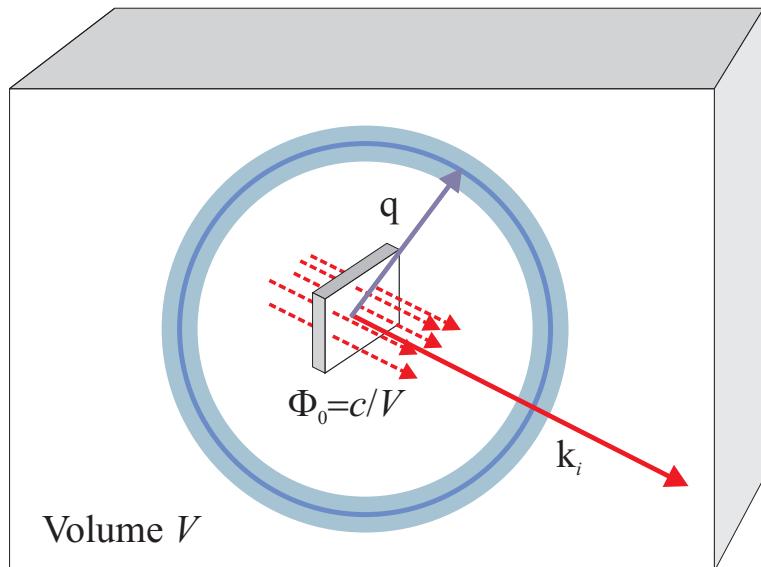
Fig. A.2 Illustration of the quantum mechanical derivation of (a) the differential scattering and (b) the absorption cross-sections. For the differential scattering cross-section, one must integrate over the values of $\mathbf{k}_f$ accessible within the solid angle element $\Delta\Omega$. For the photoelectric absorption cross-section all directions of the expelled electron must be integrated over. In both cases, energy conservation is ensured by introducing a delta function in the integrand.

or

$$\rho(\mathcal{E}_f) = \left(\frac{V}{8\pi^3}\right)\frac{d\mathbf{k}_f}{d\mathcal{E}_f} \tag{A.4}$$

The differential cross-section can then be calculated from Eq. (A.2) and (A.3) as

$$\left(\frac{d\sigma}{d\Omega}\right) = \frac{W_{\Delta\Omega}}{\Phi_0\Delta\Omega}$$

where $W_{\Delta\Omega} \equiv I_{sc}$ is the number of transitions per second into $\Delta\Omega$. The restriction on elastic scattering events is introduced by including a delta function $\delta(\mathcal{E}_f - \mathcal{E}_i)$ in Eq. (A.3), and then integrating over all $\mathcal{E}_f$, which yields

$$W_{\Delta\Omega} = \frac{2\pi}{\hbar}\int |M_{if}|^2\,\rho(\mathcal{E}_f)\,\delta(\mathcal{E}_f - \mathcal{E}_i)\,d\mathcal{E}_f \tag{A.5}$$

According to Eq. (A.4)

$$\rho(\mathcal{E}_f) = \left(\frac{V}{8\pi^3}\right)\mathbf{k}_f^2\left(\frac{d\mathbf{k}_f}{d\mathcal{E}_f}\right)\Delta\Omega$$

where the differential volume element $d\mathbf{k}_f$ has been replaced by $\mathbf{k}_f^2 d\mathbf{k}_f\Delta\Omega$ as indicated in Fig. A.2. The expression for $W_{\Delta\Omega}$ may be simplified considerably. Since $\mathcal{E}_f = \hbar\mathbf{k}_f c$, it follows that

$$\mathbf{k}_f^2\left(\frac{d\mathbf{k}_f}{d\mathcal{E}_f}\right) = \frac{1}{\hbar^3 c^3}\,\mathcal{E}_f^2 \tag{A.6}$$

With the flux given by $\Phi_0 = c/V$, we obtain

$$\boxed{\left(\frac{d\sigma}{d\Omega}\right) = \left(\frac{V}{2\pi}\right)^2\frac{1}{\hbar^4 c^4}\int |M_{if}|^2\mathcal{E}_f^2\,\delta(\mathcal{E}_f - \mathcal{E}_i)\,d\mathcal{E}_f} \tag{A.7}$$

Absorption

Calculation of the absorption cross-section proceeds along similar lines, with two main differences. The first is that the condition on the δ function that appears in Eq. (A.5) is altered, since the process is no longer elastic. In an absorption process the incident photon expels an electron from an atom with binding energy $\mathcal{E}_b$. The difference between the energy of the incident photon, $\mathcal{E} = \hbar\omega$, and the binding energy of the electron, $\mathcal{E}_b$, is the kinetic energy of the photoelectron, $\mathcal{E}_{pe} = \hbar^2\mathbf{q}^2/2m$. The second difference is that there is no restriction on the direction of $\mathbf{q}$, the wavevector of the photoelectron, so that instead of integrating over the states in $\Delta\Omega$, as was the case for the scattering cross-section, it is now necessary to integrate over the entire solid angle of 4π. Thus the absorption cross-section is

$$\sigma_a = \frac{W_{4\pi}}{\Phi_0}$$

with

$$W_{4\pi} = \int \frac{2\pi}{\hbar}|M_{if}|^2\,\rho(\mathcal{E}_{pe})\,\delta(\mathcal{E}_{pe} - (\mathcal{E} - \mathcal{E}_b))d\mathcal{E}_{pe}$$

The density of states for the photoelectron is evaluated using the same box normalization introduced for the density of X-ray states in the case of scattering discussed above. The result for the photoelecton is

$$\rho(\mathcal{E}_{pe}) = 2\left(\frac{V}{8\pi^3}\right)\left(\frac{d\mathbf{q}}{d\mathcal{E}_{pe}}\right)$$

where the factor of 2 allows for the two possible spin states of the electron. The absorption cross-section is evaluated by replacing the volume element $d\mathbf{q}$ in the above by $q^2 \sin\theta dqd\theta d\varphi$, with the integral taken over the entire solid angle of 4π, as indicated in Fig. A.2(b). It follows that the absorption cross-section is

$$\sigma_a = \frac{2\pi}{\hbar c}\frac{V^2}{4\pi^3}\int|M_{if}|^2\,\delta(\mathcal{E}_{pe}-(\mathcal{E}-\mathcal{E}_b))\,q^2\,\sin\theta dqd\theta d\varphi \qquad \text{(A.8)}$$

where once again the incident flux is given by $\Phi_0 = c/V$.

It remains of course to calculate the matrix elements M_{if} of the interaction Hamiltonian: this is described in Appendix C for the Thomson scattering cross-section, and in Chapter 7 for the absorption cross-section.

Further reading

Quantum Mechanics, A.I.M. Rae (Adam Hilger, 1986)

Quantum Mechanics, F. Mandl (John Wiley & Sons, 1992)

Classical electric dipole radiation

In Chapter 1 a classical model was used to describe the scattering of X-rays by electrons. The equation relating the strength of the radiated to incident X-ray electric fields (Eq. 1.5) was stated without proof. Here the derivation of this equation is outlined more fully.

We imagine that an electromagnetic plane wave with an electric field $\mathbf{E}_{in}$ is incident on a charge distribution, which oscillates in response to this driving field, and hence acts as a source of radiation. The problem then is to evaluate the radiated electric field at some observation point X, as shown in Fig. B.1(a). This is simplified considerably if it is assumed that r is much greater than the spatial extent of the charge distribution, and also if r is much greater than the wavelength of the radiation λ. The first of these is the *dipole approximation*, while the second assures that we can interpret the electromagnetic effects at X as radiation. Here it is further assumed that the electrons forming the charge distribution are free.

The electric and magnetic fields at X can be derived from the scalar potential Φ and the vector potential $\mathbf{A}$:

$$\mathbf{E} = -\nabla\Phi - \frac{\partial \mathbf{A}}{\partial t}$$

and

$$\mathbf{B} = \nabla \times \mathbf{A} \tag{B.1}$$

The task of evaluating the fields at X is further simplified if it is recalled that electromagnetic waves are transverse, with the fields being perpendicular to the propagation direction $\mathbf{n}$, as shown in Fig. B.1(b). We then have that $\mathbf{n}$ is colinear to $\mathbf{E} \times \mathbf{B}$, and by solving the wave equation it can be shown that $|\mathbf{E}| = c|\mathbf{B}|$. It is therefore sufficient to derive $\mathbf{B}$ from $\mathbf{A}$ (Eq. (B.1)), and then $\mathbf{E}$ follows immediately.

The vector potential is given by

$$\mathbf{A}(\mathbf{r}, t) = \frac{1}{4\pi\epsilon_0 c^2} \int_V \frac{\mathbf{J}(\mathbf{r}', t - |\mathbf{r} - \mathbf{r}'|/c)}{|\mathbf{r} - \mathbf{r}'|} \, d\mathbf{r}'$$

where $\mathbf{J}(\mathbf{r}', t)$ is the current density of the source. As the fields propagate at a finite velocity, the fields experienced at the observation point X at time t depend on the position of the electron at an earlier time $t - |\mathbf{r} - \mathbf{r}'|/c$. For this reason $\mathbf{A}$ given by the above is known as the *retarded* vector potential.

The *dipole approximation* allows us to ignore $\mathbf{r}'$ in comparison with $\mathbf{r}$, so that

$$\mathbf{A}(\mathbf{r}, t) \approx \frac{1}{4\pi\epsilon_0 c^2 \mathrm{r}} \int_V \mathbf{J}(\mathbf{r}', t - \mathrm{r}/c)\, d\mathbf{r}'$$

To proceed it is noted that the current density is equal to the product of the charge density ρ and the velocity $\mathbf{v}$,

$$\mathbf{J} = \rho\mathbf{v}.$$

For a distribution of discrete charges q_i the integral is replaced by a sum so that

$$\int_V \mathbf{J}\, d\mathbf{r}' = \int_V \rho\mathbf{v}\, d\mathbf{r}' = \sum_i q_i\mathbf{v}_i = \frac{d}{dt'}\sum_i q_i\mathbf{r}_i'$$

The last term is recognizable as the time derivative of the electric dipole moment which is written as $\dot{\mathbf{p}}$.

We now let the incident beam be linearly polarized along the z axis, so that the dipole moment and hence the vector potential will have a component along this direction only (Fig. B.1(b)). Thus for a single dipole we have

$$A_z = \left(\frac{1}{4\pi\epsilon_0 c^2 \mathrm{r}}\right)\dot{p}(t')$$

and $A_x = A_y = 0$. From Eq. (B.1) the components of the $\mathbf{B}$ field follow as

$$B_x = \frac{\partial A_z}{\partial y}; \qquad B_y = -\frac{\partial A_z}{\partial x}; \qquad B_z = 0 \tag{B.2}$$

For the x component of the $\mathbf{B}$ field we evaluate the partial derivative of A_z with respect to y as

$$\frac{\partial A_z}{\partial y} = \left(\frac{1}{4\pi\epsilon_0 c^2}\right)\frac{\partial}{\partial y}\left(\frac{\dot{p}(t')}{\mathrm{r}}\right)$$

$$= \left(\frac{1}{4\pi\epsilon_0 c^2}\right)\left[\frac{1}{\mathrm{r}}\frac{\partial \dot{p}(t')}{\partial y} - \frac{\dot{p}(t')}{\mathrm{r}^2}\frac{\partial \mathrm{r}}{\partial y}\right]$$

Since we are interested in the far-field limit of $\mathbf{B}$, we can neglect the second term in the above, while the partial derivative of the first term with respect to y can be evaluated by noting that

$$\frac{\partial}{\partial y} = \frac{\partial}{\partial t'}\frac{\partial t'}{\partial y}$$

$$= \frac{\partial}{\partial t'}\frac{\partial}{\partial y}\left(t - \frac{1}{c}\sqrt{x^2 + y^2 + z^2}\right)$$

$$= -\frac{1}{c}\left(\frac{y}{\mathrm{r}}\right)\frac{\partial}{\partial t'}$$
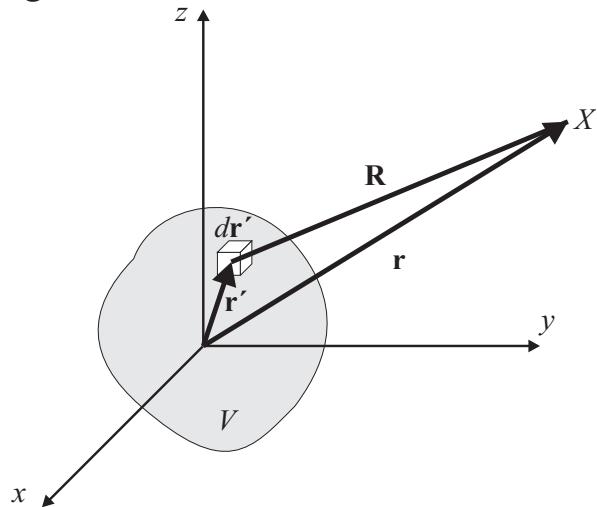
Hence the x component of the $\mathbf{B}$ field in the far field limit is

$$B_x \approx -\left(\frac{1}{4\pi\epsilon_0 c^2}\right)\frac{1}{c\mathrm{r}}\ddot{p}(t')\left(\frac{y}{\mathrm{r}}\right)$$

and the y component follows by interchanging x and y, and allowing for the minus sign in Eq. (B.2). Recalling that $\ddot{p}(t')$ is implicitly along the z axis we can generalize to any direction of $\ddot{\mathbf{p}}(t')$ by writing

$$\mathbf{B} \approx \left(\frac{1}{4\pi\epsilon_0 c^2}\right)\frac{1}{c\mathrm{r}}\ddot{\mathbf{p}}(t') \times \hat{\mathbf{r}}$$

(a) Charge distribution

(b) Electric dipole
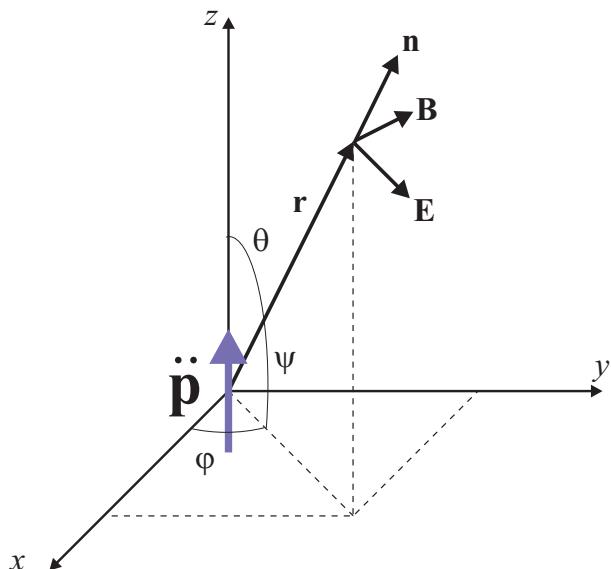
Fig. B.1 (a) The coordinate system used to calculate the electromagnetic field radiated from a charge distribution when placed in an incident plane wave. (b) An electromagnetic plane wave polarized with its electric field along the z axis forces an electric dipole at the origin to oscillate. In the far-field limit the field radiated from the dipole is approximately a plane wave with the **E** and **B** fields perpendicular to the propagation direction as indicated in the figure.

where $\hat{\mathbf{r}}$ is the unit vector $(x/\mathrm{r}, y/\mathrm{r}, z/\mathrm{r})$. The numerical value of the vector cross product is $\ddot{\mathrm{p}}\cos\psi$ where ψ is defined in Fig. B.1(b). The direction of the electric field is perpendicular to both $\hat{\mathbf{r}}$ and $\mathbf{B}$ in such a way that the cross product of $\mathbf{E}\times\mathbf{B}$ is along $\hat{\mathbf{r}}$. In particular we note that for $\psi=0$ the $\mathbf{E}$ field has the *opposite* direction of $\ddot{\mathrm{p}}$. Its magnitude is given by $|\mathbf{E}|=c|\mathbf{B}|$ so that

$$\mathrm{E}(t) = -\left(\frac{1}{4\pi\epsilon_0 c^2}\right)\frac{1}{\mathrm{r}}\ddot{\mathrm{p}}(t')\cos\psi \tag{B.3}$$

The next step is to calculate the magnitude of $\ddot{\mathrm{p}}$ in terms of the incident driving field $\mathrm{E}_{\mathrm{in}} = \mathrm{E}_0 e^{-i\omega(t-\mathrm{r}/c)}$. By definition we have

$$\ddot{\mathrm{p}} = q\ddot{z} = q\,\frac{\mathrm{Force}}{\mathrm{mass}} = q\,\frac{q\,\mathrm{E}_{\mathrm{in}}}{m} = \frac{q^2}{m}\mathrm{E}_0 e^{-i\omega(t-\mathrm{r}/c)}$$

which when inserted into Eq. (B.3) with $q=-e$, and remembering that $\omega/c=\mathrm{k}$, leads to

$$\mathrm{E}(t) = -\left(\frac{e^2}{4\pi\epsilon_0 mc^2}\right)\left(\frac{e^{i\,\mathrm{kr}}}{\mathrm{r}}\right)\mathrm{E}_{\mathrm{in}}(t)\cos\psi$$

The prefactor is the Thomson scattering length r_0, so that the ratio of the radiated to incident electric fields is given by

$$\frac{\mathrm{E}(t)}{\mathrm{E}_{\mathrm{in}}(t)} = -r_0\left(\frac{e^{i\,\mathrm{kr}}}{\mathrm{r}}\right)\cos\psi \tag{B.4}$$

The factor $\cos\psi$ in Eq. (B.3) is the origin of the polarization factor for X-ray scattering, as $\ddot{\mathrm{p}}(t')\cos\psi$ may be thought of as the apparent acceleration as seen by the observer. This is clear if we return to the case when $\mathbf{E}_{\mathrm{in}}$ is along the z axis. If $\psi=0$ the maximum acceleration is observed, whereas for $\psi=90°$ the apparent acceleration is zero. The polarization factor is discussed further in Chapter 1.

We note that the minus sign means that there is a phase shift of π between the incident and scattered fields, and it follows that the index of refraction is necessarily less than unity (see Chapter 3). This result holds in the X-ray region, where most if not all of the atomic electrons may be treated as though they are essentially free. In the visible part of the spectrum, however, we have to allow for the fact that the electrons are bound. This produces resonances in the frequency dependence of the index of refraction, and on the low frequency side of the resonances, corresponding to the visible part of the spectrum, the index of refraction is greater than one.

One way to characterize the efficiency with which an electron scatters the incident radiation is to calculate the total scattering cross-section. The power per unit area is proportional to $|\mathrm{E}|^2$, and by definition the differential cross-section is the power scattered into the solid angle $d\Omega$, normalized by the incident flux (see Appendix A). From Eq. (B.4) it follows that the differential cross-section is

$$\left(\frac{d\sigma}{d\Omega}\right) = r_0^2\cos^2\psi$$

where the factor of r in the denominator of (B.4) cancels on taking the square with a factor of r^2 that arises in converting from surface area to solid angle. The total cross-section for Thomson scattering is

found by integration over the polar angles φ and θ:

$$\sigma_{\scriptscriptstyle T} = r_0^2 \int \cos^2 \psi \, \sin \theta d\theta d\varphi = r_0^2 \int \sin^2 \theta \, \sin \theta d\theta d\varphi = \left(\frac{8\pi}{3}\right) r_0^2$$
$$= 0.665 \times 10^{-24} \text{cm}^2$$
$$= 0.665 \text{ barn} \tag{B.5}$$

The classical cross-section for the scattering of an electromagnetic wave by a free electron is therefore a constant, independent of energy.

Further reading

Foundations of Electromagnetic Theory, J.R. Reitz, F.J. Milford, and R.E. Christy (Addison-Wesley Publishing Company, 1992)

Classical Electromagnetic Radiation, M.A. Heald and J.B. Marion (Saunders College Publishing, 1995)

C

Quantization of the electromagnetic field

The cross-section for either scattering or absorption is evaluated from time-dependent perturbation theory, as outlined in Appendix A. In any perturbation problem it is of course first necessary to specify completely the non-interacting Hamiltonian, $\mathcal{H}_0$, of the system, before the effect of the perturbing Hamiltonian, $\mathcal{H}_I$, may be calculated. For the scattering or absorption of an X-ray this amounts to establishing a quantum mechanical description of both the electromagnetic field and the sample. The former may well be unfamiliar to many readers and here we explain briefly how this is achieved.

The starting point in quantizing the electromagnetic field is the classical expression for its energy in terms of the electric and magnetic fields, both of which may be derived from the vector potential **A** (Appendix B). When seeking a quantum mechanical description of the electromagnetic field it would therefore seem natural to focus on **A**. Indeed quantizing the electromagnetic field amounts to quantizing the vector potential. It also transpires that the Hamiltonian, $\mathcal{H}_I$, that describes the interaction of the X-ray and the sample, is a simple function of **A**. As a consequence the matrix elements of $\mathcal{H}_I$ that enter into the perturbation theory may be calculated readily, and in the last section we work through the example of the Thomson cross-section.

Classical energy density of the radiation field

The total energy of the electromagnetic field in *free space* is

$$\mathcal{E}_{\text{rad}} = \frac{1}{2} \int_V \left[\epsilon_0 \langle \text{E}^2 \rangle + \mu_0 \langle \text{H}^2 \rangle \right] dV$$
$$= \int_V \epsilon_0 \langle \text{E}^2 \rangle \, dV$$

Here it is assumed that the field is confined to some volume V, and $\epsilon_0 \langle \text{E}^2 \rangle = \mu_0 \langle \text{H}^2 \rangle$, where the brackets $\langle \cdots \rangle$ indicate a temporal average. The **E** field is related to vector potential **A** through

$$\mathbf{E} = -\frac{\partial \mathbf{A}}{\partial t}$$

The most general approach for dealing with $\mathbf{A}$ would be to write it as a Fourier sum of plane waves. For clarity we shall consider just one term in this series and write the vector potential as

$$\mathbf{A}(\mathbf{r}, t) = \hat{\varepsilon} A_0 \left[a_\mathbf{k} \, e^{i(\mathbf{k} \cdot \mathbf{r} - \omega t)} + a_\mathbf{k}^* \, e^{-i(\mathbf{k} \cdot \mathbf{r} - \omega t)} \right] \tag{C.1}$$

The direction of $\mathbf{A}$ is specified by the polarization unit vector $\hat{\varepsilon}$, and in addition to the amplitude coefficients $a_\mathbf{k}$ we have introduced a normalization factor A_0. The electric field is

$$\mathbf{E} = \hat{\varepsilon} A_0 \left[(i\omega) a_\mathbf{k} \, e^{i(\mathbf{k} \cdot \mathbf{r} - \omega t)} - (i\omega) a_\mathbf{k}^* \, e^{-i(\mathbf{k} \cdot \mathbf{r} - \omega t)} \right]$$

and its modulus squared is

$$\mathrm{E}^2 = \mathbf{E} \cdot \mathbf{E} = 4\omega^2 A_0^2 \, a_\mathbf{k}^* a_\mathbf{k} \cos^2(\mathbf{k} \cdot \mathbf{r} - \omega t)$$

The temporal average of the modulus squared of the field is

$$\langle \mathrm{E}^2 \rangle = 2\omega^2 A_0^2 \, a_\mathbf{k}^* a_\mathbf{k}$$

since $\langle \cos^2(\mathbf{k} \cdot \mathbf{r} - \omega t) \rangle = \frac{1}{2}$. The total energy of the electromagnetic field is therefore equal to

$$\mathcal{E}_\mathrm{rad} = \epsilon_0 \, 2\omega^2 A_0^2 \, a_\mathbf{k}^* a_\mathbf{k} \, V$$

$$= \hbar \omega a_\mathbf{k}^* a_\mathbf{k} \tag{C.2}$$

where A_0 has been chosen to be equal to

$$A_0 = \sqrt{\frac{\hbar}{2\epsilon_0 V \omega}}$$

It should be emphasized that so far we have only considered one particular $\mathbf{k}$ and polarization state, and in general we would need to sum over these quantities to obtain the total energy.

Quantization of the vector potential, $\mathbf{A}$

The normalization constant A_0 in the last section was chosen to reveal the formal equivalence of the Hamiltonian of the electromagnetic field to that of the harmonic oscillator. The quantum mechanical Hamiltonian of the latter is usually written in the form

$$\mathcal{H}_\mathrm{osc} = \hbar \omega \left(a^\dagger a + \frac{1}{2} \right) \tag{C.3}$$

A direct comparison of this expression with Eq. (C.2) should at least make this equivalence plausible (apart from the additive term of $\frac{1}{2}$ which we shall return to later). The reason for this equivalence is that when our form for $\mathbf{A}$ (Eq. (C.1)) is substituted into the wave equation, the coefficients $a_\mathbf{k}$ obey the equation of motion of the harmonic oscillator.

The operators a and $a^\dagger$ appearing in Eq. (C.3) are known as the annihilation and creation operators, since they have the properties

$$a|n\rangle = \sqrt{n}|n - 1\rangle \tag{C.4}$$

and

$$a^{\dagger}|n\rangle = \sqrt{n+1}|n+1\rangle \tag{C.5}$$

where $|n\rangle$ is an eigenfunction of $\mathcal{H}_{\text{osc}}$ with an eigenvalue

$$\mathcal{E}_n = \hbar\omega(n + \frac{1}{2})$$

and n is an integer $0, 1, 2, \cdots$. We thus quantize the electromagnetic field by requiring that the coefficients $a_{\mathbf{k}}$ in Eq. (C.2) become operators that obey the same commutation relations as the annihilation and creation operators of the harmonic oscillator. Here we must extend our notation to allow for the different possible polarization states of the photon, so that the commutation relations read

$$\left[a_{u\mathbf{k}}, a_{v\mathbf{k}'}^{\dagger} \right] = \delta_{\mathbf{kk}'}\delta_{uv}$$
$$\left[a_{u\mathbf{k}}, a_{v\mathbf{k}'} \right] = \left[a_{u\mathbf{k}}^{\dagger}, a_{v\mathbf{k}'}^{\dagger} \right] = 0$$

where the first subscript, u or v, refers to the polarization state.

The Hamiltonian of the radiation field is thus given by

$$\mathcal{H}_{\text{rad}} = \sum_u \sum_{\mathbf{k}} \hbar\omega_{\mathbf{k}} a_{u\mathbf{k}}^{\dagger} a_{u\mathbf{k}}$$

For a given value of $\mathbf{k}$ and polarization u, the eigenfunctions of $\mathcal{H}_{\text{rad}}$ are $|n_{u\mathbf{k}}\rangle$, where $n_{u\mathbf{k}}$ is the number of photons in that state. The $n_{u\mathbf{k}}$'s are sometimes referred to as the occupation numbers. It follows that a general state of the field, involving photons with different wavevectors and polarizations is a product of such states, since they are all independent. In writing down $\mathcal{H}_{\text{rad}}$ we have followed convention and set the energy of the vacuum state (all $n_{u\mathbf{k}}$=0) equal to $\frac{1}{2}\sum_u \sum_{\mathbf{k}} \hbar\omega_{\mathbf{k}}$.

The operator form of the vector potential is

$$\mathbf{A}(\mathbf{r}, t) = \sum_u \sum_{\mathbf{k}} \hat{\boldsymbol{\varepsilon}}_u \sqrt{\frac{\hbar}{2\epsilon_0 V\omega_{\mathbf{k}}}} \left[a_{u\mathbf{k}}\, e^{i(\mathbf{k}\cdot\mathbf{r}-\omega t)} + a_{u\mathbf{k}}^{\dagger}\, e^{-i(\mathbf{k}\cdot\mathbf{r}-\omega t)} \right] \tag{C.6}$$

The interaction Hamiltonian, $\mathcal{H}_I$

In the absence of any interaction between the photon field of the X-ray and the electrons in the sample the Hamiltonian is

$$\mathcal{H}_0 = \mathcal{H}_e + \mathcal{H}_{\text{rad}}$$

where $\mathcal{H}_e$ refers to the electrons and $\mathcal{H}_{\text{rad}}$ is given above. The eigenfunctions of $\mathcal{H}_0$ are a product of the eigenfunctions of $\mathcal{H}_e$ and $\mathcal{H}_{\text{rad}}$.

Classically, it can be shown[1] that the interactions between an electromagnetic field and a charge q may be allowed for by replacing the momentum $\mathbf{p}$ by $\mathbf{p} - q\mathbf{A}$. For simplicity we shall consider the

---

[1]The substitution of $\mathbf{p}$ by $\mathbf{p} - q\mathbf{A}$ can be shown to produce the correct equation of motion of a charged particle in an electromagnetic field.

case of a free electron for which $\mathcal{H}_e = \mathrm{p}^2/2m$. This allows us to write down the Hamiltonian of the interacting system as

$$\mathcal{H} = \frac{(\mathbf{p} + e\mathbf{A})^2}{2m} + \mathcal{H}_{\mathrm{rad}}$$
$$= \frac{\mathrm{p}^2}{2m} + \frac{e\mathbf{A} \cdot \mathbf{p}}{m} + \frac{e^2\mathrm{A}^2}{2m} + \mathcal{H}_{\mathrm{rad}}$$
$$= \mathcal{H}_e + \mathcal{H}_I + \mathcal{H}_{\mathrm{rad}}$$

where $\mathcal{H}_I$ is the interacting Hamiltonian

$$\mathcal{H}_I = \frac{e\mathbf{A} \cdot \mathbf{p}}{m} + \frac{e^2\mathrm{A}^2}{2m} \tag{C.7}$$

The first term is linear in $\mathbf{A}$ and gives rise to absorption of the X-ray, whereas the second is quadratic in $\mathbf{A}$ and gives rise to scattering, as we shall now explain.

The operator for $\mathbf{A}$ is linear in the annihilation and creation operators. Hence when it acts on a state $|n_{u\mathbf{k}}\rangle$ it can either destroy or create a photon in that state. Absorption corresponds to the former, and it is clear that the first term in $\mathcal{H}_I$ results in absorption. Scattering on the other hand involves the destruction of a photon in one state (labelled by $\mathbf{k}$ say), and the creation of a new photon in a state (labelled by $\mathbf{k}'$). This process then requires a combination of operators of the form $a_{\mathbf{k}'}^{\dagger} a_{\mathbf{k}}$ to act on the product states $|n_{\mathbf{k}}\rangle|n_{\mathbf{k}'}\rangle$ that are the eigenfunctions of $\mathcal{H}_{\mathrm{rad}}$. Such combinations of operators can arise only from a term in the Hamiltonian that is quadratic in $\mathbf{A}$. In the next section we explicitly calculate the cross-section arising from the second term in $\mathcal{H}_I$, and show that it is equivalent to the classical Thomson scattering of an X-ray by an electron. The absorption cross-section is derived from the first term in $\mathcal{H}_I$ in Chapter 7.

Thomson scattering cross-section

We imagine that an X-ray photon of wavevector $\mathbf{k}$ and polarization $\hat{\varepsilon}_u$ is scattered by an electron to $\mathbf{k}'$ and $\hat{\varepsilon}_v$. The scattering is restricted to be elastic, i.e. $\hbar\omega = \hbar\omega'$, which is equivalent to assuming that the energy of the X-ray is large compared to the binding energy of the electron. As the scattering is elastic the electron can be assumed to remain in its ground state $|\mathrm{p}\rangle$. The eigenfunction of the photon field on the other hand changes so that one photon is removed from the state $|n_{u\mathbf{k}}\rangle$, and one photon added to the state $|n_{v\mathbf{k}'}\rangle$. Before the scattering event we have $n_{u\mathbf{k}} = 1$ and $n_{v\mathbf{k}'} = 0$, and after $n_{u\mathbf{k}} = 0$ and $n_{v\mathbf{k}'} = 1$. We therefore write the initial and final eignestates of $\mathcal{H}_0$ as $|i\rangle = |\mathrm{p}\rangle|u1, v0\rangle$ and $|f\rangle = |\mathrm{p}\rangle|u0, v1\rangle$ respectively.

The scattering cross-section is calculated by taking the matrix element of the second term in Eq. (C.7), and using Eq. (A.7). The matrix element we need to evaluate is

$$M_{if} = \langle u0, v1|\langle \mathrm{p}|\frac{e^2}{2m}\mathrm{A}^2|\mathrm{p}\rangle|u1, v0\rangle$$

When we form the square of $\mathbf{A}$ from Eq. (C.6) there will be cross terms in the annihilation and creation operators such as $a_{i\mathbf{k}_k}^{\dagger} a_{j\mathbf{k}_l}$, which can destroy a photon in state $|n_{j\mathbf{k}_l}\rangle$, and create one in state $|n_{i\mathbf{k}_k}\rangle$. These terms give rise to scattering and, as there are two such terms, the matrix element becomes

$$M_{if} = \frac{e^2\hbar}{2m\epsilon_0 V} \frac{[\hat{\varepsilon}_u \cdot \hat{\varepsilon}_v]}{(\omega\omega')^{\frac{1}{2}}} \langle \mathrm{p}|e^{i(\omega-\omega')t}e^{i(\mathbf{k}-\mathbf{k}')\cdot\mathbf{r}}|\mathrm{p}\rangle$$

The cross-section given in Eq. (A.7) involves an integral with respect to the final X-ray energy, $\mathcal{E}_f \equiv \hbar\omega'$, whereas the matrix element is given in terms of ω. We therefore rewrite Eq. (A.7) as

$$\left(\frac{d\sigma}{d\Omega}\right) = \left(\frac{V}{2\pi}\right)^2 \frac{1}{\hbar^2 c^4} \int |M_{if}|^2 \omega'^2 \, \delta(\omega - \omega') \, d\omega'$$

Taking the square of the matrix element and inserting it into the above gives

$$\left(\frac{d\sigma}{d\Omega}\right) = \left(\frac{e^2}{4\pi\epsilon_0 mc^2}\right)^2 [\hat{\boldsymbol{\varepsilon}}_u \cdot \hat{\boldsymbol{\varepsilon}}_v]^2 \, |f(\mathbf{Q})|^2$$

This is the Thomson scattering cross-section, and should be compared with the classical result given in Chapter 1. The two descriptions are entirely equivalent, with the polarization factor given by $P = [\hat{\boldsymbol{\varepsilon}}_u \cdot \hat{\boldsymbol{\varepsilon}}_v]^2$, and the form factor by

$$f(\mathbf{Q}) = \langle p | e^{i\mathbf{Q}\cdot\mathbf{r}} | p \rangle$$

Further reading

Quantum Field Theory, F. Mandl and G. Shaw (John Wiley & Sons, 1996)

D

Gaussian statistics

In scattering theory the problem of evaluating the double sum

$$I(q) = \sum_{n,m} e^{iqr_n} e^{-iqr_m}$$

is often encountered, where the atomic positions r_n vary statistically around some average value. One example is the thermal vibrations of atoms, which leads to a reduction of the intensity of Bragg peaks with increasing wavevector Q as described by the Debye-Waller factor (see Section 5.4). By invoking translational invariance the double sum reduces to $N\langle e^{iqR} \rangle$, where $R = r_n - r_m$, and the brackets indicate an average formed by moving the origin of R over all lattice sites. We shall now prove that if the statistical variation of R is Gaussian then

$$\langle e^{iqR} \rangle = e^{-q^2 \langle R^2 \rangle / 2} \tag{D.1}$$

This is known as the Baker-Hausdorff theorem.

The proof of this theorem follows from the fact that the Fourier transform of a Gaussian is a Gaussian, as shown in Appendix E. Here a normalized Gaussian in one dimension is used, which has a Fourier transform given by

$$\frac{1}{\sqrt{2\pi\sigma^2}} \int_{-\infty}^{\infty} e^{-x^2/(2\sigma^2)} e^{iqx} dx = e^{-q^2\sigma^2/2}$$

The left hand side of this equation is by definition the average value of e^{iqx}:

$$\langle e^{iqx} \rangle = \frac{1}{\sqrt{2\pi\sigma^2}} \int_{-\infty}^{\infty} e^{-x^2/(2\sigma^2)} e^{iqx} dx$$

Also $\langle x^2 \rangle = \sigma^2$ (see the section on Gaussian integrals below), and it therefore follows that

$$\langle e^{iqx} \rangle = e^{-q^2 \langle x^2 \rangle / 2}$$

This establishes the validity of the Baker-Hausdorff theorem.

Gaussian integrals

Here the recursion relation between Gaussian integrals defined by

$$I_m(a = 1) = \int_{-\infty}^{\infty} x^m e^{-x^2}\, dx$$

is derived for $m = 0, 2, 4, \cdots$. For $m = 0$ the integral is most readily evaluated by considering its square:

$$I_0^2 = \int_{-\infty}^{\infty} e^{-x^2}\, dx \int_{-\infty}^{\infty} e^{-y^2}\, dy = \int_{-\infty}^{\infty}\int_{-\infty}^{\infty} e^{-(x^2+y^2)}\, dx dy$$

$$\equiv \int_0^{2\pi} d\theta \int_0^{\infty} r e^{-r^2}\, dr = 2\pi \frac{1}{2} = \pi$$

The integral for $m = 0$ is therefore

$$I_0 = \int_{-\infty}^{\infty} e^{-x^2}\, dx = \sqrt{\pi} \tag{D.2}$$

and

$$I_0(a) = f(a) = \int_{-\infty}^{\infty} e^{-ax^2}\, dx = \sqrt{\pi}\, a^{-1/2} \tag{D.3}$$

By differentiating Eq. (D.3) with respect to a one finds

$$-I_2(a) = f'(a) = -\int_{-\infty}^{\infty} x^2 e^{-ax^2}\, dx = \sqrt{\pi}\left(\frac{-1}{2}\right) a^{-3/2}$$

$$I_4(a) = f''(a) = +\int_{-\infty}^{\infty} x^4 e^{-ax^2}\, dx = \sqrt{\pi}\left(\frac{-1}{2}\right)\left(\frac{-3}{2}\right) a^{-5/2}$$

$$-I_6(a) = f'''(a) = -\int_{-\infty}^{\infty} x^6 e^{-ax^2}\, dx = \sqrt{\pi}\left(\frac{-1}{2}\right)\left(\frac{-3}{2}\right)\left(\frac{-5}{2}\right) a^{-7/2}$$

etc.

and in general the integrals obey the recursion relation

$$I_{2m} = I_{2m-2}\frac{2m-1}{2a}$$

E

Fourier transforms

Fourier transforms occur naturally and ubiquitously in the mathematical description of scattering. The reason is that the scattering amplitude from an extended body often appears as a Fourier transform. Here we remind the reader of a few important definitions, and work through some illustrative examples.

E.1 Definitions

The Fourier transform of the one-dimensional function $f(x)$ is defined by

$$F(q) = \int_{-\infty}^{\infty} f(x)\, e^{iqx}\, dx$$

and the inverse transform is

$$f(x) = \frac{1}{2\pi} \int_{-\infty}^{\infty} F(q)\, e^{-iqx}\, dq.$$

Evaluation of the Fourier transform is simplified if the function is either symmetric or antisymmetric with respect to the line $x = 0$. For a symmetric function $f^S(x)$ the Fourier transform is

$$
\begin{aligned}
F(q) &= \int_{-\infty}^{\infty} f^S(x)\, e^{iqx}\, dx \\
&= \int_{-\infty}^{\infty} f^S(x)\, \cos(qx)\, dx + i \int_{-\infty}^{\infty} f^S(x)\, \sin(qx)\, dx
\end{aligned}
$$

The second integral on the right-hand side is identically zero, since the product of $f^S(x)$ and sine is itself antisymmetric, and the integral of an antisymmetric function over a symmetric domain is zero. Therefore the Fourier transform of a symmetric function is real and is given by the cosine transform

$$F(q) = 2 \int_{0}^{\infty} f^S(x)\, \cos(qx)\, dx$$

Similar arguments can be used to show that the Fourier transform of an antisymmetric function $f^A(x)$ is purely imaginary and is the sine transform

$$F(q) = i\,2 \int_0^\infty f^A(x)\,\sin(qx)\,dx$$

E.2 Examples

Gaussian

Here the Gaussian function is written as

$$f(x) = A\,e^{-a^2 x^2} \tag{E.1}$$

and is plotted in Fig. E.1(a). As it is a symmetric function its Fourier transform is

$$F(q) = 2 \int_0^\infty A\,e^{-a^2 x^2}\,\cos(qx)\,dx$$

This may be evaluated by writing the cosine as the real part of a complex exponential, $\cos(qx) = Re\{e^{i\,qx}\}$. The Fourier integral then becomes

$$F(q) = 2A\,Re\left\{\int_0^\infty e^{-a^2 x^2}\,e^{i\,qx}\,dx\right\} = 2A\,Re\left\{\int_0^\infty e^{-a^2 x^2 + i\,qx}\,dx\right\}$$

$$= 2A\,e^{-q^2/(4a^2)}\,Re\left\{\int_0^\infty e^{-(ax - i\,q/(2a))^2}\,dx\right\}$$

$$= 2A\,e^{-q^2/(4a^2)}\,Re\left\{\frac{1}{a}\int_0^\infty e^{-\kappa^2}\,d\kappa\right\}$$

where κ is a complex variable defined by $\kappa = (ax - i\,q/(2a))^2)$. The real part of the last integral is equal to the standard integral

$$\int_0^\infty e^{-y^2}\,dy = \frac{\sqrt{\pi}}{2}$$

(see Eq. D.2). The Fourier transform of a Gaussian is thus

$$F(q) = \frac{A\,\sqrt{\pi}}{a}\,e^{-q^2/(4a^2)} \tag{E.2}$$

which is itself a Gaussian.

It is instructive to consider the width Δx (full width at half maximum) of the Gaussian function and the width Δq of its Fourier transform. From Eq. (E.1), $\Delta x = 2\sqrt{\log_e(2)}/a$, and from Eq. (E.2), $\Delta q = 4a\sqrt{\log_e(2)}$. The product of the widths is a constant equal to

$$\Delta x\,\Delta q = 8\log_e(2)$$

This illustrates the reciprocal nature of the description of an object in real or direct space, and the description of its Fourier transform in q space, also known as reciprocal space. If an object is extended
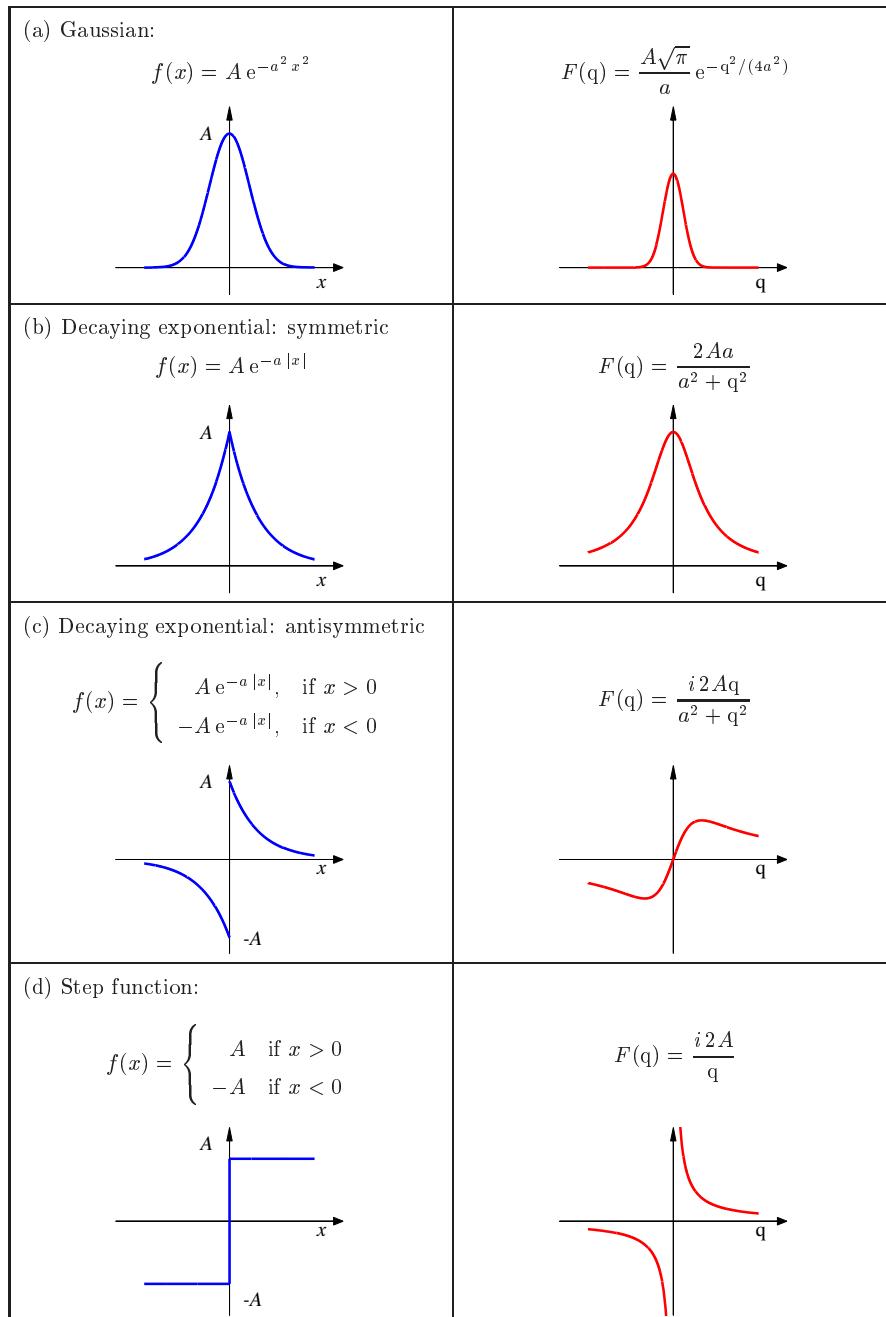
(a) Gaussian:	
$f(x) = A\,\mathrm{e}^{-a^2 x^2}$	$F(\mathrm{q}) = \dfrac{A\sqrt{\pi}}{a}\,\mathrm{e}^{-\mathrm{q}^2/(4a^2)}$
(b) Decaying exponential: symmetric	
$f(x) = A\,\mathrm{e}^{-a\,|x|}$	$F(\mathrm{q}) = \dfrac{2\,Aa}{a^2 + \mathrm{q}^2}$
(c) Decaying exponential: antisymmetric	
$f(x) = \begin{cases} A\,\mathrm{e}^{-a\,|x|}, & \text{if } x > 0 \\ -A\,\mathrm{e}^{-a\,|x|}, & \text{if } x < 0 \end{cases}$	$F(\mathrm{q}) = \dfrac{i\,2\,A\mathrm{q}}{a^2 + \mathrm{q}^2}$
(d) Step function:	
$f(x) = \begin{cases} A & \text{if } x > 0 \\ -A & \text{if } x < 0 \end{cases}$	$F(\mathrm{q}) = \dfrac{i\,2\,A}{\mathrm{q}}$

Fig. E.1 A selection of functions (left panel) and their Fourier transform (right panel).

(e) Box function	
$$f(x) = \begin{cases} A & \text{if } |x| < a \\ 0 & \text{if } |x| > 0 \end{cases}$$	$$F(q) = 2Aa\frac{\sin(qa)}{qa}$$

(f) Triangular function	
$$f(x) = \begin{cases} A(a-x)/a, & \text{for } 0 < x < a \\ A(a+x)/a, & \text{for } -a < x < 0 \\ 0, & \text{for } |x| > 1 \end{cases}$$	$$F(q) = A\frac{\sin^2(qa/2)}{(qa/2)^2}$$
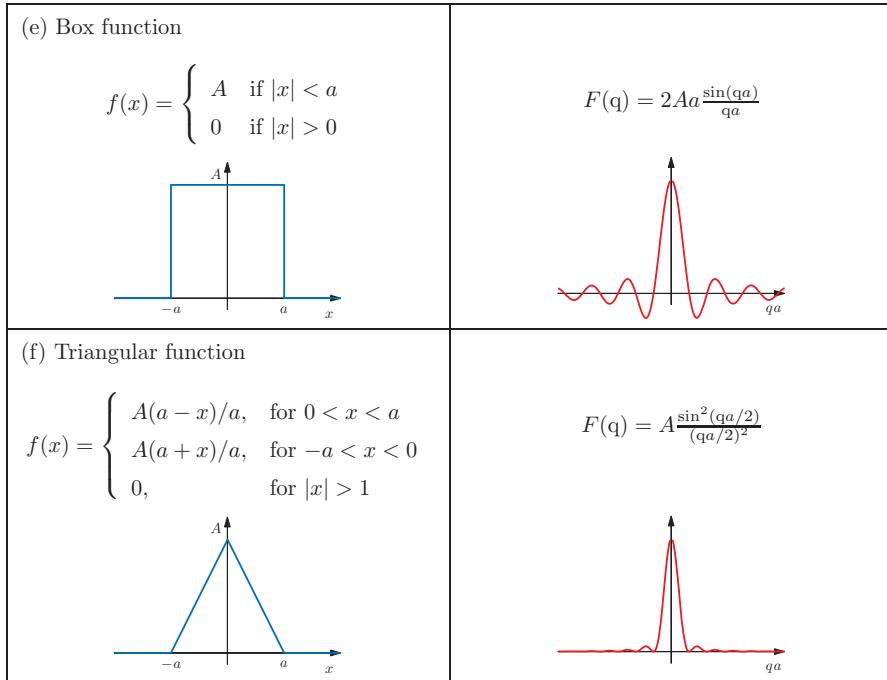
Fig. E.2 A selection of functions (left panel) and their Fourier transform (right panel).

in real space, Δx is large, and its Fourier transform is well localized in reciprocal space, i.e. Δq is small. Correspondingly, if an object is well localized in real space, then its Fourier transform is extended in reciprocal space. One extreme limit of this is a 2D object. This is infinitely thin in one direction, and hence its Fourier transform in this direction is perfectly delocalized, or in other words it has a constant value. This explains why the scattering from a two dimensional sheet of atoms forms rods perpendicular to the sheet.

Decaying exponential: symmetric

The symmetric decaying exponential is defined by

$$f(x) = A\,e^{-a|x|}$$

and is plotted in Fig. E.1(b). Its Fourier transform is

$$F(q) = 2A \int_0^\infty e^{-ax} \cos(qx)\,dx$$

The integral may be integrating by parts once to yield

$$\int_0^\infty e^{-ax} \cos(qx)\,dx = \frac{a}{q} \int_0^\infty e^{-ax} \sin(qx)\,dx$$

The right-hand side may also be integrated by parts again with the result that the cosine transform of e^{-ax} is

$$\int_0^\infty e^{-ax} \cos(qx)\, dx = \frac{a}{q}\left[\frac{1}{q} - \frac{a}{q}\int_0^\infty e^{-ax} \cos(qx)\, dx\right]$$

This can be rearranged to give

$$\int_0^\infty e^{-ax} \cos(qx)\, dx = \frac{a}{a^2 + q^2}$$

It follows that the Fourier transform of a symmetric decaying exponential is a Lorentzian:

$$F(q) = \frac{2Aa}{a^2 + q^2} \tag{E.3}$$

The product of the widths in real and reciprocal space for the symmetric decaying exponential function is

$$\Delta x\, \Delta q = 4 \log_e(2)$$

Decaying exponential: antisymmetric

The antisymmetric decaying exponential function is defined by

$$f(x) = \begin{cases} A\, e^{-a|x|}, & \text{for } x > 0 \\ -A\, e^{-a|x|}, & \text{for } x < 0 \end{cases}$$

and is plotted in Fig. E.1(c). Its Fourier transform is purely imaginary and is

$$F(q) = i\, 2 \int_0^\infty A\, e^{-ax} \sin(qx)\, dx$$

The sine transform of e^{-ax} is evaluated by integrating by parts twice, which yields

$$\int_0^\infty e^{-ax} \sin(qx)\, dx = \frac{q}{a^2 + q^2}$$

The Fourier transform of the antisymmetric decaying exponential is plotted in the right-hand panel of Fig. E.1 and is given by

$$F(q) = \frac{i\, 2Aq}{a^2 + q^2} \tag{E.4}$$

Step function

The step function

$$f(x) = \begin{cases} A, & \text{for } x > 0 \\ -A, & \text{for } x < 0 \end{cases}$$

is plotted in Fig. E.1(d). Its Fourier transform is equal to the Fourier transform of the antisymmetric decaying exponential in the limit that $a \to 0$. From Eq. (E.4) the Fourier transform of the step function is

$$F(q) = \frac{i\,2A}{q} \tag{E.5}$$

Box function

The box, or top hat, function

$$f(x) = \begin{cases} A, & \text{for } |x| \leq a \\ 0, & \text{for } x > a \end{cases}$$

is plotted in Fig. E.2(e). Its Fourier transform is

$$F(q) = \int_{-a}^{a} A e^{iqx} dx = \frac{A}{iq} \left[e^{iqa} - e^{-iqa} \right]$$

which can be rewritten as

$$F(q) = 2Aa\frac{\sin(qa)}{qa} \tag{E.6}$$

which is plotted in the right-hand column of Fig. E.2(e).

Symmetric triangle

A symmetric triangular function is plotted in Fig. E.2(f) and is given by

$$f(x) = \begin{cases} A(a - x)/a, & \text{for } 0 < x < a \\ A(a + x)/a, & \text{for } -a < x < 0 \\ 0, & \text{for } |x| > 1 \end{cases}$$

The Fourier transform of a symmetric triangle then follows as

$$F(q) = 2 \int_{0}^{\infty} \frac{A}{a}(a - x)\,\cos(qx)\,dx$$

which can be integrated by parts to yield

$$F(q) = A\frac{\sin^2(qa/2)}{(qa/2)^2} \tag{E.7}$$

which is plotted in the right-hand column of Fig. E.2(f).

E.3 Convolution theorem

One particularly useful result in the context of scattering is the Convolution Theorem. This states that the Fourier transform of the convolution of two functions $f(x)$ and $g(x)$ is equal to the product of the two individual Fourier transforms $F(q)$ and $G(q)$. The convolution or folding integral $h(x)$ of two functions $f(x)$ and $g(x)$ is defined by

$$h(x) = \int_{-\infty}^{\infty} f(x_1) g(x - x_1) \, dx_1$$

Its Fourier transform is

$$\begin{aligned} H(q) &= \int_{-\infty}^{\infty} h(x) \, e^{iqx} \, dx \\ &= \int_{-\infty}^{\infty} f(x_1) \, e^{iqx_1} \, dx_1 \int_{-\infty}^{\infty} g(x - x_1) \, e^{iq(x-x_1)} \, dx \\ &= F(q) \, G(q) \end{aligned}$$

The great utility of this result is that in many scattering problems the object of interest may be described mathematically as the convolution of two component functions in real space. One important example is a crystal lattice, for which the density may be viewed as the convolution of a lattice function and a function that describes what sits at each lattice point. The scattering amplitude is proportional to the Fourier transform of the density, and hence from the convolution theorem is equal to the product of the Fourier transforms of the component functions. If the latter are known, as is often the case, then the scattering amplitude may be obtained almost by inspection.

E.4 Patterson function

The Patterson function $P(\mathbf{r})$ is the quantity that is derived by direct Fourier transformation of the measured intensity $I(\mathbf{Q})$. Although the Patterson function does not contain any direct information on the phases (as it is the modulus squared of the scattering amplitude, $\mathcal{A}(\mathbf{Q})$, it nonetheless is a useful quantity to consider as it can be used to place constraints on the relative spacings of the scattering centres (atoms or molecules).

In one dimension, the scattered intensity $I(Q)$ may be written as

$$\begin{aligned} I(Q) &= \mathcal{A}^{\star}(Q)\mathcal{A}(Q) \\ &= \int_{-\infty}^{\infty} f^{\star}(r') \, e^{-iQr'} \, dr' \int_{-\infty}^{\infty} f(r'') \, e^{iQr''} \, dr'' = \int_{-\infty}^{\infty} \left(\int_{-\infty}^{\infty} f^{\star}(r')f(r'') \, e^{iQ(r''-r')} dr'' \right) dr' \\ &= \int_{-\infty}^{\infty} \left(\int_{-\infty}^{\infty} f^{\star}(r')f(r+r')dr' \right) e^{iQr} dr = \int_{-\infty}^{\infty} P(r) \, e^{iQr} dr \end{aligned}$$

The Patterson function is therefore defined by

$$P(r) = \int_{-\infty}^{\infty} f^{\star}(r')f(r+r')dr' \tag{E.8}$$

It is recognizable as the autocorrelation of the function $f(r)$. These concepts are readily extendible to higher dimensions.

E.5 Displacement theorem

If the function $f(x)$ is displaced by an amount x_0, then the Fourier transform $F_d(q)$ acquires the phase factor e^{iqx_0} since

$$F_d(q) = e^{iqx_0} \int f(x - x_0)e^{iq(x-x_0)}dx = e^{iqx_0}F(q) \tag{E.9}$$

Further reading

A Handbook of Fourier Transforms, D.C. Champeney (Cambridge University Press, 1987)

A Student's Guide to Fourier Transforms, J.F. James (Cambridge University Press, 1995)

F

Comparison of X-rays with neutrons

The relationship given in Eq. (3.1) between the refractive index, n, and the scattering length density ρr_0 can be derived in a different way when considering neutrons entering a material. Here the material is viewed as a continuum of nuclei, each having the scattering length b, and with a density of ρ.

An incident particle that experiences a potential $\mathcal{V}(\mathbf{r})$ from the material will be scattered. The scattering length b of a particle is related to the scattering potential $\mathcal{V}(\mathbf{r})$ in first-order perturbation theory by

$$\mathcal{V}(\mathbf{Q}) = 4\pi \left(\frac{\hbar^2}{2m_n} \right) b$$

Here $\mathcal{V}(\mathbf{Q})$ is the Fourier transform of the scattering potential:

$$\mathcal{V}(\mathbf{Q}) = \int \mathcal{V}(\mathbf{r})\, e^{i\mathbf{Q}\cdot\mathbf{r}}\, d\mathbf{r}$$

and as usual $\mathbf{Q} = \mathbf{k} - \mathbf{k}'$ is the wavevector transfer in the scattering process. This relation appears plausible when it is recalled that

(a) there is a phase difference of $\mathbf{Q}\cdot\mathbf{r}$ between the scattering from volume elements around the origin and around $\mathbf{r}$;

(b) the scattering can be thought of as a weighted superposition of the scattering from such volume elements, the weight being $\mathcal{V}(\mathbf{r})$ times the phase factor;

(c) the dimensionality in the equation relating b and $\mathcal{V}(\mathbf{Q})$ is correct, i.e. the term $(\hbar^2/2m_n)$ occurs naturally.

Of course, the factor of 4π must rely on a more rigorous treatment.

Fermi suggested that one could define a pseudo-potential between thermal neutrons and nuclei in such a way that this general first-order perturbation result would reproduce the correct scattering length. The nuclear scattering of neutrons is due to a short range potential between the neutron and the nucleus. The range of the potential is extremely short (of order 10^{-15} m) in comparison with the wavelength of

thermal neutrons (of order 10^{-10} m) so the shape of the potential is well approximated by a Dirac delta function allowing us to write

$$\mathcal{V}_F(\mathbf{r}) = C\,\delta(\mathbf{r})$$

so that

$$\mathcal{V}_F(\mathbf{Q}) = C \times 1$$

since the Fourier transform of a Dirac delta function is unity. (The properties of the Dirac delta function are reviewed in Chapter 5 on page 152.) Equating this expression for $\mathcal{V}_F(\mathbf{Q})$ with the general one given above for $\mathcal{V}(\mathbf{Q})$ allows us to identify the constant C and to write

$$\mathcal{V}_F(\mathbf{r}) = 4\pi \left(\frac{\hbar^2}{2m_n}\right) b\,\delta(\mathbf{r})$$

In refraction, the medium is considered to be a homogeneous continuum, and the change in wavenumber from k outside to nk inside the medium is due to a corresponding change in kinetic energy from $(\hbar^2/2m_n)\mathrm{k}^2$ to $(\hbar^2/2m_n)(n\mathrm{k})^2$. Energy conservation then immediately leads to

$$\left(\frac{\hbar^2}{2m_n}\right)\mathrm{k}^2 = \left(\frac{\hbar^2}{2m_n}\right)(n\mathrm{k})^2 + \langle \mathcal{V} \rangle$$

or

$$\mathrm{k}^2 - (n\mathrm{k})^2 = \left(\frac{2m_n}{\hbar^2}\right)\langle \mathcal{V} \rangle$$

Inserting the average potential

$$\langle \mathcal{V} \rangle = \frac{\int_V \mathcal{V}_F(r)\,d\mathbf{r}}{\int_V d\mathbf{r}} = 4\pi\left(\frac{\hbar^2}{2m_n}\right)b\rho$$

yields

$$\mathrm{k}^2(1 - n^2) = 4\pi\,b\rho$$

and since $(1 - n^2) = (1 + n)(1 - n) \approx 2\delta$ we obtain Eq. (3.2) with the neutron scattering length b substituting for the X-ray scattering length r_0.

Further reading

Introduction to the Theory of Thermal Neutron Scattering, G.L. Squires (Dover Publications, 1996)

Neutron Optics, V.F. Sears (Oxford University Press, 1989)

G

MATLAB® computer programs

Listings are given here of MATLAB® files which have been used to generate some of the figures in this book.

The files may be downloaded from the World Wide Web by following the link given on the home page of this book at the official John Wiley & Sons site (http://www.wiley.co.uk).

MATLAB® is a registered trademark of The MathWorks, Inc. Further information can be found at http://www.mathworks.com.

Chapter 2: Sources

Undulator characteristics, Fig. 2.11 on page 50

```
 1  function wout=undulator
 2  %
 3  % MATLAB function from:
 4  % "Elements of Modern X-ray Physics" by Jens Als-Nielsen and Des McMorrow
 5  %
 6  % Calculates: Undulator characteristics
 7  % Calls to: w1tcalc (observer phase from emitter phase)
 8  close all; clear all;
 9  set(gcf,'papertype','a4','paperunits','centimeters','units','centimeters',...
10          'position',[0.1 -8 21 26],'paperposition',[0.1 0.1 21 26]);
11
12  % (c) on-axis harmonic content for K=2
13
14  axes('position',[0.1 0.1 0.35 0.35]);
15
16  wutp=0:0.01:2*pi;                       % Emitter  phase
17  K=2; w1t=w1tcalc(wutp,K,0);             % Observer phase for K=2
18
19  xn=0:0.01:2*pi; yn=spline(w1t,2*sin(wutp),xn);
20  f=fft(yn);                              % Fourier transform displacement
21  h1=line(xn,-2*imag(f(2))/length(xn)*sin(xn),'linestyle','--',...
22      'linewidth',1.0,'color','r')
23  h3=line(xn,-2*imag(f(4))/length(xn)*sin(3*xn),'linestyle','--',...
24      'linewidth',1.0,'color','g')
25  h5=line(xn,-2*imag(f(6))/length(xn)*sin(5*xn),'linestyle','--',...
```

Elements of Modern X-ray Physics, Second Edition. Jens Als-Nielsen and Des McMorrow
© 2011 John Wiley & Sons, Ltd. Published 2011 by John Wiley & Sons, Ltd.

```
26     'linewidth',1.0,'color','b')
27  line(xn,-2*imag(f(2))/length(xn)*sin(xn)...
28          -2*imag(f(4))/length(xn)*sin(3*xn)-2*imag(f(6))/length(xn)*sin(5*xn),...
29          'color','m','linewidth',1.0)
30
31  axis([0 2*pi -2 2]); axis square
32  set(gca,'Xtick',[0 pi/2 pi 3*pi/2 2*pi],'Xticklabel',[],'Ytick',[-2 -1 0 1 2])
33  set(gca,'FontName','Times','Fontsize',16,'xgrid','on','ygrid','on','box','on')
34  ylabel('Transverse displacement')
35  xlabel(['$$\omega_1 t$$'],'position',[pi -2.5 0],'interpreter','latex');
36  text(0,-2.3,'0','horizontalalignment','center','Fontname','Times','Fontsize',16)
37  text(pi/2,-2.3,'\pi/2','horizontalalignment','center','Fontname','Times','Fontsize',16)
38  text(pi,-2.3,'\pi','horizontalalignment','center',...
39      'Fontname','Times','Fontsize',16)
40  text(1.5*pi,-2.3,'3\pi/2','horizontalalignment','center',...
41      'Fontname','Times','Fontsize',16)
42  text(2*pi,-2.3,'2 \pi','horizontalalignment','center','Fontname','Times','Fontsize',16)
43  text(0.7,0.925,'On axis, {\it K=2} (c)','horizontalalignment','center',...
44                          'Fontname','Times','Fontsize',14,'units','normalized')
45  legend([h1 h3 h5],'1^{st}','3^{rd}','5^{th}','location','southwest')
46
47  % (d) Harmonic content for K=2
48
49  axes('position',[0.6 0.1 0.35 0.35]);
50
51  hc=([-2*imag(f(2))  -2*imag(f(4))  -2*imag(f(6)) -2*imag(f(8))]/length(xn));
52  ic=(abs(hc).*[1 3^2 5^2 7^2]).^2;
53  h=bar([ic(:)/ic(1) abs(hc(:))/hc(1)],0.85,'grouped');
54  axis([0.5 4.5 0 2]); axis square
55
56  set(gca,'Box','on','xgrid','on','ygrid','on','FontName','Times','Fontsize',16,...
57          'xticklabel',['1';'3';'5';'7'])
58  set(h(1),'facecolor','k'); set(h(2),'facecolor','w')
59  xlabel('Harmonic'); ylabel('Intensity [arb. units]')
60  text(0.7,0.925,'On axis, {\it K=2} (d)','horizontalalignment','center',...
61                          'Fontname','Times','Fontsize',14,'units','normalized')
62
63  % (a) On axis radiation for  for K=1, 2 and 5
64
65  axes('position',[0.1 0.5 0.35 0.35]);
66  wutp=0:0.01:2*pi;
67
68  w1t=w1tcalc(wutp,1,0); % K=1
69  htp_k1=line(wutp,sin(wutp),'linestyle','--','color','r','linewidth',1.0);
70  htt_k1=line(w1t,sin(wutp),'linestyle','-','color','r','linewidth',1.0);
71
72  w1t=w1tcalc(wutp,2,0); % K=2
73  htp_k2=line(wutp,2*sin(wutp),'linestyle','--','color','b','linewidth',1.0);
74  htt_k2=line(w1t,2*sin(wutp),'linestyle','-','color','b','linewidth',1.0);
75
76  w1t=w1tcalc(wutp,5,0); % K=5
77  htp_k5=line(wutp,5*sin(wutp),'linestyle','--','color','m','linewidth',1.0);
78  htt_k5=line(w1t,5*sin(wutp),'linestyle','-','color','m','linewidth',1.0);
79
80  axis([0 2*pi -6 6]); axis square
81  set(gca,'Xtick',[0 pi/2 pi 3*pi/2 2*pi],'Xticklabel',[],'box','on','ygrid','on')
82  set(gca,'Ytick',[-6 -4 -2 0 2 4 6],'FontName','Times','Fontsize',16,'Xgrid','on')
83  ylabel('Transverse displacement')
84  xlabel(['$$\omega_u t^\prime$$ (' '$$\omega_1 t$$)'],...
85                          'position',[pi -7.8 0],'interpreter','latex');
86  text(0,-7.0,'0','horizontalalignment','center','Fontname','Times','Fontsize',16)
87  text(pi/2,-7.0,'\pi/2','horizontalalignment','center','Fontname','Times','Fontsize',16)
88  text(pi,-7.0,'\pi','horizontalalignment','center','Fontname','Times','Fontsize',16)
89  text(1.5*pi,-7.0,'3\pi/2','horizontalalignment','center',...
90      'Fontname','Times','Fontsize',16)
91  text(2*pi,-7.0,'2 \pi','horizontalalignment','center','Fontname','Times','Fontsize',16)
92  legend([htt_k1 htt_k2 htt_k5],'{\it K}=1','{\it K}=2','{\it K}=5',...
93      'location','southwest')
94  text(0.8,0.925,'On axis (a)','horizontalalignment','center',...
95                          'Fontname','Times','Fontsize',14,'units','normalized')
```

```
96
97  % (b) Off-axis  for K=2
98
99  axes('position',[0.6 0.5 0.35 0.35]);
100
101 wutp=0:0.01:2*pi;
102 w1t=w1tcalc(wutp,2,0);
103 hona=line(w1t,2*sin(wutp),'linestyle','-','color','k','linewidth',1.0);
104 w1t=w1tcalc(wutp,2,1);
105 hofa=line(w1t,2*sin(wutp),'linestyle','--','color','m','linewidth',1.0);
106
107 axis([0 2*pi -6 6]); axis square
108 set(gca,'Xtick',[0 pi/2 pi 3*pi/2 2*pi],'Xticklabel',[])
109 set(gca,'Ytick',[-6 -4 -2 0 2 4 6],'FontName','Times','Fontsize',16);
110 set(gca,'xgrid','on','ygrid','on','box','on')
111 ylabel('Transverse displacement')
112 xlabel(['$$\omega_1 t$$'],'position',[pi -7.8 0],'interpreter','latex');
113 text(0,-7.0,'0','horizontalalignment','center','Fontname','Times','Fontsize',16)
114 text(pi/2,-7.0,'\pi/2','horizontalalignment','center','Fontname','Times','Fontsize',16)
115 text(pi,-7.0,'\pi','horizontalalignment','center','Fontname','Times','Fontsize',16)
116 text(1.5*pi,-7.0,'3\pi/2','horizontalalignment','center',...
117      'Fontname','Times','Fontsize',16)
118 text(2*pi,-7.0,'2 \pi','horizontalalignment','center','Fontname','Times','Fontsize',16)
119 text(0.85,0.925,'{\it K=2} (b)','horizontalalignment','center',...
120                        'Fontname','Times','Fontsize',14,'units','normalized')
121 legend([hona hofa],'On axis','Off axis','location','southwest')
122
123 function [w1t]=w1tcalc(wutp,K,ratio)
124 %
125 % MATLAB function from:
126 % "Elements of Modern X-ray Physics" by Jens Als-Nielsen and Des McMorrow
127 %
128 % Calculates: observer phase (w1t) from emitter phase (wutp)
129
130 w1t=wutp+0.25*K^2/(1+ratio^2+K^2/2)*sin(2*wutp)-2*K/(1+(ratio^2)+K^2/2)*ratio*sin(wutp);
```

Chapter 3: Reflection and refraction

Fresnel reflectivity characteristics, Fig. 3.5 on page 80

```
1  function FresnelR
2  %
3  % MATLAB function from:
4  % "Elements of Modern X-ray Physics" by Jens Als-Nielsen and Des McMorrow
5  %
6  % Calculates: Fresnel reflectivity characteristics
7
8  figure; axes('position',[0.35 0.7 0.3 0.2]);
9
10 % Intensity reflectivity for different values of b_mu
11
12 tpos=-0.80;
13 q=0.01:0.001:2.5;
14 b=0.1; qp=sqrt(q.^2-1+2*sqrt(-1)*b); rq=(q-qp)./(q+qp);
15 Rq=rq.*conj(rq); Rn=Rq.*(q.^4)*(2^4);
16 iq1=find(q<1.5); iq2=find(q>1.5);
17 [ax,h1,h2]=plotyy(q(iq1),Rq(iq1),q(iq2),Rn(iq2));
18 set(h1,'color','r'); set(h2,'color','r')
19
20 axis([0 2.6 0 1.1])
21 yl=str2mat('    R(q)    ',' Fresnel ','reflectivity');
22 text(tpos,0.5,yl,'FontName','Times','rotation',90,'horizontalalignment','center');
23
24 b=0.05; qp=sqrt(q.^2-1+2*sqrt(-1)*b); rq=(q-qp)./(q+qp);
25 Rq=rq.*conj(rq); Rn=Rq.*(q.^4)*(2^4);
```

```
26  line(q(iq1),Rq(iq1),'color','g')
27  axes(ax(2)); line(q(iq2),Rn(iq2),'color','g')
28
29  b=0.01;  qp=sqrt(q.^2-1+2*sqrt(-1)*b); rq=(q-qp)./(q+qp);
30  Rq=rq.*conj(rq); Rn=Rq.*(q.^4)*(2^4);
31  axes(ax(1)); line(q(iq1),Rq(iq1),'color','b')
32  axes(ax(2)); line(q(iq2),Rn(iq2),'color','b')
33
34  b=0.001; axes(ax(1)); qp=sqrt(q.^2-1+2*sqrt(-1)*b); rq=(q-qp)./(q+qp);
35  Rq=rq.*conj(rq); Rn=Rq.*(q.^4)*(2^4);
36  line(q(iq1),Rq(iq1),'color','m')
37  axes(ax(2))
38  text(3.2,1.6,'R(q).(2Q/Q_c)^4','FontName','Times','rotation',90,...
39      'horizontalalignment','center')
40  axis([0 2.6 1 2.1])
41  set(ax,'Ycolor',[0 0 0],'Ytick',[0.5 1.0 1.5 2.0 2.5],'Xticklabels',[])
42  set(ax,'FontName','Times','Fontsize',12,'box','on');
43
44  % Penetration length
45
46  axes('position',[0.35 0.5 0.3 0.2])
47
48  q=0.01:0.01:1.4;
49  b=0.1; qp=sqrt(q.^2-1+2*sqrt(-1)*b);
50  line(q,1./imag(qp),'color','r')
51
52  b=0.05; qp=sqrt(q.^2-1+2*sqrt(-1)*b);
53  line(q,1./imag(qp),'color','g')
54
55  b=0.01; qp=sqrt(q.^2-1+2*sqrt(-1)*b);
56  line(q,1./imag(qp),'color','b')
57
58  b=0.001; qp=sqrt(q.^2-1+2*sqrt(-1)*b);
59  line(q,1./imag(qp),'color','m')
60
61  axis([0 2.6 0 1000]);
62  yl=str2mat(' \Lambda Q_c',' Penetration ','  length   ');
63  text(tpos,30,yl,'FontName','Times','rotation',90,'horizontalalignment','center');
64  set(gca,'Xticklabels',[],'Yscale','log','Ytick',[1 10 100])
65  set(gca,'FontName','Times','FontSize',12,'box','on')
66
67  % Evanescent intensity
68
69  axes('position',[0.35 0.3 0.3 0.2])
70
71  q=0.01:0.01:2.5;
72  b=0.1; qp=sqrt(q.^2-1+2*sqrt(-1)*b); ttq=2*q./(q+qp);
73  h1=line(q,ttq.*conj(ttq),'color','r');
74
75  b=0.05; qp=sqrt(q.^2-1+2*sqrt(-1)*b); ttq=2*q./(q+qp);
76  line(q,ttq.*conj(ttq),'color','g')
77
78  b=0.01; qp=sqrt(q.^2-1+2*sqrt(-1)*b); ttq=2*q./(q+qp);
79  line(q,ttq.*conj(ttq),'color','b')
80
81  b=0.001; qp=sqrt(q.^2-1+2*sqrt(-1)*b); ttq=2*q./(q+qp);
82  line(q,ttq.*conj(ttq),'color','m')
83
84  axis([0 2.6 0 4]);
85  yl=str2mat('   T(q)   ','Evanescent','intensity ');
86  hl=text(tpos,2,yl);
87  set(hl,'FontName','Times','rotation',90,'horizontalalignment','center');
88  set(gca,'Xticklabels',[],'Ytick',[1 2 3],'Yticklabel',['1';'2';'3'])
89  set(gca,'FontName','Times','FontSize',12,'box','on')
90
91  % Phase shift of reflected wave
92
93  axes('position',[0.35 0.1 0.3 0.2])
94
95  q=0.01:0.01:2.5;
```

```
96  b=0.1; qp=sqrt(q.^2-1+2*sqrt(-1)*b); rq=(q-qp)./(q+qp);
97  line(q,angle(rq),'color','r')
98
99  b=0.05; qp=sqrt(q.^2-1+2*sqrt(-1)*b); rq=(q-qp)./(q+qp);
100 line(q,angle(rq),'color','g')
101
102 b=0.01; qp=sqrt(q.^2-1+2*sqrt(-1)*b); rq=(q-qp)./(q+qp);
103 line(q,angle(rq),'color','b')
104
105 b=0.001; qp=sqrt(q.^2-1+2*sqrt(-1)*b); rq=(q-qp)./(q+qp);
106 line(q,angle(rq),'color','m')
107
108 set(gca,'FontName','Times','FontSize',12,'box','on')
109 axis([0 2.6 -pi pi/4]);
110 yl=str2mat('Phase shift of','   reflected ','    wave      ');
111 text(tpos,-pi/2,yl,'FontName','Times','rotation',90,'horizontalalignment','center');
112 text(-0.25,0,'0','horizontalalignment','center','FontName','Times','FontSize',12);
113 text(-0.25,-pi,'-\pi','horizontalalignment','center','FontSize',14);
114 xlabel('q=Q/Q_c or  \alpha/\alpha_c')
115 set(gca,'Yticklabels',[],'Ytick',[-pi -pi/2 0 pi/2],'Xtick',[0.5 1.0 1.5 2.0 2.5])
```

Kiessig fringes from a thin film, Fig. 3.7 on page 83

```
1  function kiessig
2  %
3  % MATLAB function from:
4  % "Elements of Modern X-ray Physics" by Jens Als-Nielsen and Des McMorrow
5  %
6  % Calculates: Reflectivity from a thin film of tungsten
7
8  axes('position',[0.2 0.2 0.6 0.6]);
9
10 r0=2.82e-5;        % Thompson scattering length in Angs
11 rho=4.678;         % electron density in electrons/Angs^3
12 b=0.0409;          % parameter b_mu
13 Delta=10*2*pi;     % thickness of film in Angs
14 sigma=0.0;         % surface roughness in Angs
15
16 Qc=4*sqrt(pi*rho*r0);
17
18 Q=0:0.001:1;
19 q=Q/Qc;
20 Qp=Qc*sqrt(q.^2-1+2*sqrt(-1)*b);
21
22 rQ=(Q-Qp)./(Q+Qp);
23 r_slab=rQ.*(1-exp(i*Qp*Delta))./(1-rQ.^2.*exp(i*Qp*Delta));
24 r_slab=r_slab.*exp(-Q.^2*sigma^2/2);
25 line(Q,r_slab.*conj(r_slab),'LineWidth',1.0,'Color','b');
26
27 axis([0.0 1.0 1e-10 1.5]); grid on
28 set(gca,'FontName','Times','FontSize',16,'box','on')
29 set(gca,'Ytick',[1e-10 1e-8 1e-6 1e-4 1e-2 1e0],'yscale','log')
30 xlabel('Wavevector transfer Q (Å^{-1})')
31 ylabel('|{\it r}_{slab}|^2','position',[-0.175 1e-5 0])
```

Parratt and kinematical reflectivity, Fig. 3.9 on page 88

```
1  function par_kin
2  %
3  % MATLAB function from:
4  % "Elements of Modern X-ray Physics" by Jens Als-Nielsen and Des McMorrow
5  %
6  % Calculates: Parratt and kinematical reflectivities from a multilayer
7  %             Specific case of W/Si, 10 bilayers of [10 Angs W, 40 Angs Si]
8
```

```
 9 | r0=2.82e-5;                              % Thompson scattering length in Angs
10 | Q=0.01:0.001:0.3;                        % Wavevector transfer in 1/Angs
11 | lambda=1.54;                              % wavelength in Angs
12 | rhoA=4.678; muA=33.235e-6;               % density and absorption coefficient of W
13 | rhoB=0.699; muB=1.399e-6;                % density and absorption coefficient of Si
14 |
15 | bl=[rhoA*r0+i*muA rhoB*r0+i*muB];                 % bilayer scattering factor
16 | dbl=[10 40];                                      % bilayer d-spacings
17 | ml=[bl bl bl bl bl bl bl bl bl 0.1e-20];          % multilayer scattering factor
18 | dml=[dbl dbl dbl dbl dbl dbl dbl dbl dbl dbl];    % multilayer d-spacings
19 | sml=[0 0 0 0 0 0 0 0 0 0 0 0 0 0 0 0 0 0 0 0 0];  % roughness at each interface
20 |
21 | %------ Parratt reflectivity
22 | R=parratt(Q,lambda,ml,dml,sml);
23 |
24 | axes('position',[0.2 0.15 0.7 0.4]); line(Q,R)
25 | axis([0 0.3 8e-6 2]);
26 | set(gca,'FontName','Times','FontSize',18,'box','on')
27 | set(gca,'Ytick',[1e-4 1e-3 1e-2 1e-1 1],'Yscale','log')
28 | text(0.15,5e-7,'Wavevector transfer Q (Å^{-1})',...
29 |      'FontName','Times','FontSize',18,'horizontalalignment','center')
30 | text(-0.05,1,'Reflectivity','FontName','Times',...
31 |    'FontSize',18,'horizontalalignment','center','rotation',90)
32 | text(0.20,0.7,'(b) Parratt','FontName','Times','FontSize',16)
33 |
34 | %----- kinematical reflectivity
35 | sld=bl;
36 | sigma=0; N=10; Lambda=50; Gamma=0.2;
37 |
38 | R=kinematicalR(Q,lambda,sld,sigma,N,Lambda,Gamma);
39 |
40 | axes('position',[0.2 0.55 0.7 0.4]); line(Q,R)
41 | set(gca,'FontName','Times','FontSize',18,'box','on')
42 | axis([0 0.3 8e-6 2]);
43 | set(gca,'Xticklabel','')
44 | set(gca,'Ytick',[1e-4 1e-3 1e-2 1e-1 1],'Yscale','log')
45 | text(0.20,0.7,'(a) Kinematical ','FontName','Times','FontSize',16)
46 |
47 | %%%%%%%%%%%%%%%%%%%%%%%%%%%%%%%%%%%%%%%%%%%%%%%%%%%%%%%%%%%%%%%%%%%%%%%%%%%%%%%%%%
48 | function [R]=kinematicalR(Q,lambda,sld,sigma,N,Lambda,Gamma)
49 | %
50 | % MATLAB function from:
51 | % "Elements of Modern X-ray Physics" by Jens Als-Nielsen and Des McMorrow
52 | %
53 | % Calculates: kinematical reflectivity of a multilayer
54 | % Inputs:  Q        wavevector transfer             1/Angs
55 | %          lambda   wavelength of radiation         Angs
56 | %          sld      scattering length density       1/Angs^2
57 | %                   sld=[sldA+i*muA sldB+i*muB]
58 | %          sigma    rouhgness                       Angs
59 | %          N        number of bilayers
60 | %          Lambda   length of bilayer               Angs
61 | %          Gamma    fraction of bilayer that is A
62 | % Outputs: R        Intensity reflectivity
63 |
64 | muA=imag(sld(1));
65 | muB=imag(sld(2));
66 |
67 | Dsld=real(sld(1))-real(sld(2));
68 | zeta=Q/2/pi*Lambda;
69 | beta=2*Lambda*Lambda*(muA*Gamma+muB*(1-Gamma))/lambda./zeta;
70 | r_1=-2*i*Dsld*Lambda*Lambda*Gamma./zeta;
71 | r_1=r_1.*sin(pi*Gamma*zeta)./(pi*Gamma*zeta);
72 | r_N=r_1.*(1-exp(i*2*pi*zeta*N).*exp(-beta*N))./(1-exp(i*2*pi*zeta).*exp(-beta));
73 | r_N=r_N.*exp(-((Q*sigma).^2/2));
74 | R=r_N.*conj(r_N);
75 |
76 | %%%%%%%%%%%%%%%%%%%%%%%%%%%%%%%%%%%%%%%%%%%%%%%%%%%%%%%%%%%%%%%%%%%%%%%%%%%%%%%%%%
77 | function [RR]=parratt(Q,lambda,sld,d,sigma)
78 | %
```

```
79  % MATLAB function from:
80  % "Elements of Modern X-ray Physics" by Jens Als-Nielsen and Des McMorrow
81  %
82  % Calculates: Parratt reflectivity of a multilayer
83  % Inputs: Q       wavevector transfer              1/Angs
84  %         lambda wavelength of radiation           Angs
85  %         sld    scattering length density         1/Angs^2
86  %                sld=[sld1+i*mu1 sld2+i*mu2 ....]
87  %         d      thickness of layer                Angs
88  %                d=[d1 d2 .....];
89  %         sigma  rouhgness                         Angs
90  % Outputs:R      Intensity reflectivity
91
92  k=2*pi/lambda;
93
94  %----- Calculate refractive index n of each layer
95  delta=lambda^2*real(sld)/(2*pi); beta=lambda/(4*pi)*imag(sld);
96  n=size(sld,2);
97  nu=1-delta+i*beta;
98
99  %----- Wavevector transfer in each layer
100 Q=reshape(Q,1,length(Q));
101 x=asin(Q/2/k);
102 for j=1:n
103    Qp(j,:)=sqrt(Q.^2-8*k^2*delta(j)+i*8*k^2*beta(j));
104 end
105 Qp=[Q;Qp];
106
107 %----- Reflection coefficients (no multiple scattering)
108 for j=1:n
109    r(j,:)=((Qp(j,:)-Qp(j+1,:))./(Qp(j,:)+Qp(j+1,:))).*...
110        exp(-0.5*(Qp(j,:).*Qp(j+1,:))*sigma(j)^2);
111 end
112
113 %----- Reflectivity from first layer
114 RR=r(1,:);
115 if n>1
116    R(1,:)=(r(n-1,:)+r(n,:).*...
117        exp(i*Qp(n,:)*d(n-1)))./(1+r(n-1,:).*r(n,:).*exp(i*Qp(n,:)*d(n-1)));
118 end
119
120 %----- Reflectivity from more layers
121 if n>2
122   for j=2:n-1
123      R(j,:)=(r(n-j,:)+R(j-1,:).*...
124          exp(i*Qp(n-j+1,:)*d(n-j)))./(1+r(n-j,:).*R(j-1,:).*exp(i*Qp(n-j+1,:)*d(n-j)));
125   end
126 end
127
128 %------ Intensity reflectivity
129 if n==1
130   RR=r(1,:);
131 else
132   RR=R(n-1,:);
133 end
134
135 RR=(abs(RR).^2)';
```

Reflectivity from a Langmuir film, Fig. 3.13 on page 99

```
1  function lang_ref
2  %
3  % MATLAB function from:
4  % "Elements of Modern X-ray Physics" by Jens Als-Nielsen and Des McMorrow
5  %
6  % Calculates: Reflectivity from a lanngmuir layer
7  % Data: Langmuir Vol. 10 (1994) 826
8
```

```matlab
 9 axes('position',[0.15 0.20 0.60 0.75])

10
11 Q=0:0.01:1;               % wavevector transfer in 1/Angs

12
13 %----- (a) pH

14
15 rho_hw=2.28;             % density of head group, rho_head/rho_water
16 rho_tw=1.08;             % density of tail group, rho_tail/rho_water
17 l_h=6.2;                 % length of head  in Angs
18 l_t=22.0;                % length of tail  in Angs
19 sigma=1.36;              % roughness in Angs
20 Qc=0.0217;               % critical Q for water in 1/Angs
21 mc=0.75;                 % monolayer coverage

22
23 phi1=Q*(l_h/2+l_t); phi2=Q*(l_h/2);
24 phi=exp(-Q.^2*sigma^2/2).*(rho_tw*exp(-i*phi1)+...
25     (rho_hw-rho_tw)*exp(-i*phi2)-(rho_hw-1)*exp(i*phi2));
26 R=mc*abs(phi).^2;
27 line(Q/Qc,R,'linewidth',1.5)

28
29 data_a=[0.90 1.11;1.20 1.19;1.50 1.35;1.58 1.41;1.88 1.51;2.09 1.60;2.35 1.73;...
30 2.48 1.82;2.65 1.97;2.86 2.09;3.25 2.17;3.89 2.40;4.27 2.43;4.61 2.33;4.91 2.19;...
31 5.25 2.03;5.51 1.87;5.94 1.52;6.28 1.25;6.45 1.04;6.79 0.82;7.18 0.58;7.35 0.46;...
32 7.65 0.31;8.12 0.17;8.54 0.12;9.06 0.19;9.44 0.34;9.70 0.52;10.12 0.92;10.51 1.36;...
33 10.72 1.81;11.15 2.43;11.53 3.03;11.83 3.38;12.22 3.92;12.52 4.49;12.77 4.97;...
34 13.20 5.23;13.58 5.66;13.88 5.61;14.18 5.73;14.48 6.02;14.82 5.96;15.04 5.89;...
35 15.55 5.80;15.89 5.43;16.23 5.00;16.62 4.53;16.96 4.00;17.26 3.65;17.60 3.14;...
36 17.86 2.78;18.28 2.48;18.54 1.90;18.92 1.86;19.18 1.68;19.57 1.39];
37 line(data_a(:,1),data_a(:,2),'Marker','square','MarkerSize',8,'linestyle','none')

38
39 %----- (b) pH

40
41 rho_hw=3.35;             % density of head group, rho_head/rho_water
42 rho_tw=1.01;             % density of tail group, rho_tail/rho_water
43 l_h=2.7;                 % length of head  in Angs
44 l_t=23.4;                % length of tail  in Angs
45 sigma=2.74;              % roughness in Angs
46 Qc=0.0217;               % critical Q for water in 1/Angs
47 mc=0.75;                 % monolayer coverage

48
49 phi1=Q*(l_h/2+l_t); phi2=Q*(l_h/2);
50 phi=exp(-Q.^2*sigma^2/2).*(rho_tw*exp(-i*phi1)+...
51     (rho_hw-rho_tw)*exp(-i*phi2)-(rho_hw-1)*exp(i*phi2));
52 R=mc*abs(phi).^2;
53 line(Q/Qc,R,'linewidth',1.5)

54
55 data_b=[1.03 1.03;1.24 1.17;1.46 1.27;1.88 1.41;2.40 1.54;2.65 1.63;2.95 1.70;...
56 3.34 1.71;3.64 1.76;4.15 1.76;4.41 1.66;4.67 1.62;5.18 1.47;5.52 1.31;5.69 1.12;...
57 6.12 1.00;6.51 0.81;6.89 0.60;7.28 0.46;7.49 0.34;7.79 0.23;8.26 0.11;8.56 0.06;...
58 8.82 0.12;9.25 0.19;9.54 0.34;9.76 0.50;10.10 0.69;10.40 0.90;10.87 1.19;...
59 11.13 1.44;11.56 1.70;11.94 1.98;12.20 2.13;12.51 2.51;12.93 2.70;13.40 2.62;...
60 13.57 2.73;14.12 2.79;14.34 2.75;14.81 2.79;15.19 2.86;15.54 2.71;15.88 2.62;...
61 16.22 2.46;16.69 2.32;17.08 1.78;17.38 1.57;17.76 1.16;18.15 1.36;18.49 0.87;...
62 18.96 0.79;19.18 1.09;19.56 0.81];
63 line(data_b(:,1),data_b(:,2),'Marker','diamond',...
64     'MarkerSize',8,'MarkerFaceColor','b','linestyle','none')

65
66 axis([0 20 0 7])
67 set(gca,'FontName','Times','FontSize',36,'Xtick',[5 10 15 20 ])
68 xlabel('Q/Q_c'); ylabel('{\it R}/{\it R_F}','position',[-2.5 3.5 0])
69 box on; grid on
70 text(13.5,2.0,'(b)','FontName','Times','FontSize',24)
71 text(13.5,5.,'(a)','FontName','Times','FontSize',24)
```

Chapter 4: Kinematical diffraction I: non-crystalline materials

Dependence of SAXS on shape and dimensionality, Fig. 4.14 on page 141

```matlab
function SAXS
%
% MATLAB function from:
% "Elements of Modern X-ray Physics" by Jens Als-Nielsen and Des McMorrow
%
% Calculates: Calculates SAXS from a sphere, disk and rod
% Calls to:

close all; clear all;

Q=0:0.001:2; Q2=0.1:0.002:1; Q3=0.11:0.002:1; Q4=0.25:0.002:2;
FS=12;                                  % Font size
disp('Running: may take sometime to complete')

subplot(1,2,1)                          % Plot on linear scale
axlm=[0 10 0 1.1]; axis(axlm);
c1=[0.9 0.9 1];
patch([axlm(1) axlm(2) axlm(2) axlm(1)],[axlm(3) axlm(3) axlm(4) axlm(4)],...
    [0 0 0],c1);
set(gca,'layer','top')

% Spehre

R=50;
Rg=sqrt(3/5)*R;
F1=3*(sin(Q*R)-(Q*R).*cos(Q*R))./(Q*R).^3;
hs=line(Q*Rg,F1.*F1,'color','b','linewidth',1.5,'linestyle',':');

% Disk

R=50;
Rg=sqrt(1/2)*R;
p17=2./(Q*R).^2.*(1-besselj(1,2*Q*R)./(Q*R));
hd=line(Q*Rg,p17,'color','r','linewidth',1.5,'linestyle','--');

% Rod

L=50;
for ii=1:length(Q)
    x=Q(ii)*L;
    p15(ii)=2*quadl(@si,0,x)/x-4*sin(x/2).^2./(x)^2;
end
Rg=sqrt(1/12)*L
hr=line(Q*Rg,p15,'color','m','linewidth',1.5,'linestyle','-.');

set(gca,'xscale','linear','yscale','linear','fontname','times',...
    'fontsize',FS,'linewidth',1.0,'gridlinestyle',':')
ylabel('$$\left| \mathcal F(\mathrm Q)\right|\,^2$$','interpreter','latex')
text(0.5,-0.1,'$$\mathrm Q R_g$$','interpreter','latex','FontName','Times',...
    'FontSize',12,'horizontalalignment','center','units','normalized')
axis square
box on; grid on
legend([hs hd hr],'Sphere','Disk','Rod')
text(0.07,0.07,'(a)','FontName','Times','FontSize',12,...
    'interpreter','latex','units','normalized')

subplot(1,2,2)                          % Plot on Log scale
axlm=[1 20 1e-4 1.1]; axis(axlm);
c1=[0.9 0.9 1];
patch([axlm(1) axlm(2) axlm(2) axlm(1)],[axlm(3) axlm(3) axlm(4) axlm(4)],...
    [0 0 0],c1);
set(gca,'layer','top')

% Spehre

```

```
66  R=50;
67  Rg=sqrt(3/5)*R;
68  F1=3*(sin(Q*R)-(Q*R).*cos(Q*R))./(Q*R).^3;
69  hs=line(Q*Rg,F1.*F1,'color','b','linewidth',1.5,'linestyle',':');
70  line(Q2*Rg,0.0000017./Q2.^4,'color','b','linewidth',1.0,'linestyle','-')
71
72  % Disk
73
74  R=50;
75  Rg=sqrt(1/2)*R
76  p17=2./(Q*R).^2.*(1-besselj(1,2*Q*R)./(Q*R));
77  hd=line(Q*Rg,p17,'color','r','linewidth',1.5,'linestyle','--');
78  line(Q3*Rg,0.00095./Q3.^2,'color','r','linewidth',1.0,'linestyle','-')
79
80  % Rod
81
82  L=50;
83  for ii=1:length(Q)
84      x=Q(ii)*L;
85      p15(ii)=2*quadl(@si,0,x)/x-4*sin(x/2).^2./(x)^2;
86  end
87  Rg=sqrt(1/12)*L;
88  hr=line(Q*Rg,p15,'color','m','linewidth',1.5,'linestyle','-.');
89  line(Q4*Rg,0.075./Q4.^1,'color','m','linewidth',1.0,'linestyle','-')
90
91  set(gca,'xscale','log','yscale','log','fontname','times','fontsize',FS,...
92      'linewidth',1.0,'minorgridlinestyle','none','gridlinestyle',':')
93  text(0.07,0.07,'(b)','FontName','Times','FontSize',12,...
94      'interpreter','latex','units','normalized')
95  text(0.7,0.28,'$$1/\mathrm Q^4$$','FontName','Times','FontSize',12,...
96      'interpreter','latex','units','normalized')
97  text(0.7,0.6,'$$1/\mathrm Q^2$$','FontName','Times','FontSize',12,...
98      'interpreter','latex','units','normalized')
99  text(0.7,0.83,'$$1/\mathrm Q^1$$','FontName','Times','FontSize',12,...
100     'interpreter','latex','units','normalized')
101 ylabel('$$\left| \mathcal F(\mathrm Q)\right|\,^2$$','interpreter','latex')
102 text(0.5,-0.1,'$$\mathrm Q R_g$$','interpreter','latex','FontName','Times',...
103         'FontSize',12,'horizontalalignment','center','units','normalized')
104 axis square; box on; grid on;
```

Effect of polydispersivity on SAXS, Fig. 4.15 on page 143

```
1   function Poly_Schulz
2   %
3   % MATLAB function from:
4   % "Elements of Modern X-ray Physics" by Jens Als-Nielsen and Des McMorrow
5   %
6   % Calculates: Caclulates effect of polydispersivity using Schulz
7   %              distribution
8   % Calls to:
9
10  close all
11
12  axlm=[0 0.2 1e-4 5]; axis(axlm)
13  c1=[0.9 0.9 1];
14  patch([axlm(1) axlm(2) axlm(2) axlm(1)],[axlm(3) axlm(3) axlm(4) axlm(4)],...
15      [0 0 0 0],c1);
16  set(gca,'layer','top')
17  box on; grid on
18
19  Q=0.01:0.001:1;
20
21  R=50;
22  V=4*pi/3*R^3;
23  line(Q,(3*besselj(1,Q*R)./Q/R).^2,'linewidth',1.5)
24
25  z=99;
26  line(Q,Ischulz(R,z,Q)/V^2,'linestyle','--','color','r','linewidth',1.5)
```

```
27
28 z=24;
29 line(Q,Ischulz(R,z,Q)/V^2,'linestyle','-.','color','g','linewidth',1.5)
30
31 set(gca,'xtick',[0 0.05 0.1 0.15 0.2],'ytick',[1e-4 1e-2 1])
32 set(gca,'FontName','Times','FontSize',14,'yminortick','off','xminorgrid',...
33                                'off','yminorgrid','off','yscale','log')
34 ylabel('Intensity [arb. units]')
35 xlabel('Q [$$\mathrm \AA^{-1}$$]','interpreter','latex')
36 pos=get(gca,'position'); box on;
37
38 axes('position',[pos(1)+2/3*pos(3) pos(2)+2/3*pos(4) 0.3*pos(3) 0.3*pos(4)])
39 box on
40 Rv=0:0.01:100;
41 line(Rv,schulz(Rv,50,99),'linestyle','--','color','r','linewidth',1.5);
42 line(Rv,schulz(Rv,50,24),'linestyle','-.','color','g','linewidth',1.5);
43
44 set(gca,'FontName','Times','FontSize',14,'yminortick','off')
45 ylabel('$$D(R)$$','interpreter','latex')
46 xlabel('$$R [\mathrm \AA]$$','interpreter','latex')
47
48 function Icalc=Ischulz(R,z,Q)
49 %
50 % MATLAB function from:
51 % "Elements of Modern X-ray Physics" by Jens Als-Nielsen and Des McMorrow
52 %
53 % Calculates: Calculates SAXS intensity for a polydispersed ensemble of
54 %             spheres described by the schulz distribution
55 % Calls to:
56 alphaq=(z+1)./(Q*R);
57
58 A=8*pi.^2*R^6*(z+1).^(-6).*(alphaq).^(z+7);
59
60 Icalc=A.*(...
61  alphaq.^(-1.0*(z+1))-(4+alphaq.^2).^(-1.0*(z+1)/2).*cos(zetaii(z,alphaq,1))...
62  +(z+1)*(z+2)*(alphaq.^(-1.0*(z+3))+(4+alphaq.^2).^(-1.0*(z+3)/2)...
63  .*cos(zetaii(z,alphaq,3)))...
64  -2*(z+1)*(4+alphaq.^2).^(-1.0*(z+2)/2).*sin(zetaii(z,alphaq,2)));
65
66 function Sd=schulz(R,Rbar,z)
67 %
68 % MATLAB function from:
69 % "Elements of Modern X-ray Physics" by Jens Als-Nielsen and Des McMorrow
70 %
71 % Calculates: Calculates schulz distribution
72 % Calls to:
73
74 Sd=((z+1)/Rbar).^(z+1)*R.^z.*exp(-1.0*(z+1)*R/Rbar)/gamma(z+1);
```

Chapter 5: Kinematical diffraction II: crystalline materials

The Fibonacci chain, Fig. 5.11 on page 168

```
1 function [xn]=quasi
2 %
3 % MATLAB function from:
4 % "Elements of Modern X-ray Physics" by Jens Als-Nielsen and Des McMorrow
5 %
6 % Calculates: Positionso of atoms xn in a Fibonacci chain
7 %             from the strip projection method,
8 %             and calculates the scattered intensity
9 % Calls to: pline, isinpoly, arrow
10
11 figure; axes('position',[0.15 0.15 0.8 0.8],'visible','off'); axis equal
12
```

```
13  tau=(1+sqrt(5))/2;            % golden mean
14  latp=sqrt(1+tau^2);          % lattice parameter of 2D lattice
15  Nx=10; Ny=10;                 % number of lattice points
16  angle=atan(1/tau)*180/pi;    % angle of strip
17  Delta=1+tau;                  % width of strip
18
19  %----- Draw strip and rotate
20  h=patch([0 Nx*latp/cos(angle*pi/180) Nx*latp/cos(angle*pi/180) 0],...
21          [0 0 Delta Delta],[0.7 0.7 1]);
22  rotate(h,[0 0 1],angle,[0 0 0])
23  vp=get(h,'Vertices');
24
25  %----- Draw lattice
26  x=[]; for i=0:Nx; for j=0:Ny; x=[x;i j]; end; end
27  x=x*latp;
28  line(x(:,1),x(:,2),'linestyle','none',...
29      'marker','o','markerfacecolor','g','markersize',6);
30
31  %----- Find lattice points that lie in strip
32  isp=isinpoly(x(:,1),x(:,2),vp(:,1),vp(:,2)); x(find(isp~=1),:)=[];
33
34  b=vp(2,1:2);                  % end point of line xn
35  %----- Draw perpendicular lines from points in strip to xn
36  xn=[0]; yn=[0];
37  for ix=1:length(x)
38      [intx,inty]=pline(b,x(ix,:));
39      xn=[xn; intx]; yn=[yn; inty];
40  end
41  line(x(:,1),x(:,2),'linestyle','none',...
42      'marker','o','markerfacecolor','w','markersize',6);
43
44  %------ Label the graph
45  xnd=diff(xn);L=max(xnd); S=min(xnd);
46  for id=1:length(xnd)
47  if abs(xnd(id)-L)< 0.02 ,col=[0.6 0.6 0.6]; lab='L'; else col=[1 0 0]; lab='S'; end
48  line([xn(id) xn(id+1)],[yn(id) yn(id+1)],'color',col,'linewidth',2.0)
49  text(0.5*(xn(id)+xn(id+1)),-2,lab,'color',col,'horizontalalignment','center',...
50      'Fontsize',18,'FontName','Times')
51  end
52  arrow([-2 5*latp],[-2 6*latp],8,'ends','both')
53  text(-7,5.5*latp,'\surd(1+\tau^2)','Fontsize',24,'FontName','Times')
54  arrow(b,b*1.10,10)
55  text(b(1)*1.10,b(2)*1.0-0.2,'{\it x}_n','Fontsize',24,'FontName','Times',...
56      'horizontalalignment','center')
57  h=arrow(-0.1*b,-0.1*b+[0 1+tau],10,'ends','both'); rotate(h,[0 0 1],angle,[-0.1*b 0])
58  text(-0.1*b(1),-0.1*b(1)+2.5,'\Delta','Fontsize',24,'FontName','Times')
59  circ=4.5*latp; ax=circ*cos(angle*pi/180):0.005:circ;...
60      ay=sqrt(circ^2-ax.^2); line(ax,ay);
61
62  xn=xn./cos(angle*pi/180);
63
64  %----- Calculate scttareing from chain
65
66  figure; axes('position',[0.15 0.15 0.8 0.8])
67  Q=[0:0.01:20];
68  F=sum(exp(-1)*xn*Q));
69  plot(Q,F.*conj(F))
70  set(gca,'FontName','Times','FontSize',24,'Xtick',[0 5 10 15 20])
71  xlabel('Wavevector transfer (Å^{-1})'); ylabel('Intensity')
72
73  function [intx,inty]=pline(b,c)
74  %
75  % MATLAB function from:
76  % "Elements of Modern X-ray Physics" by Jens Als-Nielsen and Des McMorrow
77  %
78  % Calculates: Draws a perpendicular line from point c(x,y)
79  %             to line that starts at origin and ends at point b(x,y)
80
81  if norm(c)==0
82      tc=0;
```

```
 83 elseif c(1)==0 & c(2)~=0
 84    tc=pi/2;
 85 else
 86    tc=atan(c(2)./c(1));
 87 end
 88 tb=atan(b(2)./b(1)); dt=tc-tb;
 89
 90 intx=norm(c)*cos(dt)*cos(tb); inty=norm(c)*cos(dt)*sin(tb);
 91 line([c(1) intx],[c(2) inty],'color','w','linewidth',1.5)
 92
 93 function  isin = isinpoly(x,y,xp,yp)
 94 % ISIN = ISINPOLY(X,Y,XP,YP)   Finds whether points with coordinates X and Y are inside
 95 %         or outside of a polygon with vertices XP, YP. Returns matrix ISIN of the same
 96 %         size as X and Y with 0 for points outside a polygon, 1 for inside points and
 97 %         0.5 for points belonging to a polygon XP, YP itself.
 98 %  Copyright (c) 1995  by Kirill K. Pankratov
 99 %         kirill@plume.mit.edu, 4/10/94, 8/26/94.
100
101 %----- Handle input
102 if nargin<4
103   fprintf('\n Error: not enough input arguments.\n\n')
104   return
105 end
106 %----- Make the contour closed and get the sizes
107 xp = [xp(:); xp(1)]; yp = [yp(:); yp(1)];
108 sz = size(x); x = x(:); y = y(:);
109 lp = length(xp); l = length(x);
110 ep = ones(1,lp); e = ones(1,l);
111 %----- Calculate cumulative change in azimuth from points x,y to all vertices
112 A = diff(atan2(yp(:,e)-y(:,ep)',xp(:,e)-x(:,ep)'))/pi;
113 A = A+2*((A<-1)-(A>1));
114 isin = any(A==1)-any(A==-1);
115 isin = (abs(sum(A))-isin)/2;
116 %----- Check for boundary points
117 A = (yp(:,e)==y(:,ep)')&(xp(:,e)==x(:,ep)');
118 fnd = find(any(A));
119 isin(fnd) = .5*ones(size(fnd));
120 isin = round(isin*2)/2;
121 %----- Reshape output to the input size
122 isin = reshape(isin,sz(1),sz(2));
```

Crystal truncation rod properties, Fig. 5.13 on page 171

```
 1 function ctr
 2 %
 3 % MATLAB function from:
 4 % "Elements of Modern X-ray Physics" by Jens Als-Nielsen and Des McMorrow
 5 %
 6 % Calculates: Properties of the Crystal Truncation Rod
 7
 8 figure
 9 set(gcf,'papertype','a4','paperunits','centimeters','units','centimeters',...
10         'position',[0.1 -8 21 26],'paperposition',[0.1 0.1 21 26]);
11
12 %Plot rod from flat surface without (beta=0) and with (beta=0.2) absorption
13
14 axes('position',[0.2 0.55 0.6 0.35])
15 axlm=[0 2 0.1 1000]; axis(axlm)
16 c1=[0.9 0.9 1];
17 patch([axlm(1) axlm(2) axlm(2) axlm(1)],[axlm(3) axlm(3) axlm(4) axlm(4)],...
18    [0 0 0 0],c1);
19
20 ell1=[0.01:0.001:0.99];     % beta=0, l range chosen to avoid Bragg peak at l=1
21 F_CTR=1./(1-exp(i*2*pi*ell1));
22 h1=line(ell1,F_CTR.*conj(F_CTR),'color','b','linewidth',1.5,'linestyle','-')
23 ell2=[1.01:0.001:1.99];
24 F_CTR=1./(1-exp(i*2*pi*ell2));
25 line(ell2,F_CTR.*conj(F_CTR),'color','b','linewidth',1.5,'linestyle','-')
```

```
26
27  ell=[0.01:0.001:1.99];        % beta=0.2, l range now includes Bragg peak at l=1
28  beta=0.2;
29  F_CTR=1./(1-exp(i*2*pi*ell)*exp(-beta));
30  h2=line(ell,F_CTR.*conj(F_CTR),'color','r','linewidth',1.5,'linestyle','-.')
31
32  set(gca,'Fontsize',16,'FontName','Times','layer','top')
33  [h,obj]=legend([h1 h2],'\beta=0','\beta=0.2')
34  set(gca,'Fontsize',18,'FontName','Times')
35  set(gca,'FontName','Times','FontSize',18)
36  xlabel('{\it l} [r.l.u.]'); ylabel('|{\it F }^{CTR}|^2'); box on
37  axis([0.0 2.0 0.1 1000])
38  set(gca,'Ytick',[0.1 1 10 100 1000],'Yscale','Log')
39
40  %Plot rod from flat surface + overlayer at different relative diplacements, z0
41
42  axes('position',[0.2 0.12 0.6 0.35])
43  axlm=[0 2 0.1 1000]; axis(axlm);
44  c1=[1 1 0.9];
45  patch([axlm(1) axlm(2) axlm(2) axlm(1)],[axlm(3) axlm(3) axlm(4) axlm(4)],...
46      [0 0 0 0],c1);
47
48  ell1=[0.01:0.001:0.99];        %l range chosen to avoid Bragg peak at l=1
49  F_CTR=1./(1-exp(i*2*pi*ell1));
50  line(ell1,F_CTR.*conj(F_CTR),'color','b','linewidth',1.5,'linestyle','-')
51  ell2=[1.01:0.001:1.99];
52  F_CTR=1./(1-exp(i*2*pi*ell2));
53  h1=line(ell2,F_CTR.*conj(F_CTR),'color','b','linewidth',1.5,'linestyle','-')
54
55  z0=0.05;                       % relative displacement of overlayer, z0=0.05
56  F_CTR=1./(1-exp(i*2*pi*ell1));
57  F_T=F_CTR+exp(-i*2*pi*(1+z0)*ell1);
58  line(ell1,F_T.*conj(F_T),'color','r','linewidth',1.5,'linestyle','--')
59  F_CTR=1./(1-exp(i*2*pi*ell2));
60  F_T=F_CTR+exp(-i*2*pi*(1+z0)*ell2);
61  h2=line(ell2,F_T.*conj(F_T),'color','r','linewidth',1.5,'linestyle','--')
62
63  z0=-0.05;                      % relative displacement of overlayer, z0=-0.05
64  F_CTR=1./(1-exp(i*2*pi*ell1));
65  F_T=F_CTR+exp(-i*2*pi*(1+z0)*ell1);
66  line(ell1,F_T.*conj(F_T),'color','g','linewidth',1.5,'linestyle','-.')
67  F_CTR=1./(1-exp(i*2*pi*ell2));
68  F_T=F_CTR+exp(-i*2*pi*(1+z0)*ell2);
69  h3=line(ell2,F_T.*conj(F_T),'color','g','linewidth',1.5,'linestyle','-.')
70
71  set(gca,'FontName','Times','FontSize',18,'layer','top')
72  xlabel('{\it l} [r.l.u.]'); ylabel('|{\it F }^{CTR}|^2'); box on
73  set(gca,'Fontsize',14,'FontName','Times')
74  [h,obj]=legend([h1 h2 h3],'{\it z}_0=0','{\it z}_0=0.05','{\it z}_0=-0.05');
75  set(gca,'Fontsize',18,'FontName','Times')
76  axis([0. 2.0 0.1 1000])
77  set(gca,'Ytick',[0.1 1 10 100 1000],'Yscale','log')
```

Debye-Waller factor of aluminium, Fig. 5.16 on page 177

```
1   function DebyeWaller
2   %
3   % MATLAB function from:
4   % "Elements of Modern X-ray Physics" by Jens Als-Nielsen and Des McMorrow
5   %
6   % Calculates:  The Debye-Waller factor for Aluminium
7   % Calls to: phiDebye
8
9   figure
10  set(gcf,'papertype','a4','paperunits','centimeters','units','centimeters',...
11          'position',[0.1 -8 21 26],'paperposition',[0.1 0.1 21 26]);
12
13  % Plot of phi(x) vs x.
```

```
14
15  axes('position',[0.30 0.70 0.45 0.225]);
16  axlm=[0 8 0 1.1]; axis(axlm);
17  c1=[0.9 0.9 1];
18  patch([axlm(1) axlm(2) axlm(2) axlm(1)],[axlm(3) axlm(3) axlm(4) axlm(4)],...
19      [0 0 0 0],c1);
20
21  x=0.01:0.02:8;
22  for il=1:length(x), phi(il)=phiDebye(x(il));    end
23
24  line(x,phi,'color','b','linewidth',1.5)
25  grid on
26  set(gca,'FontName','Times','FontSize',16,'box','on','layer','top')
27  ylabel('$$\phi(\Theta/T)$$','interpreter','latex'); xlabel('$$\Theta/T$$',...
28      'interpreter','latex')
29
30  % Plot of sqrt(u^2) vs Temperature for Al
31
32  axes('position',[0.30 0.40 0.45 0.225]);
33  axlm=[0 1050 0 0.1]; axis(axlm);
34  c1=[1 0.9 1];
35  patch([axlm(1) axlm(2) axlm(2) axlm(1)],[axlm(3) axlm(3) axlm(4) axlm(4)],...
36      [0 0 0 0],c1);
37
38  Theta_Al=394;           % Debye temperature of Al
39  A=27;                   % Atomic mass
40  nnd=4.04/sqrt(2);       % Nearest neighbour distance
41  T=x*394;
42  B_Al=11492.*T.*phi/A/Theta_Al/Theta_Al+2873/A/Theta_Al;
43  rms=sqrt(3/8/pi/pi.*B_Al);
44  iT=find(T<933); iTg=find(T>=933);
45  line(T(iT),sqrt(2)*rms(iT)/4.04,'color','g','linewidth',1.5)
46  line(T(iTg),sqrt(2)*rms(iTg)/4.04,'color','g','linewidth',1.5,'linestyle',':')
47
48  grid on
49  set(gca,'FontName','Times','FontSize',16,'box','on','layer','top')
50  xlabel('Temperature [K]','position',[500 -0.017 0])
51  ylabel('$$\frac{\sqrt{\langle u^2 \rangle}}{a\sqrt{2}}$$',...
52      'interpreter','latex')
53
54  % Temperature dependence at different Q's
55
56  axes('position',[0.30 0.10 0.45 0.225]);
57  axlm=[0 1050 0 1.1];
58  axis(axlm);
59  c1=[1 1 0.9];
60  patch([axlm(1) axlm(2) axlm(2) axlm(1)],[axlm(3) axlm(3) axlm(4) axlm(4)],...
61      [0 0 0 0],c1);
62
63  I400=exp(-(8/4.04/4.04.*B_Al))./exp(-(8/4.04/4.04.*B_Al(1)));
64  I800=exp(-(32/4.04/4.04.*B_Al))./exp(-(32/4.04/4.04.*B_Al(1)));
65
66  line(T(iT),I400(iT),'color','r','LineWidth',1.5)
67  line(T(iT),I800(iT),'color','r','Linestyle','--','LineWidth',1.5)
68
69  grid on
70  set(gca,'FontName','Times','FontSize',16,'box','on','layer','top')
71  xlabel('Temperature (K)','position',[500 -0.2 0]);
72  ylabel('Relative Intensity')
73  text(650,0.30,'(8,0,0)','FontName','Times','FontSize',16)
74  text(650,0.70,'(4,0,0)','FontName','Times','FontSize',16)
75
76  function phi=phiDebye(x)
77  %
78  % MATLAB function from:
79  % "Elements of Modern X-ray Physics" by Jens Als-Nielsen and Des McMorrow
80  %
81  % Calculates: Evaluates the integral to calculate phi(x)
82  % Calls to: phiDebyeInt
83
```

```
84 phi=quad('phiDebyeInt',0.000000001,x)./x;
85
86 function y=phiDebyeInt(xi)
87 %
88 % MATLAB function from:
89 % "Elements of Modern X-ray Physics" by Jens Als-Nielsen and Des McMorrow
90 %
91 % Calculates: Defines the integrabd used to evaluate phi(x)
92 % Note: Must be placed in a separate file called phiDebyeInt.m
93
94 y=xi./(exp(xi)-1);
```

Fibre diffraction from DNA, Fig. 5.28 on page 196

```
1  function dna
2  %
3  % MATLAB function from:
4  % "Elements of Modern X-ray Physics" by Jens Als-Nielsen and Des McMorrow
5  %
6  % Calculates: Fibre diffraction pattern from DNA
7
8  [x,y]=meshgrid(-11:0.2:11,-11:0.2:11);
9
10 iw=20;    %iw is the inverse width of a Bragg peak, here modelled as a Gaussian
11 z=zeros(size(x));
12 for il=-11:11
13    z=z+ abs((1+exp(i*il*2*pi*0.125)).*besselj(abs(il),x)).^2.*exp(-iw*(y+il).^2);
14 end
15
16 pcolor(x,y,z)
17 shading interp
18
19 axis equal; axis([-11 11 -11 11]); caxis([-0.1 2]); box on
20 set(gca,'FontName','Times','FontSize',18,'Position',[0.15 0.15 0.7 0.7])
21
22 colormap(1-gray)
23 caxis([-0.05 0.3])
24 set(gca,'dataaspectratio',[1*34/20 1 1])
```

Crystal truncation rods from O on Cu(110), Fig. 5.31 on page 202

```
1  function cuoctr
2  %
3  % MATLAB function from:
4  % "Elements of Modern X-ray Physics" by Jens Als-Nielsen and Des McMorrow
5  %
6  % Calculates: CTR of O on Cu (110) and compares with data
7  % Calls to: ff
8  % Data: Feidenhans'l et al., Phys. Rev. B., vol. 41, page 5420 (1990)
9
10 %----- Cu real and reciprocal lattice parameters
11
12 ac=3.615; ar=2*pi/(ac/sqrt(2)); br=2*pi/ac; cr=2*pi/(ac/sqrt(2));
13
14 %(1,1) rod
15
16 figure; axes('position',[0.55 0.15 0.35 0.8]);
17 axlm=[0 1 6 100000 ];
18 axis(axlm)
19 c1=[0.9 0.9 1];
20 patch([axlm(1) axlm(2) axlm(2) axlm(1)],[axlm(3) axlm(3) axlm(4) axlm(4)],...
21     [0 0 0 0],c1);
22 set(gca,'layer','top'); box on
23
24 h=1; k=1; l=0.05:0.001:1.0; Q=sqrt(h^2*ar^2+k^2*br^2+l.^2*cr^2);
```

```matlab
25
26  %----- Cu form factor
27  a=[13.338 7.1676 5.6158 1.6735]; b=[3.5828 0.2470 11.3966 64.82]; c=[1.1910];
28  f_Cu=ff(a,b,c,Q);
29
30  %------ Cu Debye-Waller factor for bulk (B) and surface (S)
31  DW_Cu_B=exp(-0.55*(Q/4/pi).^2); DW_Cu_S=exp(-1.70*(Q/4/pi).^2);
32
33  %----- O form factor
34  a=[3.0485 2.2868 1.5463 0.8670]; b=[13.2771 5.7011 0.3239 32.9089]; c=[0.2508];
35  f_O=ff(a,b,c,Q);
36
37  %----- Bulk CTR
38  Phi=pi*(h+k+l); F_CTR=f_Cu.*DW_Cu_B./(1-exp(i*Phi));
39  line(l,4*abs(F_CTR).^2,'linestyle','-.','color','g','linewidth',1.5);
40  set(gca,'FontName','Times','FontSize',16,'Ytick',[1e1 1e2 1e3 1e4 1e5],'Yscale','log')
41  text(0.1,50000,'(b) (1,1) rod','FontName','Times','FontSize',16)
42
43  %----- Add 1/2 a monolayer of Cu (no relaxation)
44  F_S=0.5*f_Cu.*DW_Cu_S*exp(i*pi*(h+k)).*exp(-i*2*pi*0.5*l);
45  F_T=F_CTR+F_S;
46  line(l,4*abs(F_T).^2,'linestyle','--','color','r','linewidth',1.5);
47
48  %----- Add 1/2 a monolayer of Cu (relaxed to z0) plus O layer (relaxed to ť-z1)
49  z0=0.1445; z1=z0-0.133;
50  F_S=0.5*exp(i*pi*(h+k))*(f_Cu.*exp(-i*2*pi*(0.5+z0)*l).*DW_Cu_S...
51                          +f_O.*exp(i*pi*k).*exp(-i*2*pi*(0.5+z1)*l));
52  F_T=F_CTR+F_S;
53  line(l,4*abs(F_T).^2,'linestyle','-','color','b','linewidth',1.5);
54
55  %----- Add 1/2 a monolayer of Cu (relaxed to z0) plus O layer (relaxed to ť+z1)
56  z0=0.1445; z1=z0+0.133;
57  F_S=0.5*exp(i*pi*(h+k))*(f_Cu.*exp(-i*2*pi*(0.5+z0)*l).*DW_Cu_S...
58                          +f_O.*exp(i*pi*k).*exp(-i*2*pi*(0.5+z1)*l));
59  F_T=F_CTR+F_S;
60  line(l,4*abs(F_T).^2,'linestyle',':','color','k','linewidth',1.5);
61
62  data=[0.0787 4.5555;0.1517 3.8388;0.2247 3.5032;0.2978 3.1584;0.3539 3.0586;...
63        0.3708 2.8954;0.4382 2.6051;0.5169 2.3692;0.5787 2.1878;0.6517 1.9700;...
64        0.7360 1.9156];
65  line(data(:,1),10.^data(:,2),'marker','o','linestyle','none','markerfacecolor','w')
66
67  %(1,0) rod
68
69  axes('position',[0.10 0.15 0.35 0.8]);
70  axlm=[0 1 6 100000 ];
71  axis(axlm)
72  c1=[1 1 0.9];
73  patch([axlm(1) axlm(2) axlm(2) axlm(1)],[axlm(3) axlm(3) axlm(4) axlm(4)],...
74      [0 0 0 0],c1);
75  set(gca,'layer','top'); box on
76
77  h=1; k=0; l=0.0:0.001:0.95; Q=sqrt(h^2*ar^2+k^2*br^2+l.^2*cr^2);
78
79  %----- Cu form factor
80  a=[13.338 7.1676 5.6158 1.6735]; b=[3.5828 0.2470 11.3966 64.82]; c=[1.1910];
81  f_Cu=ff(a,b,c,Q);
82
83  %----- Cu Debye-Waller factor for bulk (B) and surface (S)
84  DW_Cu_B=exp(-0.55*(Q/4/pi).^2); DW_Cu_S=exp(-1.70*(Q/4/pi).^2);
85
86  %----- O form factor
87  a=[3.0485 2.2868 1.5463 0.8670]; b=[13.2771 5.7011 0.3239 32.9089]; c=[0.2508];
88  f_O=ff(a,b,c,Q);
89
90  %----- Bulk unit cell SF
91  Phi=pi*(h+k+l); F_CTR=f_Cu.*DW_Cu_B./(1-exp(i*Phi));
92
93  line(l,4*F_CTR.*conj(F_CTR),'linestyle','-.','color','g','linewidth',1.5);
94  set(gca,'FontName','Times','FontSize',16,'Ytick',[1e1 1e2 1e3 1e4 1e5],'yscale','log')
```

```
95  text(0.1,50000,'(a) (1,0) rod','FontName','Times','FontSize',16)
96  ylabel('Intensity (electron units)','Fontsize',18)
97  text(1.15,2,'l (r.l.u.)','FontName','Times','FontSize',18,...
98              'HorizontalAlignment','Center')
99
100 %----- Add 1/2 a monolayer of Cu (not relaxed)
101 F_S=0.5*exp(i*pi*(h+k))*f_Cu.*DW_Cu_S.*exp(-i*2*pi*(0.5+z0)*l);
102 F_T=F_CTR+F_S.*DW_Cu_B;
103 line(l,4*abs(F_T).^2,'linestyle','--','color','r','linewidth',1.5);
104
105 %----- Add 1/2 a monolayer of Cu (relaxed to z0) plus O layer (relaxed to t-z1)
106 z0=0.1145; z1=z0-0.133;
107 F_S=0.5*exp(i*pi*(h+k))*(f_Cu.*exp(-i*2*pi*(0.5+z0)*l).*DW_Cu_S...
108                       +f_O.*exp(i*pi*k).*exp(-i*2*pi*(0.5+z1)*l));
109 F_T=F_CTR+F_S;
110 line(l,4*abs(F_T).^2,'linestyle','-','color','b','linewidth',1.5);
111
112 %----- Add 1/2 a monolayer of Cu (relaxed to z0) plus O layer (relaxed to t+z1)
113 z0=0.1145; z1=z0+0.133;
114 F_S=0.5*exp(i*pi*(h+k))*(f_Cu.*exp(-i*2*pi*(0.5+z0)*l).*DW_Cu_S...
115                       +f_O.*exp(i*pi*k).*exp(-i*2*pi*(0.5+z1)*l));
116 F_T=F_CTR+F_S;
117 line(l,4*abs(F_T).^2,'linestyle',':','color','k','linewidth',1.5);
118
119 %----- Plot data
120 data=[0.0226 1.8793;0.0960 1.9973;0.1695 2.2785;0.2429 2.4781;0.3220 2.7139;...
121       0.3955 2.8228;0.4689 2.9861;0.5480 3.1222;0.6158 3.2310;0.6949 3.4124;...
122       0.7740    3.6574];
123 line(data(:,1),10.^data(:,2),'marker','o','linestyle','none','markerfacecolor','w')
```

In-plane Bragg reflections of O on Cu(110), Table 5.2 on page 201

```
1  function Iout=cuFS(hp,k)
2  %
3  % MATLAB function from:
4  % "Elements of Modern X-ray Physics" by Jens Als-Nielsen and Des McMorrow
5  %
6  % Calculates: In-plane Bragg peak intensities for O on Cu(110)
7  % Inputs: (hp,k), Miller indices of Bragg peak
8  % Outputs: Iout, Intensity
9  % Calls to: ff
10
11 %----- Cu real and reciprocal lattice parameters
12
13 ac=3.615; ar=2*pi/(2*ac/sqrt(2)); br=2*pi/ac; cr=2*pi/(ac/sqrt(2));
14
15 l=0; Q=sqrt(hp^2*ar^2+k^2*br^2+l.^2*cr^2);
16
17 %----- Cu form factor
18 a=[13.338 7.1676 5.6158 1.6735]; b=[3.5828 0.2470 11.3966 64.82]; c=[1.1910];
19 f_Cu=ff(a,b,c,Q);
20
21 %----- Cu Debye-Waller factor for bulk and surface
22 DW_Cu_B=exp(-0.55*(Q/4/pi).^2);
23 DW_Cu_S=exp(-1.70*(Q/4/pi).^2);
24
25 %----- O form factor
26 a=[3.0485 2.2868 1.5463 0.8670]; b=[13.2771 5.7011 0.3239 32.9089]; c=[0.2508];
27 f_O=ff(a,b,c,Q);
28
29 delta=0.031/(2*ac/sqrt(2));
30
31 F_1=f_Cu.*DW_Cu_S+f_O*exp(i*pi*k);
32 F_2=(-1)^(hp/2+k+0.5)*2.*f_Cu.*DW_Cu_B*sin(2*pi*hp*delta);
33 F_S=F_1+F_2;
34 Iout=1.047539547173480e-002*abs(F_S).^2;
```

Form factor

```
1  function fofQ=ff(a,b,c,Q)
2  %
3  % MATLAB function from:
4  % "Elements of Modern X-ray Physics" by Jens Als-Nielsen and Des McMorrow
5  %
6  % Calculates: X-ray form factor as a function of Q
7  % Inputs: (a,b,c), coeffics. from ITC, Q
8  % Outputs: fofQ, form factor
9  % Note: Q is given by 4*pi*sin(theta)/lambda.
10
11 %----- Convert Q to be compatible with the definition
12 %      in the International Tables of Crystallography
13
14 Q=Q/(4*pi);
15 fofQ=a(1)*exp(-b(1)*Q.^2)+...
16     a(2)*exp(-b(2)*Q.^2)+a(3)*exp(-b(3)*Q.^2)+a(4)*exp(-b(4)*Q.^2)+c;
```

Chapter 6: Diffraction by perfect crystals

Darwin curve including absorption, Fig. 6.10 on page 228

```
1  function darabs
2  %
3  % MATLAB function from:
4  % "Elements of Modern X-ray Physics" by Jens Als-Nielsen and Des McMorrow
5  %
6  % Calculates: Darwin reflectivity curve of Si (111), including absorption
7
8  close all; clear all;
9  set(gcf,'papertype','a4','paperunits','centimeters','units','centimeters')
10 set(gcf,'position',[0.1 -8 21 26],'paperposition',[0.1 0.1 21 26])
11
12 axes('Position',[0.2 0.60 0.6 0.40])
13 axlm=[-2 2 0 1.1]; axis(axlm);
14 c1=[0.9 0.9 1];
15 patch([axlm(1) axlm(2) axlm(2) axlm(1)],[axlm(3) axlm(3) axlm(4) axlm(4)],...
16     [0 0 0 0],c1);
17 set(gca,'layer','top')
18
19 % Case 1: lambda=1.5405 Angs
20 r0=2.82E-5;                         % Thompson scattering length in Angs
21 V=160.1966;                         % unitcell vol. in Ang^3 e.g. 160.1966 for Si
22 d=3.13562;                          % d spacing for Si (111)
23 m=1;                                % order of reflection, 1= (111), 3=(333)
24 F_hkl=abs(4-4*i)*(10.54+0.25-i*0.33);  % Complex structure factor for 111
25 F_0=8*(14+0.25-i*0.33);             % Complex structure factor for 000
26 g=(2*d*d/m)*(r0/V)*F_hkl;
27 g0=g*(F_0/F_hkl);
28 [x,R]=darwin(g,g0,m); line(x,R,'color','c','linestyle','--','linewidth',1.5)
29
30 axis([-2 2 0 1.1])
31 set(gca,'Ytick',[0 0.5 1],'FontSize',20,'FontName','Times')
32 xlabel('$$x=m\pi\frac{\zeta}{\mathrm g}-\frac{\mathrm g_0}{\mathrm g}$$',...
33     'interpreter','latex','position',[0 -0.1 0]);
34 ylabel('Intensity reflectivity','position',[-2.75 0.5 0])
35 box on; grid on
36
37 % Case 2: lambda=0.70926 Angs
38 F_0=8*(14+0.082-i*0.071);           % Complex structure factor for 000
39 F_hkl=abs(4-4*i)*(10.54+0.082-i*0.071);   % Complex structure factor for 111
40 g=(2*d*d/m)*(r0/V)*F_hkl;
41 g0=g*(F_0/F_hkl);
42 [x,R]=darwin(g,g0,m);
```

```
43  line(x,R,'color','b','linestyle','-','linewidth',1.5);
44  text(-1.80,0.95,'(a)','FontName','Times','Fontsize',24)
45
46  % Plot as a function of energy and angular variable in milli degrees
47
48  axes('Position',[0.2 0.08 0.6 0.40])
49  axlm=[-3 3 0 1.1]; axis(axlm);
50  c1=[1 1 0.9];
51  patch([axlm(1) axlm(2) axlm(2) axlm(1)],[axlm(3) axlm(3) axlm(4) axlm(4)],...
52       [0 0 0 0],c1);
53  set(gca,'layer','top')
54
55  lambda=12.398/5.000;                   % 5 keV
56  theta=asin(m*lambda/2/d);
57  F_hkl=abs(4-4*i)*(10.54+0.38-i*0.8029);   % Complex structure factor for 111
58  F_0=8*(14+0.3807-i*0.8029);               % Complex structure factor for 000
59  g=(2*d*d/m)*(r0/V)*F_hkl;
60  g0=g*(F_0/F_hkl);
61  [x,R]=darwin(g,g0,m);
62  line(x*real(g/m/pi)*tan(theta)*180/pi*1e3,R,'color','b',...
63       'linestyle','--','linewidth',1.5)
64
65  lambda=12.398/10.000;                  % 10 keV
66  theta=asin(m*lambda/2/d);
67  F_hkl=abs(4-4*i)*(10.54+0.1943-i*0.2169);  % Complex structure factor for 111
68  F_0=8*(14+0.1943-i*0.2169);                % Complex structure factor for 000
69  g=(2*d*d/m)*(r0/V)*F_hkl;
70  g0=g*(F_0/F_hkl);
71  [x,R]=darwin(g,g0,m);
72  line(x*real(g/m/pi)*tan(theta)*180/pi*1e3,R,'color','r',...
73       'linestyle','--','linewidth',1.5)
74
75  lambda=12.398/50.000;                   % 50 keV
76  theta=asin(m*lambda/2/d);
77  F_hkl=abs(4-4*i)*(10.54+0.0027-i*0.0076);   % Complex structure factor for 111
78  F_0=8*(14+0.0027-i*0.0076);                 % Complex structure factor for 000
79  g=(2*d*d/m)*(r0/V)*F_hkl;
80  g0=g*(F_0/F_hkl);
81  [x,R]=darwin(g,g0,m);
82  line(x*real(g/m/pi)*tan(theta)*180/pi*1e3,R,'color','g',...
83       'linestyle','-','linewidth',1.5)
84
85  set(gca,'Xtick',[-2 -1 0 1 2],'Ytick',[0 0.5 1],'FontSize',20,'FontName','Times')
86  xlabel('\omega [milli degrees]');
87  ylabel('Intensity reflectivity','position',[-4.15 0.55 0])
88  box on; grid on
89  text(-2.85,0.25,'5 keV','FontName','Times','Fontsize',18)
90  text(-2.10,0.15,'10 keV','FontName','Times','Fontsize',18)
91  text(-1.30,0.05,'50 keV','FontName','Times','Fontsize',18)
92  text(-2.70,0.95,'(b)','FontName','Times','Fontsize',24)
93
94  function [x,R]=darwin(g,g0,m);
95  %
96  % MATLAB function from:
97  % "Elements of Modern X-ray Physics" by Jens Als-Nielsen and Des McMorrow
98  %
99  % Calculates: Darwin reflectivity R vs x  (absorption effects included)
100
101 x_m=[-5:0.01:-1]; zeta=real((g*x_m+g0)/m/pi); xc_m=m*pi*zeta/g-g0/g;
102 rc_m=xc_m+sqrt(xc_m.^2-1);
103 x_t=[-1:0.01:1]; zeta=real((g*x_t+g0)/m/pi); xc_t=m*pi*zeta/g-g0/g;
104 rc_t=xc_t-i*sqrt(1-xc_t.^2);
105 x_p=[1:0.01:5]; zeta=real((g*x_p+g0)/m/pi); xc_p=m*pi*zeta/g-g0/g;
106 rc_p=xc_p-sqrt(xc_p.^2-1);
107 x=[x_m x_t x_p]; rc=[rc_m rc_t rc_p];
108 R=abs(rc).^2;
```

Chapter 7: Photoelectric absorption

K absorption edge of Kr, Fig. 7.5 on page 250

```matlab
function kedge
%
% MATLAB function from:
% "Elements of Modern X-ray Physics" by Jens Als-Nielsen and Des McMorrow
%
% Calculates: Photoelectric absorption cross-section of Kr - comparison
%             between hydrogen-like model of K shell contribution and the
%             self-consistent Dirac-Hartree-Fock theory
%             (C.T. Chantler, J. Phys. Chem. Ref. Data vol. 24, 71 (1995))
% Calls to: loaddata

[en,sigma,thom_comp]=loaddata;           % load theoretical values

%----- Plot theoretical photoelectron and (Thomson+Compton) cross-sections

line(en,sigma,'linestyle','-.'); line(en,thom_comp,'linestyle','--')

%----- Find L shell photoelectric contribution below 14.3 keV

xl=find(en<14.3); xg=find(en>14.32);
xlog=log10(en(xl));
ylog=log10(sigma(xl));
[P,S]=polyfit(xlog,ylog,1);
ylogfit=polyval(P,log10(en));
y=10.^ylogfit;
line(en(xg),y(xg),'linestyle',':')       % Plot L contribution for E>14.32

%----- Plot theorectical absorption for K shell from Stoppe theory

en=en(xg); y=y(xg);
r0=2.82e-5;                               % Thomson scattering length
ek=14.32;                                 % K edge of Kr energy in keV
lambda=12.398./en;
xi=sqrt(ek./(en-ek));
f=2*pi*sqrt(ek./en).*exp(-4*xi.*acot(xi))./(1-exp(-2*pi*xi));
sigmaa=256/3.*lambda.*(ek./en).^2.5.*f*r0*1e8;
line(en,sigmaa+y,'color','r','linewidth',2)
axis([5 40 50 100000])
set(gca,'FontName','Times','FontSize',18,'Xtick',[5 10 20 50],...
    'Xscale','log','Yscale','log')
grid on; box on
xlabel('Photon energy [keV]');ylabel('Absorption cross-section [barn]')

text(6,150,'Thomson+Compton','FontName','Times','Fontsize',18)
text(10,20000,'L edges','FontName','Times','Fontsize',18,...
     'horizontalalignment','center')
text(25,20000,'K + L edges','FontName','Times','Fontsize',18,...
     'horizontalalignment','center')

function [en,sigma,thom_comp]=loaddata
%
% MATLAB function from:
% "Elements of Modern X-ray Physics" by Jens Als-Nielsen and Des McMorrow
%
% Photoelectric and Thomson+Compton cross-sections for Kr

en=[5.3 5.66 6.05 6.47 6.92 7.39 7.9 8.45 9.03 9.65 10.3 11 11.8 12.6 13.5 14 14.3...
 14.3 14.4 14.6 15.4 16.5 17.6 18.8 20.1 21.5 23 24.6 26.3 28.1 30 32.1 34.3 36.7 39.2];
sigma=[...
 3.83e+004 3.20e+004 2.67e+004 2.23e+004 1.87e+004 1.57e+004 1.31e+004 1.09e+004...
 9.04e+003 7.43e+003 6.11e+003 5.03e+003 4.14e+003 3.42e+003 2.82e+003 2.51e+003...
 2.40e+003 2.37e+003 1.81e+004 1.74e+004 1.49e+004 1.25e+004 1.05e+004 8.87e+003...
 7.42e+003 6.20e+003 5.17e+003 4.32e+003 3.60e+003 3.00e+003 2.48e+003 2.05e+003...
 1.69e+003 1.40e+003 1.15e+003];
thom_comp=[...
```

```
66  4.72e+002 4.49e+002 4.27e+002 4.04e+002 3.82e+002 3.61e+002 3.40e+002 3.20e+002...
67  3.00e+002 2.81e+002 2.63e+002 2.45e+002 2.29e+002 2.13e+002 1.98e+002 1.89e+002...
68  1.86e+002 1.85e+002 1.84e+002 1.81e+002 1.71e+002 1.58e+002 1.47e+002 1.36e+002...
69  1.26e+002 1.16e+002 1.07e+002 9.92e+001 9.18e+001 8.49e+001 7.85e+001 7.27e+001...
70  6.73e+001 6.24e+001 5.80e+001];
```

Chapter 9: Imaging

Numerical example of the reconstruction of a two-dimensional object from its Radon transform, Fig. 9.5 on page 311

```
1  function Sinogram
2  %
3  % MATLAB function from:
4  % "Elements of Modern X-ray Physics" by Jens Als-Nielsen and Des McMorrow
5  %
6  % Calculates: Numerical example of reconstruction of phantom
7  %             from its Sinogram
8  % Calls to: radon, iradon (part of Matlab's image processing toolbox)
9  close all; clear all;
10
11 set(gcf,'position',[100 100   560*1.3   420*1.3])
12
13 xst=0.0; yst=0.075; xsp=0.36; xln=0.3; yln=0.3
14
15 % (c) Plot phantom model
16 axes('position',[xst yst 0.3 0.3])
17 a=imread('p.jpg');   % Read in phantom (any suitable b+w jpeg will do)
18 imagesc(a')
19 colormap(hot)
20 b=double(a);         % Convert to double precision for following routines
21 axis([1 236 1 236]); daspect([1 1 1])
22 set(gca,'xticklabel',[],'yticklabel',[])
23 text(0.01,1.10,'(c) Model {\it f(x,y)}','FontName','Times','Fontsize',14,...
24     'units','normalized')
25
26 % (d) Calculate and plot Sinogram of phantom
27 axes('position',[xst+xsp yst 0.3 0.3])
28 theta3=0:2:178;
29 [R3,xp]=radon(b,theta3);
30 imagesc(theta3,xp,R3);
31 axis([min(theta3) max(theta3) min(xp)+40 max(xp)-40])
32 set(gca,'xtick',[0 50 100 150],'ytick',[-100 -50 0 50 100],...
33     'FontName','Times','FontSize',12)
34 xlabel('Projection angle \theta [Degs]'); ylabel('Position on detector x\prime');
35 text(0.01,1.10,'(d) Sinogram','FontName','Times','Fontsize',14,'units','normalized')
36
37 % (e) Reconstruct phantom from Sinogram and plot
38 axes('position',[xst+2*xsp yst 0.3 0.3])
39 [I3,H3]=iradon(R3,theta3,'Cosine');
40 imagesc(I3');
41 caxis(gca,[100 200]); axis([2 236 2 236]); daspect([1 1 1])
42 set(gca,'xticklabel',[],'yticklabel',[])
43 text(0.01,1.10,'(e) Reconstructed {\it f(x,y)}','FontName','Times',...
44     'Fontsize',14,'units','normalized')
45
46 % Add theta=0 projections
47 axes('position',[xst+0.10 yst+0.69 0.3*0.75 0.3*0.75])
48 hold on
49 axis([0 100 -100 100])
50 arrow3([0 -50],[100 -50],'r1.5',4,10); arrow3([0 -25],[100 -25],'r1.5',4,10)
51 arrow3([0 0],[100 0],'r1.5',4,10); arrow3([0 25],[100 25],'r1.5',4,10)
52 arrow3([0 50],[100 50],'r1.5',4,10)
53 axis off
54 text(0.01,0.9,'(a) \theta=0','FontName','Times','Fontsize',14,'units','normalized')
```

```
55
56 axes('position',[xst+xsp+0.05 yst+0.69 0.3*0.75 0.3*0.75])
57 a=imread('p.jpg');
58 imagesc(a)
59 colormap(hot)
60 b=double(a); % Convert to double precision for following routines
61 axis([1 236 1 236]); daspect([1 1 1])
62 set(gca,'xticklabel',[],'yticklabel',[])
63
64 ha=axes('position',[xst+2*xsp+0.69 0.3*0.75 0.3*0.75])
65 iff=find(theta3==0); ifx=find(xp<-115 | xp>115);
66 xp(ifx)=[]; R3(ifx,:)=[];
67 line(1-(R3(1:end,iff)-min(R3(:,iff)))/max(R3(1:end,iff)),xp,'linewidth',1.5)
68 axis([0 1.2 -120 120]); axis square; box on
69
70 set(gca,'xticklabel',[],'yticklabel',[],'ydir','reverse',...
71     'FontName','Times','FontSize',10)
72 xlabel('I/I_0'); ylabel('Position on detector x\prime')
73
74 % Add theta=90 projections
75 axes('position',[xst+0.10 yst+0.41 0.3*0.75 0.3*0.75])
76 hold on
77 axis([0 100 -100 100])
78 arrow3([0 -50],[100 -50],'r1.5',4,10); arrow3([0 -25],[100 -25],'r1.5',4,10)
79 arrow3([0 0],[100 0],'r1.5',4,10); arrow3([0 25],[100 25],'r1.5',4,10)
80 arrow3([0 50],[100 50],'r1.5',4,10)
81 axis off
82 text(0.01,0.9,'(b) \theta=90^o','FontName','Times','Fontsize',14,'units','normalized')
83
84 axes('position',[xst+xsp+0.05 yst+0.41 0.3*0.75 0.3*0.75])
85 a=imread('p.jpg');
86 hi=surf(double(a)); shading interp; colormap(hot)
87 b=double(a); % convert to double precision for following routines
88 axis([1 236 1 236]); daspect([1 1 1])
89 set(gca,'xticklabel',[],'yticklabel',[])
90
91 ha=axes('position',[xst+2*xsp yst+0.41 0.3*0.75 0.3*0.75])
92 iff=find(theta3==90); ifx=find(xp<-115 | xp>115);
93 xp(ifx)=[]; R3(ifx,:)=[];
94 line(1-(R3(1:end,iff)-min(R3(:,iff)))/max(R3(1:end,iff)),xp,'linewidth',1.5)
95 axis([0 1.2 -120 120]); axis square; box on
96
97 set(gca,'xticklabel',[],'yticklabel',[],'ydir','reverse',...
98     'FontName','Times','FontSize',10)
99 xlabel('I/I_0'); ylabel('Position on detector x\prime')
```

Wavefield propagation for a Fresnel zone plate, Fig. 9.15 on page 323

```
1 function Fresnel_ZP
2 %
3 % MATLAB function from:
4 % "Elements of Modern X-ray Physics" by Jens Als-Nielsen and Des McMorrow
5 %
6 % Calculates: Wavepropagation after a 1D absorption Fresnel zone plate
7 % Calls to:
8 close all; clear all; figure(1);set(gcf,'Position',[0 0 600 800])
9
10 %Define focal length.
11 f = 1e5;                      % Focus length is 10 cm = 1e5 microns
12 lambda = 1e-4;                % Wavelength is 1 \AA
13
14 % Define how many steps along the propagation distance & resolution
15 Prop_steps=500;
16 z = [0:1/Prop_steps:1]* f;    % Propagate from 0 to f
17 fieldwidth = 100;             % Total width of field (in microns)
18
19 % Define the Fresnel lens (symmetric around zero)
20 Nzones = 19;                  % Number of zones
```

```
21  zone=sqrt(f*[1:Nzones]*lambda); % Zones on zone plate
22
23  Precision=2^13;                   % Precision is on x-axis
24  x=[0:1/Precision:1]*fieldwidth;
25  plate = ones(size(x));
26  current_zone = 1;
27  for n=1:length(x)
28      if abs(x(n))<zone(current_zone)
29          plate(n) = 0.5 - 0.5*(-1)^current_zone;
30      else
31          current_zone=current_zone+1;
32          plate(n) = 0.5 - 0.5*(-1)^current_zone;
33      end
34      if current_zone>Nzones,N=n;break,end
35  end
36  plate= [fliplr(plate) plate(2:length(plate))];plate= 1-plate;
37
38  x=[-1:1/Precision:1]*fieldwidth;
39  % Define incoming wave and create the complex field
40  ampin= plate; phin = 0.*plate; % absorption plate; use line below for phase plate
41  %ampin=[zeros(1,Precision-N) ones(1,2*N+1) zeros(1,Precision-N)]; phin=pi.*plate;
42  fieldin = ampin.*exp(sqrt(-1).*phin);
43
44  % Fourier space propagation
45  uin = fftshift(fft(fieldin));               % Go to fourier space
46  fpg = exp(-sqrt(-1)*pi*lambda*z'*((x).^2)/6);   % Define matrix for different distances
47  uin = ones(size(z'))*uin;
48  uout = fpg.*uin;                            % Multiply fresnel propagator
49  fieldout = ifft((uout),[],2);               % Go back to real space
50
51  ampplot = (abs(fieldout'));
52  fieldsize=size(fieldout);
53  Plotsize = [round(fieldsize(2)/2)-2000 round(fieldsize(2)/2)+2000 1 fieldsize(1)];
54
55
56  % Plot Fresnel lens (starting field)
57  axes('Position',[0.55 0.8 0.4 0.1]);
58  area(Plotsize(1):Plotsize(2),1-abs(fieldin(Plotsize(1):Plotsize(2))),...
59      'FaceColor',[0 0 0])
60  set(gca,'FontName','Times','Xtick',[],'Ytick',[]);
61  title('Fresnel Zone Absorption Plate'); box on;
62
63  % Plot wavefield
64  axes('Position',[0.55 0.30 0.4 0.45])
65  imagesc(ampplot(Plotsize(1):Plotsize(2),Plotsize(3):Plotsize(4))');
66  colormap jet;
67  set(gca,'xtick',[],'ytick',[],'FontName','Times');
68  title('Wave Propagation');
69
70  % Plot Intensity profile
71  axes('Position',[0.55 0.10 0.4 0.15]);
72  plot(x(Plotsize(1):Plotsize(2)),ampplot(Plotsize(1):Plotsize(2),Plotsize(4)),'r-');
73  axis([x(Plotsize(1)) x(Plotsize(2)) 0 6.0])
74  set(gca,'FontName','Times');
75  title('Amplitude profile');
76  xlabel('$$x$$ [$$\mu$$m]','FontName','Times','interpreter','latex')
```

Answers to exercises and hints

2. Sources

2.1: Start from Eq. (1.1) and use the fact that 1 eV is equivalent to 1.602×10^{-19} J.

2.2: With ρ =24.8 m, I=0.2 A, and $\mathcal{E}_e$=6 GeV, $\mathcal{P}$ =1.2 MW.

2.3: For *protons*, $\gamma = 7.4 \times 10^3$, $\rho = 2.8$ km, and $\mathcal{P}$=3.9 kW. For *electrons*, $\gamma = 1.4 \times 10^7$, and $\mathcal{P}$=44 PW.

2.4: No. The characteristic energy is $\hbar\omega_c = 3\hbar c\gamma^3/(2\rho) = 44$ eV corresponding to a wavelength of λ=280 Å.

2.5: The formulae given in the question can be rearranged to read $\nu = c/(\lambda_U(1 - \beta))$, and with $\lambda = c/\nu$ and $1 - \beta = 1/(2\gamma^2)$ the desired result is obtained.

2.6: Use Eq. (2.14) as your starting point, and note that with the electron energy in GeV $1/(2\gamma^2)= (0.511 \times10^{-3})^2/ (2\mathcal{E}_e^2) =13.056\times10^{-8}/ \mathcal{E}_e^2$. An additional factor of 10^8 is introduced when converting from cm to Å.

2.7: (a) The formula for the fractional energy change can be considered as a function $\mathcal{G}(\psi)$ of the scattering angle ψ. As the initial photon energy χ_i is much less than the electron energy γ_i, and that β_i is close to unity, one obtains that $\mathcal{G}(\psi)= (1 - \cos\psi)/ (1 + (\chi_i/\gamma_i) \cos\psi)$ which clearly has a maximum when $\psi = \pi$. (b) With the same approximations as in part (a), and setting $\psi = \pi$, the fractional energy change is

$2\gamma/[\gamma(1 - \beta)] = 2/(1 - \beta) = 4\gamma^2$. The X-ray wavelength for the parameters given is 1 Å.

2.8: $u = 4 \times 10^7$ J/m^3=$\epsilon_0 c^2\langle B^2\rangle_{av}$ =$\epsilon_0 c^2 B_L^2/2$=$\epsilon_0 c^2 B_u^2/2/4$. $\therefore$ B$_u \approx 20$ T. With $K \approx 10^{-3}$, and $N = 10^4$, the flux is of order 10^{11} photons/s/0.1%BW.

3. Reflection and refraction from interfaces

3.1: Inside the material, $m\lambda' = 2d \sin\theta'$, and with $\lambda' = \lambda/n = \lambda/(1 - \delta)$ this becomes $m\lambda= 2d (1 - \delta) \sin\theta'$. Since $n \cos\theta' = \cos\theta$, we have $\sin\theta' = \sqrt{1 - \cos^2\theta'} \approx \sin\theta (1 - \delta/\tan^2\theta)$. Therefore $m\lambda= 2d \sin\theta (1 -\delta/\sin^2\theta)$, and the formula stated in the question follows on making the substitution $1/\sin\theta = 2d/(m\lambda)$.

3.2: $\alpha_c = 3$ mrad, and $\therefore \alpha = 2.4$ mrad. The minimum penetration depth is $1/Q_c=1/(2k\alpha_c) = 32$ Å.

3.3: A plot of the square of the angular position of the intensity maxima against the square of the fringe order should produce a straight line with an intercept of α_c^2 and a gradient of $(\lambda/(2t))^2$.

3.4: 1.5×10^{-2}, 2.3×10^{-3} and 6.6×10^{-4} for $m = 2$, 3 and 4, respectively.

3.5: $\alpha = 2.5$ mrad, and $\mathcal{E}_c$=24.8 keV.

3.6: $t(r) = r^2/D$, *c.f.* the equation immediately below Eq. (3.42), and $t_{av} = \int_0^{d/2} 2\pi r\, t(r)dr/$

$\int_0^{d/2} 2\pi r dr = (d/8)\alpha$ with $\alpha = d/D$.

3.7: The number of lenses required is $N=235$. The average thickness of a lens is $t_{av} = 25$ μm within the 400 μm aperture. The average transmission is 55%.

3.8: Footprint; 200 mm. $\rho_{tangential}=2$ km, $\rho_{sagittal}=5$ cm. Alignment accuracy required: 0.025 mrad.

4. Kinematical scattering I: non-crystalline materials

4.1: The intrinsic width in energy (FWHM) of the inelastic line can be estimated by subtracting in quadrature the resolution estimated from the elastic line. This assumes that both the elastic and inelastic lines may be approximated by Gaussians. The FWHM of the momentum distribution is then estimated to be ~ 0.3 Å^{-1}.

4.2: Assume that both electrons in the He atom have the same form factor given by Eq. (4.9). The desired result follows immediately, which yields essentially perfect agreement when compared with Fig. 4.5(a).

4.3: $I(Q) = 2Z^2 [1+ \sin (Qa)/(Qa)]/ [1+ (Qa/20)^2]^4$. $Qa=0$ for the first maximum. Numerical plot reveals the second maximum at $Qa \approx 6.75$.

4.4: $2f_1^2 + f_2^2 + 4f_1 f_2 \sin (Qa) / (Qa)+ 2f_1^2 \sin (2Qa) / (2Qa)$.

4.6: Integration of $\rho(r)$ over all space must yield the total charge of $6 \times 60 = 360$ electrons for the C_{60} molecule, and hence $A=360$.

4.7: Guinier approximation, $y_G= e^{-x^2/5} = 0.7020$ for $x=1.33$. Exact, $y = 3[\sin x -x \cos x]/ x^3 = 0.6954$ for $x= 1.33$.

4.10: $\mathcal{F}(Q) \approx [V_p -(1/2) \int (\mathbf{q} \cdot \mathbf{r})^2 dV_p +...] /V_p = 1- (q^2/(6V_p)) \int r^2 dV_p = 1- q^2 R_g^2/6$, and the result follows when substituting the form factor into Eq. (4.22).

5. Kinematical scattering II: crystalline materials

5.1: (a) $d_{10} = \sqrt{3}/2$, $d_{11} = 1/2$ (b) Let $\mathbf{a}_1^* = (\alpha,\beta)$ and $\mathbf{a}_2^* = (\gamma,\delta)$, then use $\mathbf{a}_i \cdot \mathbf{a}_j^* = 2\pi\delta_{ij}$ to determine the unknown coefficients α, β, γ and δ. (e) $d_{hk} = \sqrt{3}a/(2 \sqrt{h^2 + hk + k^2})$.

5.2: First show that $\sin^2 \theta$ is proportional to $h^2 + k^2 + l^2$. Then calculate the eight values of the ratio $(\sin \theta_i / \sin \theta_1)^2$ for $i= 1\cdots 8$, noting that θ is half of the given scattering angles, and compare with $h^2 + k^2 + l^2$. This allows the peaks to be indexed. Lastly compare with the selection rules for simple cubic, bcc and fcc, from which you should conclude that the sample has a simple cubic lattice.

5.3: Use Eq. (5.34) which requires evaluating the multiplicities of all reflections. Note that the (300) and (221) have the same value of $h^2 + k^2 + l^2$.

5.4: $F_{h,k,l} = 4(f_{Na} - f_H)$ for (h, k, l) all odd, and $F_{h,k,l} = 4(f_{Na} + f_H)$ for (h, k, l) all even. For X-rays, $f \propto Z$ for Q=0, and since $Z_{Na} \gg Z_H$, both types of peaks are present. In the case of neutrons, the fact that the (h, k, l) even peaks are absent implies that the scattering lengths of Na and H are of equal magnitude but of opposite sign.

5.5: Use $d_{hkl}= 2\pi/|\mathbf{G}|$.

5.6: The (1,0,0), $|F_{100}|^2=1$; and the (0,0,2), $|F_{100}|^2=4$, are the first two allowed reflections that are closet to the origin.

5.7: By definition, $M = B_T (\sin \theta/\lambda)^2 =B_T (G/4\pi)^2 =B_T(h^2 + k^2 + l^2)/(4a^2)$. From Fig. 5.16 we obtain $\phi(\Theta/T)= 0.55$, which yields $B_T = 0.32$ Å^2. Since $e^{-M} \approx 1 - M$, $M =0.55$ which when combined with the above expression for M leads to the result that the (331) reflection is the first to lose 5% of its intensity.

5.9: The contribution to the scattering amplitude from the layers above $z = 0$ form a geometric series $\eta e^{-i2\pi l} + \eta^2 e^{-i4\pi l} + \cdots$ which can be summed to yield $\eta e^{i2\pi l}/(1 - \eta e^{-i2\pi l})$. Once this amplitude has been added to the standard

expression for the crystal truncation rod scattering amplitude, the scattered intensity can be calculated. For small η, the intensity at the anti-Bragg point is $\sim 1/4 - \eta$, from which it is clear that roughness decreases the intensity in the specular CTR rod.

5.10: The scattering amplitude is: $1/(1 - e^{i2\pi l})$ $+e^{i2\pi l}/2$, and the intensity at the anti-Bragg point is zero. Thus at the anti-Bragg point $l = 0.5$ the intensity will oscillate between 0 and $|F(\mathbf{Q})|^2/4$ during layer-by-layer growth allowing the process to be studied.

6. Diffraction by perfect crystals

6.1: (a) The (400) is the first allowed symmetric Bragg peak; see Section 5.1.7. (b) The key is to use Eq. (6.1). From Table 4.1 the atomic form factor is $f(G_{400})$=7.51. The Debye-Waller factor $DW = \exp(-B_T(\sin\theta/\lambda)^2)$ at room temperature is evaluated by taking $B_T = 0.33$ (Table 5.1) and $\sin\theta/\lambda = G_{400}/4\pi$=0.3683, yielding DW=0.9562. Thus $F = 4(1 + i) f(G_{400})$ DW=57.45, and $g = 2.6 \times 10^{-6}$. (c) The required amplitude reflectivity is 1/10. From Eq. (6.20) this implies that $x + \sqrt{x^2 - 1} = 10$, or $x \approx 5$. The width of total reflection ($\Delta x = 2$) is 26.3×10^{-6} multiplied by $2\sqrt{2}/3$ or 24.8×10^{-6} (Table 6.1). The offset angle is then calculated as 5/2 times 24.8×10^{-6} multiplied by $\tan\theta$.

6.2: $x \le -1$, r is always real and negative and therefore the phase is equal to π or $-\pi$, where in our exposition we have made the latter choice; $|x| \le 1$, the phase is equal to $-$acos $(x/(x^2 + (\sqrt{1 - x^2})^2)^{1/2}) = -$acos$(x)$; $x \ge 1$, r is always real and positive and hence the phase angle is zero.

6.3: Consider Fig. 6.5 and Eq. (6.20) from which it should be clear that the correct factor is obtained from the condition that $(x - \sqrt{x^2 - 1})^2$ $= 1/2$ which has the solution $x= 3/(2\sqrt{2})$.

6.4: g is the amplitude reflectivity per layer. The amplitude reduction at the n'th layer is $\Delta\mathcal{A} = -g\mathcal{A}_n, \Rightarrow \mathcal{A}(n) = \mathcal{A}_0 \exp(-gn)$. After $N = 1/g$ layers the amplitude is reduced by a factor of

1/e. The amplitude extinction depth is therefore $Nd = d/g$. The intensity extinction depth is found from $I(n) = I_0 \exp(-2gn)$ to be $d/(2g)$.

6.5: $\Delta\theta$ [rad]=$(\zeta_D^{total}/2) (|F_0|/|F|) \tan\theta = (g/m\pi)$ $(|F_0|/|F|) \tan\theta = (g_0/m\pi) \tan\theta$ where we have used Eq. (6.28), (6.25) and (6.2), respectively. With $g_0 = m\pi\delta/\sin^2\theta$ we obtain $\Delta\theta$ [rad]=δ $\tan\theta/\sin^2\theta = 2\delta/\sin 2\theta$ as required.

6.6: (a) $\Delta\mathcal{E}/\mathcal{E}= \cot\theta\Delta\theta$. (b) $\theta = 90° \Rightarrow \lambda = 2d =$ 0.5226 Å, or $\mathcal{E}$= 23.72 keV. (c) $\mu^{-1}(23.72$ keV)= 1720 μm, from Eq. (6.33) $\Lambda_{ext} = 174$ μm, which is much less than the absorption length so dynamical diffraction applies. From Eq. (6.26) the relative bandwidth (FWHM) is 5.07×10^{-8} yielding a resolution of $\Delta\mathcal{E}$ =1.2 meV.

6.7: We have from Eq. (6.1) $g \approx 2(a^2/3)r_0/(a^3)$ $4|1 + i|Z =8(\sqrt{2}/3) (r_0/a) Z$ and an extinction depth given by $\Lambda = (a/\sqrt{3})/(2g) = a\sqrt{3/2}$ $(1/16) 1/((r_0/a)Z)$. Hence the extinction depths are estimated to be $\Lambda_C= 0.57$ μm, $\Lambda_{Si}= 0.57$ μm, and $\Lambda_{Ge}= 0.27$ μm, within a factor two of the values obtained from a full calculation.

6.8: The tabulated value of the absorption length at 12.4 keV is $\mu^{-1}= 11$ μm. The absorption depth is $(\mu^{-1}/2) \sin\theta \approx 1$ μm. The extinction length (given in the text) is 8 μm. The scattering is therefore kinematic, because absorption prevents significant multiple scattering, and the integrated intensity is proportional to $|F|^2$.

6.9: $w_{333}/w_{111}= (1/9) (|F_{333}|/|F_{111}|)$ $(\tan\theta_{333}/\tan\theta_{111}) =(1/9) (8/(4\sqrt{2})) (f_{333}/f_{111})$ $(\tan\theta_{333}/\tan\theta_{111})$.

6.10: The asymmetry parameter is $\sin(45°)/\sin(15°) \sim 3$, or its reciprocal, 1/3 . In case (a) the beam incident on the second crystal is spatially extended, so it can only accept a narrow angular range equal to $1/\sqrt{3}$ of the symmetric Darwin width. $I(\theta)$ is therefore the convolution of a top hat, say of height 1 and of width 1 from the first crystal, with a top hat of width $1/\sqrt{3}$ from the second crystal. The convolution is a parallelogram with baseline of $1+1/\sqrt{3}$ and top width of $1-1/\sqrt{3}$. With a height of 1, the integrated intensity (area) is 1. In

case (b) the convolution is also a parallelogram with baseline $\sqrt{3}+1$ and top width of $\sqrt{3}-1$. Requiring the same area means that this parallelogram has a height of $1/\sqrt{3}$.

7. Photoelectron absorption

7.1: Use Eq. (1.19) with $\sigma_a = (\mu/\rho_m)\,(M/N_A)$ from Eq. (1.18).

7.2: From Eq. (7.2), $1/\mu = 50\ \mu$m.

7.3: $1/\mu = 20\ \mu$m, which is shorter than the value at 50 μm due to the presence of the Ga and As K edges at 10.367 and 11.867 keV, respectively.

7.4: 1.7 m.

7.5: In the absence of any absorption edges, the absorption length decreases as the cube of the X-ray energy. The absorption length in air at 1 keV is approximately 1.7 mm.

7.7: The result follows from making the substitution $\kappa = 2/a$ in Eq. (4.9).

7.8: The total elastic scattering from an atom is approximately $Z(8\pi r_0^2/3)$, and equating this to Eq. (7.18) leads to the required result. The absorption and scattering cross-section are estimated to be equal at ~ 1.87 keV, which is much greater than the energy of the K edge, justifying setting the Stobbe correction factor $f(\xi)$ equal to unity.

7.9: 0.02 atm.

7.10: The second neighbour shell is at a distance of $a/\sqrt{2} = 6.48/\sqrt{2} = 4.58$ Å in good accord with the data in Fig. 7.9.

7.11: (a) $\epsilon(Z) = 0.0026Z - 0.23$. (b) $\mathcal{E}_K(\text{Ga}) = 10.367$ keV, $\mathcal{E}_K(\text{Ga}) = 11.868$ keV, both within 1 eV of their tabulated values.

8. Resonant scattering

8.1: Equation (8.13) can be rearranged to read $|f''| = \mathcal{E}[\text{keV}]\,\sigma_a[\text{Å}^2]/\,6.993 \times 10^{-6}$, which when substituted into Eq. (1.18) yields the desired result.

8.2: (a) Conventional bcc unit cell has two atoms with fractional coordinates of (0,0,0) and (1/2,1/2,1/2). Thus $F_{hkl} = f_{av.}\,(1+\exp(i\pi(h+k+l)))$ with $f_{av.} = (f_{Cu} + f_{Zn})/2$. The condition on the Miller indices is that $(h+k+l)$ must be even. (b) $F_{hkl} = (f_{Cu} \pm f_{Zn})$ where the $+$ and $-$ refer to $(h+k+l)$ even, and $(h+k+l)$ odd, respectively. (c) Ratio is approximated as $(30-29)/(30+29) \approx 0.017$.

8.3: (a) We have $\sigma_a = (4\pi r_o/k)\,|f''| = 2 \times 12.398\,r_0\,[\text{Å}]\,|f''|/\,\mathcal{E}\,[\text{keV}]$. For a composite material, $\mu = \sum_j \rho_{at,j}\,\sigma_{a,j} = (\sigma_{Cu,j} + \sigma_{Zn,j})/a^2$. The values of $a\mu$ at the four energies are 9.53, 9.24, 39.7 and 38.5 all multiplied by 10^{-6}. (b) $|F_{100}|^2$: 6.95, 57.3, 68.4, 16.7; from Eq. (5.31), I_{sc}/I_0: 7.58, 62.0, 17.5, 4.29 all multiplied by 10^{-6}. (c) 100 eV below the edge elastic scattering only and photons of 8878.9 keV will be observed. 100 eV above the edge in addition to the elastic scattering there is also fluorescence at $K_\alpha = 8.048$ keV and $K_\beta = 8.910$ keV with an intensity ratio of about 10 to 1.

8.4: (a) The beam divergence of the scattered beam is 2 mrad, and fills the detector aperture when the detector is placed a distance of $L = 500$ mm from the sample. (b) $\Delta\Omega = \pi r^2/L^2 = 3.14 \times 10^{-6}$. (c) From 8.3(b), $I_{sc}/I_0 = 4.29 \times 10^{-6}$. All incoming photons will be absorbed in the thick sample in symmetric Bragg reflection geometry. 30% will be re-emitted as fluorescence, and the fraction $\Delta\Omega/4\pi$ will reach the detector. Thus $I_f/I_0 \approx 0.075 \times 10^{-6}$, and the ratio of scattering to fluorescence is $\sim$66.

8.5: The two possibilities are $F_{111} = f_{Zn} + f_S\,e^{2\pi(1+1+1)/4}$ or $F_{\bar{1}\bar{1}\bar{1}} = f_S + f_{Zn}\,e^{2\pi(1+1+1)/4}$. Inserting $f_{Zn} = f'_{Zn} + if''_{Zn}$, etc., and rearranging leads to the desired result.

8.6: The result follows directly from the answer to Exercise 8.5.

8.8: The calculated ratios are 1.58, 1, and 0.51, in good agreement with the measured ratios.

9. Imaging

9.1: $C = 1 - e^{-(\mu_2 - \mu_1)z_2}$ if $\mu_1 < \mu_2$, and $C = 1 - e^{(\mu_2 - \mu_1)z_2}$ if $\mu_1 > \mu_2$.

9.2: $C = 0.98, 0.64, 0.32, 0.24$, ordered in terms of increasing photon energy.

9.3: Taking the over all thickness of the chest to be 30 cm, with two chest walls each of 2.5 cm, and the rib bones to have a thickness of 1 cm each, $C_{ribs} = 0.64$, $C_{tumour} = 0.30$.

9.4: (a) 267, 385 and 526 eV for C, N and O, respectively. (b) 0.52 and 7.4 μm for protein and water, respectively.

9.6: The wedge angle is determined by $\tan \omega = \sqrt{2}$, so the wedge thickness is $y = \sqrt{2}x$, with x denoting denoting the beam position. The transmission $T(x) = \exp(-y/y_0)$ with $y_0 = 184$ μm. The refracted angle is $\alpha = \delta \tan \omega = \lambda^2 [\rho r_0/(2\pi)] \sqrt{2} = 5.5 \times 10^{-6}$ radians.

9.7: The maximal intensity $< y >$ is the overlap integral of the triangular pattern with the Gaussian centred at a triangle peak position. When $(\sigma/p) \ll 1$ the overlap with neighbouring triangles can be neglected, and one finds $< y > = (\sqrt{2\pi}\sigma)^{-1} \int_{-\infty}^{\infty} \exp(-x^2/(2\sigma^2)) T(x) \, dx$ with the triangular function given by $T(x) = 1 - (2/p)x$ when $|x| < p/2$ or 0 otherwise. The integral is readily evaluated to obtain the desired result.

9.8: For a crystal of around $(500)^3$ unit cells, the integrated intensity can be calculated from Eq. (5.30), yielding ~ 300 counts per second. If we assume a detection limit of around 1 count per second, then we can estimate by considering the properties of $|\sin(x)/x|^2$ that around $4 - 5$ fringes should be visible.

9.9: From $D = 4M\Delta r_M$ one finds the number of zones $M = 500$. The outer zone width Δr_M is related to λ and f by $2\sqrt{M} \Delta r_M = \sqrt{\lambda f}$. The wavelength is determined by which depth of the zones, t, provides a phase shift of π, i.e. $t\delta k = \pi$ or $\lambda = \pi /(t\rho r_0)$. The electron density in Au is the number of electrons in the cubic fcc unit cell, $4Z$, divided by its volume, or 4.687 el. per $\mathring{A}^3$, yielding $\lambda = 2.38$ $\mathring{A}$. The focal length is equal to 21 mm. The depth of focus is approximately the resolution $1.22 \Delta r_M$ divided by the aperture angle D/f, or 12.8 μm.

Bibliography

S.K. Andersen, J.A. Golovchenko, and G. Mair. *Phys. Rev. Lett.*, 37:1141, 1976.

S.R. Andrews and R.A. Cowley. *J. Phys. C: Solid State Phys.*, 18:6247, 1985.

T. Andrews. *Phil. Transact. Roy. Soc. (London)*, 159:575, 1869.

S. Aoki, Y. Ichihara, and S. Kikuta. *Japan. J. Appl. Phys.*, 11:1857, 1972.

B.W. Batterman. *Phys. Rev.*, 133:A759, 1964.

M. Bech, O. Bunk, C. David, R. Ruth, J. Rifkin, R. Loewen, R. Feidenhans'l, and F. Pfeiffer. *J. Synch. Rad.*, 16:43, 2008.

A.S. Bhalla and E.W. White. *Acta Cryst.*, B27:852, 1971.

J.M. Bijvoet, A.F. Peerdeman, and J.A. van Bommel. *Nature*, 168:271, 1951.

M. Blume. *J. Appl. Phys.*, 57:3615, 1985.

P. Carra, B.T. Thole, M. Altarelli, and X. Wang. *Phys. Rev. Lett.*, 70:694, 1993.

C.T. Chantler. *J. Phys. Chem. Ref. Data*, 24:71, 1995.

W. Chao, B.D. Harteneck, J.A. Liddle, E.H. Anderson, and D.T. Attwood. *Nature*, 435:1210, 2005.

C.T. Chen, Y.U. Idzerda, H.-J. Lin, N.V. Smith, G. Meigs, E. Chaban, G.H. Ho, E. Pellegrin, and F. Sette. *Phys. Rev. Lett.*, 75:152, 1995.

W. Cochran, F.H.C. Crick, and V. Vand. *Acta Cryst.*, 5:581, 1952.

D. Coster, K.S. Knol, and J.A. Prins. *Z. Phys.*, 63:345, 1930.

R.A. Cowley. *Nato ASI series C Mathematical and Physical Sciences*, 432:67, 1994.

A. Damascelli, Z. Hussain, and Z.-X. Shen. *Rev. Mod. Phys.*, 75:473, 2003.

C. David, B. Nöhammer, and H. H. Solak. *Appl. Phys. Lett.*, 81:3287, 2002.

F. de Bergevin and M Brunel. *Phys. Lett.*, 39A:141, 1972.

P. Debye. *Ann. Physik*, 46:809, 1915.

Ya. S. Derbenev, A.M. Kondratenko, and E.L. Saldin. *Nuc. Instr. and Meth.*, A193:415, 1982.

H. Dosch. *Critical Phenomena at Surfaces and Interfaces: Evanescent x-ray and neutron.* Springer Tracts in Modern Physics 126, 1992.

A. Einstein. *Annalen der Physik*, 33:1275, 1910.

S. Eisebitt, J. Lüning, W.F. Schlotter, M. Lörgen, O. Hellwig, W. Eberhardt, and J. Stöhr. *Nature*, 432: 885, 2004.

P. Emma. *Proc. of the Part. Accel. Conf.*, In press, 2009.

J.L. Erskine and E.A. Stern. *Phys. Rev. B*, 12:5016, 1975.

K. Evans-Lutterodt, J.M. Ablett, A. Stein, C.C. Kao, D.M.Tennant, F. Klemens, A. Taylor, C. Jacobsen, P.L. Gammel, H. Huggins, S. Ustin, G. Bogart, and L. Ocola. *Optics Express*, 11:919, 2003.

R. Feidenhans'l, F. Grey, R.L. Johnson, S.G.J. Mochrie, J. Bohr, and M. Nielsen. *Phys. Rev. B*, 41: 5420, 1990.

J.R. Fienup. *Applied Optics*, 21:2758, 1982.

F.C. Frank. *Proc. R. Soc. London*, A215:43, 1952.

R.E. Franklin and R.G. Gosling. *Nature*, 171:740, 1953.

D. Gibbs, D.R. Harshman, E.D. Isaacs, D.B. McWhan, D. Mills, and C. Vettier. *Phys. Rev. Lett.*, 61: 1241, 1988.

W.A. Hendrickson. *Trans. Am. Crystallogr. Assoc.*, 21:11, 1985.

B.L. Henke, E.M. Gullikson, and J.C. Davis. *Atomic Data and Nuclear Data Tables*, 54:181, 1993.

M. Hoesch, X. Cui, K. Shimada, C. Battaglia, S. Fujimori, and H. Berger. *Phys. Rev. B*, 80:075423, 2009.

M. Holt, Z. Wu, H. Hong, P. Zschack, P. Jemian, J. Tischler, H. Chen, and T.-C. Chiang. *Phys. Rev. Lett.*, 83:3317, 1999.

Z. Huang and R.D. Ruth. *Phys. Rev. Lett.*, 80:976, 1998.

S. Hüfner. *Photoelectron Spectroscopy*. Springer-Verlag, Berlin, 1995.

C. Janot. *Quasicrystals: a Primer*. Oxford University Press, 1992.

J. Karle. *International Journal of Quantum Chemisry, Quantum Biology Symposium*, 7:357, 1980.

H. Kiessig. *Ann. Phys.*, 10:769, 1931.

P. Kirkpatrick and A. Baez. *J. Optic. Soc. America*, 38, 1948.

M. Kotlarchyk and S.H. Chen. *J. Chem. Phys.*, 79:2461, 1983.

G.W. Lee, A.K. Gangopadhyay, K.F. Kelton, R.W. Hyers, T.J. Rathz, J. R. Rogers, and D. S. Robinson. *Phys. Rev. Lett.*, 93:037802, 2004.

B. Lengeler, C.G. Schroer, M. Kuhlmann, B. Benner, T.F. Günzler, O. Kurapova, F. Zontone, A. Snigirev, and I. Snigireva. *J. Phys. D: Applied Physics*, 38:A212, 2005.

F. Leveiller, C. Böhm, D. Jacquemain, H. Möhwald, L. Leiserowitz, K. Kjaer, and J. Als-Nielsen. *Langmuir*, 10:819, 1994.

S.W. Lovesey and S.P. Collins. *X-ray Scattering and Absorption by Magnetic Materials*. Oxford University Press, 1996.

I. McNulty, J. Kirz, C. Jacobsen, E.H. Anderson, M.R. Howells, and D.P. Kern. *Science*, 256:1009, 1992.

J. Miao, D. Sayre, and H.N. Chapman. *J. Opt. Soc. Am. A*, 15:1662, 1998.

J. Miao, P. Charalambous, J. Kirz, and D. Sayre. *Nature*, 400:342, 1999.

A. Momose, S. Kawamoto, I. Koyama, K. Takai Y. Hamaishi, and Y. Suzuki. *Jpn. J. Appl. Phys.*, 42:L866, 2003.

J.B. Murphy and C. Pellegrini. *J. Opt. Soc. of America*, B2:259, 1985.

K. Namikawa, M. Ando, T. Nakajima, and H. Kawata. *J. Phys. Soc. Japan*, 54:4099, 1985.

L. Névot and P. Croce. *Rev. Phys. Appl.*, 15:761, 1980.

S. Nishikawa and R. Matsukawa. *Proc. Imp. Acad. Japan*, 4:96, 1928.

B. Ocko, A. Braslau, P. S. Pershan, J. Als-Nielsen, and M. Deutsch. *Phys. Rev. Lett.*, 57:94, 1986.

L.G. Parratt. *Phys. Rev.*, 95:359, 1954.

L. Pauling, R.B. Corey, and H.R. Branson. *Proc. Nat. Acad. Sci.*, 37:205, 1951.

J.S. Pedersen. *Neutrons, X-rays and Light*, chapter on Modelling of Small-Angle Scattering Data from Colloids and Polymer Systems, page 391. Elsevier Science B.V., 2002.

P. Pershan, A. Braslau, A. H. Weiss, and J. Als-Nielsen. *Phys. Rev. A*, 35:4800, 1987.

F. Pfeiffer, T. Weitkamp, O. Bunk, and C. David. *Nature Physics*, 2:268, 2006.

T. Pilo. *Fermi Surface and Phase Transitions of Layered Materials Studied by Angle-Scanned Photoemission*. University of Fribourg, 1999.

H. Reichert, O. Klein, H. Dosch, M. Denk, V. Honkimåki, T. Lippmann, and G. Reiter. *Nature*, 408:839, 2000.

H. M. Rietveld. *J. Appl. Cryst.*, 2:65, 1969.

I.K. Robinson. *Phys. Rev. B*, 33:3830, 1986.

I.K. Robinson, I.A. Vartanyants, G.J. Williams, M.A. Pfeifer, and J.A. Pitney. *Phys. Rev. Lett.*, 87, 2001.

J. Rockengerger, L. Tröger, A.L Rogach, M. Tischer, M. Grundmann, A. Eychmüller, and H. Weller. *J. Chem. Phys.*, 108:7807, 1998.

A.L. Rogach, L. Katsikas, A. Kornowski, Dansheng Su, A. Eychmüller, and H. Weller. *Ber. Bunsenges. Phys. Chem.*, 100:1772, 1996.

D. Sayre. *Acta Cryst.*, 5:843, 1952.

D. Sayre. *Imaging Processes and Coheremce in Physics*, chapter on Prospects for Long-Wavelength X-ray Miscroscopy and Diffraction, page 229. Springer-Verlag, Berlin, 1980.

G. Schütz, W. Wagner, W. Wilhelm, P. Kienle, R. Zeller, R. Frahm, and G. Materlik. *Phys. Rev. Lett.*, 58:737, 1987.

C.E. Shannon. *Proc. Inst. Radio Engrs.*, 37:10, 1949.

D. Shechtman, I. Blech, D. Gratias, and J.W. Cahn. *Phys. Rev. Lett.*, 53:1951, 1984.

S.K. Sinha, E.B. Sirota, S. Garoff, and H.B. Stanley. *Phys. Rev. B*, 38:2297, 1988.

A. Snigirev, V. Kohn, I. Snigireva, and B. Lengeler. *Nature*, 384:49, 1996.

E.A. Stern. *Scientific American*, 234(4):96, 1976.

E.A. Stern and S.M. Heald. *Handbook on Synchrotron radiation*, chapter on Basic Principles and Applications of EXAFS, pages 995–1014. North Holland, 1983.

M. Stobbe. *Ann. d. Phys.*, 7:661, 1930.

D.H. Templeton and L.K. Templeton. *Acta Cryst*, A38:62, 1982.

B.T. Thole, G. van der Laan, and G.A. Sawatzky. *Phys. Rev. Lett.*, 55:2086, 1985.

B.T. Thole, P. Carra, F. Sette, and G. van der Laan. *Phys. Rev. Lett.*, 68:1943, 1992.

G. van der Laan, B.T. Thole, , G.A. Sawatzky, J.B. Goedkoop, J.C. Fuggle, J.-M. Esteva, R. Karnatak, J.P. Remeika, and H.A. Dabkowska. *Phys. Rev. B*, 34:6529, 1986.

J.D. Watson and F.H.C. Crick. *Nature*, 171:737, 1953.

T. M. Weiss, T. Narayanan, C. Wolf, M. Gradzielski, P. Panine, S. Finet, and W.I. Helsby. *Phys. Rev. Lett.*, 94:038303, 2005.

T. Weitkamp. *Proc. SPIE*, 5536:181, 2004.

T. Weitkamp, B. Nöhammer, A. Diaz, C. David, and E. Ziegler. *Appl. Phys. Lett.*, 86:054101, 2005.

T. Weitkamp, C. David, C. Kottler, O. Bunk, and F. Pfeiffer. *Proc. SPIE*, 6318:63180S, 2006.

M.H.F. Wilkins, A.R. Stokes, and H.R. Wilson. *Nature*, 171:738, 1953.

P. Wong. *Phys. Rev. B*, 32:7417, 1985.

T. Yokoya, T. Kiss, A. Chainani, S. Shin, and K. Yamaya. *Phys. Rev. B*, 71:140504(R), 2005.

Index

List of symbols

α	fine structure constant
α_c	critical angle
β	imaginary part of deviation of refractive index from unity
β_e	electron velocity in units of c
δ	real part of deviation of refractive index from unity
$\Delta\Omega$	element of solid angle
$\hat{\varepsilon}$	polarization unit vector of X-ray electric field
ϵ_0	permittivity of free space
γ	ratio of electron energy in storage ring to rest mass energy, $\dfrac{\mathcal{E}_e}{mc^2}$
γ^{-1}	opening angle of synchrotron radiation cone
$\hbar$	Planck's constant
λ	wavelength of X-ray
λ_1	fundamental wavelength of undulator radiation
λ_u	undulator spatial period
λ_C	Compton scattering length
Λ_{ext}	extinction depth
μ	linear absorption coefficient for intensity
μ_0	permeability of free space

ω	angular frequency
ω_o	orbital angular frequency of electron in a synchrotron
$\omega_u t'$	emitter phase
$\omega_1 t$	observer phase
Φ_0	incident photon flux (photons/s/unit area)
ρ	electron number density
ρ_{at}	atomic number density
ρ_m	atomic mass density
$\rho(\mathcal{E})$	density of states
σ_a	absorption cross-section
θ	Bragg angle
ζ_D	Darwin width, relative bandwidth
$a(a^\dagger)$	annihilation (creation) operator
a_0	Bohr radius
A	atomic mass number
$\mathbf{A}$	vector potential of photon field
b	scattering length
b	asymmetry parameter
B_T	Debye-Waller factor
c	speed of light
d	lattice plane spacing
$-e$	electronic charge
$\mathcal{E}$	photon energy
$\mathcal{E}_e$	electron energy
$\mathbf{E}$	electric field
E_0	magnitude of electric field
$f(\mathbf{Q})$	atomic form factor (scattering factor)
$f^0(\mathbf{Q})$	non-resonant atomic scattering factor
f'	real part of atomic dispersion correction

f''	imaginary part of atomic dispersion correction
$F(\mathbf{Q})$	unit cell structure factor
$F^{\mathrm{CTR}}(\mathbf{Q})$	crystal truncation rod structure factor
$F^{\mathrm{mol}}(\mathbf{Q})$	molecular structure factor
$\mathbf{G}$	reciprocal lattice vector
h, k, l	Miller indices
$\mathbf{H}$	magnetic field
$\mathcal{H}_I$	interaction Hamiltonian
$\mathcal{H}_{\mathrm{rad}}$	Hamiltonian of radiation field
I_0	incident photon intensity (photons/s)
I_{sc}	scattered photon intensity (photons/s)
$\mathbf{k}$	wavevector of X-ray
K	undulator parameter
m	mass of electron
m_n	mass of neutron
m_{hkl}	multiplicity of Bragg reflection
M_{if}	matrix element between initial i and final f states
n	refractive index
N_{A}	Avogadro's number
P	polarization factor
$\mathcal{P}$	principal value
$\mathbf{p}$	momentum of electron
$\mathbf{q}$	wavevector of photoelectron
$\mathbf{Q}$	wavevector transfer (scattering vector)
r_0	Thomson scattering length (classical electron radius)
$\mathbf{R_n}$	lattice vector
$\mathbf{v}$	velocity of electron
v_c	volume of unit cell
w_{D}	Darwin width, angular
Z	atomic number

e	electron charge	1.602×10^{-19}	C
$\hbar = \dfrac{h}{2\pi}$	Planck's constant	1.055×10^{-34}	J s
m	electron mass	9.109×10^{-31}	kg
m_n	neutron mass	1.675×10^{-27}	kg
m_p	proton mass	1.673×10^{-27}	kg
c	speed of light	2.998×10^{8}	m s^{-1}
ϵ_0	permittivity of vacuum	8.854×10^{-12}	A s V^{-1} m^{-1}
$\mu_0 = \dfrac{1}{\epsilon_0 c^2}$	permeability of vacuum	$4\pi\times10^{-7}$	V s A^{-1} m^{-1}
N_A	Avogadro's number	6.022×10^{26}	mols. kmole^{-1}
k_B	Boltzmann's constant	1.381×10^{-23}	J K^{-1}
$a_0 = \dfrac{4\pi\epsilon_0\hbar^2}{me^2}$	Bohr radius	5.292×10^{-11}	m
$r_0 = \dfrac{e^2}{4\pi\epsilon_0 mc^2}$	Thomson scattering length	2.818×10^{-15}	m
$\lambda_C = \dfrac{\hbar}{mc}$	Compton scattering length	3.860×10^{-13}	m
1 Å	Ångström	1×10^{-10}	m
1 barn		1×10^{-28}	m^2